Berlin shows how biodiversity can flourish in cities p. 466

Neutrinos from an active galaxy pp. 474 & 538

Eppendorf & *Science* Prize for neural underpinnings of aggression p. 484

Science

$15
4 NOVEMBER 2022
SPECIAL ISSUE
science.org
AAAS



BRAIN CONNECTIVITY





SCIENCE FOR HUMANITY

AAAS | ANNUAL MEETING

The 2023 AAAS Annual Meeting will convene in-person in Washington, D.C. for the first time in two years. Virtual access to the meeting will be available as well.

Register today and join us March 2-5, 2023!

aaas.org/meetings | #AAASmtg

BE A PART OF THE CONVERSATION

- Diversity, Equity and Inclusion
- Research Funding and Infrastructure
- Science Communication
- Artificial Intelligence
- STEM Education
- Information Technology and Security
- International S&T Collaboration
- Science and Values
- Social and Behavioral Sciences
- Global and Public Health
- Science Policy
- Climate Change

and more...





science.org/journal/sciimmunol



READY TO PUT THE SPOTLIGHT ON YOUR RESEARCH?

Submit your research:
cts.ScienceMag.org

Science Immunology
AAAS

Twitter: @SciImmunology
Facebook: @ScienceImmunology





(**Left**) Junsuk Rho, (**Far right**) Soojin Park

The transformation of theory into practice

For researchers working in the applied sciences, the Pohang University of Science and Technology in South Korea, commonly called POSTECH, acts as an academic springboard for bringing ideas to life. After opening its doors in 1986, the university quickly established a reputation for excellence and was rated third in the Times Higher Education*'s World's Best Small University Rankings from 2019 to 2021.*

Junsuk Rho completed his Ph.D. in the United States at the University of California, Berkeley, in 2013. Now chair professor of mechanical and chemical engineering at POSTECH, he explains why he decided to continue his career researching metamaterials in South Korea.

"Everything at POSTECH, from the school's policies to the layout of the campus, is designed to improve the research atmosphere," he says.

Attracted by the university's highly collaborative and interdisciplinary research ethic, which includes partnerships with Germany's Max Planck Society for the Advancement of Science (*1*), Rho leads a world-class team that has made considerable advances in metamaterials, from developing optical materials for ultracompact, high-resolution 3D holography and ultrathin optical lenses and extended reality (XR) devices, to pushing the boundaries of fabrication techniques.

For example, in 2018, Rho's team created optically active, chiral gold nanoparticles using amino acids and peptides. The nanoparticles change color according to the degree of light polarization (*2*).

"The potential applications include active color displays, holography, biochemical sensors, and all-angle negative refractive index materials," says Rho.

Out of the lab, into the market

Currently, Rho is focused on bringing the potential of metamaterials to the mass market.

POSTECH was founded and funded by the Pohang Steel Company (POSCO), one of the world's leading steel-making companies, with a view to supporting cutting-edge scientific and technological research. In 2021, POSCO awarded Rho's lab USD 10 million to support a 10-year project to pilot a line of metamaterials that have the potential for mass production.

"This is the first time in Korea that a company has invested such a large sum of money in a single lab," says Rho.

At the same time, the Research Institute of Industrial Science and Technology (RIST), also located on the POSTECH campus, has invested USD 2 million in a high-speed electron-beam lithography system that will further support the translation of Rho's work.

"We're competing with other leading groups from places such as Harvard and Stanford, but with our high levels of funding, strong research environment, and excellent students, we are confident that we are one of the main hubs for metamaterials research," he says.

Current metamaterials that work at visible wavelengths are very expensive to make using conventional nanofabrication techniques. One of Rho's biggest challenges is to develop an economically viable way to mass produce metamaterials on a large scale. His recent success has come in the form of new techniques for fabricating nanostructures, such as a controllable lithographic method for making single-nanometer sharp bowtie nanoantennas inspired by the

PHOTOS: PROVIDED BY POSTECH

toppling of dominos (*3*), as well as single-step production of metasurfaces using a nanoparticle-embedded resin (*4*). "The former allows for the extreme confinement of light, while the latter provides a method of repeatedly printing metasurfaces at will with a single master stamp," he explains.

"This opens up the possibility for the mass production of metasurfaces, especially if such techniques can be combined with other printing methods such as roll-to-roll printing," he says.

Battery-powered future

Chair professor Soojin Park leads the Energy Materials Laboratory at POSTECH (*5*). His research focuses on battery materials and systems. For Park, the opportunities afforded by developing safer, longer-life batteries are both scientifically exciting and socially vital for a sustainable future. Park believes that battery research is key to fulfilling the energy gap that will necessarily need to be filled as the world weans itself off fossil fuels. He is also keen to explore the role battery materials can play in revolutionizing health care, as we develop devices that can monitor our physical states in real time.

Currently, rechargeable lithium-ion batteries are widely used in our daily lives, for example, in powering electric cars. However, these battery systems have drawbacks, such as being inherently flammable and having slow charging times. These batteries are not currently powerful, safe, or flexible enough to enable society to switch to battery power, he explains.

"We need to develop battery materials that can last a long time on a single charge for electric vehicles; safe and flexible power sources for electronic devices that can be attached to the skin; and light, powerful batteries that can power drones and small airplanes," he says.

Battery breakthroughs

Right now, Park's research group is conducting joint research with South Korean battery material makers and battery cell manufacturers, such as LG Energy Solution, Samsung SDI, the Hyundai Motor Company, and POSCO. His team is jointly developing battery anode materials, functional separator membranes, and functional polymeric binders for electric vehicles. Each of these materials is intended to meet the needs of future batteries, with an emphasis on fast charging capabilities, high output, high energy density, and high stability.

Park also expects his work to expand into developing energy-dense, flexible batteries that can be combined with flexible devices. Recently, his team successfully developed high-capacity silicon anode materials that realize 10 times more capacity than conventional graphite, which is the current commercialized anode material for batteries. His research group has also developed a flexible battery with high energy density that can be crumpled like paper (*6*). Furthermore, Park's group has developed a stretchable battery that can be operated while being stretched by more than 50% (*7*).

Charged with challenges

For battery materials to be commercialized, numerous scientific obstacles must be overcome, says Park.

"We're wrestling with fundamental questions: Whether low-cost, mass-production is possible. Whether we can develop batteries with a longer charged life. And whether we can genuinely make them completely safe," he says.

Silicon is a promising anode material for high-capacity batteries that can realize 10 times the capacity per weight compared to graphite, he explains. However, its capacity degrades during the charging and discharging process.

"In order for the characteristics of materials being developed at the laboratory level to match the level desired by battery cell manufacturers, many problems must be addressed," he says. "Active joint research is necessary to narrow the distance between the laboratory level and the battery makers."

To bridge the gap between research and manufacturing, POSTECH has built a dry room to manufacture and evaluate large battery cells. Additionally, the university has made the development of next-generation battery materials and systems a research priority and is in the process of building up its talent base by hiring experts in anode and cathode materials, battery systems, electrolytes, and advanced analysis.

Hub for real-life breakthroughs

POSTECH's campus offers researchers the opportunity to share their passion for futuristic technologies with a wide community of like minds and to benefit from a highly ambitious research infrastructure. "Consistently strong levels of funding, the development of centers for joint research with manufacturers, and a focus on growing our research talent base are laying the foundation for the university to become a key hub for next-generation research," says Park.

References

1. "Max Planck to Set Up Two Centres in South Korea" (2010); available at https://sciencebusiness.net/news/68020/Max-Planck-to-set-up-two-centres-in-South-Korea.
2. H.-E. Lee *et al.*, *Nature* **556**, 360–365 (2018), https://www.nature.com/articles/s41586-018-0034-1.
3. I. Kim *et al.*, *Mater. Today* **39**, 89–97 (2020), https://doi.org/10.1016/j.mattod.2020.06.002.
4. G. Yoon, K. Kim, D. Huh, H. Lee, J. Rho, *Nat. Commun.* **11**, 2268 (2020), https://www.nature.com/articles/s41467-020-16136-5.
5. "Spark Lab. Polymer Based Energy Materials Laboratory" (2019), https://www.spark-postech.com.
6. C. Hwang *et al.*, *Adv. Mater.* **30**, 1705445 (2018), https://onlinelibrary.wiley.com/doi/abs/10.1002/adma.201705445.
7. W.-J. Song *et al.*, *Adv. Energy Mater.* **8**, 1702478 (2018), https://onlinelibrary.wiley.com/doi/abs/10.1002/aenm.201702478.

Sponsored by

POSTECH
POHANG UNIVERSITY OF SCIENCE AND TECHNOLOGY

CONTENTS

4 NOVEMBER 2022 • VOLUME 378 • ISSUE 6619



Wild boars have adapted to living in Berlin. 466

NEWS

IN BRIEF

456 News at a glance

IN DEPTH

458 **Should Webb telescope's data be open to all?**
NASA plans to end policy of giving some observers 1 year's exclusive access to data *By D. Clery*

459 **Teeth record pneumonia—and racism**
Research raises standards for working with anthropological collections *By R. Pérez Ortega*

461 **A cleaner way to mine clean-energy mainstays**
An electric field can reduce the need for polluting chemicals to extract rare earth elements *By D. Normile*

462 **Prominent astronomer barred after complaints**
Tim de Zeeuw had a pattern of "extremely unacceptable" behavior, Leiden University says *By C. O'Grady*

463 **NSF to end cost-sharing requirement for some grants**
Instrumentation and teacher training programs will no longer ask institutions to provide matching funds *By J. Mervis*

464 **After Lula's win, 'a huge relief!'**
Many in Brazil's scientific community abhorred Jair Bolsonaro. But his successor faces major challenges *By S. Moutinho*

FEATURES

466 **Urban oasis**
In Berlin, pioneering research into urban ecology has found surprising biodiversity in the city's green spaces
By G. Popkin
PODCAST

INSIGHTS

PERSPECTIVES

470 **Arctic wildfires at a warming threshold**
Bigger wildfires in the Siberian Arctic signal release of more carbon to the atmosphere
By E. Post and M. C. Mack
RESEARCH ARTICLE p. 532

471 **Gene therapy for epilepsy**
On-demand inhibition of neuronal activity reduced spontaneous seizures in mice
By K. Staley
RESEARCH ARTICLE p. 523

473 **An optical interface for quantum networks**
A silicon atom embedded in diamond can be entangled with a photon *By D. Gangloff*
REPORT p. 557

474 **Neutrinos unveil hidden galactic activities**
An obscured supermassive black hole may be producing high-energy cosmic neutrinos *By K. Murase*
RESEARCH ARTICLE p. 538

475 **Molecular diversity of astrocytes**
The tissue environment influences astrocyte form and function in health and disease
By K. T. Baldwin
BRAIN CONNECTIVITY SECTION p. 486; RESEARCH ARTICLE p. 514

POLICY FORUM

477 **Protect global values of the Southern Ocean ecosystem**
Climate change and fishing present dual threats *By C. M. Brooks* et al.

BOOKS *ET AL.*

480 **Where telemedicine always falls short**
Efforts to innovate our way to better health consistently fail to deliver on equity promises
By V. Rampton

481 **Reifying racism in medicine**
False beliefs about racial differences have a long history in physician training programs *By S. Seth*

LETTERS

482 **Pakistan's floods flow from climate injustice**
By M. A. Waqas

482 **Restore Pakistan's forest to prevent floods**
By A. Ali

483 **Predicting Pakistan's next flood**
By Y. Yao and Z. A. Khan

PHOTO: GREGOR FISCHER/PICTURE ALLIANCE/GETTY IMAGES

PRIZE ESSAY

484 Boiling over
An emergent encoding of aggressive motivation in neurons of the hypothalamus
By A. Kennedy

RESEARCH

IN BRIEF

511 From *Science* and other journals

RESEARCH ARTICLES

514 Cellular neuroscience
Molecular basis of astrocyte diversity and morphology across the CNS in health and disease *F. Endo* et al.
RESEARCH ARTICLE SUMMARY; FOR FULL TEXT: DOI.ORG/10.1126/SCIENCE.ADC9020
PERSPECTIVE p. 475; BRAIN CONNECTIVITY SECTION p. 486

515 Neuroscience
Dual-polarity voltage imaging of the concurrent dynamics of multiple neuron types
M. Kannan et al.
RESEARCH ARTICLE SUMMARY; FOR FULL TEXT: DOI.ORG/10.1126/SCIENCE.ABM8797

516 Synthetic biology
Refactored genetic codes enable bidirectional genetic isolation *J. F. Zürcher* et al.

523 Neuroscience
On-demand cell-autonomous gene therapy for brain circuit disorders *Y. Qiu* et al.
PERSPECTIVE p. 471; PODCAST

532 Arctic wildfires
Unprecedented fire activity above the Arctic Circle linked to rising temperatures
A. Descals et al.
PERSPECTIVE p. 470

538 Neutrino astrophysics
Evidence for neutrino emission from the nearby active galaxy NGC 1068
IceCube Collaboration
PERSPECTIVE p. 474

543 Plant science
The control of carpel determinacy pathway leads to sex determination in cucurbits *S. Zhang* et al.

REPORTS

549 Structural biology
Molecular glue CELMoD compounds are regulators of cereblon conformation
E. R. Watson et al.

554 Volcanic plumes
The January 2022 eruption of Hunga Tonga-Hunga Ha'apai volcano reached the mesosphere *S. R. Proud* et al.

557 Quantum technology
Robust multi-qubit quantum network node with integrated error detection
P.-J. Stas et al.
PERSPECTIVE p. 473

560 Monkeypox
Multiple lineages of monkeypox virus detected in the United States, 2021–2022
C. M. Gigante et al.

DEPARTMENTS

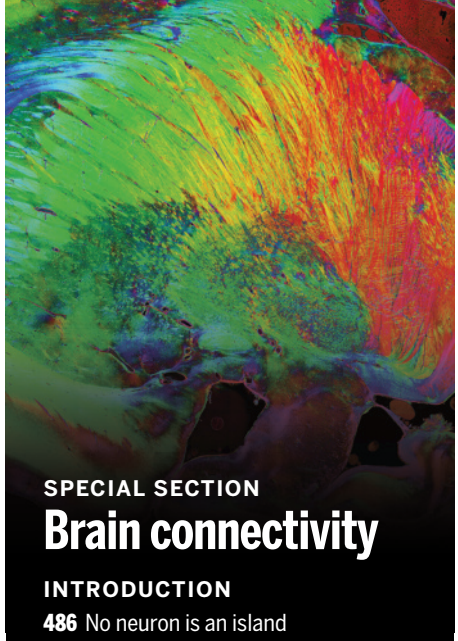
455 Editorial
Measuring emissions to manage emissions *By A. Gore*

570 Working Life
Our labor isn't free *By I. Bennett*

Science Staff 452
Science Careers 566



CREDITS (LEFT TO RIGHT): IMAGE: NASA/JPL-CALTECH; IMAGE: MARKUS AXER AND KATRIN AMUNTS/INM-1; FORSCHUNGSZENTRUM JÜLICH AND ROXANA KOOIJMANS/NETHERLANDS INSTITUTE FOR NEUROSCIENCE/HUMAN BRAIN PROJECT



SPECIAL SECTION

Brain connectivity

INTRODUCTION

486 No neuron is an island

REVIEWS

488 Atlas-based data integration for mapping the connections and architecture of the brain
T. B. Leergaard and J. G. Bjaalie

493 Solving brain circuit function and dysfunction with computational modeling and optogenetic fMRI
J. H. Lee et al.

500 Scale matters: The nested human connectome
M. Axer and K. Amunts

505 The emergent properties of the connected brain
M. Thiebaut de Schotten and S. J. Forkel

ON THE COVER

The human brain's primary interhemispheric connections have different axonal calibers. This image, from the middle of the brain, represents a cross section of the axons, with warmer colors (yellow) indicating thicker axons. These finely attuned connections allow for the perfect orchestration of the brain's symphony. See the special section beginning on page 486. *Image: Michel Thiebaut de Schotten, Stephanie Forkel/Neurofunctional Imaging Group, CNRS, CEA University of Bordeaux, France*



SEE ALSO PERSPECTIVE p. 475; RESEARCH ARTICLE p. 514

SCIENCE (ISSN 0036-8075) is published weekly on Friday, except last week in December, by the American Association for the Advancement of Science, 1200 New York Avenue, NW, Washington, DC 20005. Periodicals mail postage (publication No. 484460) paid at Washington, DC, and additional mailing offices. Copyright © 2022 by the American Association for the Advancement of Science. The title SCIENCE is a registered trademark of the AAAS. Domestic individual membership, including subscription (12 months): $165 ($74 allocated to subscription). Domestic institutional subscription (51 issues): $2212; Foreign postage extra: Air assist delivery: $98. First class, airmail, student, and emeritus rates on request. Canadian rates with GST available upon request, GST #125488122. Publications Mail Agreement Number 1069624. **Printed in the U.S.A.**
Change of address: Allow 4 weeks, giving old and new addresses and 8-digit account number. **Postmaster:** Send change of address to AAAS, P.O. Box 96178, Washington, DC 20090–6178. **Single-copy sales:** $15 each plus shipping and handling available from backissues.science.org; bulk rate on request. **Authorization to reproduce** material for internal or personal use under circumstances not falling within the fair use provisions of the Copyright Act can be obtained through the Copyright Clearance Center (CCC), www.copyright.com. The identification code for *Science* is 0036-8075. *Science* is indexed in the *Reader's Guide to Periodical Literature* and in several specialized indexes.

Science AAAS

Editor-in-Chief Holden Thorp, hthorp@aaas.org

Executive Editor Valda Vinson

Editor, Research Jake S. Yeston **Editor, Insights** Lisa D. Chong **Managing Editor** Lauren Kmec

DEPUTY EDITORS Gemma Alderton (UK),Stella M. Hurtley (UK), Phillip D. Szuromi, Sacha Vignieri **SR. EDITORS** Caroline Ash (UK), Michael A. Funk, Brent Grocholski, Pamela J. Hines, Di Jiang, Priscilla N. Kelly, Marc S. Lavine (Canada), Mattia Maroso, Yevgeniya Nusinovich, Ian S. Osborne (UK), L. Bryan Ray, Seth Thomas Scanlon (UK), H. Jesse Smith, Keith T. Smith (UK), Jelena Stajic, Peter Stern (UK), Valerie B. Thompson, Brad Wible, Yuen Yiu **ASSOCIATE EDITORS** Bianca Lopez, Corinne Simonti, Yury V. Suleymanov, Ekeoma Uzogara **LETTERS EDITOR** Jennifer Sills **LEAD CONTENT PRODUCTION EDITORS** Chris Filiatreau, Harry Jach **SR. CONTENT PRODUCTION EDITOR** Amelia Beyna **CONTENT PRODUCTION EDITORS** Julia Haber-Katris, Nida Masiulis, Abigail Shashikanth, Suzanne M. White **SR. EDITORIAL MANAGERS** Carolyn Kyle, Beverly Shields **SR. PROGRAM ASSOCIATE** Maryrose Madrid **EDITORIAL ASSOCIATE** Joi S. Granger **SR. EDITORIAL COORDINATORS** Aneera Dobbins, Jeffrey Hearn, Lisa Johnson, Shannon McMahon, Jerry Richardson, Hilary Stewart (UK), Alice Whaley (UK), Anita Wynn **EDITORIAL COORDINATORS** Maura Byrne, Alexander Kief, Ronmel Navas, Isabel Schnaidt, Qiyam Stewart, Brian White **RESEARCH & DATA ANALYST** Jessica L. Slater **ASI DIRECTOR, OPERATIONS** Janet Clements (UK) **ASI SR. OFFICE ADMINISTRATOR** Jessica Waldock (UK)

News Editor Tim Appenzeller

NEWS MANAGING EDITOR John Travis **INTERNATIONAL EDITOR** Martin Enserink **DEPUTY NEWS EDITORS** Shraddha Chakradhar, Elizabeth Culotta, Lila Guterman, David Grimm, Eric Hand (Europe), David Malakoff **SR. CORRESPONDENTS** Daniel Clery (UK), Jon Cohen, Jeffrey Mervis, Elizabeth Pennisi **ASSOCIATE EDITORS** Jeffrey Brainard, Michael Price, Kelly Servick **NEWS REPORTERS** Adrian Cho, Jennifer Couzin-Frankel, Jocelyn Kaiser, Rodrigo Pérez Ortega (Mexico City), Robert F. Service, Erik Stokstad, Paul Voosen, Meredith Wadman **INTERNS** Zack Savitsky, Viviana Flores, Katherine Irving **CONTRIBUTING CORRESPONDENTS** Warren Cornwall, Andrew Curry (Berlin), Ann Gibbons, Sam Kean, Eli Kintisch, Kai Kupferschmidt (Berlin), Andrew Lawler, Mitch Leslie, Eliot Marshall, Virginia Morell, Dennis Normile (Tokyo), Elisabeth Pain (Careers), Charles Piller, Gabriel Popkin, Michael Price, Joshua Sokol, Richard Stone, Emily Underwood, Gretchen Vogel (Berlin), Lizzie Wade (Mexico City) **CAREERS** Rachel Bernstein (Editor), Katie Langin (Associate Editor) **COPY EDITORS** Julia Cole (Senior Copy Editor), Morgan Everett, Cyra Master (Copy Chief) **ADMINISTRATIVE SUPPORT** Meagan Weiland

Creative Director Beth Rakouskas

DESIGN MANAGING EDITORS Marcy Atarod, Chrystal Smith **GRAPHICS MANAGING EDITOR** Chris Bickel **MULTIMEDIA MANAGING PRODUCER** Kevin McLean **WEB CONTENT STRATEGY MANAGER** Kara Estelle-Powers **PHOTOGRAPHY MANAGING EDITOR** Emily Petersen **DESIGNER** Christina Aycock **SENIOR SCIENTIFIC ILLUSTRATOR** Valerie Altounian **SCIENTIFIC ILLUSTRATORS** Austin Fisher, Kellie Holoski, Ashley Mastin **INTERACTIVE GRAPHICS EDITOR** Kelly Franklin **SENIOR GRAPHICS SPECIALISTS** Holly Bishop, Nathalie Cary **SENIOR PHOTO EDITOR** Charles Borst **PHOTO EDITOR** Kaitlyn Dolan **SENIOR PODCAST PRODUCER** Sarah Crespi **VIDEO PRODUCER** Meagan Cantwell **SOCIAL MEDIA STRATEGIST** Jessica Hubbard **SOCIAL MEDIA PRODUCER** Sabrina Jenkins **WEB DESIGNER** Jennie Pajerowski

Chief Executive Officer and Executive Publisher Sudip Parikh

Publisher, Science Family of Journals Bill Moran

DIRECTOR, BUSINESS SYSTEMS AND FINANCIAL ANALYSIS Randy Yi **DIRECTOR, BUSINESS OPERATIONS & ANALYSIS** Eric Knott **DIRECTOR OF ANALYTICS** Enrique Gonzales **MANAGER, BUSINESS OPERATIONS** Jessica Tierney **MANAGER, BUSINESS ANALYSIS** Cory Lipman **BUSINESS ANALYSTS** Kurt Ennis, Maggie Clark **FINANCIAL ANALYST** Isacco Fusi **BUSINESS OPERATIONS ADMINISTRATOR** Taylor Fisher **SENIOR PRODUCTION MANAGER** Jason Hillman **SENIOR MANAGER, PUBLISHING AND CONTENT SYSTEMS** Marcus Spiegler **CONTENT OPERATIONS MANAGER** Rebecca Doshi **SENIOR CONTENT & PUBLISHING SYSTEMS SPECIALIST** Jacob Hedrick **SENIOR PRODUCTION SPECIALIST** Kristin Wowk **PRODUCTION SPECIALISTS** Kelsey Cartelli, Audrey Diggs **DIGITAL PRODUCTION MANAGER** Lisa Stanford **CONTENT SPECIALIST** Kimberley Oster **ADVERTISING PRODUCTION OPERATIONS MANAGER** Deborah Tompkins **DESIGNER, CUSTOM PUBLISHING** Jeremy Huntsinger **SR. TRAFFIC ASSOCIATE** Christine Hall **SPECIAL PROJECTS ASSOCIATE** Sarah Dhere

ASSOCIATE DIRECTOR, BUSINESS DEVELOPMENT Justin Sawyers **GLOBAL MARKETING MANAGER** Allison Pritchard **DIGITAL MARKETING MANAGER** Aimee Aponte **JOURNALS MARKETING MANAGER** Shawana Arnold **MARKETING ASSOCIATES** Aaron Helmbrecht, Ashley Hylton, Mike Romano, Lorena Chirinos Rodriguez, Jenna Voris **SENIOR DESIGNER** Kim Huynh

DIRECTOR AND SENIOR EDITOR, CUSTOM PUBLISHING Sean Sanders **ASSISTANT EDITOR, CUSTOM PUBLISHING** Jackie Oberst **PROJECT MANAGER** Melissa Collins

DIRECTOR, PRODUCT & PUBLISHING DEVELOPMENT Chris Reid **DIRECTOR, BUSINESS STRATEGY AND PORTFOLIO MANAGEMENT** Sarah Whalen **ASSOCIATE DIRECTOR, PRODUCT MANAGMENT** Kris Bishop **PRODUCT DEVELOPMENT MANAGER** Scott Chernoff **PUBLISHING TECHNOLOGY MANAGER** Michael Di Natale **SR. PRODUCT ASSOCIATE** Robert Koepke **PRODUCT ASSOCIATE** Caroline Breul, Anne Mason **SPJ ASSOCIATE MANAGER** Samantha Bruno Fuller **SPJ ASSOCIATE** Casey Buchta

MARKETING MANAGER Kess Knight **BUSINESS DEVELOPMENT MANAGER** Rasmus Andersen **SENIOR INSTITUTIONAL LICENSING MANAGER** Ryan Rexroth **INSTITUTIONAL LICENSING MANAGER** Marco Castellan, Claudia Paulsen-Young **SENIOR MANAGER, INSTITUTIONAL LICENSING OPERATIONS** Judy Lillibridge **SENIOR OPERATIONS ANALYST** Lana Guz **SYSTEMS & OPERATIONS ANALYST** Ben Teincuff **FULFILLMENT ANALYST** Aminta Reyes

DIRECTOR, GLOBAL SALES Tracy Holmes **US EAST COAST AND MID WEST SALES** Stephanie O'Connor **US MID WEST, MID ATLANTIC AND SOUTH EAST SALES** Chris Hoag **US WEST COAST SALES** Lynne Stickrod **ASSOCIATE DIRECTOR, ROW** Roger Goncalves **SALES REP, ROW** Sarah Lelarge **SALES ADMIN ASSISTANT, ROW** Victoria Glasbey **DIRECTOR OF GLOBAL COLLABORATION AND ACADEMIC PUBLISHING RELATIONS, ASIA** Xiaoying Chu **ASSOCIATE DIRECTOR, INTERNATIONAL COLLABORATION** Grace Yao **SALES MANAGER** Danny Zhao **MARKETING MANAGER** Kilo Lan **ASCA CORPORATION, JAPAN** Rie Rambelli (Tokyo), Miyuki Tani (Osaka)

DIRECTOR, COPYRIGHT, LICENSING AND SPECIAL PROJECTS Emilie David **RIGHTS AND PERMISSIONS ASSOCIATE** Elizabeth Sandler **LICENSING ASSOCIATE** Virginia Warren **CONTRACT SUPPORT SPECIALIST** Michael Wheeler

MAIN HEADQUARTERS
Science/AAAS
1200 New York Ave. NW
Washington, DC 20005

SCIENCE INTERNATIONAL
Clarendon House
Clarendon Road
Cambridge, CB2 8FH, UK

SCIENCE CHINA
Room 1004, Culture Square
No. 59 Zhongguancun St.
Haidian District, Beijing, 100872

SCIENCE JAPAN
ASCA Corporation
Sibaura TY Bldg. 4F, 1-14-5
Shibaura Minato-ku
Tokyo, 108-0073 Japan

EDITORIAL
science_editors@aaas.org

NEWS
science_news@aaas.org

INFORMATION FOR AUTHORS
science.org/authors/
science-information-authors

REPRINTS AND PERMISSIONS
science.org/help/
reprints-and-permissions

MEDIA CONTACTS
scipak@aaas.org

MULTIMEDIA CONTACTS
SciencePodcast@aaas.org
ScienceVideo@aaas.org

INSTITUTIONAL SALES AND SITE LICENSES
science.org/librarian

PRODUCT ADVERTISING & CUSTOM PUBLISHING
advertising.science.org/
products-services
science_advertising@aaas.org

CLASSIFIED ADVERTISING
advertising.science.org/
science-careers
advertise@sciencecareers.org

JOB POSTING CUSTOMER SERVICE
employers.sciencecareers.org
support@sciencecareers.org

MEMBERSHIP AND INDIVIDUAL SUBSCRIPTIONS
science.org/subscriptions

MEMBER BENEFITS
aaas.org/membership/benefits

AAAS BOARD OF DIRECTORS
CHAIR Susan G. Amara
PRESIDENT Gilda A. Barabino
PRESIDENT-ELECT Keith Yamamoto
TREASURER Carolyn N. Ainslie
CHIEF EXECUTIVE OFFICER
Sudip Parikh
BOARD Cynthia M. Beall
Ann Bostrom
Janine Austin Clayton
Kaye Husbands Fealing
Maria M. Klawe
Jane Maienschein
Robert B. Millard
Babak Parviz
William D. Provine
Juan S. Ramírez Lugo
Susan M. Rosenberg

Science serves as a forum for discussion of important issues related to the advancement of science by publishing material on which a consensus has been reached as well as including the presentation of minority or conflicting points of view. Accordingly, all articles published in *Science*—including editorials, news and comment, and book reviews—are signed and reflect the individual views of the authors and not official points of view adopted by AAAS or the institutions with which the authors are affiliated.

BOARD OF REVIEWING EDITORS (Statistics board members indicated with **(S)**)

Erin Adams, *U. of Chicago*
Takuzo Aida, *U. of Tokyo*
Leslie Aiello, *Wenner-Gren Fdn.*
Deji Akinwande, *UT Austin*
Judith Allen, *U. of Manchester*
Marcella Alsan, *Harvard U.*
James Analytis, *UC Berkeley*
Paola Arlotta, *Harvard U.*
Delia Baldassarri, *NYU*
Nenad Ban, *ETH Zürich*
Christopher Barratt, *U. of Dundee*
Nandita Basu, *U. of Waterloo*
Franz Bauer, *Pontificia U. Católica de Chile*
Ray H. Baughman, *UT Dallas*
Carlo Beenakker, *Leiden U.*
Yasmine Belkaid, *NIAID, NIH*
Philip Benfey, *Duke U.*
Kiros T. Berhane, *Columbia U.*
Joseph J. Berry, *NREL*
Alessandra Biffi, *Harvard Med.*
Chris Bowler, *École Normale Supérieure*
Ian Boyd, *U. of St. Andrews*
Malcolm Brenner, *Baylor Coll. of Med.*
Emily Brodsky, *UC Santa Cruz*
Ron Brookmeyer, *UCLA* **(S)**
Christian Büchel, *UKE Hamburg*
Dennis Burton, *Scripps Res.*
Carter Tribley Butts, *UC Irvine*
György Buzsáki, *NYU School of Med.*
Mariana Byndloss, *Vanderbilt U. Med. Ctr.*
Annmarie Carlton, *UC Irvine*
Simon Cauchemez, *Inst. Pasteur*
Ling-Ling Chen, *SIBCB, CAS*
Ib Chorkendorff, *Denmark TU*
Karlene Cimprich, *Stanford U.*
James J. Collins, *MIT*
Robert Cook-Deegan, *Arizona State U.*
Virginia Cornish *Columbia U.*
Carolyn Coyne, *Duke U.*
Roberta Croce, *VU Amsterdam*
Christina Curtis, *Stanford U.*
Ismaila Dabo, *Penn State U.*
Jeff L. Dangl, *UNC*
Chiara Daraio, *Caltech*
Nicolas Dauphas, *U. of Chicago*
Frans de Waal, *Emory U.*
Claude Desplan, *NYU*
Sandra Díaz, *U. Nacional de Córdoba*
Samuel Díaz-Muñoz, *UC Davis*
Ulrike Diebold, *TU Wien*
Stefanie Dimmeler, *Goethe-U. Frankfurt*
Hong Ding, *Inst. of Physics, CAS*
Dennis Discher, *UPenn*
Jennifer A. Doudna, *UC Berkeley*
Ruth Drdla-Schutting, *Med. U. Vienna*
Raissa M. D'Souza, *UC Davis*
Bruce Dunn, *UCLA*
William Dunphy, *Caltech*
Scott Edwards, *Harvard U.*
Todd Ehlers, *U. of Tübingen*
Nader Engheta, *UPenn*
Karen Ersche, *U. of Cambridge*
Beate Escher, *UFZ & U. of Tübingen*
Barry Everitt, *U. of Cambridge*
Vanessa Ezenwa, *U. of Georgia*
Toren Finkel, *U. of Pitt. Med. Ctr.*
Gwenn Flowers, *Simon Fraser U.*
Peter Fratzl, *Max Planck Inst. Potsdam*
Elaine Fuchs, *Rockefeller U.*
Jay Gallagher, *U. of Wisconsin*
Daniel Geschwind, *UCLA*
Ramon Gonzalez, *U. of South Florida*
Sandra González-Bailón, *UPenn*
Nicolas Gruber, *ETH Zürich*
Hua Guo, *U. of New Mexico*
Taekjip Ha, *Johns Hopkins U.*
Daniel Haber, *Mass. General Hos.*
Sharon Hammes-Schiffer, *Yale U.*
Wolf-Dietrich Hardt, *ETH Zürich*
Louise Harra, *U. Coll. London*
Carl-Philipp Heisenberg, *IST Austria*
Janet G. Hering, *Eawag*
Christoph Hess, *U. of Basel & U. of Cambridge*
Heather Hickman, *NIAID, NIH*
Hans Hilgenkamp, *U. of Twente*
Janneke Hille Ris Lambers, *ETH Zürich*
Kai-Uwe Hinrichs, *U. of Bremen*
Deirdre Hollingsworth, *U. of Oxford*
Randall Hulet, *Rice U.*
Auke Ijspeert, *EPFL*
Gwyneth Ingram, *ENS Lyon*
Darrell Irvine, *MIT*
Akiko Iwasaki, *Yale U.*
Stephen Jackson, *USGS & U. of Arizona*
Erich Jarvis, *Rockefeller U.*
Peter Jonas, *IST Austria*
Johanna Joyce, *U. de Lausanne*
Matt Kaeberlein, *U. of Wash.*
William Kaelin Jr., *Dana-Farber Cancer Inst.*
Daniel Kammen, *UC Berkeley*
Kisuk Kang, *Seoul Nat. U.*
Sabine Kastner, *Princeton U.*
V. Narry Kim, *Seoul Nat. U.*
Robert Kingston, *Harvard Med.*
Nancy Knowlton, *Smithsonian Institution*
Etienne Koechlin, *École Normale Supérieure*
Alex L. Kolodkin, *Johns Hopkins U.*
LaShanda Korley, *U. of Delaware*
Julija Krupic, *U. of Cambridge*
Paul Kubes, *U. of Calgary*
Chris Kuzawa, *Northwestern U.*
Laura Lackner, *Northwestern U.*
Gabriel Lander, *Scripps Res.* **(S)**
Mitchell A. Lazar, *UPenn*
Hedwig Lee, *Duke U.*
Luis Liz-Marzán, *CIC biomaGUNE*
Omar Lizardo, *UCLA*
Jonathan Losos, *Wash. U. in St. Louis*
Ke Lu, *Inst. of Metal Res., CAS*
Christian Lüscher, *U. of Geneva*
Jean Lynch-Stieglitz, *Georgia Inst. of Tech.*
David Lyons, *U. of Edinburgh*
Fabienne Mackay, *QIMR Berghofer*
Zeynep Madak-Erdogan, *UIUC*
Anne Magurran, *U. of St. Andrews*
Ari Pekka Mähönen, *U. of Helsinki*
Asifa Majid, *U. of Oxford*
Oscar Marín, *King's Coll. London*
Charles Marshall, *UC Berkeley*
Christopher Marx, *U. of Idaho*
David Masopust, *U. of Minnesota*
Geraldine Masson, *CNRS*
C. Robertson McClung, *Dartmouth*
Rodrigo Medellín, *U. Nacional Autónoma de México*
C. Jessica Metcalf, *Princeton U.*
Baoxia Mi, *UC Berkeley*
Tom Misteli, *NCI, NIH*
Alison Motsinger-Reif, *NIEHS, NIH* **(S)**
Danielle Navarro, *U. of New South Wales*
Daniel Nettle, *Newcastle U.*
Daniel Neumark, *UC Berkeley*
Beatriz Noheda, *U. of Groningen*
Helga Nowotny, *Vienna Sci. & Tech. Fund*
Pilar Ossorio, *U. of Wisconsin*
Andrew Oswald, *U. of Warwick*
Isabella Pagano, *Istituto Nazionale di Astrofisica*
Elizabeth Levy Paluck, *Princeton U.*
Jane Parker, *Max Planck Inst. Cologne*
Giovanni Parmigiani, *Dana-Farber Cancer Inst.* **(S)**
Daniel Pauly, *U. of British Columbia*
Ana Pêgo, *U. do Porto*
Samuel Pfaff, *Salk Inst.*
Julie Pfeiffer, *UT Southwestern Med. Ctr.*
Philip Phillips, *UIUC*
Matthieu Piel, *Inst. Curie*
Kathrin Plath, *UCLA*
Martin Plenio, *Ulm U.*
Katherine Pollard, *UCSF*
Elvira Poloczanska, *Alfred-Wegener-Inst.*
Julia Pongratz, *Ludwig Maximilians U.*
Philippe Poulin, *CNRS*
Lei Stanley Qi, *Stanford U.*
Trevor Robbins, *U. of Cambridge*
Joeri Rogelj, *Imperial Coll. London*
Amy Rosenzweig, *Northwestern U.*
Mike Ryan, *UT Austin*
Miquel Salmeron, *Lawrence Berkeley Nat. Lab*
Nitin Samarth, *Penn State U.*
Erica Ollmann Saphire, *La Jolla Inst.*
Joachim Saur, *U. zu Köln*
Alexander Schier, *Harvard U.*
Wolfram Schlenker, *Columbia U.*
Susannah Scott, *UC Santa Barbara*
Anuj Shah, *U. of Chicago*
Vladimir Shalaev, *Purdue U.*
Jie Shan, *Cornell U.*
Beth Shapiro, *UC Santa Cruz*
Jay Shendure, *U. of Wash.*
Steve Sherwood, *U. of New South Wales*
Brian Shoichet, *UCSF*
Robert Siliciano, *JHU School of Med.*
Lucia Sivilotti, *U. Coll. London*
Emma Slack, *ETH Zürich & U. of Oxford*
Richard Smith, *UNC* **(S)**
John Speakman, *U. of Aberdeen*
Tara Spires-Jones, *U. of Edinburgh*
Allan C. Spradling, *Carnegie Institution for Sci.*
V. S. Subrahmanian, *Northwestern U.*
Ira Tabas, *Columbia U.*
Eriko Takano, *U. of Manchester*
A. Alec Talin, *Sandia Natl. Labs*
Patrick Tan, *Duke-NUS Med. School*
Sarah Teichmann, *Wellcome Sanger Inst.*
Rocio Titiunik, *Princeton U.*
Shubha Tole, *Tata Inst. of Fundamental Res.*
Maria-Elena Torres Padilla, *Helmholtz Zentrum München*
Kimani Toussaint, *Brown U.*
Barbara Treutlein, *ETH Zürich*
Jason Tylianakis, *U. of Canterbury*
Wim van der Putten, *Netherlands Inst. of Ecology*
Matthew Vander Heiden, *MIT*
Ivo Vankelecom, *KU Leuven*
Judith Varner, *UC San Diego*
Henrique Veiga-Fernandes, *Champalimaud Fdn.*
Reinhilde Veugelers, *KU Leuven*
Bert Vogelstein, *Johns Hopkins U.*
Julia Von Blume, *Yale School of Med.*
David Wallach, *Weizmann Inst.*
Jane-Ling Wang, *UC Davis* **(S)**
Jessica Ware, *Amer. Mus. of Natural Hist.*
David Waxman, *Fudan U.*
Chris Wikle, *U. of Missouri* **(S)**
Terrie Williams, *UC Santa Cruz*
Ian A. Wilson, *Scripps Res.* **(S)**
Hao Wu, *Harvard U.*
Li Wu, *Tsinghua U.*
Wei Xie, *Tsinghua U.*
Benjamin Youngblood, *St. Jude*
Yu Xie, *Princeton U.*
Jan Zaanen, *Leiden U.*
Kenneth Zaret, *UPenn School of Med.*
Bing Zhu, *Inst. of Biophysics, CAS*
Xiaowei Zhuang, *Harvard U.*
Maria Zuber, *MIT*

NEWS FROM Science | AAAS

Subscribe to **News from Science** for unlimited access to authoritative, up-to-the-minute news on research and science policy.



bit.ly/NewsFromScience



RUTGERS
THE STATE UNIVERSITY OF NEW JERSEY

Building the Future, One City at a Time

Our WINLAB is taking tomorrow's tech out of the lab and into the streets of New York City

Building on their extensive research with wireless testbeds, radio technology, and mobile internet architecture, the Rutgers team at the Wireless Information Network Laboratory (WINLAB) is helping to implement COSMOS, a real-world outdoor lab putting next-generation wireless technology to work.

A major partnership between WINLAB and other local innovation leaders, with funding from the National Science Foundation, COSMOS will be deployed across a square mile in Manhattan's vibrant, densely populated West Harlem neighborhood.

These urban wireless networks of the future will support data-intensive applications for a smarter, safer world.

- **Smart intersections** that can safely process vital information in real time
- Cloud-based autonomous vehicles for **reliable driverless transportation**
- **Remote surgery** enabling doctors to operate on patients across great distances
- Augmented and virtual reality to **enhance interactivity** and provide new experiences

Excellence *is Earned*
excellence.rutgers.edu

EDITORIAL

Measure emissions to manage emissions

In the 30 years since the world began negotiating the reduction of greenhouse gas (GHG) emissions, no one has identified exactly where all that pollution is coming from. That will begin to change next week when Climate TRACE (Tracking Real-Time Atmospheric Carbon Emissions)—a nonprofit coalition of artificial intelligence (AI) specialists, data scientists, researchers, and nongovernmental organizations—releases the first facility-level inventory of the largest known individual sources of the 162 million tons of GHG pollution emitted into the troposphere every day. With thousands of businesses, banks, investors, and 88 nation-states committed to reducing emissions to net zero by 2050, comprehensively tracking progress toward that goal is essential. This is especially important given last week's United Nations Emissions Gap Report indicating that the world is far behind pace for reducing emissions by 2030.

Scientists have long known the total amount of carbon dioxide (CO_2) in the atmosphere. The Keeling Curve—a daily record of global atmospheric CO_2 concentration—leaped from 313 parts per million (ppm) in March 1958 to 2021's staggering 414.72 ppm global average. Likewise, the component parts of the emissions puzzle are well understood—the burning of fossil fuels, transportation, industry, conventional agriculture, deforestation, and other sources are continually adding to the accumulation that lingers in the atmosphere. But until now, it has not been possible to precisely map and track the specific sources of GHG pollution. Climate TRACE's global database of the most substantial individual sources of emissions across two dozen sectors of the global economy will be free and publicly available.

> "...no one has identified exactly where all that pollution is coming from."

Why is this information so essential? As the eminent physicist Lord Kelvin said nearly 140 years ago, "When you can measure what you are speaking about, and express it in numbers, you know something about it; but when you cannot measure it, when you cannot express it in numbers, your knowledge is of a meagre and unsatisfactory kind; it may be the beginning of knowledge, but you have scarcely, in your thoughts advanced to the stage of science." Efforts to limit global temperature rise to 1.5°C are currently informed by rough estimates principally derived from self-reported national inventories submitted intermittently to the United Nations (UN). As of last month, no nation has submitted a complete accounting of its emissions for 2021. Indeed, 52 countries have not submitted any emissions inventories covering the past 10 years. Moreover, the inventories that do exist often have large omissions and fail to provide the granular data needed to make decisions. For example, last year, Climate TRACE found the actual emissions from global oil and gas production collectively were around double what was self-reported to the UN in 2020. Even more oil and gas emissions went uncounted by countries that are not required to report these data.

The Climate TRACE coalition is working to advance emissions monitoring closer to "the stage of science" Kelvin once described—by training AI algorithms to fuse data across multiple wavelengths and from more than 300 satellites; 11,100 air-, land-, and sea-based sensors; and other data streams to identify all of the largest point sources and track them over time. In recent years, new satellites have begun to measure methane emissions for a limited set of sources. But the atmosphere is so enriched with CO_2 that the "signal-to-noise ratio" defies the ability to measure CO_2 point-source emissions directly, leaving AI as the best recourse. The progress demonstrated by Climate TRACE mirrors the breakthroughs in AI that are ushering in a new era of radical transparency in multiple domains—making it possible to "see" specific land-use changes more clearly, and even to identify microscopic structures inside living human cells that had been impossible to "see" previously. Climate TRACE is proving that AI can do the same for emissions monitoring—making the invisible, visible.

Lord Kelvin's dictum is commonly translated in the business world as "you can only manage what you can measure." Thanks to breakthroughs in AI and other technologies, researchers, government officials, and business leaders can now manage emissions with timely, granular, and actionable climate information at their fingertips. With no time left to wait as the world burns and drowns, we can now begin to measure emissions with the precision needed to better manage their reduction—quickly.

–Al Gore

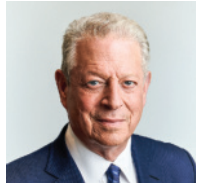


PHOTO: JASON MYERS

Al Gore
is a former vice president of the United States. He was awarded the Nobel Peace Prize, along with the Intergovernmental Panel on Climate Change (IPCC), in 2007. He is a founding member and among the funders of Climate TRACE. press@carthagegroup.com

10.1126/science.adf5788



NEWS

IN BRIEF

Edited by
Jeffrey Brainard

NATURAL HISTORY

Science society lists Earth's top 'geoheritage' sites

The International Union of Geological Sciences last week marked its 60th anniversary by announcing a list of 100 "geoheritage" sites that have substantially influenced understanding of Earth's deep history. The global list, released in collaboration with UNESCO, is meant to foster conservation and tourism. The sites include familiar ones, such as the Grand Canyon's "great unconformity," a billion-year gap in the rock record erased by erosion. More exotic examples include limestones in Germany that preserve *Archaeopteryx*, a feathered fossil that links dinosaurs to birds, and the Canary Islands' Taburiente Caldera (above), which gave such volcanic formations their name.

Antimalaria antibody delivers

INFECTIOUS DISEASES | A single intravenous infusion of lab-produced monoclonal antibodies was up to 88% efficacious in preventing malaria infection in Mali, researchers reported this week. The study, in *The New England Journal of Medicine,* offers new hope for combatting the disease, spread by parasite-laden mosquitoes. Malaria parasites have developed resistance against many drugs, and the mosquitoes that spread them have adapted to withstand some insecticides. Researchers at the U.S. National Institute of Allergy and Infectious Diseases developed the antibody, and working with colleagues at the University of Sciences, Techniques and Technology of Bamako, tested it or a placebo in 330 adult volunteers. The research team is now testing a more powerful antibody in 6- to 10-year-old children in Mali who are receiving the antibody by subcutaneous injection, a method that is much more practicable with young children than intravenous infusion. In 2020, malaria killed 627,000 worldwide, two-thirds of whom were children younger than 5 in Africa.

China completes space station

LABORATORIES | China this week launched the final module of its Tiangong-3 space station, providing the country its first long-term platform for space experiments. U.S. restrictions on use of NASA funds have blocked China from participating in research on the much larger International Space Station. Nine of Tiangong-3's research projects involve international collaborators, many from developing countries, jointly selected with a U.N. agency. These include a four-nation experiment on gamma ray bursts and a pair of infrared cameras to study Earth's humidity flows. Tiangong-3 or "Heavenly Palace" will house between three and six astronauts. It succeeds two smaller craft, Tiangong-1 and -2, that are no longer orbiting.

Oil researcher wins courage prize

SCIENTIFIC PRIZES | A biochemist in Nigeria has won this year's John Maddox Prize, which honors "standing up for science," for her tenacity in braving

PHOTO: PETER THOMPSON/HERITAGE IMAGES/GETTY IMAGES

threats while working with oil companies and local communities to clean up soil pollution near the country's oil fields. Eucharia Oluchi Nwaichi, a biochemist at the University of Port Harcourt, was threatened by representatives of an oil company who confiscated her recordings and data, according to a statement by the award's organizers, the U.K. charity Sense for Science and the journal *Nature*. She also worked to defuse a dispute between residents and a different oil company about the harmful effects of liquid waste on fish stocks, and to persuade both sides to support research to test methods to decontaminate soil, the statement says. Petroleum production in Nigeria, one of the world's largest oil exporters, has caused extensive pollution and led at times to armed conflict.

Academy probe clears biologist

RESEARCH INTEGRITY | A review by the U.S. National Academy of Medicine (NAM) has found no basis for sanctioning a member whom three leading Republicans accused of obscuring COVID-19's origin. Last year, members of the House of Representatives Committee on Energy and Commerce asked NAM to suspend and investigate conservation biologist Peter Daszak. Their complaint alleged that he violated NAM's code of conduct by refusing to share data and answer their questions about a grant awarded by the National Institutes of Health to the nonprofit he runs, the EcoHealth Alliance, which in turn shared funding with China's Wuhan Institute of Virology (WIV). Several Republicans have argued that the pandemic originated in a lab leak at WIV. Many scientists not involved in the grant have agreed with Daszak that no direct evidence supports this assertion whereas stronger evidence indicates the pandemic virus first jumped from animals to humans at a Wuhan market. In an email to members last week, NAM said its probe determined Daszak had not violated its code of conduct.

Casts of destroyed fossil found

PALEONTOLOGY | In two museums' storerooms, scientists have stumbled upon previously unknown casts of an ancient marine reptile's skeleton that was destroyed during World War II. The original fossil represented the first complete ichthyosaur, a creature that resembled a cross between a crocodile and a dolphin. Famed fossil hunter Mary Anning exhumed the specimen from Jurassic-age rocks along southern England's coastline in 1818. In 1941, the stunning, 200-million-year-old fossil was obliterated by a German bomb that hit the London museum where it was displayed. Since then, paleontologists have relied solely on a single scientific illustration of the fossil, made in 1819. The two much more detailed plaster casts were discovered in 2016 and 2019 at Yale University's Peabody Museum of Natural History and Berlin's Natural History Museum, the researchers reported this week in *Royal Society Open Science*.



On Little Bahama Bank, a tiger shark swims over manatee grass (*Syringodium filiforme*).

PHOTO: A.J. GALLAGHER *ET AL*., *NAT. COMMUN.* **13**, 6328 (2022)

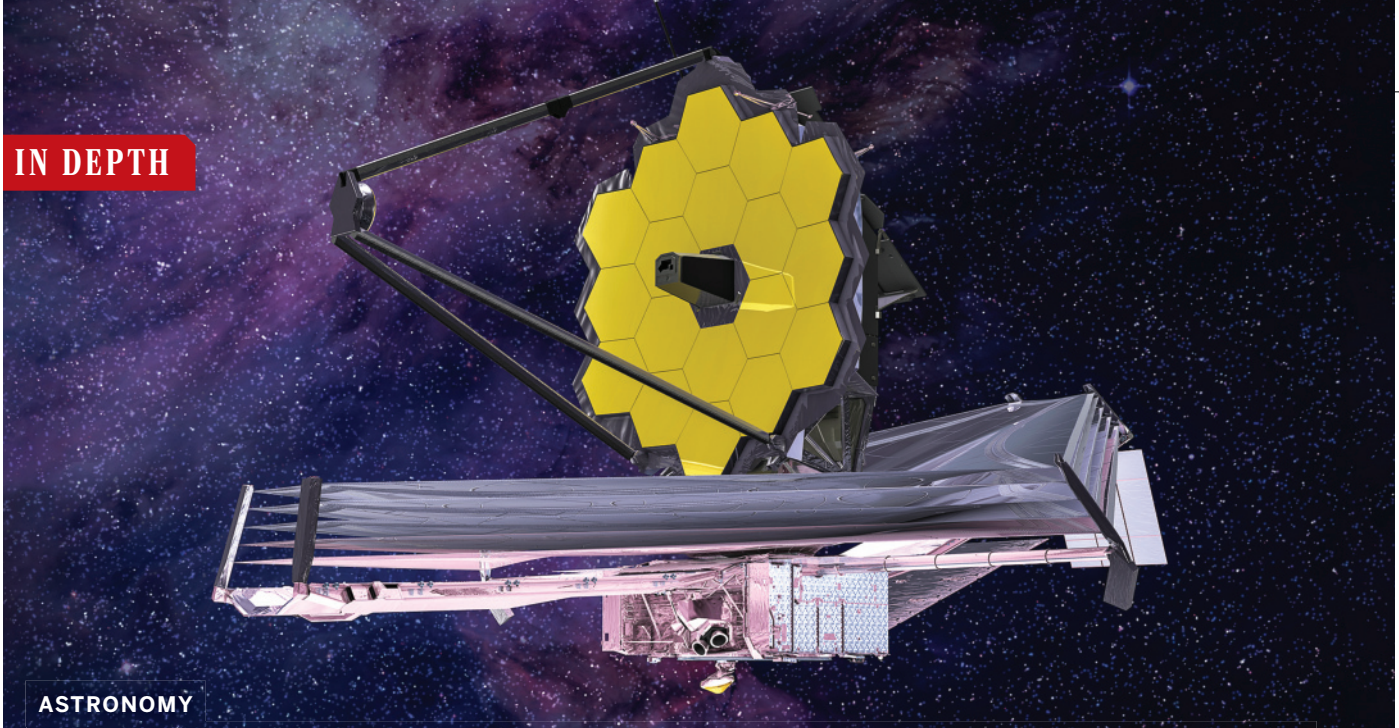
ECOLOGY

Cameras on sharks help map vast seagrass meadows

Researchers mounted cameras on tiger sharks to help measure an expanse of seagrass meadows in the Bahamas that they estimate is the world's largest, at 92,000 square kilometers. Seagrass provides a vital habitat for many other marine species, including commercially valuable fish, and the plants sequester large amounts of carbon. The new estimated size of the Bahamas' seagrass meadows, reported this week in *Nature Communications*, is about 40 times larger than the previous estimate and represents an area the size of Portugal. Tiger sharks (*Galeocerdo cuvier*) often swim over seagrass meadows, where they hunt dugongs and other herbivores. The research team fitted seven sharks with video cameras and tracking devices to map the seagrass habitat—the first use of this technique. The team used these data and diver surveys to spot-check estimates of total extent gleaned from satellite data, which can be imprecise. Measurements of carbon in seagrass sediments suggest the Bahamas could contain as much as one-quarter of the carbon stored worldwide by seagrass.

Long Covid pill trial set to begin

CLINICAL RESEARCH | Plans for the first test of whether Pfizer's COVID-19 pill known as Paxlovid can alleviate Long Covid were unveiled last week, as organizers said they expect to begin recruiting 1700 volunteers in January 2023. Patient groups and researchers have long sought such a trial to study whether suppressing the SARS-CoV-2 coronavirus can reduce Long Covid's debilitating symptoms, such as fatigue and brain fog. Participants will take either Paxlovid (a combination of the antivirals nirmatrelvir and ritonavir) or a placebo for 15 days. The Food and Drug Administration authorized the drug in December 2021 for people at high risk of severe illness from acute COVID-19. Paxlovid knocks back virus that's rapidly replicating. Researchers don't know whether such replication is happening in people with Long Covid or whether their bodies harbor virus reservoirs that help drive symptoms. The trial marks the first treatment trial backed by RECOVER, the U.S. National Institutes of Health's research effort on Long Covid, which critics charge has been slow to test therapies.



ASTRONOMY

Should Webb telescope's data be open to all?

NASA plans to end policy of giving some observers 1 year's exclusive access to data

By **Daniel Clery**

The $10 billion James Webb Space Telescope (JWST) has been observing for less than 4 months, but already a storm is brewing over access to its data. Webb images and spectra all end up in an archive at the Space Telescope Science Institute (STScI) in Baltimore, yet most of them aren't freely available until 1 year after the data were collected. This gives the researchers who proposed the observations time to analyze them and publish results without being scooped.

But some astronomers question the practice, arguing that data from federally funded projects should be free for all to use. NASA, Webb's primary backer, is facing an open data push from the White House and may soon end the restriction. Having so much Webb data locked away "doesn't pass the smell test. It's just not right," says astronomer Garth Illingworth of the University of California, Santa Cruz, who from 2009 to 2017 chaired a committee advising STScI on Webb's future science operations.

He and other proponents of an open data policy also make a practical argument. They say so-called proprietary time prevents other astronomers from using fresh data to shape their own observing plans, reducing the efficiency of a highly sought-after instrument that has consumed billions of dollars of public money.

But others say instant access to data may clash with pressing efforts to improve diversity, equity, and inclusion in astronomy. Scientists at smaller institutions, many of which serve underrepresented groups, may need more time for analysis compared with the well-resourced teams at established research universities. Eliminating proprietary time could "put people in a position where they can't succeed," says astronomer Mercedes Lopez-Morales of Harvard University, chair of the influential JWST Users Committee, which recently urged NASA to maintain a data embargo period but reduce it to 6 months.

To find a way forward, STScI will begin to poll more than 12,000 astronomers later this month about their attitudes to proprietary time. "There are mixed feelings in the community," says Neill Reid, STScI's associate director for science. "There's definitely a feeling that open access is a good way to go, but without disadvantaging [some observers]. There's not one size that fits all."

Astronomers have long been pioneers in putting data into open archives for anyone to use. Typically, data from automated survey telescopes, which systematically scan the sky night after night, are deposited straightaway. But proprietary time remains a tradition at general purpose telescopes, which give astronomers whose observing proposals are chosen exclusive access to their data for as long as 18 months.

After often-heated debate, the Webb advisory committee that Illingworth chaired before the telescope's launch urged that its proprietary period last just 6 months. Any longer, the committee concluded, and most of the data collected during the first year of observing, known as cycle 1, would be unavailable to astronomers trying to plan what to look for in cycle 2, or even some of cycle 3. For a mission then expected to only last 5 years, that was unsupportable in the view of some committee members.

In recent years, NASA has reduced the proprietary time for the Hubble Space Telescope and the Chandra X-ray Observatory to 6 months. But it did not do the same for Webb, in part because the academic teams that built its four instruments and the European and Canadian space agencies that partnered in the project had 12 months' proprietary time written into their agreements.

Webb planners did, however, adopt the committee's suggestion to provide immediate access to a key subset of data: 500 hours of observations made during the first 5 months of cycle 1, covering all Webb's key science areas and employing all its instruments and observing modes. This Early Release Science (ERS) program amounts to about 5% of cycle 1's total observing time (see table, p. 459) and its data are put in the archive immediately, providing some material for scientists devising cycle 2 proposals.

Webb's successful launch has also tempered the data-access debate somewhat because it required fewer course corrections than expected, leaving a fuel reserve that

IMAGE: NORTHROP GRUMMAN

could extend the telescope's lifetime and allow more time for observing.

But proprietary time still galls many astronomers. On 15 November, STScI will put out the call for cycle 2 proposals, for observations to start in July 2023. Although the ERS data are helping many plan future observations, most cycle 1 data are still locked up and some will remain so until the second half of 2024. NASA is also under pressure from the White House. On 25 August, the White House's Office of Science and Technology Policy ordered departments and agencies to move toward making the results of all federally funded research freely and immediately available by 2026.

In response, NASA asked the JWST Users Committee, which was meeting that same day, to look again at the telescope's proprietary time. It, too, recommended moving to 6 months. A year "won't fly anymore," Lopez-Morales says. But the committee recognized that its members, 12 senior astronomers, may have a biased view, so they asked STScI to consult with the wider community.

Mark McCaughrean, an astronomer with the European Space Agency, says the 12-month embargo should remain in place because it helps level the field. Astronomers at small universities often shoulder heavy teaching loads and other responsibilities. If their Webb observations were publicly released straight away, they could be scooped by teams at large, well-resourced research institutions before they had a chance to analyze the data over the summer, for example. The situation is trickier still for European astronomers who don't get automatic funding for postdocs and other expenses linked to winning time on a space telescope as U.S. astronomers do. "We should be aiming to improve diversity by removing structural biases against smaller institutions, early-career researchers, and historically disadvantaged groups: Fixed proprietary periods can help with this," McCaughrean says.

Illingworth says underrepresented groups could be helped by making proprietary time optional, with space in the proposal form for researchers to request it and explain their need. Marcia Rieke of the University of Arizona, principal investigator of Webb's near-infrared camera, favors the opposite: giving everyone proprietary time with the expectation that those who don't need it will give it up, or at least release their data when they publish. Proprietary time "encourages people to do a good job analyzing data," she says.

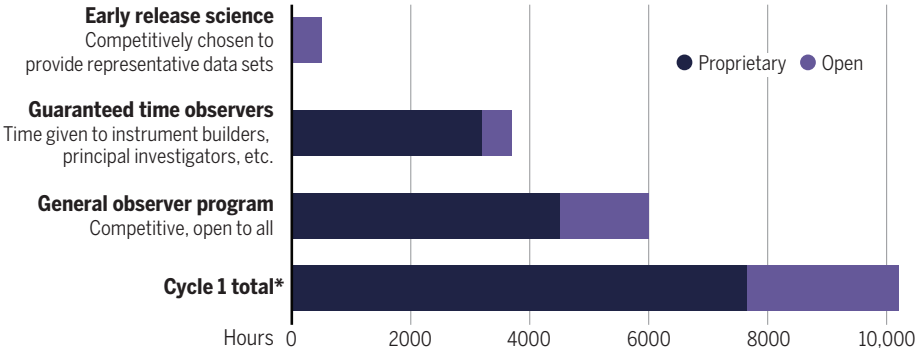
"It's complicated," Lopez-Morales concedes. On the one hand, she says, reducing proprietary time could be "in conflict with [NASA's] other efforts" to widen the pool of astronomers. Yet instant access to data means the many groups who are unsuccessful at applying for observing time—in cycle 1, the rejection rate was 75%—can still get a crack at using the data. "We need to see what the community wants," Lopez-Morales says, "and we will advocate for that."

Michael New, NASA's deputy associate director for research, says even if the community comes down in favor of 6 months, that will be a stepping stone to fully removing proprietary time. A NASA policy, now being finalized, will mandate instant access to instrument data in line with White House policy. New says the Webb agreements with other space agencies contain clauses allowing proprietary time to be reduced once the telescope is operating and discussions to do so are already taking place. "It's not if we do it, but when," he says. "Will everyone be happy? No, but we will listen to all sides."

NASA is already working to provide support for researchers who will be disadvantaged, New adds. If some are underresourced, "solve that problem, don't preserve proprietary time." ■

Private eye

Most astronomers using the James Webb Space Telescope get a yearlong "proprietary" period to exclusively analyze data from observing projects. About 75% of Webb's first year of observations is not immediately open for use.



*Hours exceed 1 year in case some observations can't be done for technical reasons.

CREDITS: (GRAPHIC) K. FRANKLIN/*SCIENCE*; (DATA) SPACE TELESCOPE SCIENCE INSTITUTE

SOCIAL JUSTICE

Teeth record pneumonia—and racism

Research raises standards for working with anthropological collections

By **Rodrigo Pérez Ortega**

In the 1930s, a 23-year-old Black man was admitted to City Hospital #2 in St. Louis and, according to his death certificate, died of pneumonia shortly after. Without his consent—or his family's—his deidentified body was included in one of the United States's most studied collections of human remains, the Robert J. Terry Anatomical Skeletal Collection, which is now at the Smithsonian Institution's National Museum of Natural History (NMNH). Almost a century later, a team of researchers has been able to confirm the pathogen that ultimately killed him by studying the plaque on his teeth, an achievement that opens new avenues for studying diseases of the past that may leave no other mark after death.

In their paper, published last month in *Communications Biology*, the researchers also took steps to address the complex issues of ethics and social justice that surround repositories such as the Terry collection. They reconstructed the context in which a now-nameless man lived, including how structural racism contributed to his death—and helped build the collection itself.

"This may be a way of doing research with the Terry collection ethically," says Carlina de la Cova, a biological anthropologist at the University of South Carolina, Columbia, who was not involved in the study. Analyzing dental calculus, she adds, is a clever, nondestructive way to learn more about an individual's past, and their disease profile. "It should not be overlooked."

"Previous research does not recognize the individual skeletons and the once-living individuals that they represent," says Molly Zuckerman, a bioarchaeologist and paleopathologist at Mississippi State University, Starkville, and a co-author of the new study. "Their humanity has been reduced or ignored, and they're turned into just a collection of objects for scientific research." As the field of biological anthropology grapples with—and tries to correct for—a



In 1923, City Hospital #2 in St. Louis, where the St. Louis Individual died, was severely overcrowded and underfunded, and had poor sanitary conditions.

PHOTO: ST. LOUIS POST-DISPATCH/POLARIS

complex history of racism, she and her colleagues aim to set a new ethical standard for studying anthropological collections with a controversial past. Rachel Watkins, a biocultural anthropologist at American University who was not involved in the study, applauds the effort. "Offering up this way of repositioning the Terry collection is really significant," she says.

The idea of using dental calculus—or hardened plaque—to study diseases of the past is not new. Accumulated over a lifetime, calculus doesn't decay after death and holds onto everything from traces of food, such as milk proteins, to fragments of bacterial DNA. In 2015, molecular anthropologist Rita Austin, then at NMNH and the University of Oklahoma, decided to see whether calculus can reveal causes of death, including so-called invisible diseases such as pneumonia, which don't leave any markings in bones and are often misdiagnosed in historical documents. "There's a lot of potential for thinking about what kind of pathogens could end up in your dental calculus," says Austin, now at the University of Oslo.

She decided to use the Terry collection because it contains more than 1700 skeletons of individuals, as well as their death certificates. If she and her team could find evidence of disease in calculus, they could compare their findings with the recorded causes of death.

Austin began by scraping the dental calculus of several individuals who had been diagnosed with tuberculosis (TB), syphilis, and pneumonia and sequencing the DNA traces it contained to make a profile of the bacteria that once lived in their mouths. What she found in one individual—whom the team named the St. Louis Individual—stood out: a diverse collection of microbes, the most abundant of which, such as *Acinetobacter nosocomialis* and *Klebsiella pneumoniae*, commonly cause pneumonia and hospital infections even today. They were direct evidence of the pneumonia that killed the man, according to his death certificate.

"Recovering biomolecular evidence that completely aligned with the recorded cause of death was just astounding for us," Zuckerman says. "It really changed our understanding of what dental calculus can tell us about the past."

But the researchers felt an obligation to probe further, into the life of the St. Louis Individual. "We didn't come to the Terry collection thinking that it was neutral," Zuckerman says, given the way Robert J. Terry, a professor of anatomy at Washington University in St. Louis (WUSTL), went about building the collection that now bears his name. Taking advantage of the lack of legal protections for marginalized people in the 19th and early 20th century, he amassed thousands of bodies of people who died in public institutions in St. Louis—most of them poor or institutionalized—and whose families didn't claim them within 36 hours after death. "These are individuals who went through a process where their identity was stripped from them," de la Cova says. "From the beginning, they were dehumanized." More than half of the individuals in the Terry collection are Black.

"It was clear that we needed to spend more time on this discussion of structural racism in St. Louis, particularly in relation to the medical profession," says Geoff Ward, a historical sociologist at WUSTL who helped with the contextual work on the St. Louis Individual. In a lengthy transparency statement in the paper—the result of feedback from colleagues from different scientific fields—the researchers outlined their efforts to "rehumanize" the St. Louis Individual and show how structural racism, from poor-quality medical care for Black people to physical violence, shaped his life and death. They hoped to "bring some of the St. Louis Individual's life history, previously obscured and erased, into broader recognition, fostering a shared remembrance of him and others in the Terry collection with similar experiences."

The team found, for example, that his skeleton showed many telltale signs of a hard life. He had a fractured jaw that had healed poorly—a possible sign of physical violence—several cavities, missing teeth, abscesses in the mouth, gingivitis, and periodontitis, all signs of poor health care. His skeleton also shows signs of a TB infection, although the researchers didn't find traces of the bacterium that causes the disease in the plaque.

Still, "It was a little bit difficult to really see this as a study of an individual, given how little access we had to the details of his life," Ward says. So the researchers supplemented their research with a review of historical documents. They used newspaper clippings to reconstruct the medical context of 1930s St. Louis, including how Black people would often delay seeking medical care because of distrust of medical institutions and how conditions at City Hospital #2 were reportedly worse than at the local zoo, according to a 1924 article in *The Pittsburgh Courier*. Jim Crow laws and local anti-Black political violence likely also worsened things for people like the St. Louis Individual. His "life was likely socially, mentally, and physiologically stressful," the researchers write, which could have made him vulnerable to a fatal pneumonia, a rare cause of death for young men even before widespread antibiotics, Zuckerman says. These very same injustices, the researchers say, allowed his body to end up in the Terry collection.

Sabrina Sholts, curator of biological anthropology at NMNH, sees the study as part of the field's broader effort to move "towards more ethical practices, and [have] conversations and priorities on fairness and



justice." Other controversial collections, such as the Samuel George Morton Cranial Collection at University of Pennsylvania Museum of Archaeology and Anthropology, for example, have recently sparked a reckoning with the racism that built them (*Science*, 9 July 2021, p. 148).

Austin, Zuckerman, and their colleagues are now working with the Smithsonian and other institutions to create new guidelines for studying anthropological collections in a more ethical way, respecting both the individuals in the collections and their modern-day communities. Since last year, NMNH no longer approves new research requests on Black individuals in their collections, Sholts says—which means the current study would now be off-limits. In May, the Smithsonian also adopted a new policy that allows its museums to share ownership of or return entirely collections based on ethical considerations, such as lack of consent. "There's so much potential to possibly identify relatives of these individuals and to offer returns," Sholts says. Even if families can't be traced, Watkins says researchers can take action. "Nothing should happen before [the] descendant community is engaged—and it needs to be Black folks," she says.

Although it's too late for this for the St. Louis Individual, whose anonymity will make it nearly impossible to find his family, the researchers are now planning to engage with community members in St. Louis to raise awareness of their findings. As Zuckerman puts it, "We want to take the messages in this paper to encourage everyone to remember these are once living individuals." ■

RESOURCES

A cleaner way to mine clean-energy mainstays

An electric field can reduce the need for polluting chemicals to extract rare earth elements

By **Dennis Normile**

Electric cars, wind turbines, and LED lighting all help keep the environment clean, but making them can be a dirty business. The high-performance magnets in motors and generators and the glowing phosphors in LEDs and flat screens all depend on substances called rare earth elements (REEs). And capturing REEs from the clay deposits in which many are found requires leaching agents that pollute soil and groundwater.

Now, a Chinese group has developed—and tested on tons of soil—an approach called electrokinetic mining that relies on electric currents to free the REEs, sharply reducing the need for polluting chemicals. The strategy, described this week in *Nature Sustainability*, could be "a game changer, providing that it is feasible at a large scale," says Anouk Borst, a geologist at KU Leuven.

Despite their name, REEs are fairly abundant in Earth's crust. It's just hard to find deposits that are economical to mine. Heavy REEs—those with high atomic numbers, including dysprosium, yttrium, and terbium—are most commonly extracted from masses of clay formed through eons of weathering of igneous rocks such as granite. In these "ion-adsorption" deposits, the elements are adsorbed—or stuck—to the surface of clay particles. They are usually extracted by pumping large quantities of ammonium sulfate or a similar solution into the ground. The leachate pulls REEs from the clay and percolates down to bedrock, where it is collected for processing.

All that can contaminate water and soil, not to mention lay waste to large tracts of land. And roughly 80% of the world's supply of heavy REEs come from ion-adsorption deposits in southern China and adjacent parts of Myanmar, where environmental regulations are poorly enforced and illegal mining is common. (The light REEs—cerium, neodymium, and praseodymium—are typically found in hard rock and are mined in a different way.)

Gaofeng Wang of the Chinese Academy of Sciences's Guangzhou Institute of Geochemistry (GIG) and his colleagues thought electrokinetic technology might offer a cleaner alternative. The approach, in which electrodes on the top and bottom of a volume of soil induce an electric field, speeding the movement of the leaching agent and the ions it extracts, is already used in soil remediation and has been proposed for copper and gold mining. It has "the real potential to outperform traditional mining techniques in terms of efficiency, environmental impacts, and economics," says Riccardo Sprocati, a specialist in the technology at the Technical University of Denmark.

The Chinese team started with a benchtop experiment, then scaled up to 20 kilograms of material, and finally moved to a field test at an actual ion-adsorption deposit, trying the technique on a 14-ton hunk of clay. The method extracted a higher percentage of the REEs more quickly than conventional leaching and needed less ammonium sulfate. It also left the soil cleaner and reduced contaminating elements in the leachate, which could simplify processing. The team calculates that the process could cut mining costs by about two-thirds.

Gareth Hatch, a rare earths expert at the Strategic Materials Advisory, a consulting firm in Manchester, England, notes that whether the technique can be scaled up "remains to be seen." The group's next test will include about 2000 tons of soil, where they will try "to optimize operating conditions," says geochemist Hongping He, director of GIG and co-author on the paper. They will divide the site into sections to keep the electric current and voltage low enough to avoid harming surrounding soil, vegetation, or fauna, He says. And they have struck an agreement with a major rare earth supplier to test the process on an even larger scale.

"As with all mining methods, it will still impact the environment," says Henning Prommer, an environmental engineer at the University of Western Australia, Perth, whose group has worked on applying electrokinetic mining to gold and copper. But, he says, "Given the crucial role that REEs play in our ambitions for a renewable energy infrastructure, any reduction in the environmental impact of mining is welcome." ■

HARASSMENT

Prominent astronomer barred after complaints

Tim de Zeeuw had a pattern of "extremely unacceptable" behavior, Leiden University says

By **Cathleen O'Grady**

A stellar international career in astronomy ended in disgrace on 18 October when Leiden University said it had "removed" a professor, later revealed to be prominent theoretical astronomer Tim de Zeeuw, for what it called "extremely unacceptable" behavior toward women colleagues. De Zeeuw, 66, will not be allowed to return to the university, but will keep his job and salary until he retires.

The Max Planck Institute for Extraterrestrial Physics, where he had an affiliation as well, has severed ties with De Zeeuw and removed his profile from its website; the European Southern Observatory (ESO), which De Zeeuw led from 2007 to 2017, says it has banned him from its premises and will revoke access to his IT account.

Leiden University has not made public a report from an independent committee that investigated complaints against De Zeeuw. But a 21 October online column by Executive Board President Annetje Ottow, addressed to the academic community, offered some details about the panel's findings. "We are talking here about … abuse of power, gender discrimination and the systematic vilification and belittling of staff," Ottow wrote. "It also includes inappropriate behaviour with an element of sexual intimidation: ranging from comments right down to unwelcome physical contact with one of the members of staff. All of this was under the constant threat of harming the complainants' careers."

De Zeeuw, in a statement sent to *Science* via his lawyer on 26 October, acknowledged having been "unpleasant and impatient in an old-fashioned way," but said he disagreed with the university's decision. "It has never been my intention to hurt or harm people. I am very sorry that people have experienced my behaviour as negative," he stated. His lawyer, Merienke Zwaan, added that media reports about De Zeeuw's "sexually transgressive behaviour towards women" were incorrect.

De Zeeuw is a "major figure" in astronomy, says Dave Clements, an astrophysicist at Imperial College London. He was appointed as a professor at Leiden University in 1990 and became director of the Leiden Observatory in 2003. From 2007 to 2017 he was director general of ESO, a 16-member intergovernmental organization headquartered in southern Germany that operates some of the world's most advanced telescopes in Chile.

Several sources who asked to remain anonymous told *Science* De Zeeuw has a reputation for being "power hungry" and for behaving "weirdly" around women, with reports of inappropriate behavior stretching back decades. An astronomer who worked at ESO as a graduate student while De Zeeuw led the institute says he was flirtatious with her and inappropriately touched her in social settings, including running his hand down her back and hugging her from behind. The researcher says she did not feel she could report the behavior but found that other women had similar experiences.



Dutch astronomer Tim de Zeeuw—seen here at the inauguration of the Extremely Large Telescope in Chile in 2017—acknowledged his behavior was "unpleasant and impatient in an old-fashioned way."

PHOTO: MARIO RUIZ/NEWSCOM

Another woman who worked closely with De Zeeuw as a junior astrophysicist at ESO more than a decade ago says he used demeaning language, such as calling her a "good girl," and that she frequently felt uncomfortable when she was alone in the office with him. Although she considers her own experience to be relatively mild, she was not surprised to hear about the independent panel's findings. Given his general demeanor, the belittling and intimidating behavior described by Leiden University was "just another little step," she says.

Leiden University reportedly asked its Complaints Committee for Unacceptable Behaviour to launch an investigation after four women at the observatory filed a complaint with the dean of the Faculty of Science in May. Although the university has publicly announced the committee's verdict, it has not mentioned De Zeeuw by name, referring to him as "a professor" instead. It wasn't until 25 October that the Dutch newspaper *NRC* first published De Zeeuw's name. The statement De Zeeuw's lawyer sent to *Science* a day later confirmed he is the accused scientist.

The decision to withhold the name set off a week of uproar and speculation that led a few colleagues to publicly deny involvement. "If you wonder whether I am the prof who was dismissed at Leiden University, it is not me," Christoph Keller, director of science at the Lowell Observatory and a guest professor at the Leiden Observatory, tweeted on 20 October. But in her column, Ottow defended the secrecy as well as the decision not to fire the accused. "There are good reasons for this relating to employment law," Ottow wrote. "Make no mistake, this is a very drastic measure for him," she added in an interview in *NRC*. "He is placed in total isolation; he is not allowed to have contact with staff or to enter the building." Others say De Zeeuw came out relatively well. The university's penalty amounts to an "unlimited sabbatical," Clements says.

The Royal Netherlands Academy of Arts and Sciences announced on 28 October that it had suspended De Zeeuw's membership, and he had resigned in response. An academy spokesperson told *Science* in an email that the resignation cut short a more thorough inquiry that would have determined whether the suspension should be permanent.

In her column, Ottow acknowledged the university had received signals about De Zeeuw's behavior before this spring, and said the university had to do better in the future. "It was noticed but regrettably, not enough was done about it," she wrote. "For this to have gone on for so long means that the work environment was not safe enough." ■



PHOTO: CHRIS WATTS/UNIVERSITY OF HOUSTON

Master teachers in Houston, part of the Robert Noyce Teacher Scholarship Program, learn to design science experiments using balloons.

U.S. SCIENCE POLICY

NSF to end cost-sharing requirement for some grants

Instrumentation and teacher training programs will no longer ask institutions to provide matching funds

By **Jeffrey Mervis**

Several U.S. government research programs require financial buy-in from institutions when their researchers apply for a grant or new instrument. The rationale for cost sharing—which can amount to half of the size of the award—is to stretch federal dollars and guarantee that every grantee has a stake in the project. But many institutions, including those serving rural areas and students from groups underrepresented in science, can't raise enough money to even compete for the grant.

So this year, Congress directed the National Science Foundation (NSF) to eliminate the requirement in two of the five agency programs that require cost sharing and see what happens. For the next 5 years, NSF will no longer require universities and other organizations to cover 30% of an award from its major research instrumentation (MRI) program, which funds new equipment. It is also ending the 50% match required by two of the four funding tracks in the Robert Noyce Teacher Scholarship Program, which trains math and science teachers.

The change was tucked into the new CHIPS and Science Act aimed at improving U.S. competitiveness with China, which President Joe Biden signed into law in August. Advocates say it's long overdue. "I'm hoping that we'll see an expanded landscape of institutions getting these grants, and that such diversity will strengthen science everywhere," says Cheryl Hayashi, provost of science at the American Museum of Natural History in New York City, which in the past has had to go to great lengths to line up the matching funds needed to win MRI and Noyce awards.

But some observers worry about possible negative repercussions. Requiring NSF to foot the entire cost of MRI and Noyce awards will mean fewer or smaller grants unless Congress increases each program's budget. (MRI's $75 million budget now supports some 150 awards annually, and Noyce makes about 60 to 70 grants a year from its $67 million budget. MRI awards range from $100,000 to $4 million, and Noyce grants can be as large as $3 million over 6 years.)

A more level playing field is also likely to generate more applications, making for even fiercer competition. Ironically, the result could be fewer awards to the very institutions the waiver is meant to aid.

"I think [the change] will open the floodgates," says Timothy Ramadhar, an organic chemist at Howard University, a historically Black institution in Washington, D.C., who recently won an MRI award for a single-crystal x-ray diffractometer to analyze molecular structures. And if NSF responds by providing smaller grants, he says, "institutions may have to settle for cheaper instruments. Maybe it'll be something that's good for teaching but not good enough to support cutting-edge research."

The CHIPS act is the latest congressional statement on cost sharing at NSF. For decades cost sharing was a routine requirement in many NSF programs. But in 2004 the agency decided it was discriminatory and dropped the requirement.

Congress thought that was too drastic a step, however. In 2007 it mandated cost sharing for the Noyce and MRI awards and told NSF to take another look at the pros and cons of cost sharing. That review led to a 2009 policy that limited cost sharing to five agency programs, including its engineering research centers program and the Established Program to Stimulate Competitive Research, which earmarks funds for states that receive little agency funding.

The new law orders NSF to report back in 5 years on how the waiver for MRI and Noyce has affected participation and the quality of the research, as well as whether it should become permanent. It also requires NSF to assess its impact on the demographics of the applicant pool. (Legislators didn't have baseline data because NSF doesn't release information on applicants to individual programs.)

One question is whether the waiver will result in more proposals from institutions that can't currently afford to compete. The MRI program currently limits institutions to submitting three applications per year, and top research universities, able to afford the cost sharing, routinely hit that cap to improve their odds of winning. In 2012, for example, the University of Oklahoma won three MRI awards.

"We didn't expect it," says meteorologist Kelvin Droegemeier, who at the time was vice president of research at the university, one of the 146 R1 institutions that perform the most research. "But we were able to come up with the required match" of $560,000, recalls Droegemeier, who led NSF's earlier cost-sharing review by the National Science Board and later served as science adviser to former President Donald Trump.

With roughly one-third of that sum to meet cost-sharing requirements in any given year, Gerald Blazey, vice president

for research at Northern Illinois University (NIU), can't afford to reach the cap. So NIU, an R2 institution, has typically submitted only one MRI proposal a year. It has won five MRI awards in the program's 30-year history, whereas some major research universities have snared more than 50.

Even without the matching requirement, Blazey must still find the money to pay for operations and maintenance of any new NSF-funded instrument. NSF imposed the cap on applications because it feared research projects might suffer or new instrument might be underutilized if universities overextended themselves. "We want to ensure that institutions are committed to the operations and maintenance of what are, typically, expensive, durable, shared-use instruments with a long life span," says Alicia Knoedler, who leads the NSF office that oversees the MRI program.

Some researchers hope NSF's new rules, expected out later this year, will remove that cap. "I'd like to see an open competition, like NSF does for most of its programs, and then fund the strongest proposals," says Pamela Clarke, head of Howard's research development office. Howard, which wants to regain R1 status by 2024, has won an MRI award in each of the past 4 years, she notes.

Another open question for NSF is whether the waiver will encourage institutions to ask for more money. "The size [of the proposal] is dictated by cost sharing," says Paige Evans, a science educator at the University of Houston who in 2018 won a $2.8 million Noyce award to train two cohorts of 15 high school teachers. Evans notes she increased her request at the last minute after university officials said they were boosting the size of the match.

The new policy could also affect how researchers go about assembling proposals. For example, before microbiologist Matthew Fields of Montana State University could ask NSF to fund a new $1.1 million digital fluorescent microscope for the Center for Biofilm Engineering that he leads, Fields first had to convince a regional foundation, the M.J. Murdock Charitable Trust, to provide some matching funds. Such conversations often make for sharper proposals and better science, Knoedler says.

Congress wants to make sure institutions don't skimp on in-house support for an MRI instrument or Noyce grant they didn't help pay for, say Democratic staffers on the House of Representatives science committee, which wrote the CHIPS provision. That possibility also worries Droegemeier.

"You need to be careful not to set [institutions] up to fail," he says. "You don't want to have them fumble the money they receive." ■

SCIENCE AND ENVIRONMENT

After Lula's win, 'a huge relief!'

Many in Brazil's scientific community abhorred Jair Bolsonaro. But his successor faces major challenges

By **Sofia Moutinho**

It was "a huge relief!" That's how Luiz Davidovich, a physicist at the Federal University of Rio de Janeiro's main campus and former president of the Brazilian Academy of Sciences, describes his feelings early on the evening of 30 October when it became clear Brazilian voters had ousted populist far-right President Jair Bolsonaro and given his left-wing rival, former President Luiz Inácio "Lula" da Silva, an unprecedented third term.

The sentiment is widely shared in Brazil's scientific community, where many feared a second term for Bolsonaro might be catastrophic for issues they care about, including support for science, climate policy, and deforestation. Lula ended up with 50.8% of the vote in the second round, the thinnest margin since Brazil's return to democracy in 1989. "Now we have the chance to start rebuilding the country's science and education, and to resume protecting the Amazon forest," Davidovich says.

> **"Brazil and the world need the Amazon alive."**
> **Luiz Inácio "Lula" da Silva**, Brazilian president-elect

Bolsonaro had stoked doubts about the election's fairness for months, and early this week, his supporters blocked roads all over the country to protest what they say was a rigged result. In a very short speech on 1 November, Bolsonaro did not formally concede, but his chief of staff later said the transition of power would begin.

Deforestation in Brazil exploded under Bolsonaro, after dropping during Lula's first stint at the helm, between 2003 and 2011. In his victory speech, Lula said he would again prioritize environmental protection, promised to crack down on illegal deforestation and mining, and signaled an openness to international cooperation to protect the rainforest. "Brazil and the world need the Amazon alive," Lula said. "We are ready to resume our leading role in the fight against the climate crisis."

Hours after the results were in, Norwegian environment minister Espen Barth Eide said his country would resume contributions to the Amazon Fund for Forest Conservation and Climate Protection, which supports programs that prevent and combat deforestation. Norway was the fund's largest contributor until it halted payments in 2019, after the Bolsonaro administration unilaterally changed the fund's targets. About $480 million in frozen contributions will now be released. Other countries welcomed Lula's promises as well.

But so far, details on Lula's environmental policies—or how he plans to balance them with bolstering the economy and meeting energy demands—have been scant. Mercedes Bustamante, an ecologist at the Federal University of Brasília and member of the Intergovernmental Panel on Climate Change, says the government should adopt a zero-tolerance policy for environmental crimes such as illegal mining. It also needs to rebuild the institutions that monitor and fight deforestation, which were weakened by the previous administration, she says (*Science*, 27 May, p. 910).

As to science, another 4 years of Lula may not be enough to repair the damage from the past 4 years, including obsolete lab equipment at public universities, a lack of research grants, and a persistent brain drain, says Renato Janine, president of the Brazilian Society for the Advancement of Science. And science will have to compete with other pressing needs—including poverty and hunger. Even though Brazil is a major food producer, the United Nations in July added the country to its Hunger Map of countries where more than 2.5% of the population faces undernourishment, 8 years after removing it from the list. "There are a lot of needs to tackle at the same time," Janine says.

But with the economy faltering, an already-approved budget for 2023 that includes cuts in research and education, and Bolsonaro's Liberal Party holding the largest number of seats in Congress, Lula's choices will be limited. "It is difficult to say what he will be able to achieve," says Luiza Duarte, a political scientist and research fellow at the Wilson Center in Washington, D.C., "but he is a very skilled politician who was able to make alliances with political enemies before." ■

Sofia Moutinho is a science journalist in Rio de Janeiro.

eppendorf & Science

PRIZE FOR NEURO BIOLOGY



Meet the Winner 2022

Eppendorf & Science Prize for Neurobiology
Congratulations to Ann Kennedy, Ph.D. on winning the 2022 Eppendorf & Science Prize for her work on the neural population dynamics that generate and maintain internal motivational states. By comparing the activation of neurons in multiple deep brain regions, Dr. Kennedy can identify differences between them that point to the role each region plays in shaping survival behaviors such as fighting or fleeing. Her work contributes to our understanding of how our emotional states arise and how they influence our actions.

The annual US$25,000 Eppendorf & Science Prize for Neurobiology honors scientists, like Dr. Kennedy, for their outstanding contributions to neurobiological research. Ann Kennedy is the 21st recipient of this international award. The winner and finalists will be honored at a Prize Ceremony on November 13, 2022 at the Hard Rock Hotel in San Diego, USA. To register to attend this event in person at 6:00 pm PST or to watch virtually live at 6:45 pm PST, go to event.eppendorf.com/prizeceremony or scan the QR code.

You could be next to win this prize.
If you are 35 years of age or younger and currently performing neurobiological research, you could be next to win the 2023 Prize. Deadline for entries is June 15, 2023.

eppendorf Science AAAS

Learn more at: eppendorf.com/prize

AAAS® and Science® are registered trademarks of the American Society for the Advancement of Science, USA. Eppendorf® and the Eppendorf Brand Design are registered trademarks of Eppendorf SE, Germany. All rights reserved, including graphics and images. Copyright © 2022 by Eppendorf SE. Photography: Saverio Truglia

URBAN OASIS

In Berlin, pioneering research into urban ecology has found surprising biodiversity in the city's green spaces

By **Gabriel Popkin**, *in Berlin*



PHOTO: MAURICE WEISS

A modest cemetery in the heart of this 3.6-million-strong capital city is hardly a likely nature haven. Yet it was here in the Domfriedhof, in Berlin's Mitte district, that Anita Grossmann, an ecologist at the Technical University of Berlin (TU Berlin), turned up 19 wild bee species in a single parched and untended patch of grasses and flowers on the graveyard's edge.

Additional surveys soon revealed this metropolis buzzes with bee diversity. The researchers tallied 106 species living in 49 grassy plots around and just outside Berlin, they reported earlier this year. Inner-city spaces such as the cemetery are "perfect for wild bees," Grossmann says. The insects love the warmth radiating from pavement and buildings—what's known as the "urban heat island." And they thrive in the diverse plant communities found outside of manicured and often chemical-soaked fields and gardens.

"You don't need a lot of space" if you're a bee, Grossmann explains. "You just need pollen, nectar, and nesting space."

The findings are the latest to emerge from one of the world's longest series of studies of a city's ecosystems. Over more than 6 decades, Berlin researchers have helped launch urban ecology as a discipline, producing sometimes surprising results that have helped promote conservation efforts and turn their city into one of the world's greenest capitals.

To be sure, the relatively modest green spaces found in Berlin and other cities cannot compensate for the destruction of larger habitats, nor stop the extinction crisis that threatens an estimated 1 million species worldwide. But a growing chorus of ecologists and environmentalists says urban habitats have been overlooked for too long, to the detriment of many of the plants and animals conservationists are trying to protect. And the Berlin study, they say, highlights the kinds of intriguing discoveries that can reward scientists willing to trade pristine forests for weedy lots and pocket parks.

Some of the findings have challenged ecological orthodoxies: that small, isolated ecosystems cannot sustain meaningful plant and wildlife populations, and that



In Berlin's Südgelände, a former railway yard has given way to a protected forest that supports numerous species.

PHOTO: MAURICE WEISS

CITIES ARE GENERALLY known for displacing nature, not conserving it. Buildings, roads, and parking lots obliterate forests and wetlands while cars, factories, and power plants pollute the air and water. Nighttime lights disrupt foraging by nocturnal animals. Wild creatures, it's generally assumed, can find better homes elsewhere.

But much of elsewhere is becoming too inhospitable. In Germany, for instance, the total biomass of flying insects in the nation's protected areas has plummeted by three-quarters since 1963, researchers reported in 2017 (*Science*, 12 May 2017, p. 576). A follow-up study published in 2019 found similar results for insects in nearly 300 forest and grassland sites. Both studies pointed the finger largely at rural land trends. Farms have expanded and consolidated to blanket much of the landscape, and agricultural chemicals have wiped out native plants and insects, leading to knock-on declines of birds and other creatures.

Studies of Berlin's urban ecology began well before such biodiversity crises hit the headlines. In the 1950s, Herbert Sukopp was a botanist at TU Berlin, located in the then-divided city's western sector, controlled by the United States, the United Kingdom, and France. (The Soviet Union controlled East Berlin and East Germany, making it difficult for researchers such as Sukopp to leave West Berlin.) As Sukopp began to investigate his city's forgotten spaces, he found habitats unlike any others: World War II had reduced much of Berlin to rubble and dramatically reduced the population of what was once among the world's largest cities—leaving extensive areas abandoned, especially former industrial zones.

At a time when most ecologists sought out remote, pristine ecosystems, Sukopp and his colleagues honed in on these distinctive disturbed landscapes, known in German as *Brachen*. They reminded him of volcanic rubble—ecological clean slates ripe for species to colonize—he recalled in a recent film.

The Berliners were the first to study how city habitats shaped the lives of their nonhuman residents. "This was a new idea of urban ecology," says Jürgen Breuste, an ecologist at the Paris Lodron University of Salzburg. "It developed really in Berlin and nowhere else in that format." Sukopp went so far as to create "red lists" of plants and animals that were rare and threatened specifically in Berlin—possibly the first urban use of the extinction risk metric, which is typically applied at larger scales.

The work carried risks. When the ecologists tried to survey abandoned railyards, which were controlled by East Berlin, police sometimes chased them away, recalls ecologist Ingo Kowarik, who studied with Sukopp and later became a professor at his university.

But the results justified the peril. The researchers discovered, for example, that in areas dominated by nonnative species such as black locust trees from North America, many organisms, such as ground beetles and spiders, were as abundant as they were in areas dominated by indigenous plants.

Even many of Berlin's red-listed species were making a good living in these "novel ecosystems"—a term coined by Australian ecologist Richard Hobbs. (Less than 6% of Berlin's endangered plants are threatened by nonnatives, according to a recent survey by experts led by Kowarik.) The mix of species often includes plants of varying heights and structures, Kowarik notes. That variation can provide more niches for insects and other animals than do many managed landscapes.

Starting in the 1980s, West Berlin began to create legally protected nature reserves in some of its *Brachen*. Then in 1989, the fall of the Berlin Wall opened a new set of wastelands for Western researchers to study. But it also triggered a multidecade real estate boom, as Berlin, once again the capital of a united Germany, prospered. As politicians and investors eyed the *Brachen* and other areas for development, ecologists armed themselves with their biodiversity data and joined political battles, eventually helping persuade city officials to protect key sites.



Ecologist Ingo Kowarik has helped lead innovative studies of Berlin's urban ecosystems.

One such area is Südgelände, a former railyard on the south side of the city. On a recent visit, Kowarik reveled in the 70-year-old forest that has grown up in the park, where he has intensively studied the interplay of natives and newcomers. "These species evolved in different botanical realms

nonnative species are always ecologically harmful. Others have shown Berlin's "wastelands"—former industrial sites colonized by novel mixtures of nonnative and native species—can harbor as much biodiversity as more natural sites. Grasshoppers, sand lizards, nightingales, and skylarks that are declining or threatened elsewhere have been found thriving in the city's green spaces. Bees are just one of several groups of organisms that often seem to prefer heavily urbanized areas.

"Cities are not these hostile places; cities are islands of biodiversity," says Sascha Buchholz, an ecologist at the University of Münster who has worked in Berlin for more than a decade. The world's cities, he says, offer "a chance for mitigating the biodiversity crisis."

and now they have come together," he said. "That's really exciting!"

A few kilometers north at the 300-hectare former Tempelhof Airport, which was decommissioned in 2008, grazing sheep and hay-cutting farmers now maintain a sprawling grassland. The site has become a key refuge for Eurasian skylarks, a bird that requires open fields that, in the countryside, have been largely overrun by crop monocultures. Grasslands are now among the most threatened ecosystems in central Europe.

"To integrate so many unusual green places into the city, with existing wild vegetation—I think this is a unique feature of Berlin," Kowarik says.

THE BERLIN SCHOOL OF ECOLOGY, as it came to be known, showed that sites like Südgelände and Tempelhof support rich and often surprising biodiversity. The next step was to explain why. In 2016 Kowarik and his colleagues, including Moritz von der Lippe, Buchholz, and Grossmann, launched a project called CityScapeLab Berlin to do just that. Borrowing an ecological gradient concept developed in the United States and Australia, the researchers quantified and mapped the degree of urbanization throughout Berlin. Such maps can help reveal how species respond to "different types of landscape configurations," says Amy Hahs, an ecologist at the University of Melbourne who has helped adapt the method for urban studies. The Berlin researchers also examined a suite of organisms, so their data would not be biased by the preferences of just one or a few species.

To generate statistically meaningful results, they focused on an ecosystem found throughout sandy Berlin: dry grasslands. Such areas can host rich mixes of grasses, wildflowers, and legumes, in part because their poor soils prevent any one species from growing too vigorously and taking over. The researchers ranked 56 grasslands in and around Berlin by a range of factors that might make life easier or harder for the species living in them, such as the amount of pavement nearby.

The researchers also pioneered the use of a metric that describes how habitats are connected to each other in 3D space. It considers not just the horizontal distance between patches, but also factors such as the height and number of buildings that could hinder animals as they try to move from one habitat to another.

In 2017 and again in 2020, the researchers surveyed what lived on their study sites. They put out brightly colored cups of formaldehyde-laced water to attract and trap pollinators. They caught carabids (ground beetles) in pitfall traps, butterflies in nets, and nocturnal moths with light traps. They painstakingly tallied plants and logged climate data.

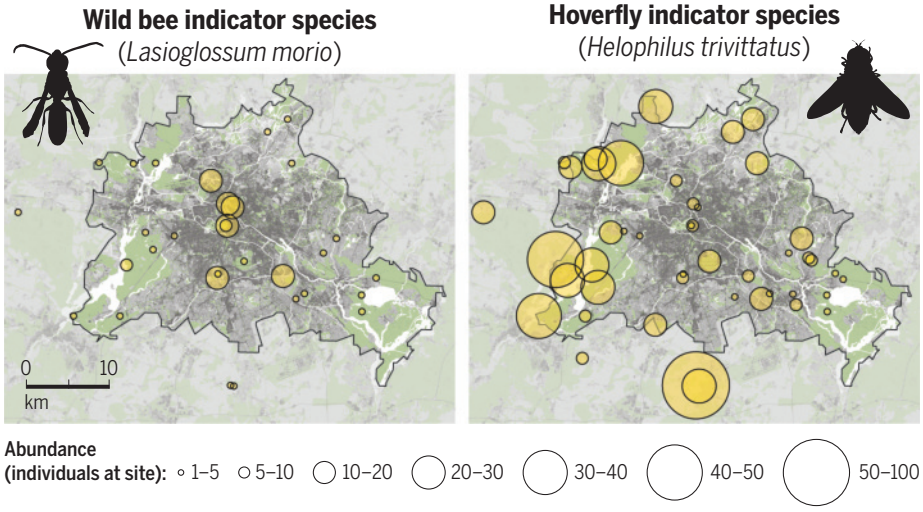
The work was often far from glamorous. In a desiccated grassy patch next to a massive 1970s-era conference center, for example, exhaust-spewing diesel trucks rumbled by just meters from where the scientists collected field data. But such unpromising places often harbored among the rarest plants and beetles, von der Lippe says. "We found a lot of really amazing endangered species on traffic greenery."

The researchers discovered that native plants, wild bees, and ground beetles were at least as diverse in highly urban sites as those located elsewhere, von der Lippe says—including many red-listed species. One reason for the unexpected abundance might be that—in contrast to intensive farming—the regular but more moderate



A buzzing metropolis

Berlin's parks and revitalized "wastelands," such as former airports and railyards, have made it one of the world's greenest capitals. Ecologists have long probed the biodiversity in these green spaces. A recent study found wild bees (below, left) thrive in inner-city sites such as cemeteries and pocket parks. By contrast, hoverflies (below, right) prefer less urban outlying areas. As cities around the globe expand and grow denser, such findings could help planners preserve urban species.





Urban grasslands are a focus of a research project called CityScapeLab Berlin. Even green patches wedged between highways have been found to support a surprising diversity of native plants, bees, and beetles.

CREDITS: (GRAPHIC) K. FRANKLIN/*SCIENCE*; (DATA) A.K. GATHOF *ET AL.*, *OECOLOGIA* **199**, 165 (2022); (PHOTO) SASCHA BUCHHOLZ

ways that humans disturb urban habitats, such as occasional mowing, can actually favor these native species.

One surprise was that areas disturbed by wild boars, which are rampant in Berlin, hosted more threatened grasshoppers and sand lizards than undisturbed areas. Boars are often considered environmentally destructive, but their rooting in the soil for food seems to create valuable niches for certain species, von der Lippe says—much as some human activity does.

Another aid to Berlin's biodiversity could be coming from the many trees and shrubs planted by city officials and residents. The plants help animals move within the urban matrix, von der Lippe suspects, making habitat fragmentation less harmful to urban wildlife than ecologists generally assume.

Ecologists have also found evidence that Berlin can serve as a refuge for species from distant regions. In July, for example, Monika Egerer, an ecologist at the Technical University of Munich (TUM), reported the discovery of a bee in a Berlin community garden that was previously known only from the south of Germany. The finding was part of a survey of 18 Berlin gardens in which Egerer and her colleagues found about 400 plant species, including four on Germany's red list. Like the Brachen, Egerer says, gardens can contain structures—such as dead, decaying wood—that provide critical niches for wildlife.

An abundance of gardens is part of what makes Berlin "an incredibly rich city from a conservation perspective," she says. And that richness can benefit city gardeners, too, Buchholz adds, as abundant bees found in cities can pollinate flowers and vegetables.

The Berlin researchers have also turned up urban losers. Grossmann and her colleagues found far fewer hoverflies, a major group of pollinating insects, in highly urban sites compared with more rural ones. She suspects the small urban grasslands the team studied lacked the moisture and structural complexity the flies need. A study of birds found some species had declined in inner-city areas, and wetland specialists such as dragonflies also fared poorly, Buchholz says.

SIMILAR FINDINGS are now flowing from researchers studying other cities in North America, Australia, Central America, and elsewhere. Wild bees, for example, appear to be thriving in many of these urban areas. So is a less celebrated group of insects, parasitoid wasps, which lay their eggs inside other insects and spiders. (Hahs likens them to "the large carnivores" of the urban environment.)

But these studies have also found discouraging signs. A global sampling of urban soils, for example, found that cities house a relatively limited set of bacteria, algae, amoebae, and fungi. "It seems to be more or less the same community everywhere," says Nico Eisenhauer, an ecologist at the German Centre for Integrative Biodiversity Research.



Sand lizards thrive in some of Berlin's wild spaces, especially those disturbed by wild boars rooting for food.

PHOTO: SASCHA BUCHHOLZ

And not everyone shares the Berlin researchers' optimism that novel urban ecosystems offer refuges from the increasingly perilous countryside. Doug Tallamy, an entomologist at the University of Delaware, Newark, doubts that nonnative trees, such as those the Berlin researchers celebrate, can support the same mix of insects and birds that Europe's native flora once did. His own studies in the mid-Atlantic United States have found that native trees support larger and more diverse populations of caterpillars—essential food for many birds—than do nonnative trees. A study he is now leading in Europe is producing similar results. "There are not different rules of ecology in Europe versus here," he says.

Breuste cautions against drawing general conclusions. So far, he notes, nearly all urban ecology research has been done in relatively wealthy cities in the temperate zone. "We need many more studies of tropical cities, of cities in dry areas, of cities with very different social-cultural conditions," he says.

Those studies can come none too soon, many researchers say, as urban ecosystems face growing peril. Demographers expect that, by 2050, two-thirds of all people will live in cities. Housing shortages could become severe, and builders and officials are eyeing green spaces for new development. And as people gain wealth, they often spend money in ways that harm biodiversity—using herbicides and pesticides in gardens, for example. Climate change is also predicted to make cities too hot and dry for many species that have long lived in them. "We're making a more and more hostile environment" for urban wildlife, says Wolfgang Weisser, a TUM ecologist.

Some ecologists are working to change that. In Berlin, Weisser has teamed with a landscape architect to develop a "biodiversity-friendly design" for a residential and commercial district being planned for the Tegel grounds. The proposal, which must be approved by the developers, builds on Weisser's work on two new apartment complexes in Munich; they provide nesting and feeding sites for species known to be harmed by urbanization, including a bat, a sparrow, a woodpecker, and a hedgehog.

In other cities, researchers have persuaded officials to mow lawns less often to allow flowers to bloom for pollinators, and at times encourage residents to do the same. Tallamy urges city and suburban dwellers to rewild their yards with native plants.

But cities could be doing much more to support biodiversity, Hahs says. Her team has found that when 30% of an urban green space is covered by shrubs and other midstory plants, more bats, birds, beetles, and other animal species live there than in a less complex habitat. But to incorporate a shrub layer into urban plantings, she says, green space managers would need to accept landscapes that are not neat and tidy, and find ways to allay concerns that bushes could encourage crime.

"We have this really good body of knowledge now for ecology in and of cities," Hahs says. "What's missing is, how do we translate that into ecology for cities?"

Even in Berlin, researchers say holding on to the wildlife they have uncovered will require an ongoing effort. "The city is rapidly densifying," Egerer says. "Are we going to be able to conserve this high biodiversity?" ■



Wildfires are becoming bigger in the Siberian peatlands, with the 2019–2020 seasons seeing as many wildfires as the preceding 40 years.

PHOTO: AP PHOTO/IVAN NIKIFOROV

CLIMATE CHANGE

Arctic wildfires at a warming threshold

Bigger wildfires in the Siberian Arctic signal release of more carbon to the atmosphere

By **Eric Post**[1] *and* **Michelle C. Mack**[2]

Vast amounts of organic carbon are stored in Arctic soils. Much of this is in the form of peat, a layer of decomposing plant matter. Arctic wildfires release this carbon to the atmosphere as carbon dioxide (CO_2) (*1*) and contribute to global warming. This creates a feedback loop in which accelerated Arctic warming (*2*) dries peatland soils, which increases the likelihood of bigger, more frequent wildfires in the Arctic and releases more CO_2, which further contributes to warming. Although this feedback mechanism is qualitatively understood, there remain uncertainties about its details. On page 532 of this issue, Descals *et al.* (*3*) analyze data from the 2019 and 2020 wildfire seasons in the Siberian Arctic and predict the extent of carbon-rich soils likely to burn in the area with future warming. Critically, they suggest that even minor increases in temperature above certain thresholds may promote increasingly larger wildfires.

Assessment of the relationship between climate warming and the frequency and extent of Arctic wildfires is complicated by several factors. Satellite data of the annual area burned by wildfires in the Arctic may require difficult-to-obtain ground-based validation to improve accuracy. Moreover, multiple factors may interact with warming in complex ways to influence fire occurrence, severity, and extent, such as lightning strikes, rainfall, and fuel load or vegetation cover. Add to this mix the uncertainty that derives from gaps in the geographic representation of data across the Arctic and the challenges seem almost insurmountable. The Siberian Arctic, for example, represents as much as 70% of the terrestrial Arctic, but year-to-year records of its burned area are sparse.

Descals *et al.* compiled multiple satellite-based estimates of the annual burned area for the Siberian Arctic from 1982 to 2020 to analyze associations between burned area and several factors (see the figure). According to their analysis across all sources of satellite data, 2019 and 2020 emerge as the biggest fire years for the Siberian Arctic, accounting for nearly half of the area burned for that region over the entire 39-year period and releasing nearly 150 million tonnes of carbon to the atmosphere. On 20 June 2020, the Russian town of Verkhoyansk set the record for the highest single-day temperature measured above the Arctic Circle (38°C) (*4*). On average, the Arctic region has warmed faster than the rest of the globe. Northern peatlands—including those in Asia, North America, and Europe—currently account for an annual carbon sink of ~100 million tonnes (*5*). The enormous carbon release of 150 million tonnes from the 2019 and 2020 Siberian

[1]Department of Wildlife, Fish, and Conservation Biology, University of California, Davis, Davis, CA, USA. [2]Center for Ecosystem Science and Society and Department of Biological Sciences, Northern Arizona University, Flagstaff, AZ, USA. Email: post@ucdavis.edu

fires demonstrates how quickly northern ecosystems can switch from carbon sinks to carbon sources under the continuous warming of the Arctic.

The authors started with individual single-predictor models, which mostly show exponential increases in burnt area across the Siberian Arctic for each of the individual drivers. These include the increases in temperature, vapor-pressure deficit (the ability of the air to dry the land surface), climatic water deficit (more water being evaporated relative to precipitation), and the number of ignition events presumably related to lightning strikes. Building on the single-predictor models, the authors then created a multivariate model, which revealed that some of the single-predictor drivers can themselves be driven by an increase in temperature. For example, warming can directly increase the number of ignition events and indirectly increase plant water stress by increasing the vapor-pressure deficit. This in turn can dry deeper soil layers and contribute to plant water stress. By linking these processes and identifying the direct and indirect effects of warming on increasing burn area, Descals *et al.* provide insights into what the future of Arctic wildfires may look like under accelerating warming.

According to their analysis, warming of mean summer air temperature past a threshold of 10°C, or of mean summer surface temperature above 17°C, would cause disproportionately large increases in the extent of carbon-rich soils burned in the Siberian Arctic. However, patterns of both local warming (*2*) and vegetation change (*6*, *7*) are highly variable across the Arctic. Therefore, additional studies in other regions of the Arctic that harbor vast expanses of peatland, such as Canada and Alaska (*5*), are needed to test these hypotheses and their general applicability to the Arctic region.

It is worth considering the implications of increasingly frequent and large wildfires for the fate of carbon that is currently locked away in the permafrost soils and sediments that underlie much of the Arctic. Increased combustion of the insulating peat layer can expose more permafrost and lead to the thaw and decomposition of an even larger reservoir of organic matter, releasing carbon that has been stored underground for centuries or even millennia (*8*). Larger and more intense wildfires could substantially accelerate the release of permafrost carbon into the atmosphere (*9*), but this interaction is not considered in current forecasts of Arctic feedback to global warming (*10*). Future studies that link rigorous assessment of wildfires with the dynamics of permafrost thaw in these remote regions are therefore needed to better quantify their impact on climate. ■

REFERENCES AND NOTES

1. M. C. Mack *et al.*, *Nature* **475**, 489 (2011).
2. M. Rantanen *et al.*, *Commun. Earth Environ.* **3**, 168 (2022).
3. A. Descals *et al.*, *Science* **378**, 532 (2022).
4. M. Allen, *Eos* **102** (2021).
5. G. Hugelius *et al.*, *Proc. Natl. Acad. Sci. U.S.A.* **117**, 20438 (2020).
6. C. G. Collins *et al.*, *Nat. Commun.* **12**, 3442 (2021).
7. I. Myers-Smith *et al.*, *Nat. Clim. Chang.* **10**, 106 (2020).
8. E. A. G. Schuur *et al.*, *Nature* **520**, 171 (2015).
9. S. M. Natali *et al.*, *Proc. Natl. Acad. Sci. U.S.A.* **118**, e2100163118 (2021).
10. Intergovernmental Panel on Climate Change, *Climate Change 2021: The Physical Science Basis. Contribution of Working Group I to the Sixth Assessment Report of the Intergovernmental Panel on Climate Change* (Cambridge Univ. Press, 2021).

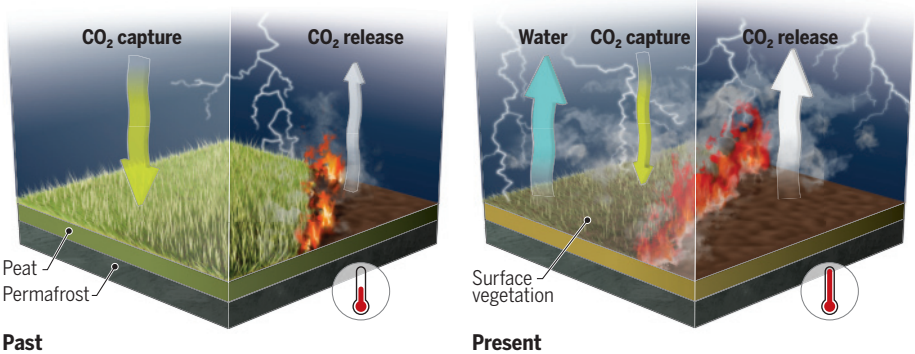
ACKNOWLEDGMENTS

The authors thank P. F. Sullivan for comments on the manuscript.

10.1126/science.ade9583

The effect of Arctic wildfires on carbon release

Arctic wildfires accelerate the release of organic carbon from the soil into the atmosphere, which can strengthen the feedback to warming.



GRAPHIC: V. ALTOUNIAN/*SCIENCE*

Past
Arctic peatlands, forests, and tundra are generally carbon sinks. Cold temperatures and wet soils keep the land relatively moist, which reduces wildfire activity

Present
Higher temperatures dry the peat layer and drive more active weather systems, which lead to more frequent lightning strikes, creating larger fires that release more carbon to the atmosphere.

NEUROSCIENCE

Gene therapy for epilepsy

On-demand inhibition of neuronal activity reduced spontaneous seizures in mice

By **Kevin Staley**

Epilepsy is the predisposition for spontaneous episodes of synchronous increases in neuronal activity, called seizures. The propensity for seizures can be reduced with antiseizure medications. But many patients do not respond (*1*), develop unacceptable side effects (*2*), or respond initially but subsequently develop tolerance (*3*). A closed-loop feedback system provides transient, on-demand treatment in response to a suprathreshold stimulus and is a potentially powerful solution to the problems of medication resistance, side effects, and tolerance (*4*). On page 523 of this issue, Qiu *et al.* (*5*) demonstrate a genetic closed-loop feedback system in mice that is designed to inhibit neurons that participate in seizure activity.

Clinically available closed-loop feedback systems use electrographic seizure detectors and intracranial electrodes; they are not capable of inhibiting neurons and can only be placed in a limited number of locations (*6*). Qiu *et al.* took a different approach to feedback: temporarily inhibiting the activity of all the neurons that participated in the last seizure. To do this, they developed a genetic strategy based on the *Fos* gene, whose expression is up-regulated by neuronal activity, including seizures (*7*, *8*).

The activity-sensitive promoter region of *Fos* was used to drive the expression of a gene encoding an inhibitory protein, voltage-gated potassium channel subunit (Kv1.1, which is encoded by *Kcna1*). Kv1.1 is opened by moderate cytoplasmic membrane depolarization (*9*). The open channel permits efflux of potassium ions and hyperpolarization of the membrane, which reduces action potential generation and neurotransmitter release by the neuron. An adeno-associated virus (AAV) vector encoding the *Fos* promoter and *Kcna1* was used to transfect neurons. When the gene therapy was expressed in cultures of mouse neurons exhibiting spontaneous synchronous activity, multielectrode arrays demonstrated a

substantial reduction in the activity of individual neurons as well as reduced synchronous activation of populations of neurons.

To test the system in the intact brain, Qiu *et al.* injected the AAV vector into the mouse hippocampus, a particularly seizure-prone region of the brain that is also critical for memory formation. After seizures that were induced by the convulsant pentylenetetrazol, they found that the *Fos* promoter drove expression of a reporter gene throughout the hippocampus, particularly in excitatory neurons. This was fortunate because suppression of the activity of inhibitory interneurons might have promoted rather than suppressed seizures. *Fos*-driven expression of Kv1.1 in the hippocampus reduced the severity of seizures induced by pentylenetetrazole 24 hours after a prior seizure that had activated Kv1.1 expression. Seizures were not entirely suppressed, but this is expected: Systemic convulsant treatment broadly affects neurons in the brain, whereas the anticonvulsant treatment was confined to the hippocampus.

Using conditions that more closely approximate human epilepsy, Qiu *et al.* injected the convulsant kainic acid into the hippocampi of mice to render them chronically epileptic—that is, subject to spontaneous seizures (*10*). Seizures were identified by using video electroencephalography (EEG) over a 2-week baseline observation period, then the mice were injected in the hippocampus with the AAV *Fos* promoter-*Kcna1* therapy. After 2 weeks for vector expression, seizures were detected during another 2-week video EEG recording, and the number of seizures was significantly decreased.

It might be expected that the seizure frequency decreased because transient, seizure-induced expression of Kv1.1 increased the interval between seizures. But it was not obviously the case that the intervals increased in this manner. The reason may be that epilepsy is also characterized by frequent, brief bursts of synchronous neuronal activity that generate spikes on the electroencephalogram (*11*). These spikes were sufficient to drive *Fos* activity in animals that were not having seizures and so would be expected to also drive Kv1.1 expression. The populations of neurons that participate in spikes and seizures are thought to overlap considerably, although the extent of this overlap varies with time (*12*). Spike-driven Kv1.1 expression could unlink its expression from seizures, providing a more consistent inhibition of epileptic neurons (see the figure).

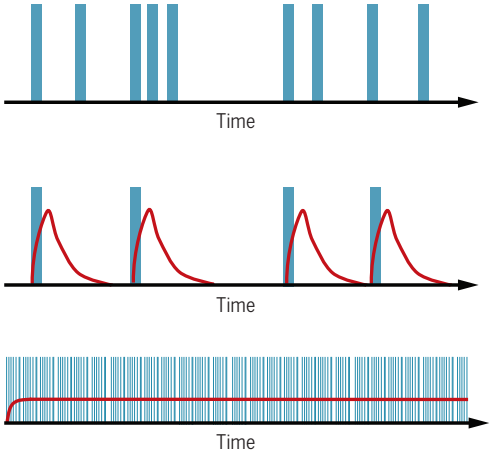
The *Fos* gene has long been studied as a model of how the brain learns from experience through altered gene expression (*7*, *13*). The findings of Qiu *et al.* support the idea that experience in the form of seizures strongly activates the *Fos* promoter. But would the exogenously expressed *Fos* promoter interfere with endogenous *Fos*-driven experiential learning? Qiu *et al.* found no evidence that seizure-induced expression of Kv1.1 interfered with the *Fos* system for experience-dependent learning in nonepileptic mice nor in mice subjected to a seizure 24 hours previously (in whom exogenous Kv1.1 should be maximally expressed). This finding is encouraging for the proposed therapeutic strategy. It also provides a new, if somewhat cryptic, clue about the nature of memory encoding: The memory engram is not influenced by the suppression of excitability in the subset of neurons expressing exogenous Kv1.1.

Would this system operate in human neurons? Qiu *et al.* treated cultures of neurons induced from human stem cells with the AAV *FOS* promoter-*KCNA1* gene therapy. Although these cultures did not generate seizures, convulsants increased neuronal activity, which drove *FOS*-mediated Kv1.1 expression and, in turn, decreased activity. These findings indicate that the *FOS* promoter-*KCNA1* feedback system is operative in human neurons. Whether the vector is also selectively expressed in excitatory human neurons and whether the system can prevent seizures in the human brain remain to be discovered.

The results of Qiu *et al.* describe a sophisticated, localizable new strategy for closed-loop feedback to control seizures. The group has been steadily improving this strategy (*9*), and many elements of the current system are more attractive than hardware-based closed-loop feedback systems. Welcome improvements would include the abilities to tune the threshold and duration of Kv1.1 expression, encode cell-specific expression, and provide a shut-off mechanism. It is also important to find out more about which neurons need to be inactivated—every neuron that is recruited into a seizure, or only those that participate in seizure initiation (*14*)? ■

Modulating neuron activity during seizures

The *Fos* promoter is engineered to drive the expression of voltage-gated potassium channel subunit (Kv1.1, which is encoded by *Kcna1*) in an adeno-associated virus (AAV) vector that is injected into the hippocampi of mice to suppress seizure-inducing neuron activity.



Seizures occur through spontaneous episodes of increased synchronous neuronal activity in the hippocampus at random intervals.

If seizures drive *Fos*-mediated *Kcna1* expression, they are inhibited for as long as the potassium channel protein is in the membrane. Seizures occurring after longer intervals are not prevented because Kv1.1 expression wanes (red).

Frequent brief bursts of synchronous neuronal activity, or **spikes, can also drive *Fos*-mediated *Kcna1* expression**, which would result in more constant Kv1.1 expression and consequently consistent seizure inhibition.

The graphs are illustrative, and *y* axes are not to scale.

Department of Neurology, Massachusetts General Hospital, Harvard Medical School, Boston, MA, USA.
Email: staley.kevin@mgh.harvard.edu

REFERENCES AND NOTES

1. P. Kwan, S. C. Schachter, M. J. Brodie, *N. Engl. J. Med.* **365**, 919 (2011).
2. J. A. Witt, C. Helmstaedter, *Epilepsy Behav.* **26**, 450 (2013).
3. W. Woldman, M. J. Cook, J. R. Terry, *Epilepsy Behav.* **94**, 264 (2019).
4. F. T. Sun, M. J. Morrell, R. E. Wharen Jr., *Neurotherapeutics* **5**, 68 (2008).
5. Y. Qiu *et al.*, *Science* **378**, 523 (2022).
6. K. L. Dell, M. J. Cook, M. I. Maturana, *Curr. Treat. Options Neurol.* **21**, 47 (2019).
7. M. Sheng, M. E. Greenberg, *Neuron* **4**, 477 (1990).
8. J. Y. Joo *et al.*, *Nat. Neurosci.* **19**, 75 (2016).
9. A. Snowball *et al.*, *J. Neurosci.* **39**, 3159 (2019).
10. F. Twele, K. Töllner, M. Bankstahl, W. Löscher, *Epilepsia Open* **1**, 45 (2016).
11. M. de Curtis, J. G. R. Jefferys, M. Avoli, in: *Jasper's Basic Mechanisms of the Epilepsies [Internet]*, J. L. Noebels, M. Avoli, M. A. Rogawski, R. W. Olsen, A. V. Delgado-Escueta, Eds. (National Center for Biotechnology Information, ed 4, 2012).
12. E. C. Conrad *et al.*, *Brain* **143**, 554 (2020).
13. F. T. Gallo, C. Katche, J. F. Morici, J. H. Medina, N. V. Weisstaub, *Front. Behav. Neurosci.* **12**, 79 (2018).
14. L. A. Lau, K. J. Staley, K. P. Lillis, *Brain* **145**, 531 (2022).

10.1126/science.ade8836

GRAPHIC: N. CARY/*SCIENCE*

QUANTUM TECHNOLOGY

An optical interface for quantum networks

A silicon atom embedded in diamond can be entangled with a photon

By **Dorian Gangloff**

Communication networks that use the quantum properties of photons and matter for transferring data are fundamentally more secure than traditional networks. The physical implementation of such a quantum network requires special devices that can convert stored information to a quantum carrier—similar to how a normal computer converts bits on a hard drive to a fiber optic signal (*1*). To enable this conversion, the device must be able to generate quantum entanglement between the stationary quantum bit and the photon used for data transfer. Once generated, the entangled photon and quantum bit can then be used to perform various tasks, such as to generate and send out an encryption key (*2*). On page 557 of this issue, Stas *et al*. (*3*) present a design for a quantum network interface and storage device, called a quantum network node, by using embedded silicon atoms inside a diamond.

There are several fundamental and practical requirements for a quantum networking node, where entanglement is generated and stored. The node must have an efficient interface to convert between photonic and matter "quantum bits," or "qubits"; it must maintain a high degree of control over the matter qubit; and it must be able to convert the information in the matter qubit to a memory qubit for longer-term storage. For practical reasons, the device should also be able to operate close to room temperature instead of extremely low temperatures, which are often required of systems that use superconducting components. The entanglement between the photon and matter qubits must also be producible on a large scale for practical applications, and the device must be able to maintain the stability of the matter qubit long enough for photonic qubits to travel between nodes.

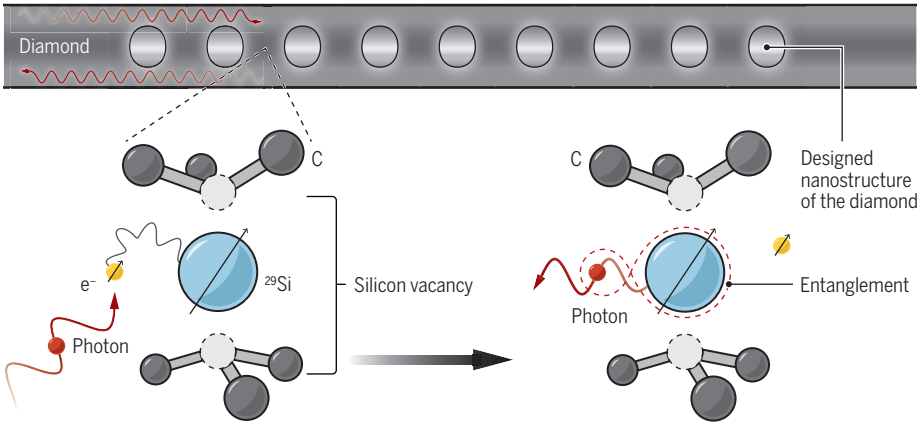
A fully functional node that fulfills all these requirements does not yet exist, but several systems have come close, with varying degrees of success. These include designs using atoms suspended in a vacuum (*4*), semiconductor nanostructures (e.g. quantum dots) (*5*), and defect centers in group IV semiconductor materials such as diamond (*6*). The list of achievements based on the use of diamond defect centers in prospective quantum technologies is long. Among them are the integration of diamond defect centers with photonics and electronics (*7*), their ability to be created and arranged in large arrays (*8*), their information storage time of up to a minute (*9*), and their operation of a qubit that is robust to control and environmental-noise errors (*10*).

Stas *et al*. show that the silicon-vacancy center in diamond is a promising system for producing and maintaining entanglement with photons, which may enable efficient quantum communication between more end users and over longer distances (*6*). The term "silicon-vacancy center" may seem like a misnomer, because it refers to a silicon atom sitting in a vacancy created by two missing carbon atoms in the diamond lattice (*11*). The silicon-vacancy center is the perfect tool for converting quantum information into photons because the photon energy is almost completely undisturbed by the surrounding lattice. The vacancy structure within the surrounding carbon lattice protects the silicon atom from vibrations and the electrical noise of charging and discharging that pervades material surfaces, making it ideal for a nanophotonic light-matter interface. Stas *et al*. use a nanostructured photonic cavity as an efficient interface to the silicon vacancy and its quantum bit consisting of an electronic spin—a fundamental quantum property of particles related to magnetism (see the figure) (*12*).

The authors selected a specific isotope, silicon-29 (^{29}Si), to be embedded at the vacancy site. The magnetically active nucleus in ^{29}Si (compared to nonmagnetic silicon-28, the most abundant isotope of silicon) helps prolong the storage time by a thousand-fold, up to 2 s. Because of the coupling between the spin of the silicon nucleus and that of the electron, the optical property of the diamond nanostructure, which acts as the photonic interface, depends on the state of the nuclear spin. This chain of dependency involving the photon, the silicon nucleus, and its electron, and the optical property of the diamond nanostructure, enables the system to be an effective device to entangle a photon and a long-lived storage element. Once the

A quantum network interface using a silicon vacancy

A silicon-29 (^{29}Si) nucleus in place of two missing carbon nuclei embedded in diamond can be used as an interface between a single-photon quantum bit and the ^{29}Si nucleus used as a nuclear spin quantum memory.



Before entanglement
An incoming photon traveling through the nanostructured diamond toward the silicon vacancy interacts with the ^{29}Si nucleus through the electron quantum bit.

After entanglement
The optical property of the diamond nanostructure depends on the state of the nucleus, which generates an entanglement between the outgoing photon and silicon atom.

GRAPHIC: A. FISHER/*SCIENCE*

Department of Engineering Science, University of Oxford, Oxford, UK. Email: dorian.gangloff@eng.ox.ac.uk

entanglement is established, the photon can be sent out and be used for quantum communication. The entanglement between the photon and the silicon nucleus can be maintained for ~2.5 ms, which is among the longest times recorded, and allows the photon to travel ~500 km before losing entanglement.

To test their device in a practical setting, Stas *et al*. created a working photon-nucleus entangling (PHONE) quantum operation and extended the ability of the typical quantum operation to generate an entangled state between a photon and the nuclear spin of the silicon. During this process, the electron spin provides an added benefit to the system. In the ideal PHONE gate, the logical state of this electron qubit should remain unchanged. However, if its state changes, it would mean that something went wrong with the data transfer. As a result, the electron qubit can be used as a natural error detection scheme, and Stas *et al*. show that by being able to monitor errors, the effective lifetime of the entangled state was extended from 1.5 ms to the reported time of 2.5 ms.

By looking through nine silicon-vacancy centers using optical spectroscopy and picking out the two with the most strain—i.e., where the nanostructure surrounding the silicon atom is the most deformed—Stas *et al*. were able to create a quantum node that operates at 4.3 K. An even larger strain surrounding the silicon vacancy may reduce the temperature sensitivity of the spin qubit more and further extend the storage lifetime (*13*). Although still an extremely low operating temperature, 4.3 K is 43 times warmer than previous systems using silicon vacancy (*14*). The temperature of 4.3 K also crosses a meaningful bar at 4.2 K, which is the boiling point of liquid helium. This means that benchtop cooling systems can be used to operate this device, and the lower cost of entry to experimenting with these systems should enable more research in the future. ■

REFERENCES AND NOTES

1. S. Wehner, D. Elkouss, R. Hanson, *Science* **362**, eaam9288 (2018).
2. A. K. Ekert, *Phys. Rev. Lett.* **67**, 661 (1991).
3. P.-J. Stas *et al*., *Science* **378**, 557 (2022).
4. D. P. Nadlinger *et al*., *Nature* **607**, 682 (2022).
5. R. Stockill *et al*., *Phys. Rev. Lett.* **119**, 010503 (2017).
6. M. Pompili *et al*., *Science* **372**, 259 (2021).
7. N. H. Wan *et al*., *Nature* **583**, 226 (2020).
8. Y.-C. Chen *et al*., *Optica* **6**, 662 (2019).
9. C. E. Bradley *et al*., *Phys. Rev.* **X 9**, 031045 (2019).
10. M. H. Abobeih *et al*., *Nature* **606**, 884 (2022).
11. C. Hepp *et al*., *Phys. Rev. Lett.* **112**, 036405 (2014).
12. C. T. Nguyen *et al*., *Phys. Rev. Lett.* **123**, 183602 (2019).
13. S. Meesala *et al*., *Phys. Rev.* **B 97**, 205444 (2018).
14. M. K. Bhaskar *et al*., *Nature* **580**, 60 (2020).

10.1126/science.ade6964



IMAGE: NASA/JPL-CALTECH

ASTRONOMY

Neutrinos unveil hidden galactic activities

An obscured supermassive black hole may be producing high-energy cosmic neutrinos

By **Kohta Murase**[1,2,3]

After relying on nothing but light to study the cosmos for centuries, the development of multimessenger astronomy in the past decade has revolutionized the field (*1*). The successful detections of the additional messengers—i.e., information carriers other than light—are only possible because of state-of-the-art, large-scale instruments, such as the detectors at the IceCube Neutrino Observatory, which are located a kilometer deep inside the Antarctic ice. High-energy cosmic neutrinos have given rise to both surprises and mysteries since their detections were reported in 2013 (*2*, *3*). On page 538 of this issue, the IceCube Collaboration (*4*) presents evidence for a neutrino source in the data recorded between 2011 and 2020. The origin of the neutrinos has been traced to the Messier 77 galaxy, also known as NGC 1068.

In space, high-energy neutrinos are mainly produced by cosmic rays—i.e., protons and atomic nuclei that are traveling at nearly the speed of light—colliding with matter or radiation, which creates subsequent particles that later decay into neutrinos and gamma rays. Such collisions occur inside astrophysical objects, such as galaxies and black hole jets, or in intergalactic space between those objects and Earth. Revealing the origin of cosmic neutrinos and the relationship among neutrinos, gamma rays, and cosmic rays is crucial to deciphering the fundamental processes that occur throughout the Universe (*1*). Neutrinos are also special because they can travel through dense environments that are impassable for photons, which allow astronomers to "see" behind gas, dust, and radiation obstructions.

Active galactic nuclei (AGNs), which exist at the centers of some galaxies, are energized by either the accretion of gas onto a supermassive black hole and/or the spin of the black hole at the center of the galaxies. They are among the most promising candidate sources of not only the highest-energy cosmic rays but also high-energy cosmic neutrinos observable from Earth (*5*, *6*). In 2018, the first candidate source of high-energy neutrinos was reported (*7*, *8*). The object, TXS 0506+056, is a blazar, which is a type of AGN with jets consisting of particles and magnetic fields ejected to point at Earth with velocities approaching the speed of light. The detection of a high-energy neutrino and data from radio, optical, ultraviolet, x-ray, and gamma-ray observations enabled a comprehensive look at the blazar jet (*7*). However, the observed x-ray and gamma-ray activities were less than what was expected based on the detected neutrinos (*7*, *8*), and a consensus on how to explain this discrepancy has not yet been reached (*1*). So far, searches relying on the population of gamma ray–detected blazars have suggested that this class of AGN alone

[1]Department of Physics, Department of Astronomy and Astrophysics, and Institute for Gravitation and the Cosmos, Pennsylvania State University, University Park, PA, USA. [2]School of Natural Sciences, Institute for Advanced Study, Princeton, NJ, USA. [3]Center for Gravitational Physics and Quantum Information, Yukawa Institute for Theoretical Physics, Kyoto, Japan. Email: murase@psu.edu

The detection of neutrinos from the Messier 77 galaxy suggests that particles are accelerated by the black hole at the galactic center, which is obscured by thick clouds of gas and dust in this artist's concept.

would not explain the amount of all cosmic neutrinos (*9*) coming from every direction in the sky (not every detected neutrino has a well-defined source of origin). This has prompted ideas for other classes of neutrino sources besides blazars.

The IceCube Collaboration (*4*) found an excess of 79 neutrinos over the background associated with NGC 1068 at a statistical significance of 4.2σ (or standard deviations). The result strengthens the previous report of neutrinos originating from NGC 1068 (*10*). This improved significance was driven by updates in the techniques for reconstructing detected neutrino events and data calibration methods, which made the location of the neutrino excess more precisely aligned with the location of NGC 1068. The improved data characterization methods enable more precise estimates for the energy and direction of each detected neutrino observed in the sky.

The source of the detected neutrinos—NGC 1068—is among the brightest and closest AGNs from Earth. It is located in the constellation Cetus, at a distance of ~46 million light-years away. Optical images of NGC 1068 show a rather normal barred spiral galaxy, with a bright starburst inner disk and star-forming regions in the outer arms. The galactic nucleus is classified as a type of AGN that is characterized by emission lines in the optical spectrum. It is also considered a radio-quiet AGN that does not have powerful jets, as seen in blazars. Its nucleus is luminous not only in the optical and infrared bands, but also in ultraviolet and x-ray bands, which are thought to largely come from the accretion disk and hot corona near the supermassive black hole at the galactic center. The black hole is estimated to be ~15 million times as massive as the Sun and is considered to be one of the most obscured supermassive black holes known, being blanketed by thick gas and dust. X-ray observations from the Nuclear Spectroscopic Telescope Array indicate that the x-rays are largely intervened by the gas (*11*), and radio data from the Atacama Large Millimeter/submillimeter Array have suggested a compact gaseous structure with a radius of ~10 light-years around the black hole (*12*). Once the x-ray emission is corrected by accounting for absorption by the gas, NGC 1068 has the brightest x-ray emission among radio-quiet AGNs in the sky region targeted by the IceCube Neutrino Observatory, which helps explain the neutrino excess.

Because the supermassive black hole at the center of NGC 1068 is obscured by gas and dust and is active with radiation, efficient neutrino production is expected to occur near the black hole. The excess of neutrino events observed from NGC 1068 may be explained by converting a part of the power extracted from accreting gas to cosmic rays (*13*, *14*), which then produce neutrinos in subsequent processes. This hypothesis proposed by the theorists is consistent with the gamma-ray data, which have an energy flux much lower than the reported neutrino energy flux (*4*). The existence of such a "hidden" neutrino source has previously been suggested by analysis of the neutrino data from the IceCube Neutrino Observatory and gamma-ray data from the Fermi Gamma-ray Space Telescope (*15*). Radio-quiet AGNs, including NGC 1068, and other low-luminosity AGNs, which are more abundant than blazars and radio-loud AGNs, might help explain the amount of all cosmic neutrinos observed by the IceCube Neutrino Observatory (*9*).

More data are needed to firmly establish NGC 1068 and other AGNs as neutrino sources. Observationally, to push the statistics over the bar of 5σ, next-generation planned detectors, such as IceCube-Gen2 at the South Pole and Pacific Ocean Neutrino Experiment off the Pacific coast of Canada as well as KM3NeT in the Mediterranean Sea and Baikal Gigaton Volume Detector in Russia, will all play important roles. In addition, a synthesis of multiwavelength observations from radio up to gamma-ray wavelengths will continue to be crucial to reveal the multimessenger connections and underlying physics. There is also much progress in numerical simulations for studying accretion flows, outflows like jets and winds, and plasma processes in AGNs (*5*). The continued collection of multimessenger data will offer rich potential for understanding the detailed nature of plasma and particle acceleration in the vicinity of a supermassive black hole. ■

REFERENCES AND NOTES

1. P. Mészáros, D. B. Fox, C. Hanna, K. Murase, *Nat. Rev. Phys.* **1**, 585 (2019).
2. IceCube Collaboration, *Phys. Rev. Lett.* **111**, 021103 (2013).
3. IceCube Collaboration, *Science* **342**, 1242856 (2013).
4. IceCube Collaboration, *Science* **378**, 538 (2022).
5. R. Blandford, D. Meier, A. Readhead, *Annu. Rev. Astron. Astrophys.* **57**, 467 (2019).
6. F. W. Stecker, C. Done, M. H. Salamon, P. Sommers, *Phys. Rev. Lett.* **66**, 2697 (1991).
7. IceCube Collaboration, *Science* **361**, eaat2890 (2018).
8. IceCube Collaboration, *Science* **361**, 147 (2018).
9. IceCube Collaboration, *Phys. Rev. Lett.* **125**, 121104 (2020).
10. M. G. Aartsen *et al.*, *Phys. Rev. Lett.* **124**, 051103 (2020).
11. A. Marinucci *et al.*, *Mon. Not. R. Astron. Soc. Lett.* **456**, L94 (2016).
12. S. García-Burillo *et al.*, *Astrophys. J. Lett.* **823**, L12 (2016).
13. K. Murase, S. S. Kimura, P. Mészáros, *Phys. Rev. Lett.* **125**, 011101 (2020).
14. Y. Inoue, D. Khangulyan, A. Doi, *Astrophys. J. Lett.* **891**, L33 (2020).
15. K. Murase, D. Guetta, M. Ahlers, *Phys. Rev. Lett.* **116**, 071101 (2016).

10.1126/science.ade4190

NEUROSCIENCE

Molecular diversity of astrocytes

The tissue environment influences astrocyte form and function in health and disease

By **Katherine T. Baldwin**

Astrocytes are morphologically complex glial cells that regulate essential aspects of central nervous system (CNS) function, including synapse formation (*1*), ion homeostasis, and neurovascular coupling (*2*). Once viewed as a homogeneous population of cells, astrocytes are now known to exhibit molecular and functional heterogeneity at the regional and cellular level (*3*). How this diversity arises is unclear. On page 514 of this issue, Endo *et al.* (*4*) investigate the molecular basis of astrocyte heterogeneity in mice, uncovering shared core features and identifying key differences that are specific to CNS regions. Their findings suggest that astrocyte diversity arises primarily from differences in the tissue microenvironment and highlight a key role for astrocyte morphological complexity in brain health and disease.

Astrocytes are ubiquitous throughout the CNS. During development, astrocytes arise from neural progenitors in the ventricular zone (VZ) and migrate to different CNS regions, where they undergo local clonal expansion and morphogenesis (*5*). Morphological complexity is a hallmark feature of astrocytes. All astrocytes possess densely branched arbors that directly contact neighboring cells and structures (*6*) to actively control the formation and function of neuronal circuits and execute a diverse array of homeostatic functions (*7*). Overall, the morphological complexity of astrocytes is a prerequisite for their functional complexity.

Astrocytes in different regions of the mouse CNS show variations in gene expression, morphology, and function (*8*).

Department of Cell Biology and Physiology, Neuroscience Center, University of North Carolina, Chapel Hill, NC, USA. Email: ktbaldwin@med.unc.edu

Heterogeneity is also observed among astrocytes within the same CNS region (*9*). What is the source of astrocyte diversity? Some aspects of heterogeneity are developmentally encoded. In the spinal cord, for example, astrocyte location and gene expression are determined by the site of origin of progenitor cells in the VZ (*10*). Heterogeneity may also arise locally (*11*), although the extent to which differences in the tissue microenvironment influence regional astrocyte diversity is largely unexplored. Questions also remain regarding the relationship between molecular diversity and morphological and functional complexity, as well as the relevance of these features to disease.

To address these knowledge gaps, Endo *et al.* analyzed anatomical, molecular, and morphological features of astrocytes across 13 different CNS regions from mice. Although neuronal density differed substantially between regions, astrocyte density was relatively constant, underscoring their importance for brain homeostasis. Accordingly, astrocytes from all brain regions shared expression of genes related to core astrocyte functions, including neurotransmitter homeostasis, cholesterol biosynthesis, and glucose metabolism. The expression of many transcriptional regulators and ligand-dependent nuclear receptors was also shared among astrocytes across regions, suggesting that common mechanisms of upstream regulation may control core functional properties.

To investigate the extent of astrocyte diversity across CNS regions, Endo *et al.* focused on astrocyte-enriched differentially expressed genes (DEGs) that were distinct to a particular region or shared by a subset of regions. DEGs from the 13 CNS regions clustered into three broad regions based on anatomical proximity: cerebrum, brain stem–spinal cord, and cerebellum. Furthermore, astrocyte region-enriched DEGs correlated with region-enriched DEGs from bulk tissue, indicating that the identity of astrocytes reflects the tissue microenvironment. Single-cell sequencing analysis of a subset of brain regions identified seven astrocyte subclusters that were present at different proportions in each brain region. Several extracellular signaling molecules were identified as upstream regulators of each cluster, suggesting that local cues may shape the identify of these subclusters. Collectively, these findings provide strong evidence that astrocyte regional heterogeneity is shaped by the tissue microenvironment.

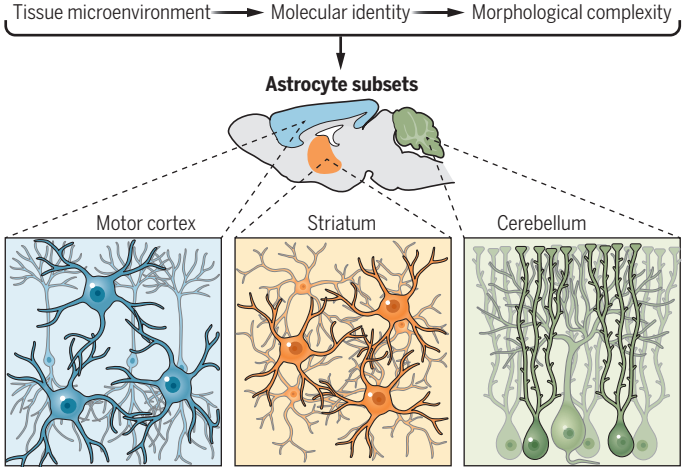
In addition to molecular heterogeneity, Endo *et al.* characterized the morphological features of astrocytes from the same 13 CNS regions and found considerable regional differences in territory size, sphericity, and branching complexity. For example, astrocytes in the motor cortex displayed the largest territory size of all CNS regions, whereas striatal astrocytes were among the smallest. Both motor cortex and striatal astrocytes had a relatively round shape, whereas astrocytes in the cerebellum had the lowest degree of circularity and the longest length (see the figure). Intriguingly, astrocyte morphological diversity correlated strongly with two gene modules from the region-specific DEGs. The authors selected top morphology-linked genes from these modules for further investigation. Deletion of morphology-linked genes from astrocytes in mice resulted in morphological and synaptic deficits and impaired spatial memory. Together, these findings establish a functional link between gene expression, astrocyte morphology, and functional output.

Astrocyte dysfunction is observed in many neurological disorders (*12*). Although astrocytes respond to disease states by undergoing molecular and functional changes that may have both beneficial and detrimental outcomes on neuronal health (*13*), increasing evidence suggests that astrocyte dysfunction could also be a cause of neuropathology (*14*). Among the genes that correlated strongly with astrocyte territory size, Endo *et al.* identified several genes associated with increased risk for Alzheimer's disease (AD). In an AD mouse model, the authors observed downregulation of several genes that positively correlate with astrocyte territory size and upregulation of genes that negatively correlate with territory size. Accordingly, the territory volume of cortical astrocytes was reduced in AD-model mice. Additionally, many of these astrocyte territory-associated genes overlapped with genes associated with other CNS disorders, including Parkinson's disease, multiple sclerosis, amyotrophic lateral sclerosis, and epilepsy. This observation suggests that changes in astrocyte morphology are a shared feature of neurological disorders.

The findings of Endo *et al.* reveal much about the heterogeneity of astrocytes, but it remains unclear how local cues shape astrocyte identity. The transcriptomic datasets will serve as a starting point to explore how transcription factors and upstream ligand-receptor signaling regulate astrocyte gene expression. These data can also be applied to investigate the cellular mechanisms that underlie key astrocyte functions, such as secretion of synaptogenic factors, regulation of ion homeostasis, and lipid synthesis, in the context of the tissue microenvironment. Whether astrocyte heterogeneity is developmentally regulated and reversible is also unknown. Exploring the upstream regulation of astrocyte heterogeneity, and to what extent astrocyte identity is plastic in the context of development and aging, will have important implications for treating astrocyte dysfunction in neurological disorders. ■

Region-specific features of astrocytes

Astrocytes in different regions of the central nervous system of mice show heterogeneity. The tissue microenvironments of these regions influence the molecular identity of astrocytes, which results in region-specific differences in gene expression and morphological complexity. For example, astrocytes in the mouse motor cortex (blue) are larger in territory size than astrocytes in the striatum (orange), whereas cerebellar astrocytes (green) are the most elongated.



GRAPHIC: K. HOLOSKI/*SCIENCE*

REFERENCES AND NOTES

1. N. J. Allen, C. Eroglu, *Neuron* **96**, 697 (2017).
2. A. Verkhratsky, M. Nedergaard, *Physiol. Rev.* **98**, 239 (2018).
3. M. Y. Batiuk *et al.*, *Nat. Commun.* **11**, 1220 (2020).
4. F. Endo *et al.*, *Science* **378**, eadc9020 (2022).
5. S. Clavreul *et al.*, *Nat. Commun.* **10**, 4884 (2019).
6. B. Torres-Ceja, M. L. Olsen, *Curr. Opin. Neurobiol.* **74**, 102550 (2022).
7. N. J. Allen, D. A. Lyons, *Science* **362**, 181 (2018).
8. H. Chai *et al.*, *Neuron* **95**, 531 (2017).
9. O. A. Bayraktar *et al.*, *Nat. Neurosci.* **23**, 500 (2020).
10. A. V. Molofsky *et al.*, *Nature* **509**, 189 (2014).
11. Y. Xie *et al.*, *Cell Rep.* **38**, 110416 (2022).
12. M. Pekny *et al.*, *Acta Neuropathol.* **131**, 323 (2016).
13. M. A. Anderson, Y. Ao, M. V. Sofroniew, *Neurosci. Lett.* **565**, 23 (2014).
14. A. J. Gleichman, S. T. Carmichael, *Neurobiol. Dis.* **142**, 104957 (2020).

10.1126/science.ade9249

POLICY FORUM

CONSERVATION

Protect global values of the Southern Ocean ecosystem

Climate change and fishing present dual threats

By **Cassandra M. Brooks[1], David G. Ainley[2], Jennifer Jacquet[3], Steven L. Chown[4], Luis R. Pertierra[5], Elizabeth Francis[6], Alex Rogers[7], Vasco Chavez-Molina[1], Louise Teh[8], U. Rashid Sumaila[8,9]**

The Southern Ocean, which comprises ~10% of the global ocean, is critically important to the homeostasis of the Earth system, exhibits distinctive marine biodiversity, and has tremendous scientific, diplomatic, and wilderness value. Yet, the region and its suite of global values are critically threatened by climate change, which is exacerbated by commercial fishing, an activity that provides value for relatively few industrial actors and compromises the greater values that the Southern Ocean ecosystem provides to the world. The Commission for the Conservation of Antarctic Marine Living Resources (CCAMLR), the arm of the Antarctic Treaty System responsible for managing Southern Ocean marine living resources, meets in October–November 2022 and is under pressure to strengthen fisheries management, especially toward climate change resilience. We encourage improved management practices that account for the environmental externalities arising from trade-offs between fishing and the global contribution of the Southern Ocean ecosystem, including under a changing climate.

With sovereignty suspended under the Antarctic Treaty, Antarctica and the Southern Ocean serve as an international space with immense global value. The Antarctic is celebrated for its rich history of exploration, vast wilderness and extraordinary austere beauty, exceptional governance prioritizing diplomacy and peace, and long history of international science collaboration (*1*). The Southern Ocean surrounding Antarctica supports exceptional marine biodiversity, including assemblages of endemic organisms and large populations of predators that rely on its rich waters (*2*). These waters harbor some of the healthiest large marine ecosystems left in the world (e.g., Ross Sea, Weddell Sea), which provide remarkable wilderness, scientific, and ecological value.

Recent assessments have highlighted the immense global value of the Southern Ocean and how those values are immediately threatened by climate change, calling for a critical evaluation of trade-offs in management, including a better understanding of the risks posed by fishing (*1–5*). Antarctic waters affect the Earth's climate, moderate sea level, and play a strong role in global ocean circulation and nutrient cycling. The Southern Ocean disproportionately absorbs global carbon dioxide and heat, thus helping to regulate temperature and buffering global impacts of climate change (*5*). The Southern Ocean biosphere also contributes to climate regulation and oxygen production through its primary production of seasonal phytoplankton blooms (*3, 5*). In addition, the Antarctic seafloor stores extensive amounts of carbon (*3*). Antarctic krill (*Euphausia superba*) play a critical role both as a central species in the Southern Ocean food web (*5*) and in biogeochemical cycles, stimulating primary production and influencing the drawdown of atmospheric carbon to the deep sea (*6*). A host of seasonally migrating iconic marine mammals and birds depend on the Southern Ocean to supply their energetic needs (*4*).

With no Indigenous Peoples in Antarctica, and no local fishing communities, exploitation of the waters surrounding Antarctica has always been the result of industrial distant water activities. Historically, prior to the existence of CCAMLR, these activities led to overexploitation and near extirpation of whales, seals, and some finfish populations (*2*). CCAMLR came into force in 1982 to regulate Southern Ocean fisheries with a mandate to ensure that fishing does not cause irreversible harm to target and nontarget populations or the marine ecosystem and to account for environmental change. Currently, fishing is restricted to CCAMLR members (comprising 25 nation states plus the European Union), and in principle any state can go through the process to join CCAMLR.

SOCIAL AND ECOLOGICAL TRADE-OFFS

Today, Southern Ocean fisheries are conducted by only ~12 countries, do not contribute to food security, and threaten the Southern Ocean ecosystem. The primary targeted species include toothfish (*Dissostichus eleginoides* and *D. mawsoni*), the region's top fish predator, and Antarctic krill, with a minor contribution of mackerel icefish (*Champsocephalus gunnari*). Although the Food and Agriculture Organization of the United Nations has suggested that Antarctic krill are underfished, with potential to contribute to food security (*7*), the krill caught are not used as a direct food source for people but as fishmeal for farmed salmon and shrimp, as well as in premium priced krill oil supplements (*8–10*). Overall, these products make up <1% of the global fishmeal and supplements markets (*3*). Toothfish are processed for human consumption, but sold as Chilean sea bass in high-end restaurants and stores in the United States, Europe, and Asia, with limited ability to reduce the food insecurity of malnourished people worldwide (*10*). There are other social consequences. Like other fisheries operating in international waters, some toothfish operations support forced labor on their vessels, and accidents with loss of life at sea are not uncommon (*11*). Finally, many of these fisheries continue to be economically viable only on account of government subsidies, which, as shown throughout the world, can contribute to overfishing *(9, 11)*.

Fishing in the Antarctic benefits very few and comes at a high cost of increasingly compromising the ecosystem. The Antarctic krill fishery recently has seen record high catches (>450,000 tonnes) (*12*). Yet, though these catch levels fall within the precautionary total allowable catch, extraction is increasingly concentrated in nearshore predator "hotspots" frequented also by fish, birds, and mammals (e.g., Scotia Sea and the west coast of the northern Antarctic Peninsula; CCAMLR Area 48) (*7, 13*). Reductions in sea ice (due to climate change) in the prime krill fishing grounds have further enabled vessel access to previously inaccessible waters and allowed for fishing year round, leading to increased competition with predators and re-

[1]Department of Environmental Studies, University of Colorado Boulder, Boulder, CO, USA. [2]H.T. Harvey & Associates Ecological Consultants, Los Gatos, CA, USA. [3]Department of Environmental Studies, New York University, New York, NY, USA. [4]Securing Antarctica's Environmental Future, School of Biological Sciences, Monash University, Victoria, Australia. [5]Department of Plant and Soil Sciences, University of Pretoria, Pretoria, South Africa. [6]The Gallifrey Foundation, Geneva, Switzerland. [7]REV Ocean, Lysaker, Norway. [8]Institute for the Oceans and Fisheries and the School of Public Policy and Global Affairs, University of British Columbia, Vancouver, Canada. [9]Institute for Environment and Development (LESTARI), National University of Malaysia, Selangor, Malaysia. Email: cassandra.brooks@colorado.edu

moval of krill from the food web (*13*). Recent research indicates that the cumulative catch in some of these coastal regions can be greater than the amount consumed by local predators, and greater than the local replenishable population of krill (*7*).

This localized depletion has substantial potential consequences for predators, including visiting whale populations, which are still recovering from historic depletion (*7, 13*). As a result of direct competition at these hotspots, in 2021, the krill fishery for the first time incidentally killed three juvenile humpback whales (*12*). This was in addition to the incidental killing of at least 16 seals and 60 petrels and other seabirds over the last two seasons (*12*). CCAMLR's mandate stipulates maintenance of ecological relationships, such that fishing should consider impacts on predators, including whales. Yet there are insufficient measures in place to ensure that the fishery is not detrimentally competing with predators or to prohibit (or even limit) incidental catch of whales in the krill fishery.

Ecosystem and target species' impacts from fishing are further compounded by climate change. Parts of the Southern Ocean, especially those adjacent to the western Antarctic Peninsula (where krill fishing is concentrated), are among the most rapidly changing regions in the world, with potential cascading impacts on the ecosystem (*2, 3*). Krill, in particular, owing to dependence on sea ice and vulnerability to acidification, are seen as extremely high risk from climate change (*3*). Benthopelagic-dwelling Antarctic toothfish, because of their limited thermal tolerance, are also at risk (*2, 3*). Antarctic finfish have shown to be easily overexploited even without the stress of climate change. For example, marbled rockcod (*Notothenia rossii*), which were severely overfished in the 1970s, remain at a fraction of their estimated pre-exploitation levels, despite ongoing regional fishery closures (*14*); bycatch of larval fish in the krill fishery may be impeding their recovery (*8, 14*). The population status of many toothfish fisheries remains unknown, including in some regions of the Southern Ocean that were heavily targeted by illegal, unregulated, and unreported fisheries in the 1990s (*12*). Meanwhile, ecosystem impacts of fishing toothfish remain largely unknown and debated. Fishing at current levels will likely exacerbate environmental impacts on toothfish and krill, along with the greater Southern Ocean ecosystem, including competing birds and mammals (*3, 13*).

Krill fishing, in particular, because of krill's critical role in the ecosystem and biogeochemical cycles, is predicted to negatively affect Southern Ocean ecosystem services (*1–3*), including reducing the carbon storage potentially provided by krill (*6*). Further, given that historic whale populations would have enhanced nutrient cycling, promoted productivity, and facilitated the drawdown of carbon and nutrients to the seafloor, allowing whales to recover (by limiting competition with fisheries) could lead to higher Southern Ocean productivity, increasing its powers of carbon sequestration (*15*). In addition, the incredible remoteness of the Antarctic means that fuel use by fishing vessels is high, leaving a disproportionate carbon footprint from fishing (*8*).



PHOTO: JOHN B. WELLER

PROTECTING THE GLOBAL VALUES

This is a critical moment for the Southern Ocean, and for CCAMLR, which showed tremendous leadership in 2016 by adopting the Ross Sea region marine protected area (MPA), among the largest MPAs in the world, but which has since waned on adopting further conservation initiatives beyond preexisting fisheries measures. This comes at a time when the global community, through the United Nations, is close to negotiating a new treaty for conserving biodiversity on the high seas. CCAMLR thus stands to either serve as a leading model or be surpassed. Continuing to authorize the removal of key prey and predator species through fishing, by a relatively small industrial fleet, will further compromise ecosystem and biosphere regulating services (as has been shown elsewhere, e.g., Peru, and Benguela current forage fish extraction). Fishing also stands to create diplomatic conflict (e.g., current conflict over toothfish fisheries at South Georgia) and erode the wilderness value of the Antarctic, without contributing to food security. Although actions must continue to be taken through national governments toward reducing global carbon emissions, CCAMLR has the responsibility to embrace the ecosystem mandates in its convention and the competency to implement a variety of tools to help immediately.

Manage for ecological and climate resilience

For three decades, CCAMLR has discussed more sophisticated spatial management for Antarctic krill (e.g., at smaller scales), yet has not been able to adopt this into practice. Thus, CCAMLR has not yet moved beyond single-species stock assessments with a large-scale static total allowable catch. Meanwhile, recent modeling has indicated that combined effects of krill fishing and climate change are potentially disastrous for populations of penguins and other predators (*13*). Historical trends suggest that the quantity of krill fished will further increase and grow more spatially concentrated in predator hotspots.

A suite of science-based tools exist for managing marine systems for ecological and climate resilience. These include using environmental and ecosystem indices to understand impacts of fishing and environmental change; considering future climate



An emperor penguin stands in front of an icebreaker on the frozen Ross Sea, Antarctica.

impacts on targeted species and the ecosystem; and employing adaptive management. Consideration of recovering whales and the provisioning needs of krill and toothfish predators must be accounted for in management, including in more refined spatial management and precautionary catch limits. All of these management ideas are being discussed among CCAMLR's Scientific Committee (which advises CCAMLR). However, data gaps and uncertainty, along with resistance to more stringent catch limits (spatially, and overall), have prevented progress. In 2022, the precautionary interim distribution of the "trigger" catch limit for krill expires. This presents a tremendous risk for fishing to be even more concentrated. Given the recent research demonstrating the risk to krill and their predators if the fishery continues under its current rules, CCAMLR has an immense opportunity and responsibility to adopt the spatially explicit precautionary management that it has been developing for decades.

Implement marine protection

Within CCAMLR's capabilities to exclude areas from fishing, MPAs, if well designed, can potentially promote adaptation to climate change and enhance Southern Ocean ecosystem resilience. MPAs can provide climate refugia and facilitate adaptation by alleviating the stressors on the ecosystem (e.g., fishing). CCAMLR's founding articles contain language that allows the closing of areas to manage fisheries, and at times it has exercised that power. Moreover, CCAMLR committed to an ecologically representative network of Southern Ocean MPAs. After adopting two MPAs (in 2009 and 2016), it has since lacked the renewed political will to move forward, with Russia and China not yet joining in consensus for the existing Southern Ocean MPA proposals under negotiation. These MPA proposals are grounded in extensive science, but likely need high-level diplomacy, one of the key facilitators of the adoption of the Ross Sea region MPA. We encourage CCAMLR states to work together to find common ground on the MPAs, which can serve as a tool for both conservation and international diplomacy, emblematic of the spirit of the Antarctic Treaty System.

Consider the full suite of values for future generations

As an international space, the Southern Ocean must be valued beyond its direct economic (extractive) value, which benefits a small number of nations (including the wealthiest on Earth) in the short term. These activities are likely also harming the wider values and functions of the Southern Ocean. A comprehensive ecosystem services assessment and mapping of the Southern Ocean urgently needs to be completed, including analyses of social perceptions from stakeholders and all nonmonetary values (*1*). This should include its support of seasonally present marine mammals and birds, and its role in the Earth system, along with its value as a global wilderness, and its history of peace and science. Further, the Southern Ocean needs to be valued for the suite of services it provides to both current and future generations. Improved management of the Antarctic could boost global climate change mitigation and ensure that Antarctica, as an exceptional global treasure, is not exploited for the benefit of short-term gain for few at the expense of many. Moreover, proximal Indigenous communities have ties to the Antarctic, though these communities have not yet had a voice at Antarctic governance meetings. Worldviews that prioritize conservation for future generations are consistent with the foundations of the Antarctic Treaty System, including the CAMLR Convention, and need to be considered and incorporated into management. CCAMLR could evaluate values, management, and trade-offs in tandem with the wider Antarctic Treaty System, providing unified management for Southern Ocean and Antarctic values.

Moratorium on fishing

Upon coming into force in 1982, CCAMLR soon thereafter closed various regions to finfish fishing to allow populations to recover, which is a powerful tool incorporated within its convention. The measure is showing effectiveness, though slowly, in the Antarctic Peninsula region (*14*). Despite working toward a more ecologically and spatially explicit management framework, CCAMLR has not used this tool under the precautionary principle despite the growing evidence of the external costs from the fishing industry. Given the clear acceleration in climate change, far more rapid now than when CCAMLR was negotiated, we argue that this conservation tool can no longer be neglected. We recommend considering a moratorium (a temporary prohibition) on fishing while a more comprehensive management assessment is undertaken. This assessment should account for all gains and losses, and consider broader climate resilience with the inclusion of regional and global trade-offs in ecosystem services. We acknowledge that among some CCAMLR member states, prohibitions on fishing may seem unreasonable, although such actions are not without historical precedent. Further, given the proven vulnerability of Southern Ocean organisms and ecosystems to climate change and ways in which fishing is known to compromise ecosystem services, a real reassessment of current practices may make an indefinite moratorium appropriate until the climate crisis is better managed. ■

REFERENCES AND NOTES

1. L. R. Pertierra *et al.*, *Ecosyst. Serv.* **49**, 101299 (2021).
2. A. D. Rogers *et al.*, *Annu. Rev. Mar. Sci.* **12**, 87 (2020).
3. R. D. Cavanagh *et al.*, *Front. Mar. Sci.* **7**, 615214 (2021).
4. E. J. Murphy *et al.*, *Front. Ecol. Evol.* **9**, 624451 (2021).
5. S. M. Grant, S. L. Hill, P. N. Trathan, E. J. Murphy, *Antarct. Sci.* **25**, 603 (2013).
6. E. L. Cavan *et al.*, *Nat. Commun.* **10**, 4742 (2019).
7. P. N. Trathan *et al.*, *J. Mar. Syst.* **225**, 103598 (2022).
8. S. Nicol, J. Foster, in *Biology and Ecology of Antarctic Krill*, V. Siegel, Ed. (Springer, 2016), pp. 387–421.</edb>
9. R. Cappell, G. MacFadyen, *Mar. Policy* **143**, 105200 (2022).
10. L. Schiller, M. Bailey, J. Jacquet, E. Sala, *Sci. Adv.* **4**, eaat8351 (2018).
11. E. Sala *et al.*, *Sci. Adv.* **4**, eaat2504 (2018).
12. CCAMLR, "Fishery Reports" (2022); https://fisheryreports.ccamlr.org/.
13. G. M. Watters, J. T. Hinke, C. S. Reiss, *Sci. Rep.* **10**, 2314 (2020).
14. E. R. Marschoff, E. R. Barrera-Oro, N. S. Alescio, D. G. Ainley, *Fish. Res.* **125-126**, 206 (2012).
15. A. J. Pershing *et al.*, *PLOS ONE* **5**, e12444 (2010).

ACKNOWLEDGMENTS

C.M.B., V.C.-M., U.R.S., and L.T. received support through the Pew Charitable Trusts. L.R.P. received support through Biodiversa ASICS. U.R.S. and L.T. also thank the University of British Columbia–based Solving Food-Climate-Biodiversity research partnership sponsored by the Social Sciences and Humanities Research Council of Canada.

Published online 20 October 2022
10.1126/science.add9480



A NASA-supported mobile health unit is prepared for deployment to the Papago Indian Reservation in 1974.

MEDICAL TECHNOLOGY

Where telemedicine always falls short

Efforts to innovate our way to better health consistently fail to deliver on equity promises

By **Vanessa Rampton**

In 2015, the Australian startup CliniCloud promised to leverage technology to disrupt medicine, making health care more accessible and affordable. The company, which had created a digital thermometer and stethoscope that paired with a smartphone app, sought to do this by allowing patients to measure their vital signs and communicate with doctors from the comfort of their own homes. Launched to much enthusiasm—its utility was endorsed by *The Lancet* and the US Food and Drug Administration—the technology's success was short-lived. By 2018, the company's online presence had disappeared, and the product had joined a long list of promising medical innovations that were soon forgotten.

CliniCloud's rapid rise and fall raises several questions: How do medical technologies age, become outmoded, and retreat from our collective consciousness? Have technologies aimed at improving health equity and democratizing health care access delivered on their creators' promises? To what extent can the provision of health care at a distance replace in-person treatment? Jeremy Greene, an emergency care physician in Baltimore and a historian of medicine at Johns Hopkins University, is well placed to answer these questions. His new book, *The Doctor Who Wasn't There*, tells a fascinating story of the hype, achievements, and inevitable shortcomings of telehealth technology.



The Doctor Who Wasn't There
Jeremy A. Greene
University of Chicago Press, 2022. 336 pp.

The technologies Greene highlights range widely. They include the original landline telephone, used by physicians to communicate with patients and with one another in the late 19th century, radio technologies that broadcast health data in the 1940s, closed-circuit televisions that enabled early telemedicine in the 1950s, and the systems that led to the creation of electronic medical records in the 1960s.

The humble telephone is a perfect case study. Almost immediately after its invention in the late 19th century, its "revolutionary" medical potential was noted—patients were going to be able to be heard in their own homes, at their convenience, and without risk of mutual infection. But it also elicited considerable concerns, for example, about the potential mechanization of physician-patient relationships. By the beginning of the 21st century, the telephone had become a routine device used by medical practitioners—a quarter of interactions between physicians and patients took place over the phone—yet it had done little to resolve unequal health outcomes. The erasure of the debates surrounding the introduction of previous forms of telehealth is a kind of power that allows technologists to ignore the pitfalls of past innovations, notes Greene. "Forgetting," he writes, "is an active as well as a passive process."

While popular histories of medicine tend to be told through a progressive lens, Greene's study reads more like an anti-progress manifesto—or at least like a story of the roads not taken. Sifting through his case studies, one is reminded not only of the complex and at times circuitous ways in which new telehealth technologies are adopted but also how they are almost always accompanied by fears that the clinician will be displaced from the diagnostic and therapeutic process.

Greene's study reminds readers that the introduction of technologies aiming to provide health care at a distance has long been bound up with recurring promises to improve health equity. And yet we know that the preservation of physical distance can have a stabilizing function, in that it prioritizes the stability of current systems over social justice (*1*). It can thus also serve to reproduce social hierarchies. During the COVID-19 pandemic, for example, telehealth technologies created new barriers to care, exacerbating the differences between those who could reliably connect to new electronic interfaces and those who could not.

Given that many of the most pressing global health problems remain unaddressed because of issues associated with resource allocation rather than a lack of available treatments, why then do we continue to focus on achieving breakthroughs rather than on using existing knowledge and technical powers to put everyone on a more equal health footing? Why, in other words, should we believe that new technologies will succeed where old ones have failed? As Greene shows, science and technology alone will never be able to deliver a more just and equitable society. ■

The reviewer is at the Department of Humanities, Social and Political Sciences, ETH Zürich, 8092 Zürich, Switzerland, and the Institute for Health and Social Policy and the Department of Philosophy, McGill University, Montréal, Quebec H3A 1G1, Canada.
Email: vanessa.rampton@gess.ethz.ch

REFERENCES AND NOTES

1. M. Kolkenbrock, *Kunst und Kirche* **4**, 4 (2020).

10.1126/science.ade1246

PHOTO: PETER RUIZ COLLECTION, ARCHIVES, HIMDAG KI TOHONO O'ODHAM NATION CULTURAL CENTER AND MUSEUM

EDUCATION

Reifying racism in medicine

False beliefs about racial differences have a long history in physician training programs

By **Suman Seth**

Masters of Health: Racial Science and Slavery in U.S. Medical Schools
Christopher D. E. Willoughby
University of North Carolina Press, 2022. 282 pp.



In 2015, a study published in *JAMA Pediatrics* found that in close to a million diagnosed cases of appendicitis, Black children were found "less likely to receive any pain medication for moderate pain and less likely to receive opioids for severe pain" (*1*). A survey conducted in 2016 by scholars at the University of Virginia offered some clues for why this might be so, revealing that striking proportions of respondents—including those with medical training—held false beliefs about differences between races (*2*). Fifty-eight percent of respondents without medical training, 42% of medical students in their second year, and 25% of residents all believed, for example, that "Blacks' skin is thicker than whites."

One conclusion we might draw from these data is that medical schools in the US are not doing enough to eradicate widely held, inaccurate ideas concerning putative biological differences between races. In his new book, *Masters of Health*, historian Christopher Willoughby suggests that this failure might be rooted in medical education's long tradition of perpetuating and reifying precisely such racial ideologies.

The book is divided into three parts. The first provides necessary background material on both the history of medicine and the history of race before the early 19th century. Even if each of these narratives is largely well known, it is nonetheless useful to have them told in tandem, so that the original and ongoing connections between medical institutions and the development of racial ideas come to the forefront. The book's third part is dedicated to locating the US within a transnational history of racial medicine. In this section, Willoughby reveals that there was much borrowing of thoughts and things between US medical men and their counterparts in the British and French empires, which covered a sizable portion of the globe by 1860.

The book's core, part two, contains the strongest and most striking material. Here, Willoughby tracks in detail the ways that early US medical students learned the racial biology that would inform their practices.

First, they encountered claims about race in their textbooks. University of Pennsylvania professor Joseph Leidy's *An Elementary Treatise on Human Anatomy* (1861), for example, introduced students to a section on the brain by suggesting that "it is the largest in the white race, and…its bulk bears a general relationship with the development of intellect." Such claims were further emphasized and elaborated on in lectures, which also allowed more visual and even tactile experiences, so that students could, for example, look at, and even handle, skulls that illustrated the arguments being made.



Racial biases were often reinforced in 19th-century anatomy lectures.

Anatomical museums rendered pedagogical lessons even more authoritative. At Harvard's museum, skulls were ordered by race: white skulls on the top shelf, South and East Asian skulls toward the middle, and African skulls at the bottom.

Willoughby also tracks how students wrote about race in their theses. Such texts were rarely terribly novel, usually summarizing extant literature rather than providing original research. As such, they serve as excellent guides for the views of leading men of 19th-century medicine. These works, Willoughby concludes, "made it clear that anatomical racial pedagogy was rigorous, standardized, and deeply influential."

We have long known that southern medical schools repeatedly made use, without consent, of the bodies of the enslaved for anatomical study. As one abolitionist newspaper put it in 1861: "What a convenience to possess for scientific purposes a class of population sufficiently human to be dissected, but not human enough to be supposed to take offence to it!"

Willoughby makes clear that northern schools may have been more circumspect, but physicians in New York and Philadelphia "preyed" on their Black population as well. The goal was to source cadavers with minimal resistance or backlash from local populations, and the wishes of free Black communities were the most easily ignored.

Where the North and South differed more dramatically was over the issue of medical experimentation, where the enslaved could not effectively resist. In research conducted for a thesis submitted to the Medical College of South Carolina in 1846, for example, C. Caldwell Higgins described experiments with no therapeutic purpose conducted on the bodies of a lactating enslaved woman and her child. The woman's body was covered with moist tobacco for almost half an hour, until she reported feeling sick. Higgins then had the women suckle her infant: "In a short time afterwards," Higgins wrote, "the child began to vomit. In fact for a while I was afraid it was going into convulsions but luckily for me it did not."

Little about *Masters of Health* makes for easy reading, but it is a text that those who have finished medical school—and those aspiring to enter it—should read with care and attention. ■

The reviewer is at the Department of Science and Technology Studies, Cornell University, Ithaca, NY 14853, USA. Email: ss536@cornell.edu

REFERENCES AND NOTES

1. M. K. Goyal, N. Kuppermann, S. D. Cleary, S. J. Teach, J. M. Chamberlain, *JAMA Pediatr.* **169**, 996 (2015).
2. K. M. Hoffman, S. Trawalter, J. R. Axt, M. N. Oliver, *Proc. Natl. Acad. Sci. U.S.A.* **113**, 4296 (2016).

10.1126/science.ade8481

IMAGE: WELLCOME COLLECTION. ATTRIBUTION-NONCOMMERCIAL 4.0 INTERNATIONAL (CC BY-NC 4.0)



Onlookers watch as pumps drain floodwaters in Dadu, Pakistan on 19 October 2022.

PHOTO: STRINGER/GETTY IMAGES

Edited by **Jennifer Sills**

Pakistan's floods flow from climate injustice

Recent flooding in Pakistan left one-third of the country under water (*1*). The floods, which affected at least 33 million people in 72% of the country's districts, were caused by an extreme monsoon season (*2*) that dropped up to five times as much rain as the average for the past 30 years (*3*). The floods led to more than 1000 human casualties and the deaths of 1.2 million livestock (*4*). Housing, education, and health infrastructures, as well as between 2.6 and 3.8 million hectares of cropland, were affected (*5*), threatening food security in Pakistan as well as in the countries to which Pakistan exported US$4.4 billion worth of food in 2021 (*6*). Communicable diseases are increasing in communities of displaced people (*5*). Pakistan's climate-driven humanitarian crisis is the result of the emissions produced by larger, more developed countries. The international community must address climate injustice.

Pakistan accounts for only 0.9% of global greenhouse gas emissions but is among the top 10 countries most affected by climate change (*7*). Ongoing global warming has caused the average annual temperature in Pakistan to increase by about 0.5°C since 1970 (*8*). Over the past three decades, the frequency of heat waves has increased five-fold, resulting in prolonged and extreme summers and accelerating evaporation and transpiration processes (*8*). Each 1°C rise in temperature allows the atmosphere to hold 7% more water (*9*), making monsoon seasons more intense. If global emissions continue to rise, the average annual temperature in Pakistan could increase by 3° to 6°C (compared with the projected global average of 1.5° to 5°C) by the end of this century (*8*, *10*), likely leading to worse devastation in the future.

Politicians, scientists, and the United Nations have spoken out against climate injustice in Pakistan (*11*), which relies on foreign grants for climate mitigation and adaptation. A global framework must be established to prevent developing countries such as Pakistan from becoming ground zero of climate change. Responsible nations must work to provide technical and economic assistance for climate change mitigation.

Muhammad Ahmed Waqas
Department of Agroecology, Aarhus University, DK-8830 Tjele, Denmark.
Email: ahmed.waqas@agro.au.dk

REFERENCES AND NOTES

1. European Space Agency, "Pakistan inundated" (2022); www.esa.int/ESA_Multimedia/Images/2022/09/Pakistan_inundated.
2. United Nations Office for the Coordination of Humanitarian Affairs (OCHA), "Pakistan: 2022 monsoon floods situation report no. 03 (as of 26 August 2022)" (2022).
3. Pakistan Meteorological Department, "Pakistan monsoon 2022 rainfall update" (2022); www.pmd.gov.pk/cdpc/Monsoon_2022_update/Pakistan_Monsoon_2022_Rainfall_Update.htm.
4. OCHA, "Pakistan: 2022 monsoon floods situation report no. 9 (as of 14 October 2022)" (2022).
5. OCHA, "Revised Pakistan 2022 floods response plan" (2022).
6. Pakistan Bureau of Statistics, "Annual analytical report on external trade statistics of Pakistan (FY 2020-21)" (Ministry of Planning, Development, & Special Initiatives, External Trade Section, Karachi, 2022).
7. Government of Pakistan, "Pakistan: Updated nationally determined contributions 2021" UN Framework Convention on Climate Change, New York (2021).
8. Q. U. Z. Chaudhry, "Climate change profile of Pakistan" (Asian Development Bank, 2017).
9. D. Coumou, S. Rahmstorf, *Nat. Clim. Change* **2**, 491 (2012).
10. J. Tollefson, *Nature* **580**, 443 (2020).
11. UN Press Release SG/SM/21519 (2022); https://press.un.org/en/2022/sgsm21519.doc.htm.

10.1126/science.ade8490

Restore Pakistan's forests to prevent floods

Forests comprise less than 5% of Pakistan's total area (*1*), and every year more forest area is destroyed by anthropogenic and natural activities. Pakistan's dwindling forest cover has exacerbated the effects of climate change (*2*). In June,

the country suffered devastating floods that threatened valuable ecosystem resources, including agricultural products, as well as the socioeconomic conditions of millions of people (*3*). Given the ability of vegetation, native biodiversity, and connected waterways and floodplains to serve as buffers for storms, rains, and floods (*4*, *5*) and mitigate climate change (*6*), Pakistan and other Asian countries must increase their environmental budgets to prioritize ecosystem restoration.

Preventing flooding in Pakistan is an ongoing challenge. In 2014, in response to widespread flooding and climate change (*7*), the country launched massive plantation projects to restore degraded forest lands and increase green job opportunities (*8*). Although the efforts made some short-term gains, they were undermined by substandard plantation designs and scientific planning, inadequate monitoring, and weak community mobilization activities (*8*, *9*). Meanwhile, natural forest degradation continued unabated (*1*, *2*, *8*).

Pakistan and other countries in the region should promote regional and global cooperation between experts in ecological science, policy, and practice (*10*, *11*) to improve on past efforts to conserve and restore natural ecosystems (particularly natural forests). Plantation locations should be selected based on the abiotic (soil, light, and water) and biotic (species facilitation) interactions underpinning targeted species. Practitioners should promote native mixed-species plantations with flood-tolerant species and heterogeneous stand structures, which would increase adaptability and resilience to future extreme climatic events (*5*, *12*). Restorations plans should also anticipate the vulnerability of new ecosystem restoration projects to natural disasters (*5*) and ensure that they are adequately protected. In addition to these improvements, developing countries in Asia should continue longstanding efforts to reduce deforestation, stop illegal infrastructure development adjacent to floodplains and waterways, and control the rate of human population growth. By investing in ecological restoration and water management, Pakistan and other at-risk countries can mitigate the damage caused by future natural disasters.

Arshad Ali
Forest Ecology Research Group, College of Life Sciences, Hebei University, Baoding, Hebei 071002, China. Email: arshadforester@gmail.com

REFERENCES AND NOTES

1. Food and Agriculture Organization of the United Nations, "Global forest resources assessment" (2020).
2. Food and Agriculture Organization of the United Nations, "2019 Forestry sector review: Pakistan" (2020).
3. S. Mallapaty, *Nature*, 10.1038/d41586-022-02813-6 (2022).
4. United Nations Environment Assembly, "Resolution 73/284: United Nations Decade on Ecosystem Restoration (2021–2030)" (2019).
5. C. J. Zabin *et al.*, *Front. Ecol. Environ.* **20**, 310 (2022).
6. B. B. N. Strassburg *et al.*, *Nature* **586**, 724 (2020).
7. K. Larkin, *Nature*, 10.1038/news.2010.409 (2010).
8. A. Ullah *et al.*, *Sci. Tot. Environ.* **772**, 145613 (2021).
9. S. Khan, "Pakistan: Environmentalists slam '10 billion trees' project," *DW Report* (2021); https://p.dw.com/p/3zom8.
10. B. B. N. Strassburg, *Science* **374**, 125 (2021).
11. C. Albert, J. H. Spangenberg, B. Schröter, *Nature* **543**, 315 (2017).
12. S. L. Stoffella *et al.*, *Ecosphere* **13**, e4223 (2022).

10.1126/science.ade9336

Predicting Pakistan's next flood

In June, the largest flooding disaster of this century hit Pakistan, flooding farmland and inducing a severe food crisis (*1*). Over 30 million people were affected, and more than 1000 people were killed (*2*). Developing countries such as Pakistan remain at high risk of disasters arising from climate change. To mitigate the damage, countries facing such threats should cooperate to improve disaster prediction capability and infrastructure.

Glacial lake outbursts combined with heavy rainfall during the monsoon period are the main causes of flooding in the Indus River basin in Pakistan (*3*). A cross-border international river, the Indus originates upstream of the Shigatse River on the Tibetan Plateau in China. Flood prediction is conducted extensively in Sindh and Punjab (the middle and lower reaches of Pakistan) (*4, 5*), but the extent to which the melting glaciers in the upper reaches will affect the middle and lower reaches of the river remains unclear. Global climate models, which predict a likely long-term warming of 1.5° or 2°C (*6*), also fail to predict extreme weather events.

Pakistan, and all countries with rivers affected by glacial meltwater (*7*), should make predicting regional hazards and extreme weather a priority. For basins such as the Indus, joint observatories and systematic simulations should be established between countries to enable the forecasting of floods related to glacier melt driven by climate change. Rather than focusing on national boundaries, climate studies should be directed toward naturally delineated basins. Aid provided by international organizations to developing countries should include not only relief supplies, but also open data sources, technology, and researchers.

Climate change will continue to affect vulnerable countries for years to come. With collaboration and investment in early warning systems and climate-resilient infrastructure, developing countries like Pakistan will be better prepared to face cascading effects, including natural disasters.

Yingying Yao[1]* and Zoon Ahmed Khan[2]
[1]Institute of Global Environmental Change, Xi'an Jiaotong University, Xi'an, China. [2]Belt and Road Strategy Institute, Tsinghua University, Beijing, China.
*Corresponding author. Email: yaoyy27@xjtu.edu.cn

REFERENCES AND NOTES

1. Q. K. Afridi, "Pakistan's disastrous floods uproot refugees and citizens," *UN Refugee Agency* (2022); www.unhcr.org/news/stories/2022/9/6311c7f54/pakistans-disastrous-floods-uproot-refugees-citizens.html.
2. P. Fihlani, "Pakistan floods: Time running out for families in Sindh," *BBC News* (2022); www.bbc.com/news/world-asia-62757605.
3. S. Mallapaty, *Nature*, 10.1038/d41586-022-02813-6 (2022).
4. M. Aslam, *Mehran Univ. Res. J. Eng. Technol.* **37**, 297 (2018).
5. I. Khan, H. Lei, A. A. Shah, I. Khan, I. Muhammad, *Environ. Sci. Pollut. Res.* **28**, 29720 (2021).
6. P. M. Forster, A. C. Maycock, C. M. McKenna, C. J. Smith, *Nat. Clim. Change* **10**, 7 (2020).
7. T. Yao *et al.*, *Nat. Rev. Earth Environ.* **3**, 618 (2022).

10.1126/science.ade7824

NEXTGEN VOICES: SUBMIT NOW

Favorite failures

Add your voice to *Science*! Our new NextGen Voices survey is now open:

Have you ever looked back and felt grateful that you experienced a setback? Describe a failure or mistake in your science career and explain how it led to a revelation, opportunity, or decision that would not have happened otherwise.

To submit, go to www.science.org/nextgen-voices

Deadline for submissions is 18 November. A selection of the best responses will be published in the 6 January 2023 issue of *Science*. Submissions should be 100 words or less. Anonymous submissions will not be considered.

PRIZE ESSAY

GRAND PRIZE WINNER

Ann Kennedy



Ann Kennedy received undergraduate degrees in Biomedical Engineering and Biology from Johns Hopkins University and a PhD in Neurobiology and Behavior from Columbia University. After completing her postdoctoral fellowship at Caltech, Ann started her laboratory in the Department of Neuroscience at Northwestern University Feinberg School of Medicine in 2020. Her laboratory develops computational methods to characterize the structure of complex behavior and model its control by the brain. **www.science.org/doi/10.1126/science.ade2128**

eppendorf & Science PRIZE FOR NEURO BIOLOGY



NEUROSCIENCE

Boiling over

An emergent encoding of aggressive motivation in neurons of the hypothalamus

By **Ann Kennedy**

Aggression between members of a species takes many forms, but the rulebook that guides it is ancient. Fighting may help resources and mates go to the fittest members of a species, as Darwin posed (*1*). This aggression can also serve as a repelling force to distribute animals evenly over an environment (*2*). In social species, aggression creates hierarchies that shape the health and behavior of group members (*3*). But picking a fight is costly because even the winner may walk away with injuries. If time allows, it is safer to begin with threat displays and posturing and only escalate to outright attack if neither side will back down (*4*).

This cautious, calculated escalation sounds cerebral: an integration of tactical observations that gradually reduce uncertainty about the opponent, with an estimate of the opponent's strength weighed against one's fitness to determine the next move. But this behavior is seen in the animal kingdom from flies to fiddler crabs to ferrets. Its importance for survival of a species means that aggressive strategies are under strong selective pressure. But what is that pressure acting on?

In 1928, Hess found that electrostimulation of a deep brain area could elicit displays of rage (*5*). Further stimulation work, as well as the rare tumor patient with aberrant aggressive behavior, pointed to the existence of a "hypothalamic attack area" (*6*, *7*). With the advent of optogenetics, this area found an identity: the ventrolateral portion of the ventromedial hypothalamus (VMHvl) (*8*). Artificial activation of VMHvl drives mice to attack and chase whatever other mouse is present; conversely, silencing VMHvl interrupts naturally occurring attacking but does not affect other behaviors, such as mating (*9*). Neighboring hypothalamic nuclei play similar dramatic roles in other behaviors—eliciting feeding, drinking, mating, or defensive reactions when stimulated.

Laboratory for Theoretical Neuroscience and Behavior, Department of Neuroscience, Northwestern University Feinberg School of Medicine, Chicago, IL, USA.
Email: ann.kennedy@northwestern.edu

PHOTOS: (LEFT TO RIGHT) COURTESY OF ANN KENNEDY; PETE OXFORD/MINDEN PICTURES

A red-legged seriema threat display. Some aggressive encounters end after opponents face off through threat displays, whereas others further escalate to outright fighting.

The combined effect of these studies paints the hypothalamic nuclei as a great internal switchboard, administered by some homuncular operator to conduct the fundamental motor acts of survival.

To see how these switches were flipped and try to understand their interaction, my collaborators and I used head-mounted miniaturized microendoscopes to capture the activity of several dozen to a few hundred hypothalamic neurons, while allowing mice to freely interact with another male or female (*10*). We studied several nuclei, including VMHvl, to look for neural signatures of an animal's decision to attack, and one of VMHvl's tightly coupled partners, the medial preoptic area (MPOA).

Neurons in MPOA were clearly and strongly modulated by animals' moment-to-moment actions, particularly reproductive behaviors. As the imaged male investigated, fought, or mated with other mice, distinct behavior-specific ensembles of neurons fired—their activity linked with the animal's actions. By contrast, VMHvl activity during social interactions was a morass—although many neurons showed a strong response to the introduction of another mouse, activity during interactions showed only weak correlation with the animal's behavior (*11*). Instead, neurons were persistently active over the duration of a social encounter, with modest fluctuations in the intensity of their activity as animals interacted.

We wondered whether we knew what we were looking for. We had defined "attack" through manual, frame-by-frame annotation—a subjective measure that may have little to do with when the mouse itself decided to start fighting. We thus opted to discard our annotations and looked at the neural activity by itself; we fit a dynamical system model to obtain a low-dimensional summary of how neurons' firing rates changed over time.

When we plotted neural activity in this summarized space, we saw the same strong response when another mouse was introduced to the imaged animal, followed by a gradual change in activity that evolved over tens of seconds (*12*). As we compared representations across nine animals, a trend emerged. In every animal, there was one "persistent" dimension of population activity: a pattern of firing across neurons that would gradually grow in prevalence and remain present for long periods of time. We reexamined our recordings and were able to point to a subset of neurons that showed the same dynamics; overall, this ramping signal captured about 20% of the variance in the data. When the level of activity along this dimension was low, mice investigated or ignored each other. As activity in the dimension increased, investigatory behavior transitioned to low-intensity aggressive actions such as dominance mounting, and as it saturated, animals began to show bouts of outright attack. Dynamics of this activation pattern mirrored animals' motivation to fight. In mice that rarely fought, any activity along this dimension quickly decayed back to baseline, but in eager fighters, activity quickly grew and remained high.

We could not identify a clear attack "decision"; during pauses between attacks, neural activity remained high. The signal looked like a level of aggressive motivation rather than a trigger for a specific motor act. This signal echoed our other data from the dorsomedial VMH (VMHdm), a region implicated in predatory defense (*13*). Predator cues or auditory threats activate VMHdm neurons for tens of seconds, during which animals exhibit freezing and defensive behaviors. We found that this VHMdm activity was necessary to keep animals in a defensive motivational state. When we showed a mouse a predator for a few seconds, removed the predator, then silenced VMHdm, the animal quickly reverted to its baseline behavior—rather than persisting to freeze and hide as mice would normally do.

Our studies suggest an alternative view of hypothalamic nuclei: not as switches for specific behaviors, as optogenetic studies suggested, but as distinct computational units (*12*). MPOA does indeed seem to reflect many moment-to-moment actions of the animal, and our dynamical systems analysis failed to find any persistent modes of its activity. But VMH is more akin to a volume dial than a switch. VMH reminded us of Konrad Lorenz's description of behavioral drives as a leaky bucket that slowly fills with water, pushing the animal to greater heights of aggression as the pressure builds (*14*, *15*).

Our observations that some animals showed more VMH persistence, and more aggression, suggests that this "leak" rate is tunable—perhaps modifying behavior in response to memories of past defeat or what is at stake in the current fight. We know many ways to tune persistence in models of biological neural populations. Now we have only to ask what molecular machinery links that tuning to experience in a living, and evolving, brain. ■

REFERENCES & NOTES

1. C. Darwin, *The Descent of Man* (D. Appleton, 1871).
2. K. Lorenz, *On Aggression* (Routledge, 1966).
3. E. O. Wilson, *Sociobiology: The New Synthesis* (Harvard Univ. Press, 1975).
4. J. Archer, F. Huntingford, in *The Dynamics of Aggression* (Psychology Press, 2013), pp. 21–50.
5. W. R. Hess, *Physiologie* **42**, 554 (1928).
6. M. R. Kruk *et al.*, *Brain Res.* **260**, 61 (1983).
7. A. G. Reeves, F. Plum, *Arch. Neurol.* **20**, 616 (1969).
8. D. Lin *et al.*, *Nature* **470**, 221 (2011).
9. H. Lee *et al.*, *Nature* **509**, 627 (2014).
10. T. Karigo *et al.*, *Nature* **589**, 258 (2021).
11. R. Remedios *et al.*, *Nature* **550**, 388 (2017).
12. A. Nair *et al.*, *bioRxiv* 10.1101/2022.04.19.488776 (2022).
13. A. Kennedy *et al.*, *Nature* **586**, 730 (2020).
14. K. C. Berridge, *Physiol. Behav.* **81**, 179 (2004).
15. K. Lorenz, P. Leyhausen, *Motivation of Human and Animal Behavior: An Ethological View* (Van Nostrand-Reinhold, 1973).

10.1126/science.ade2128

FINALIST

Kevin Guttenplan



Kevin Guttenplan received his undergraduate degree in Neuroscience and Mathematics from Pomona College. He then went to Stanford University for his PhD, where he worked first in the laboratory of B. Barres and then, after Barres's passing, in the laboratory of A. Gitler and studied the role of astrocytes in disease and injuries of the nervous system. He is now a Helen Hay Whitney postdoctoral fellow in the laboratory of M. Freeman in the Vollum Institute at Oregon Health & Science University, studying the role of astrocytes in neuronal circuits. **www.science.org/doi/10.1126/science.ade2129**

FINALIST

Filipa Cardoso



Filipa Cardoso received her bachelor's degree in Biochemistry and master's degree in Health Sciences from Universidade do Minho where she was introduced to the field of immunology, working in the immune response to tuberculosis infection and to colitis models. After her master's, she moved for a PhD in H. Veiga-Fernandes's laboratory to develop research in how the nervous and the immune systems interact to control metabolism. After completing the PhD, Filipa joined a biopharmaceutical company, LiMM Therapeutics, which stemmed from the Veiga-Fernandes laboratory. Currently, she is striving to translate the knowledge obtained from basic research to clinical application by harnessing the molecular cross-talk between neuronal and innate lymphoid cells within peripheral tissues. **www.science.org/doi/10.1126/science.ade2132**

PHOTOS: (TOP TO BOTTOM) AARON BIELECK; COURTESY OF FILIPA CARDOSO

PRIZE ESSAY

FINALIST

Kevin Guttenplan



Kevin Guttenplan received his undergraduate degree in Neuroscience and Mathematics from Pomona College. He then went to Stanford University for his PhD, where he worked first in the laboratory of B. Barres and then, after Barres's passing, in the laboratory of A. Gitler and studied the role of astrocytes in disease and injuries of the nervous system. He is now a Helen Hay Whitney postdoctoral fellow in the laboratory of M. Freeman in the Vollum Institute at Oregon Health & Science University, studying the role of astrocytes in neuronal circuits. **www.science.org/doi/10.1126/science.ade2129**

eppendorf & Science PRIZE FOR NEURO BIOLOGY

NEUROSCIENCE

Why do neurons die?

Astrocytes emerge as key mediators of neurodegeneration

By **Kevin Guttenplan**

Why do neurons die in neurodegenerative disease? Despite decades of research, this question remains a fundamental and unsolved mystery of neurobiology. One clue came when 19th-century scientists noticed that astrocytes, cells that normally support the health of neurons, dramatically change morphology after neuronal damage (*1*), a response termed "reactive astrogliosis." Almost 150 years later, researchers found that astrocytes become actively neurotoxic in mouse models of amyotrophic lateral sclerosis (ALS) (*2*, *3*), hinting that reactive astrocytes might play an important role in neurodegeneration.

Despite this evidence, researchers have been historically hampered by a lack of tools to determine how astrocytes become reactive and drive neuronal death (*4*). To unravel the mysterious connection between astrocytes and neurodegeneration, my colleagues and I have pioneered methods to track and prevent astrocyte reactivity and uncovered a mechanism underlying astrocyte-mediated toxicity.

To better understand what reactive astrocytes do, we first sought to determine what factors make nonreactive astrocytes become reactive. We characterized the gene expression profile of reactive astrocytes in vivo and screened for molecules that could replicate this reactivity signature (*5*, *6*). We found that the cytokines interleukin-1α (IL-1α), tumor necrosis factor–α (TNFα), and complement component 1q (C1q) together are able to instruct astrocytes to become reactive. To test this model in vivo, we generated a triple-knockout mouse lacking IL-1α, TNFα, and C1q and found that the reactive-astrocyte response after neuronal injury was eliminated. Importantly, this molecular cascade is highly conserved in humans: We discovered a marker of this type of reactive astrocyte in our mouse models and observed that the same marker was substantially up-regulated in brain tissue from patients with Alzheimer's disease, Parkinson's disease, ALS, and multiple sclerosis (*5*, *7*). Through these experiments, we revealed a molecular mechanism that drives reactive astrogliosis in diverse human diseases and established genetic tools to investigate the influence of astrocytes on disease pathogenesis.

Next, we asked what role reactive astrocytes play in disease and injury. We started with a simple mouse model of axonal injury. Retinal ganglion cells (RGCs) are neurons that project from the eye into the brain, and acutely injuring RGC axons leads to the death of these neurons. Surprisingly, our triple-knockout mice that lack the reactive astrocyte response were completely resistant to this injury, and none of their RGCs died after axon damage (*8*). This demonstrated that factors that drive reactive astrocyte formation also drive neurodegeneration after acute injury and that loss of these factors prevents neuronal death.

We then explored a mouse model of glaucoma in which elevated intraocular pressure leads to progressive RGC death. Just as in acute injury, inactivating the factors that induce reactive astrocytes prevented the death of neurons in this chronic injury model (*8*). Further, morphological and electrophysiological analysis of surviving neurons revealed that they retained electrical responses to light stimulation and dendritic targeting in the retina. Together, these results raise hope that damaged neurons could be reincorporated into their endogenous neural circuits and, in the case of glaucoma, restore vision (*8*).

Finally, we tested the role of astrocytes in a mouse model of ALS. By inhibiting reactive astrocytes using our triple-knockout strategy in the *SOD1*^{G93A} mouse model of ALS, we slowed the progression of motor impairment and extended the overall life span of the mice by more than 50% (*9*). This result represents one of the longest preservations of life span ever reported in *SOD1*^{G93A} mice. Combined with our data in mouse models of acute and chronic injury, this protection highlights astrocytes as drivers of neurodegeneration and could propel therapeutic strategies that target reactive astrogliosis.

Once we knew that astrocytes were involved in the brain's response to acute injury and neurodegeneration, we wondered what mechanism they used to drive neuronal death. Our first clue was that media conditioned by reactive astrocytes, but not by nonreactive astrocytes, was actively toxic to neurons (*2*, *3*, *5*). This effect indicated

Vollum Institute, Oregon Health & Science University, Portland, OR, USA. Email: guttenpl@ohsu.edu

PHOTO: AARON BIELECK

that reactive astrocytes were secreting something that could kill neurons. To identify this factor, we biochemically fractionated reactive astrocyte–conditioned media and identified candidate toxic proteins by mass spectrometry (*10*). Unexpectedly, all toxic fractions contained apolipoprotein E (ApoE) and apolipoprotein J (ApoJ). ApoE and ApoJ normally shuttle lipids between cells in structures called lipoparticles, and mutations in these genes are known to increase the risk of developing Alzheimer's disease. Notably, using antibodies to deplete ApoE- and ApoJ-containing lipoparticles from reactive-astrocyte media blocked toxicity. Although ApoE- and ApoJ-containing lipoparticles appeared to be required for astrocytes to kill neurons, additional experiments suggested that the lipoproteins themselves were not toxic. Instead, our data suggested that the toxic factor was a lipid carried within these lipoparticles.

What, then, is the lipid responsible for astrocyte toxicity? We performed mass spectrometry to compare lipids secreted by reactive versus control astrocytes and found an increase in abundance of long-chain saturated free fatty acids and phosphatidylcholines. These lipids are normally present at very low levels in the cell and can induce a form of cell death known as lipoapoptosis. To our surprise, we found that these lipids are largely responsible for astrocyte toxicity—we could kill neurons in vitro with long-chain saturated lipids and could prevent astrocyte toxicity by eliminating mediators of lipoapoptosis. We then inactivated an enzyme required for the synthesis of toxic long-chain lipids specifically in astrocytes in mice and showed that it reduced the death of RGCs after axon injury, establishing the same mechanism of lipid-mediated neuronal death in vivo.

Through this work, we developed tools to track and inhibit reactive astrogliosis, a common feature of neurodegeneration. We used these tools to reveal that reactive astrocytes drive neuronal death and disease progression in mouse models of acute injury and neurodegenerative disease. Finally, we discovered a long-sought-after and unexpected mechanism—the secretion of a lipid rather than a protein—by which astrocytes can kill neurons. These findings highlight that reactive astrocytes and the secretion of toxic lipids are powerful mediators of neurodegeneration in vitro and in vivo and are promising targets for future therapies. ■

REFERENCES AND NOTES

1. J. Grimm, *Virchows Arch.* **48**, 445 (1869).
2. F. P. Di Giorgio, M. A. Carrasco, M. C. Siao, T. Maniatis, K. Eggan, *Nat. Neurosci.* **10**, 608 (2007).
3. M. Nagai *et al.*, *Nat. Neurosci.* **10**, 615 (2007).
4. K. A. Guttenplan, S. A. Liddelow, *J. Exp. Med.* **216**, 71 (2019).
5. S. A. Liddelow *et al.*, *Nature* **541**, 481 (2017).
6. J. L. Zamanian *et al.*, *J. Neurosci.* **32**, 6391 (2012).
7. L. Barbar *et al.*, *Neuron* **107**, 436 (2020).
8. K. A. Guttenplan *et al.*, *Cell Rep.* **31**, 107776 (2020).
9. K. A. Guttenplan *et al.*, *Nat. Commun.* **11**, 3753 (2020).
10. K. A. Guttenplan *et al.*, *Nature* **599**, 102 (2021).

10.1126/science.ade2129

PRIZE ESSAY

FINALIST

Filipa Cardoso



Filipa Cardoso received her Bachelor's degree in Biochemistry and Master's degree in Health Sciences from Universidade do Minho where she was introduced to the field of immunology, working in the immune response to tuberculosis infection and to colitis models. After her Master's, she moved for a PhD in H. Veiga-Fernandes's laboratory to develop research in how the nervous and the immune systems interact to control metabolism. After completing the PhD, Filipa joined a biopharmaceutical company, LiMM Therapeutics, which stemmed from the Veiga-Fernandes laboratory. Currently, she is striving to translate the knowledge obtained from basic research to clinical application by harnessing the molecular cross-talk between neuronal and innate lymphoid cells within peripheral tissues.**www.science.org/doi/10.1126/science.ade2132**

eppendorf & Science PRIZE FOR NEURO BIOLOGY

NEUROSCIENCE

The brain-fat connection

Type 2 innate lymphoid cells shape metabolism through a brain-body circuit

By **Filipa Cardoso**

Adipose tissue is not merely a fat storage site but is, in effect, an active neuroendocrine organ that supports essential body functions, ranging from reproduction to muscle activity. These neuroendocrine functions are only possible, thanks to a complex communication network between the brain and fat tissue. Adipose tissue communicates with the brain through the release of adipokines and afferent innervation outputs, whereas the brain talks back to the tissue through systemic hormones and efferent innervation inputs (*1*). Obesity and obesity-associated conditions stem from the malfunction of this fine-tuned regulation between the brain and fat tissue.

One of the main axes of adipose tissue regulation is the sympathetic nervous system (SNS), which conveys brain-derived cues in the form of catecholamines to adipocytes and other adipose tissue cells to regulate metabolism. SNS-derived signals control many adipose tissue functions, including thermogenesis, neutral lipolysis, and immune cell function. Sympathetic output, in the form of catecholamines, can limit adiposity by acting directly on adipocytes (*2*).

Obesity-induced metabolic syndrome is driven by a state of systemic and chronic low-grade inflammation that originates in the adipose tissue. Adipose tissue is rich in immune cells, which play a vital role in its physiology. Under homeostatic conditions, type 2 innate lymphoid cells (ILC2s) promote a type 2 immune environment that protects the adipose tissue from harmful inflammation. The ILC2s achieve a protective environment through the production of interleukin-5 and interleukin-13, while also promoting energy expenditure through the release of met-enkephalin (*3*, *4*). In obesity, a gradual shift in immune mediators toward a type 1 inflammatory response leads to systemic inflammation and promotes metabolic dysfunction.

Adipose tissue biology is tightly controlled by both the SNS and the immune system, and my colleagues and I aimed to discover how these two systems interact to regulate adipose tissue metabolism (*5*). As a result, we identified a brain-adipose circuit that controls adipose tissue physiology through neuro-mesenchymal units, which modulate ILC2 function. In these circuits, sympathetic neurons activate the β2-adrenergic receptor of nearby adipose mesenchymal cells, inducing the expression of glial-derived neurotrophic factor (GDNF). Consequently, GDNF controls the activity of ILC2s in gonadal fat, which affects energy expenditure, glucose levels, and susceptibility to obesity.

Our findings indicate that synergy between the nervous and immune systems is required for adipose tissue physiology. Neuro-mesenchymal units stimulate type 2 immune responses, which disseminate and prolong the metabolic effects of sympathetic activation on adipocytes working in tandem to limit adiposity (*5*). This intercellular axis may also help to explain why, in the context of obesity, dysregulation of the immune landscape is difficult to repair. Although in a typically sized adipose depot, the SNS nerve fibers are densely distributed throughout the tissue, in an enlarged adipose tissue, sympathetic innervation is less dense because of the physical constraints imposed by expanding adipocytes. In the healthy adipose tissue, sympathetic cues promote thermogenesis, lipolysis, and type 2 immune responses. The disruption of cross-talk between the SNS and ILC2s, however, can likely limit type 2 cytokine production, which contributes to metabolic imbalance (*5*, *6*).

Retrograde tracing and chemical, surgical, and chemogenetic neuronal manipulation were used to unravel the anatomical basis for this neuroimmune regulation axis. We identified a previously unappreciated prevertebral sympathetic aorticorenal ganglion that connects to the paraventricular nucleus of the hypothalamus (PVH) and other higher-order brain areas. Manipulation of this neuronal circuit had similar effects on ILC2s as manipulating systemic sympathetic output, paving the way to potential therapeutic interventions for limiting visceral adipose tissue formation. Notably, the PVH not only coordinates whole-body metabolism through systemic leptin activity (*7*), but it also contributes to depot-specific metabolic regulation through

Champalimaud Research, Champalimaud Foundation, Lisboa, Portugal. Email: ana.cardoso@research.fchampalimaud.org

PHOTO: COURTESY OF FILIPA CARDOSO

the control of local SNS output to adipose tissue. Altogether, our study identified a neuro-mesenchymal unit that converts the activity of a brain-body circuit into adipose-resident ILC2 function, thus shaping systemic metabolism.

The integration of neuroscience and immunology techniques allowed us to add a previously unknown axis to the repertoire of neuroimmune interactions (*8*) and, most notably, to identify mesenchymal cells as the essential intermediary for this communication. This work emphasizes that the SNS is not a one-dimensional regulatory axis of adipose tissue, solely promoting lipolysis and thermogenesis through adrenergic signaling on adipocytes (*2*). Instead, an inter-organ sympathetic circuit integrates neuronal and mesenchymal signals to orchestrate ILC2 activation and to control adipose tissue physiology.

Historically, obesity treatments have targeted adipocytes (*9*), central nervous system mechanisms of metabolic regulation, or nutrient uptake. However, these treatments are not effective for all patients, and most have considerable side effects. In particular, dietary interventions have a high failure rate because of poor long-term compliance (*10*). Thus, nutritional education and lifestyle interventions are likely to be insufficient to tackle the current obesity epidemic. Accordingly, research on mechanisms of preventing fat accumulation or promoting its loss is of vital importance to control obesity and its associated comorbidities before they develop. Our work unravels the complexity of cellular interactions and brain-body mechanisms that coordinate adipose tissue metabolism. It is an enticing prospect that this previously unappreciated neuronal network will open new possibilities for fine-tuned control of obesity and related disorders. ■

REFERENCES AND NOTES

1. X. Ding *et al.*, *J. Endocrinol.* **231**, 35 (2016).
2. W. Zeng *et al.*, *Cell* **163**, 84 (2015).
3. A. B. Molofsky *et al.*, *J. Exp. Med.* **210**, 535 (2013).
4. J. R. Brestoff *et al.*, *Nature* **519**, 242 (2015).
5. F. Cardoso *et al.*, *Nature* **597**, 410 (2021).
6. X. Meng, W. Zeng, *Immunity* **54**, 2191 (2021).
7. A. K. Sutton, M. G. Myers Jr., D. P. Olson, *Annu. Rev. Physiol.* **78**, 207 (2016).
8. C. Godinho-Silva, F. Cardoso, H. Veiga-Fernandes, *Annu. Rev. Immunol.* **37**, 19 (2019).
9. M.-W. Lee *et al.*, *Cell* **160**, 74 (2015).
10. K. D. Hall, S. Kahan, *Med. Clin. North Am.* **102**, 183 (2018).

10.1126/science.ade2132

REVIEWS

Atlas-based data integration for mapping the connections and architecture of the brain p. 488

Solving brain circuit function and dysfunction with computational modeling and optogenetic fMRI p. 493

Scale matters: The nested human connectome p. 500

The emergent properties of the connected brain p. 505

RELATED ITEMS

PERSPECTIVE p. 475

RESEARCH ARTICLE p. 514

NO NEURON IS AN ISLAND

By **Peter Stern**

The brain is so much more than its constituent cells. Each neuron in the brain connects with thousands of other neurons—but instead of a cacophony of connections, we have a synchronized symphony.

Coordination of the body's myriad functions, behaviors, and thoughts requires large numbers of neurons to act cooperatively and not as isolated entities. The outcomes are driven by the connections between the neurons, whether that involves communicating with a neighboring nerve cell or sending and receiving signals to and from distant areas of the brain.

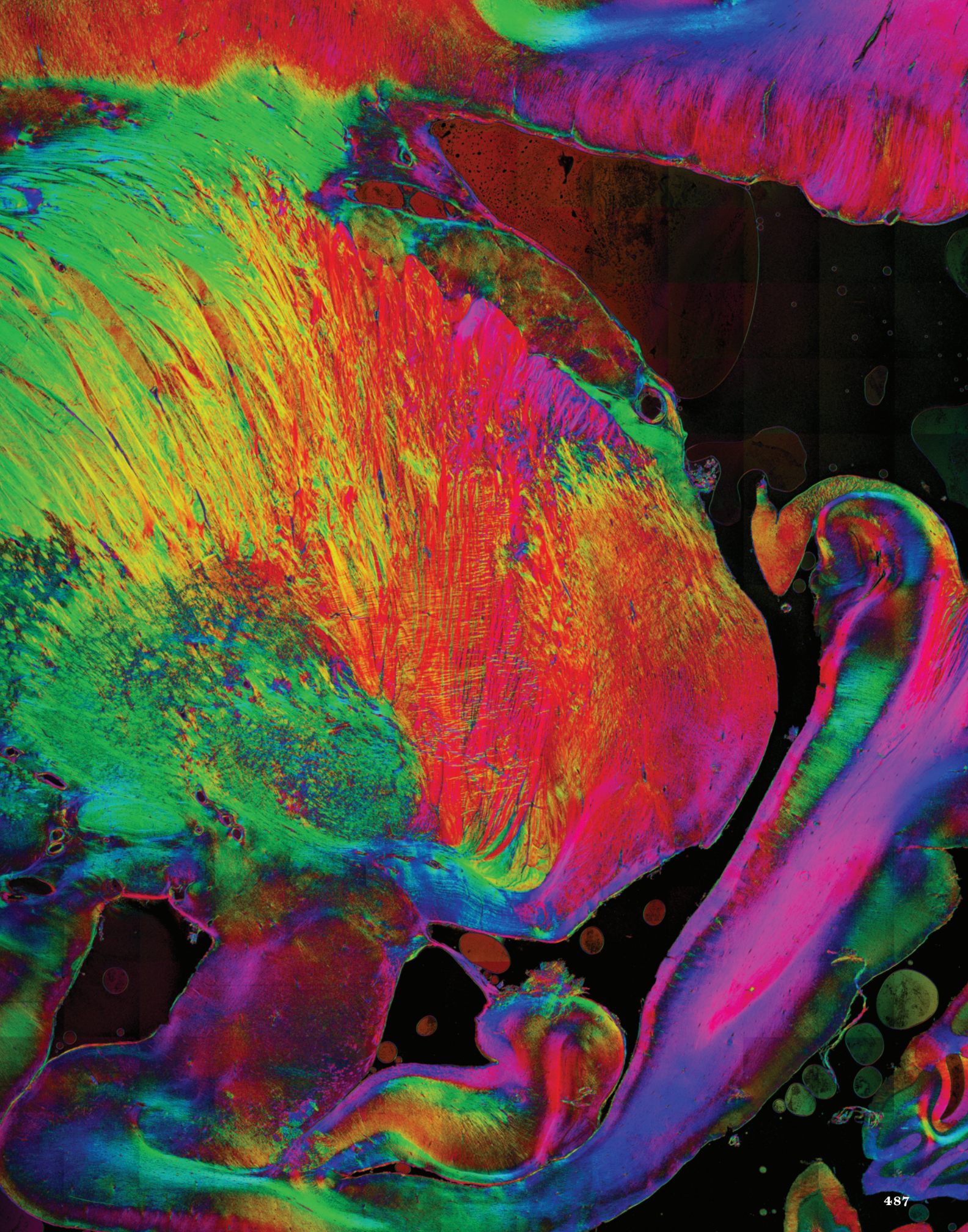
Innovative neuroscientific techniques allow researchers to specifically stimulate select groups of neurons in animals and noninvasively measure how they activate other parts of the brain, whether near or far. Advances in brain imaging reveal anatomical projections and functional connectivity patterns, allowing us to see their activation in real time. The first digital brain atlases of the mouse and rat, for example, provide astonishing insights into the connectivity of cells.

With a better understanding of the complexity of normal brain connections, we learn more about what goes wrong when they are disrupted. And the view of connectivity patterns in various organisms begins to reveal the steps involved in the evolution from the simplest neuronal nets to the multilayered, multinucleate mammalian brain.

Without connections that run smoothly, the brain is nothing more than a pile of neurons.

Details of a human brain section, which show the architecture of fibers down to single axons in cortical and subcortical structures, are revealed by three-dimensional (3D) polarized light imaging. The colors represent 3D fiber orientations and highlight pathways of individual fibers and tracts.

IMAGE: MARKUS AXER AND KATRIN AMUNTS/INM-1, FORSCHUNGSZENTRUM JÜLICH AND ROXANA KOOIJMANS/NETHERLANDS INSTITUTE FOR NEUROSCIENCE/HUMAN BRAIN PROJECT



REVIEW

Atlas-based data integration for mapping the connections and architecture of the brain

Trygve B. Leergaard* and Jan G. Bjaalie

Detailed knowledge about the neural connections among regions of the brain is key for advancing our understanding of normal brain function and changes that occur with aging and disease. Researchers use a range of experimental techniques to map connections at different levels of granularity in rodent animal models, but the results are often challenging to compare and integrate. Three-dimensional reference atlases of the brain provide new opportunities for cumulating, integrating, and reinterpreting research findings across studies. Here, we review approaches for integrating data describing neural connections and other modalities in rodent brain atlases and discuss how atlas-based workflows can facilitate brainwide analyses of neural network organization in relation to other facets of neuroarchitecture.

The brain is composed of vast numbers of neurons, glia, and vasculature, encased within a solid skull. It processes and stores information; generates memories, thoughts, and ideas; performs planning; and effectuates a wide range of behaviors. Dendrites and axons allow neurons to transmit signals across shorter or longer distances, and axons profusely branch into terminal fields with multiple synaptic contacts to other neurons. The functions performed by neurons are determined to a high degree by their connections with other neurons within and across brain regions.

Large ensembles of widely distributed neurons make up complex neural networks. The networks are highly organized, typically with different cell types distributed in layers or clusters. Within the network, populations of neurons exert specific excitatory, inhibitory, or modulatory influences on other parts of the network, and variations in the strengths and spatial distributions of the connections, including specific patterns of divergence and convergence, influence how the network subserves its functions. Overall, knowledge about the organization of the networks—the wiring patterns of the brain—is critical for understanding normal brain function and is typically embedded in network models aimed at elucidating and studying a variety of brain functions (*1*). Insight into the detailed organization of wiring patterns is also key to understanding and treating brain disorders. One example is the use of knowledge about the wiring of deep brain structures (Fig. 1, A and B) for treatment of neurological disease—e.g., the use of electrical stimulation targeting the subthalamic nucleus or specific parts of the thalamus for ameliorating symptoms of Parkinson's disease and medication-resistant tremor (*2*).

Although the patterns of neural wiring direct how neural signals are distributed through a network, the functional characteristics of a network also depend on the physiological and neurochemical properties of neurons, including their detailed local cellular relationships to other neurons (microcircuitry) and to supporting cells with sustaining or modulatory functions. Comprehensive knowledge about how the brain exerts its functions thus requires integration of knowledge about all these features. We argue that recently introduced three-dimensional (3D) digital brain atlases (*3*–*6*) offer new opportunities for extensive data integration aimed at improving our understanding of the organization of the brain. These integration efforts are accelerated by the use of tools for the registration of heterogeneous data types to the atlases in combination with computerized workflows for subsequent automated analyses of large data collections. Focusing on the rodent brain as a model system for basic neuroscience, we review approaches for the mapping of neural connections and atlas-based solutions for integrating and analyzing data and discuss future directions for advancing the field.

Mapping brain connections

A variety of techniques are available for the mapping of neural connections at different levels of granularity. The overall trajectories of fiber bundles in the brain can be visualized with myelin staining (*7*, *8*) (Fig. 2B) or polarized light imaging in histological sections (*9*) (Fig. 2B) and whole-brain diffusion magnetic resonance imaging (MRI) methods (*8*, *10*, *11*) (Fig. 2B). The neuron-by-neuron connections are mapped with the use of high-resolution

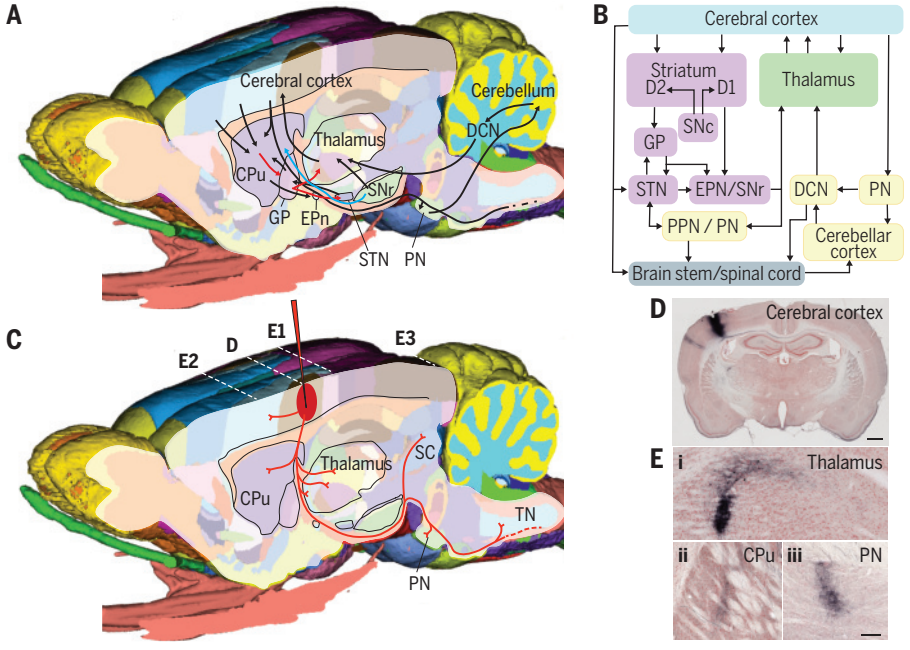


Fig. 1. Wiring patterns in the brain. (**A** and **B**) Schematic visualizations of basal ganglia and cerebellar neural networks, topologically drawn (A) in an oblique slice through the WHS rat brain atlas (RRID: SCR_017124) and as a box diagram (B). (**C**) Illustration of tract-tracing experiments in which an anterograde tracer is placed in the cerebral cortex, taken up by groups of neurons, and transported along the axons and their branches to visualize projections to intracortical and subcortical regions. (**D** and **E**) Microscopic images from a tract-tracing experiment [data from (*41*)] in which an axonal tracer (visualized as black labeling) was injected into the primary somatosensory cortex (D), giving anterograde labeling of dense axonal plexuses in the thalamus [(E), i], caudoputamen [(E), ii], and pontine nuclei [(E), iii]. CPu, caudoputamen; DCN, deep cerebellar nuclei; EPn, entopeduncular nucleus; GP, globus pallidus; SNc, substantia nigra, pars compacta; SNr, substantia nigra, pars reticulata; PN, pontine nuclei; PPN pedunculopontine nucleus; TN, trigeminal nuclei; STN, subthalamic nucleus; SC, superior colliculus. Scale bars, 1 mm (D) and 200 μm (E).

Neural Systems Laboratory, Institute of Basic Medical Sciences, University of Oslo, Oslo, Norway.
*Corresponding author. Email: t.b.leergaard@medisin.uio.no

microscopic techniques that allow the imaging of tracer-filled individual neurons (*12*, *13*) or by the use of serial electron microscopy visualization of cellular and synapse ultrastructure (*14*). The current foundation for whole-brain mapping of neuronal connections is, however, provided by invasive tract-tracing experiments in wild-type and transgenic animals (Figs. 1 and 2) (*15*, *16*). These methods are highly suitable for describing connections at the level of groups of neurons, demonstrating patterns that are persistent and reproducible among individuals and therefore useful for inferring functional properties and disease-related changes [for a discussion of different levels of connectivity analysis, see (*17*)].

In classical tract-tracing experiments, a tracer substance is deposited in a specific location in the brain and taken up by groups of neurons (Fig. 1, C to E). The tracer is transported along the axons of the neurons anterogradely, from neuronal cell bodies to their axonal terminal fields; retrogradely, from axonal terminal fields to the neurons of origin; or in both directions (*15*, *16*). Depending on the tracer used, some of the morphologies of the labeled neurons are revealed, or the tracer is transported across synapses, which allows for the identification of pre- and postsynaptic connections in a network (*16*). Creation of new animal models has also made it possible to use advanced cell type–specific tracing paradigms with genetically controlled expression signals (*18*).

A key methodological innovation for the tract-tracing methods has been serial two-photon tomography (*19*). By allowing block-face acquisition of high-resolution microscopic images, this technology has been successfully used by the Allen Institute to generate large volumes of microscopic, 3D tract-tracing image data showing brainwide connections in the mouse brain (*5*, *18*). Using a similar approach, the MouseLight project of Janelia Research Campus has created high-resolution volumetric reconstructions of individual axonal trajectories across entire mouse brains (*20*, *21*).

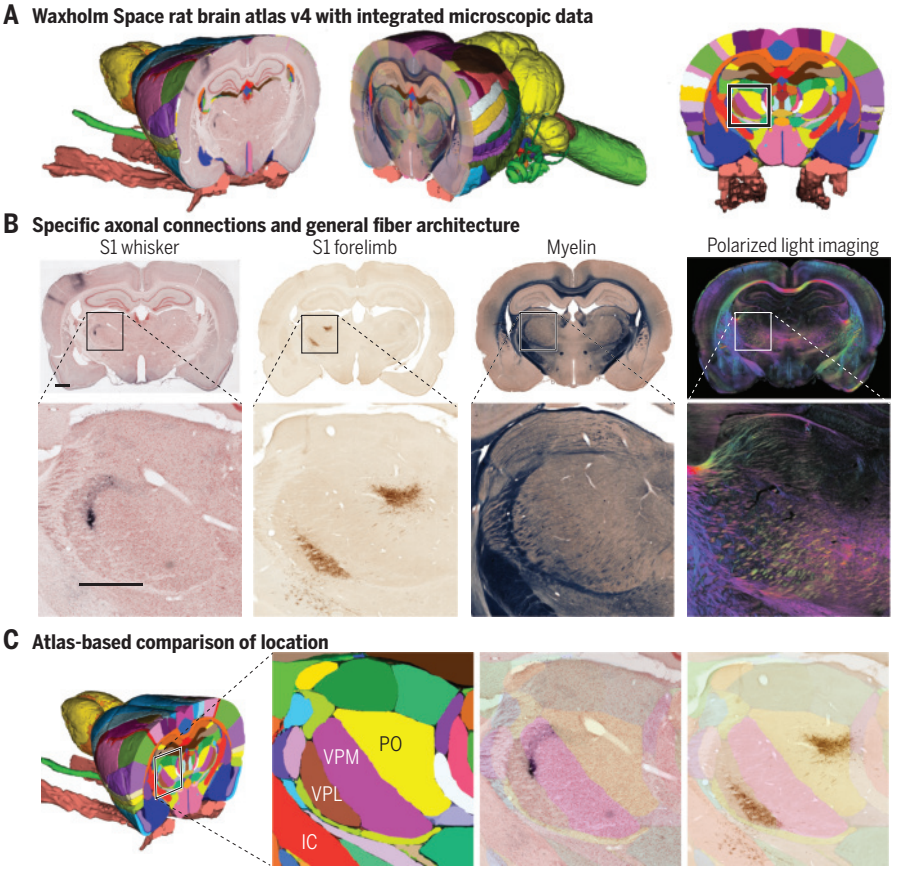


Fig. 2. WHS rat brain atlas with integrated microscopic data. The WHS rat brain atlas is enriched with spatially registered microscopic image data, which allow comparison across different experiments and data types. (**A**) Illustration of tract tracing and myelin-stained microscopic images of coronal sections registered to the brain at the level of the thalamus, indicated with a frame. (**B**) Overview and details from four different coronal microscopic images taken from the same anteroposterior level of the thalamus, including anterogradely labeled corticothalamic projections from whisker [data from (*41*)] and forelimb [data from (*42*)] representations in the primary somatosensory cortex (S1), tissue fiber orientations visualized by myelin staining [data from (*43*)], and polarized light imaging [data from (*44*)]. (**C**) WHS rat brain atlas superimposed on the tract-tracing image shown in (B), providing a starting point for interpreting the spatial location of axonal labeling across subregions of the thalamus. IC, internal capsule; PO, posterior thalamic nucleus; VPL, ventral posterolateral thalamic nucleus; VPM, ventral posteromedial thalamic nucleus. Scale bars, 1 mm.

Atlases for brainwide mapping of connections and related features

Traditionally, experimental tract-tracing studies have focused on one or a few brain regions at a time, yielding precise information about the connections among a few selected regions of interest. Extensive literature-mining efforts have aggregated information from available publications into databases to attain a more complete understanding of the connections between brain regions (*22*, *23*). However, these valuable resources are limited by the diversity of the methods used, the variable levels of precision in the reporting of brain location, and the lack of access to the underlying data (*17*, *24*). Regarding the reporting of the anatomical location of observations, a recent analysis of practices and precision from 120 different rodent brain experimental studies revealed substantial differences in the research design, interpretation of results, and reproducibility among studies (*25*). The main challenges were related to the use of different parcellation schemes and the lack of precision in the reporting of how observations would map onto a given anatomical scheme. Although atlases for mouse and rat brains (*26*–*28*) have assisted researchers for decades in assigning location to their observations, their utility is limited in that they are 2D and lack efficient and standardized tools for the registration of observations to the atlases. These limitations have been overcome with a new generation of open-access 3D atlases, which integrate information from multiple anatomical parcellation schemes and have powerful tools for the registration of data to atlases and atlas-based analyses.

For the mouse brain, the atlases developed by the Allen Institute for Brain Science have become widely used resources. The most recent version is defined in a high-resolution image volume constructed by interpolation of serial two-photon tomography (STPT) images from 1675 adult mice (the Allen Mouse Brain Common Coordinate Framework, CCFv3). In this population-averaged image volume, many anatomical delineations were defined using information from a large body of multimodal image data registered to the CCFv3 template (*6*). The underlying images included the collection of STPT data created for the Allen mouse brain connectivity atlas (*5*). Additional images were readily integrated into the atlas volume using the same high-throughput imaging and informatics pipeline, as achieved with the inclusion of more than 1000 STPT image volumes from

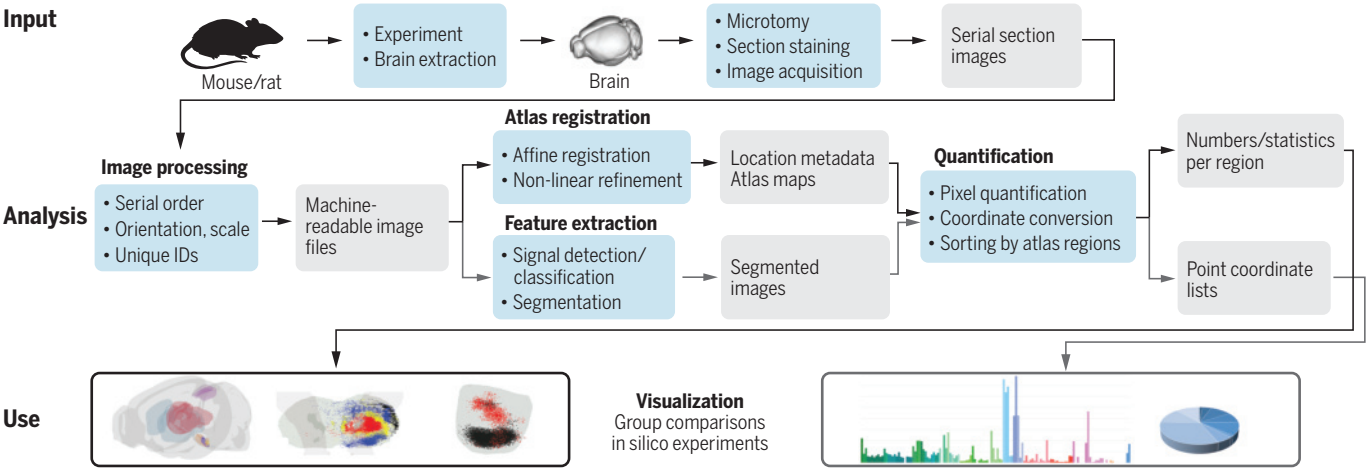


Fig. 3. Workflow for data integration and atlas-based analysis. Diagram showing key processing steps (blue) with inputs and outputs (gray) of a generic workflow for the integration of rodent brain experimental data in volumetric brain reference atlases and atlas-based analysis, yielding quantitative data and 3D point coordinate data sorted to atlas-defined brain regions. The input to the workflow is provided by experimental procedures resulting in serial microscopic images of tissue sections showing neural labeling. Preprocessing steps include validation of image order and orientation and assignment of unique serial identifiers to create machine-readable image files. Important parallel analytic steps are the spatial registration of images to a volumetric reference atlas and the extraction of labeling signals from background, providing input combined in (automated) analyses extracting quantitative measures and 3D point coordinates representing selected labeling features. The workflow output can be visualized and used in statistical analyses for characterizing and comparing labeled parameters. Point coordinates representing labeled neuronal elements are suitable for interactive 3D visualization and exploration of spatial distribution patterns and hypothesis-driven in silico experiments visualizing selected combinations of data. Usage example data are taken from (*45*–*49*).

tract-tracing experiments conducted in transgenic Cre-dependent mice (*18*).

For the rat brain, the Waxholm Space (WHS) atlas is now available in a version 4 with brain-wide parcellation (RRID: SCR_017124; https://www.nitrc.org). This atlas is based on a single high-resolution ex vivo structural and diffusion MRI volume, in which brain regions have been identified and delineated by manual interpretation of the underlying MRI data, enriched with multiple microscopic image data showing different facets of the neuroarchitecture (*4*, *29*, *30*) (see also Fig. 2). The atlas has seen broad interest, as reflected in close to 25,000 downloads, more than 300 citations, and inclusion in several services or products (e.g., EBRAINS research infrastructure, https://ebrains.eu, and the Neuroinfo software of MBF Bioscience). To facilitate comparisons of different atlas parcellation schemes, seven versions of the Paxinos and Watson rat brain atlases and four versions of the Swanson rat brain atlas were registered to the WHS rat brain atlas (*31*, *32*).

Atlas-based data integration and analysis

The 3D reference atlas spaces provided by the Allen Mouse Brain Common Coordinate Framework (CCFv3 and earlier versions) and the WHS rat brain atlas are useful frameworks for integrating heterogeneous data originating from different researchers and research projects. Recently introduced tools and workflows designed for use with the mouse and rat atlases support a three-step process for data integration and analysis (Fig. 3): (i) registration of images to an atlas, (ii) sharing of registered images with viewing and navigation of images in atlas space, and (iii) extraction of features from the images followed by quantification of the distribution of features within and across brain structures. Below, we review the principles and practical implementation of the three steps, taking a starting point in the EBRAINS Atlases services (https://ebrains.eu/services/atlases) for the mouse and rat brain and the EBRAINS Data and Knowledge services for data sharing and access (https://ebrains.eu/services/data-and-knowledge).

Registration of images to an atlas

Data integration requires that the data are made comparable, as if data of different origins were part of a single dataset. Thus, the registration of data of different origins to the same atlas framework is a key step toward integration. In EBRAINS, series of 2D histological images of mouse or rat brains are spatially registered to the atlases by an initial landmark-based anchoring of sections followed by a nonlinear adjustment. The EBRAINS tools supporting this step are the QuickNII tool for affine registration [RRID: SCR_016854; (*33*)] and the VisuAlign tool for nonlinear registration adjustments (RRID: SCR_017978). The output of the registration process is referred to as spatial metadata: a set of anchoring vectors and deformation fields that together define the transformations between the image data and the atlas. A range of other registration tools are available, with some having been developed for particular use cases, such as analyzing electrode tracts (*34*, *35*), and others suitable for many data modalities (*36*).

Sharing, viewing, and navigating images in atlas space

In addition to having spatial metadata, data are integrable only if they are properly annotated with metadata and other structured information that help us understand the data. Furthermore, the data will have to be discoverable and accessible. The approach taken by the EBRAINS Share Data service (https://ebrains.eu/service/share-data) is to provide procedures for annotation of the data with metadata according to a metadata standard and to provide descriptions and other information required to make the data interpretable and reusable. Following a curation of the metadata, the data are stored in the EBRAINS data repository, whereas the metadata are ingested in a knowledge graph that makes the data findable through a search user interface (https://search.kg.ebrains.eu) or a programmatic access route (https://ebrains.eu/service/find-data/). A search points the user to data cards with information about the data, access to the datasets, and links to a virtual microscopy viewer for inspection of the image data integrated in the atlas.

With use of the EBRAINS tools, a broad range of data generated with different methods and in different animals have been registered to the atlases. Figure 2 shows examples of histological images registered to the WHS rat brain atlas v4. In the thalamus, as the selected region of interest, data on specific connections of the

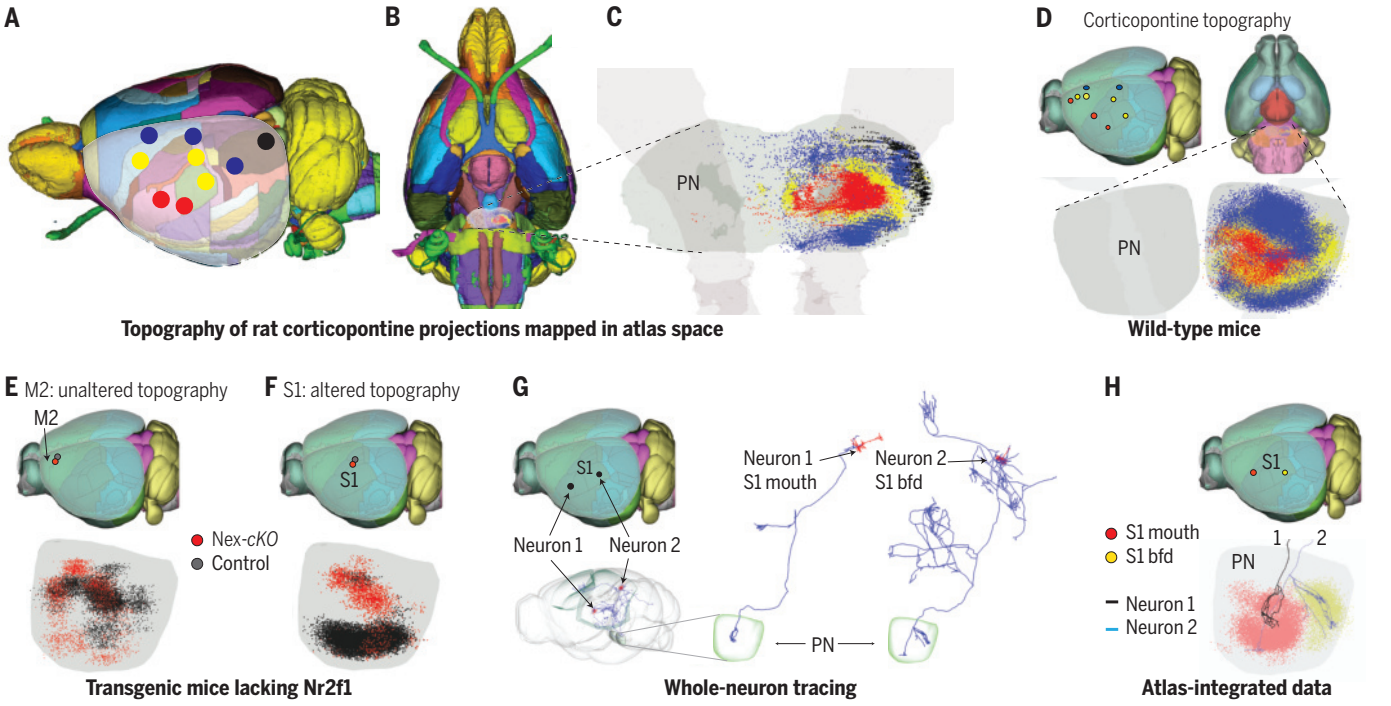


Fig. 4. 3D analysis of spatially integrated connections data. Spatial organization in the first link of the rat and mouse cerebro-cerebellar circuit, based on tract-tracing data integrated and covisualized in the WHS rat brain atlas [(A) to (C)] and the Allen Mouse Brain Common Coordinate Framework, CCFv3 [(E) to (G)]. (A to C) Data from several experiments in which an axonal tracer was placed at separate locations in the cerebral cortex. (**A**) Anterogradely labeled fibers were semiquantitatively represented as point coordinates, spatially registered within the pontine nuclei. (**B**) The WHS rat brain atlas in view from ventral. (**C**) The outer boundaries of the pontine nuclei and descending corticofugal fiber tract as gray transparent surfaces and axonal labeling from different experiments as color-coded point clouds. Shifts in location of tracer injection sites from anterolateral to dorsomedial locations (A) correspond to topographic shifts from internal to external lamellar subspaces in the pontine nuclei (C). (D to F) Data from a study of the impact of the cortical area–patterning gene *Nr2f1* on topographical organization of corticopontine projections in mice (*40*). (**D**) The distribution of corticopontine projections from different cortical locations in wild-type mice shows a similar inside-out topographical organization as that in rats (*50*) [(A) to (C)]. (**E** and **F**) Comparison of the topographical distribution of pontine projections arising from corresponding locations in the secondary motor cortex (E) and the primary somatosensory cortex (F) of Nex-cKO transgenic mice lacking Nr2f1 and control animals demonstrates that corticopontine projections from the primary somatosensory cortex are altered in Nex-cKO mice to resemble the projections from the secondary motor cortex. (G and H) Data from different sources can be integrated and compared in atlas space. (**G**) Whole-brain reconstructions of two projection neurons [from (*21*)] located in the mouth and whisker representations of the primary somatosensory cortex, with a variable amount of profusely branching axons in several subcortical regions, including the pontine nuclei. (**H**) A comparison of corticopontine projections from single neurons and anterogradely labeled projections from two populations of neurons in the mouth and whisker representations in the primary somatosensory cortex [data from (*5*)] indicating the trajectory of single-cell projections relative to the point cloud representing the spatial distribution of projections from a larger number of neurons in the same part of the cerebral cortex. The data in (A) to (C) are from (*45*) (cases R113-BDA, R118-BDA, and R124-BDA), (*46*) (case D55-FR), (*47*) (cases M27-BDA and M27-FR), and (*48*) (cases R409-BDA, R412-BDA, and R413-BDA). The data in (E), (F), and (H) are from (*51*) (wild-type cases: 100141780, 112229814, 112952510, 126908007, 127084296, 127866392, 141602484, 141603190, and 585025284; Nex-cKO cases: 11643_17 and 19423_7; littermate control case: 18035_1). The reconstructions in (G) are from (*20*, *21*) [https://www.janelia.org/project-team/mouselight: neuron AA0945 (neuron 1) and neuron AA1049 (neuron 2)]. Atlas surfaces and data points were covisualized using the MeshView web application, RRID: SCR_017222, https://www.nitrc.org. Neuron reconstructions in (G) were visualized using the Scalable Brain Atlas Composer [https://sba-dev.incf.org/composer (*52*)]. bfd, barrel field; M2, secondary motor cortex.

primary somatosensory cortex are available together with images showing bundles of axons and their orientation with myelin staining and polarized light imaging. Figure 2C demonstrates some of the basic functionalities of the virtual microscopy viewer that is available through the data cards. The viewer supports web-based pan and zoom of high-resolution images with overlays of the atlas parcellation map generated by a volumetric atlas slicer. The user can inspect the images at cellular resolution and observe brain regions, names, and boundaries and annotate points of interest to extract atlas coordinates.

Feature extraction, quantification, and distribution

Finally, features from the images can be extracted, sorted by brain region, and displayed and further analyzed in three dimensions. To this end, various approaches are used, as exemplified in the EBRAINS workflow for automation of several of the steps (*37*, *38*). This workflow consists of a registration tool, a machine learning–based tool for extraction of selected features in the images [ilastik (*39*)], and a tool for quantifying the features per atlas region [Nutil (*38*)]. The workflow allows the users to customize their analysis in many aspects, including choosing the granularity level of the atlas, defining their own regions of interest, filtrating artifacts, and applying quality control steps. It also allows for the export of coordinates to other tools for 3D visualization of the distribution of the selected features, from the whole brain or selected regions. Figure 4 shows examples of regional analysis of brain connection features extracted from images registered to the WHS rat brain atlas and the Allen Mouse Brain Common Coordinate Framework.

Figure 4 shows examples of regional analyses of brain connection features extracted from images registered to the WHS rat brain atlas or the Allen Mouse Brain Common Coordinate Framework. The data originate from different research

projects and data repositories but are integrated and made comparable by registration to the same atlas spaces. Specific combinations of tract-tracing data showing terminal fields of axons in the corticopontine projection system have been selected for analysis of topographical organization (Fig. 4, A to D) and identification of changes in topography resulting from lack of specific gene expression (Fig. 4, E and F). Furthermore, tract-tracing data showing corticopontine projections from large groups of cortical neurons have been combined with 3D reconstructions showing individual neurons and their extensive branching patterns, including branching to multiple target clusters within the pontine nuclei and elsewhere in the brain stem (Fig. 4, G and H), illustrating opportunities for parallel processing and neural circuit complexity.

Conclusion and outlook

Online repositories containing large collections of experimental data integrated in an open-access volumetric reference atlas have proven successful for mouse brain research, as made evident from the impressive data and results provided, e.g., by the Allen Institute and the Janelia Research Campus (*5*, *18*, *20*, *21*). Open-access sharing of standardized data mapped in an appropriate anatomical context makes it possible to find and efficiently use new combinations of data, suitable for characterizing and investigating many aspects of brain connections. However, despite the impressive amounts of data presented, attempts to use these generous resources may also reveal that data coverage may be insufficient to answer challenging questions, as exemplified in the recent study by Tocco *et al.* (*40*), which demonstrated that studies of topographic organization in the corticopontine projection require precisely corresponding tracer injections to detect subtle changes occurring in transgenic animals (Fig. 4, E and F). Similarly, attempts to compare the individual axonal morphologies in the pontine nuclei (using data from the MouseLight project at Janelia Research Campus) to the terminal fields visualized in tract-tracing experiments (using data from the Allen Mouse Brain Connectivity Atlas) reveal that data mapped to the same atlas allow interesting observations (Fig. 4, G and H), but these attempts also indicate that more data are needed for complete mapping of neural networks. Attempts to find, visualize, and compare such data are also hampered by technical challenges related to lack of tool interoperability. In the rat, large data collections on neural connections are not available, and, so far, few attempts have been made to systematically map brainwide connections (*24*). For these reasons, adding more data and tools will be critical for attaining an increasingly complete overview of the organization of brain connections and other features of rodent brain architecture.

The atlases play a key role in this endeavor. They provide a standardized representation of anatomical location and are embedded in software tools for integration and analysis. Data-sharing services, such as those delivered by EBRAINS, organize the data and help standardize the metadata, including metadata about the location of research data from the brain. Through the atlas frameworks, data from individual researchers published in research articles and integrated in the atlases are made directly comparable to data from large-scale mapping efforts, such as the Allen Mouse Brain Connectivity Atlas and the MouseLight project. The new paradigm for research on brain connections and brain architecture in general is to bring the research data into the same reference space, share the data, and prepare the data for systematic reanalysis and reinterpretations of our understanding of the brain. With these new approaches being introduced in neuroscience, literature mining can be supplemented with powerful mining of the data underlying the interpretations included in publications.

REFERENCES AND NOTES

1. O. Sporns, *Nat. Neurosci.* **17**, 652–660 (2014).
2. T. Wichmann, M. R. DeLong, *Neurotherapeutics* **13**, 264–283 (2016).
3. K. Amunts *et al*., *Science* **340**, 1472–1475 (2013).
4. E. A. Papp, T. B. Leergaard, E. Calabrese, G. A. Johnson, J. G. Bjaalie, *Neuroimage* **97**, 374–386 (2014).
5. S. W. Oh *et al*., *Nature* **508**, 207–214 (2014).
6. Q. Wang *et al*., *Cell* **181**, 936–953.e20 (2020).
7. T. B. Leergaard *et al*., *PLOS ONE* **5**, e8595 (2010).
8. N. S. White, T. B. Leergaard, H. D'Arceuil, J. G. Bjaalie, A. M. Dale, *Hum. Brain Mapp.* **34**, 327–346 (2013).
9. N. Schubert, M. Axer, U. Pietrzyk, K. Amunts, in *High-Resolution Neuroimaging: Basic Physical Principles and Clinical Applications*, A. M. Halefoğlu, Ed. (IntechOpen, 2017).
10. S. Mori, P. C. van Zijl, *NMR Biomed.* **15**, 468–480 (2002).
11. B. Jeurissen, M. Descoteaux, S. Mori, A. Leemans, *NMR Biomed.* **32**, e3785 (2019).
12. R. Parekh, G. A. Ascoli, *Neuroscientist* **21**, 241–254 (2015).
13. M. Wang *et al*., *Nat. Commun.* **13**, 1531 (2022).
14. N. L. Turner *et al*., *Cell* **185**, 1082–1100.e24 (2022).
15. J. L. Lanciego, F. G. Wouterlood, *J. Chem. Neuroanat.* **42**, 157–183 (2011).
16. J. L. Lanciego, F. G. Wouterlood, *Brain Struct. Funct.* **225**, 1193–1224 (2020).
17. J. W. Bohland *et al*., *PLOS Comput. Biol.* **5**, e1000334 (2009).
18. J. A. Harris *et al*., *Nature* **575**, 195–202 (2019).
19. T. Ragan *et al*., *Nat. Methods* **9**, 255–258 (2012).
20. M. N. Economo, J. Winnubst, E. Bas, T. A. Ferreira, J. Chandrashekar, *J. Comp. Neurol.* **527**, 2190–2199 (2019).
21. J. Winnubst *et al*., *Cell* **179**, 268–281.e13 (2019).
22. M. Bota, S. Talpalaru, H. Hintiryan, H. W. Dong, L. W. Swanson, *J. Comp. Neurol.* **522**, 3160–3176 (2014).
23. N. M. van Strien, N. L. Cappaert, M. P. Witter, *Nat. Rev. Neurosci.* **10**, 272–282 (2009).
24. I. M. Zakiewicz, Y. C. van Dongen, T. B. Leergaard, J. G. Bjaalie, *PLOS ONE* **6**, e22669 (2011).
25. I. E. Bjerke *et al*., *Front. Neuroanat.* **12**, 82 (2018).
26. G. Paxinos, C. Watson, *The Rat Brain in Stereotaxic Coordinates* (Academic Press, 1982).
27. L. W. Swanson, *Brain Maps: Structure of the Rat Brain* (Elsevier, 1992).
28. K. B. J. Franklin, G. Paxinos, *The Mouse Brain in Stereotaxic Coordinates* (Academic Press, 1996).
29. L. J. Kjonigsen, S. Lillehaug, J. G. Bjaalie, M. P. Witter, T. B. Leergaard, *Neuroimage* **108**, 441–449 (2015).
30. K. K. Osen, J. Imad, A. E. Wennberg, E. A. Papp, T. B. Leergaard, *Neuroimage* **199**, 38–56 (2019).
31. I. E. Bjerke, U. Schlegel, M. Puchades, J. G. Bjaalie, T. B. Leergaard, Paxinos & Watson's "The Rat Brain in Stereotaxic Coordinates" (7th edition) spatially registered to the Waxholm Space atlas of the rat brain, data set, Human Brain Project Neuroinformatics Platform (2019); https://doi.org/10.25493/APWV-37H.
32. I. E. Bjerke, U. Schlegel, M. Puchades, J. G. Bjaalie, T. B. Leergaard, Swanson's "Brain Maps: Structure of the Rat Brain" (4th edition) spatially registered to the Waxholm Space atlas of the rat brain, data set, Human Brain Project Neuroinformatics Platform (2019); https://doi.org/10.25493/486N-966.
33. M. A. Puchades, G. Csucs, D. Ledergerber, T. B. Leergaard, J. G. Bjaalie, *PLOS ONE* **14**, e0216796 (2019).
34. P. Shamash, M. Carandini, K. Harris, N. Steinmetz, bioRxiv 447995 [Preprint] (2018). https://doi.org/10.1101/447995.
35. J. Paglia, P. Saldanha, J. G. Fuglstad, J. R. Whitlock, bioRxiv 2021.10.01.462770 [Preprint] (2021). https://doi.org/10.1101/2021.10.01.462770.
36. D. Fürth *et al*., *Nat. Neurosci.* **21**, 139–149 (2018).
37. S.C. Yates *et al*., *Front. Neuroinform.* **13**, 75 (2019).
38. N. E. Groeneboom, S. C. Yates, M. A. Puchades, J. G. Bjaalie, *Front. Neuroinform.* **14**, 37 (2020).
39. S. Berg *et al*., *Nat. Methods* **16**, 1226–1232 (2019).
40. C. Tocco, M. Øvsthus, J. G. Bjaalie, T. B. Leergaard, M. Studer, *Development* **149**, dev200026 (2022).
41. I. Zakiewicz, Y. Van Dongen, T. B. Leergaard, J. G. Bjaalie, Axonal projections from the D3 whisker representation of the rat primary somatosensory cortex (case R604), data set, Human Brain Project Neuroinformatics Platform (2019); https://doi.org/10.25493/9MNV-Y97.
42. I. Zakiewicz, Y. Van Dongen, T. B. Leergaard, J. G. Bjaalie, Axonal projections from the forelimb representation of the rat primary somatosensory cortex (case R605), data set, Human Brain Project Neuroinformatics Platform (2019); https://doi.org/10.25493/ZF26-DZK.
43. T. B. Leergaard, S. Lillehaug, A. Dale, J. G. Bjaalie, Atlas of normal rat brain cyto- and myeloarchitecture, data set, Human Brain Project Neuroinformatics Platform (2018); https://doi.org/10.25493/C63A-FEY.
44. N. Schubert *et al*., Wistar rat brain fibre orientation model, data set, Human Brain Project Neuroinformatics Platform (2019); https://doi.org/10.25493/F9RX-65U.
45. T. B. Leergaard *et al*., Three-dimensional somatotopic organization of rat pontine projections from major body representations of the primary somatosensory cortex, data set, EBRAINS (2020); https://doi.org/10.25493/XQ7V-QN9.
46. T. B. Leergaard, K. D. Alloway, J. J. Mutic, J. G. Bjaalie, Three-dimensional somatotopic organization of corticopontine projections from whisker representations in the rat primary somatosensory (barrel) cortex, data set, EBRAINS (2020); https://doi.org/10.25493/NECX-22S.
47. T. B. Leergaard *et al*., Three-dimensional topography of corticopontine projections from the rat sensorimotor cortex (S1, S2, M1), data set, EBRAINS (2020); https://doi.org/10.25493/1SSX-606.
48. T. B. Leergaard, J. G. Bjaalie, Topography of the complete corticopontine projection, data set, EBRAINS (2020); https://doi.org/10.25493/ZM3M-YNJ.
49. E. R. Cullity, I. E. Bjerke, K. Kjelsberg, T. B. Leergaard, J. H. Kim, Distribution of dopamine 1 receptor positive neurons in the adult male mouse brain, data set, EBRAINS (2020); https://doi.org/10.25493/AVRZ-4JB.
50. T. B. Leergaard, J. G. Bjaalie, *Front. Neurosci.* **1**, 211–223 (2007).
51. C. Tocco *et al*., Impact of area patterning genes on corticopontine projection topography: Point coordinate data representing spatial distribution of corticopontine projections in Nr2f1 conditional knockout mice and controls (v1), data set, EBRAINS (2022); https://doi.org/10.25493/AJVE-B8G.
52. R. Bakker, P. Tiesinga, R. Kötter, *Neuroinformatics* **13**, 353–366 (2015).

ACKNOWLEDGMENTS

We thank the current and past members of the Neural Systems Laboratory for their contributions to the development, application, and validation of new methods to experimental research in small animal models and colleagues in the EBRAINS research infrastructure for their contributions to the delivery of services. **Funding:** This work was in part supported by the European Union's Horizon 2020 Framework Program for Research and Innovation under the specific grant agreement no. 945539 (Human Brain Project SGA3) and the Research Council of Norway under grant agreement no. 269774 (INCF Norwegian Node). **Competing interests:** J.G.B. is a member of the Management Board of the EBRAINS AISBL, Brussels, Belgium. The authors declare no other competing interests. **License information:** Copyright © 2022 the authors, some rights reserved; exclusive licensee American Association for the Advancement of Science. No claim to original US government works. https://www.science.org/about/science-licenses-journal-article-reuse

Submitted 21 June 2022; accepted 18 August 2022
10.1126/science.abq2594

REVIEW

Solving brain circuit function and dysfunction with computational modeling and optogenetic fMRI

Jin Hyung Lee[1,2,3,4]*, Qin Liu[1]†, Ehsan Dadgar-Kiani[1,2]

Can we construct a model of brain function that enables an understanding of whole-brain circuit mechanisms underlying neurological disease and use it to predict the outcome of therapeutic interventions? How are pathologies in neurological disease, some of which are observed to have spatial spreading mechanisms, associated with circuits and brain function? In this review, we discuss approaches that have been used to date and future directions that can be explored to answer these questions. By combining optogenetic functional magnetic resonance imaging (fMRI) with computational modeling, cell type–specific, large-scale brain circuit function and dysfunction are beginning to be quantitatively parameterized. We envision that these developments will pave the path for future therapeutics developments based on a systems engineering approach aimed at directly restoring brain function.

Can we systematically design treatments for brain disorders such as Parkinson's disease? To enable this we need a full algorithmic description beyond simple correlations of how specific cells or brain regions cooperatively contribute to a given behavior or symptom in the context of whole-brain networks. What does it take to generate such algorithms? Cell types cannot be ignored because even neurons in the same location in the brain can drive completely opposite functions and resulting behaviors (*1*, *2*). Neurons often interact with large networks across the whole brain. A limited field of view within the brain is thus insufficient to understand these algorithms. Therefore, to obtain the data necessary to reconstruct these algorithms of behavioral control we need an imaging system that can measure cell type–specific, whole-brain function. Optogenetic functional magnetic resonance imaging (ofMRI) (*3*) has begun to achieve this goal. With ofMRI, we can select cell type–specific modulation targets while monitoring the outcome of such modulation across the whole brain, in vivo with high spatiotemporal resolution. This has opened a window into the study of brain function. We can see how modulating specific elements of the brain leads to specific behaviors of interest while also directly observing the inner workings of the brain that lead to such behaviors. Through computational modeling of ofMRI signals measured across the whole brain (*4*), cell type–specific, large-scale brain function can be quantitatively described at the regional level. Once regional interaction maps are reconstructed we envision that biophysical modeling can be combined to enable cell type–specific, large-scale modeling of brain function at the single-cell-spiking level. In addition, although restoring brain function is the ultimate goal of neurological disease treatment, understanding how prominent pathology relates to brain function is also of critical importance. In this review, we will discuss approaches used to date and approaches that may be employed in the future to achieve such goals.

[1]Department of Neurology and Neurological Sciences, Stanford University, Stanford, CA 94305, USA. [2]Department of Bioengineering, Stanford University, Stanford, CA 94305, USA. [3]Department of Neurosurgery, Stanford University, Stanford, CA 94305, USA. [4]Department of Electrical Engineering, Stanford University, Stanford, CA 94305, USA.
*Corresponding author. Email: ljinhy@stanford.edu
†Present address: Brain Simulation Section, Charité – Universitätsmedizin Berlin, Berlin, Germany.

Bridging scales with optogenetic fMRI

ofMRI is a technology that combines optogenetic stimulation with fMRI readouts. Optogenetics (*5*, *6*) enables cell type–specific, millisecond-scale, activity modulation using light whereas high-field fMRI measures the resulting hemodynamic responses in live subjects across the whole brain. In the initial proof-of-concept study (*3*), motor cortex excitatory neurons triggered fMRI responses that could be measured throughout the brain with subsecond temporal resolution. To accelerate scientific discovery with ofMRI, several technological innovations were made, including development of real-time imaging with robustness to the live subject's motion which achieves data acquisition, reconstruction, and motion correction (*7*), as well as analysis of three-dimensional (3D) images with high accuracy in approximately 12 ms. To resolve cortical layer and subnuclei–specific responses, novel compressed sensing (*8*–*10*) and machine learning–based fMRI technology was developed, which achieved substantial reduction in voxel volume. MR-compatible optrodes and electrodes were also developed for simultaneous electrophysiological recordings to validate the neural basis of the ofMRI hemodynamic signal (*11*, *12*). These can achieve simultaneous acquisition of electrophysiology recordings during fMRI sessions and provide information with higher temporal resolution in regions of interest identified by ofMRI.

The capabilities and precision of ofMRI have been extensively tested using these advanced ofMRI technologies. It has been shown that location, polarity, and temporal shape of neural activity can be accurately inferred from the ofMRI signal (*3*, *13*, *14*), and that neural activity can be measured by ofMRI across multiple synapses (*11*, *15*). Stimulation cell type, location, frequency (*14*, *15*), and intensity (*11*) were shown to substantially change the location and shape of activities throughout the brain. It was also made clear that whole-brain neural dynamics as measured by ofMRI can accurately predict distinct behaviors (*2*, *14*, *15*).

Many studies have used ofMRI to improve our understanding of fundamental circuitries associated with behavior, memory, and cognition. For instance, Liu *et al*., Weitz *et al*., and Leong *et al*. identified that frequency-dependent thalamic activities drive distinct whole-brain function in circuits associated with arousal, attention, and somatosensory function (*14*, *16*, *17*). Weitz *et al*. and Takata *et al*. revealed distinct dorsal and ventral hippocampal control of brain-wide function (*15*, *18*), Jung *et al*. identified circuits associated with cell type–specific targeting of the somatosensory cortex (*19*), and Choe *et al*. revealed cerebellar cortex functional control over forebrain and midbrain (*20*). Another study revealed brain-wide dynamics that govern how the medial prefrontal cortex regulates reward-related behaviors through distant regions such as the striatum (*21*). A recent study has tried fMRI with cell type–specific activation of astrocytes (*22*). These studies have shown that the observed hemodynamic activities are closely tied to neuronal activities using either simultaneous or follow-up electrophysiology. Furthermore, although most ofMRI studies have been conducted in rodents it has also been applied to nonhuman primates, in which both saccade latencies and whole-brain activity were found to be dependent on specific neuronal targets in the motor cortex (*23*).

The ability to probe and read out whole-brain activity with ofMRI has also advanced our understanding of dysfunctional circuitry associated with neurological disorders. In studies of epilepsy ofMRI provided an advantage as it could be used to optogenetically induce seizures with precise origins on demand while measuring the resulting whole-brain activities with simultaneous electrophysiology recordings. This enabled studies that can generate models to predict and classify seizures using its early activity markers (*15*, *24*). Furthermore, longitudinal effects of seizures on global brain function could be measured to understand how the disease progresses and how seizures are generated and maintained (*25*). These advances aid our understanding of circuit mechanisms underlying seizures and help design intervention parameters such as stimulation location and frequency to effectively inhibit seizures. Optogenetic fMRI can also elucidate mechanisms behind existing therapies, such as post stroke recovery. Activation as measured by ofMRI was highly predictive of the degree of

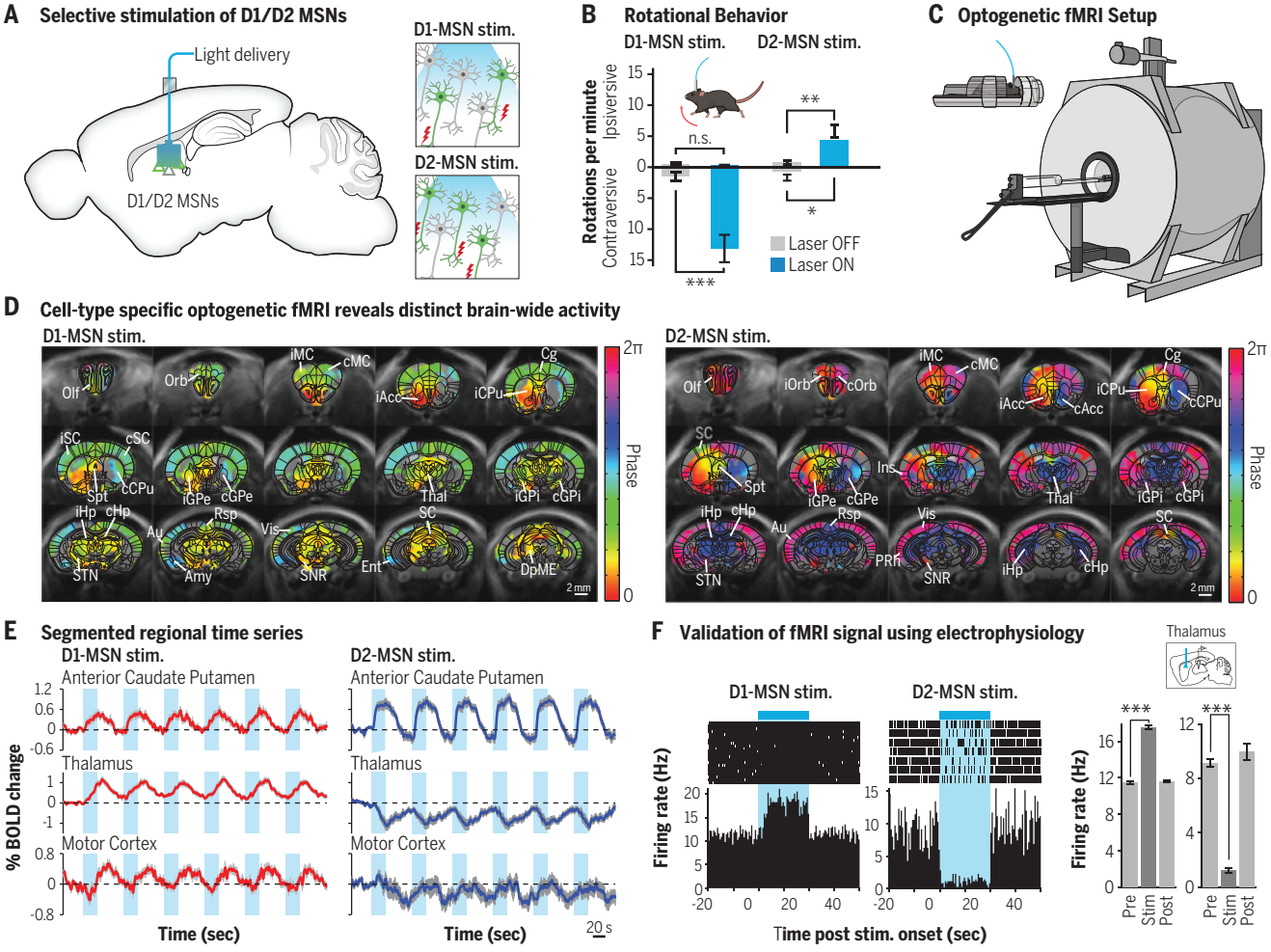


Fig. 1. Optogenetic functional magnetic resonance imaging bridges scales. (**A**) Optogenetics enable cell type–specific stimulations, such as the selective targeting of D1- or D2-MSNs in the striatum. (**B**) With selective stimulations of D1- or D2-MSNs in the striatum, mice show contraversive or ipsiversive rotations, respectively (D1-MSN stim: $n = 12$ animals, mean ± SEM, $^{***}P < 0.001$, two-tailed paired t test; D2-MSN stim: $n = 11$ animals, mean ± SEM, $^{*}P < 0.05$, $^{**}P < 0.005$, two-tailed paired t test). (**C**) Optogenetic fMRI technology combines optogenetic stimulations with fMRI readout. (**D**) ofMRI with selective stimulation of D1- and D2-MSN results in distinct brain-wide activities associated with distinct behavior ($n = 12$ animals). Group-wise phase maps, which were thresholded to only active voxels within the brain, depict the heterogeneity in the temporal dynamics of the evoked responses. (**E**) The time series of any region can be extracted from the 4D fMRI data. (**F**) Electrophysiology recordings mirror fMRI response in polarity of neural activity change. This figure is based on Lee *et al.* (*2*).

recovery and was useful in helping identify sensory circuits involved in this process (*26*).

We can now start to reveal detailed circuit mechanisms that were challenging to understand before. As an example, we will review studies uncovering how D1- and D2-receptor–expressing medium spiny neurons (MSNs) dynamically regulate global brain function and dysfunction (Fig. 1). The cortico-basal-ganglia-thalamus circuit is implicated in many important brain functions including motor control and reward mechanisms. Neurological disorders such as Parkinson's disease, Huntington's disease, addiction, and autism involve this network. The caudate putamen—which seats the D1- and D2-MSNs (Fig. 1A)—is the key node that separates the direct and indirect pathways (Fig. 1B). To assess the brain-wide dynamics driven by inhibitory D1- and D2-MSNs, Lee *et al.* performed whole-brain fMRI during repeated 20-s periods of optogenetic D1- or D2-MSN stimulations (*2*) (Fig. 1C). Active voxels were identified as those significantly synchronized to the repeated stimulations (Fig. 1D). The local signal at the site of stimulation was positive for both inhibitory D1- and D2-MSN stimulations (Fig. 1E), resolving a widely debated issue of whether inhibitory neuron activity evokes a positive or negative fMRI signal. In most regions of the ipsilateral cortico-basal-ganglia-thalamus network, the evoked response in a given region exhibited qualitatively different temporal profiles between D1- and D2-MSN stimulations (Fig. 1, D and E). Given the diversity of BOLD responses evoked by D1- and D2-MSN stimulations, using single-unit recordings we sought to verify whether the responses reflected underlying neuronal activity. For example, the fMRI time series in the thalamus exhibited robust and reliable increases and decreases upon D1- and D2-MSN stimulations, respectively (Fig. 1, D and E). Indeed, single units exhibited an increase in firing rate during D1-MSN stimulations and a decrease in firing rate during D2-MSN stimulations (Fig. 1F). These results demonstrate that ofMRI can detect cell type–specific multisynaptic activity changes across the whole brain with high spatiotemporal precision and that electrophysiological recordings alongside ofMRI can support these findings.

ofMRI has caveats for future improvements as well as potential pitfalls to avoid. Channelrhodopsin (ChR2) is known to evoke synchronized neuronal activity upon light stimulation. Therefore, before launching an ofMRI investigation the behavioral impact of the optogenetic

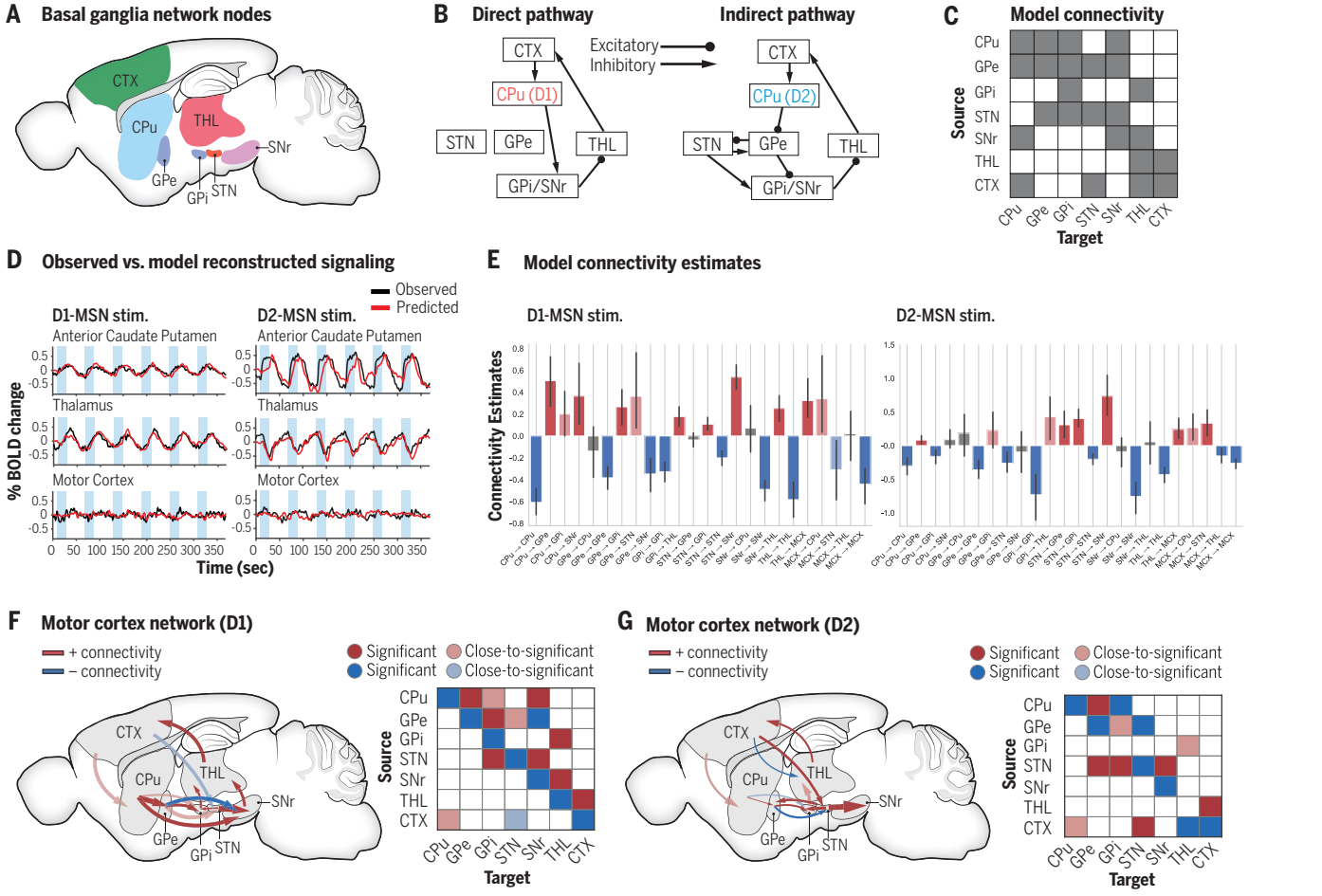


Fig. 2. Computational modeling of ofMRI data reveals brain-wide functional interaction dynamics. (**A**) The cortico-basal-ganglia-thalamus network involves a large number of network nodes across the brain. (**B**) The anatomical connectivity of direct and indirect pathways involve a large number of common anatomical regions with distinct cell types in caudate putamen (CPu). (**C**) Anatomical connections were used as an a priori generative network model. In addition to the direct and indirect pathways shown in (B), other established anatomical connection such as the hyper-direct pathway were also included. (**D**) DCM-generated fMRI time series closely match experimental ofMRI time series. (**E**) DCM used ofMRI data to estimate the causal influence (effective connectivity) among regions of interest during D1- and D2-MSN stimulations, respectively. (**F** and **G**) The graph and matrix representations of effective connectivity network for (F) D1-MSN, and (G) D2-MSN stimulations, respectively. Significant and close-to-significant represent parameters with $P < 0.05$ and $0.05 \leq P < 0.10$, respectively (one-sample t test, multiple comparison correction across connections with FDR $P < 0.10$). CPu, caudate putamen; GPe, external globus pallidus; GPi, internal globus pallidus; STN, subthalamic nucleus; SNr, substantia nigra; THL, thalamus; CTX, cortex. This figure is based on Bernal-casas *et al*. (*4*).

stimulations should first be investigated as a means to ensure that the behavior generated is of interest in either a normal physiological or pathological context. For example, in our D1- and D2-MSN stimulation ofMRI experiments, increased contralateral and ipsilateral rotations were observed, respectively (*2*) (Fig. 1B). This shows that the two separate stimulations result in opposite behaviors known to be associated with movement disorders. The fact that ChR2 evokes synchronization upon light stimulation also makes it suitable for studying pathological oscillations in a number of disease models and contexts. Excessive beta-band oscillations in Parkinson's disease have been extensively explored with ChR2-induced oscillations (*27*, *28*). Some newer opsins such as stabilized step function opsin (*29*) modulate target neurons by increasing the excitability to amplify existing spontaneous activity, which expands the application range of ofMRI to more physiological conditions. There are many aspects of ofMRI that can be further improved. For example, ofMRI will benefit greatly from higher spatio-temporal resolution, real-time feedback–based stimulation control, and imaging during behaviors (*7*, *8*).

Other technologies have also been developed for the investigation of brain circuitries, including high-speed volumetric calcium imaging (*30*, *31*), probes for high-density electrophysiology recordings (*32*, *33*), and widefield calcium and voltage imaging (*34*). Compared with ofMRI, these advances offer higher spatiotemporal resolution although they are limited by recording depths and field of view. For example, widefield "whole-cortex" calcium imaging enables up to 30 Hz simultaneous recording of cortical regions but its depth coverage is limited to superficial layers of cortex. Combining fMRI and widefield calcium imaging has been shown to mitigate the limitations of both methods (*34*). Therefore, future ofMRI studies could be integrated with other technologies for complementary strengths.

Cell type–specific modeling of large-scale brain function

Large-scale neural network models (*35*–*39*) using experimental data from positron emission tomography (*40*), fMRI (*41*), and electroencephalography (EEG)/magnetoencephalography (MEG) (*42*) have made considerable contributions to understanding of brain function. However, although these modeling efforts are based on data from carefully designed experiments that attempt to isolate specific brain functions,

without the capability to untangle contributions from different cell types across the whole brain, models have been limited in their capabilities. The development of ofMRI technology opens an opportunity in terms of whole-brain computational modeling because it measures cell type–specific whole-brain dynamics.

For example, the cortico-basal-ganglia-thalamus network features a large number of network nodes (Fig. 2A) and distinct cell types that have characteristic long-range projections. According to the canonical functional model of basal ganglia (*43*, *44*), movement initiation and suppression are mediated by direct and indirect pathways, respectively (Fig. 2B). The direct pathway promotes movements through D1-MSN excitation in the striatum followed by excitation in the thalamus and consequently the motor cortex. On the other hand, the indirect pathway is assumed to transfer the activation of D2-MSN in the striatum through complex interactions within the basal ganglia, resulting in inhibition of the thalamus and consequently the motor cortex. However, despite the wide usage and success of the canonical model in explaining experimental results, recent experimental evidence argues against the model and finds the interactions between the two pathways still puzzling. For example, the direct and indirect pathways operate simultaneously during movement onsets (*45*).

As demonstrated earlier with ofMRI, we can decompose the operation of the cortico-basal-ganglia-thalamus network by optogenetically activating D1- and D2-MSNs selectively and directly observing the corresponding brain-wide dynamics (*2*) (Fig. 1). However, the degree of connectivity in the cortico-basal-ganglia-thalamus network is too high (Fig. 2, B and C) to identify regional causal influences based on the time series alone (Fig. 2D). Through computational modeling—e.g., dynamic causal modeling (DCM)—with the precision afforded by ofMRI data, cell type–specific causal linkages among regions of interest (ROIs) in the cortico-basal-ganglia-thalamus network could be identified.

DCM is a modeling scheme that estimates the causal coupling (effective connectivity) in a multiregion network based on neuroimaging data (fMRI, MEG/EEG) (*46*–*48*). The estimations are fitted to empirical results using Bayesian techniques. One major strength of DCM is that the estimated regional connectivities are directional, which is especially valuable for networks with many reciprocal connections and feedbacks similar to the cortico-basal-ganglia-thalamus network. ofMRI can also be combined with other modeling schemes. For example, Salvan *et al.* (*49*) optogenetically modulated the entorhinal cortex and combined hidden Markov modeling with ofMRI data to study how entorhinal cortex drives frequency-dependent brain-wide dynamic states. In another study, multivariate dynamical systems (MDS) causal modeling was used with ofMRI to estimate causal brain interactions (*50*). Similar to DCM, MDS models both intrinsically and experimentally induced causal couplings in a large-scale brain network.

In our previous study (*4*) spectral DCM (*36*)—a variation of DCM that enables large-scale networks to be modeled with computational efficiency—was used to investigate the interactions within the cortico-basal-ganglia-thalamus network with ofMRI data from D1- and D2-MSN optogenetic stimulations. One recent study reported consistent results using DCM with D1- and D2-MSN stimulation ofMRI data (*51*). As illustrated in Fig. 2, combining DCM or equivalent modeling schemes with ofMRI data can accurately reveal brain-wide regional interactions. The time series is also accurately reproduced by DCM, closely matching experimental ofMRI time series (Fig. 2D). Fig. 2, E to G show the DCM estimations of between-region effective connectivity (*4*) using ofMRI data. DCM results verified the direct pathway activation during D1-MSN stimulation and indirect pathway activation during D2-MSN stimulation. The defining connections of the direct pathway model are statistically significant (CPu to SNr, GPi to thalamus, SNr to thalamus) or close to significant (CPu to GPi) with D1-MSN stimulations. In the D2-MSN stimulation network, significant connections included those of indirect pathways (CPu to GPe, GPe to STN, STN to GPi/SNr, and GPi to thalamus). The existence of cortical feedbacks can also be observed (Fig. 2, F and G). By contrast, the effective connectivity estimates by DCM also suggest several positive projections that are anatomically inhibitory and cannot be explained by the canonical direct/indirect pathway model, such as the projections from GPi to thalamus during D1-MSN stimulations, which matches several experimental reports of GPi-thalamus paradoxical coactivation (*2*, *52*–*54*). Understanding the mechanism underlying such paradoxical connections requires further microscopic investigations into the specific synaptic interactions with techniques such as single-cell-spiking level modeling and single-unit recordings, as we will discuss next.

Cell type–specific, single-cell-spiking level modeling of brain-wide function

One key strength of computational modeling is that it can bridge spatial scales, from whole-brain dynamics to single-cell activity and explain data from different experimental modalities, from fMRI to extracellular recordings (*55*, *56*). DCM and other macroscale and mesoscale brain models commonly use neural mass models or meanfield models as the basic unit describing the collective neural activity in a brain region or cortical column (*40*–*42*). By contrast, single-cell-spiking models computationally depict the microscopic biophysical features that allow for single-cell-level spiking control and modulation of brain function and dysfunction (*57*–*59*).

In addition to having the ability to capture and model the macroscale and mesoscale interactions between separate regional populations of neurons in the brain with ofMRI and DCM, there is an added advantage in modeling the interactions between individual neurons of varying cell types. Neurological disorders may differentially affect specific cell populations within one brain region. Optogenetically stimulating one type of cell population while inhibiting another type in the external globus pallidus (GPe) prolonged therapeutic effects in a mouse model of Parkinson's disease (*50*). It is widely assumed and supported by optogenetics studies that Parkinson's disease causes hyperactivity of D2-MSNs and hypoactivity of D1-MSNs, thus impairing the balance between the direct and indirect pathways (*44*, *45*, *60*). DYT1 dystonia—a genetic early onset dystonia—is related to cholinergic interneuron dysfunction and altered D2 receptor function in the striatum (*61*, *62*). Firing pattern alterations of one cell type may also contribute to large-scale changes. Optogenetic stimulation in striatal cholinergic interneurons—a subpopulation constituting less than 2% of the striatum—could generate broadband oscillations in the motor network (*27*). With cell type–specific, single-cell-spiking level modeling, it is easier to address the heterogeneity and rich microscopic interactions within one region with biophysical details. ofMRI-based DCM or other regional brain dynamics models can serve as a bridge between whole-brain dynamics and single-cell-spiking level activity, enabling construction of large-scale, cell type–specific biophysical models that can test neuronal-level hypotheses.

Cell type–specific, single-cell-spiking level models that can accurately predict circuit function and dysfunction can be very powerful tools for designing or optimizing therapy. Thus far, many large-scale models without cell type specificity have been constructed to test various hypotheses underlying deep-brain stimulation (DBS), an existing therapy for Parkinson's disease (*63*–*65*). However, because each cell type in the basal ganglia has distinct synaptic and physiological properties, accurate models would need cell type–specific parameters that can fit cell type–specifically acquired experimental data. We envision that ofMRI, DCM, and electrophysiological recordings could be combined to build large-scale biophysical models that can model brain-wide activity at the single-cell-spiking level. Figure 3A illustrates this vision. With ofMRI and electrophysiology experiments providing multiscale data and DCM providing brain-wide interaction information, single-cell level biophysical models, with accurate cell type–specific, large-scale context, can be built and validated (Fig. 3B). As illustrated

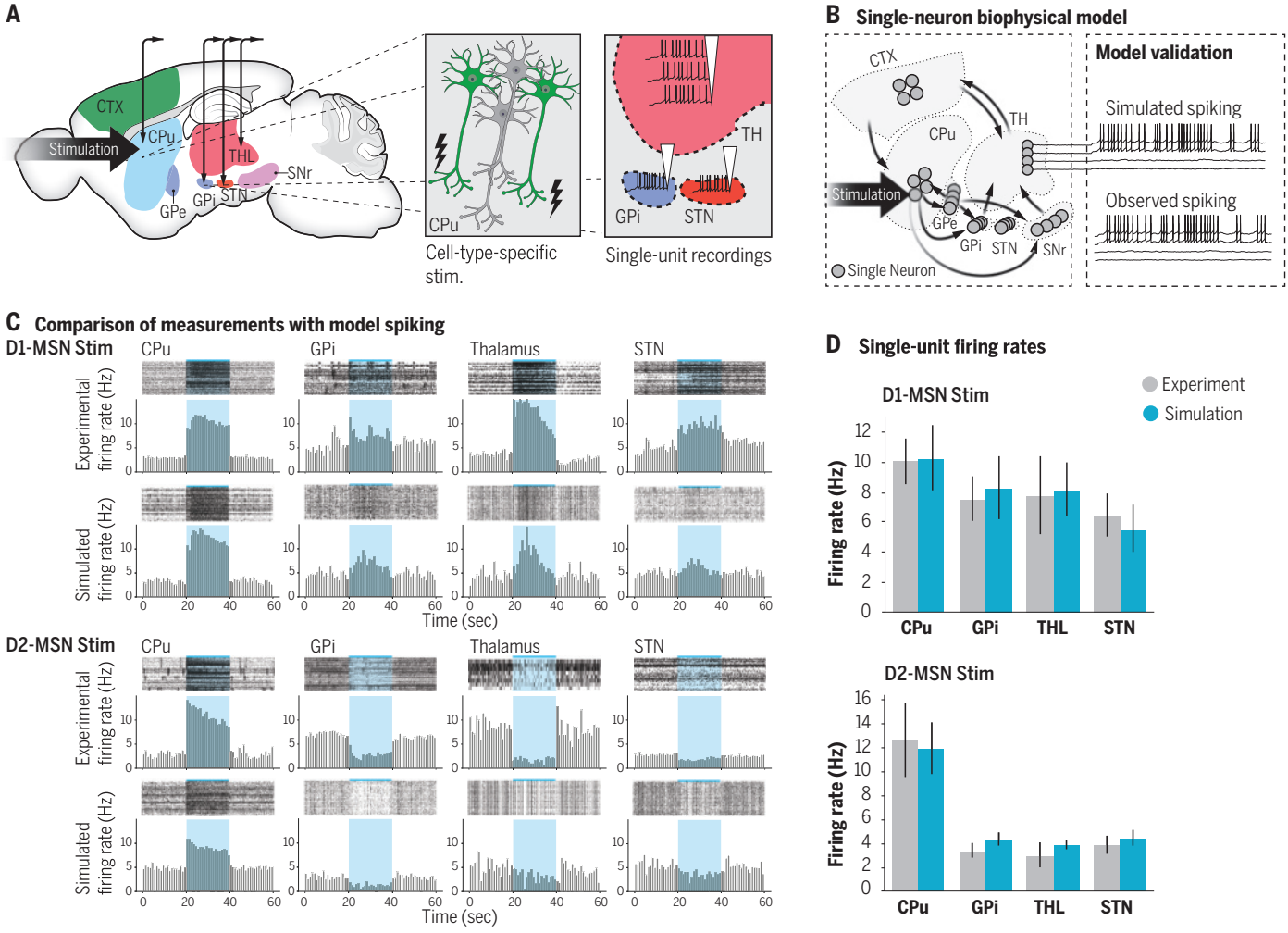


Fig. 3. Brain circuit function modeling at the single-cell-spiking level can be made possible through a multiscale approach. (**A**) Locations of optogenetic stimulation and in vivo extracellular recordings for the cortico-basal-ganglia-thalamus network study are schematically illustrated. (**B**) Single-cell-spiking level modeling with ofMRI and single-unit recording data are exemplified. A large-scale model built with ofMRI data is expanded to a single-neuron level biophysical model. Each ROI consists of many simulated single neurons. The model is validated by directly comparing simulated spiking trains with experimental data. (**C**) Models allow for direct comparison of experimental single-unit recording data and simulated data. (**D**) Models should be designed so that the spike rates of all ROIs simulated by the single-cell spiking level biophysical model statistically match experimental data. ofMRI combined with biophysics modeling can enable successful reproduction of the single-cell-spiking level dynamics induced by cell type–specific optogenetic stimulations such as D1- and D2-MSN stimulations.

single-cell level biophysical models, with accurate cell type–specific, large-scale context, can be built and validated (Fig. 3B). As illustrated in Fig. 3, C and D, a single-cell-spiking level model can be designed to reproduce experimental neuronal activity and group dynamics with high precision. With such models, we can imagine simulating brain-wide spiking activity from "virtual neuromodulations" without needing to do in vivo experiments. We would then be able to use these results to better optimize therapeutic targets and parameters in which simulated spiking matches our desired response. For example, a recent study (*66*) employed optogenetics and single-cell level computational modeling within three different cell types of the motor cortex to show that DBS on cortical somatostatin interneurons can ameliorate Parkinsonian symptoms. We envision that in the future, ofMRI-enabled brain-wide models with single-cell-spiking level precision will ultimately enable systematic design of neuromodulation therapy with predictable outcomes.

Modeling whole-brain pathology dynamics and their relationship with brain function

Brain circuitry is relevant to neurological disorders beyond use in modeling local and global brain function. It is also important for understanding the underlying pathology of many disorders. In the case of Parkinson's disease and other synucleinopathies, the seeding and gradual accumulation of pathological alpha-synuclein (α-syn) causes dopaminergic neurodegeneration, which ultimately leads to striatal imbalance and the cardinal Parkinsonian signs (*67*). Although the specific biochemical trafficking mechanisms of these proteins remain unknown, several recent studies have shown that whole-brain spreading patterns are highly dependent on the inoculation site (*68*), and that Anatomical connectivity is highly predictive of susceptible regions after induced seeding of α-syn pathology (*69*).

To understand the linkage between anatomical connections, pathology, and function, it is important to reliably measure whole-brain pathological states. The past decade has seen several prominent advancements in whole-brain tissue clearing technology. These range from hydrogel-based techniques such as CLARITY (*70*)—which enables multiplexed brain imaging but potentially requires long incubation times—to solvent-based techniques such as 3DISCO (*71*) that are generally faster but may bleach fluorescent signals. Combining these

tissue-clearing methods with whole-brain immunolabeling and light-sheet microscopy allows for high-resolution examination of whole-brain pathology using biochemical reporters (*72*, *73*). As these 3D whole-brain histological datasets now provide micron resolution and are exceeding terabytes in size, it is necessary to have automated registration and segmentation techniques (*74*) to capture the rich information provided by the data. Figure 4A depicts how a Parkinsonian disease model in which the injection of α-synuclein PFFs are used to trigger whole-brain pathology can be systematically analyzed using a computational pipeline. Brains can be immunolabeled and cleared at each time point using the iDISCO method (*72*), with the imaged aggregates automatically segmented and registered to a standardized atlas. As depicted in Fig. 4B, longitudinal analysis of pathology can demonstrate a highly dynamic, brain-wide process of spreading after seeding of α-syn, consistent with numerous histological studies (*67*, *69*). Registration to a standardized atlas can provide an enormous advantage enabling systematic statistical comparisons and analysis of disease pathology alongside connectomic (*75*), genetic (*76*), and vascular (*77*) databases, which all reside in the same reference coordinate space. Most notably, the Allen Connectivity Atlas (*75*) has been crucial in the development of models describing the spread of pathology through the connectome (*69*). For instance, network diffusion models represent whole-brain circuitry as a directed graph with neuroanatomical regions as nodes and axonal pathways as edges between these nodes (Fig. 4C). These models have found wide applicability in predicting the spread of α-syn pathology in both rodent and human imaging studies (*69*, *78*), as well as in human dementia (*79*) and supranuclear palsy neuroimaging studies (*80*). In Fig. 4C, we present an example of how a whole-brain model can accurately reconstruct the regional variability in pathology. Compared with previous models dependent upon serial histological sectioning (*69*) or in vivo human imaging data (*78*), this type of modeling can provide a more comprehensive, higher resolution description of pathology dynamics that includes all brain regions, which is important

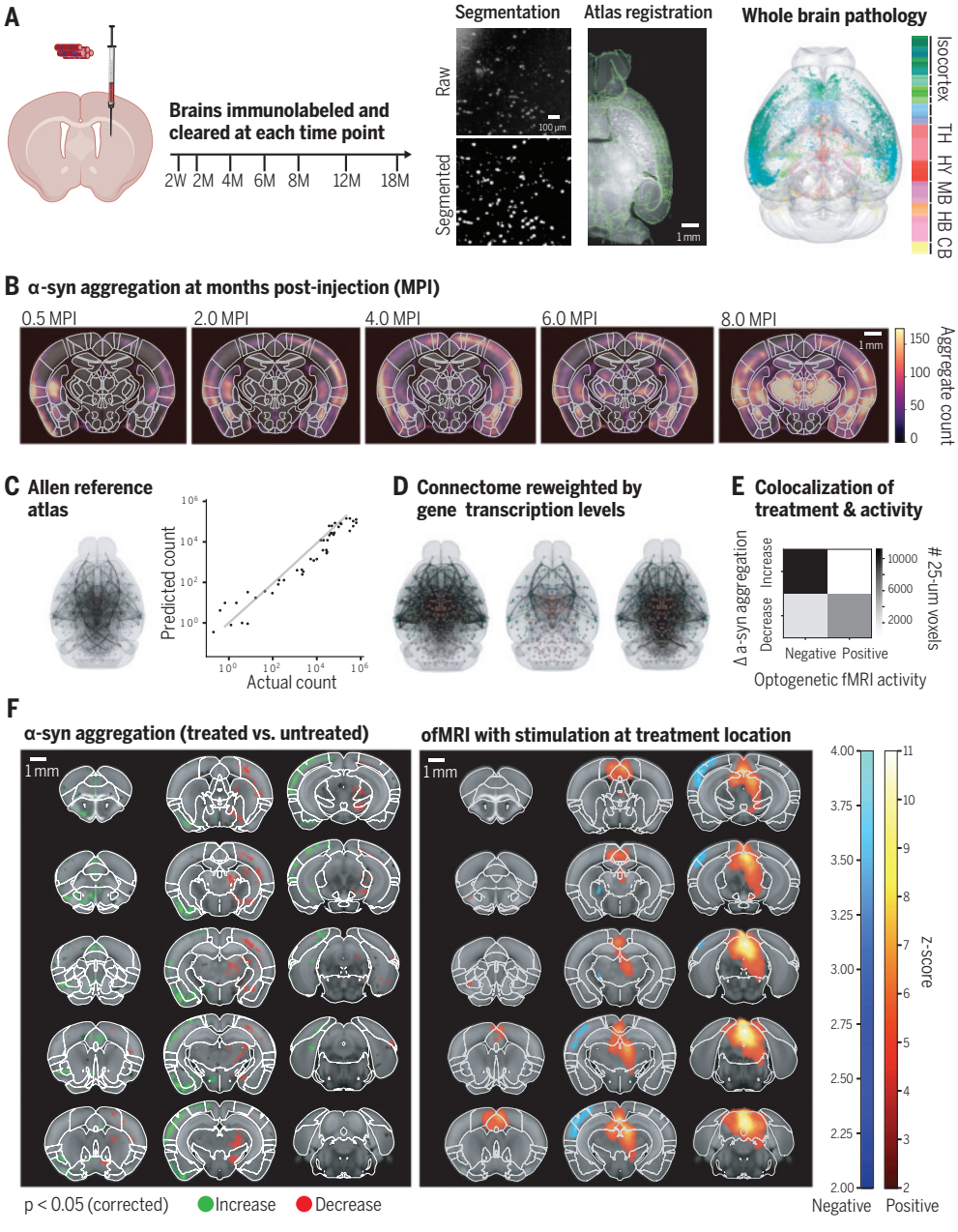


Fig. 4. To understand pathology function interaction, whole-brain pathology dynamics can be modeled alongside ofMRI. (**A**) α-synuclein PFFs injected into seed locations induce pathology at various time points post-injection, which can then be captured by iDISCO tissue clearing and light-sheet fluorescent microscopy (LSFM). Machine-learning–based, automatic segmentation and registration techniques can streamline the quantification of each pathological marker within the Allen Reference Atlas (ARA). (**B**) Comparisons of averaged heatmaps across cohorts can depict whole-brain pathology changes over many months after injection. (**C**) Modeling of longitudinal data based on whole-brain anatomical connectivity can capture regional differences in pathology. (**D**) Reweighting the connectivity matrix can allow for encoding of genetic contribution within a model. (**E**) Whole-brain colocalization analysis between optogenetic-stimulation induced alpha-synuclein pathology change and optogenetic fMRI activity can reveal the relationship between pathology and function. In this example, positive activity is colocalized with decreases in pathology, whereas negative activity is highly colocalized with increases in pathology. (**F**) Montages of the modulated alpha-synuclein pathology and ofMRI brain activity maps show a high degree of colocalization with opposite polarity.

for quantitative model descriptions. Given that transgenic mice such as those with modified LRRK2 (*69*, *81*) or SNCA (*67*) expression demonstrate significantly altered spreading patterns, models can additionally incorporate the brain's inherent genetic or cell type–specific differences. As depicted in Fig. 4D, reweighting the connectivity matrix by regional expression of a gene of interest can allow for evaluation of that gene's relevance in disease spread. Henderson *et al.* weighted a network diffusion model with SNCA expression, demonstrating that in silico simulation of circuits and genes can recover observed α-synuclein pathology (*69*).

Accurate whole-brain models of pathology dynamics that can predict both future and past states of these progressive disorders will have important clinical implications. For example, a computational model that takes an arbitrary pathological state and predicts future states could guide interventions dependent upon the predicted localization of pathology. Similarly, a model that can iterate backward and compute previous states, even back to the initial seeding site, can further aid in disease progression classification for diagnosis purposes. Because neurodegenerative disorders such as Parkinson's disease, Lewy body dementia, and multiple system atrophy have long been hypothesized to collectively form a neuropathological spectrum (*82*), modeling the various circuits that drive different pathologies and clinical manifestations will play a large part in precisely defining these disorders.

Although functional and histological readouts provide distinct information regarding the brain and disease, their colocalization is likely to be important in both furthering our understanding of neural circuitry and developing novel therapeutics. For instance, combining ofMRI and whole-brain pathological labeling could aid in the development of therapeutics that treat the underlying pathology, such as α-syn pathology in Parkinson's disease. We give an example of spatial colocalization between optogenetic stimulation–induced changes and ofMRI-measured functional changes observed during delivery of the same stimulation (Fig. 4, E and F). This optogenetic stimulation paradigm reduces the α-synuclein aggregate count at the site of stimulation and in various downstream regions. When colocalized with brain activity, their similar spatial locations but opposing polarities are apparent, revealing that positive activity is colocalized with decreases in pathology, whereas negative activity is highly colocalized with increases in pathology.

This ability to target pathology with neuromodulation, while predicting subsequent brain-wide changes in pathology could provide an alternative way of thinking about neuromodulation therapy for Parkinson's disease and related disorders. For instance, parameters such as duration and site of neuromodulation could be tailored to patients on the basis of their current pathological state and the expected impact of a given neuromodulation parameter on pathology. Taking it one step further, therapy could even be designed while taking the expected future states of pathology into consideration. Altogether, the ability to readout and model pathology with brain clearing while measuring whole-brain network function with optogenetic fMRI will allow for the development of circuit-based models that bridge pathology and function.

Conclusion

These recent advancements in cell type–specific neuromodulation, whole-brain functional imaging, and computational modeling are starting to pave a path for a major turning point in neuroscience. We aim to establish new approaches to simulating brain function that can replicate and predict behaviors of interest. This will transform the treatment of a wide array of neurological diseases including Parkinson's disease.

REFERENCES AND NOTES

1. P. Calabresi, B. Picconi, A. Tozzi, V. Ghiglieri, M. Di Filippo, *Nat. Neurosci.* **17**, 1022–1030 (2014).
2. H. J. Lee *et al.*, *Neuron* **91**, 412–424 (2016).
3. J. H. Lee *et al.*, *Nature* **465**, 788–792 (2010).
4. D. Bernal-Casas, H. J. Lee, A. J. Weitz, J. H. Lee, *Neuron* **93**, 522–532.e5 (2017).
5. F. Zhang, A. M. Aravanis, A. Adamantidis, L. de Lecea, K. Deisseroth, *Nat. Rev. Neurosci.* **8**, 577–581 (2007).
6. A. M. Aravanis *et al.*, *J. Neural Eng.* **4**, S143–S156 (2007).
7. Z. Fang, J. H. Lee, *J. Neurosci. Methods* **218**, 184–195 (2013).
8. Z. Fang, N. Van Le, M. Choy, J. H. Lee, *Magn. Reson. Med.* **76**, 440–455 (2016).
9. D. J. Holland *et al.*, *Magn. Reson. Med.* **70**, 1634–1643 (2013).
10. X. Zong, J. Lee, A. John Poplawsky, S. G. Kim, J. C. Ye, *Neuroimage* **92**, 312–321 (2014).
11. B. A. Duffy, M. Choy, M. R. Chuapoco, M. Madsen, J. H. Lee, *Neuroimage* **123**, 173–184 (2015).
12. M. R. Chuapoco *et al.*, *Neuroimage* **186**, 806–816 (2019).
13. B. Byers *et al.*, *Neuroimage* **114**, 328–337 (2015).
14. J. Liu *et al.*, *eLife* **4**, e09215 (2015).
15. A. J. Weitz *et al.*, *Neuroimage* **107**, 229–241 (2015).
16. A. J. Weitz, H. J. Lee, M. Choy, J. H. Lee, *Neuron* **104**, 1153–1167.e4 (2019).
17. A. T. Leong *et al.*, *Proc. Natl. Acad. Sci. U.S.A.* **113**, E8306–E8315 (2016).
18. N. Takata *et al.*, *PLOS ONE* **10**, e0121417 (2015).
19. W. B. Jung, H. Jiang, S. Lee, S. G. Kim, *Proc. Natl. Acad. Sci. U.S.A.* **119**, e2113313119 (2022).
20. K. Y. Choe, C. F. Sanchez, N. G. Harris, T. S. Otis, P. J. Mathews, *Neuroimage* **173**, 370–383 (2018).
21. E. A. Ferenczi *et al.*, *Science* **351**, aac9698 (2016).
22. N. Takata *et al.*, *Glia* **66**, 2013–2023 (2018).
23. A. Gerits *et al.*, *Curr. Biol.* **22**, 1722–1726 (2012).
24. B. A. Duffy, M. Choy, J. H. Lee, *Cell Rep.* **30**, 2540–2554.e4 (2020).
25. M. Choy *et al.*, *Neuron* **110**, 221–236.e4 (2022).
26. S. Vahdat *et al.*, *Sci. Adv.* **7**, eabd9465 (2021).
27. B. Crompe *et al.*, *Nat. Commun.* **11**, 1570 (2020).
28. K. Kondabolu *et al.*, *Proc. Natl. Acad. Sci. U.S.A.* **113**, E3159–E3168 (2016).
29. O. Yizhar *et al.*, *Nature* **477**, 171–178 (2011).
30. J. Demas *et al.*, *Nat. Methods* **18**, 1103–1111 (2021).
31. V. Voleti *et al.*, *Nat. Methods* **16**, 1054–1062 (2019).
32. N. A. Steinmetz *et al.*, *Science* **372**, eabf4588 (2021).
33. R. Hultman *et al.*, *Cell* **173**, 166–180.e14 (2018).
34. E. M. R. Lake *et al.*, *Nat. Methods* **17**, 1262–1271 (2020).
35. O. Sporns, *Networks of the brain*. (The MIT Press, 2016).
36. A. R. McIntosh, *Neural Netw.* **13**, 861–870 (2000).
37. X. J. Wang, *Physiol. Rev.* **90**, 1195–1268 (2010).
38. G. Deco, M. L. Kringelbach, *Neuron* **84**, 892–905 (2014).
39. A. Fornito, A. Zalesky, M. Breakspear, *Nat. Rev. Neurosci.* **16**, 159–172 (2015).
40. M. A. Tagamets, B. Horwitz, *Cereb. Cortex* **8**, 310–320 (1998).
41. K. E. Stephan *et al.*, *Neuroimage* **42**, 649–662 (2008).
42. S. J. Kiebel, O. David, K. J. Friston, *Neuroimage* **30**, 1273–1284 (2006).
43. R. L. Albin, A. B. Young, J. B. Penney, *Trends Neurosci.* **12**, 366–375 (1989).
44. M. R. DeLong, *Trends Neurosci.* **13**, 281–285 (1990).
45. J. G. Parker *et al.*, *Nature* **557**, 177–182 (2018).
46. K. J. Friston, L. Harrison, W. Penny, *Neuroimage* **19**, 1273–1302 (2003).
47. K. J. Friston, J. Kahan, B. Biswal, A. Razi, *Neuroimage* **94**, 396–407 (2014).
48. K. E. Stephan *et al.*, *Neuroimage* **49**, 3099–3109 (2010).
49. P. Salvan *et al.*, *Cell Rep.* **37**, 109954 (2021).
50. S. Ryali *et al.*, *Neuroimage* **132**, 398–405 (2016).
51. C. Grimm *et al.*, *Cell Rep.* **37**, 110161 (2021).
52. J. Kim *et al.*, *Neuron* **95**, 1181–1196.e8 (2017).
53. B. C. Schwab *et al.*, *PLOS Biol.* **18**, e3000829 (2020).
54. J. H. Goldberg, M. A. Farries, M. S. Fee, *Trends Neurosci.* **36**, 695–705 (2013).
55. G. Deco, V. K. Jirsa, P. A. Robinson, M. Breakspear, K. Friston, *PLOS Comput. Biol.* **4**, e1000092 (2008).
56. M. Schirner, A. R. McIntosh, V. Jirsa, G. Deco, P. Ritter, *eLife* **7**, e28927 (2018).
57. J. J. J. Hjorth *et al.*, *Proc. Natl. Acad. Sci. U.S.A.* **117**, 9554–9565 (2020).
58. X. Zhang, S. Santaniello, *Proc. Natl. Acad. Sci. U.S.A.* **116**, 13592–13601 (2019).
59. M. J. Bezaire, I. Raikov, K. Burk, D. Vyas, I. Soltesz, *eLife* **5**, e18566 (2016).
60. A. V. Kravitz *et al.*, *Nature* **466**, 622–626 (2010).
61. K. L. Eskow Jaunarajs, P. Bonsi, M. F. Chesselet, D. G. Standaert, A. Pisani, *Prog. Neurobiol.* **127-128**, 91–107 (2015).
62. G. Sciamanna *et al.*, *Cell Rep.* **31**, 107644 (2020).
63. J. M. Meier *et al.*, *Exp. Neurol.* **354**, 114111 (2022).
64. W. J. Neumann *et al.*, *Brain* **141**, 2655–2669 (2018).
65. E. M. Adam, E. N. Brown, N. Kopell, M. M. McCarthy, *Proc. Natl. Acad. Sci. U.S.A.* **119**, e2120808119 (2022).
66. S. Valverde *et al.*, *Nat. Commun.* **11**, 2388 (2020).
67. K. C. Luk *et al.*, *Science* **338**, 949–953 (2012).
68. Y. J. Guo, H. Xiong, K. Chen, J. J. Zou, P. Lei, *Mol. Psychiatry* **27**, 758–770 (2022).
69. M. X. Henderson *et al.*, *Nat. Neurosci.* **22**, 1248–1257 (2019).
70. K. Chung, K. Deisseroth, *Nat. Methods* **10**, 508–513 (2013).
71. A. Ertürk *et al.*, *Nat. Protoc.* **7**, 1983–1995 (2012).
72. N. Renier *et al.*, *Cell* **159**, 896–910 (2014).
73. T. Liebmann *et al.*, *Cell Rep.* **16**, 1138–1152 (2016).
74. N. Renier *et al.*, *Cell* **165**, 1789–1802 (2016).
75. S. W. Oh *et al.*, *Nature* **508**, 207–214 (2014).
76. E. S. Lein *et al.*, *Nature* **445**, 168–176 (2007).
77. C. Kirst *et al.*, *Cell* **180**, 780–795.e25 (2020).
78. S. Pandya *et al.*, *Neuroimage* **192**, 178–194 (2019).
79. A. Raj, A. Kuceyeski, M. Weiner, *Neuron* **73**, 1204–1215 (2012).
80. S. Pandya, C. Mezias, A. Raj, *Front. Neurol.* **8**, 692 (2017).
81. G. Bieri *et al.*, *Acta Neuropathol.* **137**, 961–980 (2019).
82. J. W. Langston, *Ann. Neurol.* **59**, 591–596 (2006).

ACKNOWLEDGMENTS

Funding: J.H.L., Q.L., and E.D.-K. were supported by NIH/NIMH RF1 MH114227, NIH/NINDS DP1 NS116783, and NIH S10 OD025176. J.H.L. and E.D.-K. were also supported by NIH/NIA R01 AG064051 and NIH/NIBIB R01 EB030884. **Author contributions:** J.H.L. planned and wrote the paper and made the figures, and also mentored and supported all personnel involved in the projects presented and manuscript writing. Q.L. and E.D.-K. made the figures and wrote sections of the paper. **Competing interests:** J.H.L. is a founder, consultant, and board member of LVIS. Q.L. and J.H.L are inventors on a pending patent application, titled "Joint Dynamic Causal Modeling and Biophysics Modeling to Enable Multi-Scale Brain Network Function Modeling." **Data and materials availability:** All data and materials necessary to understand and assess these conclusions are available in the manuscript.

License information: Copyright © 2022 the authors, some rights reserved; exclusive licensee American Association for the Advancement of Science. No claim to original US government works. https://www.sciencemag.org/about/science-licenses-journal-article-reuse

Submitted 28 May 2022; accepted 19 August 2022
10.1126/science.abq3868

REVIEW

Scale matters: The nested human connectome

Markus Axer[1,2]* and Katrin Amunts[1,3]

A comprehensive description of how neurons and entire brain regions are interconnected is fundamental for a mechanistic understanding of brain function and dysfunction. Neuroimaging has shaped the way to approaching the human brain's connectivity on the basis of diffusion magnetic resonance imaging and tractography. At the same time, polarization, fluorescence, and electron microscopy became available, which pushed spatial resolution and sensitivity to the axonal or even to the synaptic level. New methods are mandatory to inform and constrain whole-brain tractography by regional, high-resolution connectivity data and local fiber geometry. Machine learning and simulation can provide predictions where experimental data are missing. Future interoperable atlases require new concepts, including high-resolution templates and directionality, to represent variants of tractography solutions and estimates of their accuracy.

Cognitive abilities and behavior are closely related to the connectome, which is described as "a comprehensive description of how neurons and brain regions are interconnected. It is the indispensable foundation for understanding how brain dynamics and function emerge from their underlying structural (neural) substrate" (*1*). The human brain has ~86 billion neurons, each with up to 10,000 synapses. Neurons form hundreds of cortical areas and subcortical nuclei, which are connected by nerve fibers. Signal propagation along these fibers is an electrochemical process that includes a variety of neurotransmitters, as well as postsynaptic excitatory or inhibitory potentials, and is supported by the activity of glial cells. Consequently, a comprehensive understanding of the connectome encompasses the molecular and the cellular level up to the macro level—that is, it requires addressing a multiscale system.

To approach the entire connectome was until now only possible in the smaller brains of invertebrates such as *Caenorhabditis elegans* (*2*) and rodents such as the mouse (*3*). Mapping the mouse brain at the synaptic level now seems to be in reach (*4*). For the human brain, a comparable resolution can be achieved in small tissue blocks and slabs (e.g., using optical methods with clearing) but not yet whole-brain wide.

Here, we focus on fiber architecture because of progress made in human neuroimaging, in particular anatomical and diffusion magnetic resonance imaging (MRI), which illustrates approaches to bridging the gap to higher-resolution optical methods, and discuss the respective challenges posed by the specific characteristics of the human brain.

[1]Institute of Neurosciences and Medicine (INM-1), Research Centre Jülich, Jülich, Germany. [2]Department of Physics, School of Mathematics and Natural Sciences, Bergische Universität Wuppertal, Wuppertal, Germany. [3]Cécile and Oskar Vogt Institute for Brain Research, Medical Faculty, University Hospital Düsseldorf, Heinrich-Heine University Düsseldorf, Düsseldorf, Germany.
*Corresponding author. Email: m.axer@fz-juelich.de

Axonal architecture and nerve fibers

Axons are branches of neurons that transmit signals from one neuron to the next, sometimes over many centimeters (*5*). They are only a few micrometers thick, with a length-to-caliber ratio in the range of 100,000:1, which makes it challenging to trace a single axon over its entire extent. Many axons have a myelin sheath (a stack of lipid bilayers), and a myelinated axon is what we call a fiber. Dendrites represent the other type of branches and integrate signals from other neurons. The spatially organized neuronal cell bodies (*6*) and the neuropil (including, e.g., dendrites and glial cell processes) make up the gray matter of the brain, which includes the cerebral cortex and subcortical nuclei.

The wiring of the cerebral cortex encompasses both short-range and long-range axonal connections between neurons (Fig. 1). Short-range connections form local circuits (such as the U-shaped fibers connecting neighboring gyri), whereas long-range connections link different brain regions in the same hemisphere (long association fibers) or between them (commissural fibers). Ascending and descending connections link the cortex to subcortical nuclei and the spinal cord (projection fibers). Long-range axonal connections cluster into large, dense bundles of fibers making up the brain's white matter (stained dark in Fig. 1A).

Fibers within the cortex are less densely packed and show a high degree of structuredness in what is referred to as the myeloarchitecture. Myeloarchitectonic research was driven by Oskar and Cécile Vogt, who systematically studied differences between cortical regions, resulting in a map of >150 areas (*6*). This map, however, was not a mere mosaic of areas. Rather, it was an early attempt to group the regions on the basis of their myeloarchitectonic similarities (e.g., the expression of the stripes of Baillarger; Fig. 1A) into families and superfamilies and to build "nested" representations. In addition, the Vogts studied myeloarchitecture in combination with cellular architecture, neurophysiology, anatomy, and even genetics to understand their relationship to function and dysfunction, an early approach that viewed the human brain as a multiscale system with a nested design. Although this work of the Vogts has largely fallen into oblivion, their view of cortical areas forming nested groups and hierarchies has received ample support from recent studies of connectivity (*7*), cyto expression, receptor expression, and gene expression (*8*). Precisely what these hierarchies look like, how they are defined, and how they map to each other are ongoing topics of research (*9*).

Fibers may form polysynaptic pathways, collaterals, and feedback connections (*5*). Also targets of intensive research are the interplay of electrical and molecular-biochemical mechanisms of signal transduction at synapses; synaptic plasticity; lifelong reorganization; the relevance of fiber architecture for supporting a concrete cognitive function; the specific and dynamic consequences of variations in brain organization, including cytoarchitecture, myeloarchitecture, and chemoarchitecture; and interregional connectivity (*10*).

Two major lines of empirical research can be used to study structural connectivity in the human brain: diffusion MRI-based neuroimaging (dMRI) and methods targeting connectivity at higher spatial resolution in postmortem brains.

In vivo diffusion MRI

dMRI allows us to approach the connectome in both living subjects and in postmortem brains. In combination with tractography, functional MRI (fMRI), modeling, and (graph) theoretical approaches, it enables us to reveal fiber tracts, quantify network characteristics, and predict function.

The Human Connectome Project (HCP) enabled substantial progress in the area of in vivo neuroimaging for measures of structural and functional brain connectivity (*11*). dMRI was established as the tool of choice to study structural connectivity at the macroscale, pushed by new scanner designs and innovative white matter reconstruction methods. The HCP started with a focus on healthy young adults, explored relationships with behavior and lifestyle, and freely shared the imaging data, protocols, and software tools with the scientific community. This has become a blueprint for other large-scale cohort projects (Lifespan HCP, ABCD, UK Biobank, etc.) (*11*). These projects collect, in a systematic manner, a large amount of diffusion-based connectivity data often complemented by functional imaging, questionnaires, and neurological surveys, and they are the basis for a large body of research worldwide.

dMRI is sensitive to the random microscopic motion or diffusion of water molecules. By measuring dMRI signals along various orientations, distributions of local fiber orientations can be derived. These orientations are

used to computationally infer trajectories of white matter pathways (tractography) to estimate connectivity (Fig. 2, A to C) (*12*). Methods for tractography can be grouped according to their most distinguishing features, such as deterministic and probabilistic, local and global, shortest-path, or machine learning–based algorithms, with specific applications in research and clinical contexts (*12*–*14*).

Challenges arise in the context of interpretation and quantification. Reconstructed trajectories are modeled entities and do not necessarily represent physical nerve fibers (*14*). Basic diffusion metrics represent inferences that are based on local diffusion properties, which are not direct measures of tissue properties, nor do they provide information about the directionality of the connections. Tractography algorithms may result in false-positive and false-negative pathways, e.g., due to limited spatial and angular resolution (*15*). Given that a single voxel 1 mm in size contains hundreds of thousands of single fibers, different fiber configurations within, such as bending, fanning, crossing, and kissing, can result in the same signal, making it nearly impossible to distinguish between the different cases at the voxel level. Trajectories tend to "travel" parallel to the cortical surface, largely avoiding sulcal walls and fundi and terminating preferentially on gyral crowns. Sharp fiber turns from long-distance fibers and U-shaped fibers are not resolvable (*14*, *16*). This makes cross-validation an important topic.

Postmortem diffusion MRI

dMRI enables the study of postmortem tissues with higher resolution, down to a few hundred micrometers. It has been shown to provide meaningful measures of axonal properties such as diameters and densities (*17*) to aid in our understanding of the biological correlates of dMRI measures (*18*).

Postmortem imaging can also harness the advantages of higher magnetic field and gradient strengths, more sensitive radiofrequency coils, and longer scan times (*19*). Using tailored acquisition pulse sequences, isotropic spatial resolutions of 300 to 500 μm have been achieved. This allowed the study of the connectivity of anatomical structures such as the hippocampus (Fig. 2, D and E) (*20*), as well as whole brains (*21*). Pushing the resolution of a whole-brain dataset to this resolution leads inevitably to terabytes of data and has consequences for software and hardware demands. A human whole-brain tractogram may consist of ~100 million trajectories, posing a serious challenge for visualization and connectivity assessment.

The possibility of using the same tissue for dMRI and for microscopy opens the possibility of validating the results of tractography and providing biologically meaningful connectivity information (*22*).

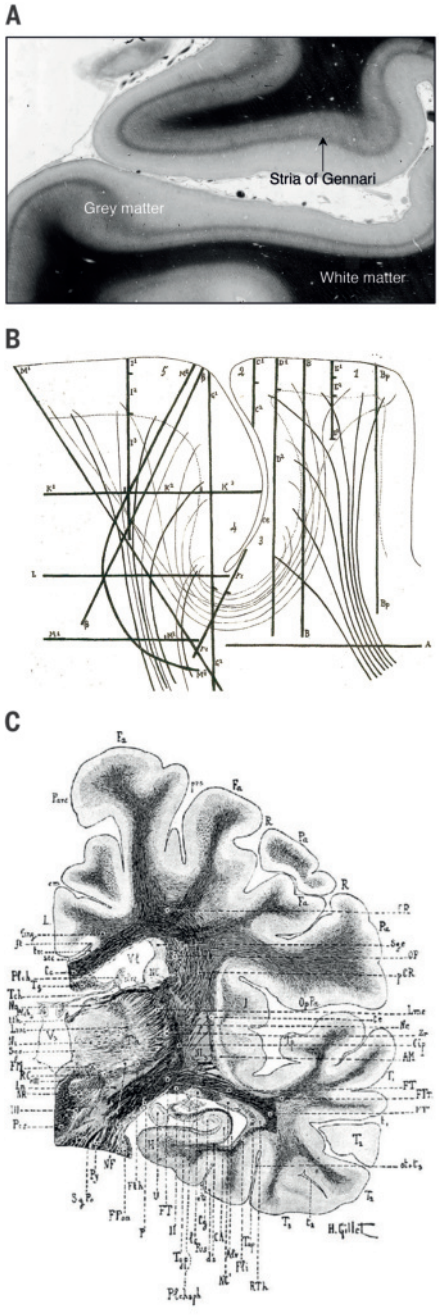


Fig. 1. Historical approaches to studying human brain connectivity showing association, commissural, and projection fibers. (**A**) Myelin-stained fibers in the primary visual cortex with the external band of Baillarger, the stria of Gennari. (Section from the brain collection of the Cécile and Oskar Vogt Institute for Brain Research, Heinrich Heine University Düsseldorf, Germany.) (**B**) Drawing of white matter tracts in the region of the central sulcus. Shown are projection fibers (thick lines), subcortical U-shaped fibers, and intersecting callosal fibers (image reproduced with permission from the archive of the Cécile and Oskar Vogt Institute of Brain Research, Heinrich Heine University Düsseldorf, Germany). (**C**) Drawing of a myelin-stained coronal human brain section [image reproduced from (*51*)].

Klingler's dissection

With the introduction of dMRI and tractography, there has been renewed interest in Klingler's dissection because it enables physically tracing white matter bundles in postmortem human brains (*23*). The process of freezing and thawing of formalin-fixed tissue facilitates the dissection of fine fiber bundles. Digitization poses a particular challenge. Laser scanning was proposed to obtain surface images to be registered to corresponding MRI scans (*24*). Dissection studies are performed on small numbers of specimens following selected long-range white matter tracts, but whole-brain or cortical connectivity analyses are currently out of reach.

Imaging with polarized light

Polarization microscopy reveals fibers and even single axons at the level of a few micrometers. It does not use contrast agents and relies exclusively on birefringence, which is an optical property of anisotropic material usually caused by orderly arranged molecules, atoms, or spatially repeating configurations, such as those found in nervous tissue.

Polarization microscopy has been used to study nerve fibers in normal and pathological tissue for >100 years and experienced a considerable boost when techniques moved from two dimensions (2D) to 3D. When polarized light passes through a thin brain section, alterations in the polarization state of the light generate contrast between fibers of different orientation and birefringence strength (reflecting myelin density). Matrix optics enables estimation of 3D orientations of fibers. 3D–polarized light imaging (3D-PLI) was introduced more than a decade ago (*25*). In this method, fiber orientations are displayed as a color-coded fiber orientation map (Fig. 3, A to F) or as glyphs when combined over a neighborhood to describe the fiber orientation distribution (Fig. 3C) (*26*). Fiber orientation distributions can be upscaled to larger voxel sizes for validating distribution functions obtained with dMRI.

3D-PLI can resolve the fine-grained fiber architecture of the cerebral cortex, as well as fibers around and within nuclei. At the same time, it enables following projection, association, and commissural pathways over large distances (Fig. 3). By contrast, conventional myelin staining stays within 2D and does not resolve fiber orientations in the densely packed white matter. Moreover, 3D-PLI contrast is generated by myelinated and unmyelinated axons, which results in rich information where myelin staining fails [e.g., mossy fibers in the hippocampus (*27*)].

Limitations of 3D-PLI include time- and labor-intensive laboratory work and inaccuracies in the 3D reconstruction of sections with distortions caused by histological processing.

Registration workflows have been developed to reduce distortions and to improve the alignment (*19*). High-throughput scanning and the use of supercomputing-based workflows allowed the reconstruction and analysis of large amounts of data (in the terabyte to petabyte range) and provided new insights into the intricate connectivity of brain regions such as the corpus callosum (*28*), sagittal stratum (*29*), and brainstem (*30*). A recent hippocampus study investigated the full topography of the different components of the perforant pathway, a key player in learning and memory (*27*). 3D-PLI can be applied in different species to reveal similarities in brain structure (*31*, *32*).

Polarization-sensitive optical coherence tomography (PSOCT) is another approach to probing birefringence and determining the orientation of fibers by means of polarized light (*33*). This technique relies on the backscattering of light from a block of tissue, analogous to ultrasound technologies. PSOCT does not require the tissue to be sectioned before it is imaged, which makes volumetric fiber visualization possible without large reconstruction artifacts. However, the technique is currently limited to cubic centimeter–sized tissue blocks, which still prevents a whole-brain approach.

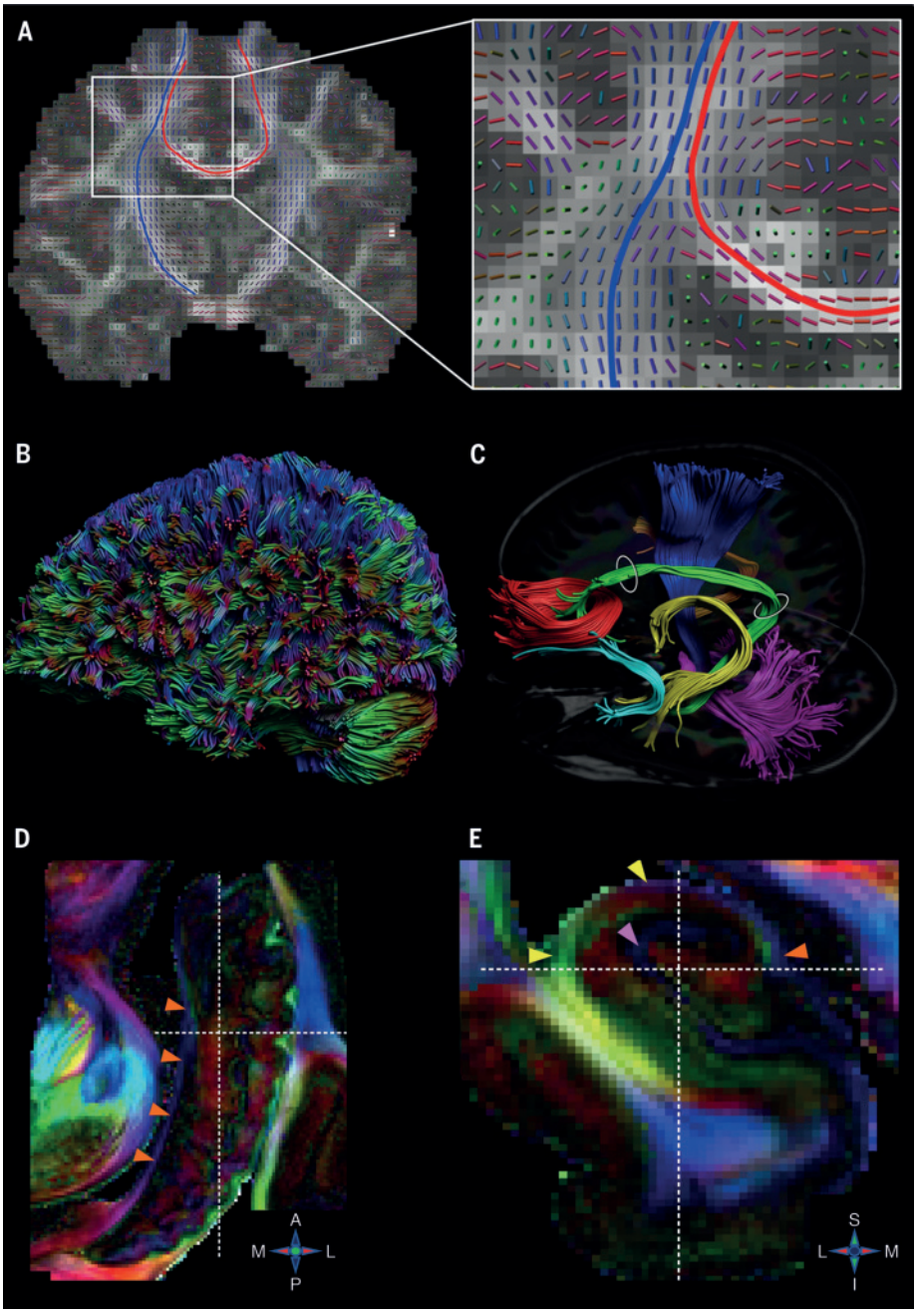


Fig. 2. Diffusion MRI and tractography. (**A**) Vector field of local predominant fiber orientations and two of its trajectories depicted on a coronal view of the human brain. The blue trajectory is part of the corticospinal tract, and the red one is part of the corpus callosum. (**B** and **C**) Whole-brain tractogram (B) and virtual dissection of multiple fiber bundles thereof (C). Bundles are selected as trajectories that pass expert-defined regions of interest. (**D** and **E**) Orientation estimation in a postmortem human hippocampus at 300-μm resolution with color-coded diffusion directions sliced along the axial (D) and the coronal (E) planes. Orange arrowheads indicate the fimbria, yellow the alveus, and pink the lacunosum-molecular layer. [Images in (A) to (C) were modified from (*14*)/CC BY 4.0, and images in (D) and (E) were modified from (*20*)/CC BY 4.0.]

Imaging at the subcellular level

Fluorescence microscopy is a rapidly growing and widely applied optical imaging technology. Key elements are tissue clearing or refractive index matching combined with labeling (e.g., lipophilic dyes or immunohistochemistry of myelin-specific proteins) and light-sheet fluorescence microscopy, two-photon fluorescence microscopy, or confocal fluorescence microscopy (*19*). These techniques are excellent for studying neural microstructures, mostly in small tissue samples. Automated fluorescence-based approaches with integrated sectioning provide distortion-free 3D reconstructions, rendering investigations of a larger number of (small) brain samples possible.

An emerging field of imaging uses the physics of scattering. Although the scattering of visible light resolves complex fiber constellations (*34*), small-angle x-ray (*35*) and neutron scattering (*36*) were shown to also quantify layers of myelin using Bragg's law of diffraction. The latter two require access to large accelerators such as the Deutsches Elektronen Synchroton (DESY) and those at the European Synchrotron Radiation Facility (ESRF) and the Stanford National Accelerator Laboratory (SLAC).

Electron microscopy can image nanometer-scale structures from tissues labeled with heavy metals (e.g., osmium) to reveal the detailed morphology of neurons and glia, myelin sheaths, synapses, microtubules, or mitochondria within the axoplasm (*37*). Various methods for 3D electron microscopy have been developed, differing in tissue processing and image acquisition. They are usually confined to sample sizes smaller than a dMRI voxel. The multibeam serial electron microscope (*38*) is the first device that provides nanometer-resolved images at the millimeter range.

Classical tracing, the gold standard for proving synaptic connectivity, is methodically highly challenging in the human brain, and only a few applications exist. For example, the Nauta method revealed callosal connectivity in early visual areas at their cytoarchitectonic borders (*39*), and carbocyanine-based tracing has been

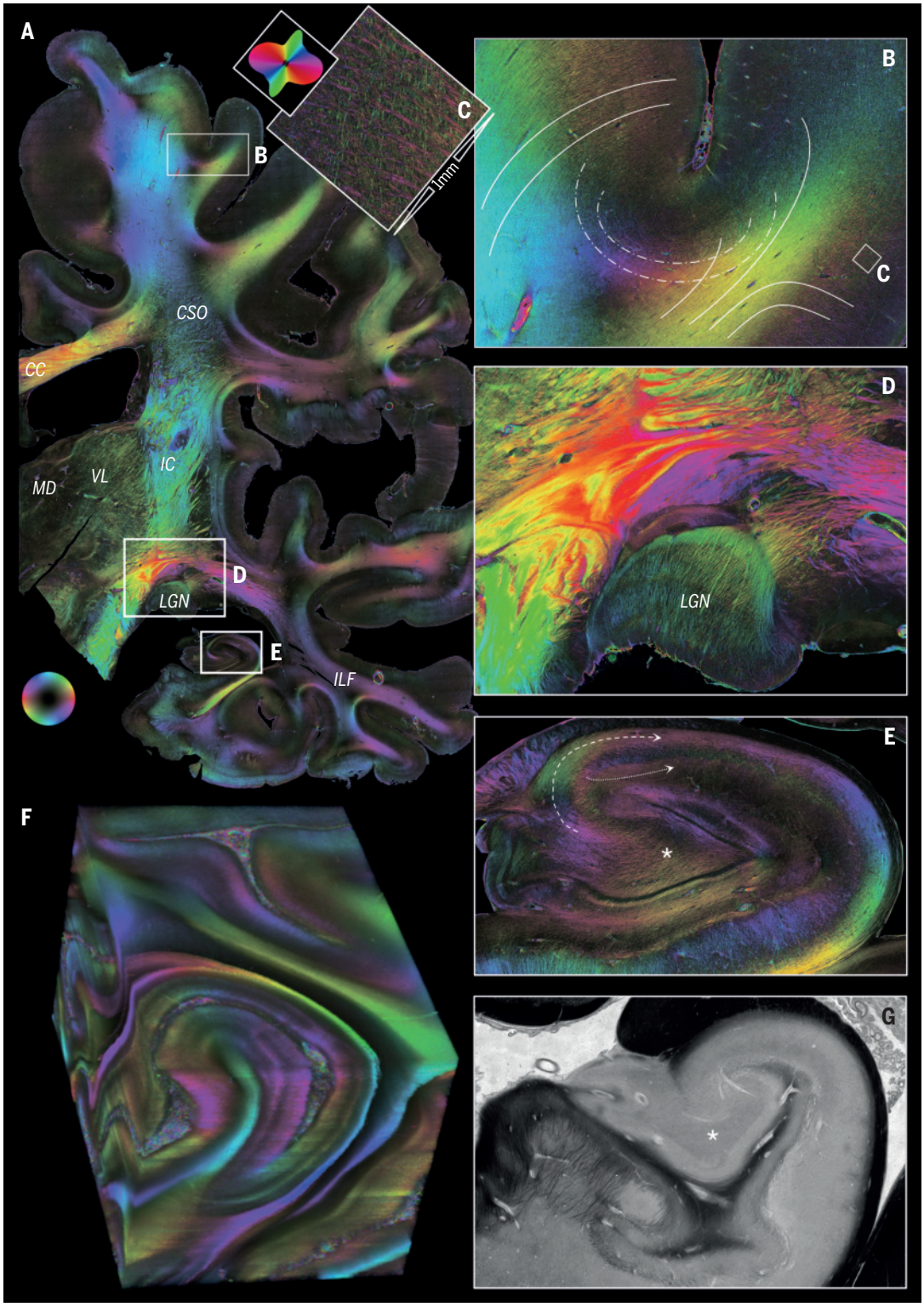


Fig. 3. Human brain fiber architecture. (**A**) Fiber orientation map of a coronal section through a human hemisphere obtained with 3D-PLI at 1.3 × 1.3 × 70 μm^3 resolution (color sphere encodes 3D fiber orientations). CC, corpus callosum; CSO, centrum semiovale; IC, internal capsule; ILF, inferior longitudinal fascicle; LGN, lateral geniculate nucleus; MD, mediodorsal thalamic nucleus; VL, ventrolateral thalamic nucleus. (**B**) Details of projection and long association fibers (continuous lines) and U-shaped fibers (dashed-dotted lines) from a region of interest at higher magnification. (**C**) Radial and horizontal cortical fiber directions for a 1 × 1 mm^2 region of interest (also visualized as a fiber orientation distribution). (**D**) Fanning and splitting of fascicles (red/yellow) and fibers in the region of the subcortical nucleus. (**E**) Human hippocampus showing dentate fibers, mossy fibers (asterisk), the endfolial pathway (dashed line), and Schaffer collaterals (dotted line). (**F**) 3D reconstruction of serial fiber orientation maps of the occipital lobe of a vervet monkey. (**G**) Myelin-stained hippocampus. The asterisk indicates the mossy fiber region, which is weakly stained, in contrast to visualization by 3D-PLI in (E). (Section from the brain collection of the Cécile and Oskar Vogt Institute for Brain Research, Heinrich Heine University Düsseldorf, Germany.)

compared with diffusion-based tractography in the same tissue and has revealed a high degree of concordance (*40*).

Mapping connectivity and sharing data

To study the connectome at multiple levels requires integration of data from different scales, modalities, and sources into an atlas framework. There is a growing number of data integration efforts; for example, a recent concordance map of human brain architecture combines histology, immunohistochemistry, and MRI (*41*). Cellular images have also been analyzed for fiber courses (*42*). One human hippocampus block was imaged using anatomical and diffusion MRI, 3D-PLI, and two-photon fluorescence microscopy and shared through the EBRAINS research infrastructure (https://doi.org/10.25493/JQ30-E08). Such multimodal datasets provide essential insights into the microstructural characteristics of complex fiber

bundles, helping to improve our understanding of MRI measurements and the reliability of tractography (*43*, *44*) and thus stimulating the field of quantitative MRI.

Tools to spatially organize connectivity data across scales are required. Mutual landmarks have to be identified and described in multimodality images at different scales. Gross anatomical structures (e.g., fiber bundles, gyri, sulci, and axon distributions) are suitable for large-volume intersubject alignment, whereas microstructure features (e.g., vasculature, individual fibers, and cell bodies) are suited for high-precision, intrasubject alignment of small tissue (sub-)samples. Knowing the precise location of each (sub-)sample is indispensable to preserving brain region–specific connectivity characteristics. MRI or en face scans accompanying tissue preparation can act as individual references to be aligned with an atlas.

New microanatomical connectivity models [equivalent to the BigBrain model (*45*)] would be helpful when used as reference data of an atlas, accommodating a broad range of formats (e.g., scalars, vectors, glyphs, and tractograms). Because the results of tractography depend on several constraints, there is a need to provide variants of tractogram solutions. This is already routine in particle physics, where an entire set of probable particle trajectories are provided to the community. Variations also exist at the level of brains (intersubject variability), which should be part of such frameworks. Thus, multiscale connectivity data can easily reach petabyte sizes (*46*).

Joint efforts would be beneficial to set up research infrastructures and establish standards. Several large brain initiatives, multipartner projects, and repositories (e.g., HBP, HCP, UK biobank, etc.) provide a broad scope of different datasets and tools. Web-based tools for the visualization and analysis of connectivity data have been developed by different consortia such as HIBALL (https://bigbrainproject.org/hiball.html), EBRAINS (https://ebrains.eu), JANELIA (https://www.janelia.org), and the Allen Brain Map (https://portal.brain-map.org). Repositories need to be interoperable to enable scaling up efforts to approach the human connectome.

Research infrastructures ideally bring together insights and data from different fields to further develop brain theory, which then can drive both empirical research and simulation. In particular, the principles of brain topography as observed by studies of cyto-, myelo-, and chemoarchitecture and interregional connectivity are likely to ultimately influence brain dynamics, including the local ratio of excitatory to inhibitory cell activity, resulting in a variable balance across different brain regions (*10*, *47*, *48*). Studies increasingly benefit from integrating the different facets under a common infrastructure (*49*).

Conclusion

Mastering the empirical, theoretical, and computational challenges for bridging the different spatial (and temporal) scales will open new perspectives for a deeper understanding of the connectome and its impact on brain function and disease. Diffusion-based imaging addresses long-distance connections and can be applied to study healthy subjects and patients, whereas the finer fiber and axonal architecture cannot be resolved. By contrast, microscopy and optical imaging provide superior contrast in the gray matter, but they are less powerful to disentangle fibers in the white matter. To take advantage of both worlds and to reduce limitations, strategies are evolving to combine methods with their respective strengths and to fill in the gaps in experimental knowledge. Digital tools such as modeling, simulation, and machine learning–based approaches are capable of predicting missing information (*50*). To constrain and validate them, "gold standards" from anatomical and physiological work are mandatory, including cross-validation in the same tissue imaged with different methods (*19*).

It is an intriguing concept to approach the connectome not only as a multiscale system in which each scale (e.g., neurons, microcircuits, and networks) has distinct features, but also as a system that has repetitive properties. However, to reveal the principles of connectivity within the experimentally accessible range of scales (from axons to pathways), in other words, to describe the human brain's "nestedness," requires critically revisiting the methodology, including tractography. Future tractography could, in a stepwise manner, move from lower to higher resolution, being informed by both regional properties of the next higher resolution (e.g., myeloarchitecture, cortical columns, and types of neurons) and the underlying geometry of fibers (e.g., fanning, crossing, converging, etc.). As a consequence, tracing algorithms need to be empowered to work at different hierarchies of discretization (e.g., scalable anisotropic voxels) during runtime.

Box 1. Topics of future research.

Connect the 3D myelo- (or axonal) architecture as a description of the gray matter with pathways of the white matter.

Assess the directionality of connections.

Correlate the axonal and network architecture with neuronal, cellular architecture.

Elucidate relationships of structural connectivity with brain dynamics and plasticity.

Build microscopical templates of connectivity, interoperable with existing atlases and maps.

Supplement the axonal by the dendritic architecture.

Predict connectivity on the basis of sparse regional information from high-resolution optical methods and electron microscopy, comparative studies, and modeling and simulation.

Develop tractography algorithms able to reproduce nested connectivity patterns.

REFERENCES AND NOTES

1. O. Sporns, G. Tononi, R. Kötter, *PLOS Comput. Biol.* **1**, e42 (2005).
2. S. J. Cook *et al*., *Nature* **571**, 63–71 (2019).
3. M. N. Economo *et al*., *eLife* **5**, e10566 (2016).
4. L. F. Abbott *et al*., *Cell* **182**, 1372–1376 (2020).
5. K. S. Rockland, *Brain Struct. Funct.* **225**, 1327–1347 (2020).
6. C. Vogt, O. Vogt, *Allgemeine Ergebnisse unserer Hirnforschung* (JA Barth, 1919), vol. 25.
7. D. J. Felleman, D. C. Van Essen, *Cereb. Cortex* **1**, 1–47 (1991).
8. D. Zachlod, S. Bludau, S. Cichon, N. Palomero-Gallagher, K. Amunts, *Neuroimage* **257**, 119286 (2022).
9. C. C. Hilgetag, A. Goulas, *Philos. Trans. R. Soc. Lond. B Biol. Sci.* **375**, 20190319 (2020).
10. G. Deco *et al*., *Curr. Biol.* **28**, 3065–3074.e6 (2018).
11. J. S. Elam *et al*., *Neuroimage* **244**, 118543 (2021).
12. F. C. Yeh, A. Irimia, D. C. A. Bastos, A. J. Golby, *Neuroimage* **245**, 118651 (2021).
13. F. Zhang *et al*., *Neuroimage* **249**, 118870 (2022).
14. B. Jeurissen, M. Descoteaux, S. Mori, A. Leemans, *NMR Biomed.* **32**, e3785 (2019).
15. K. H. Maier-Hein *et al*., *Nat. Commun.* **8**, 1349 (2017).
16. C. Reveley *et al*., *Proc. Natl. Acad. Sci. U.S.A.* **112**, E2820–E2828 (2015).
17. Y. Assaf *et al*., *Neuroimage* **80**, 273–282 (2013).
18. T. B. Dyrby, G. M. Innocenti, M. Bech, H. Lundell, *Neuroimage* **182**, 62–79 (2018).
19. A. Yendiki *et al*., *Neuroimage* **256**, 119146 (2022).
20. J. Beaujoin *et al*., *Brain Struct. Funct.* **223**, 2157–2179 (2018).
21. F. J. Fritz *et al*., *Neuroimage* **202**, 116087 (2019).
22. I. Shamir, O. Tomer, R. Krupnik, Y. Assaf, *Brain Struct. Funct.* **227**, 2153–2165 (2022).
23. T. A. Dziedzic, A. Balasa, M. P. Jeżewski, Ł. Michałowski, A. Marchel, *Brain Struct. Funct.* **226**, 13–47 (2021).
24. I. Zemmoura *et al*., *Neuroimage* **103**, 106–118 (2014).
25. M. Axer *et al*., *Neuroimage* **54**, 1091–1101 (2011).
26. A. Alimi *et al*., *Med. Image Anal.* **65**, 101760 (2020).
27. M. M. Zeineh *et al*., *Cereb. Cortex* **27**, 1779–1794 (2017).
28. J. Mollink *et al*., *Neuroimage* **157**, 561–574 (2017).
29. S. Caspers, M. Axer, D. Gräßel, K. Amunts, *Brain Struct. Funct.* **227**, 1331–1345 (2022).
30. D. J. H. A. Henssen *et al*., *Brain Struct. Funct.* **224**, 159–170 (2019).
31. M. Stacho *et al*., *Science* **369**, eabc5534 (2020).
32. H. Takemura *et al*., *eLife* **9**, e55444 (2020).
33. H. Wang *et al*., *Neuroimage* **165**, 56–68 (2018).
34. M. Menzel *et al*., *Neuroimage* **233**, 117952 (2021).
35. M. Georgiadis *et al*., *Nat. Commun.* **12**, 2941 (2021).
36. S. Maiti *et al*., *Sci. Rep.* **11**, 17306 (2021).
37. S. Loomba *et al*., *Science* **377**, eabo0924 (2022).
38. A. L. Eberle, D. Zeidler, *Front. Neuroanat.* **12**, 112 (2018).
39. S. Clarke, J. Miklossy, *J. Comp. Neurol.* **298**, 188–214 (1990).
40. A. K. Seehaus *et al*., *Cereb. Cortex* **23**, 442–450 (2013).
41. A. Alkemade *et al*., *Sci. Adv.* **8**, eabj7892 (2022).
42. R. Schurr, A. A. Mezer, *Science* **374**, 762–767 (2021).
43. S. Schiavi *et al*., *Neuroimage* **249**, 118922 (2022).
44. R. Schurr *et al*., *Neuroimage* **181**, 645–658 (2018).
45. K. Amunts *et al*., *Science* **340**, 1472–1475 (2013).
46. K. Amunts, T. Lippert, *Science* **374**, 1054–1055 (2021).
47. M. L. Kringelbach *et al*., *Proc. Natl. Acad. Sci. U.S.A.* **117**, 9566–9576 (2020).
48. D. Jancke, S. Herlitze, M. L. Kringelbach, G. Deco, *FEBS J.* **289**, 2067–2084 (2022).
49. International Brain Initiative, *Neuron* **105**, 212 (2020).
50. D. M. Camacho, K. M. Collins, R. K. Powers, J. C. Costello, J. J. Collins, *Cell* **173**, 1581–1592 (2018).
51. J. J. Déjerine, *Anatomie des Centres Nerveux* (Rueff, 1895).

ACKNOWLEDGMENTS

This work was supported by the European Union's Horizon 2020 Framework Programme for Research and Innovation (grant no. 945539: "Human Brain Project" SGA3). **License information:** Copyright © 2022 the authors, some rights reserved; exclusive licensee American Association for the Advancement of Science. No claim to original US government works. https://www.science.org/about/science-licenses-journal-article-reuse

10.1126/science.abq2599

REVIEW

The emergent properties of the connected brain

Michel Thiebaut de Schotten[1,2]* and Stephanie J. Forkel[2,3,4,5]

There is more to brain connections than the mere transfer of signals between brain regions. Behavior and cognition emerge through cortical area interaction. This requires integration between local and distant areas orchestrated by densely connected networks. Brain connections determine the brain's functional organization. The imaging of connections in the living brain has provided an opportunity to identify the driving factors behind the neurobiology of cognition. Connectivity differences between species and among humans have furthered the understanding of brain evolution and of diverging cognitive profiles. Brain pathologies amplify this variability through disconnections and, consequently, the disintegration of cognitive functions. The prediction of long-term symptoms is now preferentially based on brain disconnections. This paradigm shift will reshape our brain maps and challenge current brain models.

New ideas often emerge through close interaction between minds. Accordingly, these ideas do not solely belong to any of these individual minds but rather are the fruit of their integration—an emergent property of mutual exchange and interaction. The concept behind integration comes from emergentism, which postulates that "the whole is something besides the parts" (*1*) and that "no complex system can be understood except through careful analysis; however, the interactions of the components must be considered as much as the properties of the isolated components" (*2*). In neuroscience, there is a growing consensus that functions are an emerging property of the interaction between brain areas (*3*). Thus, function-specific brain activity involves the integrative effort of several brain regions (*4*). White matter connections support this integration by interconnecting brain regions (Fig. 1). With cortical expansion, these connections have evolved to preserve interactions between distant regions (*5*). These connections support local, intra- and interlobar associations, projection, and interhemispheric commissural circuits (*6*). These circuits create networks by stringing together many brain regions to orchestrate a brain symphony conducted by finely attuned connections with variable caliber and myelination tailored to their functional role (*7*).

Measuring brain connectivity in the living brain

Today, the connections between brain regions are noninvasively measured in the living human brain using neuroimaging methods that unveil their structure (i.e., axon bundles) and their function (i.e., synchronization of regional activity). Structurally, diffusion-weighted imaging (DWI) measures water diffusion along the directions of axons and can derive properties such as trajectory (i.e., tractography), density, caliber, and dispersion (*8*). Functionally, the communication between brain regions can be extrapolated by measuring the coherence between distant areas' activity, mainly through functional magnetic resonance imaging (fMRI). Mathematical models applied to fMRI can estimate communication strength (i.e., functional connectivity) or directionality (i.e., effective connectivity) (*9*). Because regions that fire together wire together (*10*), measuring communication between regions indicates their connections, albeit these regions are not always directly connected (*11*).

"...circuits create networks by stringing together many brain regions to orchestrate a brain symphony conducted by finely attuned connections with variable caliber and myelination..."

The integrative functional role of brain connectivity

There is, however, more to brain connections than the mere transfer of signals between brain regions. Connections can amplify or reduce brain signals (*11*) and determine the brain's cortical structure and function. Specifically, there is a similarity between the synchronized communication between brain regions at rest and their activity during tasks at the group (*12*) and the individual (*13*) levels (Fig. 2A). It is also possible to predict where a function will arise in the developing brain on the basis of the cortical projections of white matter tracts alone. For instance, the latter has been demonstrated for identifying the visual word form area, even before the acquisition of literacy (*14*). Typically, the main trends of brain connectivity capture the spatial organization of functions in the brain (*15*). Deprived of its connections, a brain region will prune its remaining dendrites and synapses, and its neurons will wither or die (*16*). Consequently, this region's network breaks down functionally [i.e., dysconnection (*17*)] and structurally (i.e., disconnection) and no longer can contribute to a function. This phenomenon, also known as diaschisis (*18*), demonstrates the critical importance of connections in maintaining the integrity of distant brain regions and their functioning. Lastly, animal studies that surgically swap connections between sensory cortices have further demonstrated the leading and decisive role of white matter connections within the brain's functional organization. Specifically, forcing visual inputs onto the auditory cortex alters it to acquire many of the cytoarchitectonic and functional properties of the visual cortex (*19*) that are associated with normal visual behavior (*20*). This indicates that cell properties are mediated by their connections through their interaction with the rest of the brain, and moreover, those brain functions are an emerging property of these integrative mechanisms. Thus, as previously hypothesized (*21*), this sum of evidence demonstrates that brain connections support the latent mechanisms that determine the function of the brain and cognition as we know it.

This shift away from considering isolated regions in favor of an integrated anatomical-functional network led to the reevaluation of functional activations with regard to their white matter connections. Accordingly, brain connections revealed by the highest-resolution tractography (*22*) can be used to systematically decipher human activation networks and recently led to the first functional white matter atlas (*23*). This atlas identifies the joint contribution—or integration—of structurally connected brain areas by a statistical association of fMRI and diffusion data (Fig. 2B). The result also revealed a leftward asymmetry between the known granularity (i.e., the level of detail) of functions of the left and the right hemispheres. This asymmetry reflects an epistemological imbalance (i.e., we know more about the cognition of the left than the right hemisphere), leading to a publication bias and triggering the necessity for more dedicated cognitive explorations of the right hemisphere, which for a long time was considered the minor or nondominant hemisphere.

The mechanisms that sustain the lateralization of brain functions are related to interhemispheric connections. Some cortical regions show increased functional asymmetries for cognitive functions such as language, perception and

[1]Groupe d'Imagerie Neurofonctionnelle, Institut des Maladies Neurodégénératives UMR 5293, CNRS, CEA, University of Bordeaux, Bordeaux, France. [2]Brain Connectivity and Behaviour Laboratory, Sorbonne University, Paris, France. [3]Donders Centre for Brain Cognition and Behaviour, Radboud University, Nijmegen, Netherlands. [4]Centre for Neuroimaging Sciences, Department of Neuroimaging, Institute of Psychiatry, Psychology, and Neuroscience, King's College London, London, UK. [5]Department of Neurosurgery, Technical University of Munich School of Medicine, Munich, Germany.
*Corresponding author. Email: michel.thiebaut@gmail.com

action, emotion, and decision-making. These cortical regions are less connected with the contralateral hemisphere via the corpus callosum (Fig. 2C) (*24*). DWI has revealed that the structure of the corpus callosum changes along with brain size across and within species (*25*, *26*). In particular, the axonal conductive properties can change (*27*), and axon calibers correlate with the interhemispheric speed of conduction (Fig. 2D) (*28*). Further, a trade-off in the number of connections exists between interhemispheric and intrahemispheric connectivity across species (*25*). Taken together, these studies suggest that during evolution, brain size expansion may have led to functional lateralization to avoid a disproportionate corpus callosum or excessive conduction delays across hemispheres.

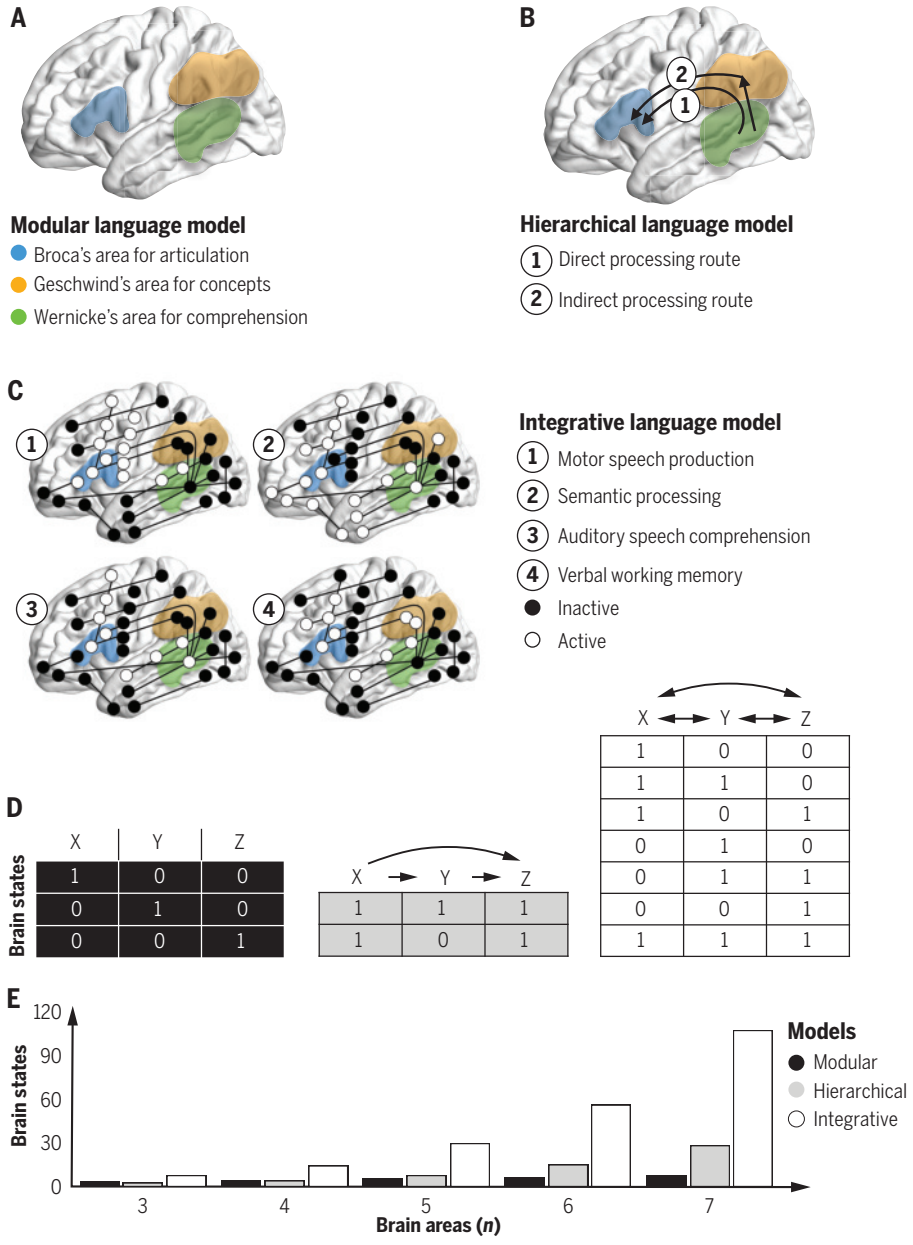


Fig. 1. The superior flexibility of the integrative brain model compared with other classical models, as exemplified by simplified language models. Brain models determine the flexibility of brain states (i.e., functions). In a modular system (**A**), one region performs one function without cross-talk, and the number of possible brain states increases linearly with the number of regions. In the hierarchical system (**B**), functions emerge from the sequential activation of regions. Accordingly, the repetition of words or sentences would rely on the temporal-parietal-frontal propagation from auditory-to-motor processes. In contrast to (A) and (B), the integrative model (**C**) offers the highest computational flexibility, allowing for the high complexity and flexibility of language processes as we know them. Each model can be translated into different brain state patterns (**D**) across brain areas X, Y, and Z. Each line indicates a brain state (function) (courtesy of Chris Foulon). (**E**) Illustration of the interaction between the brain model and the number of areas involved in the number of brain states a system can take.

Mapping evolution through connectivity

As structural connectivity can be used to decipher the brain's functional organization, multiple studies compared different primate species to understand human uniqueness and shed light on the mechanisms involved in its evolution. For instance, human language capacity parallels the extraordinary expansion of the arcuate fasciculus in the left hemisphere (Fig. 3A) (*29*). The anatomical delineation of white matter tracts (e.g., arcuate fasciculus or corpus callosum) allowed for extracting corresponding connectivity profiles across species. This point of comparison permitted the computation of deformation fields between species' brains (Fig. 3B) (*30*). These deformation fields define similarities and differences across species. Comparative studies assume that similarities between species can be traced back to a common ancestor and account for the preservation of specific functions across evolution. Recent comparative work revealed one of the first comprehensive maps of the phylogenetic organization of brain regions (*30*). Such technical advances in comparative neuroimaging will allow for targeted studies that better match human brain mechanisms to their phylogenetic counterparts. These advances may also help discover and mimic neuroprotective mechanisms in animals that could potentially translate to improving human disease models and therapeutics. For instance, frontoparietal disconnection is a very sensitive (85%) and specific (95%) biomarker for persistent disorders of visual neglect (*31*). Whereas most humans with this disconnection will fail to recover from visual neglect, monkeys with the same disconnection will recover within a few days (*32*). Hence, there is a distinctive mechanism in monkeys that facilitates brain recovery. However, this mechanism has yet to be identified, and its translatability to humans needs to be explored.

One frequent limitation of comparative studies is the small number of brains per species used (usually fewer than 10), which fails to fully capture interindividual variability. While the amount of connectivity variability (i.e., magnitude) is proportional to the brain size, its pattern of variability is similar between humans and other primates. Accordingly, brain areas that have recently evolved increasingly differ between individuals, whereas evolutionarily older areas tend to be more stable (*33*). Intraspecies variability in brain connections might therefore be a novel dimension to our understanding of evolutionary mechanisms (Fig. 3C).

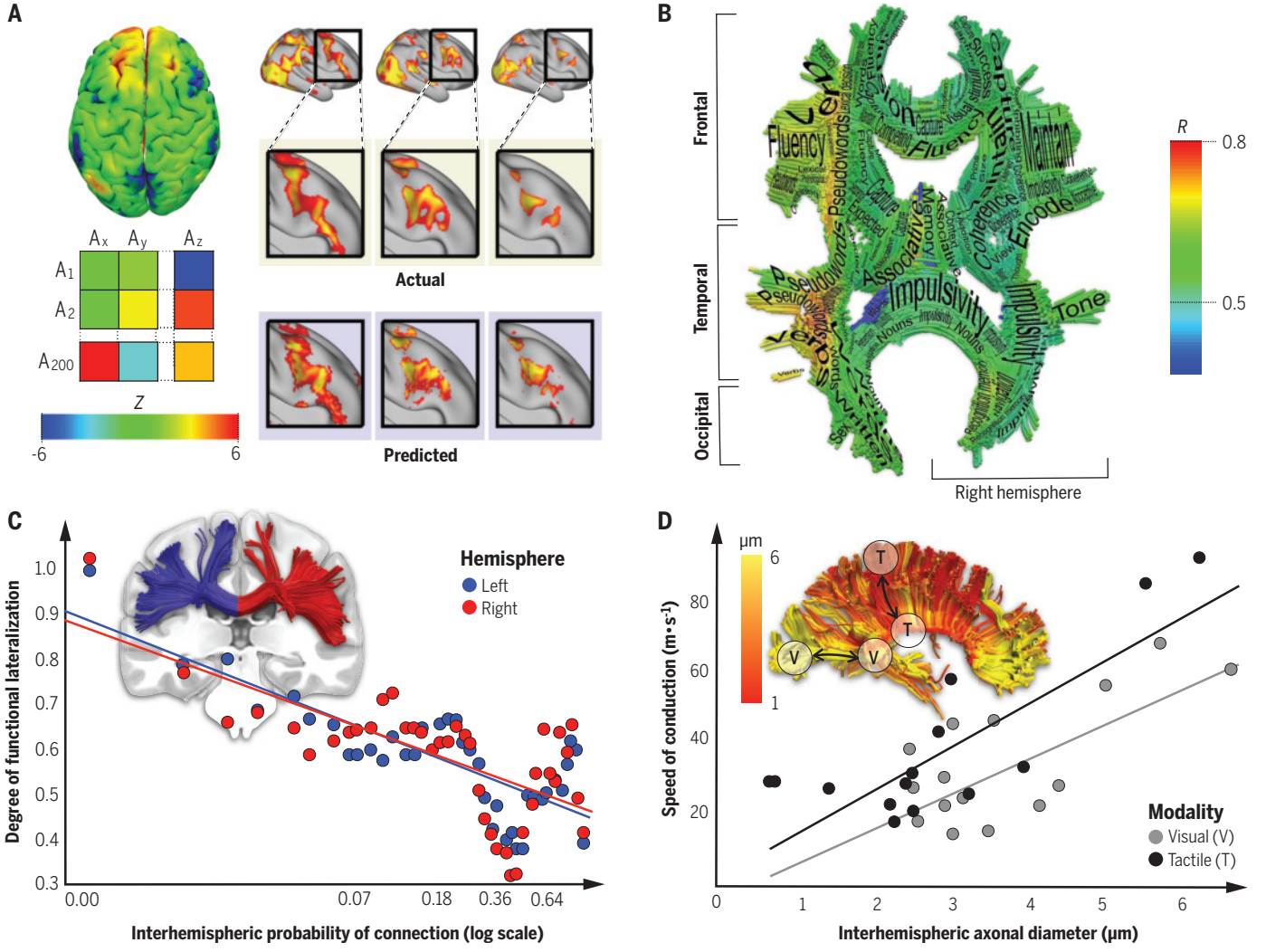


Fig. 2. Functional integration through brain connections as the latent mechanisms determining the function of the brain. (**A**) Functional connectivity (top left) can be summarized in a connectivity matrix (bottom left) that is specific to each individual (*35*). Main trends of functional connectivity can predict individual patterns of task-related activations [right; reproduced with permission from (*13*)]. A, area. (**B**) Similarly, main trends of structural connectivity can predict task-related patterns of cortical activations. The statistical association between these two modalities allows projection of the processes involved in the fMRI tasks onto the brain connections [modified from (*23*)]. *R*, goodness of fit. (**C**) The relationship between functional lateralization and interhemispheric connectivity for the left (blue) and the right (red) hemispheres [modified from (*24*)]. (**D**) Interhemispheric speed of conduction for visual (gray) and tactile (black) modalities is correlated with the strength of their interhemispheric connections [i.e., axonal diameter; modified with permission from (*28*)].

Connectivity unveils interindividual variability

This connectivity variability, or "neurovariability," is critical to the individuals we are. What we know, who we are, and how we communicate with others are ascribed through integrative brain mechanisms. Therefore, to understand the origin of our identity, we need to decipher how connections between brain regions orchestrate our brain functions at the individual level. Accordingly, the strength of communication between brain regions derived from functional connectivity can predict individual differences in brain activation during tasks (Fig. 2A) (*13*). Preliminary work has already created "fingerprints" of the brain's functional connectivity patterns in healthy volunteers that correlate with behavior and cognition [i.e., connectome-based predictive modeling (*34*)]. These fingerprints of connectivity are specific to individuals and predict fluid intelligence (*35*) and creativity (*36*) with impressive accuracy. These correlations with cognition also extend to the differences in the structure of specific brain connections [see Fig. 4A and (*37*)]. For instance, a stronger left arcuate fasciculus seems to facilitate the learning of new words (*38*). These differences affect healthy brain performance and extend to the severity of neurodevelopmental, psychiatric, and neurological symptoms (*37*). Developmental brain connectivity patterns have assisted in diagnosing neurodevelopmental learning deficits (*39*).

In neurology, a stronger arcuate fasciculus facilitates recovery after stroke (*40*), whereas its degeneration has been associated with increased symptom severity (*41*). These observations have led to new anatomical-cognitive models 150 years after the first descriptions of aphasia (i.e., language disorder) as a disconnection syndrome.

Connectivity profiles can change across a life span, leading to increasingly divergent molecular and circuit-level changes that develop over weeks, months, years, and even decades owing to environmental and learning-induced plasticity mechanisms. A good example is literacy, which alters brain connections between the visual and the auditory system even when acquired later in life (*42*). Indeed, plasticity mechanisms can limit long-term cognitive predictions, which are based on the fingerprints of brain connections.

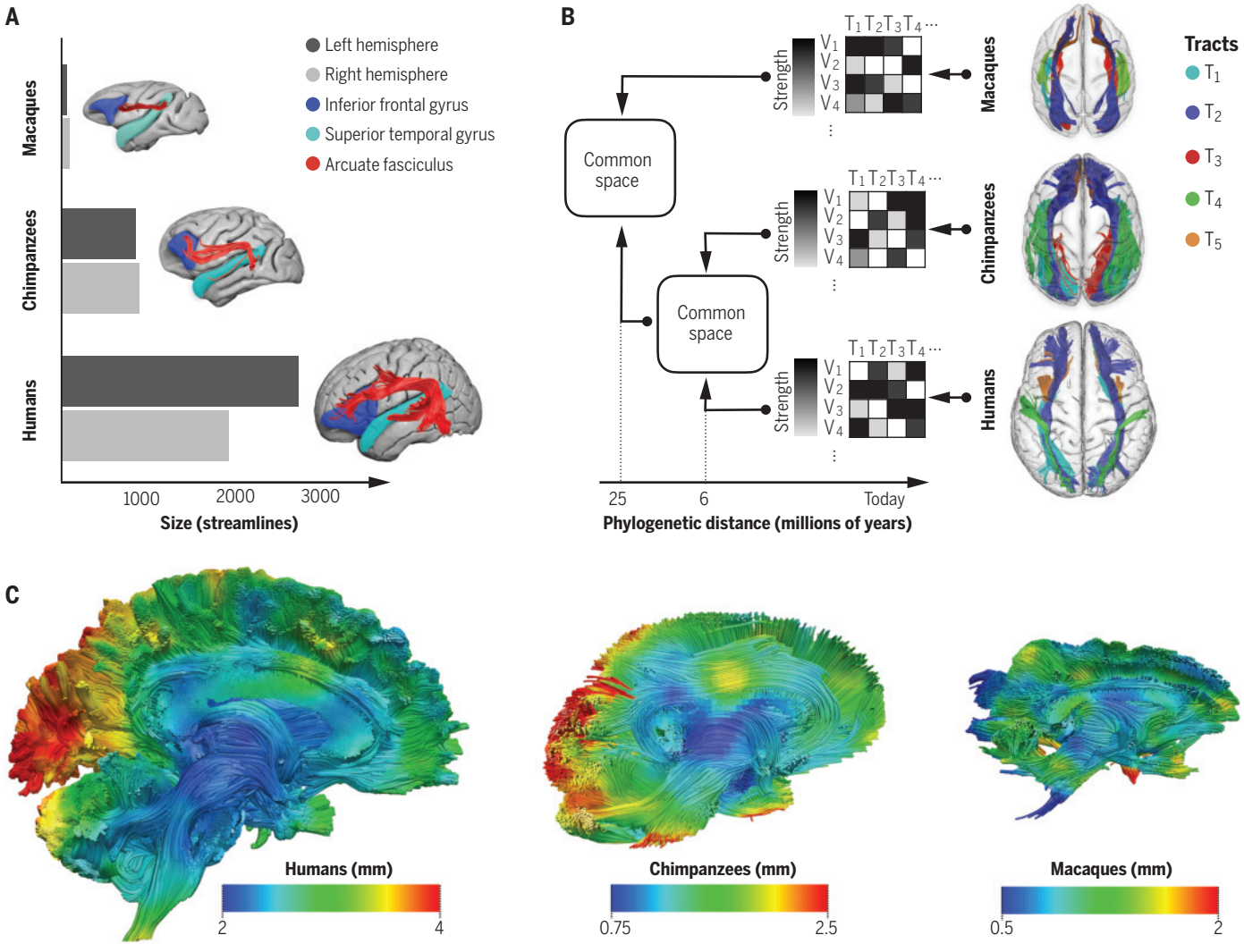


Fig. 3. Connectivity sheds light on mechanisms of brain evolution. (**A**) A comparison of the connections between frontal and temporal brain regions in humans, chimpanzees, and macaques reveals the remarkable expansion and lateralization of the arcuate fasciculus (*29*). (**B**) The extraction of a reliable connectivity profile across species permits the computation of common spaces allowing for an approximation of our ancestors' brains (*30*). In this context, the connectivity profile is defined as the number of streamlines per voxel (i.e., as a surrogate for connectivity strength) for each tract of interest. T, tract; V, voxel; Strength, connectivity strength. (**C**) Connectivity variability (i.e., average white matter deformation required to match a common species-specific template) reveals that the same variability that makes us individually different from each other is also at the root of our differences from our ancestors and our closest evolutionary relatives [modified from (*33*), thanks to data openly available at http://www.chimpanzeebrain.org]. mm, millimeters.

Importantly, while the identification of predictive biomarkers holds vast potential for changing the health of individuals and populations, it also bears fundamental ethical risks and moral challenges (e.g., treatment of predicted brain disease that may never manifest or withholding treatment on the basis of recovery predictions). Overall, these recent studies put forth evidence demonstrating that new behavioral patterns and cognitive functions can arise from even small changes in the interaction between brain regions via their connections.

Functional disintegration through disconnection

Drastic disruptions of brain interactions [i.e., disconnections (*18*)] manifest secondary to pathologies and can induce long-lasting functional symptoms. For instance, a disconnection between visual and language networks leads to irremediable alexia [i.e., inability to read (*43*)]. Although advanced neuroimaging can identify disconnections, these methods are not yet systematically available across the clinical sector. Therefore, new indirect methods that use a priori knowledge of connections (DWI or fMRI) derived from the highest-resolution datasets to estimate disconnection profiles after a brain injury are needed to reliably and statistically map the association between disconnection and symptoms (*44*). In doing so, it is possible to reevaluate classical clinical neuroanatomical phenomena within brain networks and understand the critical contribution of connections to the realization of functions. These new methods can even demonstrate that clinical-anatomical lesion studies in neuroscience's most famous cases can be extended to a disconnection paradigm. This new paradigm shows the networks considered functionally engaged for emotion and decision-making (Phineas Gage), language production (Louis Victor Leborgne), and declarative memory (Henry Molaison) in the healthy population (Fig. 4B) (*45*). Hence, consideration of brain connections appears to reconcile brain lesion studies with functional neuroimaging in healthy volunteers and provides a more comprehensive biological interpretation of clinical

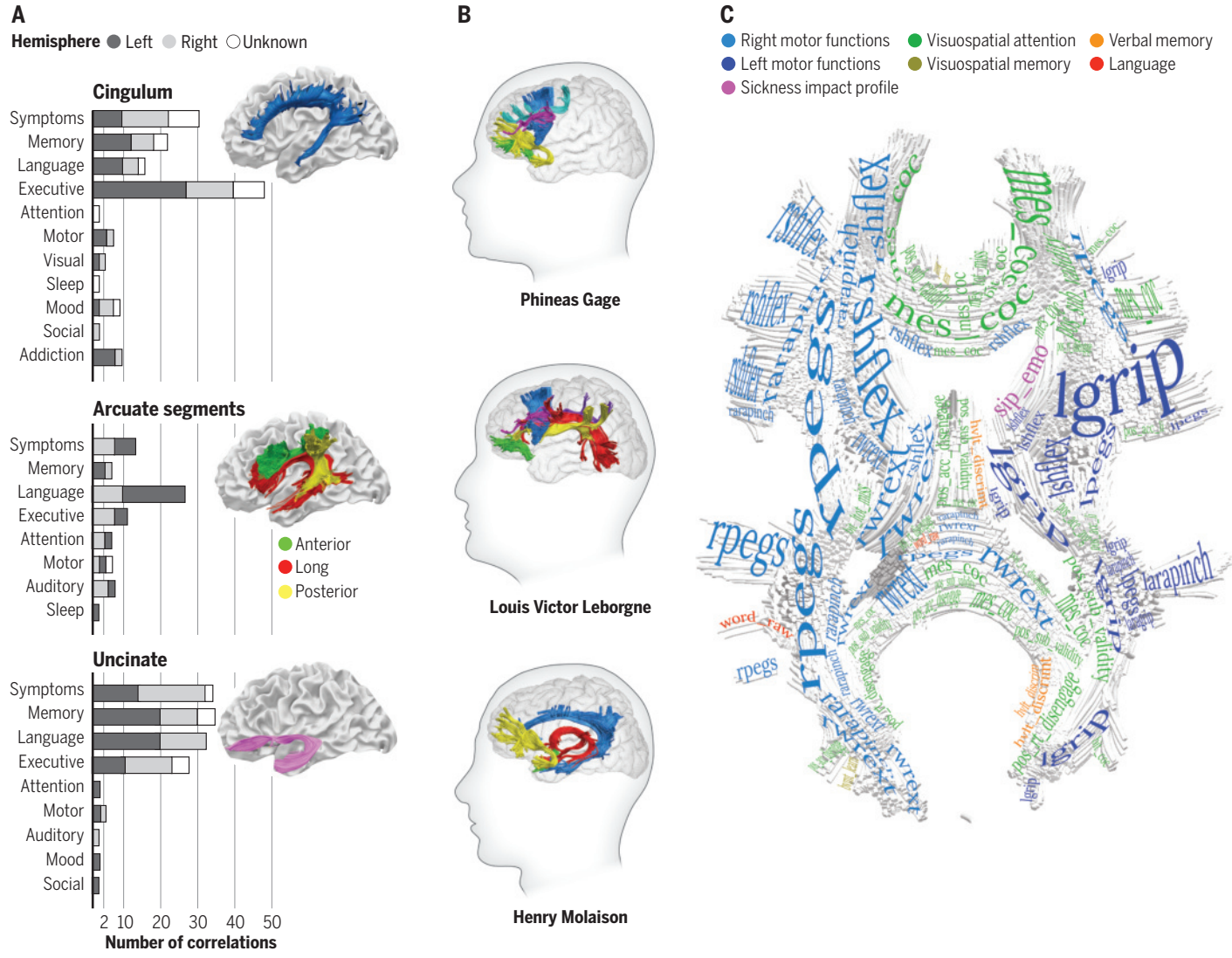


Fig. 4. Disintegration of brain functions through disconnections. (**A**) Systematic review of the relationship between variability in brain connectivity, cognitive profiles, and clinical symptoms [modified from (*37*); https://youtu.be/JVOegYHT21w]. (**B**) Connectivity revisiting neuroscience's most famous cases of neurosciences showing the tracts disconnected in classic neurobehavioral syndromes [from (*45*)]. (**C**) Neuropsychological white matter atlas highlighting the disconnection patterns causing loss of function [courtesy of (*47*); http://disconnectomestudio.bcblab.com].

manifestations with regard to the disintegration of brain processes. Further, brain disconnection results usually achieve a higher explanatory power than lesion localization alone (*46*). The disconnection framework has recently been extended to the entire brain to provide the first clinical map of symptoms associated with specific brain disconnections (Fig. 4C) (*47*). Therefore, it would prove beneficial if measures of brain connectivity were translated into advanced standard operating procedures for personalized neuroscience (*48*) that focus on rehabilitation and that support the prediction of symptom recovery while providing new targets for pharmacological treatments. The evidence presented demonstrates that the key to understanding the brain is in the interaction between multiple areas, and the best guide to its constitutional (as opposed to phasic, task-related) interactions is its connecting infrastructure.

Where do we go from here?

Despite the current progress in estimating brain connectivity, new challenges have emerged that will only be tackled by relying on synergetic efforts. First and foremost, no known method can directly measure the activation of connections in the healthy living human brain. Instead, recent indirect approaches statistically project the functional signal from the cortex onto the white matter (*49*). These indirect methods rely on a priori knowledge of the group-level probability of connections between brain regions. However, regardless of the quality of the dataset used to build these priors, axons are ~1 to 6 μm in diameter (*11*), and routine neuroimaging has a minimum resolution of 1 mm^3 in vivo and 200 μm postmortem (*50*). Similarly, monosynaptically connected areas are synchronized with a delay of 2 to 3 ms (*51*), leading to high-frequency synchronization. Yet standard functional connectivity relies on acquisitions with a temporal resolution of 1 s at best. Hence, some level of approximation exists in the estimation of the orientation of fiber populations and the estimation of the communication between brain regions, leaving room for improvement to estimate the connectome (i.e., whole-brain connectivity) accurately.

for cytoarchitecture measures and cortical thickness. Non-neuroimaging methods may get us closer to that goal. Advanced polarized light imaging (*53*) or Nissl-based structure tensor (*54*), for example, can estimate axonal orientation from postmortem tissues. However, these postmortem approaches are limited to two dimensional (2D) in-plane reconstruction and require tremendous effort to produce a whole 3D human brain comparable to BigBrain. Preliminary work already demonstrates that such an attempt is possible in macaques, and efforts are underway in humans (*55*). Future progress will serve as a cornerstone for improving structural and functional connectivity methods. These new datasets can validate current neurobiological approximations—such as axonal diameter, neurite density, the extent of myelination, information flow, or synaptic complexity at the whole-brain level—derived from neuroimaging. This step is fundamental to ensure that connectivity matrices are reliably translatable to the clinical realm and lead to advances in therapeutic interventions.

Going forward, we need to consolidate these new concepts by developing dedicated software, which provides us with additional resources to sharpen our observations. These developments will include, for example, tools that can represent high-dimensional data in the same latent space as anatomical information across scales (cells, voxels, circuits), across species (macaque, chimpanzee, human), and across imaging modalities (tracing, tractography, polarized light imaging), while accounting for neurovariability at the individual level to capture the factor interactions. To do so, researchers ought to create professional networks, integrate ideas, and share data openly. Together, these endeavors will push brain connectivity research to integrate across imaging modalities (e.g., functional white matter), formulate new frameworks (e.g., neurovariability), and foster our understanding of brain development and evolution (comparative neuroimaging and neuroecology). This joint effort will push our current frontiers and lead to advanced neuroimaging methods, personalized anatomical models, and clinical impact. Hence, it will take an integrative system of people (research consortium) to decipher this complex system within us all and discover the emergent properties of the brain.

REFERENCES AND NOTES

1. Aristotle, *Metaphysics*, C. D. C. Reeve, Transl. (Hackett Publishing Company, 2016).
2. E. Mayr, *What Makes Biology Unique? Considerations on the Autonomy of a Scientific Discipline* (Cambridge Univ. Press, 2004).
3. L. Pessoa, *The Entangled Brain: How Perception, Cognition, and Emotion Are Woven Together* (MIT Press, 2022).
4. G. Herbet, H. Duffau, *Physiol. Rev.* **100**, 1181–1228 (2020).
5. D. N. Pandya, M. Petrides, B. Seltzer, P. B. Cipolloni, *Cerebral Cortex: Architecture, Connections, and the Dual Origin Concept* (Oxford Univ. Press, 2015).
6. K. Rojkova *et al*., *Brain Struct. Funct.* **221**, 1751–1766 (2016).
7. B. Zalc, F. Rosier, *Myelin: The Brain's Supercharger* (Oxford Univ. Press, 2018).
8. Y. Assaf, H. Johansen-Berg, M. Thiebaut de Schotten, *NMR Biomed.* **32**, e3762 (2019).
9. K. J. Friston, *Brain Connect.* **1**, 13–36 (2011).
10. S. Löwel, W. Singer, *Science* **255**, 209–212 (1992).
11. G. M. Innocenti *et al*., *Prog. Neurobiol.* **208**, 102186 (2022).
12. S. M. Smith *et al*., *Proc. Natl. Acad. Sci. U.S.A.* **106**, 13040–13045 (2009).
13. I. Tavor *et al*., *Science* **352**, 216–220 (2016).
14. Z. M. Saygin *et al*., *Nat. Neurosci.* **19**, 1250–1255 (2016).
15. D. S. Margulies *et al*., *Proc. Natl. Acad. Sci. U.S.A.* **113**, 12574–12579 (2016).
16. S. A. Capurso *et al*., *J. Neurosci.* **17**, 7372–7384 (1997).
17. K. E. Stephan, T. Baldeweg, K. J. Friston, *Biol. Psychiatry* **59**, 929–939 (2006).
18. E. Carrera, G. Tononi, *Brain* **137**, 2408–2422 (2014).
19. J. Sharma, A. Angelucci, M. Sur, *Nature* **404**, 841–847 (2000).
20. L. von Melchner, S. L. Pallas, M. Sur, *Nature* **404**, 871–876 (2000).
21. R. E. Passingham, K. E. Stephan, R. Kötter, *Nat. Rev. Neurosci.* **3**, 606–616 (2002).
22. A. T. Vu *et al*., *Neuroimage* **122**, 318–331 (2015).
23. M. Thiebaut de Schotten, C. Foulon, P. Nachev, *Nat. Commun.* **11**, 5094 (2020).
24. V. R. Karolis, M. Corbetta, M. Thiebaut de Schotten, *Nat. Commun.* **10**, 1417 (2019).
25. Y. Assaf, A. Bouznach, O. Zomet, A. Marom, Y. Yovel, *Nat. Neurosci.* **23**, 805–808 (2020).
26. L. Yang *et al*., *J. Neurosci.* **42**, 3599–3610 (2022).
27. C. Sampaio-Baptista, H. Johansen-Berg, *Neuron* **96**, 1239–1251 (2017).
28. A. Horowitz *et al*., *Brain Struct. Funct.* **220**, 1777–1788 (2015).
29. F. Balezeau *et al*., *Nat. Neurosci.* **23**, 611–614 (2020).
30. R. B. Mars *et al*., *eLife* **7**, e35237 (2018).
31. M. Thiebaut de Schotten *et al*., *Cereb. Cortex* **24**, 691–706 (2014).
32. J. W. Marshall, H. F. Baker, R. M. Ridley, *Behav. Brain Res.* **136**, 257–265 (2002).
33. P. L. Croxson, S. J. Forkel, L. Cerliani, M. Thiebaut de Schotten, *Cereb. Cortex* **28**, 3829–3841 (2018).
34. X. Shen *et al*., *Nat. Protoc.* **12**, 506–518 (2017).
35. E. S. Finn *et al*., *Nat. Neurosci.* **18**, 1664–1671 (2015).
36. M. Ovando-Tellez *et al*., *Sci. Adv.* **8**, eabl4294 (2022).
37. S. J. Forkel, P. Friedrich, M. Thiebaut de Schotten, H. Howells, *Brain Struct. Funct.* **227**, 529–544 (2022).
38. D. López-Barroso *et al*., *Proc. Natl. Acad. Sci. U.S.A.* **110**, 13168–13173 (2013).
39. D. E. Astle, J. Bathelt, J. Holmes; CALM Team, *Dev. Sci.* **22**, e12747 (2019).
40. S. J. Forkel *et al*., *Brain* **137**, 2027–2039 (2014).
41. S. J. Forkel *et al*., *Neurology* **94**, e594–e606 (2020).
42. M. Thiebaut de Schotten, L. Cohen, E. Amemiya, L. W. Braga, S. Dehaene, *Cereb. Cortex* **24**, 989–995 (2014).
43. L. Cohen, S. Dehaene, S. McCormick, S. Durant, J. M. Zanker, *Neuropsychologia* **91**, 36–49 (2016).
44. M. D. Fox, *N. Engl. J. Med.* **379**, 2237–2245 (2018).
45. M. Thiebaut de Schotten *et al*., *Cereb. Cortex* **25**, 4812–4827 (2015).
46. V. Pacella *et al*., *eLife* **8**, e46075 (2019).
47. L. Talozzi *et al*., Research Square [Preprint] (2021). https://doi.org/10.21203/rs.3.rs-1181593/v1.
48. T. D. Satterthwaite, C. H. Xia, D. S. Bassett, *Neuron* **98**, 243–245 (2018).
49. V. Nozais, S. J. Forkel, C. Foulon, L. Petit, M. Thiebaut de Schotten, *Commun. Biol.* **4**, 1035 (2021).
50. S. B. Sébille, A.-S. Rolland, M.-L. Welter, E. Bardinet, M. D. Santin, *J. Neurosci. Methods* **311**, 222–234 (2019).
51. B. L. Sabatini, W. G. Regehr, *Annu. Rev. Physiol.* **61**, 521–542 (1999).
52. K. Amunts *et al*., *Science* **340**, 1472–1475 (2013).
53. M. Menzel *et al*., *Sci. Rep.* **12**, 4328 (2022).
54. R. Schurr, A. A. Mezer, *Science* **374**, 762–767 (2021).
55. A. Alkemade *et al*., *Sci. Adv.* **8**, eabj7892 (2022).

ACKNOWLEDGMENTS

The authors thank the members of the Neurofunctional Imaging Group (GIN), particularly V. Pacella, L. Talozzi, and E. Allard but also L. Sakuma, T. Orset, P. Pouget, P. Bartolomeo, P. Nachev, L. Labache, C. Foulon, L. Verhagen, R. Mars, L. Pessoa, and S. Sesack, and three anonymous reviewers for their helpful feedback and supporting material. **Funding:** This work was supported by the European Union's Horizon 2020 research and innovation programme under European Research Council (ERC) Consolidator grant agreement no. 818521 (M.T.d.S., DISCONNECTOME); University of Bordeaux's IdEx "Investments for the Future" program RRI "IMPACT," which received financial support from the French government; Marie Skłodowska-Curie grant agreement no. 101028551 (S.J.F., PERSONALISED); and the Donders Mohrmann Fellowship (S.J.F., NEUROVARIABILITY). **Competing interests:** The authors have no competing interests to declare. **License information:** Copyright © 2022 the authors, some rights reserved; exclusive licensee American Association for the Advancement of Science. No claim to original US government works. https://www.science.org/about/science-licenses-journal-article-reuse

Submitted 18 May 2022; accepted 12 August 2022
10.1126/science.abq2591

RESEARCH

IN *SCIENCE* JOURNALS

Edited by **Michael Funk**



PLANT SCIENCE

Floral sex determination

In melons, flowers initially develop bisexually, but further growth brings arrest of either carpel or stamen development, refining mature flowers into male or female. Only the female flowers produce melons. Zhang *et al.* have identified the genes involved in turning the bisexual primordial flower into either a male or female flower. The zinc finger transcription factor WIP1 interferes with carpel development, allowing male flower development to proceed. Conversely, expression of an enzyme involved in producing the hormone ethylene, perhaps supported by auxin signaling, supports and promotes female flower development. —PJH

Science, add4250, this issue p. 543

A melon vine with male (top) and female (bottom) flowers, both of which begin as bisexual buds

PHOTO: ZHANG *ET AL.*

SYNTHETIC BIOLOGY

Changing the genetic code's structure

The genetic code, the rules by which genetic information is encoded in genes within DNA, is nearly universal across all kingdoms of life, enabling the transfer of genetic information and innovation between diverse cells. Biologists have long made use of the common code for engineering microbes, crops, and animals. Zürcher *et al*. permuted the rules by which genetic information is encoded in DNA and thereby created genetically isolated organisms that cannot exchange functional genetic information with other organisms. This altered genetic code offers protection to valuable engineered organisms from natural invaders and safeguards the natural world from engineered genetic material. —DJ

Science, add8943, this issue p. 516

STRUCTURAL BIOLOGY

Closed complex for protein degradation

The ability to target endogenous proteins for degradation with small molecules has opened up avenues for treating a wide range of diseases. Watson *et al*. investigated how a class of these molecules called CELMoDs (CRBN E3 ligase modulatory drugs) alter the conformational landscape of cereblon (CRBN), the enzyme that recognizes and marks substrates for degradation. The authors found that CELMoD compounds trigger a conformational rearrangement of CRBN from an entirely open and defunct form to an active closed form, but only for a subset of CRBN proteins. Next-generation CELMoDs, which are more effective therapies, appear to activate many more CRBN proteins by promoting closure much more efficiently, and future drug development may be able to harness this allosteric effect to improve efficacy. —MAF

Science, add7574, this issue p. 549

QUANTUM TECHNOLOGY

A robust quantum network node

The ability to develop quantum networks and communicate quantum information over long distances requires quantum memory nodes with efficient optical interfaces and long memory times. Because of their long coherence times and efficient optical interface, color centers in diamond are promising candidates to achieve this goal. Stas *et al*. used silicon vacancies in diamond and integrated the properties into a single device (see the Perspective by Gangloff). The authors demonstrate a quantum memory with a lifetime exceeding 2 seconds and full optical control of the quantum states of the two-qubit register. With the capability of

built-in error detection, such a platform is promising for the development of scalable quantum networks. —ISO

Science, add9771, this issue p. 557; see also ade6964, p. 473

PLASMA CELLS

Long-lived plasma cell production

High-affinity antibodies that provide durable protective immunity are produced by long-lived bone marrow plasma cells that differentiate from germinal center (GC) B cells. However, the kinetics with which these plasma cells occupy survival niches in the bone marrow after immunization is poorly understood. Robinson *et al.* constructed a genetic time-stamping mouse model to mark plasma cells generated at specific stages of an immune response, which enabled them to track the fate of plasma cells over time. The formation of new long-lived plasma cells started early in the GC response after immunization and progressed at a linear rate. These findings suggest that vaccine formulations that can extend the duration of the GC response will boost the number of long-lived antigen-specific plasma cells generated after immunization. —IRW

Sci. Immunol. **7**, eabm8389 (2022).

PHYSIOLOGY

Semaphorin 4D as cartilage destroyer

Various proinflammatory cytokines contribute to cartilage destruction in joint diseases. Murakami *et al*. found that the cytokine Semaphorin 4D (Sema4D) was released by inflamed macrophages and stimulated cartilage matrix degradation in articular chondrocytes and cartilage explants. In a mouse model of inflammatory arthritis, loss of Sema4D protected against cartilage degeneration. Sema4D stimulated the expression of transcripts encoding matrix-degrading enzymes downstream of intracellular signaling pathways that were distinct from those by which Sema4D regulates cell morphology and motility. —AMV

Sci. Signal. **15**, eabl5304 (2022).

VOLCANIC PLUMES

Reaching new heights

Large, explosive volcanic eruptions can loft material such as ash, gases, and water all the way into the stratosphere, with measurable impacts on atmospheric composition and climate. Proud *et al*. used geostationary satellite images of the January 2022 Hunga-Tonga volcano eruption, one of the largest eruptions ever recorded, to show that its volcanic cloud reached an altitude of 57 kilometers, well past the stratosphere and into the mesosphere and higher than any volcanic plume previously recorded. This is the first time a plume has been seen to penetrate the stratopause. —HJS

Science, abo4076, this issue p. 554

MONKEYPOX

Deaminase drives viral evolution

Monkeypox cases have occurred sporadically around the world for several decades. However, May 2022 saw a surge of reports of monkeypox infections outside of endemic regions and concentrated in the community of men who have sex with men. Fortunately, modifications of the smallpox vaccine are effective against monkeypox. Gigante *et al*. identified two lineages occurring in the United States showing evidence of the antiviral activity of host apolipoprotein B editing complex (APOBEC3) cytosine deaminase. APOBEC3 editing is unusual for poxviruses, but it looks to be driving recent monkeypox virus evolution. —CA

Science, add4153, this issue p. 560

IN OTHER JOURNALS

Edited by **Caroline Ash** *and* **Jesse Smith**



BIOGEOGRAPHY

Imperial affiliations for alien flora

One legacy of empires is the alien plant life that was intentionally spread around the world by colonists, often for economic reasons. Some of these alien species have since become damagingly invasive, and floristic homogenization and ecosystem degradation have become widespread. Lenzner *et al.* used zeta diversity to capture the contribution of rare and widespread species to compositional similarity and turnover of a flora. Species turnover was determined largely by climate and modified by the length of time of colonization. Given its size and relatively recent expansion, the British empire has had the greatest influence on alien invaders. Despite increased global plant trade since World War II, the specific signatures of pre-war colonial power in a region can still be traced in the composition of its alien flora. —CA

Nat. Ecol. Evol. 10.1038/s41559-022-01865-1 (2022).

Captain James Cook's ship *Endeavour* (a modern replica of the barque is shown) carried the botanist Joseph Banks, who was a towering figure in plant collection and dispersal around the British empire.

PHOTO: PATRICK EDEN/ALAMY STOCK PHOTO

EVOLUTION

Why are worms not afraid of cyanide?

Amygdalin, the Greek word for "almond," is a natural chemical compound found in many plants, including in the seeds of apples, peaches, cherries, and almonds. Amygdalin is a cyanogenic glycoside that is poisonous to many animals, but bacteria and plants have enzymes that can detoxify cyanide. The nematode *Caenorhabditis elegans*, a tiny roundworm that, when it is not being used as a model

organism, normally lives in temperate soils and is able to tolerate amygdalin. Interestingly, this worm seems to have acquired resistance to the toxin by horizontal transfer of two genes, one of which encodes a detoxifying enzyme, from green algae. In nature, *C. elegans* lives within rotten fruit, where it likely encounters plant-derived cyanide. —DJ

Curr. Biol. 10.1016/j.cub.2022.09.041 (2022).

SOCIAL RELATIONSHIPS

Stay well together

Inflammation is thought to be an important neurobiological mediator between romantic emotions and physical vigor, but this connection is controversial. Jolink *et al.* measured blood levels of an inflammatory marker, C-reactive protein (CRP), in romantically attached couples. The authors confirmed that just being in the presence of the other partner affected systemic inflammation. Indeed, the more time (measured in minutes per 24 hours) spent within the same physical space as the long-term partner, the lower the CRP levels recorded. Simply spending time together appears to be a good explanation for how high-quality relationships sustain physical health among adult humans by reducing systemic inflammation. —MM

Brain Behav. Immun. **107**, 132 (2022).

QUANTUM KEYS

Chip-based quantum key distribution

The flow of information between sender and receiver is typically encrypted with secret keys to ensure privacy. With the development of quantum computers, however, it has been shown that classical encryption methods are susceptible to hacking. Quantum key distribution (QKD) is a provably robust method for ensuring security against such quantum hackers, but the generation and transmission of the quantum keys have been impractically slow. Beutal *et al.* present a chip-based, fully integrated four-channel wavelength-division multiplexed QKD receiver that can achieve a key distribution of more than 12 megabits per second. Readily scalable by adding more wavelength channels, the architecture presents a viable route to developing secure, high-rate transmission of information across communication networks. —ISO

Optica **9**, 1121 (2022).

SOCIAL SCIENCE

Political rallies can bias policing

Campaign rallies by Donald Trump influenced law enforcement behavior toward racial minorities for up to 2 months afterward. Grosjean *et al.* used data from 35 million US traffic stops from 2015 to 2017, including in 141 counties that hosted rallies. In these counties, there was a nearly 6% post-rally increase in the probability that a stopped driver was Black. This was not due to any changes in the behavior or racial composition of drivers. Effects were most pronounced among officers whose prior treatment of Black versus white drivers was most biased. Among those officers, effects were exacerbated when rallies mentioned racial issues. —BW

Q. J. Econ. 10.1093/qje/qjac037 (2022).

FERROELECTRICS

The best way to relax

Relaxor ferroelectrics have both a polarization and a strain response to an external electric field, making them of great interest for various applications. However, the origin of this effect has been challenging to fully resolve. Kim *et al.* looked at the evolution of nanoscale polar nanodomains under varying epitaxial strains using diffused x-ray scattering, microdiffraction, electron microscopy, and molecular dynamics simulations. The authors found that structural transition between polar nanodomain configurations not only forms the basis for rotation of polarization but also for large electromechanical coupling. —BG

Nat. Phys. 10.1038/s41567-022-01773-y (2022).



PLANT SCIENCE

Adaptive diversity

Insight into local adaptation of long-lived trees, which are often foundational species in their habitats, can aid restructuring of forest populations that have been overtaken by climate change. Capblancq *et al.* studied the interaction between distribution and genomic adaptation for the red spruce (*Picea rubens*), which is found from Nova Scotia to North Carolina, areas that include a range of precipitation, moisture, and temperature extremes. The authors found that red spruce seedlings grew more poorly the farther they were transplanted from the site and environmental conditions local to their mother tree because of genetic selection for local conditions. —PJH

New Phytol. 10.1111/nph.18465 (2022).

Red spruce grows along a wide latitudinal gradient in the eastern United States, across which it displays genomic adaptation for local conditions.

PHOTO: BLICKWINKEL/ALAMY STOCK PHOTO

ALSO IN *SCIENCE* JOURNALS

Edited by **Michael Funk**

CELLULAR NEUROSCIENCE

Astrocyte diversity and morphology

Astrocytes are the major type of glia, displaying complex bushy morphologies as their defining feature. Endo *et al*. studied astrocyte similarities, diversity, and morphology across the mouse central nervous system (CNS) (see the Perspective by Baldwin). They identified gene networks related to astrocyte morphology between CNS regions, several of which unexpectedly included genes related to risk of Alzheimer's disease (AD). When expression of these genes was reduced in mice, astrocyte morphological complexity was diminished, and mice exhibited impairments in a cognitive test. Remarkably, the same genes are down-regulated in both a mouse model of AD and in human AD and several other CNS disorders. These findings suggest that loss of astrocyte morphology may be therapeutically targetable in diverse CNS disorders. —SMH

Science, adc9020, this issue p. 514; see also ade9249, p. 475

NEUROSCIENCE

Real-time voltage imaging of neurons

How different subpopulations of neurons coordinate their activity patterns in real time to control network output is still not fully understood. This is in part because of our inability to simultaneously measure the voltage dynamics within and across targeted cell ensembles. Kannan *et al*. developed a suite of mutually compatible, genetically encoded voltage indicators for high-speed voltage imaging of multiple genetically identified neurons in awake behaving animals. These indicators can be uniquely combined for simultaneous recordings of spiking by ensembles of neurons. This technical advance enables the first comprehensive studies of the real-time, millisecond-scale interactions between neurons of distinct genetic classes. —PRS

Science, abm8797, this issue p. 515

NEUROSCIENCE

Selectively silencing abnormal neurons

Nearly one-third of epilepsy patients do not respond to currently available anti-epileptic drugs. Several gene therapy approaches have been suggested, but these methods tend to indiscriminately target all neurons in a given brain region. Qiu *et al*. developed a gene therapy strategy that self-selects neurons that are pathologically overactive and down-regulates their excitability in a closed loop (see the Perspective by Staley). They put the *KCNA1* gene, which encodes a potassium channel, under the control of an immediate early gene promoter with activity that is switched on by intense neuronal firing. The treatment switches itself off once brain circuit activity has returned to baseline. This approach could in principle be used to treat any neuropsychiatric disorder in which only a subpopulation of neurons is pathologically overactive. —PRS

Science, abq6656, this issue p. 523; see also ade8836, p. 471

ARCTIC WILDFIRES

Getting burned

Global warming is exacerbating the conditions that cause wildfires in many regions, including the Arctic, where extensive peatlands hold large amounts of carbon. However, is the extent of wildfires there increasing as would be expected given the changing conditions? Descals *et al*. found that during the summer of 2020, which was the warmest in four decades, Arctic fires burned an unprecedentedly large area of carbon-rich soils (see the Perspective by Post and Mack). They project that near-term climatic warming will cause an exponential increase in burned area in Arctic carbon-rich soils before mid-century. —HJS

Science, abn9768, this issue p. 532; see also ade9583, p. 470

NEUTRINO ASTROPHYSICS

Nearby active galaxy emits neutrinos

Observations have shown a diffuse background of high-energy neutrinos, which is known to be of extragalactic origin. However, it has been difficult to identify individual sources that contribute to this background. The IceCube Collaboration reanalyzed the arrival directions of astrophysical neutrinos and then searched for point sources (see the Perspective by Murase). They identified evidence for neutrino emission from NGC 1068 (also known as Messier 77), a nearby active galaxy. Its properties are quite different from TXS 0506+056, which was found to be a neutrino source in 2018, leading the investigators to suggest that there might be more than one population contributing to the neutrino background. —KTS

Science, abg3395, this issue p.538; see also ade4190, p. 474

MYOCARDITIS

Of myocarditis and women

Inflammation of the heart muscle, or myocarditis, is an off-target effect of anticancer treatments such as immune checkpoint inhibitor (ICI) therapy. Studying sex differences in ICI myocarditis, Zhang *et al.* observed greater T cell infiltration and cardiac dysfunction in female mice with this disorder and identified down-regulation of two genes, *MANF* and *HSPA5*, in the heart. In a mouse model, cardiac depletion of *Manf* worsened ICI myocarditis, whereas addition of the recombinant MANF protein improved heart function. Treating cardiomyocytes derived from human induced pluripotent stem cells with estrogen or estrogen receptor β agonist induced MANF and HSPA5 expression. Treating female tumor-bearing mice with estrogen receptor β agonist during ICI treatment reduced T cell infiltration and preserved heart function. Hormone therapy could thus potentially limit ICI myocarditis by promoting the protective effects of MANF. —CC

Sci. Transl. Med. **14**, eabo1981 (2022).

ANIMAL BEHAVIOR

Complex cognition in songbirds

A cornerstone of symbolic cognition is recursion, the capacity to embed structures within similar structures. This capacity has only been identified in primates, but Liao *et al.* found that carrion crows (*Corvus corone*), a songbird family that demonstrates complex cognition, can parse, learn, and generate recursive sequences of visual stimuli. The birds reached a level of performance comparable to that of 3- to 4-year-old human children and superior to that of nonhuman primates after only a few learning trials. Given the parallels between songbird communication and human language, these findings shed light on the fundamental cognitive abilities that underlie complex communication between conspecifics. —AF

Sci. Adv. 10.1126/sciadv.abq3356 (2022).

Science
JOURNALS AAAS



Publish your research in the *Science* family of journals

The *Science* family of journals (*Science, Science Advances, Science Immunology, Science Robotics, Science Signaling*, and *Science Translational Medicine)* are among the most highly-regarded journals in the world for quality and selectivity. Our peer-reviewed journals are committed to publishing cutting-edge research, incisive scientific commentary, and insights on what's important to the scientific world at the highest standards.

Submit your research today!

Learn more at **Science.org/journals**

RESEARCH ARTICLE SUMMARY

CELLULAR NEUROSCIENCE

Molecular basis of astrocyte diversity and morphology across the CNS in health and disease

Fumito Endo, Atsushi Kasai, Joselyn S. Soto, Xinzhu Yu, Zhe Qu, Hitoshi Hashimoto, Viviana Gradinaru, Riki Kawaguchi, Baljit S. Khakh*

INTRODUCTION: The central nervous system (CNS) comprises a large population of non-neuronal cells called glia. The predominant type of glia are astrocytes, which were discovered ~140 years ago. Astrocytes tile the entire CNS, serve critical homeostatic functions, and display complex, "bushy" morphologies—their defining feature. Unlike CNS neurons, which are highly diverse, astrocytes have historically been considered largely homogenous, serving as a type of omnipresent glue that is equivalent between CNS areas. Although recent studies have challenged this belief, there has been no broad assessment of astrocyte diversity, similarity, or morphology across the CNS of any species. An important goal, therefore, is to rigorously understand the molecular similarities and differences between astrocytes in the CNS, to determine how they affect astrocyte morphology, and to determine how these properties relate to normal and disease conditions.

RATIONALE: It is critical to understand all cell types of the CNS in detail as part of our quest to explore fundamental biology and to develop new therapeutic strategies to treat CNS disorders. We studied astrocyte regional diversity and major signaling pathways using whole-brain imaging, astrocyte-neuron density, marker expression, astrocyte-specific and bulk tissue gene expression, single-cell gene expression, astrocyte morphology, and interrelationships between gene expression and morphology using bioinformatic methods across the CNS. The data were mined to identify genes and pathways related to astrocyte morphological complexity, which we explored experimentally using gene knockdowns. We then compared these morphology-related genes with astrocytic differentially expressed genes from an Alzheimer's disease (AD) mouse model displaying reduced astrocyte morphology, as well as in relation to gene expression in AD and other CNS disorders.

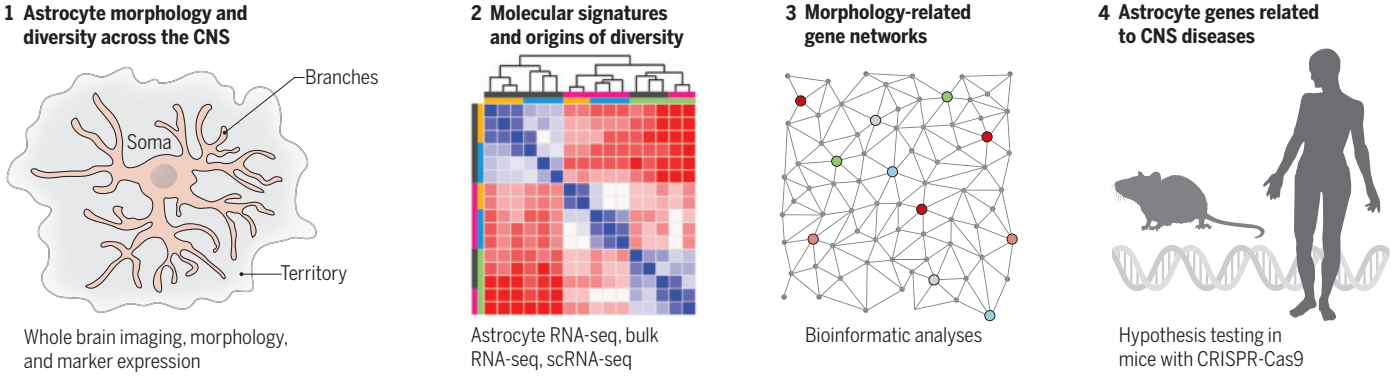
RESULTS: We found several hundred genes that were enriched within and shared among astrocytes in the CNS, with functions related to metabolism, cholesterol, and neurotransmitter uptake and biosynthesis. These genes represent the core functions of astrocytes, but little is known about approximately a third of them, implying that understanding the fundamental physiology of astrocytes across CNS areas is an important ongoing experimental goal. Our data also reveal that astrocytes have molecular features and functions specific to CNS regions, and that these region-specific functions arise from the local tissue environment and by variable representation of seven distinct astrocyte subclusters.

We mined our data to identify gene networks related to astrocyte morphology, and unexpectedly discovered several AD risk genes. We developed astrocyte-specific CRISPR/Cas9–based gene knockdown to reduce the expression of such genes in the hippocampus. We found a reduction of astrocyte morphology with changes in a cognitive task after knockdown of key morphology-related genes, indicating that astrocyte morphological changes affect neural circuit function. In addition to AD risk genes that were astrocyte morphology related, we found a significant association between morphology-related genes and those related to several other common CNS disorders.

CONCLUSION: We provide comprehensive molecular data that will allow many new types of experiments to explore core features of astrocytes across the CNS, in particular, those unique to specific regions and how they relate to the dynamics and biophysics of neural circuits in specific CNS regions. We used our data to identify the molecular underpinnings of astrocyte morphology between CNS regions and to show that reduced astrocyte morphological complexity, and the attendant loss of tissue support, is common to diverse CNS disorders. This raises the prospect that restoring astrocyte morphology, and thus the ensuing neuronal and tissue support functions, may be therapeutically beneficial in disease. Our findings provide the molecular basis to explore such strategies and to unravel the nascent underlying biology determining how astrocytes contribute to CNS function and dysfunction. ■

The list of author affiliations is available in the full article online.
*Corresponding author. Email: bkhakh@mednet.ucla.edu
Cite this article as F. Endo *et al.*, *Science* **378**, eadc9020 (2022). DOI: 10.1126/science.adc9020

READ THE FULL ARTICLE AT
https://doi.org/10.1126/science.adc9020



Astrocyte diversity and morphology across the CNS. (1) Astrocyte morphology and gene expression was measured across CNS regions. (2) Gene expression data revealed the molecular signatures of astrocyte diversity and its origins. (3) Gene expression and morphological data identified gene networks related to complex morphology. Causal roles were explored. (4) Several astrocyte morphology genes were Alzheimer's disease risk genes, a disorder in which astrocytes displayed reduced morphology.

RESEARCH ARTICLE

CELLULAR NEUROSCIENCE

Molecular basis of astrocyte diversity and morphology across the CNS in health and disease

Fumito Endo[1], Atsushi Kasai[2], Joselyn S. Soto[1], Xinzhu Yu[1]†, Zhe Qu[3], Hitoshi Hashimoto[2,4,5,6,7], Viviana Gradinaru[3], Riki Kawaguchi[8], Baljit S. Khakh[1,9]*

Astrocytes, a type of glia, are abundant and morphologically complex cells. Here, we report astrocyte molecular profiles, diversity, and morphology across the mouse central nervous system (CNS). We identified shared and region-specific astrocytic genes and functions and explored the cellular origins of their regional diversity. We identified gene networks correlated with astrocyte morphology, several of which unexpectedly contained Alzheimer's disease (AD) risk genes. CRISPR/Cas9–mediated reduction of candidate genes reduced astrocyte morphological complexity and resulted in cognitive deficits. The same genes were down-regulated in human AD, in an AD mouse model that displayed reduced astrocyte morphology, and in other human brain disorders. We thus provide comprehensive molecular data on astrocyte diversity and mechanisms across the CNS and on the molecular basis of astrocyte morphology in health and disease.

To explore how the brain performs its functions, it is critical to understand its diverse cell populations in detail, as articulated by the BRAIN Initiative (*1*, *2*). Furthermore, it is important to explore both neuronal and non-neuronal cells such as glia (*1*–*3*).

Astrocytes, the most populous glial cells, were documented at the same time as neurons, but for a long time their role was relegated to a type of "glue" that held the brain together (*4*). With recent technical advances (*5*), these fascinating cells are emerging as essential contributors of brain physiology, animal behavior, and disease (*6*, *7*). Astrocytes are ubiquitous, morphologically complex, bushy cells that make extensive contacts with other brain cells. They serve diverse roles, including ion and neurotransmitter homeostasis, synapse formation and removal, synaptic modulation, and contributions to neurovascular coupling and the blood–brain barrier. Astrocytes are widely implicated in neurological and psychiatric diseases (*7*, *8*).

[1]Department of Physiology, University of California Los Angeles, Los Angeles, CA, USA. [2]Laboratory of Molecular Neuropharmacology, Graduate School of Pharmaceutical Sciences, Osaka University, Suita, Osaka, Japan. [3]Division of Biology and Biological Engineering, California Institute of Technology, Pasadena, CA, USA. [4]Molecular Research Center for Children's Mental Development, United Graduate School of Child Development, Osaka University, Suita, Osaka, Japan. [5]Division of Bioscience, Institute for Datability Science, Osaka University, Suita, Osaka, Japan. [6]Open and Transdisciplinary Research Initiatives, Osaka University, Suita, Osaka, Japan. [7]Department of Molecular Pharmaceutical Science, Graduate School of Medicine, Osaka University, Suita, Osaka, Japan. [8]Center for Neurobehavioral Genetics, Semel Institute for Neuroscience and Human Behavior, University of California Los Angeles, Los Angeles, CA, USA. [9]Department of Neurobiology, University of California Los Angeles, Los Angeles, CA, USA.
***Corresponding author. Email: bkhakh@mednet.ucla.edu**
†Present address: Department of Molecular and Integrative Physiology, Beckman Institute, University of Illinois at Urbana-Champaign, Urbana, IL 61801, USA.

Unlike neurons, which are extremely diverse within neural circuits, astrocytes have traditionally been viewed as being homogeneous. However, recent gene expression and functional studies using different methods in the context of health and brain tumors have shown that astrocytes are separable between several central nervous system (CNS) regions (*9*–*18*). This has led to the realization that astrocytes may be diverse, an attribute that, together with their highly complex morphology, may allow them to mediate their multiple roles in different parts of the CNS. However, there has been no broad molecular assessment of astrocyte diversity, similarity, or morphology across the CNS of any species.

Results

Strategy

We studied astrocytes from 13 regions of the adult mouse CNS (Fig. 1A): the olfactory bulb (OB), motor cortex (MCX), somatosensory cortex (SCX), visual cortex (VCX), hippocampus (HIP), striatum (STR), thalamus (TH), hypothalamus (HY), cerebellum (CB), midbrain (MB), hindbrain (HB), ventral spinal cord (VSC), and dorsal spinal cord (DSC). First, we assessed astrocyte-neuron density and astrocyte marker expression in different CNS regions. Next, we assessed molecular profiles and signaling pathways using astrocyte-specific RNA sequencing (RNA-seq), bulk tissue RNA-seq, and single-cell RNA-seq (scRNA-seq). Additionally, we documented the morphology of astrocytes and used weighted gene coexpression network analyses (WGCNA) to identify gene networks correlated with morphological complexity. We also tested the consequences of reducing the expression of genes predicted to affect astrocyte morphology using CRISPR/Cas9. Then, we related molecular signatures of astrocyte morphology to gene expression and astrocyte morphological changes in an Alzheimer's disease (AD) mouse model and to human CNS disorders, including AD.

Cellular and anatomical evaluation of astrocytes

We mapped astrocyte density across 13 CNS regions by using whole-brain imaging by block-face serial microscopy tomography (FAST) (*19*) in mice expressing tdTomato in astrocytes (*20*) (from *Aldh1l1* locus; Fig. 1B). We observed tdTomato$^+$ astrocytes throughout the brain (movie S1) and spinal cord, with densities that varied between regions but overlapped with Sox9 (*21*) by 95 ± 2% (Fig. 1C and figs. S1 and S2). Although *Aldh1l1* and Sox9 are reliable markers of astrocytes (*20*, *21*), no marker labels all astrocytes, and 100% overlap was therefore not expected. We quantified tdTomato$^+$ astrocyte density and found significant but modest twofold differences between areas (Fig. 1, C and D; $N = 3$ to 6 mice; all regions in fig. S1). Next, we labeled neurons and most astrocytes by immunohistochemistry (IHC) for S100β; and glial fibrillary acidic protein (GFAP) in mice expressing GCaMP6f in astrocytes (fig. S3). The astrocyte-neuron ratios varied almost 10-fold, being highest in the ventral spinal cord and lowest in the cerebellum, where our evaluations included Bergmann glia (Fig. 1E; $N = 8$ mice). These differences were not driven by major variation in astrocytes but by differences in neurons (Fig. 1, F and G; $N = 8$ mice). There was no one-to-one scaling between neuron and astrocyte density across regions, although the two parameters were correlated ($r = 0.495$, $P = 0.118$; Fig. 1H). These data show that the density of astrocytes per region did not scale simply with neuron density, but that astrocytes tiled the CNS with modest variation, likely reflecting homeostatic functions. Large variations of the astrocyte-neuron ratios between CNS regions were driven by neurons. Because astrocytes form part of the neurovascular unit, we also mapped astrocyte-endothelial cell density and ratios across CNS regions (fig. S4, A to D). We found that endothelial cell and astrocyte density were strongly correlated (fig. S4E), reflecting critical neurovascular unit biology.

We performed IHC for GFAP, S100β, and GCaMP6f (from the *Aldh1ll* locus) to determine whether these markers were equivalent or dissimilar between CNS regions (*20*). There was an ~500-fold variation between CNS regions for these established markers (fig. S5; $N = 8$ mice; movie S2). Although the density of astrocytes varied little (Fig. 1), quantitative IHC experiments (fig. S5) provided evidence for the diversity between CNS regions.

Shared CNS-wide astrocyte genes and pathways

To evaluate astrocyte gene expression, we performed astrocyte-specific RNA-seq (*9*).

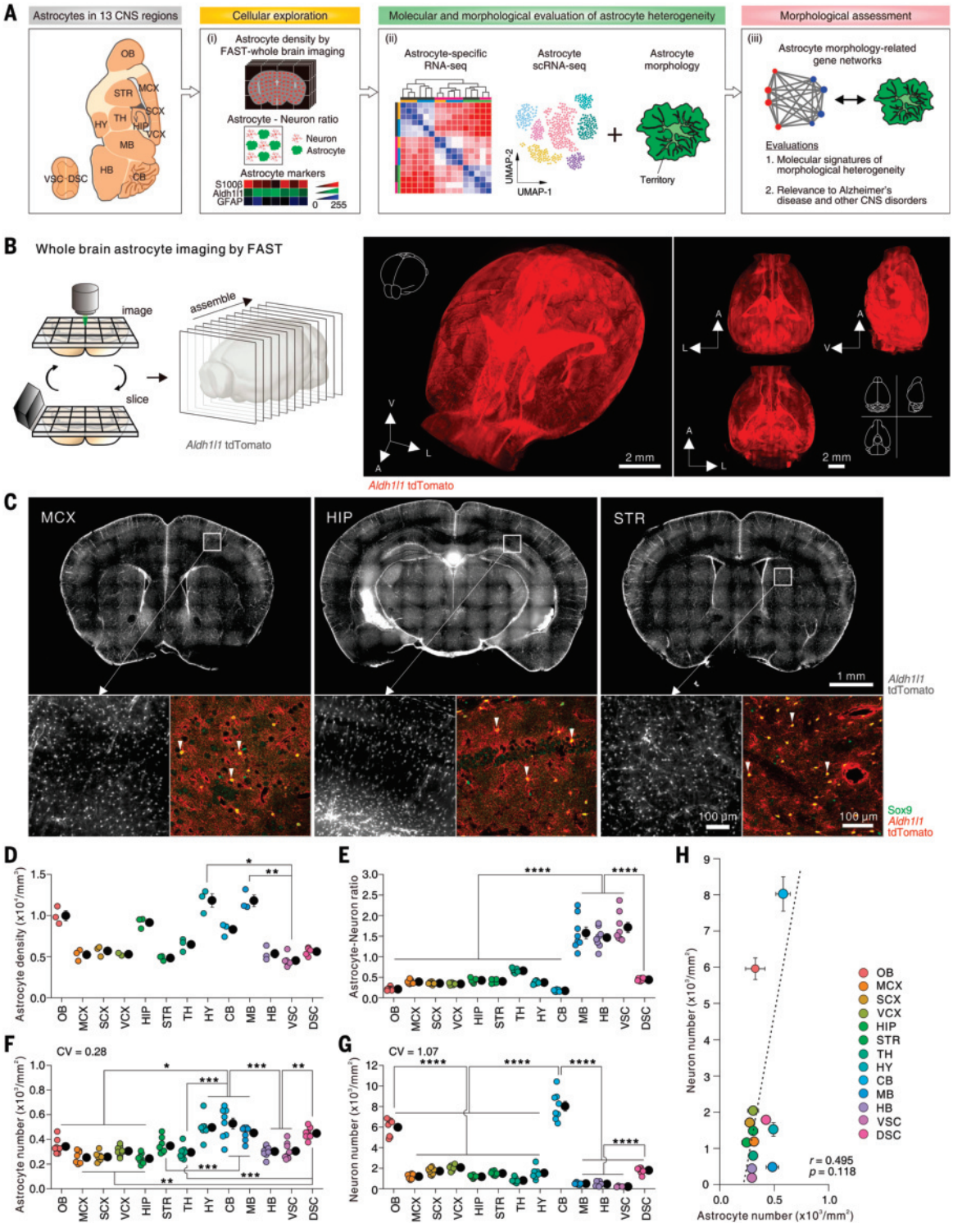


Fig. 1. Astrocyte density and astrocyte-to-neuron ratios across the mouse CNS. (**A**) Experimental design for investigating astrocytes in 13 CNS regions. CB, cerebellum; DSC, dorsal spinal cord; HB, hindbrain; HIP, hippocampus; HY, hypothalamus; MB, midbrain; MCX, motor cortex; OB, olfactory bulb; SCX, somatosensory cortex; STR, striatum; TH, thalamus; VCX, visual cortex; VSC, ventral spinal cord. (**B**) Illustration and representative images of whole-brain astrocyte imaging by FAST. A, anterior; L, lateral; V, vertical. The brains were from *Aldh1l1*-Cre/ERT2 x Ai14 (*Aldh1l1* tdTomato) mice. (**C**) Representative coronal sections of *Aldh1l1*-Cre/ERT2 x Ai14 (*Aldh1l1* tdTomato) mouse brains imaged by FAST. Magnified images show tdTomato$^+$ astrocytes in the MCX, HIP, and STR; the other 10 regions are shown in fig. S1. The color images show exemplar Sox9- and *Aldh1l1*-driven tdTomato images (see fig. S2). (**D**) Astrocyte density measurements by FAST in 13 CNS regions (N = 6 mice for spinal cord; N = 3 mice for brain). (**E**) Plot showing the astrocyte-to-neuron ratio in 13 CNS regions (N = 8 mice). (**F** and **G**) Plot of astrocyte and neuron numbers in 13 CNS regions. (**H**) Correlation between astrocyte and neuron numbers. Data are shown as means ± SEM.

Whole-tissue (input) and astrocyte RNA (immunoprecipitated) was extracted from 13 regions (Fig. 2A; N = 3 to 5 mice). Multidimensional scaling showed separation among input, immunoprecipitation, and CNS areas (Fig. 2B). Immunoprecipitated fractions were enriched with astrocyte markers (fig. S6A).

We identified 4314 astrocyte-enriched genes [relative to input; $\log_2$ ratio > 1; false discovery rate (FDR) < 0.05, fragments per kilobase of transcript per million mapped reads (FPKM) > 1], and of these, 825 (~20%) were common across the 13 regions and called "shared" (fig. S6, B to D). A total of 939 genes (~22%) were "unique" to a particular region, and the remaining 2588 genes (~60%) were "partially shared" in two to 12 regions (fig. S6, B to D). To explore the pathways and signaling mechanisms shared by astrocytes across all regions, we assessed the molecules represented by the 825 genes. About half were related to enzymatic and transporter activity or transcriptional regulation (fig. S6E). Figure 2C shows the top 50 astrocyte-enriched genes shared across 13 regions in order of enrichment, with the color scale representing abundance and annotations illustrating the major signaling mechanisms. Recalling IHC (Fig. 1 and fig. S2), *Aldh1l1* and Sox9 were abundant across regions (Fig. 1C) and known astrocyte genes (e.g., *Kcnj10*, *Slc1a2*, and *Apoe*) were among the top 50 highly expressed (Fig. 2C). Unbiased analyses for the 825 shared astrocyte-enriched genes showed that the top pathways were related to neurotransmitter homeostasis, cholesterol biosynthesis, and glucose metabolism (Fig. 2D).

We performed several analyses for astrocytes across 13 regions (figs. S7 and S8). For K^+ homeostasis, the most highly expressed genes were *Kcnj10*, *Kcnj16,* and *Atp1a2*, encoding K^+ channels and Na^+/K^+ ATPase (fig. S7A). Astrocytes highly expressed genes related to neurotransmitter transport and metabolism but they lacked or expressed at very low levels the genes related to Ca^{2+}-dependent vesicular release (fig. S7, B to E). Shared functional properties of astrocytes may be cell-autonomously regulated because >50% of all upstream regulators were categorized as transcriptional regulators and ligand-dependent nuclear receptors (fig. S8, A and B). The top 20 genes across 13 regions reflecting functional classes of molecules such as enzymes, transporters, kinases, receptors, peptidases, and ion channels are provided in fig. S8, C to J. For example, the G protein–coupled receptor (GPCR) genes *Gpr37l1*, *S1pr1*, *Ntsr2*, *Ednrb*, *Smo*, *Adora2b*, *Olfr287*, *Gpr146*, *Agtrap*, *Fzd1*, *Fzd9*, and *Npr2* were expressed in astrocytes across the CNS. These evaluations of shared genes and pathways represent core features of CNS astrocytes (Fig. 2, C and D, and table S1). Little is known about the physiology of many astrocyte genes within the top 50 (Fig. 2C).

Region-specific astrocyte genes and pathways

We analyzed astrocyte differentially expressed genes (DEGs) in each CNS area relative to the other 12 regions and identified 3500 that were region enriched (Fig. 2E). Hierarchical clustering of these region-enriched DEGs revealed a trend consistent with anatomical proximity (Fig. 2F). Thus, astrocytes from the cerebrum (OB, MSC, SCX, VCX, HIP, and STR) were clustered distinctly from broad regions of the brain stem and spinal cord (TH, HY, MB, VSC, and DSC) and the cerebellum (Fig. 2, E and F). The number of region-enriched genes varied (fig. S9A), but regional differences were mainly driven by up-regulated genes (fig. S9A). Overlap of the top 100 astrocyte region–enriched DEGs is illustrated in fig. S9B for the cerebrum, brain stem and spinal cord, and cerebellum. Clustering for the bulk tissue–specific DEGs, with or without astrocyte-enriched genes for the 13 CNS regions, showed a similar pattern as astrocyte DEGs (fig. S9, C to E), suggesting that the regional identity of astrocytes reflects the region-specific microenvironment (as reflected in the bulk RNA-seq data), as well as astrocyte lineage–related gene expression (as reflected in the immunoprecipitated RNA-seq data).

Because astrocytes from 13 CNS regions clustered into three broad anatomical classes, we identified the top 10 marker genes from the cerebrum, brain stem and spinal cord, and cerebellum (Fig. 2G). Furthermore, we identified region-specific astrocyte marker genes for each of the 13 CNS areas (Fig. 2H) and classified the top 20 on the basis of their functions (fig. S10). Some of the genes we identified as being regionally enriched within astrocytes (e.g., *Chrdl1* and *Crym*) were known (*9*, *14*, *22*), but many were new. We validated expression of the genes for which reliable antibodies were available: IHC for proteins encoded by *Sphk1*, *Ccnd1*, *Crym,* and *Sept4* confirmed regional location at the protein level (Fig. 2, I to L; N = 4 mice). Additional analyses for the astrocyte region–enriched genes across the 13 CNS regions revealed differences and similarities in transcription factors that may partly explain the interregional differences of astrocytes (fig. S11A). Gene ontology analysis for the region-enriched DEGs identified putative astrocyte region–specific functions (fig. S11B). We also assessed genes related to astrocyte functions such as phagocytosis, synapses, reactivity (fig. S12), and Ca^{2+} signaling (fig. S13), noting differences between regions for transmembrane Ca^{2+} flux pathways and GPCR signaling (fig. S13, E and F) that foreshadow functional studies.

Bioinformatic evaluation of astrocyte diversity

To explore how differences between astrocytes from different CNS regions may arise, we performed scRNA-seq for the cortex, hippocampus, and striatum, which we chose because they shared the same anatomical area (Fig. 2, E and F) and are widely studied in the field. We asked several questions. First, do subclusters of astrocytes exist within these regions? Next, do different combinations of these subclusters contribute to the regional nature of astrocytes? Moreover, are regional differences between astrocytes related to a metric of the local tissue in which they reside?

We analyzed scRNA-seq data of 89,553 cells from the cortex, hippocampus, and striatum, (Fig. 3, A and B, and fig. S14A; N = 13 mice). Astrocytes accounted for ~15% (fig. S14B), which is consistent with expectations (*4*). However, this percentage should be treated cautiously because it results from tissue dissociation, but the percentage of $Sox9^+$ and $tdTomato^+$ astrocytes relative to 4′,6-diamidino-2-phenylindole–positive ($DAPI^+$) cells (e.g., from fig. S2) in the cortex, hippocampus, and striatum was 10 ± 1, 11 ± 1, and 13 ± 1%, respectively (N = 3). Further analysis showed that these CNS regions shared seven astrocyte subclusters (AST1 to AST7; Fig. 3C) representative of the cortex, hippocampus, and striatum (Fig. 3D). Genes known to be enriched in cortical (*Chrdl1*), hippocampal (*Gfap*), and striatal (*Crym*) astrocytes showed high expression within their cognate region (Fig. 3E). By analyzing the subclusters, we identified the top 100 genes enriched within each (Fig. 3F). Furthermore, the seven subclusters represented different proportions of astrocytes per brain region, implying that regional diversity may be cast partly from variable representation of the subclusters (Fig. 3G). For example, subcluster AST2 was dominant in the cortex, subcluster AST1 was dominant in the hippocampus, and subclusters AST5 and AST6 were dominant in the striatum (Fig. 3G). Upstream analysis for the seven subclusters revealed differences and similarities in the top five upstream transcriptional regulators (fig. S14C). We also found upstream regulators related to external cues such as neurotransmitters [e.g., γ-aminobutyric acid (GABA)], growth factors [e.g., epidermal growth factor (EGF)], and cytokines [e.g., interleukin-9 (IL-9); fig. S14D], implying that astrocyte regional differences were related to tissue-dependent profiles within the local microenvironment. We assessed functional features of the astrocyte subclusters (fig. S14E) and performed candidate gene analyses (fig. S15). Genes related to glucose homeostasis were up-regulated in AST2, AST4, AST5, and AST6 (fig. S15A). Related to K^+ homeostasis, *Kcnj10* was up-regulated in AST2, whereas *Atp1a2* and *Atp1b2* were up-regulated in AST1 (fig. S15B). Subcluster-specific enrichment was observed for genes related to cholesterol homeostasis, neurotransmitter homeostasis, dopamine metabolism, synapse function, and phagocytosis (fig. S15), indicating that combinations of subclusters between CNS regions

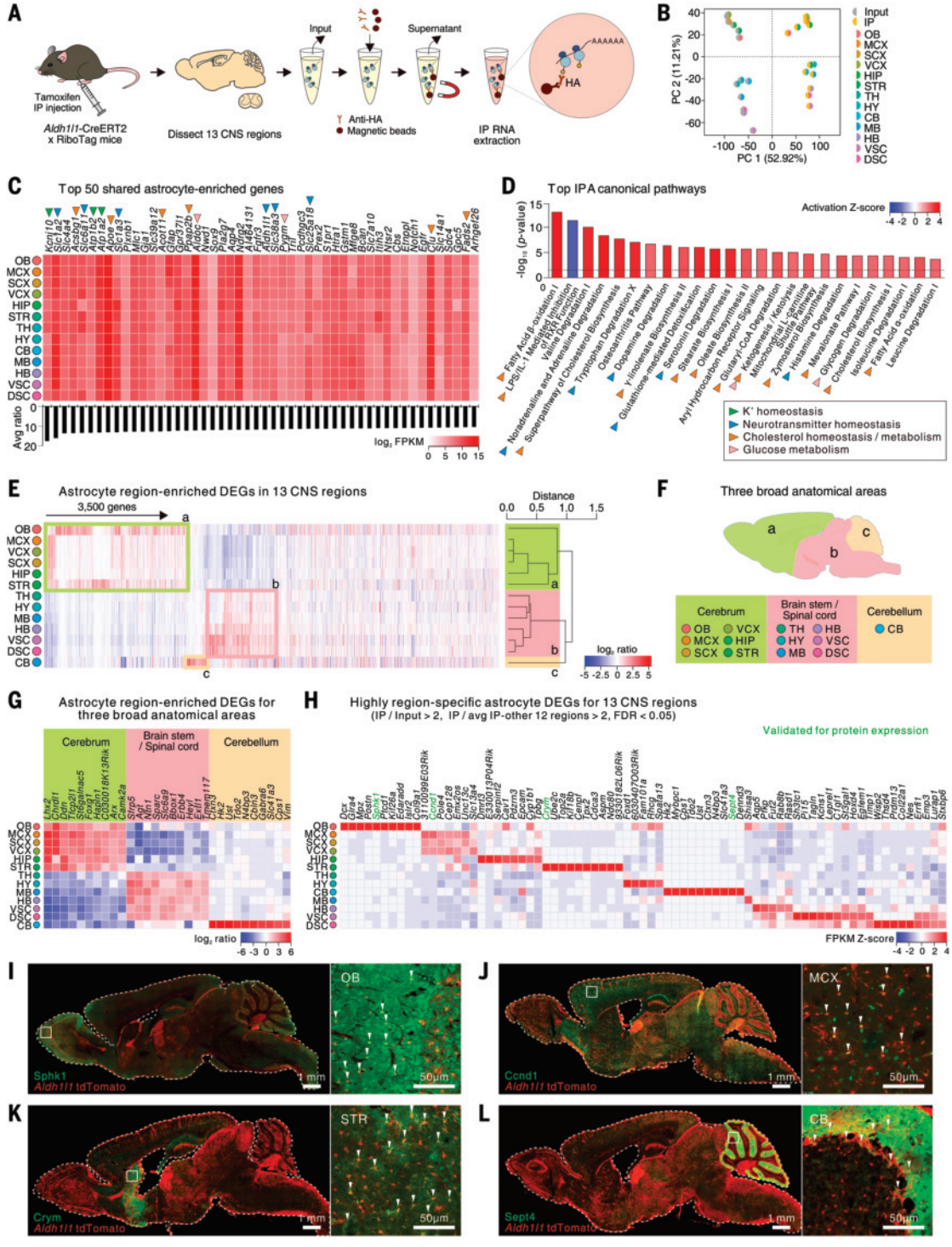


Fig. 2. Shared and unique astrocyte CNS molecular signatures and mechanisms. (**A**) Approach for astrocyte-specific RNA-seq. (**B**) Multi-dimensional scaling plot for input and immunoprecipitated (N = 3 to 5 mice) RNA-seq data. (**C**) Heat map showing the $\log_2$ FPKM values of the top 50 most enriched astrocyte genes shared in the 13 CNS regions. The bar graph shows the average ratio of immunoprecipitation versus input. Colored arrowheads indicate functional class. (**D**) Bar graph showing the top 25 ingenuity pathway analysis (IPA) canonical pathways for the 825 shared astrocyte-enriched genes with a threshold of P value < 0.05. The colored arrowheads indicate functional class. (**E**) Heat map showing 3500 astrocyte region–enriched DEGs in 13 CNS regions with a cluster dendrogram. Astrocyte region–specific DEGs were defined by comparing immunoprecipitation in one CNS region with the average of immunoprecipitated samples from the other 12 regions with a threshold of $\log_2$ ratio > 1, FDR < 0.05, and FPKM > 1. From the dendrogram, astrocytes could be classified into three broad groups. Genes defining OB, MCX, SCX, HIP, and STR (cerebrum) are outlined in green ("a"). Genes highly expressed within and defining TH, HY, MB, HB, VSC, and DSC (brain stem or spinal cord) are outlined in pink ("b"). Genes highly expressed within and defining the CB are outlined in orange ("c") and include Bergmann glia genes. (**F**) Schematic of anatomical grouping of astrocytes in 13 CNS regions based on RNA-seq. (**G**) Heat map showing the $\log_2$ ratio of immunoprecipitation versus the averaged immunoprecipitation from the other 12 regions of the top 10 astrocyte-specific DEGs for anatomically relevant CNS regions. (**H**) Heat map showing the top region-specific astrocyte genes from RNA-seq. (**I** to **L**) Representative (N = 4 mice) IHC images for *Sphk* (I), *Ccnd1* (J), *Crym* (K), and *Sept4* (L), which reproduced regional expression in OB, MCX, STR, and CB, respectively.

imparted separable functional features to astrocytes in different CNS regions.

The existence of several extracellular species in the top 10 upstream regulators for the astrocyte subclusters [e.g., GABA, IL-4, EGF, tumor necrosis factor (TNF), and IL-5; fig. S14D] suggested that regional astrocyte diversity may reflect the tissue microenvironment, which we explored using astrocyte-specific and bulk RNA-seq data (Fig. 2). As shown in Fig. 2, astrocyte RNA-seq data for the 13 CNS regions could be hierarchically clustered into three broad anatomical regions. This trend was also observed when we compared the percentage of shared genes between all 13 regions

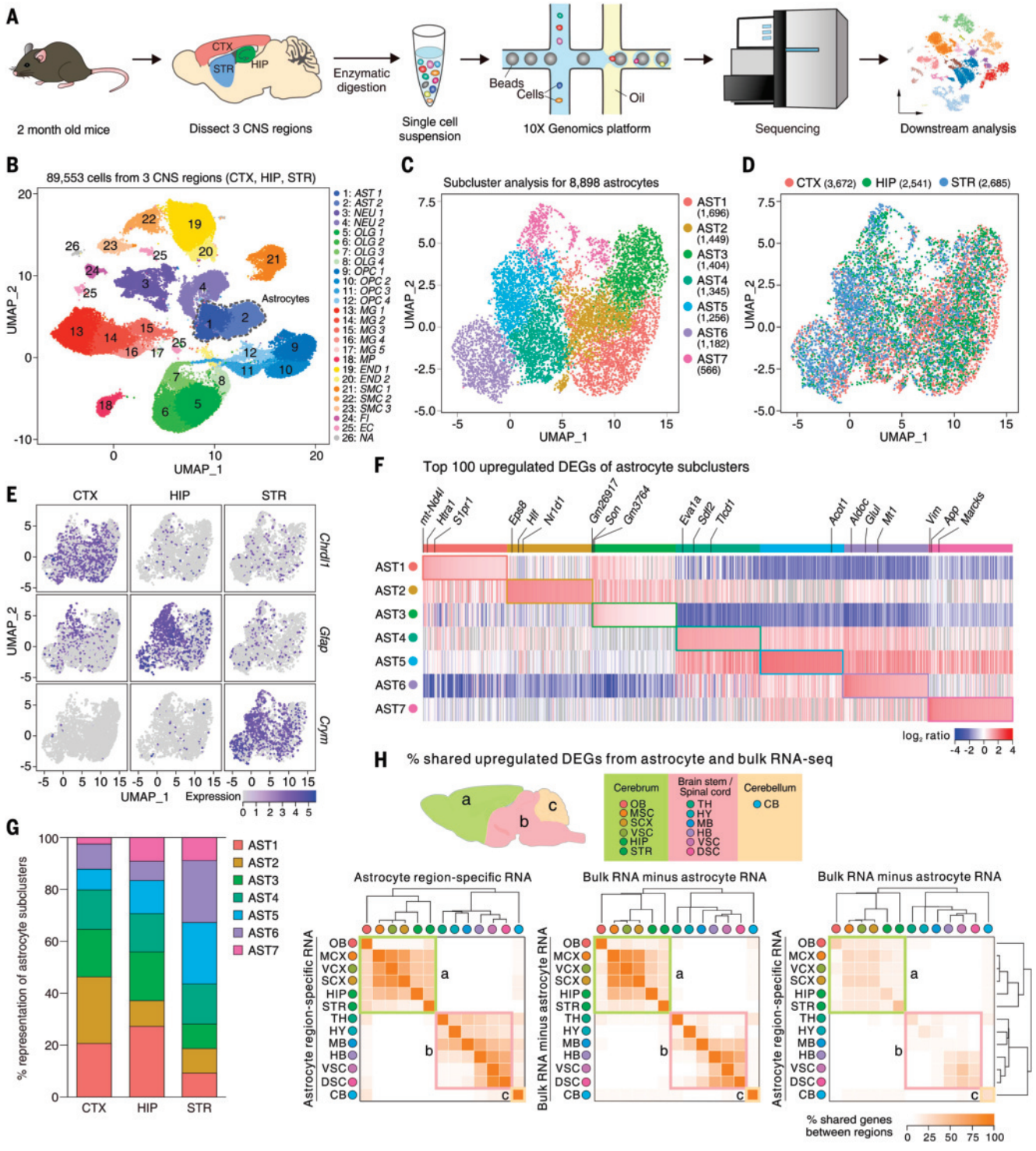


Fig. 3. Origins of astrocyte diversity from regional and scRNA-seq data. (**A**) Experimental procedure for scRNA-seq. Single cells were dissociated from the cortex, hippocampus, and striatum of wild-type mice (N = 4 to 7 mice). Data for striatal cells were partly from our recent study (*34*) and combined with new cortical, hippocampal, and striatal single-cell data. (**B**) Uniform manifold approximation and projection (UMAP) plot of 89,553 brain cells from three CNS regions grouped by expression similarity identified 26 major cell populations (10 major cell types). (**C**) UMAP plot of cluster analysis for 8898 astrocytes [*AST1* and *AST2* in (B)] from three CNS regions. The cell numbers of astrocyte subclusters are shown as AST1 to AST7. (**D**) UMAP plot of the astrocyte subclusters to illustrate the three different brain regions examined. (**E**) UMAP plots from (C) showing the expression of *Chrdl1*, *Gfap*, and *Crym*. (**F**) Heat map shows the top 100 genes that were up-regulated in each astrocyte subcluster relative to the others. Example genes are identified. (**G**) Proportional bar graph showing the percentage of each astrocyte subcluster representation in the three CNS regions from scRNA-seq data. (**H**) Correlations between astrocyte region–specific RNA-seq data (left), bulk RNA-seq data (middle), and bulk RNA-seq minus astrocyte region–specific RNA-seq data (right) that were gathered as part of Fig. 2. The correlation plots show that astrocytes grouped into three broad anatomical areas ("a," "b," and "c").

in a pairwise manner for astrocyte RNA-seq and bulk RNA-seq data (Fig. 3H). Next, we compared the percentage of shared genes between the astrocyte region–specific RNA-seq data with the bulk RNA-seq data (minus astrocyte enriched genes) and found a similar trend (Fig. 3H). Because the astrocyte-specific RNA-seq data were correlated with the equivalent bulk RNA-seq data per region, these data provide evidence that region-specific features were shaped, at least in part, by the local tissue environment (Fig. 3H) and by variable representation of the subclusters in a region-specific manner (Fig. 3G). This recalls the finding that many postnatal cortical astrocytes arise from local proliferation and are likely tuned to their environment (*23*). Our analyses provide the rationale and data to explore such relationships when specific genetic tools become available.

Astrocyte morphology–related gene networks

A key feature of astrocytes is their morphological complexity. To exploit transcriptomic datasets, we documented the two-dimensional (2D) morphological features of astrocytes from 13 CNS regions and related these to RNA-seq data using WGCNA. To quantify the morphology of astrocytes, we expressed GCaMP6f sparsely in astrocytes, obtained diffraction-limited 2D images from flattened confocal volumes using IHC (Fig. 4, A and B, and fig. S16), and subjected them to identical evaluations (Fig. 4A and fig. S16). For example, astrocytes in MCX displayed the largest territory size and showed a relatively round shape, whereas astrocytes in CB (Bergmann glia) showed the most elongated shape (fig. S16, B to I). We found no differences in the number of major branches per astrocyte from the 13 CNS regions (average: 4.0 to 5.6; fig. S16J). The fractal dimension, a parameter reflecting morphological complexity, revealed significant differences between astrocytes in 13 CNS regions (fig. S16, K to N). Astrocytes in each region showed distinct morphological features, which were summarized with a *z* score (Fig. 4C). By assessing the correlation coefficient for the morphological *z* score of astrocytes in 13 CNS regions, we found strong concordance among astrocytes from four closely related forebrain regions (Fig. 4D), recalling RNA-seq (Fig. 2).

We performed WGCNA for astrocyte RNA-seq data of the 13 CNS regions and identified 62 module eigengenes (fig. S17). We compared morphological parameters and the 62 modules for astrocytes from the 13 CNS regions and found significant correlations between the two (Fig. 4E). We identified several modules with high correlation to astrocyte morphological parameters (red box in Fig. 4E). Of these, we focused on two modules, "darkmagenta" and "turquoise" (Fig. 4F), because they displayed the highest correlation with other modules ("cyan" and "lightyellow") and astrocyte territory size and with Feret's minimum and maximum (Fig. 4, E and F). We analyzed genes within these modules using stringent criteria of more than fourfold enrichment within astrocytes for both hippocampus and cortex (MCX, SCX, and VCX) and by focusing on the top 5% of genes displaying the highest significance (Fig. 4, G and H). Using these criteria, within the darkmagenta module, we identified genes *Rorb*, *Fermt2*, *Gstm5*, *Slc9a3r1*, *Slc1a2, Limd1*, and *Ppara*. Within the turquoise module, we identified genes *Tank*, *Tspan7*, *Ezr*, *Crot*, *Oaf*, *Psat1*, *Mertk,* and *Celsr1*. We also assessed morphology-related genes (top 5%) in astrocyte subclusters from scRNA-seq (Fig. 4I). Most of the genes positively correlated with astrocyte territory size were highly expressed in subcluster AST2 and depleted in subcluster AST6. Because astrocytes in the cortex (MCX, SCX, and VCX) displayed larger territory size than the striatum (Fig. 4, B and C, and fig. S16) and because subcluster AST2 was dominant in the cortex, whereas subcluster AST6 was dominant in the striatum (Fig. 3G), our data suggest that distinct astrocyte subclusters contribute morphological features of astrocytes.

Evaluation of astrocyte morphology–related genes with CRISPR/Cas9

From analyses of astrocyte territory size–related modules (Fig. 4), our attention was drawn to the proteins encoded by *Fermt2* and *Ezr*, i.e., FERMT2 (FERM Domain Containing Kindlin 2) and ezrin, because they are known putative actin-interacting proteins that may contribute to astrocyte morphology. To test this possibility, we used astrocyte-specific CRISPR/Cas9–based gene knockdown by expressing *Staphylococcus aureus* Cas9 (SaCas9) in astrocytes together with guide RNAs (gRNAs) to reduce the expression of candidate genes in astrocyte reporter mice to image astrocyte morphology (*Aldh1l1*-Cre/ERT2 x Ai95; Fig. 5, A to C, and fig. S18). We focused on *Fermt2* and *Ezr*, achieving cell-specific SaCas9 expression within astrocytes (Fig. 5, D and E; $N = 3$ mice) and 72 and 75% reduction in Fermt2 and Ezr expression relative to controls, respectively (Fig. 5, F to I, and fig. S18, A and B; $N = 6$ to 7 mice). Having established a significant reduction of Fermt2 and Ezr, we assessed the morphology of sparsely labeled hippocampal CA1 astrocytes (Fig. 5, J and K, and fig. S18C). We found that astrocytes with reduced Fermt2 or Ezr showed significantly reduced territory sizes and Feret's dimensions by ~20% (22% for Fermt2 and 19% for Ezr; Fig. 5, J and K, and fig. S18, D and E), showing that they are involved in the maintenance of astrocyte morphology, supporting the predictions from WGCNA (Fig. 4). The observed ~20% reductions in astrocyte morphology ($P < 0.0001$) are consistent with single-gene evaluations (*24*–*28*) and suggest that multiple mechanisms contributed to astrocyte morphology, as reflected within the WGCNA modules.

We also performed experiments using the object location memory test as a measure of cognition in the *Fermt2* and *Ezr* knockdown mice and noted significant impairments relative to controls (Fig. 5, L and M; $N = 10$ mice). At a cellular level, these impairments were accompanied by elevated activity-dependent immediate early gene (cFos) expression in neurons of the CA1 pyramidal cell layer (Fig. 5, N and O; $N = 5$ to 7 mice) and reduced co-localization between the pre- and postsynapse markers PSD-95 and VGLUT1 (Fig. 5, P and Q), which was accompanied by reduced immunostaining for these molecules (fig. S19). Thus, these data show that reducing expression of genes predicted from our WGCNA modules to contribute to astrocyte morphology led to reduced astrocyte morphology and to cognitive, cellular, and synaptic deficits (Fig. 5).

Astrocyte morphology–related genes in AD

We identified several known AD risk genes (e.g., *Apoe*, *Clu*, and *Fermt2*) among the WGCNA module genes that were highly correlated with astrocyte territory size (Fig. 4, F to H). These were enriched in astrocytes from the cortex and hippocampus, areas that are affected in AD (fig. S20A). To explore a possible association between morphology-related genes and AD, we performed scRNA-seq on 10- to 11-month-old APP/PS1 AD model mice (*29*) relative to controls to identify astrocyte DEGs. We sequenced 45,391 cortical cells, and found 640 astrocyte DEGs (Fig. 6, A and B). Eleven DEGs were up-regulated relative to controls and 629 were down-regulated ($P < 0.05$, $\log_2$-fold change > 0.1 or < −0.1; Fig. 6B). As shown from the volcano plots, several of the down-regulated genes in AD were related to those correlated with astrocyte morphology, implying that astrocyte territory size may be reduced in AD. We also assessed genes related to astrocyte reactivity and found no significant trend in scRNA-seq of APP/PS1 mice or snRNA-seq of human AD (fig. S20C), recalling recent work (*30*).

We determined how many of the astrocyte territory size–related genes (from the top 5%; Fig. 4, F to H) were also significantly up- or down-regulated DEGs in APP/PS1 mice (adjusted $P < 0.05$). We found that 40 genes that were positively correlated with astrocyte territory size were down-regulated, and five genes that were negatively correlated with astrocyte territory size were up-regulated in APP/PS1 mice, and this trend was similar in human AD snRNA-seq data (Fig. 6C) (*31*). To further explore these associations, we performed subcluster analysis for astrocytes in APP/PS1 mice and found that wild-type (WT) and transgenic APP/PS1 mice shared seven astrocyte subclusters

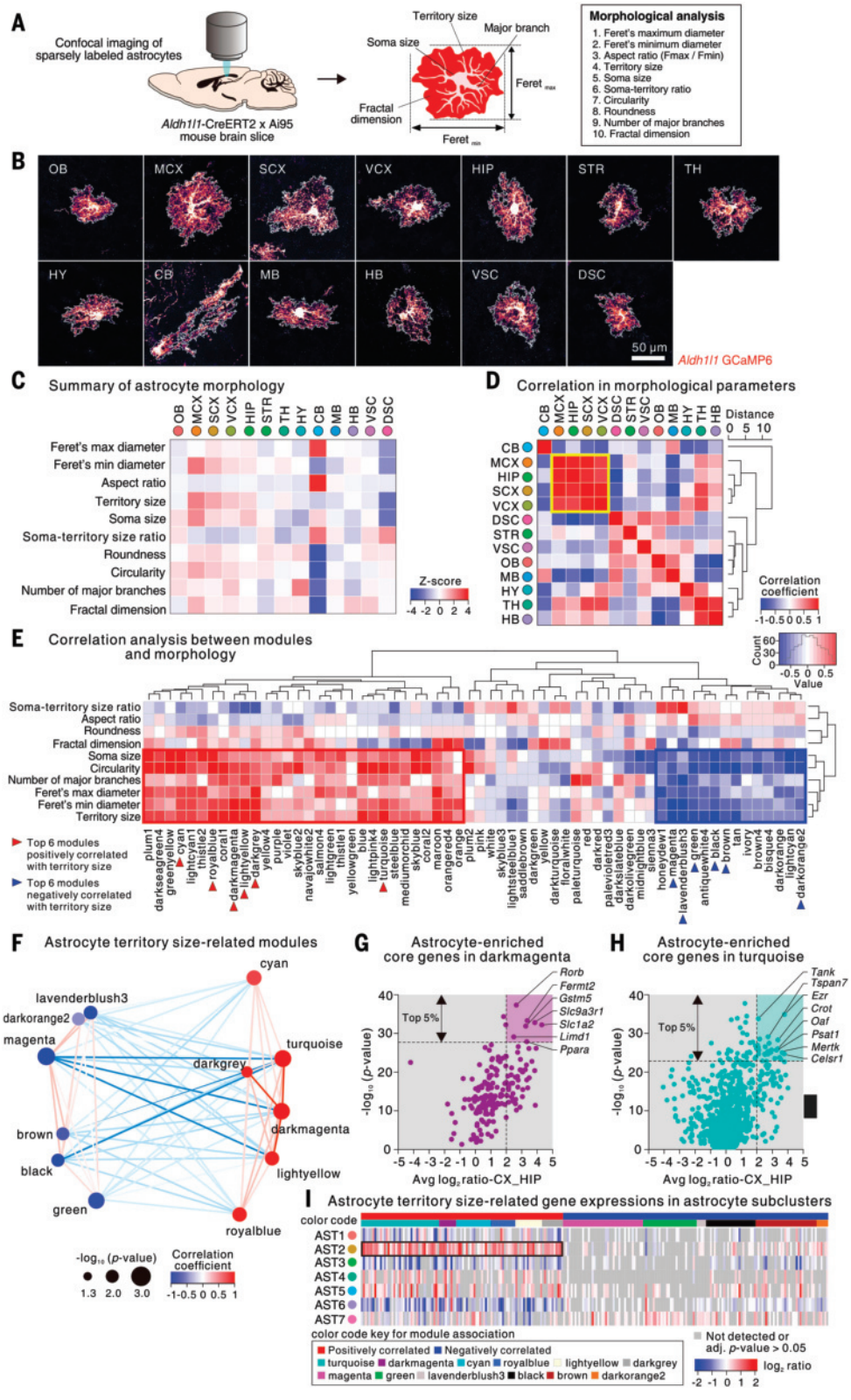


Fig. 4. Astrocyte morphology–related gene networks. (**A**) Procedure for morphological analysis of astrocytes (an artificial red color was used). (**B**) Representative images of single astrocytes from 13 CNS regions. (**C**) Heat map of aggregate *z* score of the astrocyte morphological parameters across 13 CNS regions (raw data are provided in fig. S16). (**D**) Heat map showing the correlation coefficient along with a cluster dendrogram of morphological parameter *z* scores of astrocytes in 13 CNS regions. Four regions (MCX, SCX, VCX, and HIP) that are the most correlated are outlined in yellow. (**E**) Heat map showing correlation coefficients along with cluster dendrograms among 62 module eigengenes (MEs) in WGCNA and the morphological parameters of astrocytes from 13 CNS regions. Histogram in the color scale represents the coefficient values. The WGCNA modules that were highly correlated with morphological parameters, including for territory size, are outlined in red (positive correlation) or blue (negative correlation). (**F**) Multi-dimensional scaling plot of MEs significantly correlated with astrocyte territory size ($P < 0.05$). Size of the node indicates *P* value, color of the node indicates correlation coefficient with astrocyte territory size, and color of the line indicates correlation coefficient between two MEs. (**G** and **H**) Scatter plots showing $\log_2$ ratio (immunoprecipitation versus input) for the average value from MCX, SCX, VCX, and HIP and $-\log_{10}$ (*P* value) for correlation of genes within the darkmagenta (G) and turquoise (H) modules. Several genes are named, and the top 5% are emphasized in the graphs with background coloring. (**I**) Heat map showing the expression of the top 5% morphology-related genes within astrocyte subclusters from the three CNS regions identified in Fig. 3.

in distinct proportions. Subcluster AST1 was significantly increased and subcluster AST6 was significantly decreased in APP/PS1 mice compared with wild-type mice (Fig. 6D and fig. S20D). We assessed the expression of the top 5% of morphology-related genes in astrocyte subclusters from APP/PS1 mice. Most of the genes that were positively correlated with astrocyte territory size were highly expressed in subcluster AST6 and depleted in subcluster AST1 (Fig. 6E), indicating that astrocyte territory size may be reduced in the context of AD. To test this, we injected AAV PHP.eB: *GfaABC$_1$D* Lck-GFP (*32*) into the retro-orbital sinus of 9-month-old wild-type and APP/PS1

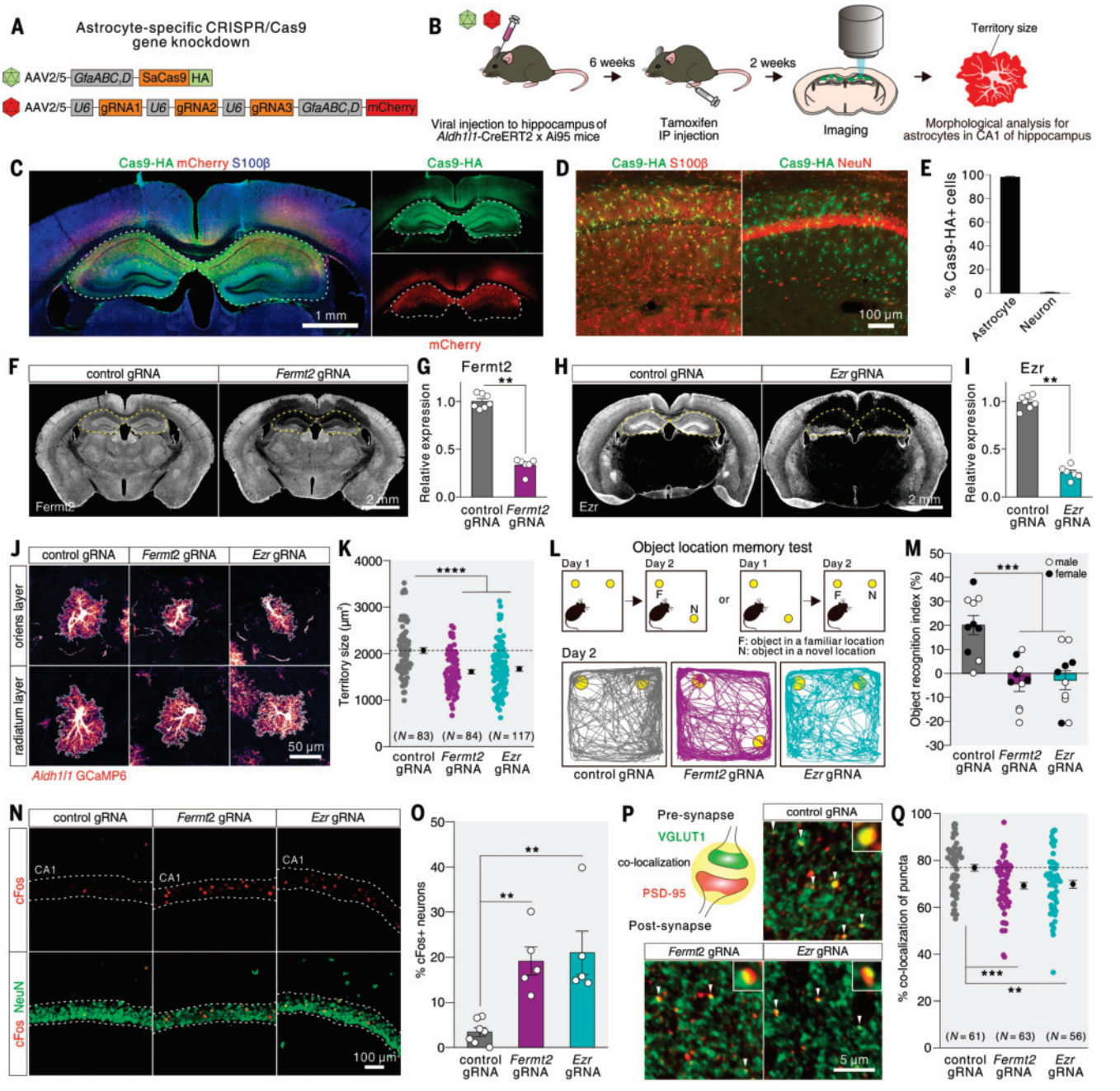


Fig. 5. Evaluation of astrocyte morphology–related genes with CRISPR/Cas9. (**A**) AAVs used for astrocyte-specific CRISPR-Cas9 gene knockdown. (**B**) Schematic of morphology analysis of hippocampal astrocytes using astrocyte-specific CRISPR/Cas9 gene knockdowns. (**C**) Exemplar images of brain sections immunostained for SaCas9-HA (green) and mCherry (red). (**D**) Images of hippocampal astrocytes in 2- to 3-month-old wild-type mice injected with AAV for astrocyte-specific SaCas9 immunostained for SaCas9-HA (green), S100β (red, left), or NeuN (red, right). (**E**) Percentage of SaCas9-HA$^+$ astrocytes or neurons in the hippocampus of wild-type mice injected with AAV for SaCas9 (N = 3). (**F**) Exemplar images of sections immunostained with Fermt2 antibody. Brains were microinjected with AAV for astrocyte-specific SaCas9 and with AAV for control gRNAs or AAV for *Fermt2* gRNAs in the hippocampus. Loss of *Fermt2* immunostaining was observed in the hippocampus. (**G**) Knocking-down efficiency for *Fermt2* protein in the hippocampus of *Aldh1l1*-Cre/ERT2 x Ai95 mice injected with astrocyte-specific AAV for SaCas9 and AAV for *Fermt2* gRNAs (N = 6 to 7). (**H** and **I**) As in (F) and (G) but for Ezr (N = 6 to 7). (**J** and **K**) Images and data for astrocytes in the hippocampal CA1 layers of *Aldh1l1*-Cre/ERT2 x Ai95 mice injected with AAV for astrocyte-selective SaCas9 and AAV for control gRNAs, *Fermt2* gRNAs, or *Ezr* gRNAs (83 to 117 astrocytes from N = 3 mice per group). (**L** and **M**) Object location memory test to assess control, *Fermt2*, and *Ezr* knockdown mice. Schematic, representative traces, and average data are shown (N = 10 mice; males and females are shown). The differences were significant for both sexes (P = 0.015 for males, P = 0.0076 for females) and for pooled data (P < 0.0001) using ANOVA; sex differences were not our focus, so average data are shown. (**N** and **O**) Representative images and average data for cFos$^+$ neurons (NeuN) in the CA1 region of the hippocampus from control, *Fermt2*, and *Ezr* knockdown mice (N = 5 to 7 mice). (**P** and **Q**) Representative images and average data for VGLUT1 and PSD-95 co-localization in the CA1 region of the hippocampus from control, *Fermt2*, and *Ezr* knockdown mice (25 to 35 images from N = 5 to 7 mice per group). The graph shows the percentage of PSD95 puncta co-localized with VGLUT1. In (Q), the points represent the average co-localization between VGLUT1 and PSD-95 puncta for each image (see fig. S19 for additional analyses). Data are shown as means ± SEM.

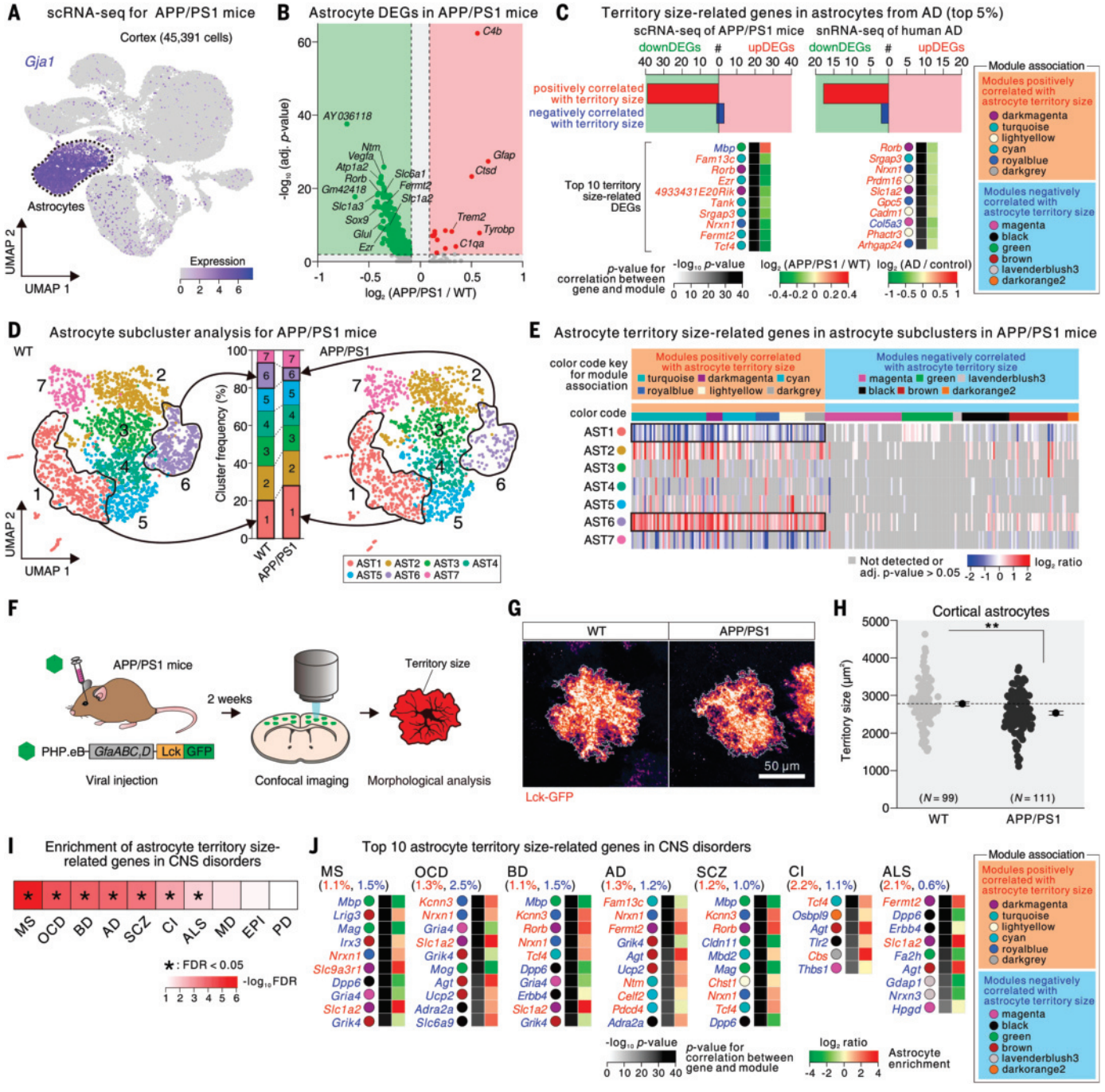


Fig. 6. Astrocyte morphology–related genes in an AD mouse model, human AD, and for other CNS disorders. (**A**) UMAP plot (45,391 cells) from the cortex of wild-type and APP/PS1 mice grouped by expression similarity identified 10 cell populations (fig. S20B). Astrocytes were identified by the expression of *Gja1*. (**B**) Volcano plot showing DEGs within astrocytes of APP/PS1 versus wild-type mice (adjusted *P* value < 0.05, $\log_2$-fold change > 0.10 or < −0.10); several genes are named. (**C**) Top graphs show the number of territory size–related genes from the up- and down-regulated DEGs in astrocytes that were altered in scRNA-seq data from APP/PS1 mice and in human AD snRNA-seq data. The heat maps show the top 10 territory size–related genes that displayed high-$\log_{10}P$ values in the WGCNA analyses (from the top 5% from WGCNA). The WGCNA modules that the genes belong to are on the right. (**D**) UMAP plot of cluster analysis (3808 astrocytes) from WT and APP/PS1 mice in relation to the bar graph showing cluster frequency of astrocyte subclusters for WT and APP/PS1 mice (*N* = 9 to 10 mice). (**E**) Heat map showing the expression of the morphology-related genes (top 5% from Fig. 4) within astrocyte subclusters in APP/PS1 mice. Genes positively correlated with astrocyte morphology were enriched in cluster 6, which was reduced in APP/PS1 mice. By contrast, genes positively correlated with morphology were depleted in cluster 1, which was increased in APP/PS1 mice. (**F**) Procedure for morphology analysis of cortical astrocytes in APP/PS1 mice. (**G**) Images of single astrocytes from the cortex labeled with Lck-GFP in WT and APP/PS1. (**H**) Analysis of Lck-GFP–labeled astrocyte territory size in the cortex of WT and APP/PS1 mice (*N* = 99 to 111 astrocytes from *N* = 3 mice per group). (**I**) Hypergeometric heat map showing the enrichment of astrocyte territory–related genes within those associated with CNS disorders. *Significance with FDR < 0.05. (**J**) Top 10 astrocyte territory size–related genes that overlapped with genes associated with AD, amyotrophic lateral sclerosis (ALS), cerebral infarction (CI), multiple sclerosis (MS), schizophrenia (SCZ), bipolar disorder (BD), and obsessive-compulsive disorder (OCD). Data are shown as means ± SEM.

mice and measured territory sizes of sparsely labeled astrocytes at ~10 months age (Fig. 6F). Astrocyte territory sizes were significantly reduced in the cortex of APP/PS1 mice relative to controls (Fig. 6, G and H, and fig. S20E and F), which was consistent with our predictions (Fig. 5) and notable because astrocytes were assessed irrespective of subcluster identity. Furthermore, because physiological functions of astrocytes are implicated in the pathophysiology of AD (*7*, *33*), we performed candidate gene analyses for the astrocyte subclusters and found that genes related to cholesterol homeostasis, K^+ homeostasis, neurotransmitter homeostasis, and synapse function were enriched in subcluster AST6 and depleted in subcluster AST1 (fig. S20, G to J). scRNA-seq data lack spatial information, which could be evaluated by mapping of astrocyte types in relation to plaque markers in AD model mice and in human tissue. Our data on disease-specific astrocyte subclusters (AST1 and AST6) suggest these as potential therapeutic targets for AD.

Astrocyte morphology–related genes in other CNS disorders

Our analysis of astrocytes in wild-type mice identified genes associated with astrocyte territory sizes (Fig. 4), which we tested with CRISPR/Cas9–mediated knockdown (Fig. 5). Furthermore, these genes were down-regulated in human AD and in a mouse model of AD that displayed reduced astrocyte territory sizes (Fig. 6). To further explore such associations, we evaluated astrocytes from Huntington's disease (HD), because they displayed reduced territory sizes (*27*, *28*, *34*, *35*). In accord with our AD findings, we found down-regulation of genes positively correlated with astrocyte territory sizes, and up-regulation of genes negatively correlated with astrocyte territories in a HD mouse model and postmortem human HD tissue (fig. S21) (*36*). To explore the association between astrocyte territory-related genes and other common CNS disorders, we identified disease-associated genes from Phenopedia (*37*) for AD, Parkinson's disease, amyotrophic lateral sclerosis, cerebral infarction, multiple sclerosis, epilepsy, schizophrenia, major depression, bipolar disorder, and obsessive-compulsive disorder and performed hypergeometric analyses. Significant enrichment of astrocyte territory–related genes was found for multiple sclerosis, obsessive-compulsive disorder, bipolar disorder, AD, schizophrenia, cerebral infarction, and amyotrophic lateral sclerosis (Fig. 6I). Figure 6J shows the top 10 astrocyte territory size–related genes that overlapped with the genes associated with these CNS disorders, indicating that astrocyte morphological changes may be a common underappreciated feature of diverse CNS disorders.

Discussion

There is renewed interest in understanding astrocyte biology in health and disease, necessitating the exploration of astrocytes with high-dimensional molecular data in different regions (*9*–*18*). By comparing astrocytes across 13 CNS regions, we found ~850 genes that were shared, with functions related to metabolism, cholesterol biosynthesis, and neurotransmitter uptake and biosynthesis. These represent the core functions of astrocytes, i.e., to maintain tissue homeostasis, and this realization is important because many of these pathways are disrupted in brain disorders. However, of the top genes shared between astrocytes, little is known about nearly a third of them, implying that fully understanding the core functions of astrocytes across CNS areas is an important experimental goal. For example, K^+ homeostasis is a core function of astrocytes, and both Kir4.1 and ATP1A2 contribute (*38*). Our data show that both *Kcnj10* and *Atp1a2* are highly expressed in astrocytes across the CNS. Further studies are needed to explore which dominates under specific settings. Across all regions, we found little evidence for the molecular machinery supporting astrocyte Ca^{2+}-dependent vesicular glutamate release. We found abundant evidence that cholesterol metabolism and fatty acid β-oxidation were core functions of astrocytes.

Our data provided strong evidence to indicate that astrocytes have molecular features and functions specific to CNS regions, and suggested that these region-specific functions arise from the local tissue environment and by variable representation of subclusters AST1 to AST7 in a region-specific manner. Once specific genetic tools become available, it will be possible to disentangle these two contributions to astrocyte diversity. Our data also provide molecules that are highly enriched within astrocytes from specific brain regions. For example, *Chrdl1* is highly enriched in cortical astrocytes and regulates synaptic function (*22*). *Crym*, encoding μ-crystallin, was unique to striatal astrocytes, but its functional relevance has been unexplored. Region-specific genes suggest that it may be possible to target astrocytes in a brain region–specific manner to investigate neural circuits and for therapeutic strategies.

A cardinal feature of astrocytes is their bushy morphology. We mined our data to explore the molecular underpinning of morphological differences between astrocytes from different CNS regions. Several previously proposed molecules were detected, including *Ntrk2* (*39*), *Hepacam*, *Gja1* (*24*), *Gjb6* (*40*), *Nlgn1-3* (*25*), β-integrin signaling genes (*41*), and *Mertk*, *Chrdl1*, and *Cyp4f15* (*14*, *42*). We then identified gene networks related to astrocyte morphology across 13 CNS regions by assessing the correlation of 10 morphological parameters to modules from astrocyte RNA-seq. To test the hypothesis that the astrocyte morphology–related genes contributed to morphology, we developed astrocyte-specific CRISPR/Cas9–based gene knockdown to reduce the expression of core genes in the hippocampus, where astrocytes showed the highest morphological complexity. We found a significant reduction of hippocampal astrocyte territory sizes after the reduction of *Fermt2* and *Ezr* proteins. We also observed concomitant changes in a cognitive task, cFos expression in neurons, and co-localization of pre- and postsynapse markers. This suggested that the astrocyte morphological changes that accompany disease states have causal effects on neural circuit and synaptic function, thus contributing to disease phenotypes. Our molecular studies portend physiological studies to explore these relationships systematically for AD across age and sex.

Unexpectedly, we identified several known AD risk genes, *Apoe*, *Clu*, and *Fermt2*, as being significant astrocyte morphology–related genes. This is notable because astrocyte morphology changes in neurological and psychiatric diseases, including AD (*43*–*46*). Moreover, disease-associated astrocytes displayed higher *Gfap* expression in an AD mouse model (*47*). By exploring associations between astrocyte morphology–related genes and AD, we found that positively correlated morphology-related genes were predominantly down-regulated. A similar trend was also observed for human AD (*31*) and for mouse and human HD (*28*, *34*, *35*). Because our findings predicted that astrocyte territory size might be reduced in the context of AD, we assessed astrocyte territory sizes in APP/PS1 mice and found that astrocyte territory sizes were indeed significantly reduced in the cortex of these mice. In subcluster analysis for astrocytes, we identified seven astrocyte subclusters in distinct proportions. Subcluster AST1 was significantly increased and subcluster AST6 was significantly decreased in APP/PS1 mice. The increased subcluster AST1 population was characterized by higher *Gfap* and reduced homeostatic and morphology-related genes in APP/PS1 mice. Conversely, subcluster AST6, which was decreased, was characterized by lower *Gfap* and by up-regulated homeostatic and morphology-related genes. These data indicate dynamic alterations of astrocytes in response to early pathological states in an amyloid AD model, reflecting morphology and cellular composition.

We provide comprehensive molecular data permitting new physiological and hypothesis-driven experiments for astrocytic genes and pathways that are core features across the CNS and for those unique to specific regions. Our findings identify the molecular basis of complex astrocyte morphology and indicate that reduced astrocyte morphological complexity, and the attendant loss of homeostatic and

metabolic tissue support, is a common feature of CNS disorders that is potentially amenable to therapeutic manipulation.

Methods summary

All animal experiments were conducted in accordance with the National Institutes of Health's *Guide for the Care and Use of Laboratory Animals* and approved by the Chancellor's Animal Research Committee at the University of California, Los Angeles (UCLA). Mice were housed in the vivarium managed by the Division of Laboratory Animal Medicine at UCLA with a 12-hour light/dark cycle and ad libitum access to food and water. All animals were healthy with no obvious behavioral phenotype at the start of the experiments other than those expected, were not involved in previous studies, and were sacrificed during the light cycle. Mice were assigned randomly to the experiments on the basis of genotype. WT C57BL/6NTac mice were maintained in an in-house breeding colony or purchased from Taconic Biosciences. Ai95 [B6;129S-Gt(ROSA)26Sortm95.1(CAG-GCaMP6f)Hze/J, JAX stock no. 028865] or Ai14 [B6;129S6-Gt(ROSA)26Sortm14(CAG-tdTomato)Hze/J, JAX stock no. 007908] mice were acquired from JAX and crossed with *Aldh1l1*-Cre/ERT2 BAC mice [B6N.FVB-Tg(*Aldh1l1*-Cre/ERT2)1Khakh/J, JAX stock no. 029655] fully backcrossed to C57BL/6NTac background in an in-house breeding colony. RiboTag mice (B6N.129-Rpl22tm1.1Psam/J, JAX stock no. 011029) were acquired from JAX and crossed with *Aldh1l1*-Cre/ERT2 mice. APP/PS1dE9 mice [B6;C3-Tg(APPswe,PSEN1dE9)85Dbo/Mmjax, JAX MMRRC stock no. 034829-JAX] were acquired from the JAX Mutant Mouse Regional Resource Center (MMRRC) and maintained in an in-house breeding colony. APP/PS1 mice carry human transgenes for both APP bearing the Swedish mutation and PSEN1 bearing the deletion mutation of exon 9, both under the control of the mouse prion promoter.

All statistical tests were performed in GraphPad Prism 9. Power analyses were performed in GraphPad StatMate 2.0. The graphs were created in OriginPro 2018b and assembled in CorelDraw 2018. Data are presented as means ± SEM along with the individual data points. In some of the graphs, the error bars representing the SEM were smaller than the symbols representing the mean. OriginPro 2018b was used to determine whether the data were normally distributed. Parametric tests were used for normally distributed datasets, and nonparametric tests were applied to data not normally distributed or to data with a small sample size. For comparisons of two groups, paired and unpaired two-tailed Student's *t* tests or two-tailed Mann-Whitney tests were used. For comparisons of more than three groups, one-way ANOVA tests followed by Tukey's or Kruskal-Wallis tests were used. In the figures, *P* values are indicated as follows: $*P < 0.05$, $**P < 0.01$, $***P < 0.001$, and $****P < 0.0001$. When *P* values were > 0.05, this was considered nonsignificant (n.s.). The number of replicates (*n* values), exact *P* values, sample numbers, and details of statistical analyses in each case are provided in table S4 for every experiment.

REFERENCES AND NOTES

1. C. Bargmann *et al*., "BRAIN 2025: A scientific vision" (National Institutes of Health, 2014); https://braininitiative.nih.gov/sites/default/files/pdfs/brain2025_508c.pdf.
2. T. R. Insel, S. C. Landis, F. S. Collins, The NIH BRAIN Initiative. *Science* **340**, 687–688 (2013). doi: 10.1126/science.1239276; pmid: 23661744
3. B. A. Barres, The mystery and magic of glia: A perspective on their roles in health and disease. *Neuron* **60**, 430–440 (2008). doi: 10.1016/j.neuron.2008.10.013; pmid: 18995817
4. N. J. Allen, D. A. Lyons, Glia as architects of central nervous system formation and function. *Science* **362**, 181–185 (2018). doi: 10.1126/science.aat0473; pmid: 30309945
5. X. Yu, J. Nagai, B. S. Khakh, Improved tools to study astrocytes. *Nat. Rev. Neurosci.* **21**, 121–138 (2020). doi: 10.1038/s41583-020-0264-8; pmid: 32042146
6. J. Nagai *et al*., Behaviorally consequential astrocytic regulation of neural circuits. *Neuron* **109**, 576–596 (2021). doi: 10.1016/j.neuron.2020.12.008; pmid: 33385325
7. H. G. Lee, M. A. Wheeler, F. J. Quintana, Function and therapeutic value of astrocytes in neurological diseases. *Nat. Rev. Drug Discov.* **21**, 339–358 (2022). doi: 10.1038/s41573-022-00390-x; pmid: 35173313
8. K. W. Kelley, H. Nakao-Inoue, A. V. Molofsky, M. C. Oldham, Variation among intact tissue samples reveals the core transcriptional features of human CNS cell classes. *Nat. Neurosci.* **21**, 1171–1184 (2018). doi: 10.1038/s41593-018-0216-z; pmid: 30154505
9. H. Chai *et al*., Neural circuit-specialized astrocytes: Transcriptomic, proteomic, morphological and functional evidence. *Neuron* **95**, 531–549.e9 (2017). doi: 10.1016/j.neuron.2017.06.029; pmid: 28712653
10. E. S. Akdemir *et al*., Lunatic fringe-GFP marks lamina-specific astrocytes that regulate sensory processing. *J. Neurosci.* **42**, 567–580 (2022). doi: 10.1523/JNEUROSCI.1392-21.2021; pmid: 34872929
11. A. Y. Huang *et al*., Region-specific transcriptional control of astrocyte function oversees local circuit activities. *Neuron* **106**, 992–1008.e9 (2020). doi: 10.1016/j.neuron.2020.03.025; pmid: 32320644
12. C. C. John Lin *et al*., Identification of diverse astrocyte populations and their malignant analogs. *Nat. Neurosci.* **20**, 396–405 (2017). doi: 10.1038/nn.4493; pmid: 28166219
13. B. Lozzi, T. W. Huang, D. Sardar, A. Y. Huang, B. Deneen, Regionally distinct astrocytes display unique transcription factor profiles in the adult brain. *Front. Neurosci.* **14**, 61 (2020). doi: 10.3389/fnins.2020.00061; pmid: 32153350
14. O. A. Bayraktar *et al*., Astrocyte layers in the mammalian cerebral cortex revealed by a single-cell in situ transcriptomic map. *Nat. Neurosci.* **23**, 500–509 (2020). doi: 10.1038/s41593-020-0602-1; pmid: 32203496
15. A. V. Molofsky *et al*., Astrocyte-encoded positional cues maintain sensorimotor circuit integrity. *Nature* **509**, 189–194 (2014). doi: 10.1038/nature13161; pmid: 24776795
16. M. Y. Batiuk *et al*., Identification of region-specific astrocyte subtypes at single cell resolution. *Nat. Commun.* **11**, 1220 (2020). doi: 10.1038/s41467-019-14198-8; pmid: 32139688
17. M. M. Boisvert, G. A. Erikson, M. N. Shokhirev, N. J. Allen, The aging astrocyte transcriptome from multiple regions of the mouse brain. *Cell Rep.* **22**, 269–285 (2018). doi: 10.1016/j.celrep.2017.12.039; pmid: 29298427
18. L. Morel *et al*., Molecular and functional properties of regional astrocytes in the adult brain. *J. Neurosci.* **37**, 8706–8717 (2017). doi: 10.1523/JNEUROSCI.3956-16.2017; pmid: 28821665
19. K. Seiriki *et al*., High-speed and scalable whole-brain imaging in rodents and primates. *Neuron* **94**, 1085–1100.e6 (2017). doi: 10.1016/j.neuron.2017.05.017; pmid: 28641108
20. R. Srinivasan *et al*., New transgenic mouse lines for selectively targeting astrocytes and studying calcium signals in astrocyte processes in situ and in vivo. *Neuron* **92**, 1181–1195 (2016). doi: 10.1016/j.neuron.2016.11.030; pmid: 27939582
21. W. Sun *et al*., SOX9 is an astrocyte-specific nuclear marker in the adult brain outside the neurogenic regions. *J. Neurosci.* **37**, 4493–4507 (2017). doi: 10.1523/JNEUROSCI.3199-16.2017; pmid: 28336567
22. E. Blanco-Suarez, T. F. Liu, A. Kopelevich, N. J. Allen, Astrocyte-secreted chordin-like 1 drives synapse maturation and limits plasticity by increasing synaptic GluA2 AMPA receptors. *Neuron* **100**, 1116–1132.e13 (2018). doi: 10.1016/j.neuron.2018.09.043; pmid: 30344043
23. W. P. Ge, A. Miyawaki, F. H. Gage, Y. N. Jan, L. Y. Jan, Local generation of glia is a major astrocyte source in postnatal cortex. *Nature* **484**, 376–380 (2012). doi: 10.1038/nature10959; pmid: 22456708
24. K. T. Baldwin *et al*., HepaCAM controls astrocyte self-organization and coupling. *Neuron* **109**, 2427–2442.e10 (2021). doi: 10.1016/j.neuron.2021.05.025; pmid: 34171291
25. J. A. Stogsdill *et al*., Astrocytic neuroligins control astrocyte morphogenesis and synaptogenesis. *Nature* **551**, 192–197 (2017). doi: 10.1038/nature24638; pmid: 29120426
26. B. Zhou *et al*., Astroglial dysfunctions drive aberrant synaptogenesis and social behavioral deficits in mice with neonatal exposure to lengthy general anesthesia. *PLOS Biol.* **17**, e3000086 (2019). doi: 10.1371/journal.pbio.3000086; pmid: 31433818
27. R. Jiang, B. Diaz-Castro, L. L. Looger, B. S. Khakh, Dysfunctional calcium and glutamate signaling in striatal astrocytes from Huntington's disease model mice. *J. Neurosci.* **36**, 3453–3470 (2016). doi: 10.1523/JNEUROSCI.3693-15.2016; pmid: 27013675
28. J. C. Octeau *et al*., An optical neuron-astrocyte proximity assay at synaptic distance scales. *Neuron* **98**, 49–66.e9 (2018). doi: 10.1016/j.neuron.2018.03.003; pmid: 29621490
29. J. L. Jankowsky *et al*., Mutant presenilins specifically elevate the levels of the 42 residue beta-amyloid peptide in vivo: Evidence for augmentation of a 42-specific gamma secretase. *Hum. Mol. Genet.* **13**, 159–170 (2004). doi: 10.1093/hmg/ddh019; pmid: 14645205
30. Z. Jiwaji *et al*., Reactive astrocytes acquire neuroprotective as well as deleterious signatures in response to Tau and Aß pathology. *Nat. Commun.* **13**, 135 (2022). doi: 10.1038/s41467-021-27702-w; pmid: 35013236
31. H. Mathys *et al*., Single-cell transcriptomic analysis of Alzheimer's disease. *Nature* **570**, 332–337 (2019). doi: 10.1038/s41586-019-1195-2; pmid: 31042697
32. R. C. Challis *et al*., Systemic AAV vectors for widespread and targeted gene delivery in rodents. *Nat. Protoc.* **14**, 379–414 (2019). doi: 10.1038/s41596-018-0097-3; pmid: 30626963
33. B. De Strooper, E. Karran, The cellular phase of Alzheimer's disease. *Cell* **164**, 603–615 (2016). doi: 10.1016/j.cell.2015.12.056; pmid: 26871627
34. X. Yu *et al*., Context-specific striatal astrocyte molecular responses are phenotypically exploitable. *Neuron* **108**, 1146–1162.e10 (2020). doi: 10.1016/j.neuron.2020.09.021; pmid: 33086039
35. A. Benraiss *et al*., Cell-intrinsic glial pathology is conserved across human and murine models of Huntington's disease. *Cell Rep.* **36**, 109308 (2021). doi: 10.1016/j.celrep.2021.109308; pmid: 34233199
36. H. Lee *et al*., Cell type-specific transcriptomics reveals that mutant huntingtin leads to mitochondrial RNA release and neuronal innate immune activation. *Neuron* **107**, 891–908.e8 (2020). doi: 10.1016/j.neuron.2020.06.021; pmid: 32681824
37. W. Yu, M. Clyne, M. J. Khoury, M. Gwinn, Phenopedia and Genopedia: Disease-centered and gene-centered views of the evolving knowledge of human genetic associations. *Bioinformatics* **26**, 145–146 (2010). doi: 10.1093/bioinformatics/btp618; pmid: 19864262
38. N. MacAulay, Molecular mechanisms of K^+ clearance and extracellular space shrinkage-Glia cells as the stars. *Glia* **68**, 2192–2211 (2020). doi: 10.1002/glia.23824; pmid: 32181522
39. L. M. Holt *et al*., Astrocyte morphogenesis is dependent on BDNF signaling via astrocytic TrkB.T1. *eLife* **8**, e44667 (2019). doi: 10.7554/eLife.44667; pmid: 31433295
40. U. Pannasch *et al*., Connexin 30 sets synaptic strength by controlling astroglial synapse invasion. *Nat. Neurosci.* **17**, 549–558 (2014). doi: 10.1038/nn.3662; pmid: 24584052
41. S. Cho, A. K. Muthukumar, T. Stork, J. C. Coutinho-Budd, M. R. Freeman, Focal adhesion molecules regulate astrocyte

morphology and glutamate transporters to suppress seizure-like behavior. *Proc. Natl. Acad. Sci. U.S.A.* **115**, 11316–11321 (2018). doi: 10.1073/pnas.1800830115; pmid: 30327343
42. D. Lanjakornsiripan *et al*., Layer-specific morphological and molecular differences in neocortical astrocytes and their dependence on neuronal layers. *Nat. Commun.* **9**, 1623 (2018). doi: 10.1038/s41467-018-03940-3; pmid: 29691400
43. A. M. Arranz, B. De Strooper, The role of astroglia in Alzheimer's disease: Pathophysiology and clinical implications. *Lancet Neurol.* **18**, 406–414 (2019). doi: 10.1016/S1474-4422(18)30490-3; pmid: 30795987
44. M. Pekny *et al*., Astrocytes: A central element in neurological diseases. *Acta Neuropathol.* **131**, 323–345 (2016). doi: 10.1007/s00401-015-1513-1; pmid: 26671410
45. M. Pekny, M. Pekna, Astrocyte reactivity and reactive astrogliosis: Costs and benefits. *Physiol. Rev.* **94**, 1077–1098 (2014). doi: 10.1152/physrev.00041.2013; pmid: 25287860
46. C. Escartin *et al*., Reactive astrocyte nomenclature, definitions, and future directions. *Nat. Neurosci.* **24**, 312–325 (2021). doi: 10.1038/s41593-020-00783-4; pmid: 33589835
47. N. Habib *et al*., Disease-associated astrocytes in Alzheimer's disease and aging. *Nat. Neurosci.* **23**, 701–706 (2020). doi: 10.1038/s41593-020-0624-8; pmid: 32341542

ACKNOWLEDGMENTS

We thank F. Gao and the UCLA Neuroscience Genomics Core for assistance with RNA-seq, M. Gangwani for AAV delivery (Fig. 6F) and discussions, S. Cheong for help counting astrocytes (Fig. 1D), D. Geschwind for discussion about gene expression analysis, A. Huang and L. Wu for comments, and N. Okabe for IHC guidance. The sequencing core was supported partly by the Genetics, Genomics and Informatics Core of the Semel Institute of Neuroscience. **Funding:** B.S.K., J.S., F.E., and X.Y. were supported by the National Institutes of Health (NIH grants R01DA047444, R35NS111583, and R01AG0759655), an Allen Distinguished Investigator Award, a Paul G. Allen Frontiers Group advised grant of the Paul G. Allen Family Foundation, and the Ressler Family Foundation (B.S.K.). J.S.S. was supported by the National Science Foundation Graduate Research Fellowship Program (NSF-GRFP; DGE-2034835) and by a UCLA Eugene V. Cota-Robles Fellowship. A.K. and H.H. were supported by JSPS KAKENHI grants JP21K19335 (H.H.), JP20H00492 (H.H.), and JP20H03391 (A.K.); MEXT KAKENHI grant JP18H05416 (H.H.); AMED grant JP21dm0207117 (H.H.); and the Takeda Science Foundation, Japan (A.K., H.H.). V.G. was supported by the NIH (Pioneer Award DP1OD025535), the Vallee Foundation, the CZI Neurodegeneration Challenge Network, and the Beckman Institute for CLARITY, Optogenetics and Vector Engineering Research (CLOVER) for technology development and dissemination. **Author contributions:** F.E. performed most experiments and analyzed data. A.K. and H.H. performed FAST. X.Y. performed striatal scRNA-seq. J.S. conducted stereotactic AAV microinjections and made SaCas9 plasmids. Z.Q. and V.G. made PHP.eB:*GfaABC$_1$D* Lck-GFP AAV. R.K. guided RNA-seq analyses. B.S.K. conceived the study, planned and directed the experiments, and produced the figures with help from F.E. B.S.K. wrote the paper with help from F.E., and all authors approved the final version. **Competing interests:** The authors declare no competing interests. **Data and materials availability:** RNA-seq data are available at the Gene Expression Omnibus (GEO) under GSE198032 subseries GSE19824 and are also provided in tables S1 to S3. scRNA-seq data are available at the GEO under GSE 198032 subseries GSE198027. **License information:** Copyright © 2022 the authors, some rights reserved; exclusive licensee American Association for the Advancement of Science. No claim to original US government works. https://www.science.org/about/science-licenses-journal-article-reuse

SUPPLEMENTARY MATERIALS

science.org/doi/10.1126/science.adc9020
Materials and Methods
Figs. S1 to S21
References (*48*–*62*)
MDAR Reproducibility Checklist
Tables S1 to S4
Movies S1 and S2

Submitted 7 May 2022; accepted 16 September 2022
10.1126/science.adc9020

RESEARCH ARTICLE SUMMARY

NEUROSCIENCE

Dual-polarity voltage imaging of the concurrent dynamics of multiple neuron types

Madhuvanthi Kannan*†, Ganesh Vasan*†, Simon Haziza†, Cheng Huang, Radosław Chrapkiewicz, Junjie Luo, Jessica A. Cardin, Mark J. Schnitzer*, Vincent A. Pieribone*

INTRODUCTION: Signal processing in the brain involves the concerted dynamics of multiple distinct cell subtypes that belong to excitatory and inhibitory neuron populations. To uncover how they synergize their activities in real time, it is important to record the voltage dynamics of multiple identified subtypes simultaneously. Genetically encoded fluorescent voltage indicators (GEVIs) are ideally suited to reveal the millisecond-scale activation dynamics of one or more genetically identified neuron types in awake animals.

RATIONALE: We previously introduced the green and red fluorescence resonance energy transfer (FRET)–opsin GEVIs Ace-mNeon and VARNAM, which are fusion proteins of voltage- sensitive rhodopsin from *Acetabularia* with bright fluorescent proteins mNeonGreen and mRuby3, respectively. Ace-mNeon and VARNAM exhibit fluorescence decreases during voltage depolarization events such as action potentials (APs) and together constitute a pair of mutually compatible GEVIs that can be genetically targeted to two distinct neuron types for simultaneous dual-color voltage recordings. Using protein engineering and high-throughput voltage screening, we uncovered the second-generation GEVIs Ace-mNeon2 and VARNAM2, which have improved voltage sensitivities. We also identified the respective reverse response-polarity variants, pAce and pAceR, which exhibit fluorescence increases during APs. We reasoned that the four new indicators make up a suite of mutually compatible tools for multipopulation voltage recordings in behaving animals. When targeted to distinct neuron types, the indicators enable unambiguous cell-type identification from the voltage readout based on their fluorescence spectra, optical spike polarity, or both.

RESULTS: Our improved indicators exhibit enhanced voltage sensitivities to enable low-power (<25 mW mm^{-2}) recordings of spiking and transmembrane voltage dynamics from >50 individual neurons at a time in running mice and ~30-min continuous imaging in flies. Ace-mNeon2 voltage imaging from ~1200 neurons revealed visual cortical cell type–specific responses to behavioral-state transitions in awake mice. Cortical interneurons expressing somatostatin (SST) exhibited the most profound activation during a quiescence-to-arousal transition. Further, using simultaneous dual-polarity voltage recordings with Ace-mNeon2 and pAce, we examined the functional dynamics of pairs of neuron types. We unveiled a time-varying, state-dependent mutual antagonism in the voltage dynamics of SST- and vasoactive intestinal peptide (VIP)–expressing interneurons.

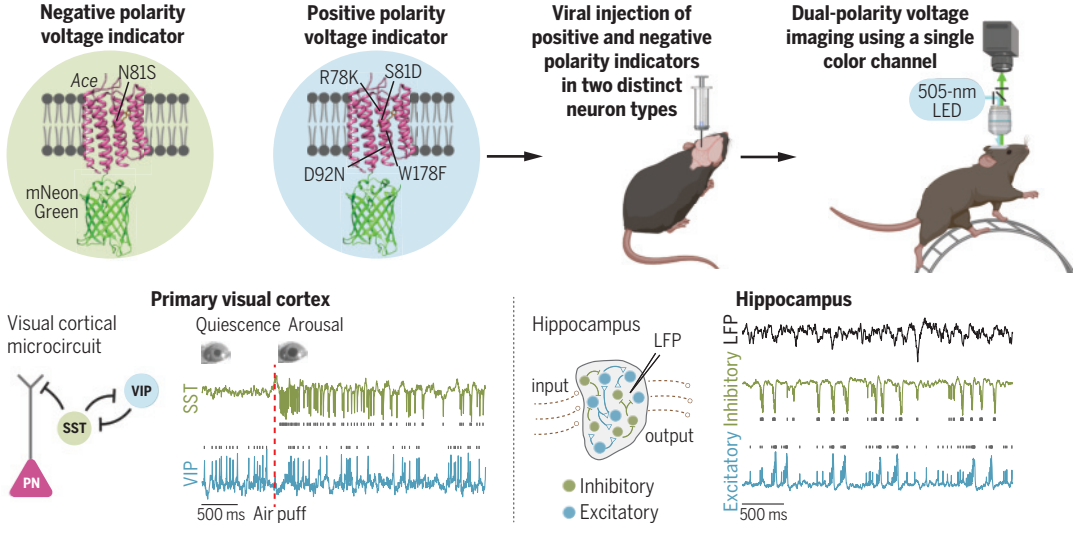
In the hippocampus, dual-polarity voltage imaging uncovered the differential contributions of distinct cell classes to the local field potential (LFP). Spiking in entorhinal cortex (EC)–projecting neurons, but not in SST interneurons, consistently phase-locked to the LFP. Moreover, using dual-color voltage imaging, we found that anterior cingulate cortex (ACC)– and EC-projecting excitatory subclasses differ in their responses to state change; the former uniformly increase their firing rates, but the latter do not.

Finally, by combining dual-polarity and dual-color imaging using three mutually compatible sensors from our suite, we extracted the simultaneous, real-time voltage dynamics of three neuron types. These subtypes belong to excitatory and inhibitory interneuronal subpopulations in the visual cortex and hippocampus of running mice.

CONCLUSION: Our work reveals functional correlations between targeted neuron types in visual cortical circuits during altered behavioral states as well as the contributions of distinct cell subclasses to hippocampal LFPs in running mice. Together, our findings benchmark multipopulation voltage imaging for investigations of the concerted dynamics of multiple cell classes in behaving animals. ■

The list of author affiliations is available in the full article online.
*Corresponding author. Email: mkannan@umn.edu (M.K.); gvasan@umn.edu (G.V.); mschnitz@stanford.edu (M.J.S.); vincent.pieribone@yale.edu (V.A.P.)
†These authors contributed equally to this work.
Cite this article as M. Kannan *et al.*, *Science* **378**, eabm8797 (2022). DOI: 10.1126/science.abm8797

READ THE FULL ARTICLE AT
https://doi.org/10.1126/science.abm8797



Dual-polarity imaging of the simultaneous voltage dynamics of two neuron types in running mice. Newly characterized negative- and positive-polarity GEVIs enable unambiguous identification of neuron types based on the optical spike polarity in single-color voltage imaging. Using this technique, we uncover a state-dependent antagonism between visual cortical SST and VIP interneurons as well as relative contributions to the LFP from hippocampal excitatory and inhibitory neurons. N81S, Asn^{81}→Ser; R78K, Arg^{78}→Lys; S81D, Ser^{81}→Asp; D92N, Asp^{92}→Asn; W178F, Trp^{178}→Phe; LED, light-emitting diode; PN, pyramidal neuron.

RESEARCH ARTICLE

NEUROSCIENCE

Dual-polarity voltage imaging of the concurrent dynamics of multiple neuron types

Madhuvanthi Kannan[1,2]*†‡, Ganesh Vasan[1,2]*†‡, Simon Haziza[3,4]†, Cheng Huang[3], Radosław Chrapkiewicz[3,4], Junjie Luo[3,4,5], Jessica A. Cardin[6,7,8], Mark J. Schnitzer[3,4,5]*, Vincent A. Pieribone[1,2,6]*

Genetically encoded fluorescent voltage indicators are ideally suited to reveal the millisecond-scale interactions among and between targeted cell populations. However, current indicators lack the requisite sensitivity for in vivo multipopulation imaging. We describe next-generation green and red voltage sensors, Ace-mNeon2 and VARNAM2, and their reverse response-polarity variants pAce and pAceR. Our indicators enable 0.4- to 1-kilohertz voltage recordings from >50 spiking neurons per field of view in awake mice and ~30-minute continuous imaging in flies. Using dual-polarity multiplexed imaging, we uncovered brain state–dependent antagonism between neocortical somatostatin-expressing (SST^+) and vasoactive intestinal peptide–expressing (VIP^+) interneurons and contributions to hippocampal field potentials from cell ensembles with distinct axonal projections. By combining three mutually compatible indicators, we performed simultaneous triple-population imaging. These approaches will empower investigations of the dynamic interplay between neuronal subclasses at single-spike resolution.

The dynamic interplay of multiple excitatory and inhibitory neuronal subtypes is central to how the brain processes information. During motor or sensory processing, the external environment and an animal's internal state can affect the activity of neocortical interneurons, which in turn modulate excitatory projection neurons (*1*–*5*). Likewise, in the hippocampus, different ensembles of projection neurons exhibit state-dependent changes in spiking activity related to learning and memory (*6*–*9*). However, how different neural subclasses coordinate their dynamics in real time remains poorly understood, owing to an inability to measure the spiking activity of two or more genetically defined or projection-targeted neural ensembles simultaneously.

Genetically encoded voltage indicators (GEVIs) enable targeted recordings of spiking and subthreshold activity with submillisecond temporal precision (*10*–*12*). Although extensive protein engineering has spawned a host of new sensors (*13*–*24*), existing GEVIs are not optimized for concurrent, targeted recordings from two or more neuron types in behaving animals.

We previously introduced the green and red fluorescence resonance energy transfer (FRET)–opsin GEVIs Ace-mNeon and VARNAM (*17*, *18*). FRET-opsin GEVIs are fusions of a bright fluorescent protein (FP; the FRET donor) to a transmembrane opsin with a voltage-sensitive light absorption spectrum (the FRET acceptor) (*25*, *26*). This modular design enables voltage imaging in live animals with a high dynamic range of fluorescence signaling but at far-lower illumination levels (~25 mW mm^{-2}) than those (1 to 10 W mm^{-2}) required by opsin voltage indicators (*16*, *19*, *22*, *23*, *27*). Imaging studies using FRET-opsins have generally monitored the time-dependent emissions of the bright FRET donor but not those of the opsin FRET acceptor, because the latter's fluorescence is too dim to augment the detection of voltage signals. Thus, only one fluorescence channel is needed to image a FRET-opsin GEVI, with excitation and emission wavelength bandwidths matching those of the bright donor (*17*, *18*, *25*). Ace-mNeon and VARNAM comprise a fusion of the *Acetabularia* (Ace) rhodopsin (*17*, *18*) to the bright FP mNeonGreen (*28*) or mRuby3 (*29*), respectively. Notably, Ace-mNeon and VARNAM have demonstrated optical compatibility for concurrent recordings in live flies (*18*).

Protein engineering of negative- and positive-polarity FRET-opsins

To improve the sensitivities of Ace-mNeon and VARNAM for recordings in awake mice, we performed protein engineering and high-throughput screening of voltage responsivity in excitable human embryonic kidney (HEK) cells (Fig. 1, A and B) (*18*, *30*, *31*). Our screening platform scores GEVIs for brightness, voltage sensitivity, and kinetics in a plate-based format, achieving a capacity of 120 unique variants per day with a sample content of ~2000 cells per variant (*18*).

In Ace-mNeon and VARNAM, depolarization-dependent quenching by Ace of fluorescence from the FP leads to depolarization-evoked fluorescence decreases as the readout of voltage changes. To improve voltage sensitivity, we sought to enhance the FRET transfer by optimizing the Ace-FP linker (*32*). In Ace-mNeon, we also performed site-saturation mutagenesis at Ace N81 (Asn^{81}) and screened a library of N81X positional mutants (where X is any amino acid) (Fig. 1A and fig. S1) (*18*). Screening of mutagenic libraries uncovered variants with increased response amplitudes (Fig. 1B and fig. S2). Ace-mNeon N81S G229Y (Asn^{81}→Ser and Gly^{229}→Tyr) and VARNAM Δ228W Δ229R G231I (deletion of Trp^{228} and Arg^{229}, and Gly^{231}→Ile) (henceforth, Ace-mNeon2 and VARNAM2, respectively) exhibited significantly improved fluorescence responses to depolarizing voltages compared with their predecessors in patch-clamp recordings from transfected cells [the ratio of fluorescence change to baseline fluorescence ($\Delta F/F$) values for 120-mV steps were (mean ± SEM) −31.3 ± 0.7% for Ace-mNeon2 (n = 13 cells) versus −13.9 ± 0.6% for Ace-mNeon (n = 11 cells), P < 0.0001, Mann-Whitney test; and −22.9 ± 0.7% for VARNAM2 (n = 13 cells) versus −14.1 ± 0.5% for VARNAM (n = 8 cells), P < 0.0001, Mann-Whitney test] (Fig. 1, C and D; figs. S3 to S5; and table S1).

We next screened a library of Ace-mNeon2 D92X positional mutants, owing to the highly conserved role of the N81/D92 (D, Asp) pair in opsin proton-pumping and photosensing (*33*, *34*). We uncovered several variants with response polarity reversals that exhibited fluorescence increases during depolarization (fig. S6). Although the best-performing positive variant Ace-mNeon2 D92N exhibited slower kinetics, reciprocal S81X saturation mutagenesis revealed kinetics rescue mutants (figs. S6 and S7). Among them, the S81D mutant also provided the largest voltage sensitivity. The 92N/81D reversed polarity phenotype is transposable across other Ace-based indicators, including VARNAM and Voltron (*13*, *18*).

For further engineering, we targeted residues lining Ace's photosensing helix C, amino acids involved in stabilizing its voltage-sensitive intermediate state, and those near the chromophore (Fig. 1A and fig. S1) (*34*–*36*). Voltage screening of mutagenic libraries uncovered positive variants with enhanced sensitivities (fig. S8). Ace-mNeon2 R78K S81D D92N W178F and VARNAM2 R78E S81D D92N, henceforth pAce (positive Ace) and pAceR (positive Ace in

[1]The John B. Pierce Laboratory, New Haven, CT 06519, USA. [2]Department of Cellular and Molecular Physiology, Yale University, New Haven, CT 06520, USA. [3]James H. Clark Center, Stanford University, Stanford, CA 94305, USA. [4]CNC Program, Stanford University, Stanford, CA 94305, USA. [5]Howard Hughes Medical Institute, Stanford University, Stanford, CA 94305, USA. [6]Department of Neuroscience, Yale University, New Haven, CT 06520, USA. [7]Kavli Institute of Neuroscience, Yale University, New Haven, CT 06520, USA. [8]Wu Tsai Institute, Yale University, New Haven, CT 06520, USA.
*Corresponding author. Email: mkannan@umn.edu (M.K.); gvasan@umn.edu (G.V.); mschnitz@stanford.edu (M.J.S.); vincent.pieribone@yale.edu (V.A.P.)
†These authors contributed equally to this work.
‡Present address: Department of Neuroscience, University of Minnesota, Minneapolis, MN 55455, USA.

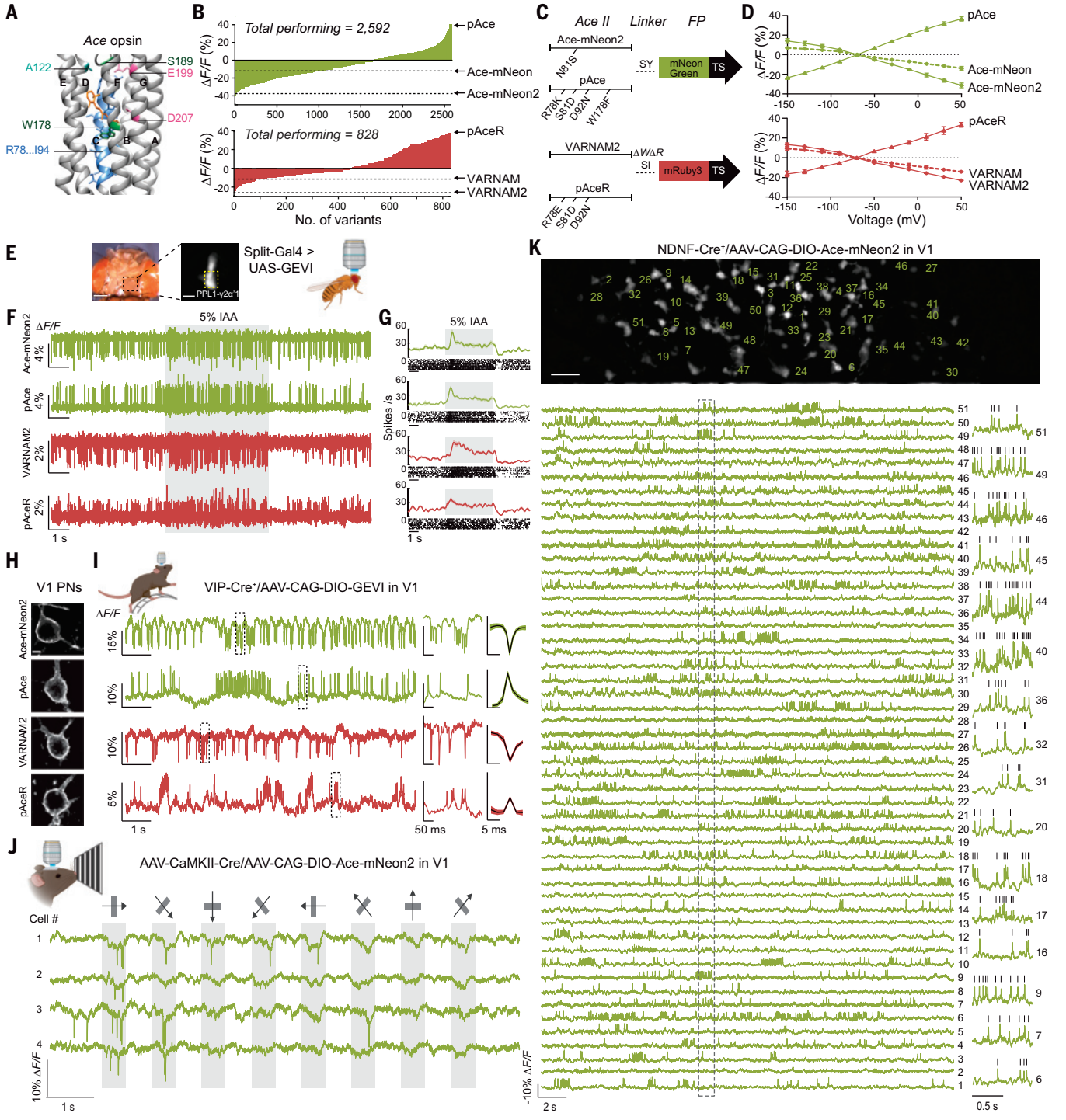


Fig. 1. Design and characterization of Ace-mNeon2, VARNAM2 and reverse polarity variants pAce and pAceR. (**A**) Crystal structure of Ace [Protein Data Bank (PDB) ID 3AM6], showing residues targeted for site-directed saturation mutagenesis on Ace-mNeon and VARNAM. The seven transmembrane helices are labeled A to G. Amino acids R78 through I94 on helix C and specified loci on other helices were targeted. A, Ala; W, Trp; R, Arg; I, Ile; S, Ser; E, Glu; D, Asp. (**B**) Distribution of fluorescence responses to field stimulation acquired from spiking HEK cells expressing Ace-mNeon (top) and VARNAM (bottom) variants obtained on the high-throughput platform. (**C**) Schematic representations of Ace-mNeon2, pAce, VARNAM2, and pAceR constructs, depicting the point mutations in Ace and the Ace-FP linker. SI is Ser, Ile; SY is Ser, Tyr; and TS is Thr, Ser. (**D**) *ΔF-ΔV* curves obtained using whole-cell recordings and concurrent fluorescence imaging of HEK cells transfected with Ace-mNeon, Ace-mNeon2, and pAce (top) and VARNAM, VARNAM2, and pAceR (bottom). Values represent mean ± SEM. (**E**) In vivo voltage imaging (left) through a transparent surgical window implanted on a fly head (graphic on right). Each of the indicators was selectively expressed in a PPL1-γ2α′1 dopaminergic neuron using a split-GAL4 system (center). The yellow dashed box indicates the axonal region of PPL1-γ2α′1. Scale bars, 200 μm (left) and 20 μm (right). (**F**) Representative recordings from PPL1-γ2α′1 using the four GEVIs, showing odor-evoked spiking elicited by 5-s delivery (gray shading) of 5% isoamyl acetate (IAA). (**G**) Spiking rates (mean ± SEM) during odor delivery and raster plots of individual trials in (F) (*n* = 10 trials, two trials

per fly). (**H**) Confocal images from coronal cortical slices of V1 PNs expressing the indicated sensors. Scale bar, 5 μm. (**I**) Example fluorescence traces showing spontaneous spiking obtained from awake, head-restrained mice selectively expressing the indicators in V1 VIP$^+$ interneurons (left); the boxed areas on the traces shown at an expanded time scale (center); and optical spike waveforms (mean ± SEM) (right) [n = 5 neurons per condition ranked in order of decreasing signal-to-noise ratios, three mice each (Ace-mNeon2 and pAce) and two mice each (VARNAM2 and pAceR)]. (**J**) Example visual responses from layer 2/3 PNs to drifting gratings presented at eight different orientations, acquired using Ace-mNeon2 in an awake mouse. Arrows indicate stimulus orientation. Gray shading denotes stimulus periods. (**K**) Representative epifluorescence image of a single field of view from a NDNF-*Cre*$^+$ mouse expressing *Cre*-dependent soma-targeted Ace-mNeon2 in V1 (scale bar, 50 μm) (top) and $\Delta F/F$ traces showing spontaneous activity from the numbered cells (bottom). Fluorescence traces are inverted for visualization. The region enclosed by the dashed box is shown at an expanded time scale on the right for select cells. Gray ticks denote identified spikes.

Red), exhibited $\Delta F/F$ values of 36.6 ± 0.7% (mean ± SEM) and 33.4 ± 1.1% (n = 11 cells each), respectively, per 120 mV in cultured HEK cells (Fig. 1, B to D; and figs. S5, S9, and S10) (E, Glu; F, Phe; K, Lys). Because these positive variants have the same signaling dynamic range as Ace-mNeon2 and VARNAM2 but in the opposite direction, they have slightly lower resting fluorescence intensities than the latter and reduced resting-state photobleaching, similar to other positive GEVIs (fig. S11) (*14*, *37*).

All indicators except pAceR showed submillisecond kinetics at room temperature (fig. S5 and table S1). Overall, Ace-mNeon2, VARNAM2, and pAce exhibited the largest effective $\Delta F/F$ (%) for single action potentials (APs) compared to prior negative- and positive-polarity GEVIs in 1-ms impulse response computations (fig. S12 and table S1).

Sensor characterization in awake flies and mice

For voltage imaging in live animals for all studies described in this paper, we used high-speed (400 or 600 Hz in mice, 1 kHz in fruit flies), widefield one-photon epifluorescence microscopy. We first expressed each of our four GEVIs in the PPL1-$\gamma 2\alpha'1$ dopaminergic neuron in flies, in which they reported spontaneous and odor-evoked spiking with comparable baseline- and evoked spike rates (Fig. 1, E to G). Compared with their red counterparts, the green GEVIs exhibited greater response amplitudes and values of d', a signal detection theory metric that characterizes how the ratio of fluorescence signals to background fluctuations sets the spike detection fidelity (*38*) [$\Delta F/F$, d' (mean ± SEM): 3.1 ± 0.2%, 14.5 ± 1.4 (Ace-mNeon2); 4.0 ± 0.1%, 13.4 ± 0.8 (pAce); 1.1 ± 0.1%, 7.4 ± 0.4 (VARNAM2); 0.9 ± 0.03%, 6.5 ± 0.3 (pAceR)]. We also compared the performance of all four GEVIs in the PPL1-$\alpha'2\alpha2$ neuron, where they had greater d' values than their parent indicators Ace-mNeon and VARNAM [~10.8 (Ace-mNeon2), ~8.7 (pAce), ~7.0 (VARNAM2), and ~6.7 (pAceR) versus reported values of ~6.9 (Ace-mNeon) and ~6.6 (VARNAM)] (fig. S13) (*18*). The higher $\Delta F/F$ values and superior photostability of pAce enabled extended duration (30 min) continuous recordings with stable d' values throughout imaging sessions with illumination powers of ~5 mW mm^{-2} (fig. S14).

For studies in live mice, our epifluorescence imaging methodology was designed to allow cellular resolution recordings in cortical brain tissue and to reduce both tissue autofluorescence and background fluorescence from scattered or out-of-focus indicator emissions. Specifically, we (i) were able to use modest illumination intensities (typically, 25 mW mm^{-2}), owing to the high brightness of our indicators; (ii) achieved relatively sparse fluorescence labeling (<370 labeled cells per mm^2) by targeting specific cell classes through virally mediated projection targeting or using cell type–specific *Cre*- or *Flp*-driver mouse lines (*39*–*42*); and (iii) generated soma-targeted versions of Ace-mNeon2, VARNAM2, pAce, and pAceR, which mainly trafficked to cell body membranes (Fig. 1H) (*43*). With this labeling and trafficking approach, <4.2% (and usually much less) of the area of each imaging plane was occupied by labeled cell bodies. Further, for data analyses, we used automated algorithms designed to extract neuronal activity traces with minimal contamination from physiologic artifacts or background activity (*44*–*46*) (fig. S15 and Materials and methods).

We expressed each of our four GEVIs in vasoactive intestinal peptide–expressing (VIP$^+$) interneurons in primary visual cortex (V1), in which they successfully reported single action potentials (Fig. 1, H and I). The $\Delta F/F$ values per spike (mean ± SEM) were −16.5 ± 1.9% for Ace-mNeon2 (n = 127 spikes), 10.7 ± 1.4% for pAce (n = 87 spikes), −7.3 ± 1.2% for VARNAM2 (n = 49 spikes), and 3.2 ± 0.5% for pAceR (n = 48 spikes).

To record stimulus-evoked activity, we used axonal projection targeting to express our best-performing GEVI, Ace-mNeon2, in a sparse subset of V1 layer 2/3 pyramidal neurons (PNs) ~100 to 200 μm beneath the pia (Fig. 2E). Specifically, we targeted PNs projecting to the anteromedial visual cortical area (AM) (*39*, *42*) by injecting an adeno-associated virus (AAV) expressing *Cre*-dependent Ace-mNeon2 into area V1 of wild-type mice along with a retrograde AAV expressing *Cre* under the CaMKII promoter into the AM. Voltage imaging of these V1→AM projecting neurons during presentations of drifting grating visual stimuli revealed the cells' orientation-selective visual responses (Fig. 1J).

To showcase imaging of neural ensemble dynamics, we used *Cre*-driver mice to target Ace-mNeon2 to neuron-derived neurotrophic factor–expressing (NDNF$^+$) interneurons, ~50 to 70 μm below the pia (*41*, *47*, *48*) (Fig. 2B), and recorded spiking in up to 51 cells at once (Fig. 1K) for 4 to 5 min continuously (fig. S16). Similarly, using other *Cre*- or *Flp*-driver lines, we respectively targeted Ace-mNeon2 or pAce to layer 2/3 somatostatin-expressing (SST$^+$) interneurons [~200 to 350 μm deep (*40*)] or VIP$^+$ interneurons [~50 to 300 μm below the pia (*49*)] to capture voltage signals from multiple cells of each neuron type (Fig. 2, C and D; and fig. S17). Across these different cortical subtypes, d' values ranged from 9.9 to 17.5, implying spike detection error rates ranging from 0.04 spike min^{-1} to infinitesimal values (fig. S18) (*38*). This high level of spike detection fidelity allowed us to extract spike trains and spike timing estimates that were invariant to the use of different cell-extraction algorithms (fig. S15, A, B, D, and G).

Voltage imaging of visual cortical ensembles during behavioral state transitions

In neocortex, interneuron activity is strongly influenced by an animal's internal state and, in turn, modulates excitatory cells (*1*–*5*). However, the extent to which different interneuron types respond to state transitions and how distinct brain states affect the millisecond-scale interactions between subtypes remain unknown.

To address these questions, we selectively targeted Ace-mNeon2 to NDNF$^+$, VIP$^+$, or SST$^+$ interneurons in area V1, or to V1→AM projecting neurons, by using the same mouse lines and viruses as described earlier in the text (Fig. 2A) (*40*, *41*). Voltage imaging in V1 of awake, head-restrained mice revealed spontaneous spiking rates (mean ± SEM) of 4.72 ± 0.01 Hz for NDNF$^+$ neurons (n = 192 cells, seven mice), 6.52 ± 0.23 Hz for VIP$^+$ neurons (n = 49 cells, five mice), 4.71 ± 0.21 Hz for SST$^+$ neurons (n = 43 cells, five mice), and 0.93 ± 0.34 Hz for PNs (n = 53 cells, five mice). These values are consistent with estimated spike rates of V1 layer 2/3 PNs and SST$^+$ cells obtained using electrophysiological recordings in awake mice (*4*, *50*). Likewise, the higher spontaneous firing rates of VIP$^+$ versus SST$^+$ interneurons have been observed across distinct cortical areas (*51*, *52*).

To induce a change in brain state by increasing arousal, we delivered a brief air puff to the mouse's back while monitoring its pupil

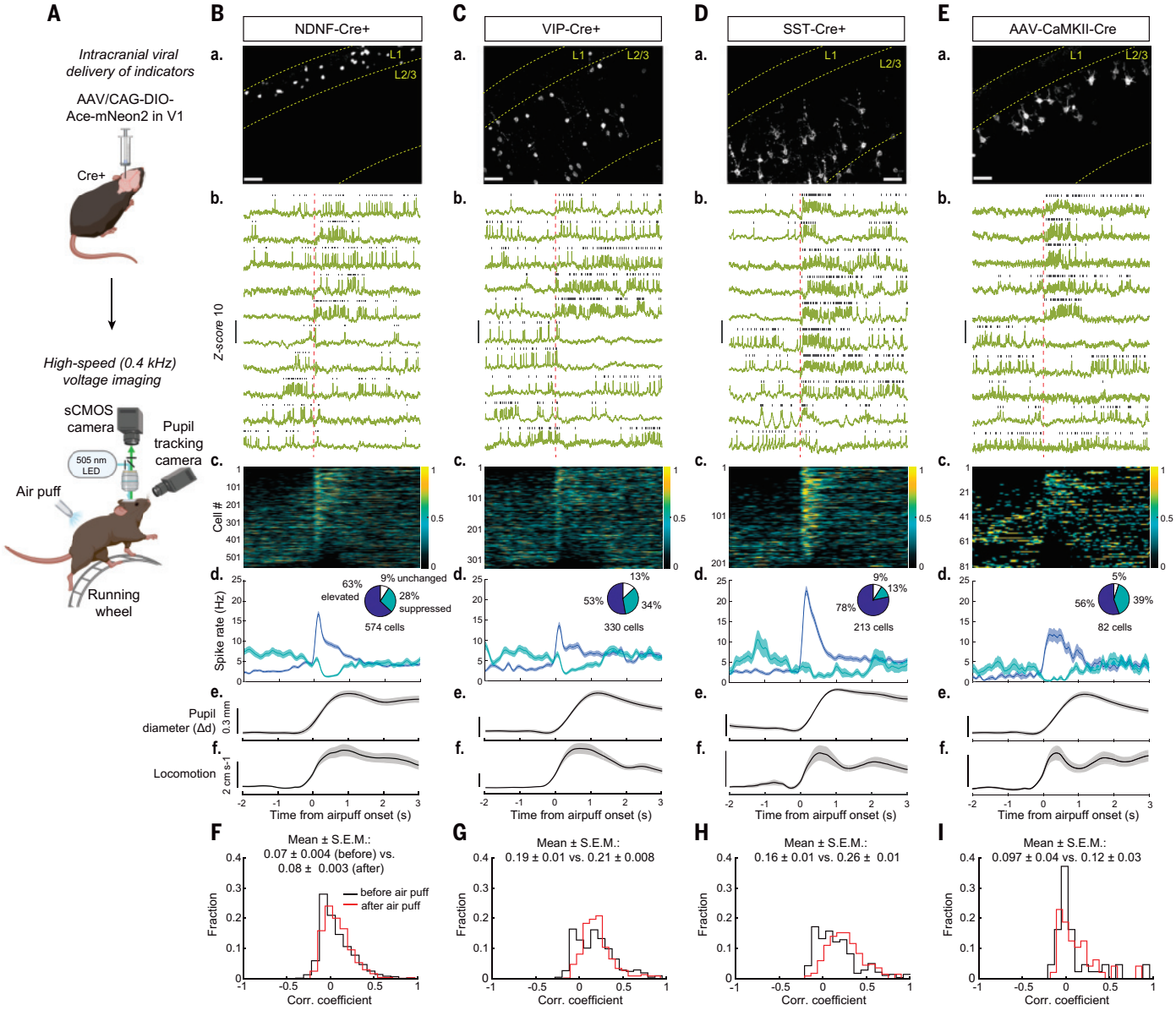


Fig. 2. Ace-mNeon2 voltage imaging unveils state-dependent modulation of spontaneous firing in excitatory and inhibitory cell types in V1.
(**A**) Schematic of AAV injection and experimental setup. LED, light-emitting diode; sCMOS, scientific complementary metal oxide semiconductor. (**B**) Ace-mNeon2 voltage imaging of NDNF$^+$ neurons during air puff delivery. (a) Confocal images of soma-targeted Ace-mNeon2 expression in NDNF$^+$ interneurons. Scale bar, 50 μm. (b) Representative fluorescence-time traces from individual cells (inverted for visualization purposes). The vertical dashed line in red indicates air-puff onset. Gray ticks denote identified spikes. (c) *Z*-scored firing rate for all NDNF$^+$ interneurons (n = 574 cells, six mice). Cells are arranged in order of decreasing spike modulation indices (Materials and methods). (d) Firing rate (mean ± SEM) aligned to air-puff onset for activated (dark blue) and suppressed (cyan) fractions. Pie chart insets indicate the percentage of cells with increased (dark blue), suppressed (cyan), or unchanged (white) spike rates after air puff. (e) Pupil diameter (mean ± SEM). (f) Locomotor speed (mean ± SEM). (**C**) Same as (B) for VIP$^+$ interneurons (n = 330 cells, five mice). (**D**) Same as (B) for SST$^+$ interneurons (n = 213 cells, six mice). (**E**) Same as (B) for PNs (n = 82 cells, four mice). (**F**) Distribution of pairwise correlation coefficients of mean firing rates across a sliding 20-ms window, as determined for 3-s intervals, before (black) and after (red) air puff for NDNF$^+$ interneurons (2300 cell pairs in the same fields of view, six mice; P = 0.0021; Wilcoxon matched-pairs signed rank test for before versus after air puff). The mean ± SEM correlation coefficient values are shown above the distribution plots. (**G**) Same as (F) for VIP$^+$ interneurons (n = 442 pairs, five mice; P = 0.0011). (**H**) Same as (F) for SST$^+$ interneurons (n = 334 pairs, six mice; P < 0.0001). (**I**) Same as (F) for PNs (n = 51 pairs, four mice; P = 0.03).

diameter, which is a commonly used, simple metric of arousal (Fig. 2A) (*53*, *54*). The evoked arousal was often accompanied by the onset of locomotion and robust modulations of spiking across all neuron classes studied (Fig. 2, B to E). However, the distinct cell classes differed regarding both the fractions of cells that increased or decreased their spiking and the magnitudes of spike rate modulation (Fig. 2, B to E).

We imaged the spiking dynamics of ~1200 neurons across the different cell types. Upon arousal, SST$^+$ interneurons exhibited the most substantial state-dependent modulation, with 78% of SST$^+$ cells increasing their spontaneous spiking rates and only 13% decreasing their spiking rates (Fig. 2D). SST$^+$ cells also underwent the greatest increases in spike rates among the cell types imaged, from 2.5 ± 0.4 Hz (mean ±

SEM) under baseline conditions to 22.5 ± 1.2 Hz after air puff (Fig. 2D). Sixty-three percent of NDNF$^+$ interneurons also increased their spiking, from 2.6 ± 0.3 to 16.8 ± 0.7 Hz, whereas 28% decreased their spiking after air puff (Fig. 2B). VIP$^+$ neurons and PNs exhibited comparable state-dependent responses, with half of each population showing increased spiking (53 and 56%, respectively) and a third showing suppressed spiking (34 and 39%, respectively) after air puff. These latter two classes also had similar spike rate increases during arousal (from 3.8 ± 0.5 to 13.7 ± 0.8 Hz for VIP$^+$ cells and 0.9 ± 0.3 to 11.8 ± 1.6 Hz for PNs) (Fig. 2, C and E). That each neuron type that we studied exhibited a subset of cells that decreased their spiking argues against the possibility that the net spiking increases were motion-related artifacts stemming from the locomotion that often occurred after the air puff. Further supporting this point, during air-puff trials in which there was no locomotor increase, we still observed comparable modulations in neural activity (fig. S19). Among the cell types imaged, the air puff–evoked rise in spiking among SST$^+$ cells returned the fastest toward baseline levels, whereas VIP$^+$ and NDNF$^+$ interneurons, which receive inhibitory inputs from SST$^+$ cells (*47*, *55*), returned more gradually to baseline spiking levels (Fig. 2, B to D).

To characterize the degree of spiking synchronization between the cells of each type, we computed pairwise correlation coefficients for the time-dependent spike rates of each cell pair and compared the distributions of these coefficients as determined before versus after air puff. Both SST$^+$ and VIP$^+$ cells exhibited positive intrapopulation coupling of spontaneous activity (*56*), which rose slightly during arousal, especially among SST$^+$ cells. By comparison, NDNF$^+$ interneurons and PNs showed weaker intrapopulation correlations (*57*), which were unaltered by air puff (Fig. 2, F to I).

Dual polarity multiplexed voltage imaging

Although arousal increases the net spontaneous activity of multiple cell subtypes (Fig. 2), how it alters the fine-scale dynamic relationships between two or more subtypes remains unknown. Thus, we turned to simultaneous multipopulation voltage imaging using our improved GEVIs.

Multipopulation recordings using fluorescent Ca^{2+} or voltage sensors were previously done by targeting spectrally orthogonal sensors to distinct cell types (*18*, *58*–*61*). We reasoned that a pair of GEVIs operating in the same spectral channel but with opposite response polarities should be mutually compatible, allowing studies of two cell types per color channel. The cells of each type can be distinguished by the directionality of their optical spike waveforms (fig. S20).

We performed dual-polarity multiplexed voltage imaging (DUPLEX) in awake mice, where we targeted Ace-mNeon2 and pAce either to two distinct inhibitory or to one excitatory and one inhibitory cell type by using *Cre*- and *Flp*-dependent expression strategies (Fig. 3A and Materials and methods). We virally expressed *Cre*-dependent Ace-mNeon2 and *Flp*-dependent pAce in area V1 of NDNF-*Cre*$^+$/VIP-*Flp*$^+$ or SST-*Cre*$^+$/VIP-*Flp*$^+$ double-transgenic mice (Fig. 3, B to G). Alternatively, we injected recombinase-dependent Ace-mNeon2 and pAce viruses along with AAV-CaMKII-*Cre* into VIP-*Flp*$^+$ mice (fig. S21). High-speed epifluorescence imaging in a single color channel revealed the joint dynamics of NDNF$^+$ and VIP$^+$ cells, SST$^+$ and VIP$^+$ cells, or PNs and VIP$^+$ cells, respectively, in these mice while they were awake but head restrained (Fig. 3, B to G; and fig. S21).

To estimate the degree of functional connectivity within and across cell types, we computed pairwise correlation coefficients for the time (t)–varying activity traces, $\Delta F/F(t)$, as well as for the spike rates of cell pairs in the same fields of view. NDNF$^+$ and VIP$^+$ interneurons had positive intrapopulation correlations but NDNF$^+$- VIP$^+$ pairs had virtually uncorrelated dynamics (Fig. 3, D, H, and I). The mean ± SEM correlation coefficients were 0.19 ± 0.02 ($\Delta F/F$) and 0.15 ± 0.02 (spike rates) for NDNF$^+$-NDNF$^+$ pairs, 0.31 ± 0.04 ($\Delta F/F$) and 0.29 ± 0.09 (spike rates) for VIP$^+$-VIP$^+$ pairs, and −0.09 ± 0.04 ($\Delta F/F$) and 0.02 ± 0.02 (spike rates) for NDNF$^+$-VIP$^+$ pairs (Fig. 3I), in accord with reports that the two subtypes may receive distinct inputs or not strongly target each other (*47*, *48*).

By comparison, DUPLEX imaging of SST$^+$ and VIP$^+$ cells revealed slightly negatively correlated intertype dynamics, whereas the intratype dynamics were positively correlated [mean ± SEM correlation coefficients were 0.37 ± 0.04 ($\Delta F/F$) and 0.11 ± 0.03 (spike rates) for SST$^+$-SST$^+$ pairs, 0.51 ± 0.05 ($\Delta F/F$) and 0.30 ± 0.07 (spike rates) for VIP$^+$-VIP$^+$ pairs, and −0.22 ± 0.04 ($\Delta F/F$) and −0.04 ± 0.01 (spike rates) for SST$^+$-VIP$^+$ pairs] (Fig. 3, G, J, and K). DUPLEX imaging of PNs and VIP$^+$ cells revealed very low correlations between the two neuron types [−0.009 ± 0.03 ($\Delta F/F$) and 0.06 ± 0.02 (spike rates)], whereas the intrapopulation correlation coefficients were higher [0.23 ± 0.10 ($\Delta F/F$) and 0.15 ± 0.08 (spike rates) for PN pairs; 0.32 ± 0.07 ($\Delta F/F$) and 0.16 ± 0.05 (spike rates) for VIP$^+$-VIP$^+$ pairs] (Fig. 3, L and M; and fig. S21).

To examine how spiking by one interneuron subtype relates to membrane potential dynamics of cells in the same or another interneuron subtype, we computed cross-correlation functions between one cell's spike rate and the subthreshold part of another cell's time-varying activity trace, $\Delta F/F(t)$, averaged over all pairs of cells of the two subtypes in the same field of view (fig. S22). The results verified that SST$^+$ and VIP$^+$ cells had positive intrapopulation correlations, whereas SST$^+$-VIP$^+$ pairs had negatively correlated dynamics, and that the dynamics of NDNF$^+$ cells were only weakly correlated with those of other NDNF$^+$ cells and VIP$^+$ cells. These results are consistent with paired recordings in live-brain slices that have revealed a bidirectional inhibition between SST$^+$ and VIP$^+$ neurons and nonoverlapping synaptic inputs to the two subtypes (*55*, *62*).

DUPLEX imaging in hippocampal area CA1

Past studies using GEVIs have assessed relationships between specific neuron classes and the local field potential (LFP) in hippocampal area CA1 (*23*, *63*). Using DUPLEX imaging, we tracked the concurrent dynamics of two CA1 neuron classes by expressing our two red GEVIs in distinct cell types (fig. S23) or by using our two green GEVIs in tandem while also recording LFPs (Fig. 4A and fig. S24). In a running mouse expressing Ace-mNeon2 in entorhinal cortex (EC)–projecting excitatory neurons in the *stratum pyramidale* (~150 to 200 μm below a glass window) and pAce in SST$^+$ interneurons in the *stratum oriens* (~25 to 150 μm below a glass window), we tracked 10 excitatory and 18 SST$^+$ cells in the same field of view and distinguished the two cell types by the opposing polarities of their optical spike waveforms (Fig. 4, B to D). Spike detection fidelity indices (d') in CA1 neurons ranged from 10.6 to 17.6, implying spike detection error rates of 0.007 spike min^{-1} or less (fig. S18) (*38*).

SST$^+$ interneurons had greater baseline spike rates and burstiness than the EC-projecting neurons [19.8 ± 1.8 versus 14.7 ± 0.5 Hz (mean ± SEM), $P < 0.01$] (Fig. 4E). We assessed the extent to which spiking by the excitatory and inhibitory neurons was phase-locked to membrane potential oscillations in these specific cell types or to CA1 LFP signals. Across a total of 157 neurons, spiking from both cell types was locked with greater precision to intrapopulation subthreshold oscillations than to the LFP; notably, SST$^+$ cells and EC-projecting PNs spiked at distinct phases of their intrinsic theta (4 to 9 Hz) membrane potential dynamics [13.8° ± 2.6° and −1.3 ± 4.8°, respectively (mean ± SEM, $P < 0.01$)] (Fig. 4, F to H). Spiking in EC-projecting cells but not SST$^+$ cells also consistently phase-locked to the LFP ($P < 0.001$ and $P = 0.82$, respectively) (Fig. 4, G and H).

We next assessed the relationships between the LFP and the cell type–specific subthreshold dynamics, as well as those between the subthreshold dynamics of the two subtypes. We found strong subthreshold coherence between both cell types and the LFP in the theta frequency band ($P < 0.0001$ and $P < 0.0001$, respectively) (Fig. 4, I to L; and fig. S24, A to D). We also found strong intra- and

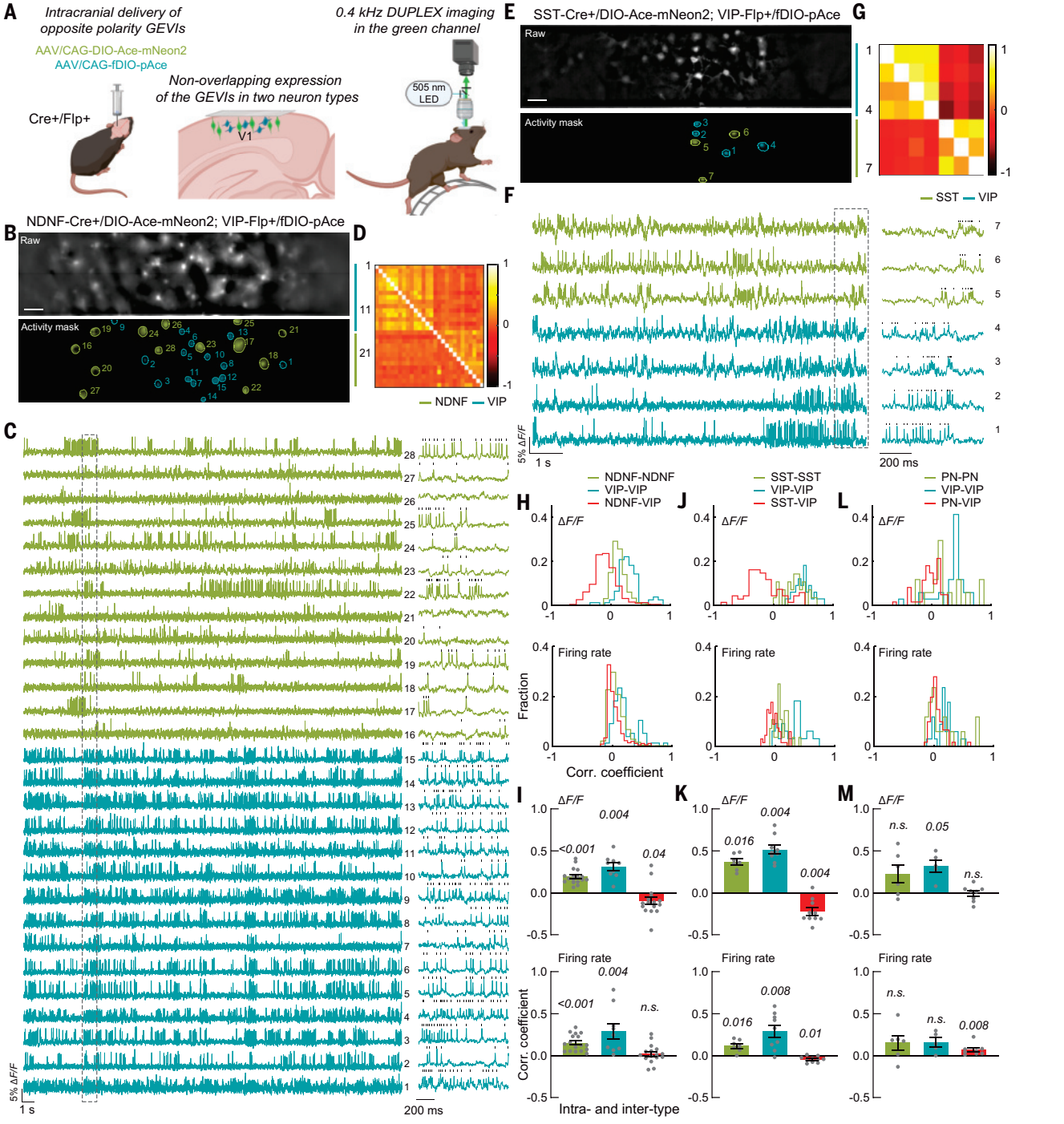


Fig. 3. DUPLEX captures the concerted activation dynamics between cell types in V1. (**A**) Schematic of AAV injections and experimental setup. (**B** to **G**) Example DUPLEX recordings from two targeted cortical cell types. (B) and (E) show raw epifluorescence (top) and activity-mask (bottom) images of single fields of view from a (B) NDNF-*Cre*$^+$/VIP-*Flp*$^+$ mouse expressing Ace-mNeon2 in NDNF$^+$ interneurons (green) and pAce in VIP$^+$ cells (blue) and (E) SST-*Cre*$^+$/VIP-*Flp*$^+$ mouse expressing Ace-mNeon2 in SST$^+$ interneurons (green) and pAce in VIP$^+$ interneurons (blue). Active cells are numbered. Scale bar, 50 μm. (C) and (F) show Δ*F*/*F* traces from the cells numbered in (B) and (E), respectively. Ace-mNeon2 traces are inverted for visualization purposes. The regions enclosed by the dashed boxes in (C) and (F) are shown at an expanded time scale to the right. Gray ticks indicate identified spikes. (D) and (G) show intra- and interpopulation correlation coefficient matrices of pairwise, zero time-lag correlation coefficients of the Δ*F*/*F* traces (upper triangle) and spiking rates (lower triangle), determined using a 20-ms sliding window for the cells in (C) and (F), respectively. (**H**) Distribution of pairwise correlation coefficients for Δ*F*/*F* traces (top) and spiking rates (bottom) across all mice for NDNF/VIP recordings (n = 1795 NDNF-NDNF pairs, 77 VIP-VIP pairs, and 373 NDNF-VIP pairs; 208 NDNF-neurons and 54 VIP-neurons, five mice). (**I**) Mean ± SEM pairwise correlation coefficients for Δ*F*/*F* traces (top) and spiking rates (bottom) for the NDNF/VIP dataset in (H) (n = 17 fields of view). P values are italicized (one-sample Wilcoxon test against zero). n.s., not significant. (**J** and **K**) Same as (H) and (I) for SST/VIP recordings (n = 28 SST-SST pairs, 33 VIP-VIP pairs, and 67 SST-VIP pairs; 25 SST$^+$ neurons and 29 VIP$^+$ neurons, 10 fields of view, three mice). (**L** and **M**) Same as (H) and (I) for PN/VIP recordings (n = 17 PN-PN pairs, 34 VIP-VIP pairs, and 61 PN-VIP pairs; 20 PNs and 22 VIP$^+$ neurons, eight fields of view, three mice).

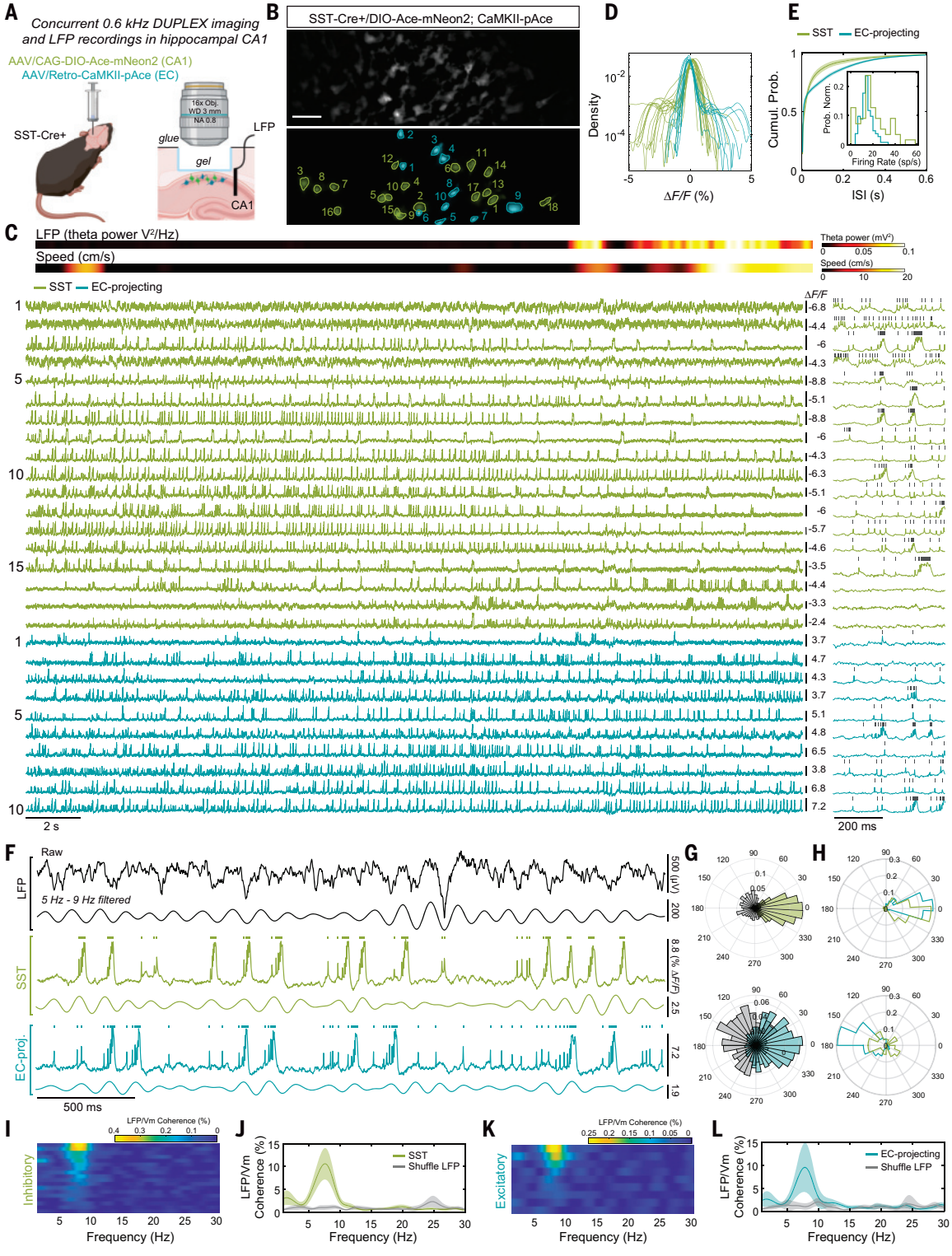


Fig. 4. DUPLEX uncovers cell class–specific contributions to the LFP in hippocampal CA1. (**A**) Schematic of AAV injections and experimental setup. (**B**) Representative raw epifluorescence image (top) and spatial footprint of negative-polarity signals (green) and positive-polarity signals (blue) of 18 and 10 identified neurons, respectively (bottom). Scale bar, 50 μm. (**C**) Δ*F*/*F* traces (bottom) for all the neurons in (B) along with wheel speed and LFP theta (top). Ace-mNeon2 traces are inverted for visualization purposes. The first 500 ms are shown at the expanded time scale to the right. Gray ticks denote identified spikes. (**D**) Fluorescence trace amplitude distributions for all neurons across all fields of view. Note the opposite polarities within similar dynamic ranges for Ace-mNeon2 and pAce. (**E**) Cumulative distributions of interspike intervals (ISIs) and firing rates (inset; sp/s, spikes per second) for all recorded neurons (n = 55 SST$^+$ interneurons and 102 projection neurons, six fields of view, one mouse). The shaded area represents the 95% confidence interval (CI). (**F**) Phase relationships between spike and theta oscillations extracted from the LFP or cellular transmembrane voltage oscillations for projection neurons and SST$^+$ cells recorded simultaneously. Shown here are the raw LFP trace (top) and the theta-filtered (5 to 10 Hz) (center) and unfiltered (bottom) excitatory and inhibitory

traces. (**G**) Spike-theta phase relationship for the two neurons in (F). Color and gray represent the optically acquired theta transmembrane voltage (V_m) and theta LFP, respectively. Note that both neurons are phase-locked to their own V_m and to the LFP but with approximately opposite phases. (**H**) Polar histogram of the probability density of the average spike-theta phase relationship for all 157 neurons, computed against their respective theta V_m (top) or theta LFP (bottom). For each neuron, average spike timing relative to the theta cycle was computed using the circular mean. (**I** to **L**) LFP-subthreshold coherence of all neurons in (C), showing that a fraction of [(I) and (J)] SST^+ interneurons and [(K) and (L)] EC-projecting excitatory neurons are phase-locked to theta LFP. For (I) and (K), raster plots are sorted in decreasing order of theta-band coherence strength. For (J) and (L), LFP coherence is averaged across all neurons in (I) and (K). The shaded area represents the 95% CI.

interpopulation coherence in the beta frequency band (15 to 25 Hz) (fig. S24, E to H), in contrast to the lack of beta frequency band coherence with the LFP (fig. S24, A to D).

DUPLEX imaging in live flies

To showcase the use of DUPLEX for multi–cell type recordings across species, we expressed pAce in the γ-aminobutyric acid–signaling (GABAergic) MBON-γ1pedc>α/β neuron and Ace-mNeon2 in the PPL1-α′2α2 dopaminergic neuron in fruit flies (fig. S25A). Both these cells receive excitatory olfactory inputs from mushroom body Kenyon cells, and MBON-γ1pedc>α/β also exerts feedback inhibition onto PPL1-α′2α2 axons (*64*). When we exposed the double-labeled flies to odorants, DUPLEX imaging of PPL1-α′2α2 axons and MBON-γ1pedc>α/β dendrites revealed that MBON-γ1pedc>α/β was strongly activated throughout exposure to an attractive odor [apple cider vinegar (ACV)] but was more transiently activated by a repulsive odor [benzaldehyde (BEN)]. By contrast, PPL1-α′2α2 was strongly inhibited by ACV but weakly excited by BEN, in accord with the known inhibitory connection from MBON-γ1pedc>α/β to PPL1-α′2α2 (fig. S25, B and C).

Interpopulation correlations of spiking dynamics during state transitions

We next used DUPLEX to examine how state transitions affect the interactions between cortical subtypes. In green DUPLEX recordings from $NDNF^+$ and VIP^+ interneurons in layer 1 of V1 (~50 to 100 μm below the pia), spike rates were uncorrelated across the two populations under baseline conditions (Fig. 5, A to C), and air puff–induced arousal had no impact on this uncorrelated behavior [mean ± SEM correlation coefficients: 0.07 ± 0.02 before air puff versus 0.10 ± 0.03 after] (Fig. 5C). To quantify the effects of air puff on the spiking of individual cells, we also computed a spike modulation index from −1 to 1 (Material and methods). Spiking by $NDNF^+$ and VIP^+ cells was significantly positively modulated by air puff [mean ± SEM; median values: 0.27 ± 0.02; 0.32 ($P < 0.0001$, one-sample Wilcoxon signed rank test against zero) and 0.11 ± 0.03; 0.08 ($P = 0.006$), respectively] (Fig. 5D).

In DUPLEX recordings from SST^+ and VIP^+ interneurons (~200 to 250 μm below the pia), spiking by the two subtypes became significantly more anticorrelated after air puff (mean ± SEM correlation coefficients: −0.02 ± 0.01 before air puff versus −0.14 ± 0.03 after) (Fig. 5, E to G). The spike modulation indices also revealed that most SST^+ cells were positively modulated by the air puff [mean ± SEM; median values: 0.43 ± 0.05; 0.57 ($P < 0.0001$, one-sample Wilcoxon test)], whereas VIP^+ cells imaged concurrently at the same tissue depth and in the same fields of view more commonly had negative values of the spike modulation index [mean ± SEM; median values: −0.07 ± 0.05; −0.12 ($P = 0.14$)] (Fig. 5H).

DUPLEX studies in PNs and VIP^+ cells (~150 to 200 μm below the pia) revealed uncorrelated dynamics for these cell classes before and after air puff (mean ± SEM correlation coefficients were 0.04 ± 0.02 before versus 0.05 ± 0.02 after air puff) (Fig. 5, I to K). The spike modulation indices revealed a small positive modulation of both populations by the air puff [mean ± SEM; median values: 0.19 ± 0.09; 0.44 ($P = 0.06$, one-sample Wilcoxon test) and 0.08 ± 0.05; 0.07 ($P = 0.14$), respectively] (Fig. 5L).

Dual-color voltage imaging of hippocampal projection neurons

Although DUPLEX can dissect activity patterns among nonoverlapping populations, such as discrete excitatory and interneuron subtypes, when the level of overlap between two neuronal subclasses is unknown, their activities can instead be distinguished by simultaneous dual-color voltage imaging. We used Ace-mNeon2 and VARNAM2 to examine the extent to which two subclasses of CA1 projection neurons, targeting distinct cortical regions, modulate their spiking during a rest-to-run behavioral transition. We expressed Ace-mNeon2 and VARNAM2 in anterior cingulate cortex (ACC)– and EC-projecting CA1 PNs, respectively, using retrograde AAV labeling. We then performed simultaneous dual-color voltage imaging in an injected mouse, which was head restrained on a running wheel, and used a brief air puff to elicit a rest-to-run behavioral transition (Fig. 5M).

We imaged a total of 101 ACC-projecting and 34 EC-projecting neurons from five fields of view in the same animal, with a single field of view containing as many as 30 and 13 cells of the two subclasses, respectively (Fig. 5, M and N; and fig. S26). Both Ace-mNeon2 and VARNAM2 captured a diversity of cell dynamics, including isolated spikes, spike bursts, and subthreshold oscillations.

We assessed whether the ACC- and EC-projecting cell ensembles had distinct supra- and subthreshold dynamics across the behavioral state transition (*6*–*9*). Whereas EC-projecting cells did not significantly change their spike rates after the onset of locomotion, ACC-projecting cells did [$\log_2$ fold change (mean ± SEM): 0.0 ± 0.2 for EC-projecting cells versus 0.9 ± 0.1 for ACC-projecting cells; $P = 0.59$ and $P < 0.0001$; rank sum test between real data and spike trains circularly permuted in time] (Fig. 5, O to Q; and fig. S26). We also observed greater coherence in subthreshold activity after the behavioral transition, but interestingly, each subclass synchronized at distinct frequencies (7.3 ± 0.3 and 4.2 ± 0.2 Hz, respectively, for ACC- and EC-projecting cell pairs; $P < 0.0001$; rank sum test computed for run epochs against levels estimated from neurons belonging to different fields of view) (Fig. 5, R to T).

Simultaneous voltage imaging of three cell populations

Together, our indicators enable discriminations of distinct targeted subtypes or projection-specific cell subclasses based on the polarity of optical spike waveforms as well as spectral orthogonality. Thus, in principle, the four GEVIs are mutually compatible and allow recordings from up to four distinct neuron types at once. To demonstrate dual polarity and dual-color multiplexing, we performed proof-of-concept voltage imaging from three distinct cell populations simultaneously.

In an SST-*Cre*$^+$/VIP-*Flp*$^+$ double-transgenic mouse, we injected AAVs encoding both *Cre*-dependent Ace-mNeon2 and *Flp*-dependent pAce into V1, along with a retrograde AAV expressing CaMKII-VARNAM2 in area AM to label a subset of excitatory projection neurons (Fig. 6A). We then performed voltage imaging in V1 using dual-color, widefield epifluorescence microscopy to record from SST^+, VIP^+, and excitatory neurons concurrently (Fig. 6, B and C).

To image three neuron classes at once in the hippocampus, we retrogradely labeled EC- and lateral septum (LS)–projecting CA1 PNs and SST^+ interneurons, using viruses to express Ace-mNeon2, pAce, and pAceR, respectively, in a SST-*Cre*$^+$ mouse (Fig. 6D). With simultaneous dual-color imaging, we captured the concurrent spiking and subthreshold activity of as many as 57 cells in one field of view belonging to the three subpopulations (21 EC-projecting, 15 LS-projecting, and 21 SST^+ cells). These ensembles comprised nonoverlapping cell populations (Fig. 6E), and all three GEVIs reported spiking at high signal-to-noise ratios (Fig. 6F).

Conclusion

Our suite of mutually compatible GEVIs allows simultaneous high-speed voltage imaging of

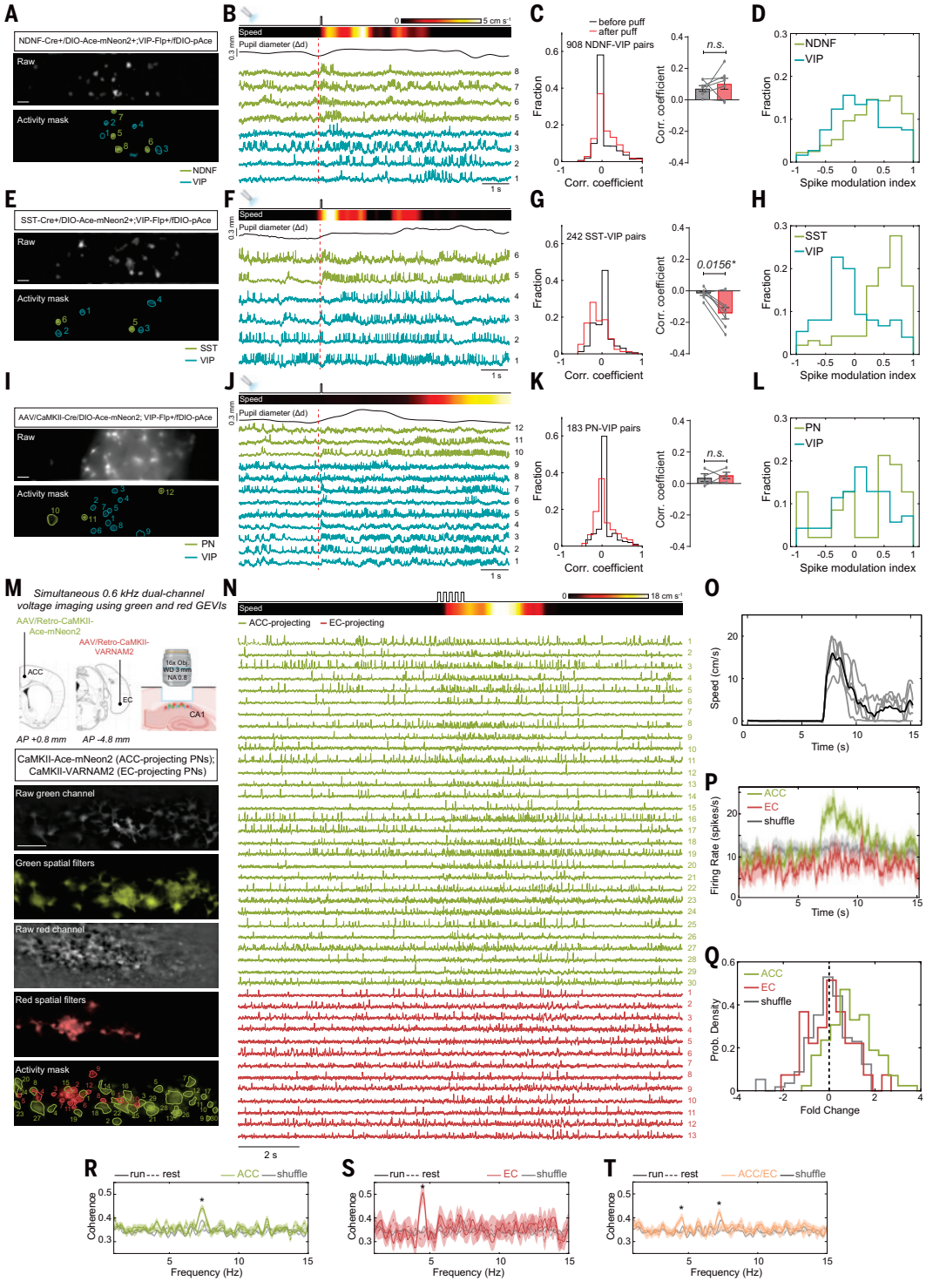


Fig. 5. Dual population recordings in V1 and CA1 during state transitions. DUPLEX recordings in V1 are shown in (A) to (L). (**A**) Representative raw epifluorescence (top) and activity-mask (bottom) images of a single field of view from a NDNF-*Cre*$^+$/VIP-*Flp*$^+$ mouse expressing Ace-mNeon2 in NDNF$^+$ interneurons (green) and pAce in VIP-cells (blue). Scale bar, 50 μm. (**B**) Δ*F*/*F* traces from the cells numbered in (A) aligned to air-puff onset (vertical dashed line). Ace-mNeon2 traces are inverted for visualization purposes. Also shown at the top are air-puff onset, locomotion speed, and pupil diameter. (**C**) Distribution of pairwise intertype correlation coefficients of spike rates (left) determined using a 20-ms sliding window for a 3-s interval before (black) or after (red) air puff (n = 908 NDNF-VIP pairs from 393 NDNF$^+$ and 188 VIP$^+$ cells, seven mice) and mean ± SEM correlation coefficients by mouse (right) (n = 7 mice; one-tailed Wilcoxon matched-pairs signed rank test). (**D**) Distribution of spike modulation indices for all NDNF$^+$ and VIP$^+$ neurons in (C). (**E** to **G**) Same as (A) to (C) for DUPLEX recordings in SST-*Cre*$^+$/VIP-*Flp*$^+$ mice (n = 242 SST-VIP pairs from 103 SST$^+$ and 79 VIP$^+$ cells, six mice; *P < 0.05, one-tailed Wilcoxon matched-pairs signed rank test). (**H**) Same as (D) for all SST$^+$ and VIP$^+$ neurons. (**I** to **K**) Same as (A) to (C) for DUPLEX recordings in AAV-CaMKII-*Cre*/VIP-*Flp*$^+$ mice (n = 183 PN-VIP pairs from 75 PNs and 67 VIP$^+$ cells, four mice; one-tailed Wilcoxon matched-pairs signed-rank test). (**L**) Same as (D) for all PNs and VIP$^+$ neurons. Dual-color voltage recordings from hippocampal projection neurons are shown in (M) to (T). (**M**) Schematic of the experimental approach (top) and representative field of view of the red and green channels in grayscale, their respective overlay of spatial filters estimated by EXTRACT for each spiking neuron in each spectral channel, and the overlay of the spatial filter contours for all 30 and 13 identified projection specific neurons, respectively (bottom). Scale bar, 50 μm. (**N**) Δ*F*/*F* traces for all neurons in (M), aligned to the rest-run transition. Also shown at the top are the onset of five consecutive air puffs and wheel speed. (**O**) Average mouse speed for five trials (black). Individual trials are shown in gray. (**P**) Average firing rate (250-ms window) for each projection-specific class. Shuffle is computed by random circular permutations of each neuron's spike train. The shaded area represents the 95% CI. (**Q**) Fold-change in the cells' spiking rates, computed across 2-s intervals before and after air puff. Shuffle is computed using a random circular permutation of each neuron's spike train. (**R** to **T**) Average pairwise coherence of the subthreshold dynamics of neurons belonging to the ACC-projecting subclass [(R); n = 101 neurons], the EC-projecting subclass [(S); n = 34 neurons], and across the two subclasses [(T); n = 135 neurons, five fields of view, one mouse]. P < 0.0001 (rank sum test computed during epochs of running, against levels estimated from neurons belonging to different fields of view). Shaded areas represent the 95% CI.

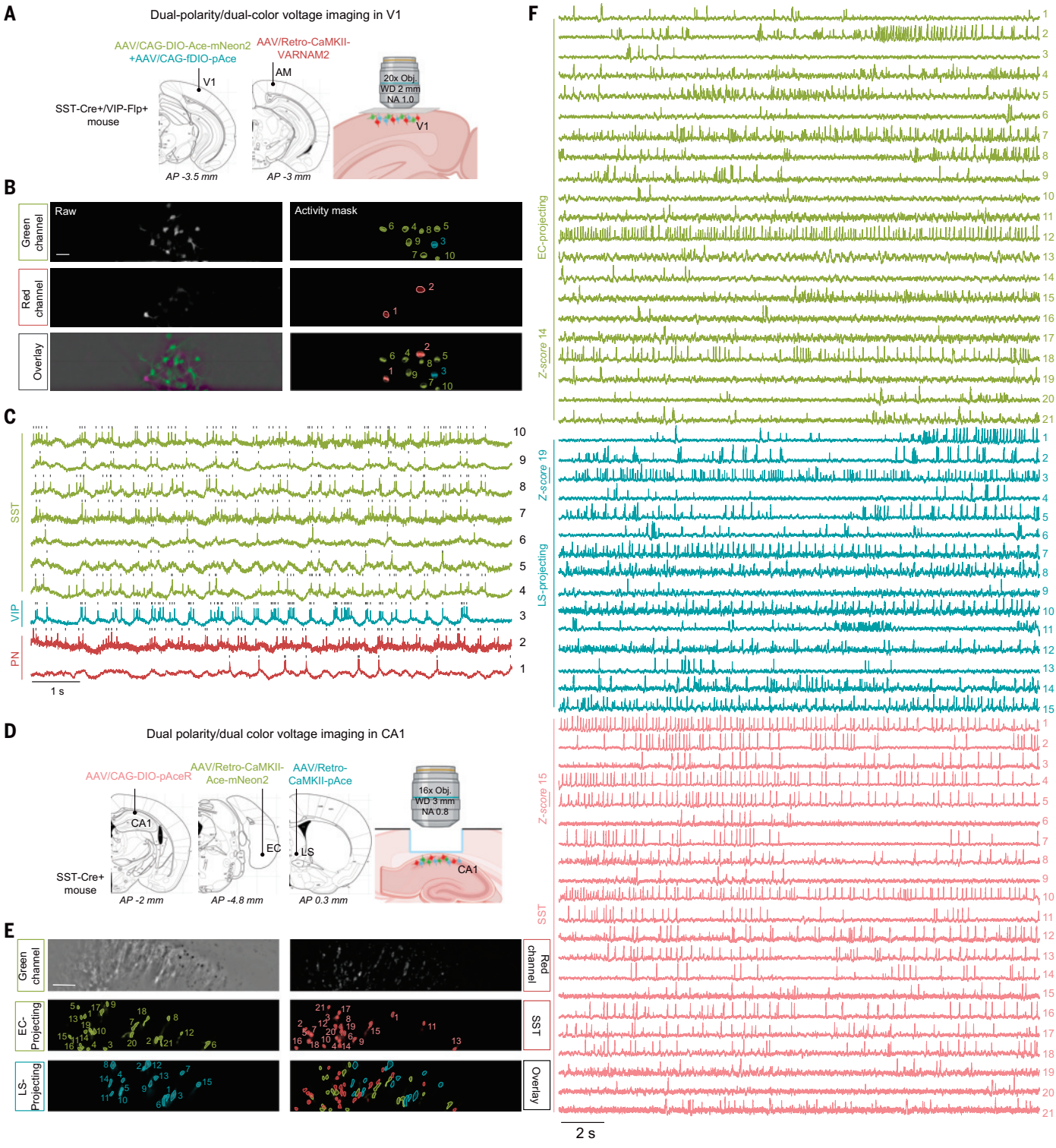


Fig. 6. Simultaneous dual-polarity and dual-color imaging capture the voltage dynamics of three distinct targeted subtypes or cell subclasses in awake mice. (**A**) Schematic of AAV injections for three–cell type V1 imaging. (**B**) Raw epifluorescence (left) and activity-mask (right) images of a single field of view in the green and red channels and overlay. Scale bar, 50 μm. (**C**) $\Delta F/F$ traces from the cells numbered in the mask overlay image in (B) and representing SST^+ interneurons, VIP^+ interneurons, and PNs expressing Ace-mNeon2 (green), pAce (blue), and VARNAM2 (dark red), respectively. Ace-mNeon2 and VARNAM2 traces are inverted for visualization purposes. (**D**) Schematic of AAV injections for three–cell class voltage imaging in CA1. (**E**) Representative field of view of the red and green channels with the respective spatial footprint of the identified neurons belonging to each of the three cell classes. Scale bar, 50 μm. (**F**) $\Delta F/F$ traces for all neurons in (E), representing EC- and LS-projecting excitatory neurons and SST^+ interneurons expressing Ace-mNeon2 (green), pAce (blue), and pAceR (light red), respectively. Ace-mNeon2 traces are inverted for visualization purposes.

multiple genetically identified ensembles in awake animals. Notably, our indicators can provide large datasets for quantitative characterizations of the spiking patterns of targeted neuron types in behaving flies and mice. This provides a starting point for future studies in which the fine-scale dynamics between targeted cell types can be examined toward dissecting the circuit basis of animal behavior. The FRET-opsin GEVIs introduced here are bright and can be used with illumination levels far lower than those needed for imaging opsin GEVIs (*16*, *22*, *23*, *27*). They are hence compatible with both widefield epifluorescence microscopy and specialized microscopy methods that use sculpted illumination patterns (*16*, *22*, *24*), facilitating broad dissemination of our voltage imaging approaches.

Our V1 data, acquired from ~1200 cells using Ace-mNeon2, reveal that SST^+ interneurons exhibit a major increase in spontaneous firing during arousal, recapitulating the results of targeted patch recordings (*4*). Although our results do not confirm the VIP^+ neuron-centered PN disinhibition model (VIP ⊣ SST ⊣ PN), which was proposed based on Ca^{2+} imaging data (*2*, *65*, *66*), the distinct findings might stem from key experimental differences, such as the presence or absence of visual stimuli (*67*). However, past interpretations of Ca^{2+} imaging data might be confounded by subtype-specific differences in intracellular Ca^{2+} dynamics or cytosolic Ca^{2+} release, which in turn may be influenced by state-dependent neuromodulatory effects (*67*). A prior alternative to Ca^{2+} imaging was to perform targeted whole-cell patch electrode recordings, but the invasiveness of the technique and the availability of fewer healthy cells for successful patching makes it challenging to sample large numbers of cells from sparse populations (e.g., VIP^+ interneurons) (*2*). The use of GEVIs avoids such limitations of electrodes and Ca^{2+} imaging, and our suite of four compatible GEVIs enables unprecedented studies of spiking in multiple identified neuron classes at once.

Notwithstanding, our imaging methodology does have limitations. Our widefield one-photon epifluorescence imaging studies in the mouse neocortex, like other recent voltage-imaging studies (*13*, *16*, *23*, *24*), were limited to supragranular cortical layers, relatively sparse fluorescence labeling patterns, and moderately sized fields of view. Similarly, our studies of the CA1 hippocampal area were limited to its two most superficial layers. In these regions, by combining high brightness indicators with cell type–specific and soma-targeted labeling strategies, we achieved high signal-to-background fluorescence and exceptional d' values for accurate spike detection and timing estimation (fig. S18), independent of the cell-extraction algorithm used (fig. S15, B, D, and G).

To access cells in deeper cortical layers, the use of patterned illumination strategies to reduce background fluorescence may improve imaging depths (*16*, *22*, *24*, *68*). Alternatively, imaging of voltage dynamics in infragranular cortical layers or deep brain areas with a microprism (*69*) or gradient index (GRIN) microendoscope (*70*) should also be feasible, especially if high numerical aperture lenses (*71*) for enhanced fluorescence collection are used instead of those typically used for Ca^{2+} imaging (*72*). Further, although the densities of labeled cells in our recordings (<370 cells mm^{-2}) were comparable to those of past voltage-imaging studies (*13*, *16*, *22*, *23*), they were low compared with the total neuronal density in the mammalian cortex. Thus, our imaging approach may not generalize to studies requiring pan-neuronal or other dense labeling strategies. That said, recent work has aimed to delineate the large number of mammalian neuron types in the cortex (*73*), so we expect that upcoming studies that seek to differentiate the functional attributes of these distinct cell types will require targeted labeling strategies such as those used here. With continued progress in scientific-grade image sensor chips, we also expect improved high-speed cameras that will enable voltage imaging over larger fields of view and of more cells than those studied here.

We quantified the veracity of optically detected spike trains using the d' metric, but measuring the fidelity of optically detected, subthreshold membrane potential changes is more challenging because the relevant fluorescence signals and noise fluctuations are not just frequency-dependent but also nonstationary. Although the subthreshold components of the estimated neural activity traces, $\Delta F/F(t)$, did vary to a modest extent with the use of different cell-extraction algorithms (fig. S15), likely due to different efficacies in computationally removing background fluorescence contaminants or heartbeat artifacts, the biological conclusions obtained about cell class interactions using spike rate correlations and subthreshold correlations were in general agreement with each other (Fig. 3, H to M) and did not depend on the analytic approach to cell extraction (fig. S22). Nonetheless, further progress in cell-extraction algorithms that are tailored for voltage-imaging studies remains important.

Traditionally, multipopulation imaging has been achieved using spectrally orthogonal indicators (*18*, *58*–*61*). Yet, likely due to the limited set of mutually compatible sensors or the need for tailored optical hardware, simultaneous multichannel imaging is not widely performed in live animals. DUPLEX offers a simple alternative to distinguish between two neuron types using one fluorescence channel. Here, DUPLEX unveiled anticorrelated dynamics among pairs of visual cortical SST^+ and VIP^+ interneurons during arousal. In the hippocampus, DUPLEX revealed cell type–specific subthreshold activity, which allowed us to characterize how the dynamics of excitatory and inhibitory populations relate to those of the LFP. Our results fit with the hypothesis that excitatory neurons contribute more strongly to the LFP because of their spatial organization and temporal synchronization (*74*).

Whereas DUPLEX allows recordings from nonoverlapping cell types, our green and red indicators can be combined for studies of two cell populations that overlap or for which the degree of overlap is unknown. The ACC- and EC-projecting CA1 ensembles represent spatially distinct subpopulations, as seen from the nonoverlapping expression of Ace-mNeon2 and VARNAM2 (Fig. 5M). This anatomical distinction and the separate dynamical attributes of the two cell classes (Fig. 5, P to T) are in line with the idea that there are heterogeneous parallel modules in the hippocampus (*75*).

Looking ahead, that our two green GEVIs of opposite polarities can be further combined with our red GEVIs should enable many different voltage-imaging studies of three or four cell classes simultaneously (Fig. 6). Thus, the new indicators collectively empower neuroscientists to unravel intercellular interactions within and between targeted neuron classes in awake behaving animals.

Materials and methods

Plasmids

For high-throughput screening in HEK cells, VARNAM and Ace-mNeon were inserted into a modified pCAGGS backbone (*18*). A nuclear localization sequence (NLS)–tagged FP reporter (mCerulean for VARNAM and mCherry for Ace-mNeon) was fused to the C terminus of the indicator interspersed by a T2A ribosomal skipping signal. For in vivo voltage imaging, the indicators were cloned in AAV backbones. pAAV-CaMKII-Ace-mNeon2, pAAV-CaMKII-VARNAM2, and pAAV-CaMKII-pAce were cloned by inserting the respective indicator sequences in place of enhanced green fluorescent protein (EGFP) between the Kpn I and Hind III sites of pAAV-CaMKII-EGFP (Addgene #50469). *Cre*-dependent constructs for Ace-mNeon2 and pAceR were generated by cloning the respective inverted open reading frame (ORF) sequences in pAAV-CAG-Flex-EGFP (Addgene #59331) by replacing the floxed EGFP cassette between the Asc I and Nhe I sites. Likewise, *Flp*-dependent VARNAM2 and pAce constructs were cloned by introducing the respective inverted ORF sequences in place of the floxed mNeonGreen between the Asc I and Nhe I sites in pAAV-CAG-fDIO-mNeonGreen (Addgene #99133). All AAV constructs above included a Golgi–endoplasmic reticulum export sequence and a Kv2.1 proximal restriction and clustering sequence (*43*) at the C terminus of the indicator sequence for

improved membrane trafficking and perisomatic localization, respectively.

Fly stocks

To create transgenic flies carrying the four improved FRET-opsin GEVIs, we synthesized codon-optimized transcripts for Ace-mNeon2, VARNAM2, pAce, and pAceR using a commercial gene synthesis service (GenScript) and then inserted them in place of green fluorescent protein (GFP) in the *pJFRC7-20×UAS-IVS-mCD8::GFP* (Addgene #26220) and *pJFRC19-13×LexAop2-IVS-myr::GFP* backbones (Addgene #26224). After verifying the sequences of the plasmids, we inserted the plasmids into the attP40 or VK00027 phiC31 docking site to generate *20×UAS-Ace-mNeon2*, *13×LexAop-Ace-mNeon2*, *20×UAS-pAce*, *13×LexAop-pAce*, *20×UAS-VARNAM2*, *13×LexAop-VARNAM2*, *20×UAS-pAceR*, and *13×LexAop-pAceR* flies using a commercial transformation service (Bestgene Inc.).

We obtained MB058B, MB296B, and MB085C split-GAL4 lines from the FlyLight team at Janelia Research Campus and *R82C10-LexA* (#54981) from the Bloomington Stock Center. We raised all flies on standard cornmeal agar media under a 12-hour light-dark cycle at 25°C and 50% relative humidity.

Site-directed saturation mutagenesis

Mutagenic libraries were generated on Ace-mNeon-T2A-NLS-mCherry and VARNAM-T2A-NLS-mCerulean backbones using a preestablished protocol (*18*). Briefly, a set of four forward primers containing degenerate codons WKC, NMC, VWG, or DGG at the target site was pooled with a single, partially overlapping reverse primer, and mutagenizing polymerase chain reaction (PCR) reactions were set up using CloneAmp polymerase (Clontech). After Dpn I treatment to digest unmutated template, the linear PCR products were circularized using InFusion ligase (Clontech) and transformed in TOP10 competent cells (Invitrogen). To obtain up to 19 unique amino acid substitutions at a single target site, 48 colonies were picked and cultured in 96–deep-well culture plates. Plasmid DNA was isolated using Nucleospin 96 Plasmid kit (Macherey-Nagel) on an epMotion 5075 liquid handling workstation (Eppendorf), and purified DNA was collected in 96-well plates. The libraries were sequenced after voltage screening to identify the individual mutations and ensure that at least 19 variants were obtained at every site.

Maintenance and transfection of HEK and excitable HEK cells

HEK293 cells (ATCC® CRL-1573™) were maintained in high-glucose Dulbecco's minimum essential medium (DMEM)/10% fetal bovine serum (FBS). Excitable HEK cells (ATCC CRL-3269) (*30*, *31*) were maintained in DMEM/F12, 10% FBS, 1% penicillin (100 U ml^{-1}), streptomycin (100 μg ml^{-1}), geneticin (500 μg ml^{-1}), and puromycin (2 μg ml^{-1}) as described previously. About 24 hours before transfection, the cells were plated on poly L-lysine–coated 12-mm coverslips or 96-well glass-bottomed plates in antibiotic-free media. Plasmid DNA (0.5 μg per 12-mm coverslip or 0.2 μg per well of a 96-well plate) was transfected using Lipofectamine (ThermoFisher), and cells were imaged 1 to 2 days after transfection. Both cell lines served solely as a system for the expression and characterization of voltage indicators rather than the subject of investigation.

High-throughput semi-automated voltage screening

High-throughput voltage screening (Fig. 1B) was performed on a custom-built platform described previously (*18*). A white-light source pE-4000 (CoolLED, UK) was used for sample illumination. For imaging Ace-mNeon, we used a 472/30-nm excitation filter, 495-nm dichroic mirror, and 520/35-nm emission filter (Semrock). For VARNAM and mCherry (reporter fluorophore in Ace-mNeon constructs), we used a 560/40-nm excitation filter, 585-nm dichroic mirror, and 630/75-nm emission filter (Chroma Technologies Corporation). mCerulean reporter in the VARNAM constructs was imaged using a 455/40-nm excitation filter, 458-nm dichroic mirror, and 480/30-nm emission filter (Semrock). After identifying transfected cells in the reporter channel, time-series fluorescence images were captured in the respective GEVI channels using an ORCA Flash4.0 sCMOS camera (Hamamatsu) at 50 Hz. A single pulse of 60 V/0.5 ms was applied using a Grass S48 Stimulator, 1 s after baseline fluorescence acquisition (F_0). The percent change in fluorescence at time t was obtained using the formula

$$\frac{\Delta F}{F_0}\% = \frac{F(t) - F_0}{F_0} \times 100$$

Platform automation, sample illumination, data acquisition and parallel data analysis were controlled using custom-written virtual instruments in LabView.

Fluorescence voltage imaging in cultured HEK cells

Whole-cell voltage-clamp recordings were performed between 22° and 25°C. The bath solution contained (in mM) 125 NaCl, 2 KCl, 10 HEPES, 30 glucose, 3 $CaCl_2$, 1 $MgCl_2$ (~310 mOsm $liter^{-1}$, pH 7.3). The intracellular solution consisted of (in mM) 125 K-gluconate, 8 NaCl, 0.6 $MgCl_2$, 0.1 $CaCl_2$, 1 EGTA, 4 Mg_2-ATP, 0.4 Na-GTP, and 10 HEPES. Patch pipettes had tip resistances of 4 to 5 megaohms, yielding series resistances of <20 megaohms. In the voltage-clamp mode, voltage steps in increments of 20 mV/ 0.5 s were applied using a MultiClamp amplifier controlled by pClamp10 software.

Fluorescence recordings were obtained using an Olympus upright microscope. Cells were visualized under a 1.0 NA 60× water-immersion objective lens. Ace-mNeon and pAce were imaged using a 505-nm light-emitting diode (LED) (Thorlabs) and a filter set composed of a 509/22-nm excitation filter, 526-nm dichroic mirror, and 544/24-nm emission filter (Semrock). VARNAM and pAceR were illuminated using a 565-nm LED (Thorlabs), 560/40-nm excitation filter, 585-nm dichroic mirror, and 630/75-nm emission filter (Semrock). The illumination intensity at the sample plane for all indicators was 15 to 20 mW mm^{-2}. Fluorescence time-series images (1 to 5 kHz) were captured using a NeuroCCD camera, controlled via NeuroPlex software (RedShirtImaging, GA). Fluorescence response traces were extracted by ranking each pixel by their signal-to-noise ratios, where the noise was calculated as the root mean square value of the baseline fluorescence fluctuations. The top 25% of the SNR-ranked pixels were used to calculate the $\Delta F/F$ values shown in Fig. 1D and fig. S5. Probe kinetics for activation (τ_{ON}) and deactivation (τ_{OFF}) were calculated from 5-kHz recordings obtained in HEK cells, by fitting the first 50 ms of the step responses using a double exponential equation as described previously (*76*).

Surgical dissection of live flies

We created an optical window on the fly head using an ultraviolet (UV) laser microsurgery system, as described previously (*77*). In brief, we anesthetized the flies by placing them on ice for 1 min and then transferring them to a cooled surface (~4°C) consisting of an aluminum thermoelectric cooling block. We then glued the fly's thorax with a 125-μm-diameter fused silica optical fiber (PLMA-YDF-10/125, Nufern) on a custom-made plastic fixture. To minimize head motion, we glued the fly's head to the thorax using a UV light curing epoxy (NOA 89, Norland). After transferring the mounted fly to the surgery station, we created an optical window in the cuticle by laser-drilling a 150-μm-diameter hole (30 to 40 pulses, delivered at 100 Hz, 36 mJ per pulse, as measured at the specimen plane). Immediately after surgery, we applied 1 ml of UV epoxy (NOA 68, Norland; refractive index: 1.54; transmission 420 to 1000 nm: ~100%) and cured it for ~30 s to seal the cuticle opening.

Visual cortical surgeries

Animal experiments were performed according to the guidelines of the National Institutes of Health and approved by The John B. Pierce Laboratory Animal Care and Use Committee.

Intracranial AAV injections

C57BL/6J wild-type and VIP-*Cre*, SST-*Cre*, VIP-*Flp*, and NDNF-*Cre* transgenic mice were

purchased from The Jackson Laboratory (JAX #664, #31628, #13044, #28578, #28536). NDNF-*Cre*$^{+/+}$ or SST-*Cre*$^{+/+}$ mice were crossed with VIP-*Flp*$^{+/+}$ to generate the NDNF-*Cre*$^{+}$/VIP-*Flp*$^{+}$ and SST-*Cre*$^{+}$/VIP-*Flp*$^{+}$ double driver lines. The following AAV vectors were custom-produced at the University of North Carolina Vector Core at high titers (>1 × 10^{13} GC ml^{-1}): AAV/DJ-CAG-DIO-Ace-mNeon2, AAV2/Retro-CaMKII-Ace-mNeon2, AAV/DJ-CAG-fDIO-pAce, AAV2/Retro-CaMKII-pAce, AAV/DJ-CAG-fDIO-VARNAM2, AAV2/Retro-CaMKII-VARNAM2, and AAV/DJ-CAG-DIO-pAceR. All AAV vectors above encode soma-targeted versions of the indicators. AAV5-CaMKII-mCherry-*Cre* and AAV2/Retro-EF1A-mCherry-IRES-*Cre* viruses were purchased from the UNC Vector Core and Addgene (#55632), respectively.

Mice were used without regard to sex; we used a total of 21 males and 23 females in this study. Stereotactic AAV injections were performed in 3- to 4-month-old mice under 1.5% (v/v) isoflurane anesthesia. Each animal received five injections in area V1. The coordinates for the V1 injections (Figs. 1, H to K; 2; 3; 5, A to L; and 6, A to C; and figs. S16, S17, S19, and S21) were [in mm from Bregma; (AP, ML, and DV): 2.5, 2.5, and 0.2 (site 1); 2.8, 2.0, and 0.2 (site 2); 3.0, 2.5, and 0.2 (site 3); 3.4, 2.0, and 0.2 (site 4); 3.6, 2.75, and 0.2 (site 5). For PN projection labeling in the anteromedial (AM) visual cortical area (Figs. 1J and 2E and fig. S21), the coordinates were (AP, ML, and DV): 3.0, 0.96, and 0.4. Injections were performed using beveled glass micropipettes delivering a total of 50 to 100 nl virus per site at a rate of 100 nl/min.

For targeted recordings from identified neuron types (Figs. 1, H to K, and 2; and figs. S16, S17, and S19), AAV/DJ-CAG-DIO-Ace-mNeon2 (or AAV/DJ-CAG-fDIO-pAce) was injected in *Cre*- (or *Flp*)-recombinase–expressing transgenic driver lines. For DUPLEX imaging (Figs. 3 and 5, A to L), AAV/DJ-CAG-DIO-Ace-mNeon2 and AAV/DJ-CAG-fDIO-pAce viruses were mixed at a 1:3 (v/v) ratio for injections in NDNF-*Cre*$^{+}$/VIP-*Flp*$^{+}$ or at a 1:1 ratio for injections in SST-*Cre*$^{+}$/VIP-*Flp*$^{+}$ mice. For DUPLEX recordings from PNs with VIP^{+} interneurons in VIP-*Flp*$^{+}$ mice (Figs. 3, L and M, and 5, I to L; and fig. S21), the AAV/DJ-CAG-DIO-Ace-mNeon2 virus was mixed with the AAV5-CaMKII-mCherry-*Cre* virus for Ace-mNeon2-labeling of PNs and injected together with an equal volume of the AAV/DJ-CAG-fDIO-pAce virus for pAce-labeling of VIP^{+} interneurons. To lower PN labeling densities by labeling a subset of neurons projecting to a higher-order visual cortical area (Figs. 1J and 2E), the AAV/DJ-CAG-DIO-Ace-mNeon2 virus was injected locally in V1, whereas the AAV2/Retro-EF1A-mCherry-IRES-*Cre* virus was delivered to the AM cortical area.

For dual-color imaging (Fig. 6, A to C), AAV/DJ-CAG-DIO-Ace-mNeon2 and AAV/DJ-CAG-fDIO-VARNAM2 were mixed at a 1:1 (v/v) ratio for injections in an SST-*Cre*$^{+}$/VIP-*Flp*$^{+}$ background.

Histology and confocal imaging

For confocal imaging of the cell type–specific expression of Ace-mNeon2 in area V1 (Fig. 2, B to E, subpanel a), injected mice were transcardially perfused with ice-cold Sorenson's buffer (pH 7.4) followed by 4% paraformaldehyde. The brains were isolated and post-fixed overnight at 4°C. Forty- to 60-μm-thick coronal sections comprising the visual cortical areas were prepared on a Leica vibratome and mounted on gelatin-coated glass microscope slides using ProlongGold (Invitrogen). Confocal micrographs were obtained using Zeiss LSM 710 under a 20× air objective.

Headpost and cranial window implantation

Headpost and cranial windows were implanted between 25 and 30 days after injection with some modifications to a preestablished protocol (*78*). Mice were anesthetized using a mixture of ketamine (100 mg/kg) and xylazine (16 mg/kg). A custom-designed titanium head post was affixed to the skull using C&B Metabond (Parkell), after which a 3-mm-diameter circular craniotomy was made over the injection area in V1. A sterile double-glass window, assembled by gluing one each of 3-mm- and 5-mm-diameter circular coverslips (Warner), was secured in place using Vetbond, as previously described (*78*). C&B Metabond was applied over the window margins and the remainder of the exposed skull. Carprofen (5 mg/kg, subcutaneously, every 24 hours for 48 hours) and buprenorphine (100 μg/kg, subcutaneously, every 12 hours for 48 hours) were administered as part of postoperative analgesia. Before awake imaging experiments, the headposted mice were handled and habituated to run on a custom wheel every day for up to 2 weeks in 10- to 20-min training sessions. Imaging began once the animal was fully wheel trained.

Hippocampal CA1 surgeries

The Stanford Administrative Panel on Laboratory Animal Care (APLAC) approved all procedures involving animals, and we complied with all ethical regulations.

Hippocampal AAV injections

C57BL/6J wild-type and SST-*Cre* transgenic mice were purchased from The Jackson Laboratory (JAX #664 and #013044). Mice (aged 8 to 16 weeks at start) underwent two surgical procedures under isoflurane anesthesia (1.5 to 2% in O_2). In the first procedure, we injected AAVs to express the fluorescent voltage indicators. In the second procedure, performed about a week after viral injection, we inserted a cannular implant for hippocampal imaging.

The coordinates for CA1 injections in Figs. 4 and 6, D to F, and figs. S23 and S24, were (in mm from Bregma; AP, ML, DV) −1.8, −2.5, −1.1 and −1.3, −1.3, −1.1. The coordinates for retrograde labeling in the lateral septum (LS) (Fig. 6, D to F), entorhinal cortex (EC) (Figs. 5, M to T and 6, D to F; and figs. S23, S24, and S26), and anterior cingulate cortex (ACC) (Fig. 5, M to T; and fig. S26) were, respectively (in mm from Bregma; AP, ML, DV) 0.3, 0.3, −3; −4.8, 3.3, −3.5; and 0.8, 0.2, −1.5. We used the viruses AAV/DJ-CAG-DIO-Ace-mNeon2 and AAV2/Retro-CaMKII-pAce to label SST^{+} neurons and EC-projecting neurons, respectively (Fig. 4); AAV2/Retro-CaMKII-VARNAM2 and AAV2/Retro-CaMKII-Ace-mNeon2 to label EC-projecting and ACC-projecting neurons, respectively (Fig. 5); AAV2/Retro-CaMKII-Ace-mNeon2, AAV2/Retro-CaMKII-pAce, and AAV/DJ-CAG-DIO-pAceR to label EC-projecting and LS-projecting neurons and SST^{+} neurons, respectively (Fig. 6); and AAV/DJ-CAG-DIO-pAceR and AAV2/Retro-CaMKII-VARNAM2 to label SST neurons and EC-projecting neurons, respectively (fig. S23). All viral vectors had titers of >10^{12} genome copies ml^{-1} and were custom produced at the UNC Vector Core.

Cannular implant fabrication and preparation of LFP electrodes

Cannula implants were prepared under a stereomicroscope (Leica MZ7-5) with a fully equipped solder station. The hippocampal cannula consisted of a circular borosilicate cover glass (3 mm in diameter, 170 ± 5 mm thickness, Schott) glued to the end of a 3-mm outer diameter (OD), 1.5-mm-long stainless-steel ring, using UV-curable adhesive (Loctite 3105) (Figs. 5, M to T, and 6; and fig. S23).

For the dual-modality optical-LFP hippocampal recordings (Fig. 4), we affixed three ~1-cm-long, ~50-μm-diameter tungsten wires coated with single polyimide insulation (M215580, California Fine Wire) to the optical cannula at three different axial positions, spaced in increments of ~50 μm. The tip of one of the three tungsten wires was placed flush with the optical window, and the tips of the other two extended beyond the optical window. This set of electrode placements was chosen to maximize the chances that at least one of the electrodes would provide high-quality LFP signals, given that our surgical placement of the implant was performed without fine visual feedback about the exact location of the ~100-μm-thick CA1 pyramidal cell layer. We glued these tungsten wires onto the optical cannula with UV light–cured adhesive, which constrained the electrodes to be laterally offset by 1.5 mm from the center of the imaging window. Next, we soldered a gold-plated pinhead (NC0102069, WPI) onto the end of each tungsten wire projecting away from the imaging window. The reference electrode was

composed of a ~5-mm-long, ~127-μm-diameter, uncoated, stainless-steel wire (#791600, A-M Systems) soldered to a gold-plated pinhead (NC0102069, WPI). Separately, we fabricated a four-channel connector using four gold-plated sockets (NC1456862, WPI) and a connector board (EIB8, Neuralynx).

Hippocampal cannular implantation

To implant the optical cannula, we resected the skin and scalp to expose the dorsal surface of the cranium and removed any remaining connective tissue by cleaning the exposed skull with hydrogen peroxide (H_2O_2). To ensure strong adhesion between the cannula implant and the skull, we slightly roughened the skull surface using a drill bit and then rinsed the cranium with Ringer's solution. We drilled a 3-mm-diameter opening above the right dorsal CA1, sized to allow the cannula implant to fit in snugly. We aspirated the cortex above dorsal CA1 using a 30-gauge blunt needle, under irrigation with ice-cold Ringer's solution. We proceeded with cortical aspiration until the light-scattering, myelinated axon bundles of the corpus callosum became visible. Of the three superimposed layers of myelinated axons, which were visually distinguishable by their distinct orientations, we removed the top two layers with gentle air suction, while making sure to leave intact the *stratum oriens* layer of the hippocampus. (We excluded from further study any mice with surgical damage to CA1, because such damage can lead to local epileptiform activity.) The cannula implant was then inserted and affixed to the skull using UV-curable adhesive (Loctite 3105).

For studies in which LFP recordings were to be performed concurrently with imaging, we drilled a 0.5-mm-diameter hole into the skull above the cerebellum, inserted the reference electrode into cerebellar tissue and then affixed it to the skull with UV-curable adhesive (Loctite 3105). Carprofen (5 mg kg^{-1}) was administered 30 min before the end of the surgery to mitigate pain. To enable head-fixation during in vivo imaging, we secured a custom stainless steel head bar to the mouse's skull using blue light-cured resin (Flow-it ALC, Pentron). Carprofen (5 mg kg^{-1}) was administered up to 2 days after surgery as part of postoperative analgesia. Mice recovered for ~2 weeks before the start of voltage imaging sessions.

Voltage imaging in awake flies

The fly data was acquired at Stanford University. The optical instrumentation described below was used to obtain the data in Fig. 1, E to G; and figs. S13, S14, and S25.

Instrumentation and imaging

To image voltage dynamics in flies, we used a custom-built upright epi-fluorescence microscope and a 1.0 numerical aperture (NA) 20× water-immersion objective (XLUMPlanFL, Olympus). For Ace-mNeon and pAce imaging, we used a 503/20-nm excitation filter (Chroma), 518-nm dichroic (Chroma), and 534/30-nm emission filter (BrightLine). We illuminated the sample using the 500-nm wavelength module of a solid-state light source (Spectra X, Lumencor), with 5 to 7 mW of optical power at the specimen plane. For VARNAM and pAceR imaging, we used a 559/25-nm excitation filter (Semrock), 580-nm dichroic (Chroma), and 630/50-nm emission filter (Semrock). We illuminated the sample using the 550-nm wavelength module of the light source, with 8 to 10 mW of optical power at the specimen plane. We acquired images at 1000 Hz, using a scientific-grade CCD camera (Zyla 4.2, Andor) and 2 pixel–by–2 pixel binning.

Odor delivery

To image odor-evoked activity, we perfused odors to the flies' antennae using a custom-built olfactometer that delivered constant airflow (200 ml min^{-1}) to either the control path (mineral oil) or the odor path (odorant dissolved in mineral oil). We presented 5% isoamyl acetate (CAS# 123-92-2, Sigma-Aldrich Inc.), 3% benzaldehyde (CAS# 100-52-7, Sigma-Aldrich Inc.), or apple cider vinegar (Bragg Inc.) to the fly using a probe needle [1.7 mm inner diameter (ID), Grainger Inc.], ~3 mm in front of the antenna. Each odor delivery trial lasted for 5 s.

Spike extraction

To extract the voltage data, we motion-corrected the raw videos using the Turboreg algorithm for image registration (http://bigwww.epfl.ch/thevenaz/turboreg/) (*79*). We then selected pixels whose mean fluorescence intensity, averaged over the entire movie, was in the top 10% of all pixels across the field of view; we defined the union of these high-ranking pixels as the region of interest (ROI). We corrected for photobleaching by fitting a double exponential function to the spatially averaged fluorescence across the ROI, $F(t)$, and then dividing $F(t)$ by the fitted double exponential trace. We then computed time-dependent changes in the relative fluorescence intensity, $\Delta F(t)/F = (F'(t)-F_0)/F_0$, where $F'(t)$ was the time-dependent fluorescence intensity trace across the ROI after the photobleaching correction and F_0 was the time-averaged baseline intensity in the ROI after the photobleaching correction. To identify individual spikes, we high-pass filtered the $\Delta F(t)/F$ trace by subtracting a median-filtered (40-ms window) version of the trace and identified spikes as local peaks that surpassed a set threshold (3 SD for PPL1-DANs, 2 SD for MBON-γ1pedc>α/β). We estimated the instantaneous, time-dependent spike rate by tabulating the number of spikes within a 100-ms sliding window.

To determine the mean spike waveform, we averaged the waveforms of all spikes across a trial. We then performed a spline interpolation (10-μs intervals) of the mean waveform and, from the resultant, determined the spike amplitude and duration. Determinations of the spike detection fidelity for studies in live flies were performed using the same formulas as were used for the studies in mice (see section Determinations of the spike detection fidelity index, d').

Single- and dual-channel voltage imaging in V1 in running mice

All data from brain area V1 (Figs. 1, H to K; 2, B to E; 3; 5, A to L; and 6, A to C; and figs. S16, S17, S19, S21, and S22) were acquired at the John B. Pierce Laboratory. Before the awake animal experiments, head-posted mice were handled and acclimated to a custom 15-cm-diameter 3D-printed wheel for ~2 weeks in training sessions of 10 min per day.

Instrumentation and imaging

For in vivo neocortical voltage imaging, mice implanted with cranial windows were head-fixed by securing the head post to two points on the custom wheel with thumbscrews. Neurons expressing soma-targeted indicators at cortical depths of ~50 to 200 mm below the pial surface (Fig. 2, B to E, subpanel a) were imaged on a custom-built dual-channel upright fluorescence microscope equipped with an epi-illuminator module (WFA2001, Thorlabs), an EYFP/mCherry (59026, Chroma) dual-bandpass filter set (comprising a 59026× excitation filter with passbands of 503/12 and 575/15, a 69008bs dichroic mirror with passbands of 470/20, 540/25 and 630/50, and a 59026m emission filter with passbands of 535/15 and 635/35), and a 20X 1.0 NA Olympus XLUMPLFLN water immersion objective.

The illumination from a pair of LEDs, emitting light of 505- and 565-nm wavelengths (M505L4 and M565L3, Thorlabs, respectively), was collimated with a pair of aspheric condenser lenses (ACL2520U-A), one for each LED. For dual-channel imaging (Fig. 6, A to C), illumination from the two LEDs was combined using a 550-nm long-pass dichroic mirror (T550 LPXR, Chroma). The illumination intensity at the sample plane in each of the red and green channels was ~25 mW mm^{-2}.

Fluorescence emissions returning from the sample plane were directed by a 585-nm long-pass dichroic mirror (T585 LPXR, Chroma) into the two fluorescence detection arms of the microscope. Emissions from Ace-mNeon2 and/or pAce passed through a 520/35-nm bandpass filter (FF01-520/35-25, Semrock). Emissions from VARNAM2 and/or pAceR passed through a 630/75-bandpass filter (ET630/75m, Chroma). Within each fluorescence detection arm, a 0.75× camera tube lens (WFA4101, Thorlabs) focused the fluorescence onto a high-speed sCMOS camera (Orca Flash 4.0 v3, Hamamatsu).

For the dual-color, dual-polarity imaging studies of V1 using Ace-mNeon2, pAce, and VARNAM2 in Fig. 6, A to C, both the 505- and 565-nm LEDs were ON concurrently, and we acquired data simultaneously from both cameras. For synchronized registration of the images, the two cameras were operated in their external trigger mode, allowing us to trigger image acquisition on both cameras by sending them a single, common transistor-transistor logic (TTL) pulse. We further verified that image acquisition by the two cameras was synchronized by using the time stamps on the two videos. To ensure that images from the two channels were spatially aligned, we calibrated images against an alignment target and confirmed this during each imaging session based on reference points, e.g., the location of landmark vasculature.

For all experiments in Figs. 1, H to K; 2, B to E; 3; 5, A to L; and 6, A to C; and figs. S16, S17, S19, S21, and S22, fluorescence time-series images (2048 pixels by 512 pixels) were collected at 400 Hz with 4-by-4 binning. We typically acquired 3 or 4 trials of data from each imaging field of view, and we imaged ~6 to 8 fields of view per session. Over the course of several days, but in some cases over 3 to 4 weeks, we revisited and reimaged each field of view two or three more times, using vascular landmarks to identify the approximate tissue locations of prior imaging sessions.

We inferred the cortical depth of the imaged neurons based on the laminar organization, as reported in the published scientific literature, of the different cortical cell types that we examined. Specifically, we inferred that we recorded neurons in cortical layers 1, 2, and 3 based on published evidence that (i) cortical $NDNF^+$ interneurons are layer 1 specific (*41*, *47*, *48*) and that (ii) cortical PNs, selectively targeted using CaMKII, and SST^+ interneurons, selectively targeted using the published SST-*Cre* transgenic line (*40*) are both absent in cortical layer 1. PN projection neurons from the AM area reside in cortical layer 2/3, between 100 and 200 μm below the pial surface (*39*, *42*). SST^+ interneurons reside at depths >200 μm beneath the pial surface (*40*), and VIP^+ interneurons reside at depths >50 to 100 μm below the pia (*49*). Confocal micrographs showing cell subtype–specific labeling in V1 (Fig. 2, B to E, subpanel a) further confirmed the laminar organization of the imaged cortical cell classes in the supragranular layers and the relative cortical depths of the distinct neocortical subclasses.

Visual stimulus presentations

In Fig. 1J, visual stimuli were generated using the Psychophysics toolbox on MATLAB and were presented to awake, stationary mice on an LCD video monitor (1280 pixels by 1024 pixels, 20 inches by 16 inches, 60-Hz refresh rate, mean luminance of 250 cd m^{-2}). The monitor was placed ~15 cm from the animal, perpendicular to the surface of the right eye (contralateral to the injection area). To map the receptive field of an imaged neuron, static bright and dark stimuli were presented individually in a pseudorandom sequence within each square of a 3-by-4 grid extending across the entire video monitor. Once the cell's receptive field location was approximately mapped, to characterize the cell's orientation-selective responses, we sequentially presented a set of drifting sinusoidal gratings at one of eight orientations, spaced by increments of 45° and presented in a pseudorandom sequence. The spatial frequency of the grating was 0.04 cycles per division, and the temporal frequency was 2 Hz. Each trial lasted 16 s, with interstimulus intervals of 500 ms.

Induced state transitions and pupillometry

In Figs. 2, B to E, and 5, A to L, to induce a change of state, a brief 50-ms air puff was delivered to mice at rest using a small tube aimed at the back of the animal. Wheel position was tracked using a programmable angle sensor (KMA210, Digikey). A data acquisition device (NI USB-6259, National Instruments) registered the wheel's position and delivered TTL pulses to initiate image acquisition. Software code that was custom written in LabView 2019 (National Instruments) controlled data acquisition.

For the state-transition experiments in Figs. 2, B to E, and 5, A to L, an infrared camera (Basler A602f) was used to measure the pupil diameter at a frame rate of 15 Hz. Pupil diameter was measured in real time using custom code written in LabView. An annulus region of interest was drawn over the pupil, with the inner circle located at the center of the eye and the outer circle extending past the edge of the pupil. The edge-detection functionality of the LabView Vision Development Module was used to detect dark-to-light transition points along a set of radial measurement lines drawn from the inner circle and extending to the outer circle. The pupil diameter was calculated by fitting a circle to the set of detected dark-to-light transition points. The threshold level for edge detection and the number of transition points were manually optimized for each individual mouse.

Single- and dual-channel voltage recordings in CA1 in running mice

All imaging studies of hippocampal area CA1 were performed at Stanford University. The optical instrumentation described below was used to acquire the CA1 data shown in Figs. 4; 5, M to T; and 6, D to F; and figs. S23, S24, and S26.

Instrumentation and imaging

For green DUPLEX studies (Fig. 4), simultaneous dual-color (Fig. 5, M to T; and figs. S24 and S26), and triple-population voltage imaging (Fig. 6, D to F), we used a custom-built microscope with a 16× 0.80 NA, 3.0-mm working distance (WD), water immersion objective lens (Nikon N16XLWD-PF). For red-DUPLEX (fig. S23), we used a 25× 1.0 NA, 4.0-mm WD, water immersion lens (Olympus XLPLN25XSVMP2). The recording depth for all hippocampal data was ~50 to 100 μm, as set by the intrinsic cellular organization of the dorsal CA1 area. A motorized stage (Sutter MP-285) was used for fine axial focusing.

Illumination from two LEDs (UHP-F-470 and UHP-F-545, Prizmatix) was combined using a long-pass dichroic mirror (511 nm, Prizmatix) and then filtered using a dual-bandpass clean-up filter (Semrock, FF01-482/563-25, with passbands of 482/18 and 563/9 nm). A dual-band dichroic mirror (Semrock, Di01-R488/561-25x36, with passbands of 525/40 and 690/108 nm) reflected the combined illumination toward the specimen and transmitted the returning fluorescence emissions. The illumination intensity at the sample plane from each LED was ~25 to 75 mW mm^{-2}.

In the emission pathway, to separate fluorescence in the two color channels, we used a 550-nm short-pass dichroic mirror (70 mm by 100 mm, custom designed, Alluxa) and a pair of emission filters, each of which was specific for one of the two color channels: 520/41 nm (70-mm diameter, custom designed, Alluxa) for Ace-mNeon2 and pAce and 609/62 nm (Semrock, FF01-609/62-50) for VARNAM2 and pAceR.

Each arm of the fluorescence collection pathway was composed of a tube lens of 85-mm effective focal length (Canon, EF 85 mm f/1.2L II USM) and a high-speed scientific-grade CMOS camera (Hamamatsu ORCA Fusion Digital CMOS camera; Hamamatsu Photonics K.K., C14440-20UP). Data acquisition was controlled by custom software with a field programmable gate array (FPGA)–based (Xilinx Z-7010) back end and a front end written in LabView 64-bit 2019 (National Instruments). Note that although our labs were acquainted with and therefore used LabView to implement the hardware control, other programming languages (e.g., C++, MATLAB, Python) can also be used to control data acquisition if the camera manufacturer provides an appropriate software development package.

As with dual-channel imaging in V1, dual-channel imaging in CA1 (Figs. 5, M to T, and 6, D to F) was performed with both the 470- and 545-nm illumination sources turned ON (or OFF) simultaneously at the beginning (or end) of each trial. Frame acquisitions were synchronized across the two cameras using an external electronic trigger generated by the FPGA. We achieved subpixel spatial alignment between the fields of view of the two cameras by registering them with an alignment target. We verified proper registration using image landmarks, e.g., large blood vessels.

Images were collected at 600 Hz with no spatial binning. Live data from each camera were stored as native DCAM image files (.dcimg) on two separate 2-TB SSD drives. The data were batch-processed offline using the custom pipeline SpikeImagingAnalysis (see section Data extraction pipeline and downstream analyses of hippocampal CA1 datasets for details), which we wrote in MATLAB (Mathworks).

Rest-to-run state transition

For the studies in Fig. 5, M to T, we used a mouse's running wheel (8 cm wide, 13 cm in diameter) that was 3D-printed in PLA plastic. The wheel surface was covered with a self-adherent wrap (Coban, 3M). Angular displacements of the wheel were tracked using a rotary encoder (Optical AB Phase Quadrature Encoder 600P/R, Amazon). A data acquisition interface (BNC-2090A, National Instruments) controlled from LabView was used to acquire the wheel displacement data.

Mice were habituated on the wheel for at least 2 days, for at least 15 min per day, before brain-imaging sessions began. To trigger rest-to-run behavioral state transitions, a brief air puff was delivered to the mouse's back. The air puff intensity was ~30 psi and was administered with a 20-gauge blunt needle placed 1 to 2 cm away from the mouse. For each field-of-view, we performed high-speed voltage imaging across a 30-s trial (18,000 frames at 600 Hz), starting with the mouse at rest. Within each trial, a TTL signal (five pulses at 5 Hz) triggered the air puff delivery after 10 or more seconds of baseline data had been acquired. Each experimental session involved imaging six fields of view, with one air-puff trial per field of view.

LFP recordings

We amplified the electrophysiological signals using a digital recording head-stage (RHD 16-Channel, Part #C3334, Intantech) that was attached to our custom-designed connector. We then acquired the digital data at a sampling rate of 2 kHz using a USB data acquisition board (RHD USB interface board, Part #C3100, Intantech).

To synchronize the optical and electrical recording instruments, we generated a synchronizing digital signal (hereafter called "syncTTL"), which was composed of a square wave signal with a 50% duty ratio and a 1-s-long on-state but with intervals of random duration between pulses, to enable unambiguous temporal alignments. The syncTTL signal was externally and independently generated by a data acquisition system (USB-6003, National Instruments) and was recorded concurrently by both the electrical and the optical data acquisition systems (at 600 Hz and 2 kHz, respectively).

To temporally align the optical and electrical physiological signals (recorded at 600 Hz and 2 kHz, respectively), we first bandpass-filtered the LFP traces (the filter's 3-dB high-frequency cutoff was 500 Hz and the 3-dB low-frequency cutoff was 0.1 Hz). Then, we interpolated the LFP traces and the squared syncTTL signal so that the sampling rates of the resulting traces matched the 600-Hz sampling frequency of the optical data. We used the MATLAB function *interp1* with the "spline" method to interpolate the continuously valued LFP trace. To interpolate the binary- valued syncTTL signal, we used the *interp1* function with the "nearest" method. Finally, we temporally aligned the optical and electrical traces according to the temporal registration provided by the paired set of syncTTL recordings.

Data extraction pipeline and downstream analyses of V1 datasets

Extraction of individual neurons and their fluorescence activity traces for imaging studies in area V1 (Figs. 1, H to K; 2; 3; 5, A to L; and 6, A to C; and figs. S15 and S17 to S22) was performed at the John B. Pierce Laboratory using the open-access Python-based automated pipeline VolPy (*44*), which consisted of the following steps:

1) File loading. We modified the VolPy code to support the .dcimg file format of the data taken with the Hamamatsu camera.

2) Motion correction. Each movie was motion-corrected using the NoRMCorre algorithm (*80*), which is built into the VolPy pipeline.

3) Cell segmentation. Steps 3 and 4 are included as part of the updated SpikePursuit algorithm (*13*) that is built into the VolPy pipeline (*44*) for spike extraction and denoising. Whereas the original version of SpikePursuit used manual input parameters to identify the location of each neuron (*13*), in the updated version, neuron identification and segmentation are performed automatically using a convolutional neural net known as "Mask R-CNN" (*81*), which provides binary masks covering each identified cell.

4) Trace denoising and spike extraction. Fluorescence activity traces are extracted from the regions of the movie covered by spatial masks (ROIs) from step 3. and are then corrected for photobleaching using a high-pass filter (third-order Butterworth filter, 1/3 Hz cut-off). For each ROI, the following two steps are then executed in a loop for three iterations. The first step estimates spike times and the second refines the spatial filter. (Step 1) To estimate spike times, the first eight principal components of background pixels (at >12 pixels from the ROI) are extracted and removed from the fluorescence movie using ridge regression. The resulting trace of fluorescence activity within the ROI after background removal is then high-pass-filtered (fifth-order Butterworth filter, 1 Hz cut-off) to obtain a trace, t_s, that contains activity at frequencies typical of neural oscillations and spikes. Spikes are identified as threshold crossing events, and the spike waveforms are averaged to obtain a spike template. A matched filter (*82*) is then derived from this spike template and from additive white Gaussian noise, with the goal of identifying a template waveform that can be applied to a noisy signal. To denoise traces, the matched filter is applied to t_s and spikes are detected again. Lastly, the reconstructed fluorescence trace representing the spike train t_{rec} is obtained by convolving the spike template and the inferred spike train. (Step 2) To refine each cell's spatial mask, its reconstructed trace t_{rec}, is regressed onto the fluorescence movie using ridge regression.

Automated assignment of cell classes in DUPLEX recordings

To identify the polarity of the neural spike waveforms in DUPLEX recordings (Figs. 3; 5, A to L; and 6, A to C; and figs. S20 to S22), for each cell, we identified putative spikes in the t_{rec} trace as negative- or positive-going that deviated >3 SD from baseline noise levels. We identified the polarity of the indicator expressed in the cell according to whether it exhibited more negative- or positive-going events (fig. S20). Because VolPy extracts action potentials (APs) through template-matching (*44*), only typical AP waveforms were considered during polarity assignment. Traces with no spikes were not assigned and were removed manually from downstream analyses (see analysis pipeline, fig. S20).

Spike rate, spike modulation index, and correlational analyses

We exported data from VolPy as MATLAB files for downstream analyses. Each cell's firing rate (FR) was estimated by sliding a rectangular window (of 100 ms for Fig. 2 and fig. S19 or 20 ms for Figs. 3, H to M, and 5, C, G, and K; and fig. S17) along the spike train followed by smoothing with a Gaussian kernel of 100 ms using the *smooth* function in MATLAB. The air puff–induced spike modulation indices in Fig. 2, B to E (subpanel d) and 5, D, H, and L; and fig. S19 were calculated as $(FR_{arousal} - FR_{baseline})/(FR_{arousal} + FR_{baseline})$, where FR is the mean firing rate over a 750-ms time window that was either before or after the air puff. In Fig. 2, B to E (subpanels c and d), we temporally aligned the spike rates to the air-puff onset. Pairwise correlation coefficients and cross-correlation values in Figs. 2, F to I; 3, H to M; and 5, C, G, and K; and figs. S17, S21, and S22 were calculated using the *corrcoef* and *xcorr* functions in MATLAB.

Data extraction pipeline and downstream analyses of hippocampal CA1 datasets

Trace extraction for the hippocampal data (Figs. 4; 5, M to T; and 6, D to F; and figs. S18, S23, S24, and S26) was performed at Stanford University using a custom pipeline written in

MATLAB (SpikeImagingAnalysis, https://github.com/sihaziza/SpikeImagingAnalysis_public). This pipeline consisted of the following steps:

1) File loading and motion correction. Raw 16-bit .dcimg video files from voltage-imaging sessions were loaded into memory, underwent spatial (2 by 2) binning, and saved in .h5 data format. Movies underwent motion-correction using NoRMCorre (*79*) and were then cropped so as to remove parts of the images that did not contain fluorescently labeled brain tissue. The NoRMcorre parameter shift_method was set to "cubic," instead of the default "fft."

2) Detrending. To account for fluorescence photobleaching, at each time point in the fluorescence video, $F(t)$, we normalized each pixel by $F_0(t)$, the time-varying value of the pixel's baseline fluorescence, which we computed using a temporal low-pass filter (fourth-order Butterworth filter, 0.5-Hz cut-off frequency). The resultant is the detrended movie, $F(t)/F_0(t)$.

3) Cell extraction. We extracted individual neurons and their time traces of membrane voltage activity using the automated cell-extraction algorithm EXTRACT (*45*, *46*). EXTRACT is generally agnostic about cells' morphologies and activity patterns and therefore has broad applicability to both one- and two-photon fluorescence imaging studies of neural activity. It is based on the mathematical framework of robust statistics, which generally allows it to surpass other widely used cell-extractions algorithms, such as CNMF (*83*) and PCA/ICA (*84*), in the removal of background fluorescence contaminants and cross-talk between overlapping cells (*46*).

In brief, EXTRACT is designed to automatically identify each neuron's spatial profile, S, and retrieve its activity trace, T, using an iterative process that is applied to individual cells, one at a time. This "cell finding" process is followed by an iterative "cell refinement" process.

During cell finding, EXTRACT finds a seed pixel that attains the movie's maximum fluorescence intensity and initializes a candidate cell image at that pixel. The estimates of S and T are iteratively updated in an alternating manner by using a robust regression at each step and a one-sided Huber loss function (*46*). Once the estimates of S and T stabilize for an individual cell, the cell's inferred fluorescence contribution is subtracted from the movie, and the entire set of steps is repeated for another cell. This process continues until no more putative cells are found, which is determined to occur when the peak value for the activity trace of the seed pixel falls below a predefined threshold value (>3× SD of background noise).

During the iterative process of "cell refinement," at each iteration, the set of estimated traces {T} is updated using robust estimation while holding fixed the set of cells' spatial profiles. Next, the spatial profiles {S} are updated using robust estimation while holding fixed the activity traces, {T}. A validation procedure then checks each putative cell against a set of predetermined quality metrics and removes any cell with metrics below predetermined threshold values. This three-step process runs for a fixed number of iterations, and EXTRACT outputs the final estimates of each cell's spatial profile and activity trace.

For DUPLEX studies that involved a pair of similarly colored GEVIs but with opposite polarities, we ran EXTRACT twice: once on the detrended video, $F(t)/F_0$, to identify active neurons expressing the positive polarity indicator, and once on a sign-inverted version of the detrended video, $F(t)/F_0$, to identify active neurons expressing the negative polarity indicator.

4) Spike timing estimation. To precisely estimate each cell's spike train based on its fluorescence activity trace, we used the statistical method MLspike (*85*), which outputs the spike train that is most likely to have led to the observed fluorescence trace. The algorithm requires five input parameters: the saturation S, single-spike amplitude A, single-spike time constant τ, baseline fluctuation "drift," and noise level σ. The saturation parameter, defined as the number of spikes at which the indicator provides a full-amplitude response, was set at S = 1. We estimated A and τ using a double-exponential fit to the mean spike waveform, which we computed using only temporally isolated spikes. We empirically estimated the parameter, "drift," by computing peak-to-peak amplitude variation of a low-pass-filtered (fourth-order Butterworth filter, 50-Hz cut-off frequency) version of the cell's activity trace that retained subthreshold activity up to the gamma frequency band but not spiking activity. σ was estimated as the standard deviation of the residual signal, defined as the difference between the raw and a denoised version of the cell's fluorescence activity trace (we obtained by applying a wavelet denoising of degree one).

Computations of oscillatory phase

In Fig. 4, G and H, to calculate the phase of spiking with respect to theta oscillations (5 to 10 Hz), we first band-pass-filtered both the optical voltage trace and the LFP trace at the theta frequencies using the *butter* and *filtfilt* MATLAB functions (fourth-order Butterworth filter, cut-off frequency of 5 to 10 Hz). We then computed the phase of each filtered trace by performing a Hilbert transform (*hilbert* and *angle* functions). For Fig. 4G, we calculated the timing of each spike relative to the period of that oscillation cycle (in degrees). For each cell, we then computed the circular mean to generate Fig. 4H.

Spike-rate analyses

In Fig. 5, O to Q, all traces (spike rasters and speed traces) were temporally aligned to the rest-to-run transition, which we detected as a discrete change in the running speed (thresholded at >2 cm s^{-1}). We then computed the cells' time-varying spiking rates using a 100-ms sliding window. For each neuron type studied, we averaged the time-varying spike rate across all cells to determine the mean spike rate (Fig. 5P). To assess the rest-to-run fold change in instantaneous spiking rates (Fig. 5Q), we computed the spiking rate in the 2-s intervals immediately before and immediately after the state transition.

Analyses of subthreshold activity

In Fig. 5, R to T, neuronal traces from all fields of view were temporally aligned to the rest-to-run transition. To compute coherence of subthreshold activity between pairs of cells, in either the running or resting states, we first estimated the subthreshold dynamics of each cell by computing low-pass filtered versions (fourth-order Butterworth low-pass filter, cut-off frequency of 50 Hz) of the "drift" output of ML spike for each cell. Next, we computed the magnitude-squared coherence between the two low-pass-filtered time traces by using the MATLAB function *mscohere*, which we applied to 1-s-long segments of data, chosen such that temporally successive segments from the traces overlapped by 0.8 s. To estimate the noise level in such computations, we computed the pairwise coherence of cells belonging to two separate fields of view. In Fig. 4, I to L, we computed the neuron-LFP coherence in a pairwise manner, between the subthreshold activity of each cell and the LFP, determined in the same way as for cell pairs in Fig. 5.

Comparisons of cell-extraction methods

We compared the results from VolPy and EXTRACT to a simple ROI-based approach for cell extraction. For this comparison, we used DUPLEX data providing joint recordings of $NDNF^+$ and VIP^+ interneurons in V1 (Fig. 3, B and C; and fig. S15).

Unlike ROI-based cell extraction, both VolPy and EXTRACT performed comparably in terms of removal of cellular cross-talk (fig. S15, A to H), neuropil contamination (fig. S15, I to N), and hemodynamic artifacts (fig. S15, O to T). Moreover, the inferred biological conclusions were independent of the algorithm used, in that the results obtained using both VolPy and EXTRACT were identical and indicated positively correlated activity within each interneuronal population but no significant correlation of the voltage signals between $NDNF^+$ and VIP^+ interneurons (fig. S15, F to H). However, traces extracted using an ROI-based approach showed spurious pairwise correlated activity, suggestive of increased cellular cross-talk, and the presence of hemodynamic artifacts in the subthreshold traces. In addition, the data obtained from ROI-extracted traces were

inconsistent with prior observations as they showed highly positively correlated activity not only within populations but also anomalously between NDNF$^+$ and VIP$^+$ interneurons (*47*, *48*).

Computations of GEVI impulse responses

In fig. S12, activation and deactivation kernels for each GEVI were determined using a biexponential function from the empirically measured values of each indicator's fast and slow time constants and the relative amplitudes of the fast and slow relaxation processes associated with the indicator's activation and deactivation responses. The empirical values used and the publications from which they are taken are indicated in the caption for table S1.

We determined each GEVI's impulse response function (fig. S12, A and B) by convolving its activation kernel with the rising edge of a 1-ms-duration square voltage pulse (+100-mV depolarization, starting from −70 mV) and its deactivation kernel with the falling edge of the square pulse, and then summing the two resultants at a sampling rate of 5 kHz. To isolate the kinetic aspects of the indicator response, we defined the excursion rate (fig. S12A) as the time-dependent fluorescence emission rate response to the 100-mV voltage pulse, normalized by the indicator's steady-state fluorescence emission rate in response to a maintained 100-mV depolarization (i.e., a 100-mV step function). To account for the different response amplitudes of different GEVIs, we performed the same calculation for each GEVI but without normalizing by the steady-state response amplitude; the resulting plots, termed the "effective 1× AP-$\Delta F/F$" plots (fig. S12B), show each indicator's estimated response to a 1-ms action potential of 100-mV amplitude. To evaluate how different GEVIs respond to a burst of action potentials in quick succession (fig. S12C), we computed indicator responses to a set of three spikes, with each spike modeled as a 1-ms-duration square pulse of 100-mV depolarization, and with the spikes spaced in 3-ms increments. To assess the capability to resolve action potential bursts under typical imaging conditions, we then down-sampled the computed traces to 1 kHz (fig. S12C).

Determinations of the spike detection fidelity index, d′

To compute d', we used a signal detection theory framework that accounts for both the duration and intensity of fluorescence waveforms in optical recordings of action potentials and that characterizes the ability to correctly distinguish instances of a spike from background noise fluctuations within the fluorescence trace (*17*, *38*). As described in our prior work (*38*), if we use N successive samples from a fluorescence detector, $F = (F_1, F_2, \ldots, F_N)$, to detect spikes, the distribution of F follows Poisson statistics in the shot-noise-limited regime. Given a specific observation, F, the Poisson distribution of F enables one to estimate the a posteriori likelihood of two mutually exclusive hypotheses: the null hypothesis, $H^{(0)}$, which posits the absence of a spike; and the alternative, $H^{(1)}$, which posits that a spike occurred. d' can then be calculated as

$$d' = \left(\mu_L^{(1)} - \mu_L^{(0)}\right)/\sigma_L \quad (1)$$

in which μ_L and σ_L respectively represent the mean and variance of the (approximately normal) probability distributions of the log-likelihood ratio, $L(f)$, of the two hypotheses, in the cases when there actually is or is not a spike. The mean, μ_L, and variance, σ_L, of these log-likelihood ratio distributions are given by

$$\mu_L^{(0)} = \frac{F_0}{\nu}\sum_{n=1}^{N}\log(1+s_n) - \frac{F_0}{\nu}\sum_{n=1}^{N}s_n \quad (2)$$

$$\mu_L^{(1)} = \frac{F_0}{\nu}\sum_{n=1}^{N}(1+s_n)\log(1+s_n) - \frac{F_0}{\nu}\sum_{n=1}^{N}s_n \quad (3)$$

$$\sigma_L \approx \sigma_L^{(1)} \approx \sigma_L^{(0)} = \sqrt{\frac{F_0}{\nu}\sum_{n=1}^{N}\log^2(1+s_n)} \quad (4)$$

Where ν is the sampling rate, F_0 represents the baseline fluorescence intensity in time periods that contain no neural spike, and s_n is the mean fluorescence signal at each time bin within a time period that contains the optical waveform of the identified spikes for each neuron. For studies in flies (figs. S13 and S14C), we determined each neuron's d' value by first computing its mean spike waveform, s_n, over an interval of [−25 ms, +25 ms] relative to the spike occurrence time, and then using Eq. 1 to 4 to compute d'.

For studies in mice (figs. S16, F and H; and S18), we first used Eq. 1 to 4 to compute a d' value for each action potential fired by an individual cell and then determined the mean d' value averaged across all spikes in the cell's spike train. We used only spikes that were temporally separated from other action potentials by >10 ms, so as to avoid computational biases that could be introduced by spike bursts, e.g., by instances when a cell does not return to its resting membrane potential between spikes. For each isolated spike, we estimated d' using data within a time interval of [−10 ms, +20 ms] relative to the spike's occurrence time.

To determine how the spike detection error rate depended on the imaging frame rate (fig. S18, A and B), we treated the case in which the decision boundary for classifying instances of $H^{(0)}$ and $H^{(1)}$ was set midway between the two log-likelihood probability distributions [see, e.g., figure 1 of (*38*)]. In other words, false-negative and false-positive spikes were considered equally deleterious. When there are abundant fluorescence photons, the two log-likelihood distributions are each approximately Gaussian, with means that differ by d' in units of σ_L. We used the complementary error function *erfc* in MATLAB to compute the proportion of the area under each log-likelihood probability distribution that was on the opposite side of the decision boundary from the mean of the distribution [i.e., the proportion of cases representing spike detection errors; see figure 1 of (*38*)].

Statistics

For both the V1 and CA1 datasets, we performed statistical tests using standard MATLAB functions or built-in tests in Prism 8 (GraphPad). For two-sample comparisons of a single variable, we always used nonparametric tests, as described in this section.

In Fig. 1D, to test for significant differences in the mean $\Delta F/F$ values of the indicators, we used Mann-Whitney test. In Figs. 2, F to I, and 5, C, G, and K, for comparisons of pairwise correlation coefficients of spike rates for time bins before versus after air puff, we performed Wilcoxon matched-pairs signed rank test. In Fig. 3, I, K, and M, to assess whether neuron pairs exhibited positively versus negatively correlated activity, we compared the mean pairwise correlation coefficients to zero using one-sample Wilcoxon test. In Fig. 4H, to assess statistical differences in the polar plots, we computed the mean and standard deviation of each data distribution and made statistical comparisons between different distributions using circular statistics. Specifically, we used the Hodges-Ajne test to test the hypothesis of nonuniformity of circular data and the Watson-Williams multisample test to test the hypothesis of equal means. In Fig. 5, D, H, and L, to assess whether neuronal spike rates were positively versus negatively modulated by the air puff, we tested whether mean spike modulation indices were significantly different from zero using a one-sample Wilcoxon test.

We did not use power analysis or statistical methods to estimate sample sizes but instead estimated useful sample sizes based on published reports and our prior experiences with voltage imaging. Data exclusion criteria were not preestablished. However, recordings with no spiking neurons were excluded.

REFERENCES AND NOTES

1. K. A. Ferguson, J. A. Cardin, Mechanisms underlying gain modulation in the cortex. *Nat. Rev. Neurosci.* **21**, 80–92 (2020). doi: 10.1038/s41583-019-0253-y; pmid: 31911627

2. Y. Fu *et al*., A cortical circuit for gain control by behavioral state. *Cell* **156**, 1139–1152 (2014). doi: 10.1016/j.cell.2014.01.050; pmid: 24630718
3. C. C. Y. Lee, E. Kheradpezhouh, M. E. Diamond, E. Arabzadeh, State-dependent changes in perception and coding in the mouse somatosensory cortex. *Cell Rep.* **32**, 108197 (2020). doi: 10.1016/j.celrep.2020.108197; pmid: 32997984
4. P.-O. Polack, J. Friedman, P. Golshani, Cellular mechanisms of brain state-dependent gain modulation in visual cortex. *Nat. Neurosci.* **16**, 1331–1339 (2013). doi: 10.1038/nn.3464; pmid: 23872595
5. J. Schiemann *et al*., Cellular mechanisms underlying behavioral state-dependent bidirectional modulation of motor cortex output. *Cell Rep.* **11**, 1319–1330 (2015). doi: 10.1016/j.celrep.2015.04.042; pmid: 25981037
6. B. K. Hulse, E. V. Lubenov, A. G. Siapas, Brain state dependence of hippocampal subthreshold activity in awake mice. *Cell Rep.* **18**, 136–147 (2017). doi: 10.1016/j.celrep.2016.11.084; pmid: 28052244
7. P. Rajasethupathy *et al*., Projections from neocortex mediate top-down control of memory retrieval. *Nature* **526**, 653–659 (2015). doi: 10.1038/nature15389; pmid: 26436451
8. K. Q. Shan, E. V. Lubenov, M. Papadopoulou, A. G. Siapas, Spatial tuning and brain state account for dorsal hippocampal CA1 activity in a non-spatial learning task. *eLife* **5**, e14321 (2016). doi: 10.7554/eLife.14321; pmid: 27487561
9. C. Xu *et al*., Distinct hippocampal pathways mediate dissociable roles of context in memory retrieval. *Cell* **167**, 961–972.e16 (2016). doi: 10.1016/j.cell.2016.09.051; pmid: 27773481
10. M. Kannan, G. Vasan, V. A. Pieribone, Optimizing strategies for developing genetically encoded voltage indicators. *Front. Cell. Neurosci.* **13**, 53 (2019). doi: 10.3389/fncel.2019.00053; pmid: 30863283
11. T. Knöpfel, C. Song, Optical voltage imaging in neurons: Moving from technology development to practical tool. *Nat. Rev. Neurosci.* **20**, 719–727 (2019). doi: 10.1038/s41583-019-0231-4; pmid: 31705060
12. H. H. Yang, F. St-Pierre, Genetically encoded voltage indicators: Opportunities and challenges. *J. Neurosci.* **36**, 9977–9989 (2016). doi: 10.1523/JNEUROSCI.1095-16.2016; pmid: 27683896
13. A. S. Abdelfattah *et al*., Bright and photostable chemigenetic indicators for extended in vivo voltage imaging. *Science* **365**, 699–704 (2019). doi: 10.1126/science.aav6416; pmid: 31371562
14. A. S. Abdelfattah *et al*., A general approach to engineer positive-going eFRET voltage indicators. *Nat. Commun.* **11**, 3444 (2020). doi: 10.1038/s41467-020-17322-1; pmid: 32651384
15. S. Chamberland *et al*., Fast two-photon imaging of subcellular voltage dynamics in neuronal tissue with genetically encoded indicators. *eLife* **6**, e25690 (2017). doi: 10.7554/eLife.25690; pmid: 28749338
16. L. Z. Fan *et al*., All-optical electrophysiology reveals the role of lateral inhibition in sensory processing in cortical layer 1. *Cell* **180**, 521–535.e18 (2020). doi: 10.1016/j.cell.2020.01.001; pmid: 31978320
17. Y. Gong *et al*., High-speed recording of neural spikes in awake mice and flies with a fluorescent voltage sensor. *Science* **350**, 1361–1366 (2015). doi: 10.1126/science.aab0810; pmid: 26586188
18. M. Kannan *et al*., Fast, in vivo voltage imaging using a red fluorescent indicator. *Nat. Methods* **15**, 1108–1116 (2018). doi: 10.1038/s41592-018-0188-7; pmid: 30420685
19. K. D. Piatkevich *et al*., A robotic multidimensional directed evolution approach applied to fluorescent voltage reporters. *Nat. Chem. Biol.* **14**, 352–360 (2018). doi: 10.1038/s41589-018-0004-9; pmid: 29483642
20. V. Villette *et al*., Ultrafast two-photon imaging of a high-gain voltage indicator in awake behaving mice. *Cell* **179**, 1590–1608.e23 (2019). doi: 10.1016/j.cell.2019.11.004; pmid: 31835034
21. H. H. Yang *et al*., Subcellular imaging of voltage and calcium signals reveals neural processing in vivo. *Cell* **166**, 245–257 (2016). doi: 10.1016/j.cell.2016.05.031; pmid: 27264607
22. Y. Adam *et al*., Voltage imaging and optogenetics reveal behaviour-dependent changes in hippocampal dynamics. *Nature* **569**, 413–417 (2019). doi: 10.1038/s41586-019-1166-7; pmid: 31043747
23. K. D. Piatkevich *et al*., Population imaging of neural activity in awake behaving mice. *Nature* **574**, 413–417 (2019). doi: 10.1038/s41586-019-1641-1; pmid: 31597963
24. S. Xiao *et al*., Large-scale voltage imaging in behaving mice using targeted illumination. *iScience* **24**, 103263 (2021). doi: 10.1016/j.isci.2021.103263; pmid: 34761183
25. Y. Gong, M. J. Wagner, J. Zhong Li, M. J. Schnitzer, Imaging neural spiking in brain tissue using FRET-opsin protein voltage sensors. *Nat. Commun.* **5**, 3674 (2014). doi: 10.1038/ncomms4674; pmid: 24755708
26. P. Zou *et al*., Bright and fast multicoloured voltage reporters via electrochromic FRET. *Nat. Commun.* **5**, 4625 (2014). doi: 10.1038/ncomms5625; pmid: 25118186
27. D. R. Hochbaum *et al*., All-optical electrophysiology in mammalian neurons using engineered microbial rhodopsins. *Nat. Methods* **11**, 825–833 (2014). doi: 10.1038/nmeth.3000; pmid: 24952910
28. N. C. Shaner *et al*., A bright monomeric green fluorescent protein derived from *Branchiostoma lanceolatum*. *Nat. Methods* **10**, 407–409 (2013). doi: 10.1038/nmeth.2413; pmid: 23524392
29. B. T. Bajar *et al*., Improving brightness and photostability of green and red fluorescent proteins for live cell imaging and FRET reporting. *Sci. Rep.* **6**, 20889 (2016). doi: 10.1038/srep20889; pmid: 26879144
30. J. Park *et al*., Screening fluorescent voltage indicators with spontaneously spiking HEK cells. *PLOS ONE* **8**, e85221 (2013). doi: 10.1371/journal.pone.0085221; pmid: 24391999
31. H. Zhang, E. Reichert, A. E. Cohen, Optical electrophysiology for probing function and pharmacology of voltage-gated ion channels. *eLife* **5**, e15202 (2016). doi: 10.7554/eLife.15202; pmid: 27215841
32. L. Stryer, Fluorescence energy transfer as a spectroscopic ruler. *Annu. Rev. Biochem.* **47**, 819–846 (1978). doi: 10.1146/annurev.bi.47.070178.004131; pmid: 354506
33. T. Kikukawa *et al*., Photochemistry of *Acetabularia* rhodopsin II from a marine plant, *Acetabularia acetabulum*. *Biochemistry* **50**, 8888–8898 (2011). doi: 10.1021/bi2009932; pmid: 21905737
34. T. Wada *et al*., Crystal structure of the eukaryotic light-driven proton-pumping rhodopsin, *Acetabularia* rhodopsin II, from marine alga. *J. Mol. Biol.* **411**, 986–998 (2011). doi: 10.1016/j.jmb.2011.06.028; pmid: 21726566
35. D. Maclaurin, V. Venkatachalam, H. Lee, A. E. Cohen, Mechanism of voltage-sensitive fluorescence in a microbial rhodopsin. *Proc. Natl. Acad. Sci. U.S.A.* **110**, 5939–5944 (2013). doi: 10.1073/pnas.1215595110; pmid: 23530193
36. L. Zimányi *et al*., Pathways of proton release in the bacteriorhodopsin photocycle. *Biochemistry* **31**, 8535–8543 (1992). doi: 10.1021/bi00151a022; pmid: 1327104
37. J. Platisa, G. Vasan, A. Yang, V. A. Pieribone, Directed evolution of key residues in fluorescent protein inverses the polarity of voltage sensitivity in the genetically encoded indicator ArcLight. *ACS Chem. Neurosci.* **8**, 513–523 (2017). doi: 10.1021/acschemneuro.6b00234; pmid: 28045247
38. B. A. Wilt, J. E. Fitzgerald, M. J. Schnitzer, Photon shot noise limits on optical detection of neuronal spikes and estimation of spike timing. *Biophys. J.* **104**, 51–62 (2013). doi: 10.1016/j.bpj.2012.07.058; pmid: 23332058
39. M. E. Garrett, I. Nauhaus, J. H. Marshel, E. M. Callaway, Topography and areal organization of mouse visual cortex. *J. Neurosci.* **34**, 12587–12600 (2014). doi: 10.1523/JNEUROSCI.1124-14.2014; pmid: 25209296
40. H. Taniguchi *et al*., A resource of Cre driver lines for genetic targeting of GABAergic neurons in cerebral cortex. *Neuron* **71**, 995–1013 (2011). doi: 10.1016/j.neuron.2011.07.026; pmid: 21943598
41. B. Tasic *et al*., Adult mouse cortical cell taxonomy revealed by single cell transcriptomics. *Nat. Neurosci.* **19**, 335–346 (2016). doi: 10.1038/nn.4216; pmid: 26727548
42. J. Zhuang *et al*., An extended retinotopic map of mouse cortex. *eLife* **6**, e18372 (2017). doi: 10.7554/eLife.18372; pmid: 28059700
43. S. T. Lim, D. E. Antonucci, R. H. Scannevin, J. S. Trimmer, A novel targeting signal for proximal clustering of the Kv2.1 K^+ channel in hippocampal neurons. *Neuron* **25**, 385–397 (2000). doi: 10.1016/S0896-6273(00)80902-2; pmid: 10719893
44. C. Cai *et al*., VolPy: Automated and scalable analysis pipelines for voltage imaging datasets. *PLOS Comput. Biol.* **17**, e1008806 (2021). doi: 10.1371/journal.pcbi.1008806; pmid: 33852574
45. H. Inan, M. A. Erdogdu, M. J. Schnitzer, "Robust estimation of neural signals in calcium imaging" in *NIPS'17: Proceedings of the 31st International Conference on Neural Information Processing Systems*, U. von Luxburg, I. Guyon, S. Bengio, H. Wallach, R. Fergus, S. V. N. Vishwanathan, R. Garnett, Eds. (Curran Associates Inc., 2017).
46. H. Inan *et al*., Fast and statistically robust cell extraction from large-scale neural calcium imaging datasets. bioRxiv 2021.2003.2024.436279 [Preprint] (2021); doi: 10.1101/2021.03.24.436279
47. E. Abs *et al*., Learning-related plasticity in dendrite-targeting layer 1 interneurons. *Neuron* **100**, 684–699.e6 (2018). doi: 10.1016/j.neuron.2018.09.001; pmid: 30269988
48. K. Cohen-Kashi Malina *et al*., NDNF interneurons in layer 1 gain-modulate whole cortical columns according to an animal's behavioral state. *Neuron* **109**, 2150–2164.e5 (2021). doi: 10.1016/j.neuron.2021.05.001; pmid: 34038743
49. M. He *et al*., Strategies and tools for combinatorial targeting of GABAergic neurons in mouse cerebral cortex. *Neuron* **92**, 555 (2016). doi: 10.1016/j.neuron.2016.10.009; pmid: 27764676
50. H. Adesnik, W. Bruns, H. Taniguchi, Z. J. Huang, M. Scanziani, A neural circuit for spatial summation in visual cortex. *Nature* **490**, 226–231 (2012). doi: 10.1038/nature11526; pmid: 23060193
51. L. Mesik *et al*., Functional response properties of VIP-expressing inhibitory neurons in mouse visual and auditory cortex. *Front. Neural Circuits* **9**, 22 (2015). doi: 10.3389/fncir.2015.00022; pmid: 26106301
52. J. Yu, H. Hu, A. Agmon, K. Svoboda, Recruitment of GABAergic interneurons in the barrel cortex during active tactile behavior. *Neuron* **104**, 412–427.e4 (2019). doi: 10.1016/j.neuron.2019.07.027; pmid: 31466734
53. M. Vinck, R. Batista-Brito, U. Knoblich, J. A. Cardin, Arousal and locomotion make distinct contributions to cortical activity patterns and visual encoding. *Neuron* **86**, 740–754 (2015). doi: 10.1016/j.neuron.2015.03.028; pmid: 25892300
54. J. Reimer *et al*., Pupil fluctuations track fast switching of cortical states during quiet wakefulness. *Neuron* **84**, 355–362 (2014). doi: 10.1016/j.neuron.2014.09.033; pmid: 25374359
55. C. K. Pfeffer, M. Xue, M. He, Z. J. Huang, M. Scanziani, Inhibition of inhibition in visual cortex: The logic of connections between molecularly distinct interneurons. *Nat. Neurosci.* **16**, 1068–1076 (2013). doi: 10.1038/nn.3446; pmid: 23817549
56. U. Knoblich, L. Huang, H. Zeng, L. Li, Neuronal cell-subtype specificity of neural synchronization in mouse primary visual cortex. *Nat. Commun.* **10**, 2533 (2019). doi: 10.1038/s41467-019-10498-1; pmid: 31182715
57. L. Cossell *et al*., Functional organization of excitatory synaptic strength in primary visual cortex. *Nature* **518**, 399–403 (2015). doi: 10.1038/nature14182; pmid: 25652823
58. J. Akerboom *et al*., Genetically encoded calcium indicators for multi-color neural activity imaging and combination with optogenetics. *Front. Mol. Neurosci.* **6**, 2 (2013). doi: 10.3389/fnmol.2013.00002; pmid: 23459413
59. H. Dana *et al*., Sensitive red protein calcium indicators for imaging neural activity. *eLife* **5**, e12727 (2016). doi: 10.7554/eLife.12727; pmid: 27011354
60. M. Inoue *et al*., Rational design of a high-affinity, fast, red calcium indicator R-CaMP2. *Nat. Methods* **12**, 64–70 (2015). doi: 10.1038/nmeth.3185; pmid: 25419959
61. M. Inoue *et al*., Rational engineering of XCaMPs, a multicolor GECI suite for in vivo imaging of complex brain circuit dynamics. *Cell* **177**, 1346–1360.e24 (2019). doi: 10.1016/j.cell.2019.04.007; pmid: 31080068
62. M. M. Karnani *et al*., Opening holes in the blanket of inhibition: Localized lateral disinhibition by VIP interneurons. *J. Neurosci.* **36**, 3471–3480 (2016). doi: 10.1523/JNEUROSCI.3646-15.2016; pmid: 27013676
63. W. Akemann *et al*., Imaging neural circuit dynamics with a voltage-sensitive fluorescent protein. *J. Neurophysiol.* **108**, 2323–2337 (2012). doi: 10.1152/jn.00452.2012; pmid: 22815406
64. F. Li *et al*., The connectome of the adult Drosophila mushroom body provides insights into function. *eLife* **9**, e62576 (2020). doi: 10.7554/eLife.62576; pmid: 33315010
65. J. Jackson, I. Ayzenshtat, M. M. Karnani, R. Yuste, VIP+ interneurons control neocortical activity across brain states. *J. Neurophysiol.* **115**, 3008–3017 (2016). doi: 10.1152/jn.01124.2015; pmid: 26961109
66. J. Reimer *et al*., Pupil fluctuations track rapid changes in adrenergic and cholinergic activity in cortex. *Nat. Commun.* **7**, 13289 (2016). doi: 10.1038/ncomms13289; pmid: 27824036
67. J. M. P. Pakan *et al*., Behavioral-state modulation of inhibition is context-dependent and cell type specific in mouse visual cortex. *eLife* **5**, e14985 (2016). doi: 10.7554/eLife.14985; pmid: 27552056
68. S. Xiao, H. A. Tseng, H. Gritton, X. Han, J. Mertz, Video-rate volumetric neuronal imaging using 3D targeted illumination. *Sci. Rep.* **8**, 7921 (2018). doi: 10.1038/s41598-018-26240-8; pmid: 29784920
69. M. L. Andermann *et al*., Chronic cellular imaging of entire cortical columns in awake mice using microprisms. *Neuron* **80**, 900–913 (2013). doi: 10.1016/j.neuron.2013.07.052; pmid: 24139817
70. J. C. Jung, A. D. Mehta, E. Aksay, R. Stepnoski, M. J. Schnitzer, In vivo mammalian brain imaging using one- and two-photon

fluorescence microendoscopy. *J. Neurophysiol.* **92**, 3121–3133 (2004). doi: 10.1152/jn.00234.2004; pmid: 15128753
71. R. P. Barretto, B. Messerschmidt, M. J. Schnitzer, In vivo fluorescence imaging with high-resolution microlenses. *Nat. Methods* **6**, 511–512 (2009). doi: 10.1038/nmeth.1339; pmid: 19525959
72. R. P. Barretto, M. J. Schnitzer, In vivo optical microendoscopy for imaging cells lying deep within live tissue. *Cold Spring Harb. Protoc.* **2012**, 1029–1034 (2012). doi: 10.1101/pdb.top071464; pmid: 23028071
73. Allen Institute for Brain Science, Cell types: Overview of the data, Allen cell types database; https://celltypes.brain-map.org/.
74. G. Buzsáki, C. A. Anastassiou, C. Koch, The origin of extracellular fields and currents—EEG, ECoG, LFP and spikes. *Nat. Rev. Neurosci.* **13**, 407–420 (2012). doi: 10.1038/nrn3241; pmid: 22595786
75. I. Soltesz, A. Losonczy, CA1 pyramidal cell diversity enabling parallel information processing in the hippocampus. *Nat. Neurosci.* **21**, 484–493 (2018). doi: 10.1038/s41593-018-0118-0; pmid: 29593317
76. L. Jin *et al*., Single action potentials and subthreshold electrical events imaged in neurons with a fluorescent protein voltage probe. *Neuron* **75**, 779–785 (2012). doi: 10.1016/j.neuron.2012.06.040; pmid: 22958819
77. C. Huang *et al*., Long-term optical brain imaging in live adult fruit flies. *Nat. Commun.* **9**, 872 (2018). doi: 10.1038/s41467-018-02873-1; pmid: 29491443
78. G. J. Goldey *et al*., Removable cranial windows for long-term imaging in awake mice. *Nat. Protoc.* **9**, 2515–2538 (2014). doi: 10.1038/nprot.2014.165; pmid: 25275789
79. P. Thévenaz, U. E. Ruttimann, M. Unser, A pyramid approach to subpixel registration based on intensity. *IEEE Trans. Image Process.* **7**, 27–41 (1998). doi: 10.1109/83.650848; pmid: 18267377
80. E. A. Pnevmatikakis, A. Giovannucci, NoRMCorre: An online algorithm for piecewise rigid motion correction of calcium imaging data. *J. Neurosci. Methods* **291**, 83–94 (2017). doi: 10.1016/j.jneumeth.2017.07.031; pmid: 28782629
81. K. He, G. Gkioxari, P. Dollar, R. Girshick, Mask R-CNN. *IEEE Trans. Pattern Anal. Mach. Intell.* **42**, 386–397 (2020). doi: 10.1109/TPAMI.2018.2844175; pmid: 29994331
82. F. Franke, R. Quian Quiroga, A. Hierlemann, K. Obermayer, Bayes optimal template matching for spike sorting - combining fisher discriminant analysis with optimal filtering. *J. Comput. Neurosci.* **38**, 439–459 (2015). doi: 10.1007/s10827-015-0547-7; pmid: 25652689
83. E. A. Pnevmatikakis *et al*., Simultaneous denoising, deconvolution, and demixing of calcium imaging data. *Neuron* **89**, 285–299 (2016). doi: 10.1016/j.neuron.2015.11.037; pmid: 26774160
84. E. A. Mukamel, A. Nimmerjahn, M. J. Schnitzer, Automated analysis of cellular signals from large-scale calcium imaging data. *Neuron* **63**, 747–760 (2009). doi: 10.1016/j.neuron.2009.08.009; pmid: 19778505
85. T. Deneux *et al*., Accurate spike estimation from noisy calcium signals for ultrafast three-dimensional imaging of large neuronal populations in vivo. *Nat. Commun.* **7**, 12190 (2016). doi: 10.1038/ncomms12190; pmid: 27432255
86. M. Kannan *et al*, Dual-polarity voltage imaging of the concurrent activation dynamics of multiple neuron types. Zenodo (2022); doi: 10.5281/zenodo.6361012

ACKNOWLEDGMENTS

We thank Pierce scientific staff members C. Gardiner, M. Izydorsczak, P. O'Brien, X. Liu, T. Liu, and R. O'Brien for technical assistance; Pierce workshop members J. Buckley and A. Wilkins; G. Lur (University of California, Irvine) and K. Ferguson (Yale School of Medicine, New Haven) for advice on V1 imaging; and J. Verhagen (Yale Neuroscience) for comments on the manuscript. We further thank members of the Schnitzer laboratory: J. Li for animal husbandry and genotyping, Y. Zhang for virus handling and surgical advice, G. Delamare for instrumentation support, and F. Dinc and J. Li for computational consultations. All schematics were created using BioRender. **Funding:** This study was supported by NIH BRAIN Initiative grants U01NS103517 (V.A.P.), U01NS120822 (M.J.S. and G.V.), UF1NS107610 (M.J.S. and H. Zheng), and U19NS104590 (M.J.S. and I. Soltesz); and NSF NeuroNex grant DBI-1707261 (M.J.S. and K. Deisseroth). This research was funded in part by the Defense Advanced Research Projects Agency (DARPA) of the United States, contract nos. N6600117C4012 (NESD) and N6600119C4020 (N3) (V.A.P.). The views, opinions and/or findings expressed are those of the authors and should not be interpreted as representing the official views or policies of the Department of Defense or the US government. **Author contributions:** M.K. and G.V. conceived the project; designed, screened and characterized the sensors; and performed molecular biology and rAAV cloning. M.K. performed visual cortical surgeries. G.V. built the in vivo setup and wrote the software for V1 imaging. M.K. and G.V. conceived and performed in vivo V1 experiments and data analyses. S.H. conceived and performed the hippocampal experiments, wrote the SpikeImagingAnalysis pipeline, and performed data analyses for CA1 studies. C.H. performed and analyzed the fly experiments. R.C. built the optical setup used for CA1 imaging. J.L. designed the transgenic flies. J.A.C. shared the running wheel and provided advice on V1 imaging. M.K. and G.V. wrote the manuscript with contributions from all authors. M.J.S. developed data analyses, edited the manuscript, and supervised work at Stanford. V.A.P. supervised work at John B. Pierce and Yale. **Competing interests:** The authors declare no competing interests. **Data and materials availability:** All sequence information is available on GenBank (accession numbers OM687163 to OM687166 for soma-targeted Ace-mNeon2, pAce, VARNAM2, and pAceR, respectively). Plasmids and rAAVs will be made available through Addgene (help@addgene.org). Fly stocks have been deposited at the Bloomington Drosophila Stock Center, and all data and codes are available at Zenodo (*86*). **License information:** Copyright © 2022 the authors, some rights reserved; exclusive licensee American Association for the Advancement of Science. No claim to original US government works. https://www.science.org/about/science-licenses-journal-article-reuse. This research was funded in whole or in part by the Howard Hughes Medical Institute, a cOAlition S organization. The authors will make the Author Accepted Manuscript (AAM) version available under a CC BY public copyright license.

SUPPLEMENTARY MATERIALS

science.org/doi/10.1126/science.abm8797
Figs. S1 to S26
Table S1
References (*87*, *88*)
MDAR Reproducibility Checklist

Submitted 22 October 2021; accepted 3 October 2022
10.1126/science.abm8797

RESEARCH ARTICLES

SYNTHETIC BIOLOGY

Refactored genetic codes enable bidirectional genetic isolation

Jérôme F. Zürcher[1], Wesley E. Robertson[1], Tomás Kappes[2], Gianluca Petris[1], Thomas S. Elliott[1], George P. C. Salmond[2], Jason W. Chin[1]*

The near-universal genetic code defines the correspondence between codons in genes and amino acids in proteins. We refactored the structure of the genetic code in *Escherichia coli* and created orthogonal genetic codes that restrict the escape of synthetic genetic information into natural life. We developed orthogonal and mutually orthogonal horizontal gene transfer systems, which permit the transfer of genetic information between organisms that use the same genetic code but restrict the transfer of genetic information between organisms that use different genetic codes. Moreover, we showed that locking refactored codes into synthetic organisms completely blocks invasion by mobile genetic elements, including viruses, which carry their own translation factors and successfully invade organisms with canonical and compressed genetic codes.

The near-universal genetic code defines the correspondence between codons in genes and amino acids in proteins (*1*, *2*). Because all forms of life use essentially the same genetic code, evolutionary innovation can be shared through horizontal gene transfer (HGT) between organisms (*3*, *4*), and this is a major driver of evolution (*5*).

However, the near-universal genetic code is also a liability for organisms; mobile genetic elements (or selfish genetic elements)—including transposons, viruses, and plasmids—exploit the universality of the code and co-opt the host cell's machinery to read their genes and propagate at the expense of host organisms. There is a clear tension between maintaining a common genetic code, to allow the acquisition of beneficial innovation through HGT, and excluding selfish genetic elements that exploit the common code for their own ends (*3*, *6*).

Several deviations from the standard genetic code have been documented in mitochondria and chloroplasts, and most characterized code reassignments involve stop codons (*7*–*9*). Known sense codon reassignments in the nuclear genome are rare. The "CTG yeast" decodes the CUG codon (which encodes leucine in the standard code) primarily as serine (97%, with the remaining 3% still assigned to leucine) (*10*). Viruses for the CTG yeasts are essentially unknown, which suggests that sense codon reassignment may protect against viruses (*11*). There are no experimentally validated examples of sense codon reassignment in bacteria, although computational evidence supports arginine codon reassignment in bacilli (*12*).

Genome synthesis (*13*, *14*) and editing provide the opportunity to rewrite the genetic code and create organisms with new properties (*14*–*19*). We synthesized a 4-Mb *Escherichia coli* genome in which we replaced all annotated occurrences of the TCG and TCA serine codons with the synonymous AGC and AGT codons using defined recoding rules (*20*); we also replaced the TAG stop codon with TAA. This created Syn61, an organism with a compressed genetic code (*14*). We further evolved the strain and deleted the genes for the tRNAs that decode TCG and TCA codons (*serU*, $tRNA_{CGA}^{Ser}$; *serT*, $tRNA_{UGA}^{Ser}$) and the gene for RF-1 (*prfA*) that terminates protein synthesis at the TAG stop codon. The resulting organism, Syn61Δ3, cannot read all the codons in the near-universal genetic code and therefore cannot read horizontally transferred genes that contain the codons deleted from its genome, as exemplified by resistance to a range of bacteriophage (*18*).

It has been widely hypothesized that refactoring the structure of the genetic code, through the reassignment of sense codons to distinct canonical amino acids, would create organisms with new properties and could create a genetic firewall to limit the escape of genetic information from synthetic organisms to natural organisms (*4*, *6*, *21*–*23*). In this work, we tested these hypotheses.

Compressed codes are nonorthogonal

A spectinomycin resistance gene written in the canonical genetic code [SpecR wild type (WT)] was correctly read in, and conferred spectinomycin resistance to, cells that contain the full complement of tRNAs to read the canonical code. However, consistent with previous observations (*18*), SpecR WT did not confer spectinomycin resistance to Syn61Δ3 cells (Fig. 1).

We created a recoded spectinomycin resistance gene [recSpecR (ΔTCG, TCA)], with the compressed genetic code used in the Syn61 genome. recSpecR (ΔTCG, TCA) conferred spectinomycin resistance to Syn61Δ3 cells (Fig. 1). The recSpecR (ΔTCG, TCA) gene also conferred spectinomycin resistance to cells that read the canonical genetic code; this was expected because the compressed genetic code uses a subset of the codons used in the canonical genetic code. We made similar observations with hygromycin resistance genes written in canonical and compressed codes (fig. S1).

These experiments demonstrated that genetic information written in the canonical code can be read in cells that decode the canonical code, but not in cells with genome-wide code compression and cognate tRNA deletion. However, code-compressed genes can be read in both cells with cognate tRNA deletion and cells that decode the canonical code. Therefore, there is no barrier limiting the flow of genetic information from engineered organisms with compressed genetic codes to natural forms of life. Creating orthogonal genetic codes that actively restrict the transfer of genetic information from engineered biological systems to natural systems is an important and unaddressed challenge.

tRNAs enable invasion of codon-compressed organisms

A WT F plasmid [F (WT)], written in the canonical genetic code, was efficiently transferred to cells that read the canonical code. By contrast, F (WT) was not transferred to Syn61Δ3 (Fig. 1 and data file S1), as expected. However, upon selecting for the conjugation of F (WT) from cells that read the canonical code into Syn61Δ2 cells (Syn61 cells deleted for *serU* and *serT* but containing *prfA*), we obtained two viable colonies in which recipient cells had received F (WT) (fig. S2). These colonies corresponded to rare events, which appeared at a frequency 10^6-fold less than the colonies resulting from conjugation of F (WT) into cells that read the canonical code. Sequencing the two clones revealed that they had acquired sequences that contained *serT* from the donor cell. This provided direct experimental evidence that selection for transfer of a mobile genetic element that uses the canonical code to recipients that cannot read the entire canonical code can enable selection for recipients that acquire the tRNA genes necessary to read the canonical genetic code.

To follow the effects of introducing *serT* into recipient cells in a reproducible system, we created the mobile genetic element F (WT + *serT*), a variant of F (WT) that contains *serT*. We demonstrated that F (WT + *serT*)

[1]Medical Research Council Laboratory of Molecular Biology, Cambridge, UK. [2]Department of Biochemistry, University of Cambridge, Cambridge, UK.
*Corresponding author. Email: chin@mrc-lmb.cam.ac.uk

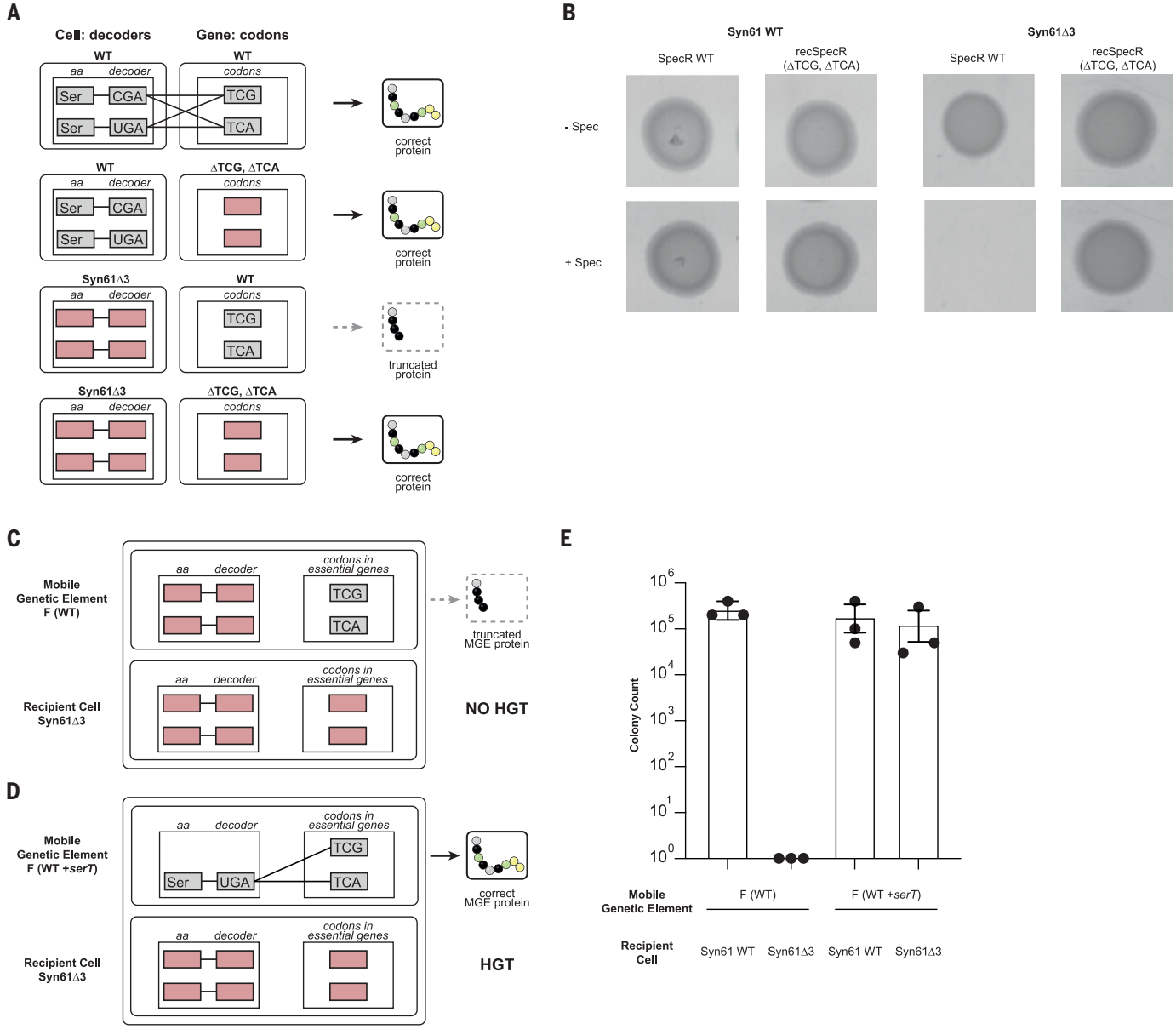


Fig. 1. Compressed genetic codes are nonorthogonal. (**A**) The relationship between the TCG and TCA codons in genes, the decoders for these codons in cells with canonical (WT) decoding and Syn61Δ3 decoding (ΔTCG, ΔTCA), and the corresponding protein sequence synthesized. The anticodon of the tRNAs that read TCG or TCA codons is indicated (decoder). The amino acid (aa) used by the tRNA is indicated. Gray for a decoder indicates that the tRNA is loaded with serine. Gray for a codon indicates that the codon is within a non–codon-compressed gene, and its decoding as serine will make the correct protein sequence. Pink for a decoder–amino acid pair indicates that the tRNA is deleted. Pink for a codon indicates the codon is absent from the gene because the gene has been designed with codon compression. (**B**) Functional assessment of SpecR WT and codon-compressed spectinomycin resistance [recSpecR (ΔTCG, TCA)] genes in (left) cells that use the full complement of tRNAs to decode all the codons in the reading frame (Syn61 WT) and (right) cells in which the tRNAs that decode TCG and TCA codons have been deleted (Syn61Δ3). Cells were spotted on agar plates in the presence or absence of spectinomycin and incubated overnight. The growth of cells in the presence of spectinomycin indicates that the indicated SpecR gene is functional in the indicated strain. (**C** and **D**) Predicted protein synthesis and HGT outcomes from mobile genetic elements (MGEs) and recipient cells with the indicated decoders and codons in essential genes. (C) A mobile genetic element encoding its genes according to the canonical genetic code, in which TCG and TCA encode serine, cannot be horizontally transferred to Syn61Δ3 cells that have no decoders for TCG and TCA codons. Translation will stall at TCG and TCA codons, and no full-length protein will be synthesized from the essential genes within the mobile genetic element that contain TCG and TCA codons. (D) A mobile genetic element encoding its genes according to the canonical genetic code that also carries a gene for a tRNA decoding TCG and TCA codons can be horizontally transferred to Syn61Δ3 cells. The tRNA encoded on the mobile genetic element can rescue decoding of TCG and TCA codons within essential genes in the mobile genetic element to make the correct MGE proteins. (**E**) Transfer of mobile genetic elements through conjugation. Colony count indicates successful transconjugants received from ~10^6 cells. A WT mobile genetic element (F WT) can be transferred into cells that read the canonical code (Syn61 WT) but not into cells that lack tRNAs decoding TCG and TCA (Syn61Δ3). A WT mobile genetic element that encodes a tRNA decoding TCG and TCA codons as serine [F (WT + *serT*)] can be transferred to both Syn61 WT and Syn61Δ3.

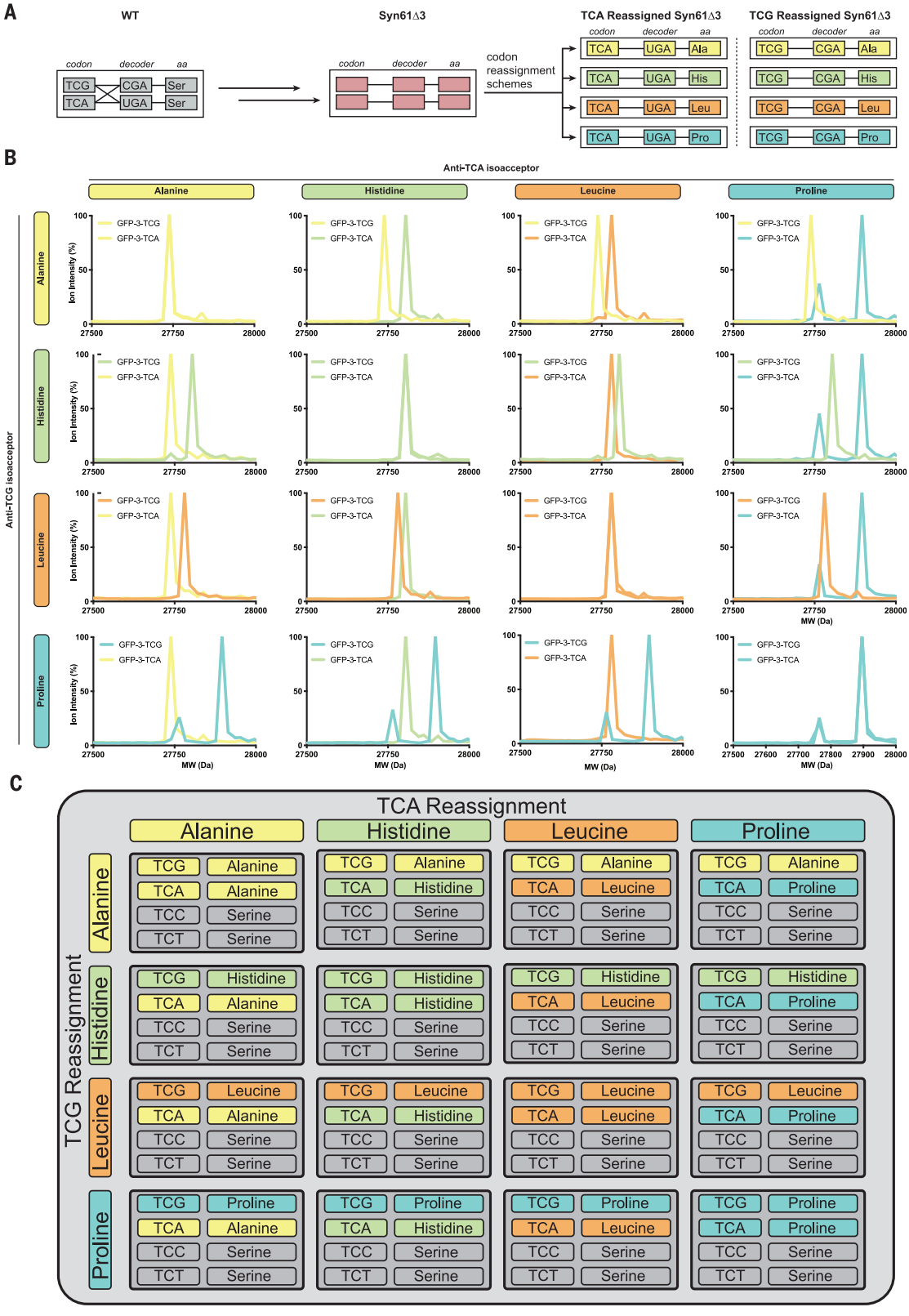


Fig. 2. Sense codon reassignment generates genetic codes. (**A**) Total synthesis of a codon-compressed genome followed by tRNA and release factor deletion yielded Syn61Δ3. The discovery of tRNAs that direct the incorporation of distinct canonical amino acids in response to TCG or TCA codons enables sense codon reassignment to create new genetic codes. (**B**) Isoacceptor tRNAs for the indicated amino acids with anticodons altered to the Watson-Crick complement of TCG or TCA codons were introduced into Syn61Δ3 in the indicated pairwise combinations. We read out the identity of the amino acid incorporated into each codon using GFP genes with TCG or TCA codons at position 3 and electrospray ionization mass spectrometry. When pairs of isoacceptors for distinct amino acids were used, each codon led to the specific incorporation of the amino acid attached to the Watson-Crick–paired isoacceptor. The secondary peak measured in the proline incorporations results from incomplete methionine cleave at the N terminus. A complete list of found and expected masses are provided in data file S2. MW, molecular weight. (**C**) Sixteen genetic codes in which TCG and TCA codons are reassigned to alanine, histidine, leucine, and proline.

can be transferred to Syn61Δ3 cells and that this transfer is dependent on *serT* (Fig. 1). We conclude that acquisition of *serT* is sufficient to circumvent the genetic isolation that is provided by code compression and cognate tRNA deletion in Syn61Δ3. These experiments highlight that creating systems that actively obstruct invasion by mobile genetic elements that carry their own decoders is an important challenge.

Refactoring code structure

We found that chimeric tRNAs for alanine ($tRNA_{CGA}^{Ala}$, $tRNA_{UGA}^{Ala}$), histidine ($tRNA_{CGA}^{His}$, $tRNA_{UGA}^{His}$), leucine ($tRNA_{CGA}^{Leu}$, $tRNA_{UGA}^{Leu}$), and proline ($tRNA_{CGA}^{Pro}$, $tRNA_{UGA}^{Pro}$) specifically

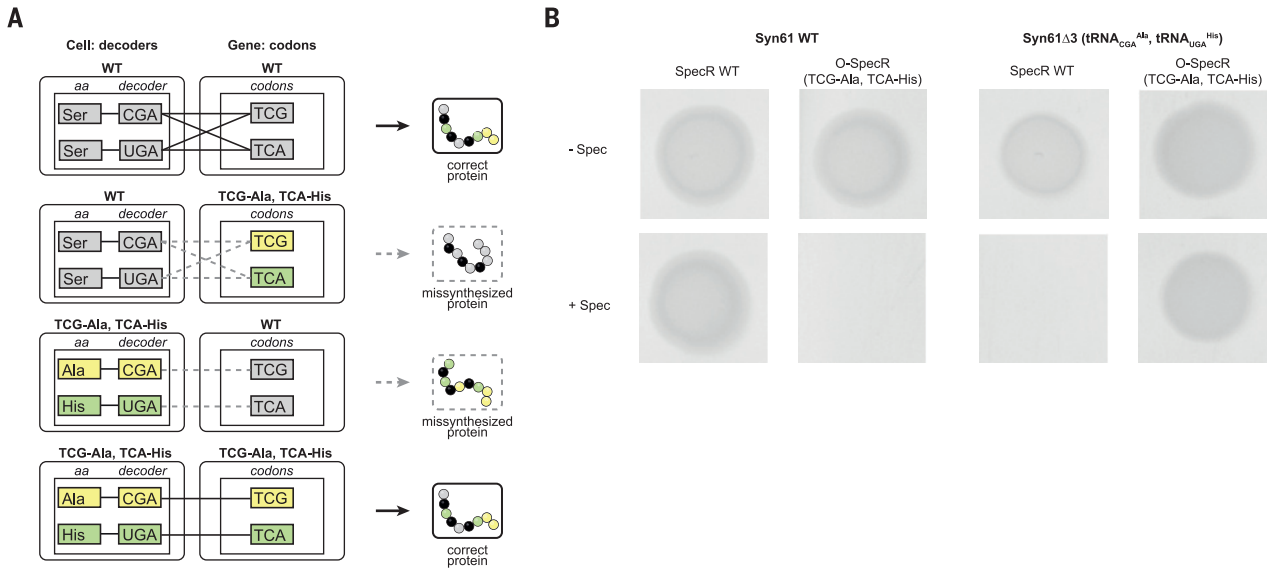


Fig. 3. Orthogonal genetic systems. (**A**) Relationship between the TCG and TCA codons in genes; the decoders for these codons in cells with canonical (WT) decoding and decoding by $tRNA_{CGA}^{Ala}$, $tRNA_{UGA}^{His}$ in Syn61Δ3; and the corresponding protein sequence synthesized. The anticodon of the tRNAs that read TCG or TCA codons is indicated (decoder). The amino acid (aa) used by the tRNA is indicated. Gray for a codon indicates that its decoding as serine will make the correct protein sequence. Yellow for a codon indicates that its decoding as alanine will make the correct protein sequence. Green for a codon indicates that its decoding as histidine will make the correct protein sequence. (**B**) Functional assessment of SpecR WT (written in the canonical genetic code) and O-SpecR (TCG-Ala, TCA-His), which is codon-compressed according to the Syn61 recoding scheme and has alanine codons replaced with TCG and histidine codons replaced with TCA. The genes are read in cells that read the canonical code (Syn61 WT), and cells where TCG is decoded as alanine and TCA is decoded as histidine [Syn61Δ3 ($tRNA_{CGA}^{Ala}$, $tRNA_{UGA}^{His}$)]. Cells were spotted on agar plates in the presence or absence of spectinomycin and incubated overnight. The growth of cells in the presence of spectinomycin indicates that the indicated SpecR gene is functional in the indicated strain.

direct the incorporation of the amino acid defined by the parent isoacceptor tRNA in response to their cognate codon (TGC or TCA) at position 3 in superfolder green fluorescent protein (sfGFP) or position 11 in ubiquitin in Syn61Δ3 (Fig. 2, figs. S3 to S13, and data files S2 and S3) and produce good yields of protein (fig. S3). The fidelity of $tRNA_{UGA}^{Leu}$ was lower than that of other tRNAs (data file S3 and fig. S5). We investigated alanyl and leucyl-tRNAs because their anticodons are not identity elements for their cognate aminoacyl-tRNA synthetases, and they were therefore expected to be permissive to anticodon mutation; the other tRNAs were identified through a screen (fig. S14). We found that unlike $tRNA_{CGA}^{Ser}$ and $tRNA_{UGA}^{Ser}$, our chimeric tRNAs specifically decode the Watson-Crick complement of their anticodon sequence; for example, $tRNA_{CGA}^{Ala}$ decodes TCG codons in preference to TCA codons, and $tRNA_{UGA}^{Ala}$ decodes TCA codons in preference to TCG codons (figs. S3 and S5). These tRNAs are also specific with respect to other TCN codons (figs. S6 and S7), and most reassigned strains grew comparably with parental strains (fig. S15). Our data show that we can independently reassign the TCA and TCG codons to alanine, histidine, leucine, or proline in Syn61Δ3 and thereby create 16 new genetic codes (Fig. 2B, figs. S3 and S5, and data files S2 and S3). In each of these genetic codes, we changed the identity of the canonical amino acids encoded at specific sense codons with respect to both the canonical code and the other 15 codes we have created (Fig. 2C). Our reassignment strategy is analogous to models that have been proposed for codon capture in natural evolution (*24*).

Overall, we have refactored the structure of the genetic code. Our genetic codes expand the number of codons used to encode alanine and proline (from four to six), double the number of codons used to encode histidine from two to four, and increase the number of codons used to primarily encode leucine from six to eight. These experiments also show that the UCN codon box, which encodes serine in the canonical code, can be split to encode additional canonical amino acids.

Orthogonal code–orthogonal decoder pairs

Genes that are written by using the canonical genetic code, in which TCG and TCA codons encode serine, will make the correct protein product in natural cells that read these codons as serine. However, these genes will yield the incorrect, likely nonfunctional protein product in cells that decode these codons to incorporate amino acids other than serine.

Similarly, synthetic genes—in which we compress the genetic code using the Syn61 recoding scheme and replace codons for specific natural amino acids with TCG and TCA codons—will make the correct protein product in cells that decode the TCG and TCA codons to incorporate the correct amino acid. However, these synthetic genes will yield an incorrect, likely nonfunctional protein product in cells that read the canonical genetic code (Fig. 3).

We converted all 27 GCN codons (which encode alanine in the canonical code) to TCG codons and all six CAT/C codons (which encode histidine in the canonical code) to TCA codons in recSpecR (ΔTCG, TCA). This created the orthogonal resistance gene O-SpecR (TCG-Ala, TCA-His). We demonstrated that O-SpecR (TCG-Ala, TCA-His) can be decoded in, and confer spectinomycin resistance to, Syn61Δ3 ($tRNA_{CGA}^{Ala}$, $tRNA_{UGA}^{His}$) cells, in which TCG is read as alanine and TCA is read as histidine. We further demonstrated that O-SpecR (TCG-Ala, TCA-His) did not confer spectinomycin resistance to cells that read the canonical genetic code. Last, we demonstrated that SpecR WT, in which serine is encoded by using TCG and TCA codons, cannot confer spectinomycin resistance to Syn61Δ3 ($tRNA_{CGA}^{Ala}$, $tRNA_{UGA}^{His}$) cells (Fig. 3). We extended this approach to six other reassignment schemes, as well as to other genes (fig. S16).

These experiments demonstrated that we can create a genetic code–decoder pair for synthetic genes that is functionally orthogonal with respect to the canonical genetic code–decoder pair for natural genes. The orthogonal

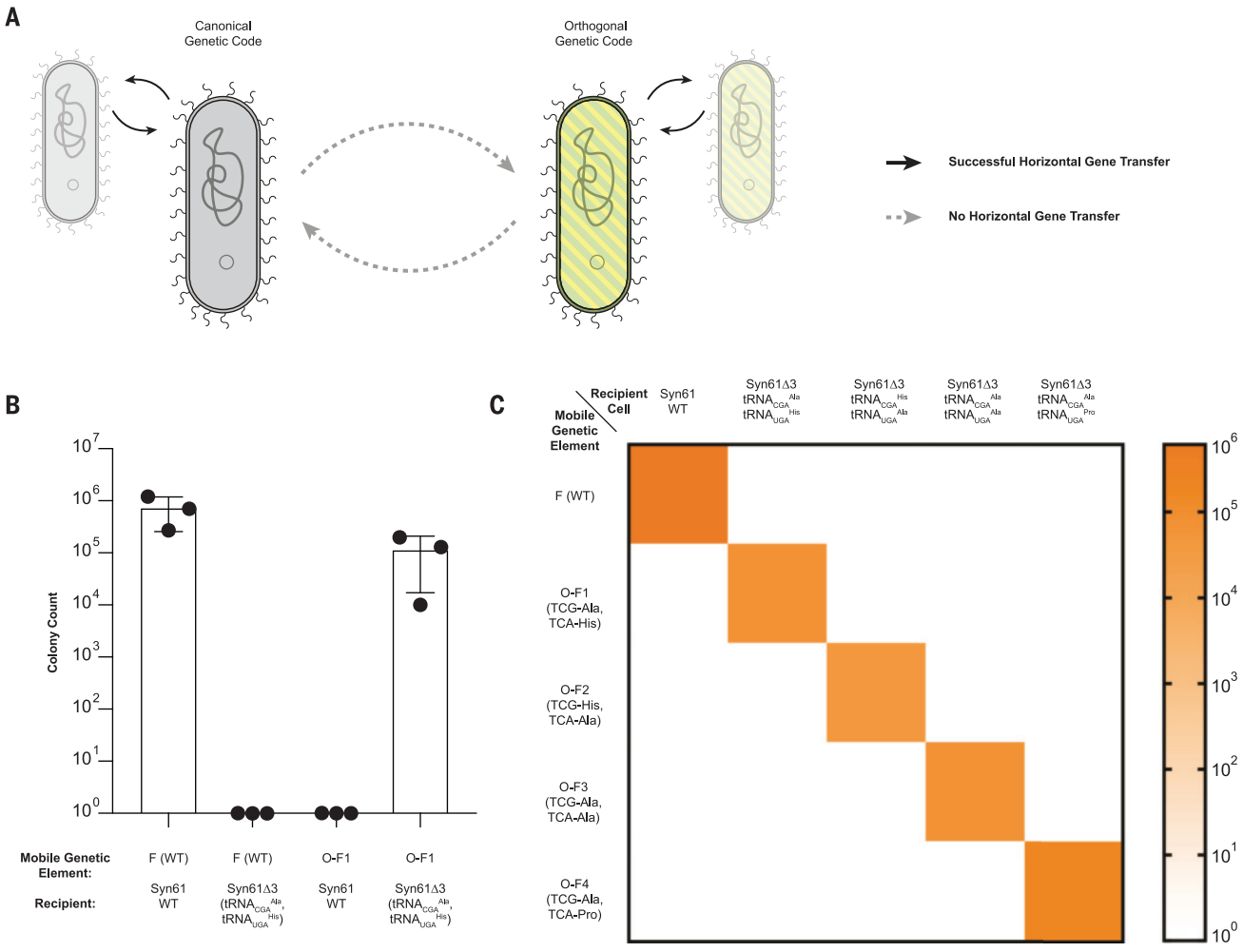


Fig. 4. Orthogonal and mutually orthogonal HGT systems. (**A**) HGT between organisms that use distinct, orthogonal genetic codes is prohibited (dashed gray arrows), whereas HGT can occur between cells that share a common genetic code (solid arrows). (**B**) Orthogonal horizontal transfer of mobile genetic elements. Colony count indicates the number of transconjugants received from ~10^6 donor cells that bear the indicated mobile genetic element. A WT mobile genetic element [F (WT)] was transferred into cells that read the canonical genetic code (Syn61 WT) but not into cells where TCG is reassigned to alanine and TCA is reassigned to histidine [Syn61Δ3 ($tRNA_{CGA}^{Ala}$, $tRNA_{UGA}^{His}$)]. An orthogonal mobile genetic element (O-F1), in which alanine codons were replaced with TCG and histidine codons were replaced with TCA, was transferred into Syn61Δ3 ($tRNA_{CGA}^{Ala}$, $tRNA_{UGA}^{His}$) but not into Syn61 WT. (**C**) Mutually orthogonal HGT systems. Colony count (orange heat map) indicates successful transconjugants received from ~10^6 donor cells bearing the indicated mobile genetic element.

code, written in synthetic genes, is correctly read by the cognate orthogonal decoder but not by the canonical decoder. The canonical code, written in natural genes, is correctly read by the canonical decoder but not by the orthogonal decoder.

The functional orthogonality of genes in cells with altered decoders will depend on the frequency of reassigned codons and the functional consequences of codon reassignments. The consequences of amino acid substitutions—a result of codon reassignment—may globally and crudely correlate with differences in amino acid polarity and hydrophobicity (*6*, *25*). The consequences of amino acid substitutions at particular sites in proteins may be predicted by using computational approaches that leverage evolutionary sequence- and/or structural information (*26*–*29*). Although the composition of natural genes is fixed, the codon usage in synthetic genes—written in the standard code or any orthogonal code—can be simply designed to maximize the number of codons that are subject to reassignment, which may maximize the functional orthogonality of synthetic genes.

Orthogonal HGT

Next, we created orthogonal HGT (O-HGT) systems composed of an orthogonal decoder and a mobile genetic element that uses an orthogonal genetic code. Cells that read the canonical code can transfer a WT mobile genetic element between themselves but cannot transfer the WT mobile genetic element to cells that contain orthogonal decoders. Cells that contain O-HGT systems can transfer their mobile genetic element to cells that contain a compatible orthogonal decoder but cannot transfer their mobile genetic element to cells that contain an incompatible orthogonal decoder or to cells that read the canonical code.

A mobile genetic element [F (WT)] written in the canonical code was transferred to cells that read the canonical code, as expected. We also showed that F (WT) could not be transferred to Syn61Δ3 ($tRNA_{CGA}^{Ala}$, $tRNA_{UGA}^{His}$)

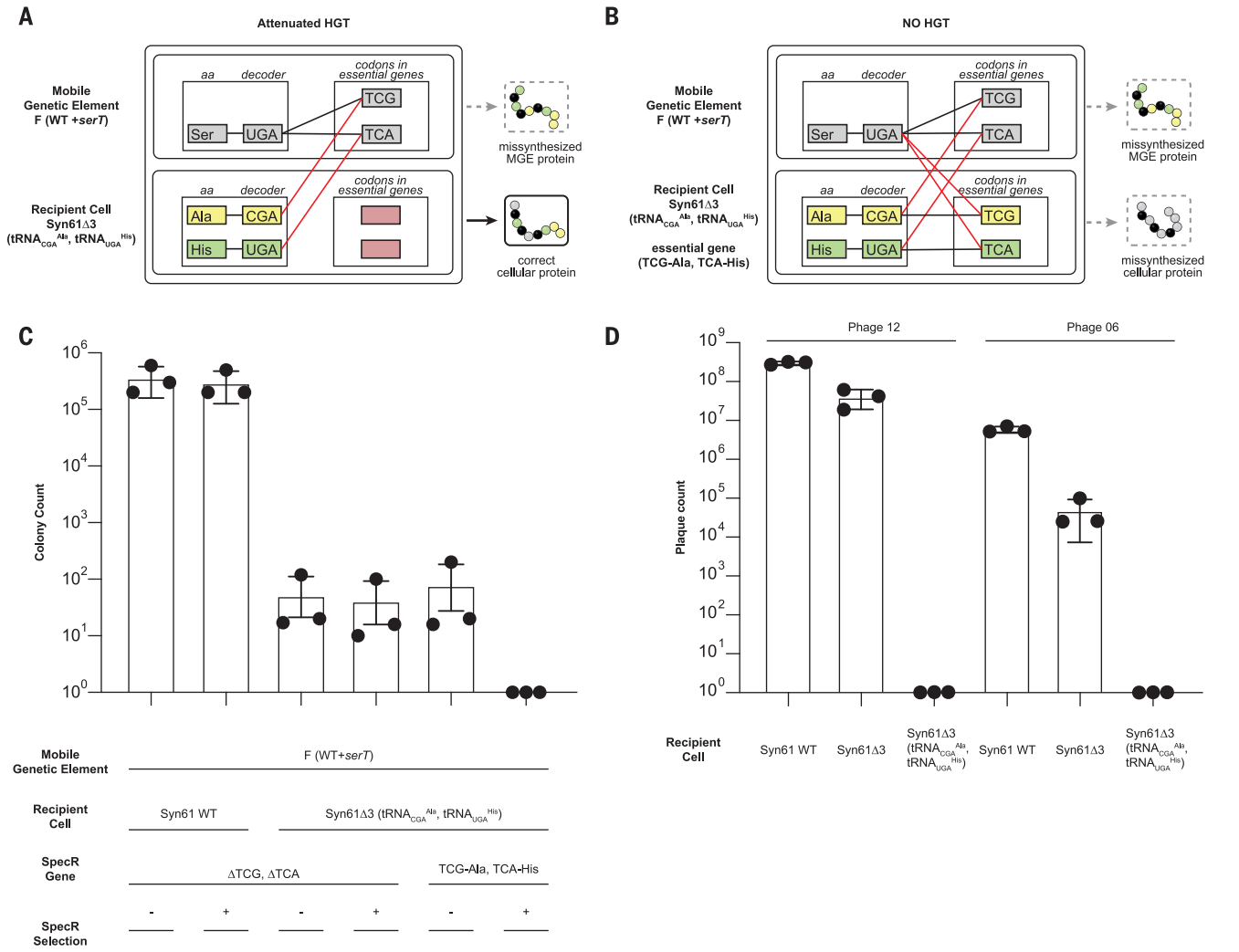


Fig. 5. Orthogonal code locking blocks invading codes. (**A** and **B**) Predicted protein synthesis and HGT outcomes from mobile genetic elements (MGEs) and recipient cells with the indicated decoders, and codons in essential genes. (A) Transfer of a WT mobile genetic element that encodes for a tRNA decoding TCG and TCA codons as serine into a cell where TCG is reassigned to alanine and TCA is reassigned to histidine. Essential genes in the WT mobile genetic element, which contain TCG and TCA codons, will be missynthesized, with each TCG and TCA codon in the gene being stochastically decoded as serine or alanine/histidine. This is predicted to attenuate HGT. (B) Transfer of a WT mobile genetic element that encodes for a tRNA decoding TCG and TCA codons as serine into a cell where TCG is reassigned to alanine and TCA is reassigned to histidine. Essential genes in the WT mobile genetic element, which contain TCG and TCA codons, will be missynthesized, with each TCG and TCA codon in the gene being stochastically decoded as serine or alanine/histidine. In addition, essential genes in the host cell, in which TCG is used to encode alanine and TCA is used to encode histidine, will be missynthesized. This is predicted to further restrict HGT. (**C**) HGT of a WT mobile genetic element [F (WT + *serT*)] is ablated in cells that use a refactored genetic code in essential genes. Colony count indicates successful transconjugants received from ~10^6 cells. Recipient cells and spectinomycin resistance gene variant (SpecR gene) in the recipient cell are indicated. Correctly reading the indicated SpecR gene in the recipient cell is made essential by addition of spectinomycin. (**D**) T4-like phage encoding a seryl-tRNA$_{UGA}$ infect Syn61Δ3 but not cells that bear orthogonal genetic codes. Plaque count indicates the number of successfully replicating phage obtained from infection with 1.1×10^{10} plaque-forming units (PFU)/ml (phage 12) and 7.5×10^9 PFU/ml (phage 6). Cells contain cognate spectinomycin resistance genes, as in (C); all experiments were performed in the presence of spectinomycin.

cells, in which TCG codons are read as alanine and TCA codons are read as histidine (Fig. 4).

Next, we investigated HGT for mobile genetic elements written in altered genetic codes. We synthesized the mobile genetic element O-F1 (TCG-Ala, TCA-His). The genetic code in all annotated open reading frames of this F plasmid was compressed by using the Syn61 scheme, and GCN codons (which encode alanine in the canonical code) and CAT/C codons (which encode histidine in the canonical code) were converted to TCG and TCA codons, respectively, within the *trfA* gene; this gene is essential for the replication of the mobile genetic element (*30*).

O-F1 (TCG-Ala, TCA-His) was horizontally transferred to Syn61Δ3 (tRNA$_{CGA}^{Ala}$, tRNA$_{UGA}^{His}$) cells. We further demonstrated that O-F1 (TCG-Ala, TCA-His) was not horizontally transferred to cells that read the canonical genetic code (Fig. 4). These experiments demonstrated that we can create O-HGT systems. We created additional HGT systems that are orthogonal to the natural genetic system and mutually orthogonal to each other (Fig. 4 and fig. S17). Overall, we demonstrated the scalability of our approach through the creation of five mutually orthogonal HGT systems.

Blocking invading codes

We hypothesized that reassigning TCA and TCG codons to specific natural amino acids and replacing codons for specific natural amino acids in essential genes with TCA and TCG codons in Syn61Δ3 (Fig. 5) would obstruct the *serT*-mediated HGT we observed in this strain (Fig. 1).

Transfer of F (WT + *serT*) to Syn61Δ3 ($tRNA_{CGA}^{Ala}$, $tRNA_{UGA}^{His}$, O-SpecR [TCG-Ala, TCA-His]) was obstructed (10^4-fold) in the absence of spectinomycin because $tRNA_{CGA}^{Ala}$ and $tRNA_{UGA}^{His}$ compete with $tRNA_{UGA}^{Ser}$ in the recipient cell to decrease the production of functional proteins from the mobile genetic element. However, this obstruction was not sufficient to completely ablate transfer of F (WT + *serT*). Upon the addition of spectinomycin, which makes O-SpecR (TCG-Ala, TCA-His) an essential gene in the cell, the decoding of TCG codons as alanine and the decoding of TCA codons as histidine become essential and "locked in." Under these conditions, the transfer of F (WT + *serT*) was completely ablated (Fig. 5). Similar results were obtained with other refactored codes and other essential genes (figs. S18 and S19).

To extend our approach to viral infection, we identified pools of phage from the River Cam that can infect Syn61Δ3 (data file S4 and supplementary materials, materials and methods). From these pools, we isolated two individual phage (12 and 06, both T4-like phage), which carry an identical $tRNA_{UGA}^{Ser}$ gene and infect Syn61Δ3 (fig. S20); some viruses are known to carry their own tRNAs and other translation factors to augment the cellular pool of translation factors and assist in the translation of codons within their own genes (*9*, *31*, *32*). As expected, expression of this tRNA in Syn61Δ3 is sufficient to confer susceptibility to infection by (otherwise noninfectious) T4 phage (fig. S21). We demonstrated that unlike Syn61Δ3, several refactored, code-locked strains were completely resistant to infection with phage 06 and phage 12 (Fig. 5 and fig. S22).

Our results demonstrate that cells with refactored genetic codes resist invasion by mobile genetic elements that use competing codes. Locking the refactored codes into essential genes in the cell enhances this resistance and can ablate transfer of mobile genetic elements with competing codes.

Discussion

Previous work has shown that the choice of synonymous codons in individual genes and viruses can alter their robustness and evolvability (*33*–*35*), but such approaches are limited to exploring subsets of the canonical code. Although a large body of theoretical work and a limited number of in vitro experiments have considered the relationship between the structure of the genetic code and its robustness and evolvability (*21*, *22*), it has been impossible to investigate the resulting hypotheses through experiments in living cells. Refactoring the structure of the genetic code directly alters the number and types of amino acids that can be accessed by point mutations in live cells (figs. S23 and S24) and provides opportunities to experimentally test how altered codes affect the robustness and evolvability of protein and cellular function. In future work, we will aim to leverage genetic code refactoring to accelerate directed evolution.

Competition between pools of genotypes written in different genetic codes may have led to a universal code being fixed in extant life. Future work may exploit organisms with refactored and mutually orthogonal codes to experimentally investigate competition between codes and the role of HGT in fixing and maintaining a universal genetic code (*4*, *36*).

Shielding synthetic organisms from environmental genetic elements may be valuable for biotechnological applications on an industrial scale, for which contamination with mobile genetic elements, including viruses, can cause financial losses and disrupt vital supply chains (*37*). Synthetic organisms with decoders for an orthogonal code and essential genes that lock the cognate orthogonal code into the organism exhibit resistance to mobile genetic elements that are written in the canonical code. This resistance extends to mobile genetic elements that carry tRNA genes that otherwise allow correct reading of the canonical code in their genes. Our work defines a paradigm for creating organisms that actively resist invasion by foreign codes.

Our refactored genetic codes limit the transfer of genetic information from synthetic organisms to natural organisms and may form the basis of genetic firewalls that isolate synthetic genetic systems from the environment. Such genetic firewalls complement strategies for controlling the survival and growth of synthetic organisms, to realize biocontainment (*16*, *38*, *39*). This is especially important when considering applications of engineered organisms outside the laboratory.

The strategies that we have described should be generally applicable to any gene or genetic system added to the synthetic organism. Because the canonical genetic code is near universally conserved, we anticipate that the principles we have established may be applied to a broad range of organisms.

REFERENCES AND NOTES

1. F. H. Crick, L. Barnett, S. Brenner, R. J. Watts-Tobin, *Nature* **192**, 1227–1232 (1961).
2. M. W. Nirenberg, J. H. Matthaei, *Proc. Natl. Acad. Sci. U.S.A.* **47**, 1588–1602 (1961).
3. R. J. Hall, F. J. Whelan, J. O. McInerney, Y. Ou, M. R. Domingo-Sananes, *Front. Microbiol.* **11**, 1569 (2020).
4. K. Vetsigian, C. Woese, N. Goldenfeld, *Proc. Natl. Acad. Sci. U.S.A.* **103**, 10696–10701 (2006).
5. S. M. Soucy, J. Huang, J. P. Gogarten, *Nat. Rev. Genet.* **16**, 472–482 (2015).
6. E. V. Koonin, A. S. Novozhilov, *IUBMB Life* **61**, 99–111 (2009).
7. M. Kollmar, S. Mühlhausen, *BioEssays* **39**, 1600221 (2017).
8. J. Ling *et al*., *Nucleic Acids Res.* **42**, 499–508 (2014).
9. A. L. Borges *et al*., *Nat. Microbiol.* **7**, 918–927 (2022).
10. M. A. Santos, A. C. Gomes, M. C. Santos, L. C. Carreto, G. R. Moura, *C. R. Biol.* **334**, 607–611 (2011).
11. D. J. Taylor, M. J. Ballinger, S. M. Bowman, J. A. Bruenn, *PeerJ* **1**, e50 (2013).
12. Y. Shulgina, S. R. Eddy, *eLife* **10**, e71402 (2021).
13. D. G. Gibson *et al*., *Science* **319**, 1215–1220 (2008).
14. J. Fredens *et al*., *Nature* **569**, 514–518 (2019).
15. M. J. Lajoie *et al*., *Science* **342**, 357–360 (2013).
16. D. J. Mandell *et al*., *Nature* **527**, 264–264 (2015).
17. A. J. Rovner *et al*., *Nature* **527**, 264 (2015).
18. W. E. Robertson *et al*., *Science* **372**, 1057–1062 (2021).
19. D. de la Torre, J. W. Chin, *Nat. Rev. Genet.* **22**, 169–184 (2021).
20. K. Wang *et al*., *Nature* **539**, 59–64 (2016).
21. G. Pines, J. D. Winkler, A. Pines, R. T. Gill, *mBio* **8**, e01654-17 (2017).
22. J. Calles, I. Justice, D. Brinkley, A. Garcia, D. Endy, *Nucleic Acids Res.* **47**, 10439–10451 (2019).
23. P. Marliere, *Syst. Synth. Biol.* **3**, 77–84 (2009).
24. S. Osawa, T. H. Jukes, *J. Mol. Evol.* **28**, 271–278 (1989).
25. M. Schmidt, V. Kubyshkin, *ChemBioChem* **22**, 1268–1284 (2021).
26. J. Frazer *et al*., *Nature* **599**, 91–95 (2021).
27. S. Teng, A. K. Srivastava, C. E. Schwartz, E. Alexov, L. Wang, *Int. J. Comput. Biol. Drug Des.* **3**, 334–349 (2010).
28. V. Parthiban, M. M. Gromiha, D. Schomburg, *Nucleic Acids Res.* **34**, W239–W242 (2006).
29. P. C. Ng, S. Henikoff, *Annu. Rev. Genomics Hum. Genet.* **7**, 61–80 (2006).
30. I. Konieczny, K. S. Doran, D. R. Helinski, A. Blasina, *J. Biol. Chem.* **272**, 20173–20178 (1997).
31. V. A. Delesalle, N. T. Tanke, A. C. Vill, G. P. Krukonis, *Bacteriophage* **6**, e1219441 (2016).
32. M. Bailly-Bechet, M. Vergassola, E. Rocha, *Genome Res.* **17**, 1486–1495 (2007).
33. B. A. Renda, M. J. Hammerling, J. E. Barrick, *Mol. Biosyst.* **10**, 1668–1678 (2014).
34. G. Moratorio *et al*., *Nat. Microbiol.* **2**, 17088 (2017).
35. J. R. Coleman *et al*., *Science* **320**, 1784–1787 (2008).
36. V. Kubyshkin, C. G. Acevedo-Rocha, N. Budisa, *Biosystems* **164**, 16–25 (2018).
37. P. W. Barone *et al*., *Nat. Biotechnol.* **38**, 563–572 (2020).
38. P. Marlière *et al*., *Angew. Chem. Int. Ed.* **50**, 7109–7114 (2011).
39. J. W. Lee, C. T. Y. Chan, S. Slomovic, J. J. Collins, *Nat. Chem. Biol.* **14**, 530–537 (2018).

ACKNOWLEDGMENTS

We thank J. Fredens (National University of Singapore) for advice on conjugation assays; S. Grazioli and A. Kleefeldt for help with de novo assembly of phage genomes; and the LMB mass spectrometry facility, especially S.-Y. Peak-Chew, for performing mass spectrometry experiments. **Funding:** This work was supported by the Medical Research Council (MRC), UK (MC_U105181009, MC_UP_A024_1008 to J.W.C.); G.P. was supported by a Marie Skłodowska-Curie European Postdoctoral Fellowship (897663). Work in the G.P.C.S. laboratory was supported by award BB/W000105/1 from the Biotechnology and Biological Sciences Research Council, UK (UKRI). **Author contributions:** J.F.Z. and J.W.C. conceptualized and planned the project, with input from W.E.R.; J.F.Z. demonstrated unidirectional genetic isolation and loss of isolation through tRNA import. J.F.Z., T.S.E., G.P., and W.E.R. designed and characterized tRNAs for genetic code refactoring. J.F.Z. demonstrated bidirectional genetic isolation and (mutually) orthogonal HGT systems. J.F.Z. demonstrated improved genetic isolation through code refactoring and genetic code locking. J.F.Z. and T.K. performed phage experiments under supervision of G.P.C.S. J.W.C. and J.F.Z. wrote the manuscript, with input from all authors. J.W.C. supervised the project. **Competing interests:** The MRC has filed a provisional patent application related to this work on which J.F.Z., W.E.R., and J.W.C. are listed as inventors. J.W.C. has a commercial interest in Constructive Bio. **Data and materials**

availability: The GenBank accession nos. for all the plasmids described in the text are provided in data file S5, and the authors agree to provide any materials and strains used in this study upon request. All data are available in the main text or supplementary materials. **License information:** Copyright © 2022 the authors, some rights reserved; exclusive licensee American Association for the Advancement of Science. No claim to original US government works. https://www.sciencemag.org/about/science-licenses-journal-article-reuse

SUPPLEMENTARY MATERIALS
science.org/doi/10.1126/science.add8943
Materials and Methods
Figs. S1 to S24
References (*40*–*44*)
Data Files S1 to S5
MDAR Reproducibility Checklist

Submitted 12 July 2022; accepted 7 October 2022
Published online 20 October 2022
10.1126/science.add8943

NEUROSCIENCE

On-demand cell-autonomous gene therapy for brain circuit disorders

Yichen Qiu[1], Nathanael O'Neill[1], Benito Maffei[1], Clara Zourray[1,2], Amanda Almacellas-Barbanoj[1], Jenna C. Carpenter[1], Steffan P. Jones[1], Marco Leite[1], Thomas J. Turner[1], Francisco C. Moreira[1], Albert Snowball[1], Tawfeeq Shekh-Ahmad[1]†, Vincent Magloire[1], Serena Barral[2], Manju A. Kurian[2,3], Matthew C. Walker[1], Stephanie Schorge[4], Dimitri M. Kullmann[1]*, Gabriele Lignani[1]*

Several neurodevelopmental and neuropsychiatric disorders are characterized by intermittent episodes of pathological activity. Although genetic therapies offer the ability to modulate neuronal excitability, a limiting factor is that they do not discriminate between neurons involved in circuit pathologies and "healthy" surrounding or intermingled neurons. We describe a gene therapy strategy that down-regulates the excitability of overactive neurons in closed loop, which we tested in models of epilepsy. We used an immediate early gene promoter to drive the expression of Kv1.1 potassium channels specifically in hyperactive neurons, and only for as long as they exhibit abnormal activity. Neuronal excitability was reduced by seizure-related activity, leading to a persistent antiepileptic effect without interfering with normal behaviors. Activity-dependent gene therapy is a promising on-demand cell-autonomous treatment for brain circuit disorders.

Many neurodevelopmental and neuropsychiatric circuit disorders are characterized by intermittent episodes of pathological activity (*1*–*3*). Pharmacotherapy is focused on reducing the frequency and/or severity of such episodes, but often with limited success. For example, 30% of people with epilepsy are refractory to pharmacological treatment, even with drugs that act in a use-dependent manner on their molecular targets (*4*). Genetic therapies are promising strategies to treat these pathologies because of their ability to modulate neuronal excitability in a region-specific and cell type–specific manner (*5*–*9*). However, current experimental genetic therapies do not discriminate between neurons involved in triggering circuit paroxysms and healthy surrounding or intermingled neurons (*10*–*16*). There is a need to develop methods that select and treat only those neurons involved in the generation of crises (*17*, *18*).

[1]Department of Clinical and Experimental Epilepsy, UCL Queen Square Institute of Neurology, University College London, London, UK. [2]Department of Developmental Neurosciences, Zayed Centre for Research Into Rare Disease in Children, GOS–Institute of Child Health, University College London, London, UK. [3]Department of Neurology, Great Ormond Street Hospital for Children, London, UK. [4]Department of Neuroscience, Physiology and Pharmacology, University College London, London, UK.
***Corresponding author. Email: g.lignani@ucl.ac.uk (G.L.); d.kullmann@ucl.ac.uk (D.M.K.)**
†Present address: Department of Pharmaceutics, The Hebrew University of Jerusalem, Jerusalem, Israel.

In the case of epilepsy, subpopulations of neurons exhibit stereotypical patterns of pathological discharges during seizures (*19*, *20*). Targeting these neurons specifically would be an important step toward a rational treatment with minimal side effects.

Activity-dependent promoters, typically of immediate early genes (IEGs), respond rapidly to increases in neuronal activity (*21*–*23*) and have been used to identify hyperactive cells recruited during seizures (*24*). Although seizures often start and terminate abruptly, they can occur in clusters with intervals comparable with the kinetics of IEGs (*25*). We therefore asked whether an activity-dependent promoter could be used to drive a therapeutic transgene to reduce neuronal excitability in closed loop. Epileptiform hyperactivity should reduce their likelihood to fire while leaving other neurons unaffected (Fig. 1A). Once seizures resolve, the genetic therapy should switch itself off, unless and until excessive activity occurs again (Fig. 1B).

Results

Activity-dependent gene therapy follows neuronal dynamics, decreases network hyperexcitability in vitro

We used an adeno-associated virus (AAV) to express a destabilized version of the fluorescent reporter green fluorescent protein (dsGFP) under the promoter of an extensively characterized IEG, c-Fos (AAV9 *cfos*-dsGFP; shortened to *cfos*-dsGFP) (*21*–*24*), and verified that dsGFP expression dynamically follows epileptiform network activity in vitro. Primary neuronal cultures were infected at 7 days in vitro and grown either on multielectrode arrays (MEAs) to record network activity or on coverslips for imaging (Fig. 1, C to F). At 18 days in vitro, we blocked γ-aminobutyric acid type A ($GABA_A$) receptors with picrotoxin (PTX) to mimic an epileptic seizure and then recorded network activity or, in parallel, fixed a subset of coverslips, at 2, 6, 24, and 48 hours in the continued presence of PTX. MEA recordings revealed an increase in network activity that peaked 6 hours after addition of PTX and then returned to baseline after 48 hours (Fig. 1D and fig.S1). c-Fos expression and dsGFP fluorescence followed a similar time course (Fig. 1, E and F, and fig. S2).

We next placed a transgene that decreases neuronal and network activity under the same *cfos* promoter. We used a codon-optimized version of *KCNA1*, which encodes the potassium channel Kv1.1, with an $Ile^{400}Val$ mutation to bypass the need for posttranscriptional editing and facilitate recovery from inactivation (*15*). We refer to this engineered potassium (K+) Channel as EKC. Kv1.1 overexpression decreases both neuronal excitability and synaptic neurotransmitter release (*26*). Kv1.1 overexpression using KCNA1, EKC, or transcriptional upregulation has also been used in experimental antiepileptic gene therapies targeting excitatory neurons (*11*, *12*, *15*, *27*, *28*). Because of the innate propensity of primary neuronal cultures in vitro to exhibit bursting activity as they mature, we transduced neurons plated on MEAs at 7 days in vitro with either *cfos*-dsGFP or AAV9 *cfos*-EKC (*cfos*-EKC) and recorded network activity at 21 days in vitro (Fig. 2, A and B). As hypothesized, cultures treated with *cfos*-EKC showed less network activity than that of cultures treated with *cfos*-dsGFP (Fig. 2C). Spike frequency, burst frequency, and number of spikes per burst were all significantly lower in cultures treated with *cfos*-EKC (Fig. 2D and fig. S3). We also asked whether an experimental perturbation aimed at transiently increasing activity is followed by a rapid decrease in neuronal excitability, as would be expected from the activity-dependent promoter driving EKC expression (fig. S5). We increased spontaneous activity by adding PTX for 30 min and then silenced network activity for 2 hours with tetrodotoxin (TTX) before washing off the blockers and recording neuronal firing. We

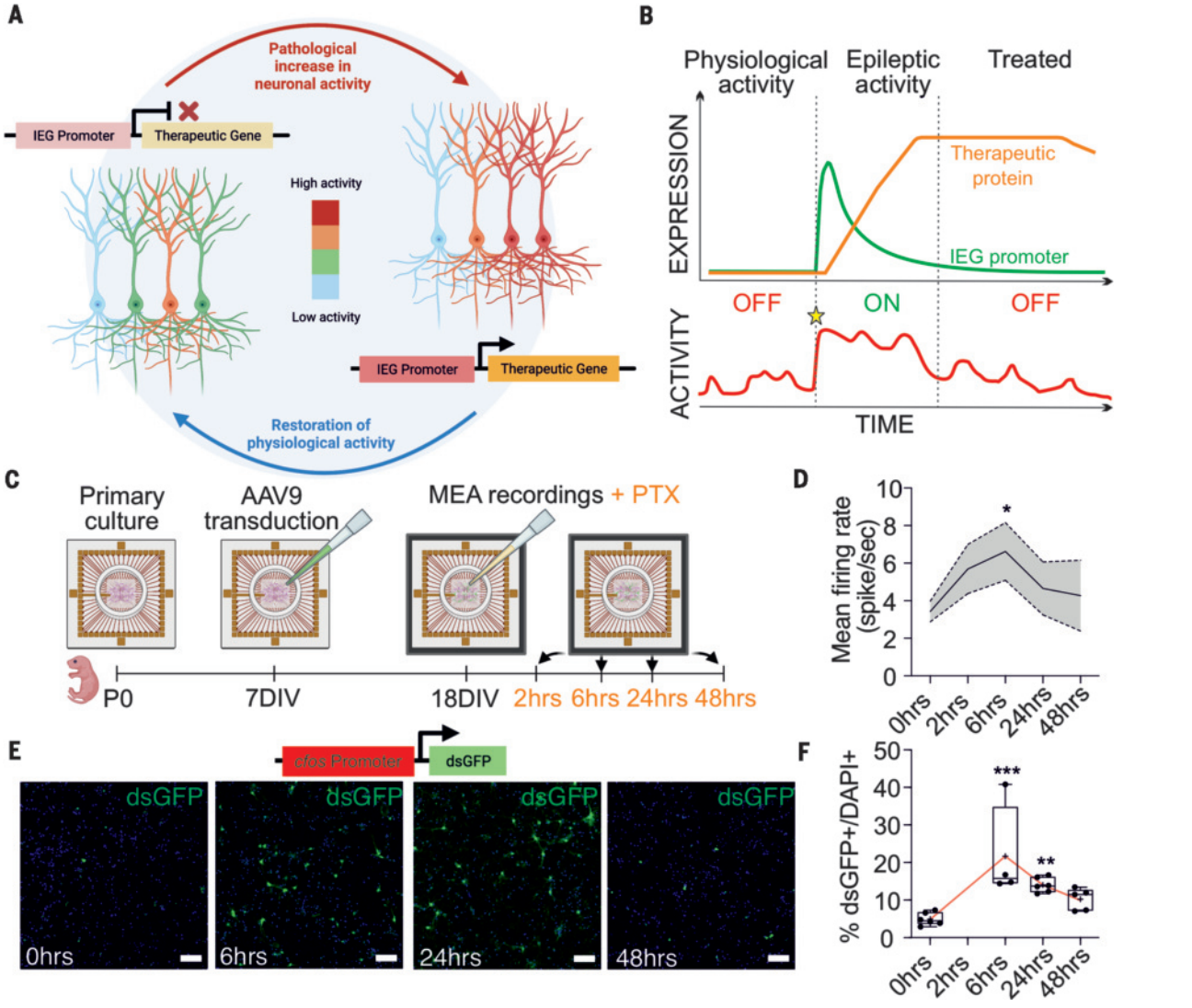


Fig. 1. Activity-dependent gene therapy paradigm. (**A**) Cartoon illustrating the activity-dependent strategy. (**B**) Schematic sequence of activity-dependent promoter and transgene expression. The star indicates the beginning of the pathological event. (**C**) Timeline of MEA recordings from primary cultures. (**D**) Network mean firing rate after disinhibition with PTX application [*P < 0.05; one-way analysis of variance (ANOVA) followed by Bonferroni multiple-comparison test versus 0 hours]. (**E**) dsGFP expression in primary neurons transduced with cfos-dsGFP 0, 6, 24, and 48 hours after addition of PTX. Scale bars, 100 μm. (**F**) dsGFP-positive neurons expressed as a percentage of all 4′,6-diamidino-2-phenylindole (DAPI)–positive neurons at different time points after PTX application (**P < 0.01; ***P < 0.001; one-way ANOVA followed by Bonferroni multiple-comparison test versus 0 hours).

observed a net decrease in firing rate in dsGFP-positive neurons treated with *cfos*-EKC compared with *cfos*-dsGFP (fig. S5).

We asked whether the results with *cfos*-EKC would generalize to other activity-dependent promoters and transgenes (fig. S6). We compared the promoters of several IEGs (*cfos*, *arc*, and *egr1*) as well as synthetic activity–dependent promoters [enhanced synaptic activity-responsive element (ESARE) and NPAS4 robust activity marker (NRAM)], which have different properties (*21*, *29*–*31*) (table S2), in combination with three transgenes: the control reporter dsGFP; EKC as above; or another potassium channel gene, *KCNJ2*, which encodes the muscle inward-rectifier Kir2.1 (*32*, *33*). Although some promoter-transgene combinations were effective in reducing spiking and/or bursting, none was as consistent across the different electrophysiological measures as *cfos*-EKC (fig. S6).

We sought to determine whether *cfos*-EKC dampens the effect of a proconvulsant manipulation in vitro. However, the lower baseline activity in *cfos*-EKC–treated cultures (Fig. 2D) precluded a simple comparison with *cfos*-dsGFP. Instead, we modified a previously described method, CRISPR activation (CRISPRa), based on dual-AAV9 delivery of a single guide RNA (sgRNA) and a nuclease-defective "dead" Cas9 (dCas9) controlled by doxycycline (*14*, *34*). One AAV9 carried a TeT-ON promoter driving dCas9 fused to a transcriptional activator. The other AAV9 expressed the *cfos* promoter driving the tetracycline trans-activator rtTa linked to enhanced GFP (EGFP) with a T2A peptide, as well as a U6 promoter driving either an sgRNA targeting the endogenous *Kcna1* promoter or an sgRNA designed to target the yeast LacZ gene as control (Fig. 2E) (*14*, *34*). In this system, endogenous *Kcna1* overexpression was designed to be switched on only when all three of the following conditions are met: (i) neurons are cotransduced with both AAV9s, (ii) doxycycline is applied, and (iii) activity is sufficient to activate the *cfos* promoter. Primary cultures plated on MEAs were treated with both AAVs at 7 days in vitro. We then obtained an initial (baseline) recording of network

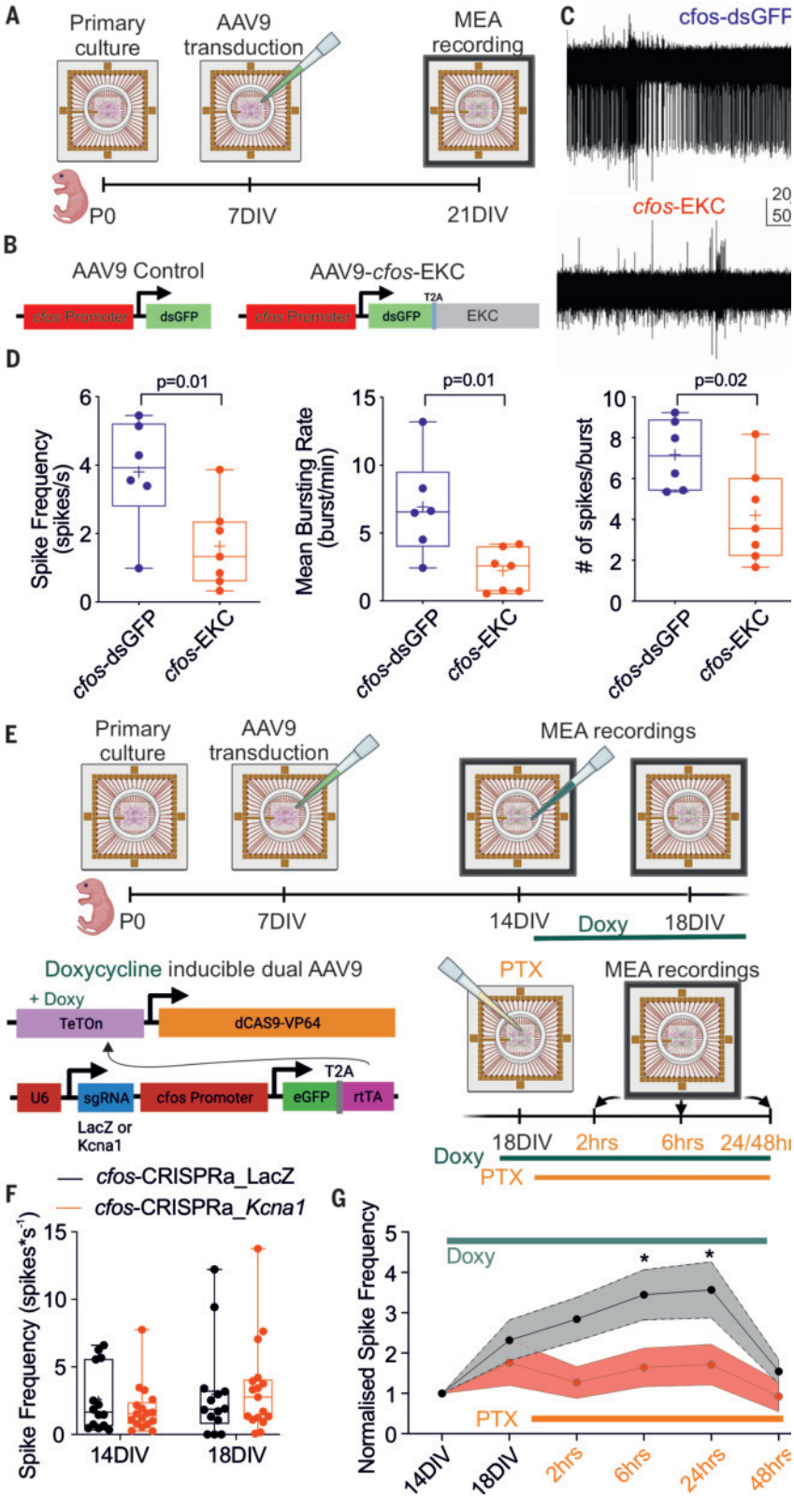


Fig. 2. Activity-dependent gene therapy decreases epileptiform activity in vitro. (**A**) Timeline of MEA recordings in primary cultures. DIV, days in vitro. (**B**) Primary cultures were transduced with either cfos-dsGFP as control or cfos-EKC. (**C**) MEA traces. (**D**) Effect of cfos-EKC compared with cfos-dsGFP on spike frequency, mean bursting rate, and average number of spikes per burst. Student's *t* test corrected for multiple comparisons, $\alpha = 0.02$. (**E**) Timeline of MEA recordings in primary cultures transduced with dual AAVs controlled by doxycycline: one expressing an inducible dCAS9 fused to a transcriptional activator, and the other carrying an sgRNA targeting either the *Kcna1* promoter or a LacZ sequence. (**F**) Spike frequency before PTX addition was similar between neurons transduced with *cfos*-CRISPRa_LacZ and *cfos*-CRISPRa_*Kcna1*. (**G**) Spike frequency over time normalized to network activity recorded at 14 days in vitro (*$P < 0.05$; two-way ANOVA followed by Bonferroni multiple-comparison test; interaction time × sgRNA, $P = 0.006$). (F) and (G) use the same color scheme.

activity at 14 days in vitro without doxycycline treatment. There was no difference in network excitability between cultures transduced with either *cfos*-CRISPRa_*Kcna1* or *cfos*-CRISPRa_LacZ (Fig. 2F). We then added doxycycline to activate CRISPRa and recorded from the same cultures 4 days later. We again observed no significant difference in network activity. Last, we added PTX and recorded from the same cultures 2, 6, 24, and 48 hours later. This revealed a clear difference between cultures treated with *cfos*-CRISPRa_*Kcna1* and *cfos*-CRISPRa_LacZ. Indeed, PTX failed to increase network activity in cultures treated with *cfos*-CRISPRa_*Kcna1* (Fig. 2G and fig. S7).

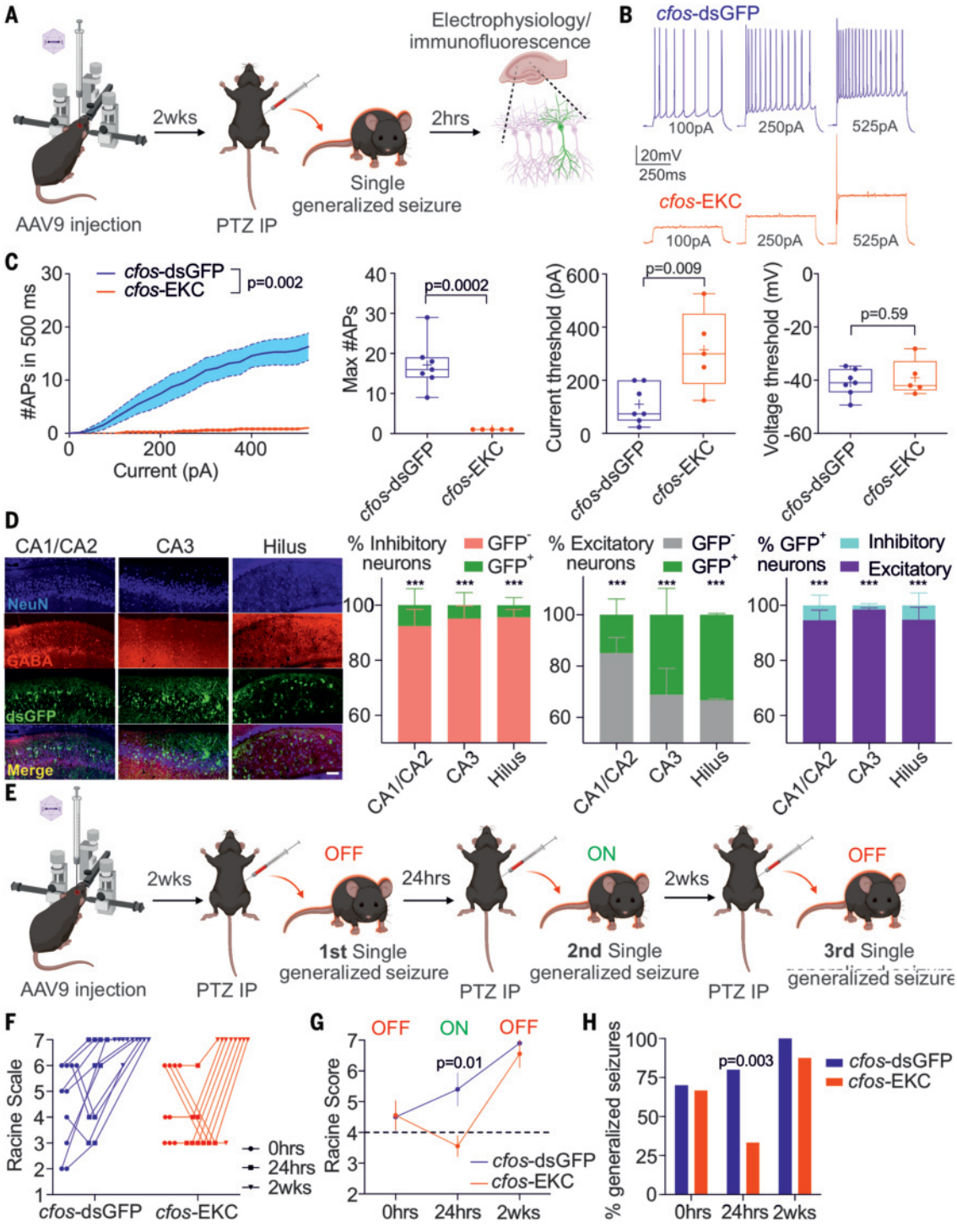


Fig. 3. Activity-dependent gene therapy is effective in decreasing excitatory neuronal excitability and in protecting against sequential chemoconvulsant challenges. (**A**) Illustrative timeframe for electrophysiology and immunofluorescence analysis. (**B**) Evoked trains of action potentials recorded in neurons transduced with either *cfos*-dsGFP or *cfos*-EKC. (**C**) Neuronal excitability parameters of neurons expressing either *cfos*-dsGFP or *cfos*-EKC after a single generalized seizure. (Left) Number of action potentials evoked by increasing current steps. (Middle) Maximum number of evoked action potential. (Right) Current and voltage thresholds. Input/output, two-way ANOVA; other graphs, Student's *t* test corrected for multiple comparisons, $\alpha = 0.02$. (**D**) Immunofluorescence images and analysis of the percentage of inhibitory neurons positive or negative for dsGFP, of excitatory neurons positive or negative for dsGFP, and of dsGFP positive neurons identified as excitatory or inhibitory ($n = 3$ animals) (***$P < 0.001$ two-way ANOVA followed by Bonferroni multiple-comparison test). Scale bar, 100 μm. (**E**) Illustrative timeline for repeated PTZ injections. OFF, basal *cfos*-driven transgene expression; ON, seizure-induced *cfos*-driven expression. (**F**) Raw Racine scale data in animals transduced with either *cfos*-dsGFP or *cfos-KCNA1* and then injected with PTZ at three time points (0 hours, 24 hours, and 2 weeks). (**G**) Averaged Racine scores of data shown in (F). Racine score of >4 was considered as a generalized seizure. Two-way ANOVA followed by Bonferroni multiple-comparison test. (**H**) Percentage of mice experiencing generalized seizures from (F) (χ^2 test).

Activity-dependent gene therapy decreases neuronal excitability in a transient, cell-autonomous, on-demand fashion

We next asked whether the strategy is effective in vivo. In the first set of experiments, we asked how the *cfos* promoter behaves in response to chemoconvulsant-evoked seizures. Mice were injected with either *cfos*-dsGFP or AAV9 *CaMKII*-dsGFP (shortened to *CaMKII*-dsGFP) in the visual cortex. The *CaMKII* promoter was chosen as a control because it has previously been used to bias expression to forebrain principal cells in constitutive antiepileptic gene therapies (*10*, *15*). Two weeks later, we injected either pilocarpine into the same brain region to induce a focal seizure (*35*) or saline as a control (fig. S8) and sacrificed the mice 2 hours later. Animals treated with *CaMKII*-dsGFP showed widespread expression of GFP whether saline or pilocarpine was injected. By contrast, mice treated with *cfos*-dsGFP showed focal expression of GFP only after pilocarpine injection (fig. S8).

To test whether activity-dependent expression of EKC driven by the *cfos* promoter can affect neuronal excitability, we injected either *cfos*-dsGFP or *cfos*-EKC in the hippocampus of adult mice. Two weeks later, we elicited a single generalized seizure with an intraperitoneal pentylenetetrazole (PTZ) injection. Mice were monitored to verify that they reached stage 5 on a revised Racine scale (equivalent to a generalized tonic-clonic seizure) (*36*) and were sacrificed after 2 hours to prepare acute hippocampal slices for electrophysiological recordings from dsGFP-positive CA1 pyramidal neurons (Fig. 3A). dsGFP-positive neurons treated with *cfos*-EKC exhibited a profound decrease in excitability when compared with *cfos*-dsGFP treated neurons (Fig. 3, B and C), with robust decreases in the maximal firing frequency and in the slope that relates action potential frequency to depolarizing current injection. There was also an increase in current threshold for triggering the first action potential and an increase in the size of the afterhyperpolarization, but other parameters were not affected (Fig. 3C and fig. S9). The effect of activity-dependent EKC expression was more pronounced than previously observed with constitutive expression (*11*, *14*). We were unable to measure the effect of *cfos*-EKC in the absence of seizures because we could not identify the transduced neurons without activation of the fluorescent reporter.

We also tested other activity-dependent promoter-transgene combinations. These revealed a consistent effect of EKC overexpression on action potential firing, independent of the promoter (figs. S10 and S11). When the *KCNJ2* transgene was used, however, neurons exhibited a hyperpolarized resting membrane potential, as expected from the intrinsic properties of this channel (*32*), but inconsistent changes in firing (figs. S10 and S11 and supplementary text).

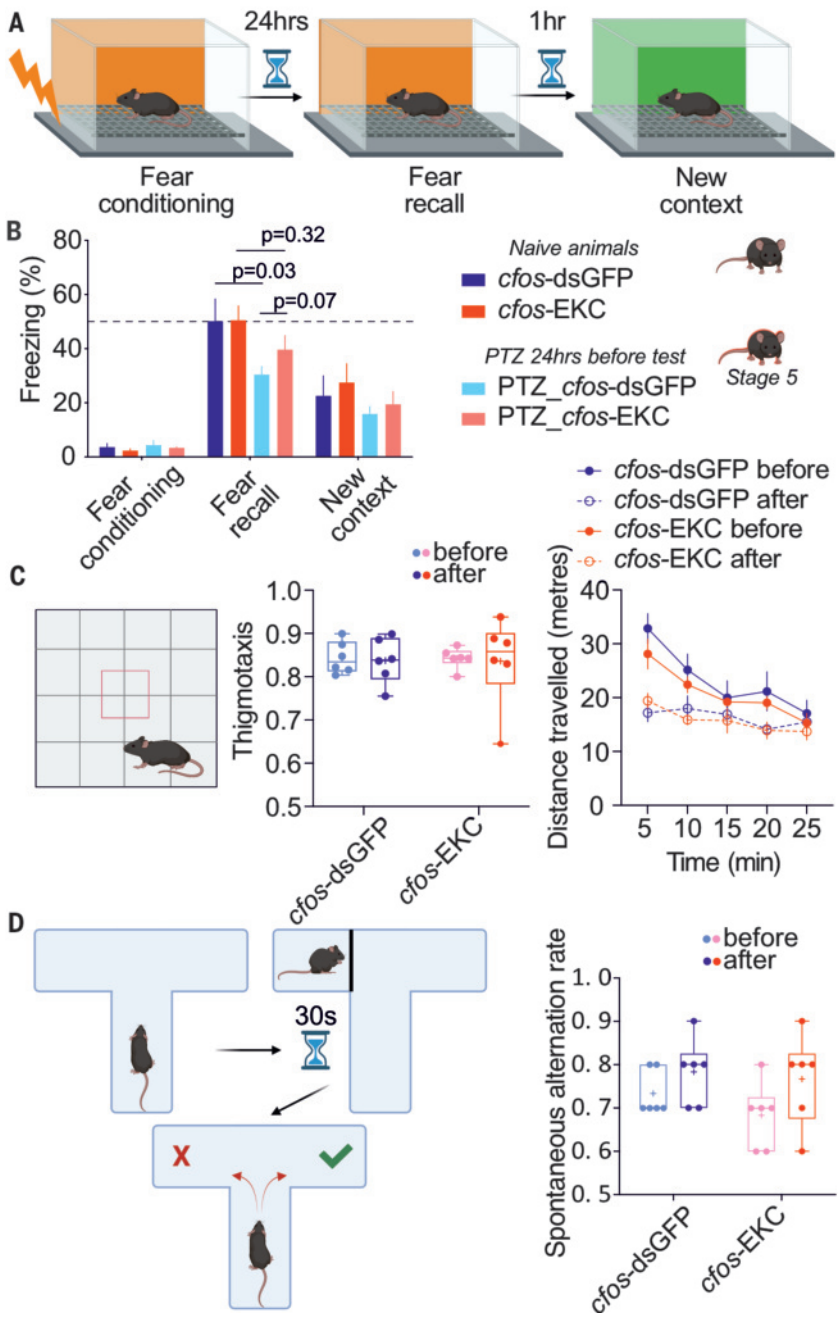


Fig. 4. Activity-dependent gene therapy does not affect normal behavior. (**A**) Schematic of the CFC test. (**B**) Percentage of freezing time for naïve or PTZ-treated mice injected with either *cfos*-dsGFP (n = 7 and 8, respectively) or *cfos*-EKC (n = 7 and 9, respectively) during fear conditioning, fear recall, and in a new context. Two-way ANOVA followed by Bonferroni multiple-comparison test. (**C**) Open field test. Shown is thigmotaxis (fraction of time spent in the periphery) and distance traveled before and after either *cfos*-dsGFP or *cfos*-EKC injection in both hippocampi. (**D**) Spontaneous T-maze alternation test. Shown are the spontaneous alternation rates before and after either *cfos*-dsGFP or *cfos*-EKC injection.

To better understand which neurons were activated after a single generalized PTZ-evoked seizure, we performed immunohistochemical analysis in different hippocampal regions (CA1/2, CA3, and hilus) in animals treated with different IEG promoters driving dsGFP in the hippocampus (Fig. 3D and figs. S12 to S17). dsGFP driven by *cfos* was mainly expressed in excitatory neurons, with a very low percentage of inhibitory neurons or of parvalbumin-positive neurons expressing the reporter (Fig. 3D and fig. S15). Although ESARE-driven dsGFP

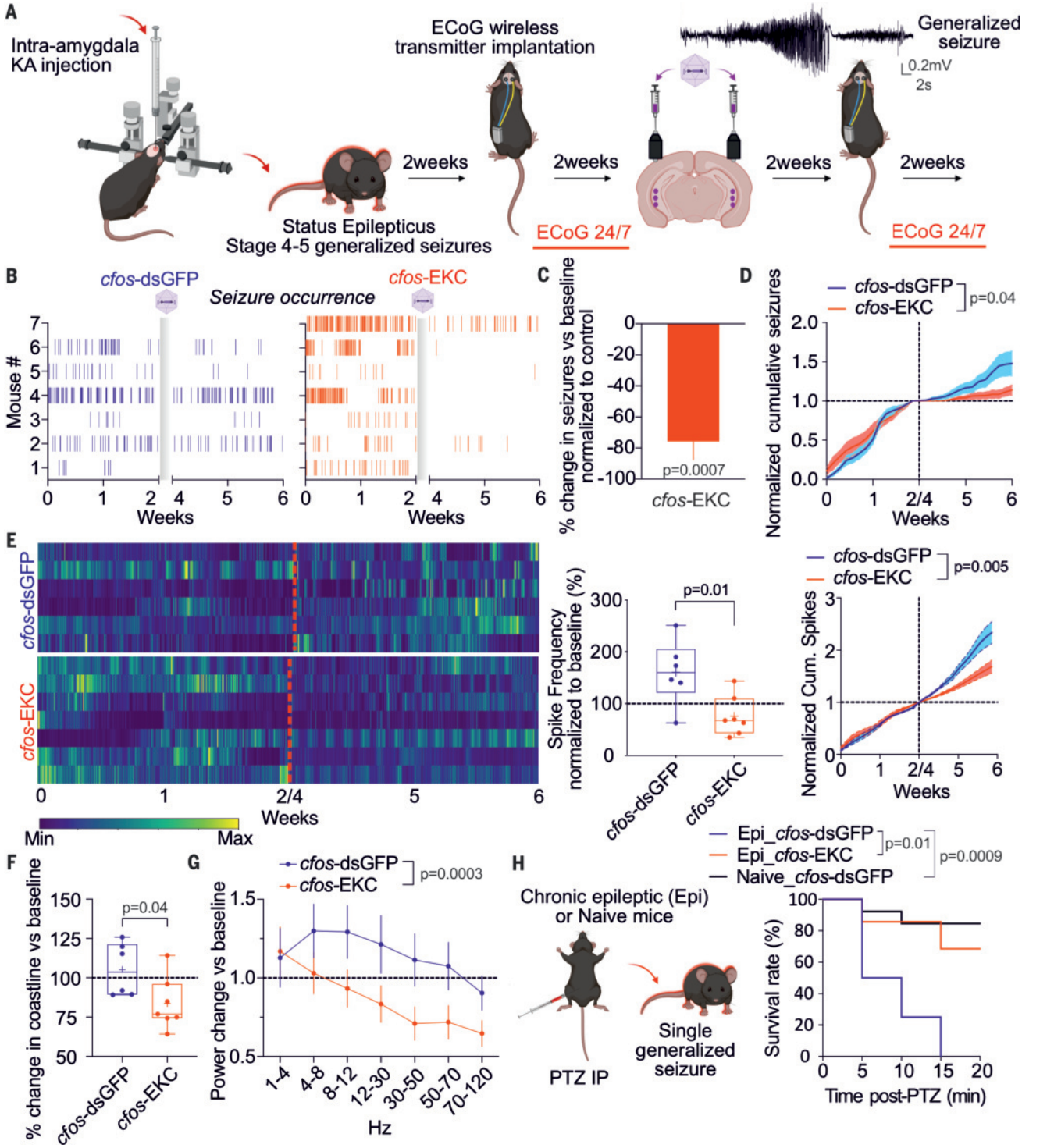


Fig. 5. Activity-dependent gene therapy decreases spontaneous generalized seizures and interictal spikes and protects against a subsequent chemoconvulsant challenge. (**A**) Schematic of the preclinical trial. (**B**) Seizures (vertical bars) over time for each mouse. Gray boxes indicate the viral injection, either with *cfos*-dsGFP or *cfos*-EKC, followed by a 2-week period to allow viral expression. (**C**) Percentage change in spontaneous generalized seizures after *cfos*-EKC treatment compared with baseline, normalized to the same percentage of change in *cfos*-dsGFP treated mice. One Sample *t* test versus 0 hours. (**D**) Weighted cumulative plot normalized by the total seizure count before treatment. Two-way ANOVA. (**E**) (Left) Number of spikes per hour plotted against time. Red dotted lines indicate the viral injection, with either *cfos*-dsGFP or *cfos-KCNA1*. Spike rates were normalized to the maximum for each animal (yellow, maximum; blue, minimum spike rate). (Middle) Spike frequency normalized to baseline (before viral injection) (Student's *t* test). (Right) Weighted cumulative plot normalized by the total interictal spike count before viral treatment (two-way ANOVA). (**F**) Percentage change in coastline normalized to baseline (before viral injection). Student's *t* test. (**G**) Percentage power change versus baseline in different frequency bands (two-way ANOVA). (**H**) Chronic epileptic animals or naïve animals (injected with *cfos*-dsGFP) received an intraperitoneal PTZ injection at the end of the study. Kaplan-Meier plot showing survival rate. Log-rank (Mantel-Cox) test.

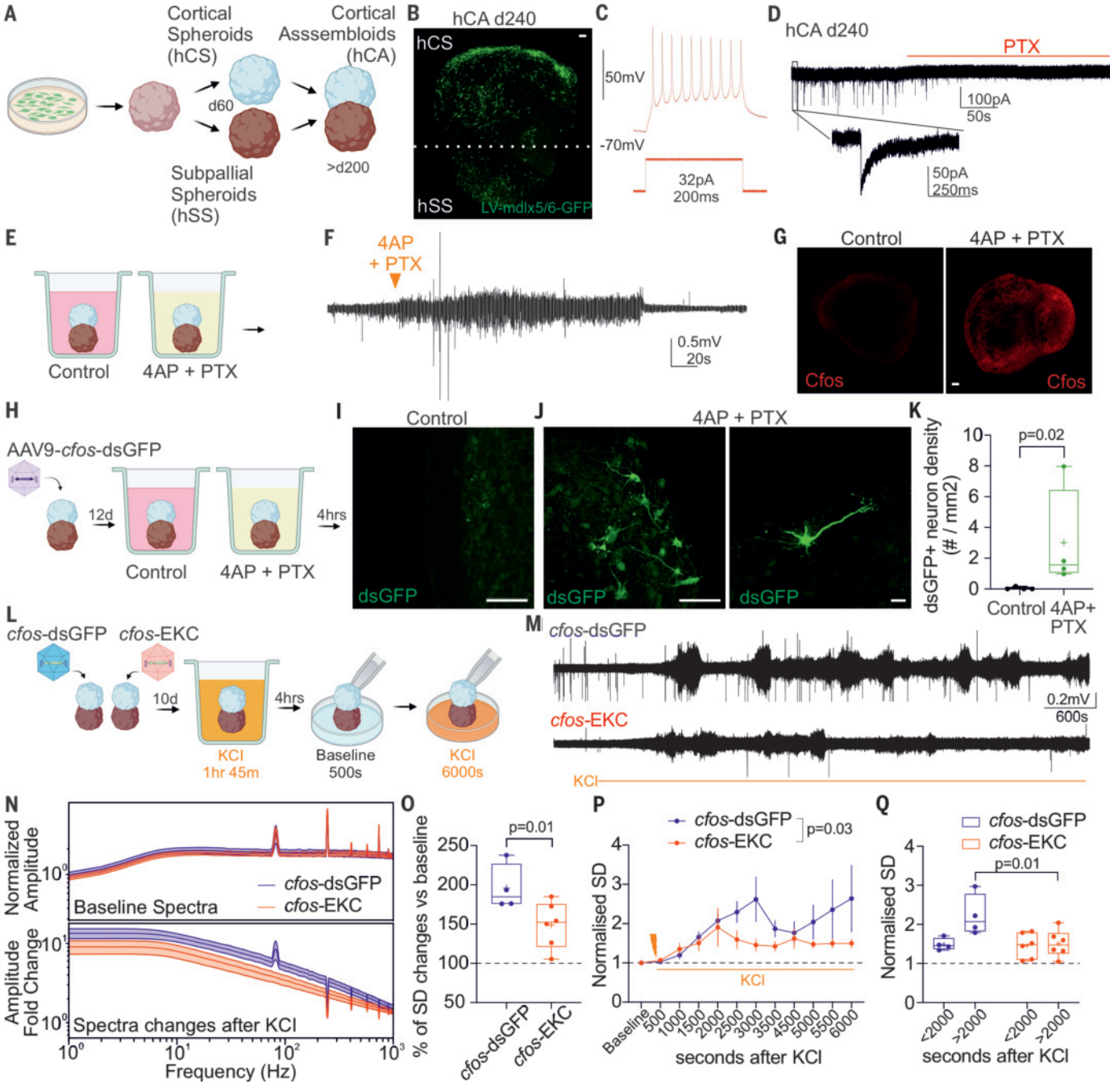


Fig. 6. Activity-dependent gene therapy decreases epileptiform activity in hCAs. (**A**) Schematic representation for the generation of human forebrain assembloids after fusion of hCSs and hSSs. (**B**) Inhibitory neurons migrate from hSS to hCS, recapitulating human cortical development. Scale bar, 100 mm. (**C** and **D**) Trains of evoked action potentials and spontaneous inhibitory postsynaptic events recorded in excitatory neurons in cortical assembloids at the latest stage of differentiation (d240). (**E**) Cortical assembloids were maintained either in control medium or in a medium with 4AP and PTX. (**F**) Local field potential showing an increase in activity after addition of 4AP and PTX (orange triangle). (**G**) Immunofluorescence images of cfos obtained 4 hours after control medium (left) or medium supplemented with 4AP and PTX (right). Scale bar, 100 μm. (**H**) Cortical assembloids were transduced with cfos-dsGFP and then, 12 days later, moved to either control medium or medium supplemented with 4AP and PTX. (**I** to **K**) After 4 hours, cortical assembloids were fixed and stained for dsGFP, and the density of dsGFP-positive neurons was plotted. Scale bars, (I) and (J), 100 μm; (K) 10 μm. Student's *t* test. (**L**) Schematic representation for a test of activity-dependent gene therapy in hCAs. (**M**) Local field potential showing a decrease in activity after addition of KCl (orange line) in hCAs transduced with *cfos*-EKC compared with *cfos*-dsGFP. For the purpose of illustration, the voltage range illustrated is ± 0.5 mV. (**N**) (Top) Baseline LFP amplitude spectra for hCAs treated with *cfos*-dsGFP or *cfos*-EKC. (Bottom) Amplitude changes across frequencies after KCl. (**O**) Percentage change in the median standard deviation (SD), normalized to baseline activity, as a proxy for network activity. Student's *t* test. (**P**) Time course of SD during the experiment. Two-way ANOVA. (**Q**) Change in SD in hCA transduced with either *cfos*-dsGFP or *cfos*-EKC divided into two periods: <2000 s before *cfos* activation and >2000 s after *cfos* activation (two-way ANOVA followed by Bonferroni multiple comparison test).

expression was mainly in excitatory neurons, dsGFP driven by a minimal *arc* promoter (mArc) showed a significantly higher percentage of expression in inhibitory neurons (≈12%) (figs. S14, S16, and S17). With *cfos*-dsGFP, there was a trend for a lower percentage of excitatory neurons in CA1/2 to express dsGFP compared with CA3 and hilus (Fig. 3D).

We hypothesized that expression of EKC in response to an evoked generalized seizure should attenuate the effect of a second chemoconvulsant challenge if delivered during the time that potassium channel overexpression persists, but that this protective effect should fade with time. We therefore performed three consecutive intraperitoneal PTZ injections in the same animals (Fig. 3E). We first expressed either *cfos*-dsGFP or *cfos*-EKC in both hippocampi and, after 2 weeks, gave the first PTZ injection. This injection triggered a single generalized seizure with no difference in severity between the two groups (Fig. 3, E to H), which was as expected because the *cfos* promoter is normally inactive under baseline condition. We then administered a second PTZ injection 24 hours later. This led to markedly attenuated seizures in the animals injected with *cfos*-EKC compared with those injected with *cfos*-dsGFP, with the majority of animals failing to reach a Racine score of 4 (Fig. 3, E to H). Last, to test whether this effect persists, we gave a third PTZ injection after 2 weeks, by which time we anticipated that overexpression of Kv1.1 channels had returned to baseline, as expected from their membrane persistence (*37*). At this time point, no difference was observed between the two groups (Fig. 3, E to H). Activity-dependent induction of EKC expression thus protects against generalized convulsions, which are associated clinically with mortality and morbidity, in a time-limited manner.

Activity-dependent gene therapy does not affect normal behavior

A potential limitation of *cfos*-EKC treatment is that it might interfere with normal brain function. Indeed, the *cfos* promoter is recruited during physiological behaviors such as memory formation and learning (*38*). We therefore asked whether salient sensory and aversive stimuli could lead to the overexpression of Kv1.1 sufficient to interfere with normal behavior. *Cfos* activation has previously been harnessed to manipulate a memory trace or engram, with behavioral readout in a contextual fear conditioning (CFC) task: Chemogenetic or optogenetic modulation of neurons "tagged" in a *cfos*-dependent manner during this test can alter fear recall 24 hours after memory consolidation (*39*–*41*). We repeated this behavioral paradigm after bilateral intrahippocampal expression of either *cfos*-dsGFP or *cfos*-EKC and performed the CFC test 2 weeks later (Fig. 4A). We tested this paradigm both in naïve animals and in animals that had received a single PTZ injection 24 hours before fear conditioning (leading to a stage 5 seizure in all such animals). In the naïve animals, no difference in freezing behavior was observed between *cfos*-dsGFP– and *cfos*-EKC–treated groups, either during fear conditioning or 24 hours later during fear recall, or when animals were exposed to a new context (fig. S18). In animals that had received a PTZ injection, we observed a nonsignificant trend for greater freezing during fear recall in the *cfos*-EKC group than in the *cfos*-dsGFP group (Fig. 4B). When animals were tested in several other behavioral tasks, *cfos*-EKC–expressing animals again performed similarly to *cfos*-dsGFP–expressing animals: No differences were observed before or after viral injection (Fig. 4, C and D, and fig. S19) in an open field test to monitor anxiety and locomotor activity (Fig. 4C), a T-maze test to assess working memory (Fig. 4D), or an olfactory discrimination test (fig. S19).

Activity-dependent gene therapy suppresses spontaneous seizures and interictal activity in a chronic model of intractable epilepsy

Although treatment with *cfos*-EKC is effective in protecting against a second chemoconvulsant challenge delivered shortly after a first, it remained to be determined whether it could modify the disease course in epilepsy, in which seizures occur sporadically. We therefore switched to a model of chronic limbic epilepsy. We used a clinically relevant model of drug-resistant epilepsy that consists of an intra-amygdala kainic acid (KA) injection to induce a period of status epilepticus (*14*, *42*, *43*). Mice started to exhibit spontaneous seizures after 2 weeks and were implanted with wireless electrocorticogram (ECoG) transmitters (Fig. 5A). We recorded spontaneous generalized seizures for 2 weeks and then randomized animals for injection with either *cfos*-dsGFP or *cfos*-EKC in both hippocampi. Two weeks later, after waiting for viral expression, the ECoG was recorded for 2 more weeks (Fig. 5A). *cfos*-EKC–treated animals showed a robust decrease in the number of spontaneous seizures when compared with animals receiving *cfos*-dsGFP (Fig. 5, B to D).

We also analyzed interictal spike activity in the same animals (Fig. 5E). We observed a net decrease in spike activity in animals treated with *cfos*-EKC compared with *cfos*-dsGFP (Fig. 5E), with a trend to more consistently follow a circadian rhythm (fig. S20). Despite a slight decrease in seizure frequency with time in *cfos*-dsGFP–treated animals, interictal spike frequency increased, suggesting that this phenomenon is a natural evolution of this chronic model. By contrast, animals treated with *cfos*-EKC showed significant decreases in both spontaneous seizures and interictal spike activity, suggesting a broader impact of the treatment than only raising the seizure threshold. Indeed, treatment efficacy was reflected in significant decreases in ECoG coastline (a measure of overall activity) and in total power, especially at higher frequencies (Fig. 5, F and G).

We also asked whether the activity-dependent transgene expression was maintained in the absence of overt seizures. *cfos*-dsGFP was injected bilaterally in the dentate gyrus. Two weeks later, KA was injected unilaterally, also in the dentate gyrus. After 5 days, at which stage interictal spikes occur without seizures (and dsGFP induced by KA has been degraded), we sliced the brain and observed ipsilateral *cfos*-dsGFP expression (fig. S21). This finding suggests that interictal activity is sufficient for activation of the treatment.

At the end of the chronic epilepsy study, we asked whether the treatment protected animals from a lethal dose of PTZ (Fig. 5H). We observed a significant survival advantage in animals injected with *cfos*-EKC compared with *cfos*-dsGFP, with a survival rate close to that of *cfos*-dsGFP–transduced naïve animals injected with the same PTZ dose (85%) (Fig. 5H).

We also tested the effect of *cfos-KCNJ2* on spontaneous seizures in the same chronic epilepsy model (fig. S22). In contrast to *cfos*-EKC, no impact on seizure frequency was observed in animals injected with *cfos-KCNJ2* when compared with *cfos*-dsGFP (fig. S22), implying that transient Kir2.1 expression does not have an antiepileptic action.

Last, we asked whether treatment with *cfos*-EKC affected performance in behavioral tests that are affected by chronic epilepsy. Having quantified several behavioral defects in chronic epileptic animals compared with naïve animals, we injected either *cfos*-dsGFP or *cfos*-EKC in epileptic animals and waited 4 weeks to measure the same behavioral parameters (figs. S23 to S25). We observed no worsening in animals treated with *cfos*-EKC compared with *cfos*-GFP in either T-maze, open field, or olfactory discrimination tests (figs. S23 to S25).

Activity-dependent gene therapy suppresses epileptiform activity in human neurons

We asked whether *cfos* can be activated by epileptiform activity in human neurons. We used an induced pluripotent stem cell line to derive human cortical assembloids (hCAs) by fusing cortical spheroids (hCSs) with subpallial spheroids (hSSs) (Fig. 6A) (*44*–*47*). Immunofluorescence analysis at different time points showed expression of hCS and hSS region-specific transcription factors [forkhead box G1 (FOXG1), paired box 6 (PAX6), and NK2 homeobox 1 (NKX2.1)] and mature neuronal markers [microtubule associated protein 2 (MAP2), NeuN, and GABA)] (fig. S26). We

demonstrated successful fusion of hCSs and hSSs, with inhibitory neurons migrating to, and integrating with, the cortical side (Fig. 6B). We then performed electrophysiological recordings in neurons located in the hCS area of acute hCA slices and showed that neurons can fire trains of action potentials and exhibit spontaneous PTX-sensitive inhibitory postsynaptic currents, confirming that interneurons integrate in the network (Fig. 6, C and D). We treated mature hCAs with 4-aminopyridine (4AP) and PTX to increase network excitability and recorded epileptiform activity using local field potentials (Fig. 6, E and F). Four hours later, we observed *cfos*-positive neurons that were not present when hCAs were treated with a control solution (Fig. 6G). Last, we transduced hCAs with AAV9 *cfos*-dsGFP and after 12 days incubated them in either a control solution or 4AP and PTX (Fig. 6H). No dsGFP-positive neurons were present in the control condition (Fig. 6I). By contrast, we observed dsGFP-positive neurons in hCAs treated with 4AP and PTX, suggesting that this minimal promoter is also activated in human neurons after epileptiform activity (Fig. 6, J and K). Last, we tested the ability of *cfos*-EKC to suppress epileptiform activity in hCAs. We transduced hCAs with a lentivirus expressing either *cfos*-dsGFP or *cfos*-EKC and after 10 days treated them for 1 hour and 45 min with 55 mM KCl (fig. S27). Four hours later, we recorded baseline local field potential activity and then added 55 mM KCl a second time (Fig. 6L). We observed a clear reduction in overall network activity in hCAs transduced with *cfos*-EKC compared with cfos-dsGFP (Fig. 6, M to Q).

Discussion

We have reported an activity-dependent, cell-autonomous, on-demand gene therapy that follows network dynamics, driving the expression of a transgene that in turn decreases neuronal excitability (Fig. 1, A and B). This approach is specific for neurons that participate in pathological network activity but is also time-limited in that transgene expression persists only for as long as neurons are hyperactive (Fig. 3, E to H). In a chronic model of epilepsy, we achieved a greater decrease in seizure frequency than previously reported for gene therapy with constitutive promoters or with widely used antiseizure drugs (*11*–*13*, *43*), and without deleterious effects on normal behaviors (Figs. 4 and 5). Given that the components of activity-dependent gene therapy are normal mammalian genetic elements packaged in a well-tolerated viral vector that is already in the clinic, there is a relatively straightforward path to first-in-human studies. The translational potential is underlined by the preliminary evidence of effectiveness in hCAs (Fig. 6).

Cfos tagging has been used to track the recruitment of neurons in pathological behaviors and as a test of causality in CFC (*39*–*41*). The combination of *cfos* with EKC proved highly effective in down-regulating neuronal excitability after chemoconvulsants and in suppressing spontaneous seizures, without deleterious effects in a battery of behavioral tests. We observed less consistent effects on neuronal excitability with other promoters. Why other IEG promoters, and synthetic promoters, were less effective is unclear. Among factors determining their potential utility are the different time courses of activation and deactivation, and the triggering mechanisms for each promoter. For example, mArc activation has been linked to synaptic transmission and plasticity processes rather than simply responding to increases in neuronal activity, as is the case for *cfos*, although the intermediate intracellular signaling cascades overlap (*21*). We also found that *KCNJ2* could not be substituted for EKC, even though it profoundly hyperpolarized neurons when driven in an activity-dependent manner (fig. S4). If anything, animals treated with AAV9 *cfos*-*KCNJ2* had a worse outcome in the chronic epilepsy study when compared with animals injected with *cfos*-dsGFP (fig. S10). A possible explanation for the efficacy of Kv1.1 overexpression is that it reduces not only excitability but also neurotransmitter release through a modulatory effect on the presynaptic action potential waveform (supplementary text) (*26*, *48*).

It remains to be determined whether the powerful antiepileptic effect of *cfos*-EKC depends on suppressing the excitability of a small number of "detonator" or "hub" neurons responsible for triggering seizures, or of a network of neurons whose activity is prone to reaching a critical point (*20*, *49*). The data are therefore silent on whether successive seizures arise from a stereotypical or variable pattern of neuronal recruitment in an ictogenic network.

Because patients with focal epilepsy often experience two or more seizures within 24 hours (*25*), *cfos*-EKC would be expected to abort such clusters. However, we observed the persistence of the antiepileptic treatment in the chronic model despite evidence from the PTZ injections that the effect of a single evoked seizure faded by 2 weeks (Figs. 3 and 5). A possible explanation is that in the chronic epilepsy model, interictal discharges repeatedly reactivated the *cfos* promoter, so that the epileptiform activity remained below threshold for generalization. This is supported by the findings that interictal activity is sufficient to activate *cfos*-driven dsGFP expression (fig. S21) and that treated animals were relatively protected from the effects of a chemoconvulsant challenge despite a prolonged absence of overt seizures (Fig. 5H).

A cell-autonomous self-regulated tool that normalizes network dynamics has potential clinical applications beyond epilepsy. Several other neuropsychiatric diseases are characterized by circuit hyperactivity, including early stages of schizophrenia [in which anterior hippocampal hyperactivity has been implicated (*50*)], Parkinson's disease [subthalamic nucleus (*51*)], migraine and cluster headache [posterior hypothalamus (*52*)], and obsessive-compulsive disorder [anterior cingulate cortex (*53*)]. Early hyperactivity has also been documented in mouse models of Alzheimer's disease and is associated with high levels of *arc* expression (*54*). In this case, *arc* or ESARE could represent appropriate therapeutic activity-dependent promoters.

REFERENCES AND NOTES

1. P. Fusar-Poli *et al*., *JAMA Psychiatry* **70**, 107–120 (2013).
2. S. Harvey, M. D. King, K. M. Gorman, *Front. Neurol.* **12**, 659064 (2021).
3. K. Staley, *Nat. Neurosci.* **18**, 367–372 (2015).
4. M. J. Brodie, *CNS Drugs* **31**, 527–534 (2017).
5. D. M. Kullmann, S. Schorge, M. C. Walker, R. C. Wykes, *Nat. Rev. Neurol.* **10**, 300–304 (2014).
6. T. J. Turner, C. Zourray, S. Schorge, G. Lignani, *J. Neurochem.* **157**, 229–262 (2021).
7. K. M. Tye, *Neuron* **83**, 1259–1261 (2014).
8. R. C. Wykes, G. Lignani, *Neuropharmacology* **132**, 108–117 (2018).
9. B. E. Deverman, B. M. Ravina, K. S. Bankiewicz, S. M. Paul, D. W. Y. Sah, *Nat. Rev. Drug Discov.* **17**, 641–659 (2018).
10. A. Lieb *et al*., *Nat. Med.* **24**, 1324–1329 (2018).
11. R. C. Wykes *et al*., *Sci. Transl. Med.* **4**, 161ra152 (2012).
12. D. Kätzel, E. Nicholson, S. Schorge, M. C. Walker, D. M. Kullmann, *Nat. Commun.* **5**, 3847 (2014).
13. F. M. Noe, A. T. Sorensen, M. Kokaia, A. Vezzani, in *Jasper's Basic Mechanisms of the Epilepsies*, J. L. Noebels, M. Avoli, M. A. Rogawski, R. W. Olsen, A. V. Delgado-Escueta, Eds. (Oxford Univ. Press, 2012).
14. G. Colasante *et al*., *Brain* **143**, 891–905 (2020).
15. A. Snowball *et al*., *J. Neurosci.* **39**, 3159–3169 (2019).
16. A. Nanobashvili *et al*., *Gene Ther.* **26**, 65–74 (2019).
17. P. Kwan, S. C. Schachter, M. J. Brodie, *N. Engl. J. Med.* **365**, 919–926 (2011).
18. F. Tang, A. M. S. Hartz, B. Bauer, *Front. Neurol.* **8**, 301 (2017).
19. W. Truccolo *et al*., *Nat. Neurosci.* **14**, 635–641 (2011).
20. M. Wenzel, J. P. Hamm, D. S. Peterka, R. Yuste, *Cell Rep.* **19**, 2681–2693 (2017).
21. S. W. Flavell, M. E. Greenberg, *Annu. Rev. Neurosci.* **31**, 563–590 (2008).
22. E. L. Yap, M. E. Greenberg, *Neuron* **100**, 330–348 (2018).
23. T. Kawashima, H. Okuno, H. Bito, *Front. Neural Circuits* **8**, 37 (2014).
24. N. Dabrowska *et al*., *Brain* **142**, 2336–2351 (2019).
25. S. R. Haut, R. B. Lipton, A. J. LeValley, C. B. Hall, S. Shinnar, *Neurology* **65**, 1313–1315 (2005).
26. J. H. Heeroma *et al*., *Dis. Model. Mech.* **2**, 612–619 (2009).
27. A. L. Lee *et al*., *J. Neurochem.* **86**, 1079–1088 (2003).
28. H. J. Wenzel *et al*., *Epilepsia* **48**, 2023–2046 (2007).
29. T. Kawashima *et al*., *Nat. Methods* **10**, 889–895 (2013).
30. A. T. Sørensen *et al*., *eLife* **5**, e13918 (2016).
31. X. Sun *et al*., *Cell* **181**, 410–423.e17 (2020).
32. N. A. Hager, C. K. McAtee, M. A. Lesko, A. F. O'Donnell, *Front. Cell Dev. Biol.* **9**, 796136 (2022).
33. C. R. Yu *et al*., *Neuron* **42**, 553–566 (2004).
34. G. Colasante *et al*., *Mol. Ther.* **28**, 235–253 (2020).
35. V. Magloire, J. Cornford, A. Lieb, D. M. Kullmann, I. Pavlov, *Nat. Commun.* **10**, 1225 (2019).
36. J. Van Erum, D. Van Dam, P. P. De Deyn, *Epilepsy Behav.* **95**, 51–55 (2019).
37. E. F. Fornasiero *et al*., *Nat. Commun.* **9**, 4230 (2018).
38. F. T. Gallo, C. Katche, J. F. Morici, J. H. Medina, N. V. Weisstaub, *Front. Behav. Neurosci.* **12**, 79 (2018).

39. K. Minatohara, M. Akiyoshi, H. Okuno, *Front. Mol. Neurosci.* **8**, 78 (2016).
40. K. Z. Tanaka *et al*., *Neuron* **84**, 347–354 (2014).
41. A. R. Garner *et al*., *Science* **335**, 1513–1516 (2012).
42. E. M. Jimenez-Mateos *et al*., *Nat. Med.* **18**, 1087–1094 (2012).
43. P. J. West *et al*., *Exp. Neurol.* **349**, 113954 (2022).
44. S. P. Paşca, *Nat. Neurosci.* (2018).
45. S. A. Sloan, J. Andersen, A. M. Paşca, F. Birey, S. P. Paşca, *Nat. Protoc.* **13**, 2062–2085 (2018).
46. C. Zourray, M. A. Kurian, S. Barral, G. Lignani, *Front. Mol. Neurosci.* **15**, 839366 (2022).
47. F. Birey *et al*., *Nature* **545**, 54–59 (2017).
48. U. Vivekananda *et al*., *Proc. Natl. Acad. Sci. U.S.A.* **114**, 2395–2400 (2017).
49. L. A. Lau, K. J. Staley, K. P. Lillis, *Brain* **145**, 531–541 (2022).
50. M. McHugo *et al*., *Am. J. Psychiatry* **176**, 1030–1038 (2019).
51. M. Jahanshahi, I. Obeso, C. Baunez, M. Alegre, P. Krack, *Mov. Disord.* **30**, 128–140 (2015).
52. P. J. Goadsby *et al*., *Physiol. Rev.* **97**, 553–622 (2017).
53. K. D. Fitzgerald *et al*., *Biol. Psychiatry* **57**, 287–294 (2005).
54. M. Przybyla *et al*., *Brain* **143**, 1889–1904 (2020).

ACKNOWLEDGMENTS

We thank I. Zalivina and L. Ussingkaer for the help in preparing AAVs; M. Weston for help in behavioral assessment; I. Colombi and M. Chiappalone for the MEA analysis software; and T. Smart, M. Hausser, and B. Clark for facilitating the CFC experiments. We are thankful to all members of the Experimental Epilepsy Group at UCL and C. Bernard for helpful discussions. The figures were created with Biorender.com under a license granted to G.L. **Funding:** This work was supported by Epilepsy Research UK Emerging Leader Fellowship F1701 (G.L.), Medical Research Council New Investigator Project Grant MR/S011005/1 (G.L.), Medical Research Council PhD studentship for Y.Q. (D.M.K. and G.L.), UCL Technology Fund UTF-20-005 (G.L. and D.M.K.), Sir Jules Thorn Trust Studentship for C.Z. (G.L., S.B., M.A.K., and S.S.), Wellcome Trust Investigator Award 212285/Z/18/Z (D.M.K.), Sir Jules Thorn Trust Award for Biomedical Research (M.A.K.), NIHR Research Professorship NIHR-RP-2016-07-019) (M.A.K.), and NIHR Great Ormond Street Hospital Biomedical Research 17BR09 (S.B.). **Author contributions:** Conceptualization: G.L., D.M.K., and S.S. Funding acquisition: G.L., D.M.K., S.S., M.A.K., and S.B. Methodology: Y.Q., N.O., B.M., C.Z., A.A.-B., J.C.C., S.P.J., F.C.M., M.L., A.S., T.S.-A., V.M., S.S., G.L., and D.M.K. Investigation: Y.Q., N.O., B.M., C.Z., A.A.-B., J.C.C., S.P.J., M.L., T.J.T., A.S., and T.S.-A. Formal analysis: Y.Q., N.O., B.M., C.Z., A.A.-B., S.P.J., F.C.M., M.L., and G.L. Supervision: G.L., D.M.K., S.S., M.C.W., M.A.K., S.B., V.M., and J.C.C. Writing – original draft: G.L. and D.M.K. Writing – review and editing: G.L. and D.M.K. **Competing interests:** G.L., D.M.K., S.S., Y.Q., and M.C.W. are listed as inventors on patent WO2021191474A1. G.L., D.M.K., S.S., and M.C.W. have equity in a company that aims to bring epilepsy gene therapy to the clinic. **Data and materials availability:** All Python and Matlab scripts are available at https://github.com/KullmannLab/Qiu_et_al_2022. PyEcog software is available here: https://www.pyecog.com. All the vectors used in this manuscript will be made available on a suitable platform. All data are stored in the UCL cloud database. All raw data supporting the main and supplementary figures are available here: https://doi.org/10.5522/04/20867117. **License information:** Copyright © 2022 the authors, some rights reserved; exclusive licensee American Association for the Advancement of Science. No claim to original US government works. https://www.science.org/about/science-licenses-journal-article-reuse

SUPPLEMENTARY MATERIALS

science.org/doi/10.1126/science.abq6656
Materials and Methods
Supplementary Text
Figs. S1 to S27
Tables S1 and S2
References (*55*–*77*)
MDAR Reproducibility Checklist

Submitted 27 April 2022; accepted 14 September 2022
10.1126/science.abq6656

ARCTIC WILDFIRES

Unprecedented fire activity above the Arctic Circle linked to rising temperatures

Adrià Descals[1,2]*, David L. A. Gaveau[3], Aleixandre Verger[1,2,4], Douglas Sheil[5,6], Daisuke Naito[6,7], Josep Peñuelas[1,2]

Arctic fires can release large amounts of carbon from permafrost peatlands. Satellite observations reveal that fires burned ~4.7 million hectares in 2019 and 2020, accounting for 44% of the total burned area in the Siberian Arctic for the entire 1982–2020 period. The summer of 2020 was the warmest in four decades, with fires burning an unprecedentedly large area of carbon-rich soils. We show that factors of fire associated with temperature have increased in recent decades and identified a near-exponential relationship between these factors and annual burned area. Large fires in the Arctic are likely to recur with climatic warming before mid-century, because the temperature trend is reaching a threshold in which small increases in temperature are associated with exponential increases in the area burned.

Emissions from Arctic wildfires jeopardize global climate goals (*1*). The Arctic is warming rapidly because of a climate change–related phenomenon known as "Arctic amplification" (*2*); annual mean temperature has already increased more than 2°C compared with that of the preindustrial era (*3*) and is expected to reach 3.3° to 10°C above the 1985–2014 average by 2100 (*4*). These increased temperatures result in thawing of permafrost and deterioration of peatlands with emissions of carbon dioxide and methane (*5*–*7*). High-latitude peatlands are expected to become a net carbon source as a consequence of global warming (*8*). The release of carbon creates positive feedback with additional emissions contributing to further warming and thawing with further peatland degradation and emissions. In this context, the numerous fires identified by satellite thermal sensors in eastern Siberia in 2020 (*9*) raise particular concerns because of the resulting emissions (*10*).

Wildfires are common in the Arctic and Subarctic (*11*), but their size, frequency, and intensity are expected to increase as the climate warms (*12*). Extreme weather, such as that in 2020 in the Siberian Arctic (*13*), is expected to become more severe as Arctic oscillations weaken over time (*14*). Previous research in the Alaskan tundra suggests that the annual burned area might be two times greater than in the 1950–2010 period by the end of the century as warmer and drier conditions coincide more frequently (*15*). The conditions that affected the Arctic fire seasons of 2019 and 2020 in the Siberian Arctic have provided new empirical observations between climatic factors and burn extent and may already be indicating the changes in fire regimes expected by the end of the century. The fire seasons of 2019 and 2020, however, raised two uncertainties—first, whether the annual burned area above the Arctic Circle was actually increasing. Satellite-derived burned-area products tend to underestimate the true extent of burning (*12*), and rigorous validation techniques are required (*16*). Second, even if the burned areas in 2019 and 2020 were the largest yet observed, the links to other trends required evaluation.

We assessed annual burned area in the Siberian Arctic (latitudes >66.5°N) for 1982–2020 using six satellite-derived maps of burned areas (fig. S1). We investigated the Siberian Arctic because it is where most burning occurs above the Arctic Circle and fire frequency appeared to be increasing (*9*). We investigated 10 factors associated with the likelihood of fire: six climatic variables [air and surface temperature, total precipitation, wind speed and direction, and vapor-pressure deficit (VPD)], three variables describing the vegetation conditions [length of the growing season, mean normalized difference vegetation index ($NDVI_{mean}$), and climatic water deficit (CWD)], and the number of ignitions, a direct factor associated with the likelihood of fires. We evaluated how these factors have varied over the past four decades and their relationships with satellite-derived estimates of annual burned areas. Lastly, we investigated the future trends of annual burned area and fire emissions under future Representative Concentration Pathways (RCPs).

Results

Trends of burned area for 1982–2020

Between 1982 and 2020, the satellite burned-area products indicate that 12.97 million hectares (Mha) burned in the circumpolar region (latitudes >66.5°N). The Siberian Arctic, a region with continuous permafrost, accounted

[1]CREAF, Centre de Recerca Ecològica i Aplicacions Forestals, Cerdanyola del Vallès, 08193 Barcelona, Catalonia, Spain. [2]CSIC, Global Ecology Unit CREAF-CSIC-UAB, Bellaterra, 08193 Barcelona, Catalonia, Spain. [3]TheTreeMap; Bagadou Bas, 46600 Martel, France. [4]CIDE, CSIC-UV-GV, 46113 València, Spain. [5]Forest Ecology and Forest Management Group, Wageningen University and Research, Wageningen, Netherlands. [6]Center for International Forestry Research (CIFOR), Bogor 16000, Indonesia. [7]Graduate School of Agriculture, Kyoto University, Kitashirakawa Oiwake-cho, Sakyo-ku, Kyoto 606-8502, Japan.
*Corresponding author. Email: a.descals@creaf.uab.cat

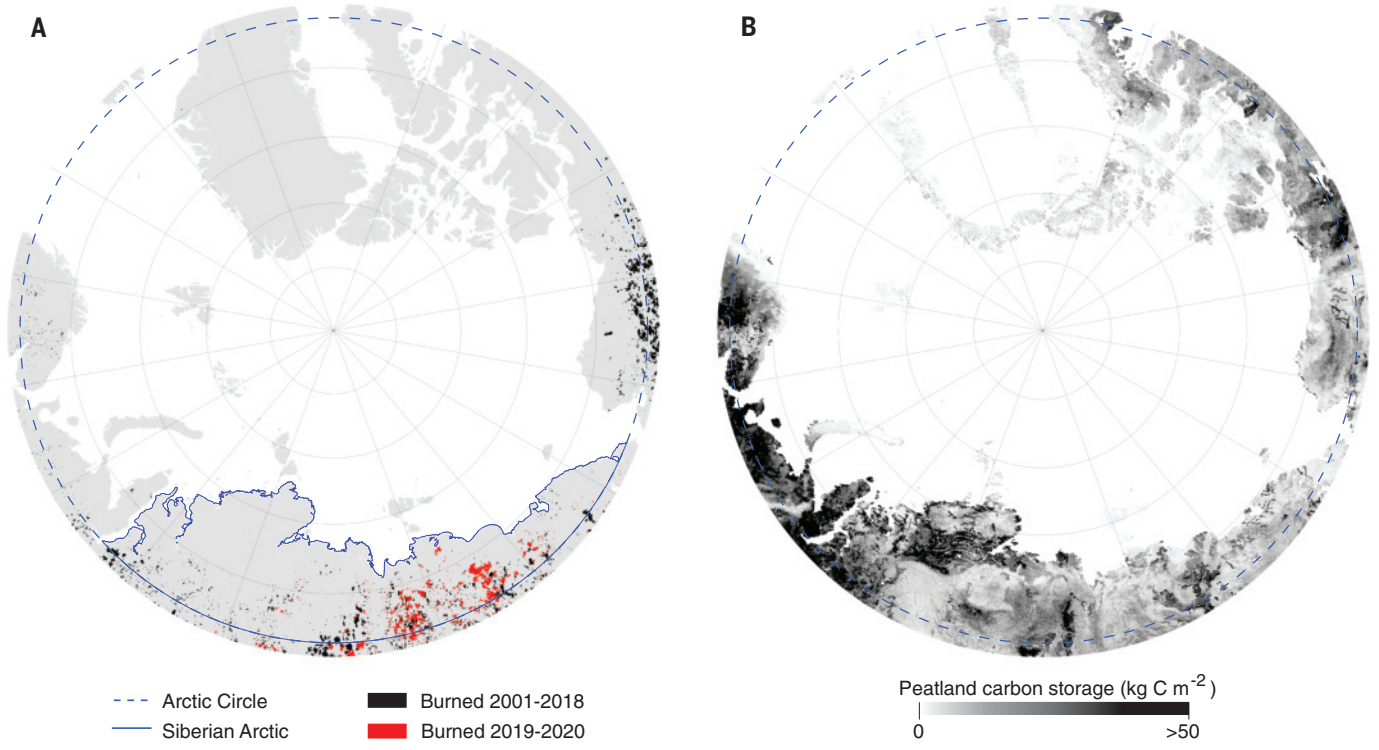


Fig. 1. Maps of burned area for 2001–2020 and peatland carbon storage in the circumpolar region. (**A**) Extent of the burns for 2001–2018 is from the FireCCI51 product, and the extent for 2019 and 2020 is the union of the C3SBA10 product and the Sentinel-2 burned-area map developed in this study. The Siberian Artic is the area inside the blue outline. Black represents areas that burned at least once for 2001–2018, and red represents areas that burned in 2019 and 2020. Areas that burned at least once in both periods, in 2001–2018 and 2019–2020, are also depicted in red; these areas represent only 3% of total burning above the Arctic Circle during the 2001–2020 period. We show the annual burned area from 2001 to 2020, which is the period when the occurrence of fires accelerated. (**B**) Estimated storage of organic carbon in peatlands from a reference dataset (*8*).

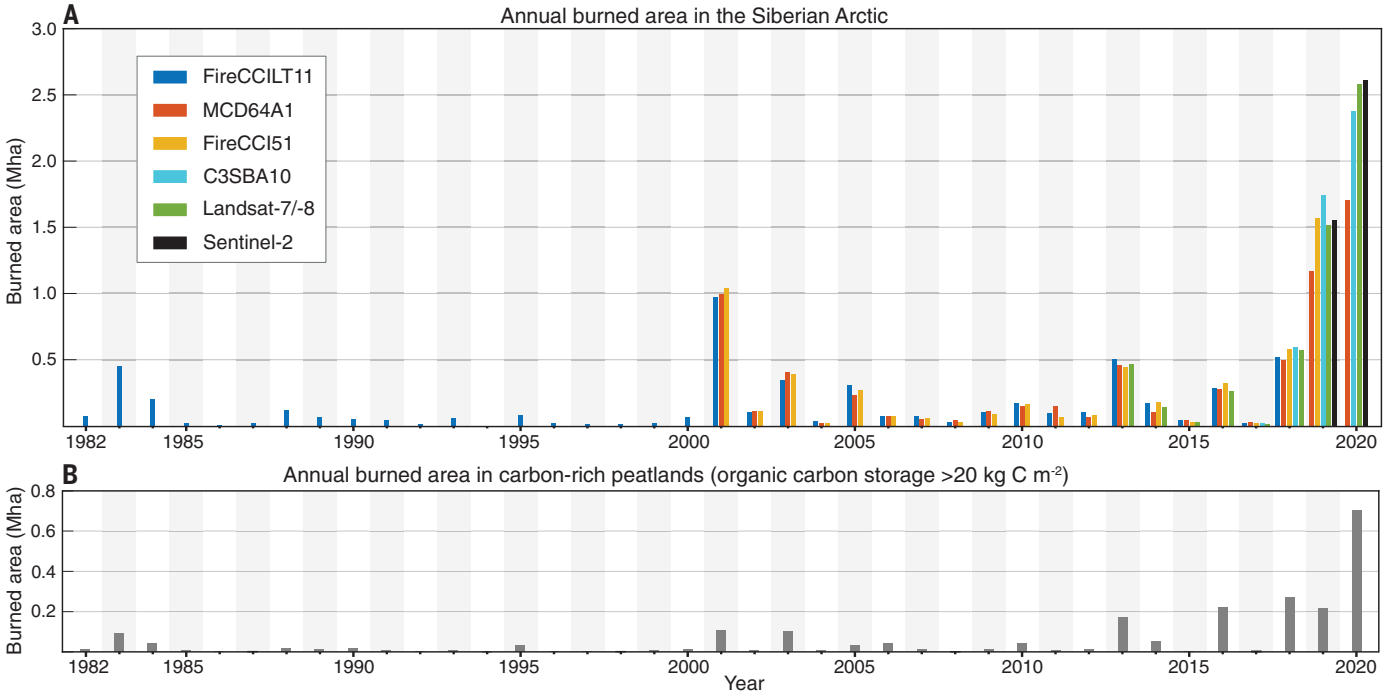


Fig. 2. Annual burned area in the Siberian Arctic and in carbon-rich peatlands for 1982–2020. (**A**) Annual burned area in the Siberian Arctic derived from remotely sensed data from six products. (**B**) Annual burned area in carbon-rich peatlands; >20 kg C m^{-2} in storage of organic carbon obtained from a reference dataset (*8*). The annual burned area in carbon-rich peatlands represents the median burned area for the available satellite products. Satellite burned-area products contain no data for 1994.

for 71% of this burned area. The years 2019 and 2020 had the greatest mapped burned area in Siberia above the Arctic Circle (Fig. 1A) (see supplementary text A for consistency of the time series of the burned area and fig. S2), which represents 44% of the total mapped burned area (9.24 Mha) in the region from 1982 to 2020. The burned area mapped in the Siberian Arctic varied between the satellite products, most notably the MCD64A1 product for 2019 and 2020 (Fig. 2A). The burned areas for 2020 were 1.71, 2.38, 2.59, and 2.62 Mha for MCD64A1, C3SBA10, Landsat, and Sentinel-2, respectively.

The sampling-based burned area in 2020, based on an assessment of errors of omission and commission (*16*), was nearly 3 Mha (MCD64A1 = 2.83 ± 0.26 Mha, C3SBA10 = 2.92 ±

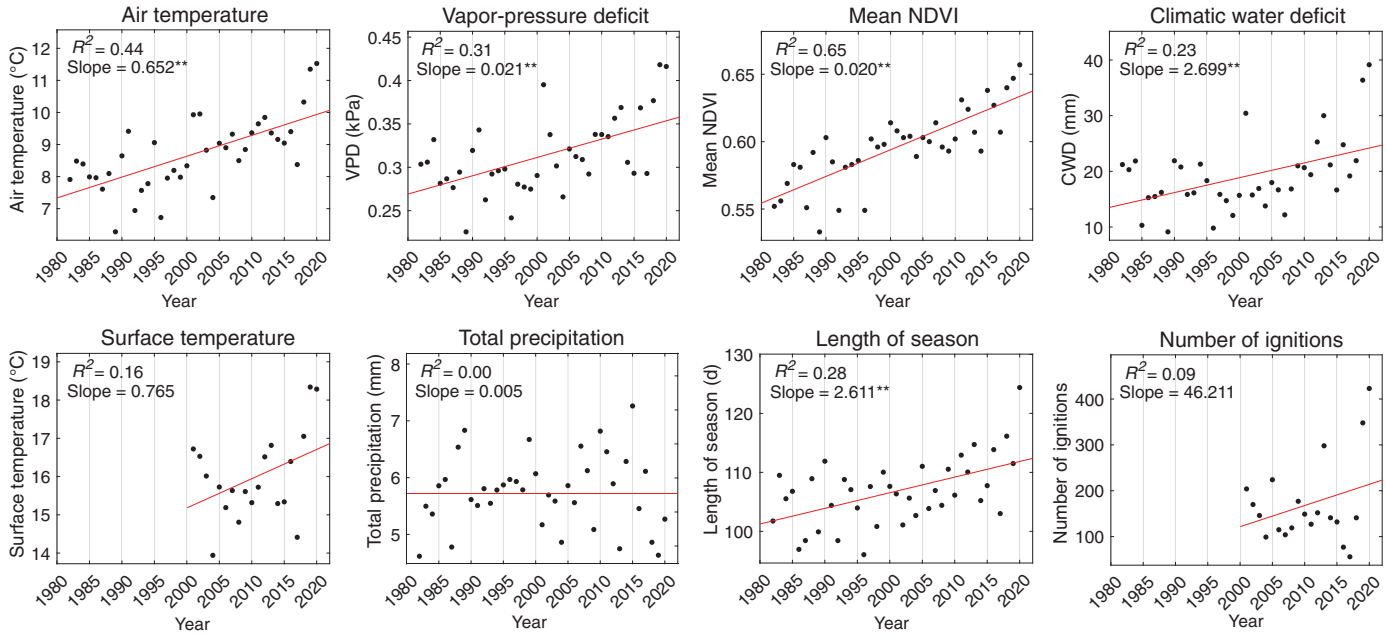


Fig. 3. Trends of eight fire factors in the Siberian Arctic during 1982–2020. Factors are the mean summer air and surface temperature, mean VPD, total summer precipitation, mean CWD, mean NDVI depicting vegetation green biomass, the length of the growing season, and the number of detected ignitions. The red lines are linear regressions; slopes are estimated on a decadal time scale. *p < 0.05; **p < 0.01.

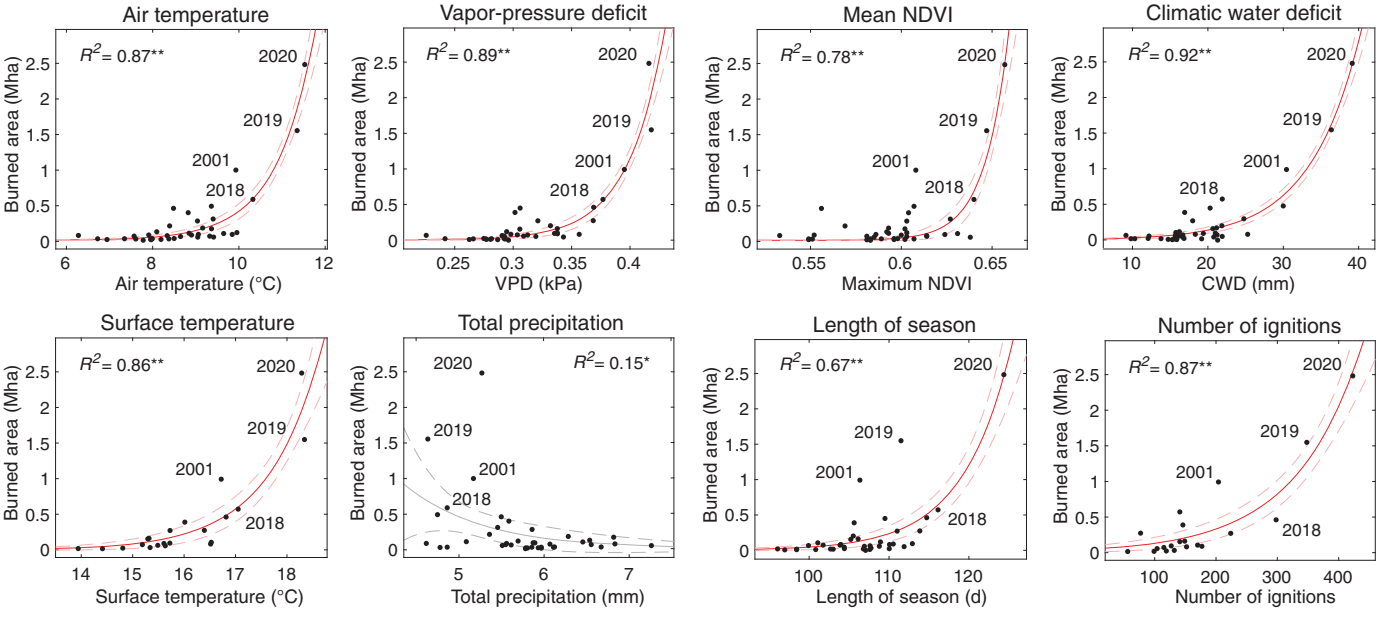


Fig. 4. Regression between the annual burned area and eight fire factors in the Siberian Arctic during 1982–2020. Solid lines are the best regression (linear or exponential), based on the coefficient of determination (R^2; *p < 0.05; **p < 0.01). The best regression model was the exponential for all the factors. The annual burned area is the median burned area for the available satellite products. The factors are the mean summer air and surface temperature, mean VPD, total precipitation, mean CWD, mean NDVI depicting green biomass, the length of the growing season, and the number of ignitions. Red solid lines depict a fit with a significant correlation (p < 0.01). The dashed lines are the 95% prediction limits of the regressions.

0.17 Mha, Landsat = 2.92 ± 0.15 Mha, and Sentinel-2 = 2.99 ± 0.14 Mha) (see full assessment of accuracy in table S1 and a description of the results in supplementary Text B). The area estimate for 2019 and 2020 amounts to ~4.7 Mha. The mapped burned area is less than the estimated burned area for all four products because the omission errors of the "burned" class (ranging from 15.5 to 53.7%) are higher than the commission errors (ranging from 3.2 to 23.0%). Our estimates of carbon emissions from burning were 55.3 and 90.4 Tg C for 2019 and 2020, respectively, which is 156.7 and 256.1 Tg CO_2-eq (including CO_2 and CH_4) (fig. S3). Fires in 2020 damaged a wide area (0.71 Mha) of carbon-rich peatlands (organic carbon storage >20 kg C m^{-2}), indicated with a reference map of soil carbon storage (Fig. 1B) (*8*). The area of carbon-rich peatlands affected by fires has also recently expanded: 70% of total burned area occurred in these areas within the past 8 years of the record, and 30% occurred in 2020 (Fig. 2B).

Trends of the fire factors for 1982–2020

Various factors that may exacerbate the risk of fire have increased significantly over the past four decades in the Siberian Arctic (Fig. 3 and fig. S4). Air temperature, NDVI, the length of the growing season, and VPD have steadily risen. The average increase in summer air temperature was 0.66°C per decade. In 2019 and 2020, the mean summer air temperature was 11.35° and 11.53°C, which was 2.65° and 2.82°C higher than the 1982–2020 average, respectively. CWD, a proxy of plant water stress defined as the difference between potential and actual evapotranspiration, also increased between 1982 and 2020, although the linear trend likely began in the 2000s. More surprising, however, was the abrupt increase in CWD in 2019 and 2020. The estimated number of ignitions, total precipitation, and wind speed all had strong interannual variations, and the slope of their trends was not significantly different from zero.

The annual number of detected ignitions was relatively consistent, with a median of 143, but high counts were observed in specific years, peaking at 423 in 2020. Seventy-two percent of these 2020 ignitions were detected within 20 days, between 13 June and 3 July, reaching Siberian Arctic regions as far north as 72.9° (fig. S5). Notably, these ignitions coincided with anomalously high values of convective available potential energy (CAPE) (fig. S6), an indicator of convective storms and lightning. Between 13 June and 3 July, satellite thermal sensors registered a rapid increase in the number of active fire detections, which accounts for 40.6% of all hot spots detected in 2020. By contrast, hot spots detected before 13 June represented only 1.1%. Similar peaks in the number of detected ignitions, preceding high rates of active fire detection, occurred concurrently with high CAPE values in 2002, 2005, 2013, and 2018.

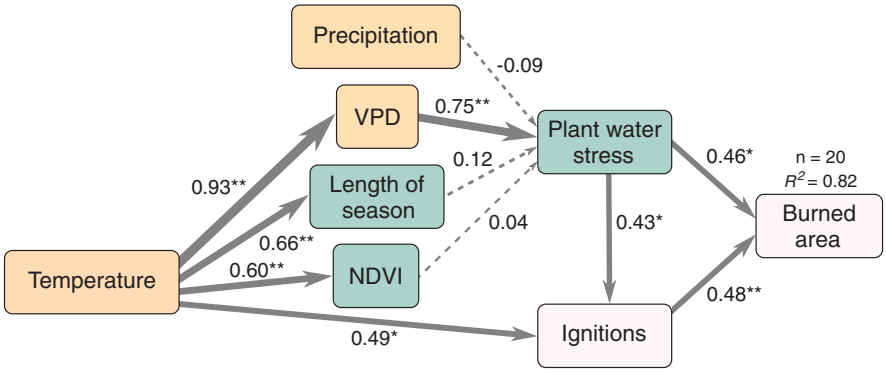


Fig. 5. Causality networks for the association among factors of fire in the Siberian Arctic for 2001–2020. Variables are categorized as climate (mean summer surface temperature, total precipitation, and mean VPD) (yellow), vegetation (mean summer NDVI depicting green biomass, the length of the growing season, and plant water stress measured by mean summer CWD) (green), and fire (number of detected ignitions and annual burned area) (light red). Factor loadings between variables are shown next to lines (*, $p < 0.05$; **$p < 0.01$). The width of the lines depicts the magnitude of the effect, and dashed lines represent nonsignificant effects. R^2 is the variance explained for the annual burned area.

Sensitivity of the burned area to the fire factors

Linear and exponential regressions were used to analyze the best association between the annual burned area (aggregated with the median across available satellites for each year) and the factors of fire regime. An exponential regression was the best regression model (Fig. 4); the annual burned area accelerated when specific thresholds were exceeded. For example, the four years with the largest mapped burned areas (2001, 2018, 2019, and 2020) had a mean summer air temperature >10°C. The best fit was for CWD, which explained 92% of the interannual variability in the burned area. Other factors with a high coefficient of determination (R^2) were summer air temperature (87%), VPD (89%), and number of ignitions (87%). The annual burned area was correlated most weakly with total precipitation (15%). We also detrended the fire factors using the linear regression shown in Fig. 3 before determining the correlation with the annual burned area to reduce the potential of spurious correlations. The detrended correlations (fig. S7) confirmed the high R^2 for CWD (90%), air temperature (80%), VPD (51%), and number of ignitions (86%), but the correlation decreased for $NDVI_{mean}$ (from 78 to 11%).

We further examined the potential relationships among the fire-related factors in a structural equation modeling (SEM) (the rationale of the proposed relationships is described in the materials and methods). The hypothesized causal model outperformed the model validity analysis ($p > 0.05$ in the chi-square test; details on the covariances and residuals in the model are shown in table S2). The SEM supported the role of temperature in controlling other factors that affect the extent of burning (Fig. 5 and fig. S8). Temperature showed significant positive relationships with the lengthening of the growing season (0.66), the vegetation green biomass represented by $NDVI_{mean}$ (0.60), and atmospheric dryness measured by VPD (0.93). We hypothesized that these temperature-regulated factors and total precipitation would influence plant water stress, measured by CWD, but only VPD showed a significant effect (0.75) for the low number of observations (n = 20). Despite this, the hypothesized relationships displayed the expected sign. Temperature and CWD had a positive relationship with the number of detected ignitions (0.49 and 0.43, respectively). Annual burned area presented an R^2 of 0.82 and was directly explained by the number of detected ignitions (0.48) and the CWD (0.46).

Climate factors may differ locally and throughout the fire season. An additional analysis based on local weather conditions during the burning revealed that ignitions affecting areas larger than 4000 ha occurred with average hourly maximum temperatures of 28.6°C (SD = 3.4°C) and mean wind direction from the northeast (fig. S9). Thirty-day preignition precipitation was 0.37 mm (SD = 0.81 mm), and mean wind speed was 0.96 m s^{-1} (SD = 0.55 m s^{-1}). Ignitions that lead to burned areas larger than 4000 ha represent only 10% of all counts but account for 81% of all burned areas that were mapped between 2001 and 2020.

Projections of annual burned area and carbon emissions under warming scenarios

Annual burned area in 2018, 2019, and 2020 more than doubled the long-term average, which was 0.24 Mha for the period 1982–2020 in the Siberian Arctic. Summer 2001, with a mean temperature nearing 10°C, was the first

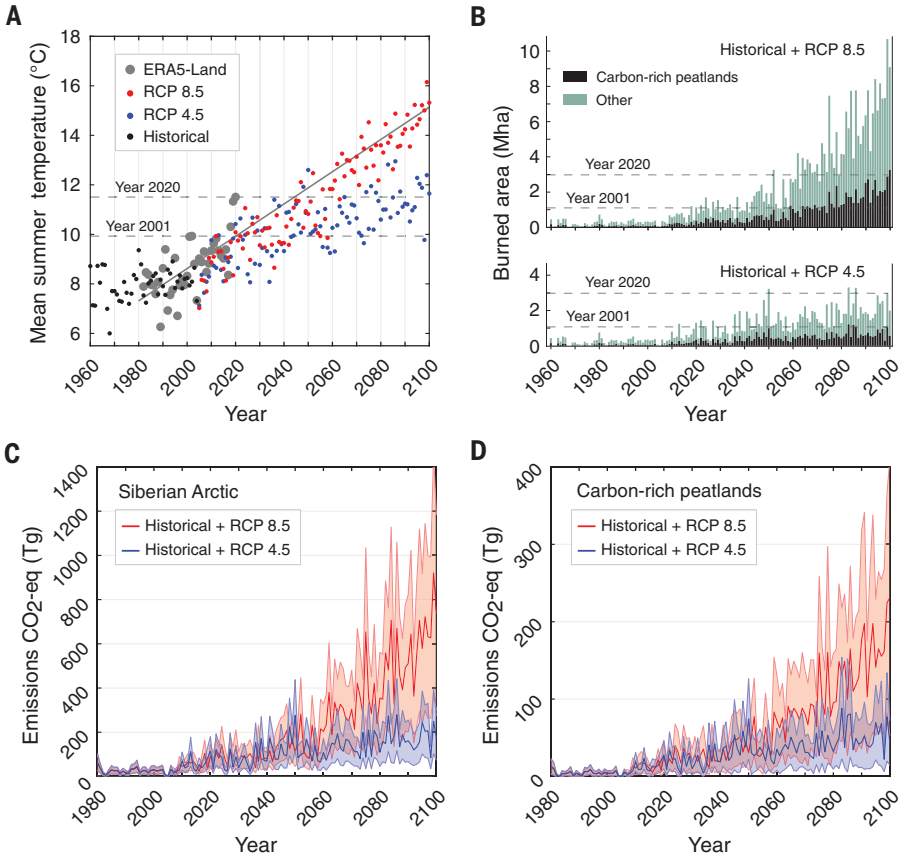


Fig. 6. Projected temperatures, annual burned areas, and emissions from fire in the Siberian Arctic. (**A**) Mean summer air temperatures from climate reanalysis (ERA-5 Land) during 1982–2020 and historical and projected temperatures under the RCP 4.5 and 8.5 scenarios based on HadGEM2-CC model. (**B**) Annual burned areas for the historical period and under the RCP 4.5 and 8.5 scenarios for carbon-rich peatlands (organic carbon storage >20 kg C m^{-2}) and other regions of the Siberian Arctic. (**C** and **D**) Projected CO_2-eq emissions under the RCP 4.5 and 8.5 in the Siberian Arctic (C) and carbon-rich soils (D).

year on record to have a mapped burned area over twice that of the long-term average. The exponential regression between the burned area and temperature (Fig. 4) indicated that an annual burn of 0.5 Mha occurred at a mean summer temperature of 10.2°C. The 10°C threshold also indicated the rapid growth of the annual burned area in 2018, 2019, and 2020. This indicates that small increases in summer mean temperature above the 10°C threshold tend to be associated with extensive annual burned areas.

The linear trend of mean summer air temperature (Fig. 3) indicated that temperatures would reach 10.2°C by 2024 and reach the levels in 2020 by 2045 if mean summer temperatures continued to increase linearly at the current rate. (Fig. 6A). The RCP 4.5 and 8.5 scenarios also indicated an increase in temperatures that could substantially expand the burned area in the Siberian Arctic; annual burned area could range from 0.5 to 2.5 Mha before the middle of the century under RCP 4.5 and RCP 8.5 (Fig. 6B). This would result in a mean annual emission of 37.8 (SD = 14.4) Tg C $year^{-1}$ and 107.0 (SD = 40.7) Tg CO_2-eq $year^{-1}$ under RCP 8.5 between 2030 and 2050 (Fig. 6C), of which 27.6% would come from carbon-rich peatlands (Fig. 6D). Large fires of the magnitude observed in 2020 (burned area > 2.5 Mha) might recur on a yearly basis at the end of the century under RCP 8.5, with annual mean carbon emissions of 135.0 (SD = 69.0) Tg C $year^{-1}$ and 382.5 (SD = 195.6) Tg CO_2-eq $year^{-1}$ (27.9% from carbon-rich peatlands). Under the RCP 4.5 scenario, annual carbon emissions would stabilize [51.7 (SD = 18.8) Tg C $year^{-1}$] in the second half of the century, and fires such as those in 2020 (>2.5 Mha) would become less frequent in the Siberian Arctic, with a 10-year return interval if greenhouse gas concentrations stabilize by the middle of the century.

Discussion

The Siberian Arctic burned at the highest rates in 2019 and 2020, based on the burning trends over four decades of satellite data. Burning was sevenfold higher in 2020 than the 1982–2020 average and damaged an unprecedented area of peatlands. We found that temperature-related factors of fire regime have increased significantly over the past four decades and identified an exponential relationship between these factors and annual burned area, accounting for the unprecedented extent of the burns in 2019 and 2020.

The SEM results confirmed the positive association between higher temperatures, longer growing season, and greener vegetation. Higher temperatures account for the earlier snowmelt, permitting vegetation growth (*17*) and increased green biomass (*18*), which increases fuel availability. This earlier start of the growing season, also reported more widely (*19*), modifies water use and availability such that plants may also experience water stress earlier in the season (*20*). According to the SEM results, the lengthening of the growing season and increasing green biomass of vegetation were associated with increased plant water stress, but the association was not significant, likely owing to the limited number of observations.

The increasing vulnerability to drought is exacerbated by extreme heatwaves, as in 2020, which can potentially desiccate plants and reduce moisture in peat and thus increase the severity of burning (*21*). This is reflected by the high influence of atmospheric dryness, measured by VPD, on plant water stress, represented by CWD, and its high correlation with annual burned area. Furthermore, CWD encompasses climatic factors, the water balance, and phenological changes that influence the susceptibility of vegetation to fire, so the interconnection of the fire factors with CWD may explain why CWD was best correlated with the annual burned area.

Climate warming and extreme weather may also account for the increase in the number of ignitions for specific years. The year 2020 had record-breaking temperatures and caused drought conditions early during the growing season (*13*). Recent warm winters, such as 2020, appear associated with abnormal circulation patterns that also favor the early spring snow melt and lower albedo that maintain warm conditions (*22*). Heatwaves and, more especially, increased surface temperatures are associated with convective storms and ignitions, as confirmed with the SEM. Whereas lightning remains infrequent at high latitudes, it is expected to increase as the climate warms (*23*). Climatic warming thus has a dual effect on fire regimes; warming increases the susceptibility of vegetation and peatlands to fire and increases the number of lightning-caused ignitions.

Increased winter warmth, as seen in 2020, reflects changes in circulation that draw more heat and moisture from lower latitudes (*24*). Circulation in eastern Siberia draws air and moisture from all directions of the compass (*25*) and is not immune to the so-called circulation "blocking" (*26*) seen elsewhere across the continent (*27*). Nonetheless, most burning

occurs during relatively gentle winds blowing from the northeast, indicating that the processes that promote flammability may be distinct from those that promote the subsequent burning.

Our ignition detection method indicated that numerous fires started near simultaneously across a vast region during a period of atmospheric instability in the 2020 fire season, from which we speculate that lightning was the main cause of ignition, but local observations are required to verify this supposition. An alternative, or additional, explanation is that fires emerge from smoldering material that has persisted through the winter to reemerge when conditions permit a broader conflagration (*28*, *29*). We also found that satellite thermal sensors showed that fires spread quickly after high CAPE values and midseason ignitions, which suggests that most of the annual burned area is caused by fires that started during that time.

The link we see between fires and temperature suggests that severe fire years, such as 2020, will become increasingly common and resulting carbon emissions will rise. The magnitude of future fires and carbon emissions, however, remains uncertain. First, although the frequency of lightning strikes appears likely to increase as temperatures rise (*23*), the scale of any resulting fires depends on specific local weather and vegetation conditions, which remain challenging to predict. Second, we only considered direct emissions from burning and disregarded indirect emissions, although these are not necessarily negligible. Burning removes the peat that insulates permafrost, exposing it to thawing, which promotes soil respiration and the production of carbon dioxide and methane (*30*). Estimates from field studies in two different boreal forests in Alaska suggest that post-fire carbon emissions range from one-third to more than double those that occur during burning (*31*). Furthermore, permafrost prevents deeper burning in peatlands (*21*). As permafrost retreats, high temperatures and drying conditions may favor higher combustion rates (*32*). We used combustion rates ranging from 2.0 kg C m^{-2} for tundra to 3.4 kg C m^{-2} for boreal forests (*31*), but dry peatlands can release up to 16.8 kg C m^{-2} (*21*), indicating that much higher emissions are credible.

A previous study proposed temperature and rainfall thresholds for the annual burned areas in the Alaskan tundra (*15*). The extensive area burned in 2019 and 2020 corroborated the proposed curve-growth relationship between annual burned area and climate-related factors for the Alaskan tundra. Hu *et al.* (*15*) forecasted that the annual burned area would double in the Alaskan tundra by the end of the century. We found, however, that the annual burned area in the Siberian Arctic already doubled the long-term average in the past 3 years of the record. This increase in annual burned area suggests that the Arctic is already experiencing a change in fire regimes caused by climatic warming. The burned areas in 2019 and 2020 might be exceptional occurrences, but the recent temperature trend and projected scenarios indicate that temperatures are reaching a threshold in which small increases above 10°C can alter fire-related factors and result in exponentially increasing burned area and associated fire emissions in the next decades. Forthcoming fires can potentially affect peatlands and deteriorate the permafrost, which in turn will exacerbate the carbon emissions from carbon-rich soils.

REFERENCES AND NOTES

1. S. M. Natali *et al*., *Proc. Natl. Acad. Sci. U.S.A.* **118**, e2100163118 (2021).
2. M. C. Serreze, J. A. Francis, *Clim. Change* **76**, 241–264 (2006).
3. E. Post *et al*., *Sci. Adv.* **5**, eaaw9883 (2019).
4. Arctic Monitoring and Assessment Programme, *Arctic Climate Change Update 2021: Key Trends and Impacts. Summary for Policy-Makers* (Arctic Monitoring and Assessment Programme, 2021).
5. E. A. Schuur *et al*., *Nature* **520**, 171–179 (2015).
6. K. Dutta, E. Schuur, J. Neff, S. Zimov, *Glob. Change Biol.* **12**, 2336–2351 (2006).
7. M. R. Turetsky *et al*., *Nat. Geosci.* **13**, 138–143 (2020).
8. G. Hugelius *et al*., *Proc. Natl. Acad. Sci. U.S.A.* **117**, 20438–20446 (2020).
9. A. Witze, *Nature* **585**, 336–337 (2020).
10. M. C. Mack *et al*., *Nature* **475**, 489–492 (2011).
11. N. H. French *et al*., *Int. J. Wildland Fire* **24**, 1045–1061 (2015).
12. J. L. McCarty *et al*., *Biogeosciences* **18**, 5053–5083 (2021).
13. A. Ciavarella *et al*., *Clim. Change* **166**, 9 (2021).
14. O. V. Churakova Sidorova, R. T. W. Siegwolf, M. V. Fonti, E. A. Vaganov, M. Saurer, *Sci. Rep.* **11**, 19010 (2021).
15. F. S. Hu *et al*., *Front. Ecol. Environ.* **13**, 369–377 (2015).
16. P. Olofsson *et al*., *Remote Sens. Environ.* **148**, 42–57 (2014).
17. A. Descals *et al*., *Sci. Total Environ.* **742**, 140637 (2020).
18. L. T. Berner *et al*., *Nat. Commun.* **11**, 4621 (2020).
19. S. Piao *et al*., *Glob. Chang. Biol.* **25**, 1922–1940 (2019).
20. J. Peñuelas, T. Rutishauser, I. Filella, *Science* **324**, 887–888 (2009).
21. M. R. Turetsky, W. F. Donahue, B. W. Benscoter, *Nat. Commun.* **2**, 514 (2011).
22. A. B. M. Collow *et al*., *J. Clim.* **35**, 3075–3090 (2022).
23. Y. Chen *et al*., *Nat. Clim. Chang.* **11**, 404–410 (2021).
24. Q. You *et al*., *Earth Sci. Rev.* **217**, 103625 (2021).
25. J. Piao, W. Chen, S. Chen, H. Gong, Q. Zhang, *J. Clim.* **33**, 3883–3899 (2020).
26. C. You, M. Tjernström, A. Devasthale, D. Steinfeld, *Geophys. Res. Lett.* **49**, e2022GL097899 (2022).
27. T. Nakamura, T. Sato, *Environ. Res.* **209**, 112881 (2022).
28. R. C. Scholten, R. Jandt, E. A. Miller, B. M. Rogers, S. Veraverbeke, *Nature* **593**, 399–404 (2021).
29. J. L. McCarty, T. E. Smith, M. R. Turetsky, *Nat. Geosci.* **13**, 658–660 (2020).
30. J. E. Holloway *et al*., *Permafr. Periglac. Process.* **31**, 371–382 (2020).
31. S. Veraverbeke *et al*., *Curr. Opin. Environ. Sci. Health* **23**, 100277 (2021).
32. M. R. Turetsky *et al*., *Nat. Geosci.* **8**, 11–14 (2015).
33. A. Descals, adriadescals/ArcticFires: Arctic Fire repository, *Zenodo* (2022). https://doi.org/10.5281/zenodo.6907765.
34. E. Chuvieco, M. L. Pettinari, G. Otón, ESA Fire Climate Change Initiative, (Fire_cci): AVHRR-LTDR Burned Area Grid product, Centre for Environmental Data Analysis, Version 1.1 (2020). http://dx.doi.org/10.5285/62866635ab074e07b93f17fbf87a2c1a
35. L. Giglio, C. Justice, L. Boschetti, D. Roy, MCD64A1 MODros. Inf. Serv./Terra+ aqua burned area monthly L3 global 500m SIN grid V006, NASA EOSDIS. Inf. Serv. Land Processes DAAC (2015). https://doi.org/10.5067/MODIS/MCD64A1.006.
36. E. Chuvieco, M. Pettinari, J. Lizundia-Loiola, T. Storm, M. Padilla Parellada, ESA Fire Climate Change Initiative, (Fire_cci): MODros. Inf. Serv. Fire_cci burned area pixel product, Centre for Environmental Data Analysis, version 5.1 (2018). https://doi.org/10.5285/58f00d8814064b79a0c49662ad3af537.
37. Copernicus Climate Change Service, Fire burned area from 2001 to present derived from satellite observations, Copernicus Climate Change Service (C3S) Climate Data Store (CDS) (2019). https://doi.org/10.24381/cds.f333cf85.
38. Z. Wan, S. Hook, G. Hulley, MOD11A2 MODIS/Terra land surface temperature/emissivity 8-day L3 global 1km SIN grid V006, NASA EOSDIS Land Processes DAAC (2015). https://doi.org/10.5067/MODIS/MOD11A2.006.
39. J. Muñoz Sabater, ERA5-Land monthly averaged data from 1950 to present, Copernicus Climate Change Service (C3S) Climate Data Store (CDS) (2019). https://doi.org/10.24381/cds.68d2bb30.
40. J. T. Abatzoglou, S. Z. Dobrowski, S. A. Parks, K. C. Hegewisch, Monthly climate and climatic water balance for global terrestrial surfaces from 1958-2015, University of Idaho (2017). ttps://doi.org/10.7923/G43J3B0R.
41. H. Wouters, J. Berckmans, R. Maes, E. Vanuytrecht, K. De Ridder, Global bioclimatic indicators from 1950 to 2100 derived from climate projections, Copernicus Climate Change Service (C3S) Climate Data Store (CDS) (2021). https://doi.org/10.24381/cds.a37fecb7.
42. K. Didan, MOD13Q1 MODIS/Terra vegetation indices 16-day L3 global 250m SIN grid V006, NASA EOSDIS. Inf. Serv. Land Processes DAAC (2015). https://doi.org/10.5067/MODIS/MOD13Q1.006.

ACKNOWLEDGMENTS

Funding: This work was funded by the Ministry of Agriculture, Forestry and Fisheries (MAFF) of the government of Japan and the Center for International Forestry Research ("CIFOR"), through the project "Transitions to Climate Resilient Landscapes: Reducing and Mitigating Boreal and Tropical Forest Fires to Promote Sustainable Rural Livelihoods." We acknowledge funds from the Spanish Government grant PID2019-110521GB-I00, the Fundación Ramón Areces grant CIVP20A6621, and the Catalan Government grant SGR 2017-1005. This work represents a contribution to CSIC PTI-TELEDETECT. **Author contributions:** Conceptualization: A.D., D.L.A.G., and J.P. Methodology: A.D. and D.L.A.G. Investigation: A.D. and D.L.A.G. Visualization: A.D., D.L.A.G., and J.P. Supervision: J.P. Writing – original draft: A.D. and D.L.A.G. Writing – review and editing: A.D., D.L.A.G., A.V., D.S., D.N., and J.P. **Competing interests:** Authors declare that they have no competing interests. **Data and materials availability:** All source code and the Sentinel-2 and Landsat-8 burned-area maps are available at Zenodo (*33*). Other data that support the findings of the study are openly available. The burned area time series derived from AVHRR sensors (FireCCILT11) (*34*) is available at https://doi.org/10.5285/62866635ab074e07b93f17fbf87a2c1a. The burned area time series derived from MODIS sensors are available at https://doi.org/10.5067/MODIS/MCD64A1.006 for the MCD64A1 product (*35*) and https://doi.org/10.5285/58f00d8814064b79a0c49662ad3af537 for the FireCCI51 (*36*) product. The burned area time series derived from Sentinel-3 (C3SBA10) (*37*) is available at https://doi.org/10.24381/cds.f333cf85. The Landsat-7 and -8 surface reflectance datasets are available at https://earthexplorer.usgs.gov, and the Sentinel-2 Level-2A surface reflectance at https://scihub.copernicus.eu. The active fire datasets obtained from MODIS is available at https://firms.modaps.eosdis.nasa.gov/active_fire. Fire emission datasets were downloaded from the FIRECAM platform https://globalfires.earthengine.app/view/firecam. Land surface temperature from MODIS (MOD11A2) (*38*) is available at https://doi.org/10.5067/MODIS/MOD11A2.006. Climate reanalysis ERA5-Land Monthly (*39*) is available at https://doi.org/10.24381/cds.68d2bb30, and TERRACLIMATE dataset (*40*) is available at https://doi.org/10.7923/G43J3B0R. The downscaled air temperature projections from the HadGEM2-CC model (*41*) are available at https://doi.org/10.24381/cds.a37fecb7. The storage of organic carbon from peatlands is available at https://bolin.su.se/data/hugelius-2020. Lastly, the NDVI time series from the GIMMS3g dataset is available at https://www.nasa.gov/nex/data, and the NDVI from the MOD13Q1v6 product (*42*) at https://doi.org/10.5067/MODIS/MOD13Q1.006. **License information:** Copyright © 2022 the authors, some rights reserved; exclusive licensee American Association for the Advancement of Science. No claim to original US government works. https://www.sciencemag.org/about/science-licenses-journal-article-reuse

SUPPLEMENTARY MATERIALS

science.org/doi/10.1126/science.abn9768
Materials and Methods
Supplementary Text
Figs. S1 to S9
Tables S1 and S2
References (*43*–*65*)

Submitted 7 January 2022; accepted 13 September 2022
10.1126/science.abn9768

NEUTRINO ASTROPHYSICS

Evidence for neutrino emission from the nearby active galaxy NGC 1068

IceCube Collaboration*†

A supermassive black hole, obscured by cosmic dust, powers the nearby active galaxy NGC 1068. Neutrinos, which rarely interact with matter, could provide information on the galaxy's active core. We searched for neutrino emission from astrophysical objects using data recorded with the IceCube neutrino detector between 2011 and 2020. The positions of 110 known gamma-ray sources were individually searched for neutrino detections above atmospheric and cosmic backgrounds. We found that NGC 1068 has an excess of 79^{+22}_{-20} neutrinos at tera–electron volt energies, with a global significance of 4.2σ, which we interpret as associated with the active galaxy. The flux of high-energy neutrinos that we measured from NGC 1068 is more than an order of magnitude higher than the upper limit on emissions of tera–electron volt gamma rays from this source.

Observations of high-energy cosmic rays (protons and atomic nuclei from space), up to 10^{19} to 10^{20} eV (*1*–*3*), have demonstrated that powerful cosmic particle accelerators must exist, but their nature and location remain unknown. Interstellar magnetic fields change the direction of charged cosmic particles during their propagation to Earth, concealing their sources. High-energy photons and neutrinos are not deflected, so they could be used to locate the cosmic accelerators. Both travel along straight paths and are produced wherever cosmic rays interact with ambient matter or light, in or near the acceleration sites (*4*, *5*). Depending on the environment in which these interactions occur, gamma rays could rapidly lose energy through several processes, including pair-production in interactions with lower-energy photons. Above tera–electron volt energies, gamma rays are strongly absorbed over cosmological distances through interactions with the extragalactic background light and the cosmic microwave background (*6*). Neutrinos are not affected by intergalactic absorption, so they could potentially be used to probe tera–electron volt cosmic accelerators.

Active galaxies, those that host an active galactic nucleus (AGN) (*7*), are characterized by a very bright central region powered by the accretion of material onto a supermassive black hole (SMBH). The accretion flow of matter into the SMBH is usually surrounded by an obscuring, dusty torus, causing the observable characteristics of an AGN to depend on the viewing angle from Earth. For example, Seyfert II galaxies (*8*) are thought to be viewed edge on, with the line of sight passing directly through the obscuring torus (*9*). In some cases, the AGN can launch a strong, narrow jet of accelerated plasma. If such a jet is oriented close to the line of sight, the AGN is observed as a blazar (*10*). AGNs are potential neutrino emitters (*11*, *12*); if a plasma jet is present, it might dominate the emission (*13*, *14*).

The IceCube Neutrino Observatory (*15*) is based at the Amundsen-Scott South Pole Station in Antarctica and has been operating since 2010. The observatory uses 1 km^3 of optically transparent glacial ice as a detection medium to measure Cherenkov light—ultraviolet and blue photons emitted by charged secondary particles traveling at a speed above the phase velocity of light in the ice. These relativistic (close to the speed of light) secondary particles are produced when neutrinos interact with nuclei in or near the instrument. A total of 5160 digital optical modules (DOMs) are installed on 86 vertical cables (strings), spaced 125 m apart to form a three-dimensional array in the ice. Each DOM records the number of induced photoelectrons (charges) as a function of time.

The measured flux of astrophysical neutrinos (*16*) is largely isotropic, equally distributed among neutrino flavors, and can be described by a single power-law energy distribution that extends from ~10 TeV to peta–electron volt energies (*17*, *18*). A specific source of high-energy cosmic neutrinos was reported after the spatial and temporal coincidence of a high-energy IceCube neutrino (*19*) with a gamma-ray flaring blazar, TXS 0506+056 (*20*–*22*). TXS 0506+056 contains a typical accretion disk and a dusty torus, which emits high-energy radiation and, possibly, cosmic rays (*22*). Neutrinos detected using IceCube were correlated with a catalog of 110 known gamma-ray emitters, with a significance of 3.3σ (*23*). The individual sources that made the largest contribution to the total significance of that catalog were the active galaxy NGC 1068 and the blazars TXS 0506+056, PKS 1424+240, and GB6 J1542+6129. The significance of the neutrino excess from the direction of NGC 1068 was reported as 2.9σ, which is insufficient to claim a detection (*23*).

Searching for point-like neutrino emission

We analyzed data collected with IceCube between 13 May 2011 and 29 May 2020. This period begins with the installation of the full 86-string detector configuration. Previous searches for cosmic neutrino sources (*23*) included data collected with the incomplete detector with fewer strings going back to 2008 and the full detector up to the spring of 2018. We only used the full detector data because our methods depend on uniformly processed data. The IceCube dataset we used (*24*) has consistent selection criteria (*25*). We reprocessed these data uniformly to remove data sample fragmentation, align different data-taking conditions and calibrations, and improve event reconstructions

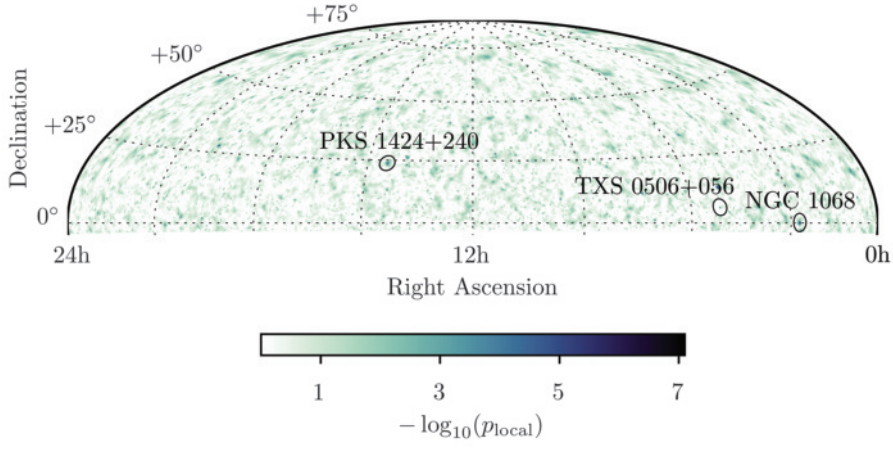


Fig. 1. Sky map of the scan for point sources in the Northern Hemisphere. The color scale indicates the logarithm of the local *P* value (P_{local}) obtained from our maximum likelihood analysis, evaluated (with the spectral index as a free parameter) at each location in the sky. The map is shown in equatorial coordinates on a Hammer-Aitoff projection. The black circles indicate the three most significant objects in the source list search, which are labeled. The circle around NGC 1068 contains the most significant location in the Northern Hemisphere, shown in higher resolution in Fig. 2A.

*Corresponding authors: analysis@icecube.wisc.edu; F. Halzen (francis.halzen@icecube.wisc.edu)
†IceCube Collaboration authors and affiliations are listed in the supplementary materials.

(*26*). We applied the directional track reconstruction method SplineReco (*26*, *27*, *28*) to all events in our dataset (*26*). We incorporated additional calibration information in the extraction of the charges at each DOM and in the corresponding arrival times of Cherenkov photons. Compared with previous work (*23*), this introduces small changes in the reconstructed event energies and some reconstructed event directions (*26*). To ensure a uniform detector response, the DOMs of the DeepCore subarray, intended to study ≲100-GeV neutrinos, were excluded (*25*). Our resulting dataset, which is optimized for track-like events induced by muon (anti-)neutrinos $\left[\overset{(-)}{\nu}_{\mu}\right]$, has a total exposure time of 3186 days.

We restricted our searches to the Northern Hemisphere from declination $\delta = -3°$ to 81°, where IceCube is most sensitive to astrophysical sources. IceCube uses Earth as a passive cosmic muon shield and as a target material for neutrinos. Hence, by selecting only upward-going events, we reduced the atmospheric muon background, which contributes <0.3% to our final event sample (*25*). Declinations higher than 81° are excluded because low-energy events from those directions are closely aligned with the strings of IceCube, complicating our distinction between the signal and background (*26*). The resulting loss of sky coverage is <1%.

A total of ~670,000 neutrino-induced muon tracks pass the final event selection criteria (*25*). However, only a small fraction of these events originate from neutrinos produced in astrophysical sources. Most arise from the decay of particles (specifically mesons) that are produced in the interaction of cosmic rays with nuclei in Earth's atmosphere. To discriminate neutrinos that originate from individual astrophysical sources from the background of atmospheric and diffuse astrophysical neutrinos, we used a maximum-likelihood method and likelihood ratio hypothesis testing, based on the estimated energy, direction, and angular uncertainty of each event (*26*). The median angular resolution of each neutrino arrival direction, composed of reconstruction uncertainty and the kinematic angle between the parent neutrino and the muon, is 1.2° at 1 TeV, 0.4° at 100 TeV, and 0.3° at 1 PeV. We assume any point source emits a neutrino flux $\Phi_{\nu_\mu+\bar{\nu}_\mu}$ described by a generalized power-law energy spectrum, $\Phi_{\nu_\mu+\bar{\nu}_\mu}(E_\nu) = \Phi_0 \cdot (E_\nu/E_0)^{-\gamma}$, with normalization energy $E_0 = 1$ TeV, where E_ν is the neutrino energy and the spectral index γ and the flux normalization Φ_0 are free parameters (*26*). This corresponds to two correlated model parameters that we express as a pair (μ_{ns}, γ), where μ_{ns} is the mean number of astrophysical neutrino events associated with a given point in the sky. Using the energy- and declination-dependent effective area of the detector and assuming a spectral index γ, μ_{ns} can be directly converted to Φ_0 (*26*). Hence, the tuple of μ_{ns} and γ fully determines the flux of muon neutrinos, $\Phi_{\nu_\mu+\bar{\nu}_\mu}$, at any given energy.

We performed three different searches (*26*). The first search consists of three discrete scans of the Northern Hemisphere to identify the location of the most statistically significant excesses of high-energy neutrino events. These scans use three different hypotheses for the spectral index: γ as a free parameter, γ fixed to 2.0, and γ fixed to 2.5. The other two searches use a list of 110 preselected astronomical objects, all located in the Northern Hemisphere: The second search is for the most significant candidate neutrino source in the list, whereas the third search consists of a binomial test to evaluate the significance of observing an excess of k sources with local P values below or equal to a chosen threshold, with k being an index from 1 to 110. The binomial test is repeated under the same three spectral index hypotheses as the sky scan.

All analysis methods, including the selection of the hypotheses to be tested, were formulated a priori. The performance of each method was evaluated using simulations and randomized experimental data (*26*). The local P values are determined as the fraction of background-only simulations that yield a test statistic greater than (or equal to) the test statistic obtained from the experimental data. The global P values are determined from the smallest local P value after correcting for testing multiple locations (the look-elsewhere effect) (*26*). We use this global value to assess the evidence that the data provide against a background-only null hypothesis (that the data consist purely of atmospheric background and isotropic cosmic neutrinos).

Table 1. Summary of final *P* values. For each of the three tests performed, we report the most significant local and global P values.

Test type	Pretrial P value, P_{local} (local significance)	Posttrial P value, P_{global} (global significance)
Northern Hemisphere scan	5.0×10^{-8} (5.3σ)	2.2×10^{-2} (2.0σ)
List of candidate sources, single test	1.0×10^{-7} (5.2σ)	1.1×10^{-5} (4.2σ)
List of candidate sources, binomial test	4.6×10^{-6} (4.4σ)	3.4×10^{-4} (3.4σ)

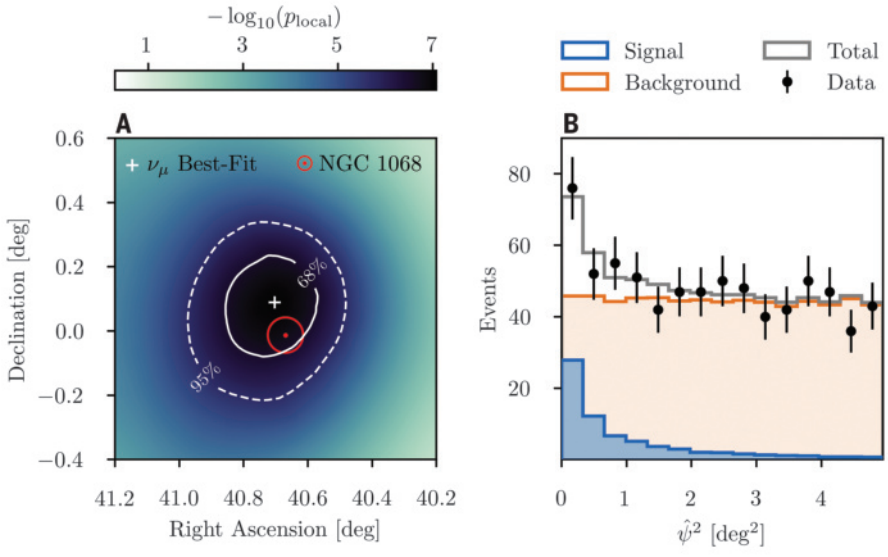


Fig. 2. High-resolution scan around the most significant location. (**A**) High-resolution scan around the most significant location marked by a white cross, with contours showing its 68% (solid) and 95% (dashed) confidence regions. The red dot shows the position of NGC 1068, and the red circle is its angular size in the optical wavelength (*61*). (**B**) The distribution of the squared angular distance, $\hat{\psi}^2$, between NGC 1068 and the reconstructed event directions. We estimated the background (orange) and the signal (blue) from Monte Carlo simulations, assuming the best-fitting spectrum at the position of NGC 1068. The superposition of both components is shown in gray and the data in black. This representation of the result ignores the energy and angular uncertainty of the events.

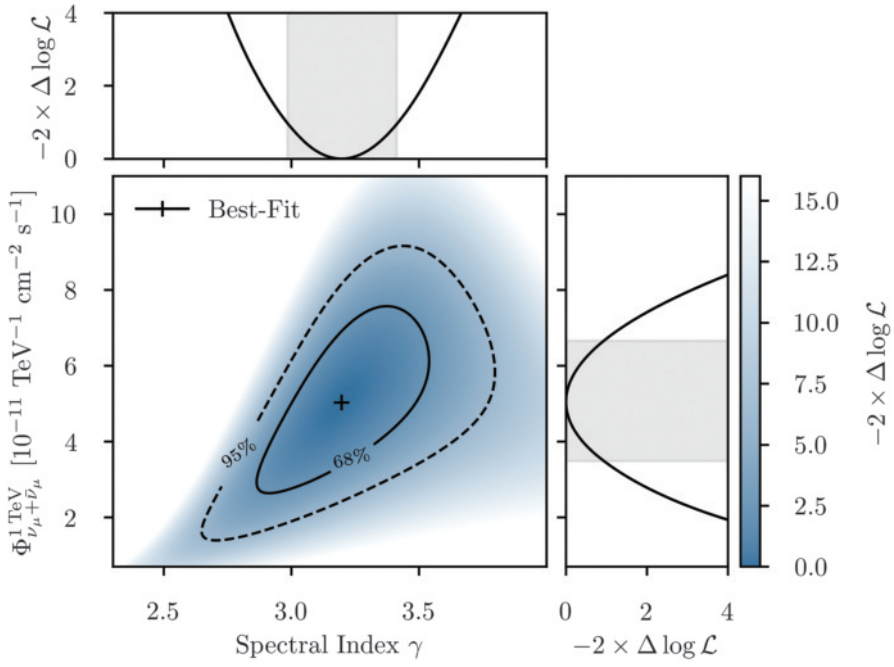


Fig. 3. Source parameters of NGC 1068. The best-fitting flux values are shown as the black cross, with the solid and dashed contours representing the 68% and 95% confidence levels, respectively. These were derived from Wilks' theorem—i.e., by using the log-likelihood ratio (color scale), $-2\Delta \log \mathcal{L}$, between any fixed values for the two flux parameters $\left(\gamma, \Phi^{1\,\mathrm{TeV}}_{\nu_\mu+\bar{\nu}_\mu}\right)$ and the overall best-fitting point marked by the cross. The side panels show the corresponding one-dimensional projections (profile likelihoods) as black solid lines, with the gray shaded areas showing the one-dimensional 68% confidence levels (as reported in the text). All contours include only statistical uncertainties.

The discrete scan of the sky maximizes the signal and background likelihood functions at each point on an ~(0.2° × 0.2°) grid, determining the local value of the test statistic, the best-fitting value of the mean number of astrophysical neutrino events $(\hat{\mu}_{\mathrm{ns}})$, and the mean spectral index $(\hat{\gamma})$. The scan is repeated with fixed spectral indices $\gamma = 2.0$ and $\gamma = 2.5$ to reduce the impact of background fluctuations, which arise from atmospheric neutrinos. The atmospheric spectrum, produced by the decay of charged pions and kaons as well as the muons produced when pions and kaons decay, follows a power law with $\gamma \approx 3.7$ (*29*), and thus those fluctuations typically yield $\hat{\gamma} \gtrsim 3$. Fixing the spectral index therefore increases the sensitivity to astrophysical sources with $\gamma < 3$. For the 20 most significant locations in each of the three searches, we scan the 1.5° × 1.5° vicinity using increased resolution of ~(0.03° × 0.03°) on a square grid. We find the most significant location identified in the first scan (with free spectral index) at right ascension 40.69° and declination 0.09° (J2000 equinox) with $\hat{\gamma} = 3.2$ and $\hat{\mu}_{\mathrm{ns}} = 81$.

Sky scan search

The full sky map of the discrete scan is shown in Fig. 1. At the most significant location, the local *P* value is 5×10^{-8}, which corresponds to a local significance of 5.3σ. After including a penalty for the multiple tests performed—i.e., how likely it is to observe an equal or larger significance when scanning many independent sky positions under the three spectral index hypotheses (*26*)—the global *P* value corresponds (*26*) to 2.0σ and is therefore not significant without additional prior information. The high-resolution scan around the most significant location is shown in Fig. 2A.

We searched a posteriori for astrophysical counterparts in close proximity to the direction of the five most significant locations in each of the three sky maps. The nearby active galaxy NGC 4151 (*8*) is located at ~0.18° from the fourth most significant location in the map obtained with $\gamma = 2.5$.

Source list search

Searching the entire Northern Hemisphere requires a strong numerical penalty because of testing multiple locations. This trials factor can be reduced by restricting the search to a list of a priori selected positions based, for example, on known gamma-ray emission (*30*). To avoid confirmation bias, we maintain the previous selection method (*23*), which was adopted before there was any indication for neutrino emission from NGC 1068 (*31*). This approach identified a total of 110 objects within the declination range we analyzed, $-3° \leq \delta \leq 81°$. The number of objects in the list was chosen such that a local 5σ detection corresponds to a global detection >4σ after accounting for the number of trials. The 110 astronomical objects were selected from the gamma-ray flux weighted by the IceCube sensitivity. Using the gamma-ray flux above 1 GeV (*32*), the list contains 95 blazars, 5 AGNs, and 9 other types of galaxies. One galactic source is added because of its tera–electron volt gamma-ray emission (*26*, *33*). We do not assume or require any relationship between the observed gamma-ray flux and the hypothesized neutrino flux during our hypothesis testing (*26*).

Of the 110 astronomical objects tested, NGC 1068 is the most significant with a local *P* value of 1×10^{-7} (5.2σ); it has best-fitting values of spectral index $\hat{\gamma} = 3.2^{+0.2}_{-0.2}$ and mean number of signal events $\hat{\mu}_{\mathrm{ns}} = 79^{+22}_{-20}$. NGC 1068 is contained within the 68% confidence region around the most significant location in the sky scan, offset by 0.11° (less than the directional uncertainty), consistent with neutrino emission from NGC 1068 (Fig. 2). After correcting for having tested the 110 sources in the catalog, the global *P* value for NGC 1068 is 1.1×10^{-5}, corresponding to a significance of 4.2σ.

Binomial test

We performed a binomial test to investigate how likely it is to find an excess of k sources from the catalog with local *P* values below or equal to a threshold (*26*), as defined a priori. By scanning the *P* value threshold, we find the smallest background probability for an excess of $k = 3$ sources, under the free spectral index hypothesis, with local *P* values $\leq 4.6 \times 10^{-6}$. This is equivalent to a local significance of 3.7σ, a small increase from the previous search (*23*). After correcting for having tested three different spectral index hypotheses, we obtain a posttrial significance of 3.4σ for the binomial test. Besides NGC 1068, the other two objects contributing to the excess are the blazars PKS 1424+240 and TXS 0506+056 (Fig. 1), for which we found potential neutrino emission with local significances of 3.7σ and 3.5σ, respectively. This significance of TXS 0506+056 relates to a time-integrated signal over the duration of our dataset, whereas previous analyses have found evidence for transient emission (*20*, *21*, *34*). A search for transient emission has a lower effective background than our time-integrated searches. The total number of contributing candidate sources ($k = 3$) in the binomal test is lower than the four previously reported (*23*). Although the local significance of PKS 1424+240 increased from 3.0σ to 3.7σ, the local significance of GB6 J1542+61 decreased from 2.9σ to 2.2σ, falling below the threshold corresponding to the best-fitting binomial *P* value. The results of all three searches (*26*) are summarized in Table 1.

Neutrino emission from NGC 1068

The high-resolution scan around the most significant location in the Northern Hemisphere is shown in Fig. 2A, with NGC 1068 located inside the 68% confidence region. The position of NGC 1068 produced $\hat{\mu}_{ns} = 79^{+22}_{-20}$ more events than expected from the atmospheric and diffuse astrophysical neutrino backgrounds. Figure 2B shows the distribution of the angular separation of these events from NGC 1068. Among the 79 most contributing events, 63 were included in a previous analysis (*23*). The systematic uncertainty on $\hat{\mu}_{ns}$ is ~2 events (*26*). The measured spectral index is $\hat{\gamma} = 3.2^{+0.2}_{-0.2}$ with an estimated systematic uncertainty of ±0.07 (*26*), consistent with previous results (*23*). We estimate these systematic uncertainties by analyzing simulated data, assuming a source with flux equal to the one measured for NGC 1068 but varying assumptions about the detector response (*26*). Systematic uncertainties arise mainly from the modeling of the photon propagation in the glacial ice—e.g., scattering and absorption—and the efficiency with which photons are detected by the IceCube optical modules. Systematic uncertainties are smaller than statistical uncertainties for directional track reconstructions (*26*) but have a nonnegligible effect on the energy reconstructions.

The properties of the source spectrum are shown in Fig. 3, which shows the likelihood as a function of the model parameters (Φ_0, γ) evaluated at the coordinates of NGC 1068. The conversion of $\hat{\mu}_{ns}$ to the flux Φ_0 accounts for the contribution from tau neutrino interactions (which produce muons) assuming an equal neutrino flavor ratio. The best-fitting flux averaged over the data-taking period, at a neutrino energy of 1 TeV, is $\Phi^{1\mathrm{TeV}}_{\nu_\mu+\bar{\nu}_\mu} = (5.0 \pm 1.5_{\mathrm{stat}} \pm 0.6_{\mathrm{sys}}) \times 10^{-11}\,\mathrm{TeV}^{-1}\,\mathrm{cm}^{-2}\mathrm{s}^{-1}$. This systematic uncertainty was estimated by varying the flux normalization under different ice and detector properties, such that we reproduce the observed values of $\hat{\gamma}$ and $\hat{\mu}_{ns}$ in the median case.

Our analysis assumed that the spectrum follows an unbroken power law over the entire energy range of the dataset. However, our results show that the main contribution to the excess (and thus the measured spectral index and flux normalization) comes from neutrinos in an energy range from 1.5 to 15 TeV, which contributes 68% to the total test statistic. Outside this energy range, the data do not strongly constrain the inferred flux properties. Our results strengthen the suggestion (*23*) that NGC 1068 could be a neutrino source; we find a higher statistical significance for this result (4.2σ versus 2.9σ).

Incrementally removing the most contributing neutrino events one by one from the vicinity of NGC 1068 shows that the excess persists, which indicates that it is not dominated by one or a few single events but is the result of an accumulation of neutrinos (*26*). We visually inspected all neutrino events contributing to the excess from NGC 1068, finding typical, well-reconstructed, horizontal, and approximately tera–electron volt–energy tracks with no sign of unexpected contamination or anomalies (*26*). Out of the 20 events contributing the most to the test statistic, 19 were included in the previous analysis (*23*). Although the location is therefore dominated by the same neutrinos, the

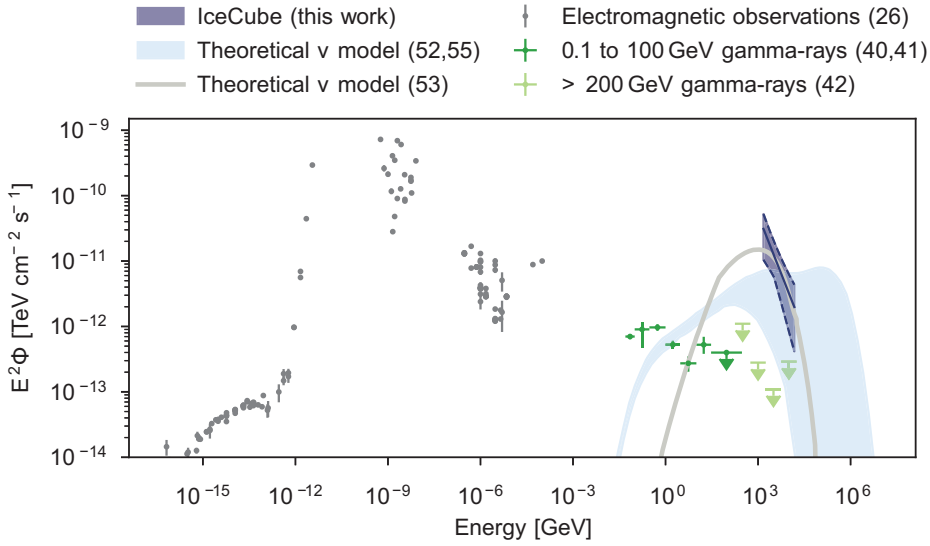


Fig. 4. Multimessenger spectral energy distribution of NGC 1068. Gray points show multifrequency observations (data sources listed in table S1). Dark and light green points indicate gamma-ray observations at 0.1 to 100 GeV (*40*, *41*) and >200 GeV (*42*), respectively. Arrows indicate upper limits, and error bars are 1σ confidence intervals. The solid, dark blue line shows our best-fitting neutrino spectrum with the dark blue shaded region indicating the 95% confidence region. We restrict this spectrum to the range between 1.5 and 15 TeV, where the flux measurement is well constrained (*26*). Two theoretical predictions are shown for comparison: The light blue shaded region and the gray line show the NGC 1068 neutrino emission models from (*52*, *55*) and (*53*), respectively. The shaded region covers possible values of the gyrofactor $30 \le \eta_g \le 10^4$ used to describe uncertainty in the efficiency of the underlying particle acceleration (*55*). All fluxes Φ are multiplied by the energy squared E^2.

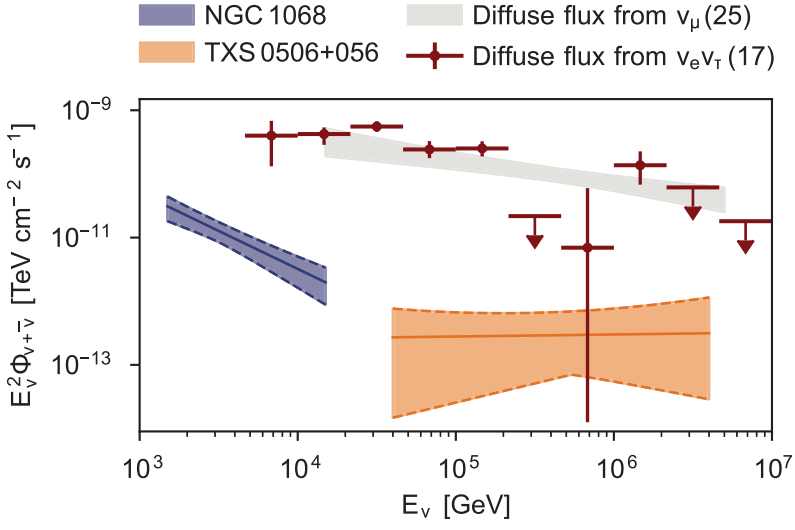


Fig. 5. Comparison of point-source fluxes with the total diffuse astrophysical neutrino flux. Fluxes for NGC 1068 (blue line, this work), TXS 0506+056 (orange line, this work), and the diffuse neutrino background [brown data points and gray band (*17*, *25*)] are given for a single flavor of neutrinos and antineutrinos. All fluxes $\Phi_{\nu+\bar{\nu}}$ are multiplied by the neutrino energy squared E^2_ν. For the conversion of the diffuse astrophysical flux measured from the $\nu_e\nu_\tau$ channel (*17*), we assume an equal flavor ratio. Shaded regions and dashed lines indicate 68% confidence intervals. Downward arrows are 68% upper limits.

differences in the data processing modify their contribution to the likelihood function. These changes are small but consistently cause the reconstructed neutrinos to align more closely with the direction of NGC 1068, thus strengthening the association (*26*).

Astrophysical interpretation

The flux we measured from the direction of NGC 1068 was 79^{+22}_{-20} muon-neutrino events over a period of 3186 days, corresponding to $\Phi^{1\,\mathrm{Tev}}_{\nu_\mu+\bar{\nu}_\mu} = (5.0 \pm 1.5_{\mathrm{stat}}) \times 10^{-11}\ \mathrm{TeV}^{-1}\ \mathrm{cm}^{-2}\mathrm{s}^{-1}$. If all neutrino flavors contribute equally, as expected for sources dominated by pion decay and neutrino oscillations over cosmic distances (*35*, *36*), the all-flavor flux is a factor of 3 higher. We adopt a distance of 14.4 Mpc for NGC 1068 (*37*), although values in the literature range from 10.3 ± 3 Mpc (*38*) to 16.5 Mpc (*39*). For comparison, assuming isotropic emission, this leads to a redshift-corrected equivalent neutrino luminosity L_ν, from 1.5 to 15 TeV and at 14.4 Mpc, of $L_\nu = (2.9 \pm 1.1_{\mathrm{stat}}) \times 10^{42}\ \mathrm{erg\ s^{-1}}$. This is higher than the equivalent gamma-ray luminosity of $1.6 \times 10^{41}\ \mathrm{erg\ s^{-1}}$ observed in the energy range 100 MeV to 100 GeV (*40*, *41*) and higher than the upper limits reported above 200 GeV (*42*) (Fig. 4).

High-energy neutrinos are generated in or near astronomical sources as decay products of charged mesons, which are themselves produced in proton-proton interactions (*4*), or interactions between protons and low-energy ambient radiation (*5*). Gamma rays are also produced in the same processes, through the decay of neutral mesons. Neutrinos escape the site without further interactions, whereas photons may experience additional interactions depending on the optical depth of the environment. Therefore, the connection between neutrinos and gamma rays is highly dependent on the astrophysical environment. NGC 1068 (*8*) is a nearby Seyfert II galaxy that hosts a Compton-thick AGN (*43*–*45*), has vigorous starburst activity (*46*, *47*) and outflows (*48*), and for these reasons has previously been discussed as a potential source of high-energy neutrinos (*49*–*51*). Neutrino emission models (*52*, *53*) have predicted the production of neutrinos and gamma rays within the heavily obscured environment around the NGC 1068 AGN (*49*, *54*). In those models, the SMBH in the AGN provides the acceleration conditions, with x-ray photons generated through photon Comptonization from the accretion disk in the hot plasma above the disk, called the corona, providing the conditions for the production of neutrinos and absorption of gamma rays. Figure 4 compares our neutrino flux measurement with the model predictions (*52*, *53*).

The evidence of neutrino emission from NGC 1068 suggests that AGNs could make a substantial contribution to the diffuse neutrino flux. Figure 5 compares the neutrino fluxes from the AGN NGC 1068 and the blazar TXS 0506+056 with the overall diffuse flux of astrophysical neutrinos. These two sources contribute ~1% of the total diffuse flux in their observed energy ranges. For NGC 1068, the observed energy range does not strongly overlap with the diffuse flux, and its best-fitting spectral index of $\hat{\gamma} = 3.2^{+0.2}_{-0.2}$ is higher than the diffuse flux with $\gamma = 2.53^{+0.07}_{-0.07}$ (*17*). Nonetheless, it is evident that the diffuse flux could contain additional bright and nearby sources, like NGC 1068, a large population of faint sources, or both. For example, the nearby Seyfert I galaxy NGC 4151 has previously been suggested as a potential neutrino source (*55*, *56*, *57*). Depending on the luminosity function and cosmological evolution, the contribution from many faint sources at large distances (redshift $z \gtrsim 1$) could be large (*58*, *59*).

We cannot characterize the underlying source population with so few known point sources. However, our observation of neutrino emission from NGC 1068 can place constraints on the density ρ of AGNs with similar or greater neutrino luminosity in the local Universe, independent of the precise emission process or processes. If there is one source within a spherical volume of radius 14.4 Mpc (*37*), the distance to NGC 1068, then $\rho \lesssim 10^{-4}\ \mathrm{Mpc^{-3}}$. This density estimate relies on the observation of a single source, which may or may not be representative of the population, so this is an upper limit. Simulations of populations with various luminosity functions (*60*) have an uncertainty of more than an order of magnitude. Nevertheless, given the differences in spectrum and distance between NGC 1068 and TXS 0506+056, which is ~100 times farther away, we suggest that there are at least two populations of neutrino sources, which could differ in both density and luminosity by orders of magnitude.

We have observed evidence for neutrino emission from the active galaxy NGC 1068 at the 4.2σ level of significance, which we interpret as a signature of hadronic particle acceleration. The observation is consistent with phenomenological models (*52*, *53*) that predicted neutrino emission and absorption of gamma-ray photons in this source. Like the blazar TXS 0506+056 (*21*), the active galaxy NGC 1068 is a point source of high-energy neutrinos.

REFERENCES AND NOTES

1. J. Abraham *et al*., *Nucl. Instrum. Methods Phys. Res. A* **523**, 50–95 (2004).
2. The Pierre Auger Collaboration, *Nucl. Instrum. Methods Phys. Res. A* **798**, 172–213 (2015).
3. T. Abu-Zayyad *et al*., *Nucl. Instrum. Methods Phys. Res. A* **689**, 87–97 (2012).
4. S. R. Kelner, F. A. Aharonian, V. V. Bugayov, *Phys. Rev. D* **74**, 034018 (2006).
5. S. R. Kelner, F. A. Aharonian, *Phys. Rev. D* **78**, 034013 (2008).
6. A. De Angelis, G. Galanti, M. Roncadelli, *Mon. Not. R. Astron. Soc.* **432**, 3245–3249 (2013).
7. P. Padovani *et al*., *Astron. Astrophys. Rev.* **25**, 2 (2017).
8. C. K. Seyfert, *Astrophys. J.* **97**, 28 (1943).
9. R. Antonucci, *Annu. Rev. Astron. Astrophys.* **31**, 473–521 (1993).
10. C. M. Urry, P. Padovani, *Publ. Astron. Soc. Pac.* **107**, 803 (1995).
11. D. Eichler, *Astrophys. J.* **232**, 106 (1979).
12. V. S. Berezinsky, V. L. Ginzburg, *Mon. Not. R. Astron. Soc.* **194**, 3–14 (1981).
13. K. Mannheim, P. L. Biermann, *Astron. Astrophys.* **221**, 211–220 (1989).
14. F. Halzen, E. Zas, *Astrophys. J.* **488**, 669–674 (1997).
15. M. G. Aartsen *et al*., *J. Instrum.* **12**, P03012 (2017).
16. IceCube Collaboration, *Science* **342**, 1242856 (2013).
17. M. G. Aartsen *et al*., *Phys. Rev. Lett.* **125**, 121104 (2020).
18. R. Abbasi *et al*., *Phys. Rev. D* **104**, 022002 (2021).
19. M. G. Aartsen *et al*., *Astropart. Phys.* **92**, 30–41 (2017).
20. IceCube Collaboration *et al*., *Science* **361**, eaat1378 (2018).
21. IceCube Collaboration, *Science* **361**, 147–151 (2018).
22. P. Padovani, F. Oikonomou, M. Petropoulou, P. Giommi, E. Resconi, *Mon. Not. R. Astron. Soc.* **484**, L104–L108 (2019).
23. M. G. Aartsen *et al*., *Phys. Rev. Lett.* **124**, 051103 (2020).
24. M. G. Aartsen *et al*., *Eur. Phys. J. C* **79**, 234 (2019).
25. M. G. Aartsen *et al*., *Astrophys. J.* **833**, 3 (2016).
26. Materials and methods are available as supplementary materials.
27. J. Ahrens *et al*., *Nucl. Instrum. Methods Phys. Res. A* **524**, 169–194 (2004).
28. R. Abbasi *et al*., *J. Instrum.* **16**, P08034 (2021).
29. R. Abbasi *et al*., *Astropart. Phys.* **34**, 48–58 (2010).
30. T. K. Gaisser, R. Engel, E. Resconi, *Cosmic Rays and Particle Physics: Second Edition* (Cambridge Univ. Press, 2016).
31. M. Aartsen *et al*., *Astrophys. J.* **835**, 151 (2017).
32. S. Abdollahi *et al*., *Astrophys. J. Suppl. Ser.* **247**, 33 (2020).
33. S. P. Wakely, D. Horan, *International Cosmic Ray Conference*, vol. 3 of *International Cosmic Ray Conference* (2008), pp. 1341–1344.
34. P. Padovani *et al*., *Mon. Not. R. Astron. Soc.* **480**, 192–203 (2018).
35. M. Bustamante, J. F. Beacom, W. Winter, *Phys. Rev. Lett.* **115**, 161302 (2015).
36. C. A. Argüelles, T. Katori, J. Salvado, *Phys. Rev. Lett.* **115**, 161303 (2015).
37. J. Bland-Hawthorn *et al*., *Astrophys. Space Sci.* **248**, 9–19 (1997).
38. B. F. Madore, in *27th Rencontres de Moriond: Physics of Nearby Galaxies: Nature or Nurture?*, T. X. Thuan, J. Tran Thanh Van, C. Balkoski, Eds. (Ed. Frontieres, 1992), pp. 25–28.
39. Gravity Collaboration, O. Pfuhl *et al*., *Astron. Astrophys.* **634**, A1 (2020).
40. M. Ajello *et al*., *Astrophys. J.* **892**, 105 (2020).
41. S. Abdollahi *et al*., *Astrophys. J. Suppl. Ser.* **247**, 33 (2020).
42. V. A. Acciari *et al*., *Astrophys. J.* **883**, 135 (2019).
43. C. Ricci *et al*., *Astrophys. J. Lett.* **815**, L13 (2015).
44. A. Marinucci *et al*., *Mon. Not. R. Astron. Soc.* **456**, L94–L98 (2016).
45. A. Zaino *et al*., *Mon. Not. R. Astron. Soc.* **492**, 3872–3884 (2020).
46. A. B. Romeo, K. Fathi, *Mon. Not. R. Astron. Soc.* **460**, 2360–2367 (2016).
47. B. Eichmann, J. B. Tjus, *Astrophys. J.* **821**, 87 (2016).
48. G. Cecil, J. Bland, R. B. Tully, *Astrophys. J.* **355**, 70 (1990).
49. R. Silberberg, M. M. Shapiro, *Neutrinos as a Probe for the Nature of and Processes in Active Galactic Nuclei*, vol. 10 of *16th International Cosmic Ray Conference*, S. Miyake, N. G. Kaigi, N. B. Gakkai, Eds. (Institute for Cosmic Ray Research, 1979), p. 357.
50. T. M. Yoast-Hull, J. S. Gallagher III, E. G. Zweibel, J. E. Everett, *Astrophys. J.* **780**, 137 (2014).
51. A. Lamastra *et al*., *Astron. Astrophys.* **596**, A68 (2016).
52. Y. Inoue, D. Khangulyan, A. Doi, *Astrophys. J. Lett.* **891**, L33 (2020).
53. K. Murase, S. S. Kimura, P. Mészáros, *Phys. Rev. Lett.* **125**, 011101 (2020).
54. R. Silberberg, M. M. Shapiro, in *Composition and Origin of Cosmic Rays*, M. M. Shapiro, Ed., vol. 107 of *NATO Advanced Study Institute (ASI) Series C* (Springer, 1983), pp. 231–244.
55. Y. Inoue, D. Khangulyan, S. Inoue, A. Doi, *Astrophys. J.* **880**, 40 (2019).
56. F. W. Stecker, C. Done, M. H. Salamon, P. Sommers, *Phys. Rev. Lett.* **66**, 2697–2700 (1991).
57. R. Silberberg, M. M. Shapiro, C. H. Starr, in *Particle Astrophysics and Cosmology*, M. M. Shapiro, R. Silberberg, J. P. Wefel, Eds., vol. 394 of *NATO Advanced Study Institute (ASI) Series C* (Springer, 1993), p. 53.
58. K. Murase, E. Waxman, *Phys. Rev. D* **94**, 103006 (2016).

59. F. Capel, D. J. Mortlock, C. Finley, *Phys. Rev. D* **101**, 123017 (2020).
60. C. F. Tung *et al.*, *J. Open Source Softw.* **6**, 3194 (2021).
61. G. Paturel *et al.*, *Astron. Astrophys.* **412**, 45–55 (2003).

ACKNOWLEDGMENTS

We dedicate this work to our recently deceased colleagues, Thomas K. Gaisser and P. Buford Price. The IceCube Collaboration acknowledges contributions to this manuscript from H. Niederhausen and T. Glauch. **Funding:** The authors gratefully acknowledge support from the following agencies and institutions. USA: US National Science Foundation–Office of Polar Programs, US National Science Foundation–Physics Division, US National Science Foundation–EPSCoR, Wisconsin Alumni Research Foundation, Center for High Throughput Computing (CHTC) at the University of Wisconsin–Madison, Open Science Grid (OSG), Extreme Science and Engineering Discovery Environment (XSEDE), the Frontera computing project at the Texas Advanced Computing Center, US Department of Energy–National Energy Research Scientific Computing Center, the Particle Astrophysics research computing center at the University of Maryland, Institute for Cyber-Enabled Research at Michigan State University, and the astroparticle physics computational facility at Marquette University. Belgium: Funds for Scientific Research (FRS-FNRS and FWO), FWO Odysseus and Big Science programs, and Belgian Federal Science Policy Office (Belspo). Germany: Bundesministerium für Bildung und Forschung (BMBF), Deutsche Forschungsgemeinschaft (DFG), Helmholtz Alliance for Astroparticle Physics (HAP), Initiative and Networking Fund of the Helmholtz Association, Deutsches Elektronen Synchrotron (DESY), and the High Performance Computing cluster of the RWTH Aachen. Sweden: Swedish Research Council, Swedish Polar Research Secretariat, Swedish National Infrastructure for Computing (SNIC), and Knut and Alice Wallenberg Foundation. Australia: Australian Research Council. Canada: Natural Sciences and Engineering Research Council of Canada, Calcul Québec, Compute Ontario, Canada Foundation for Innovation, WestGrid, and Compute Canada. Denmark: Villum Fonden and Carlsberg Foundation. New Zealand: Marsden Fund. Japan: Japan Society for Promotion of Science (JSPS) and Institute for Global Prominent Research (IGPR) of Chiba University. Korea: National Research Foundation of Korea (NRF). Switzerland: Swiss National Science Foundation (SNSF). UK: the Department of Physics of the University of Oxford. **Author contributions:** The IceCube Collaboration designed, constructed, and now operates the IceCube Neutrino Observatory. Data processing and calibration, Monte Carlo simulations of the detector and of theoretical models, and data analyses were performed by a large number of collaboration members, who also discussed and approved the scientific results presented here. The manuscript was reviewed by the entire collaboration before publication, and all authors approved the final version. Contributions listed below are in the following areas: (a) Conceptualization, formal analysis, and methodology; (b) Data curation and resources; (c) Funding acquisition and project administration; (d) Investigation; (e) Software; (f) Supervision; (g) Validation; (h) Writing – original draft and visualization; and (i) Writing – review and editing. Specific contributions are as follows: R. Abbasi (d), M. Ackermann (d), J. Adams (c, d), J. A. Aguilar (c, d), M. Ahlers (d), M. Ahrens (d), J. M. Alameddine (d, e), A. A. Alves Jr. (d), N. M. Amin (d), K. Andeen (b, c, d), G. Anton (c, d), C. Argüelles (b, d), Y. Ashida (d), S. Axani (b, d, e), X. Bai (b, c, e), A. Balagopal V. (d), B. Bastian (d), V. Basu (d), S. Baur (d), J. J. Beatty (d), K.-H. Becker (d), J. Becker Tjus (c), C. Bellenghi (a, b, e, g, h, i), S. BenZvi (b, c, d, i), D. Berley (c), E. Bernardini (d), D. Bindig (d), E. Blaufuss (b, c, d, e, i), S. Blot (d, i), F. Bontempo (d), J. Borowka (g, i), S. Böser (c, d), O. Botner (a, b, c, d, i), J. Böttcher (b, e, g, i), E. Bourbeau (d), F. Bradascio (d), J. Braun (b, d, e), J. Brostean-Kaiser (d), S. Browne (d), A. Burgman (d), R. T. Burley (d), R. S. Busse (d), M. A. Campana (d), E. G. Carnie-Bronca (d), C. Chen (d), D. Chirkin (b, d, e), B. A. Clark (b, d, e, i), L. Classen (d), A. Coleman (b, d, e), G. H. Collin (b, d, e), J. M. Conrad (b, c, d), P. Coppin (d), P. Correa (d), R. Cross (b, d), C. Dappen (b, g, i), P. Dave (d), C. De Clercq (d), J. J. DeLaunay (d), D. Delgado López (d), H. Dembinski (b, d, e), K. Deoskar (d), A. Desai (d), P. Desiati (b, c, d, e), K. D. de Vries (d), G. de Wasseige (d), T. DeYoung (b, c, d), A. Diaz (b, d, e), J. C. Díaz-Vélez (b, d, e), M. Dittmer (d), H. Dujmovic (d), M. A. DuVernois (b, d), E. Dvorak (b, e), T. Ehrhardt (b, d), P. Eller (b, e, i), R. Engel (c), H. Erpenbeck (b, g, i), J. Evans (d), P. A. Evenson (b, d), K. L. Fan (d, e), A. Fedynitch (d), N. Feigl (d), S. Fiedlschuster (d), C. Finley (a, c, d, i), L. Fischer (d), A. Franckowiak (d), E. Friedman (b, d, e), A. Fritz (d), P. Fürst (b, e, g, i), T. K. Gaisser (a, b, c, d), E. Ganster (b, e, g, i), A. Garcia (d), S. Garrappa (d), L. Gerhardt (d), C. Glaser (c, d), T. Glauch (a, b, c, d, e, f, g, h, i), T. Glüsenkamp (d), A. Goldschmidt (d), J. G. Gonzalez (b, c, d, e), D. Grant (c, d, i), S. Griswold (b, d), C. Günther (g, i), P. Gutjahr (d), C. Haack (a, b, e, f, g, h), A. Hallgren (a, b, c, d), R. Halliday (b, d), L. Halve (g, i), F. Halzen (a, b, c, d, e, h, i), M. Ha Minh (e, i), K. Hanson (b, c, d, e), J. Hardin (b, d, e), A. A. Harnisch (d, e), A. Haungs (c, d), K. Helbing (d), F. Henningsen (e, i), S. Hickford (d), C. Hill (d), G. C. Hill (a, b, c, d), K. D. Hoffman (c, d), R. Hoffmann (d), K. Hoshina (b, d, e), M. Huber (a, e), T. Huber (d), K. Hultqvist (c, d), M. Hünnefeld (d), R. Hussain (b, d, e), K. Hymon (d), S. In (d), N. Iovine (d), A. Ishihara (d, e), M. Jansson (d), M. Jeong (d), M. Jin (d), B. J. P. Jones (b, c, d, e), D. Kang (d), W. Kang (d), X. Kang (d), A. Kappes (c, d), D. Kappesser (d), L. Kardum (d), T. Karg (d), M. Karl (a, e, i), A. Karle (a, b, c, d, e, i), U. Katz (c, d), M. Kauer (b, d, e), M. Kellermann (g, i), J. L. Kelley (b, c, d, e), A. Kheirandish (d, i), K. Kin (d), T. Kintscher (d), S. R. Klein (c, d), R. Koirala (d), H. Kolanoski (d), T. Kontrimas (a, b, e, g, h, i), L. Köpke (a, c, d), C. Kopper (b, c, e, f, i), D. J. Koskinen (d), P. Koundal (d), M. Kovacevich (d), M. Kowalski (d), T. Kozynets (d), N. Kurahashi (b, c, d, e), N. Lad (d), C. Lagunas Gualda (d), M. J. Larson (b, c, d, e), F. Lauber (d), J. P. Lazar (b, d), K. Leonard (b, d, e), A. Leszczyńska (d), Q. R. Liu (b, d, e), E. Lohfink (d), C. J. Lozano Mariscal (d), L. Lu (b, d, e), F. Lucarelli (a, b), A. Ludwig (e), W. Luszczak (b, d, e), Y. Lyu (d), W. Y. Ma (d), J. Madsen (c, d, e), Y. Makino (b, d), S. Mancina (b, d, e), I. C. Mariş (d), I. Martinez-Soler (d), K. Mase (e), F. McNally (d), J. V. Mead (d), K. Meagher (b, d, e), S. Mechbal (d), A. Medina (d, e), M. Meier (d), S. Meighen-Berger (e, i), J. Micallef (d, e), D. Mockler (d), T. Montaruli (a, b, c, d, e, f, i), R. Morse (a, b, c, d, e), M. Moulai (b, d, e), R. Naab (d), R. Nagai (d), U. Naumann (d), J. Necker (d), H. Niederhausen (a, b, c, d, e, f, g, h, i), M. U. Nisa (d), S. C. Nowicki (d), A. Obertacke Pollmann (d), M. Oehler (d), A. Olivas (b, c, d, e), E. O'Sullivan (c, d), H. Pandya (d), N. Park (a, d, i), G. K. Parker (b, d, e), E. N. Paudel (d), L. Paul (b, d), C. Pérez de los Heros (a, b, c, d), L. Peters (b, g, i), S. Philippen (a, b, e, g, i), S. Pieper (d), A. Pizzuto (b, c, d, e), M. Plum (b, d), Y. Popovych (d), M. Prado Rodriguez (b, c, d, e), C. Raab (d), J. Rack-Helleis (d), K. Rawlins (b, c, d, e), A. Rehman (d), R. Reimann (a, b, e, g, i), G. Renzi (d), E. Resconi (a, b, c, f, h), S. Reusch (d), W. Rhode (c, d), B. Riedel (b, c, d, e), E. J. Roberts (d), S. Robertson (d), G. Roellinghoff (d), M. Rongen (c, d), C. Rott (d), T. Ruhe (c, d), D. Ryckbosch (c, d), D. Rysewyk Cantu (d), I. Safa (b, d, e), J. Saffer (d), S. E. Sanchez Herrera (d), A. Sandrock (d, e), J. Sandroos (d), M. Santander (c, d, i), S. Sarkar (Oxford U.) (d), K. Satalecka (d), M. Schaufel (g, i), H. Schieler (d), S. Schindler (d), T. Schmidt (b, d, e), A. Schneider (b, d, e), J. Schneider (d), F. G. Schröder (b, c, d), L. Schumacher (a, b, e, f, i), G. Schwefer (g, i), S. Sclafani (b, d), D. Seckel (a, b, c, d), S. Seunarine (d), A. Sharma (d), S. Shefali (d), M. Silva (b, d, e), B. Skrzypek (d), B. Smithers (b, d, e), R. Snihur (b, d, e), J. Soedingrekso (d, e), D. Soldin (b, c, d, e), C. Spannfellner (i), G. M. Spiczak (d), C. Spiering (d), J. Stachurska (d), M. Stamatikos (d), T. Stanev (a, d), R. Stein (d), J. Stettner (a, b, e, g, i), A. Steuer (d), R. Stokstad (a, c, d), T. Stürwald (d), T. Stuttard (b, e), G. W. Sullivan (b, c, d), I. Taboada (c, d, i), S. Tilav (a, b, c, d, e, g), F. Tischbein (g, i), K. Tollefson (d), C. Tönnis (d), S. Toscano (d), D. Tosi (b, d, e), A. Trettin (d), M. Tselengidou (d), C. F. Tung (d), A. Turcati (a, e), R. Turcotte (d), J. P. Twagirayezu (d), M. A. Unland Elorrieta (d), N. Valtonen-Mattila (b, d), J. Vandenbroucke (b, c, d, e, h, i), N. Van Eijndhoven (c, d), D. Vannerom (d, e), J. van Santen (d), C. Walck (d), C. Weaver (b, d, e), P. Weigel (d, e), A. Weindl (b), J. Weldert (d), C. Wendt (b, c, d, e), J. Werthebach (d), M. Weyrauch (d), N. Whitehorn (c, d, e, i), C. H. Wiebusch (a, c, f, g, i), D. R. Williams (c, d), M. Wolf (a, b, c, d, e, f, g, h), G. Wrede (d), J. Wulff (e, g), S. Yoshida (d, e), S. Yu (d), T. Yuan (b, c, d, e), and P. Zhelnin (d). **Competing interests:** There are no competing interests to declare. **Data and materials availability:** Numerical results for all 110 sources are listed in table S3. All data and software used in this paper, including the event list and analysis scripts, are available from the IceCube data archive at https://icecube.wisc.edu/science/data/neutrino-emission-from-ngc-1068. **License information:** Copyright © 2022 the authors, some rights reserved; exclusive licensee American Association for the Advancement of Science. No claim to original US government works. https://www.science.org/about/science-licenses-journal-article-reuse

SUPPLEMENTARY MATERIALS

science.org/doi/10.1126/science.abg3395
Materials and Methods
Supplementary Text
Figs. S1 to S30
Tables S1 to S4
IceCube Collaboration Author List
References (*62*–*98*)

Submitted 19 November 2021; accepted 22 September 2022
10.1126/science.abg3395

PLANT SCIENCE

The control of carpel determinacy pathway leads to sex determination in cucurbits

Siqi Zhang[1]†, Feng-Quan Tan[1]†, Ching-Hui Chung[1], Filip Slavkovic[1], Ravi Sureshbhai Devani[1], Christelle Troadec[1], Fabien Marcel[1], Halima Morin[1], Céline Camps[1], Maria Victoria Gomez Roldan[1], Moussa Benhamed[1], Catherine Dogimont[2], Adnane Boualem[1], Abdelhafid Bendahmane[1]*

Male and female unisexual flowers evolved from hermaphroditic ancestors, and control of flower sex is useful for plant breeding. We isolated a female-to-male sex transition mutant in melon and identified the causal gene as the carpel identity gene *CRABS CLAW (CRC)*. We show that the master regulator of sex determination in cucurbits, the transcription factor *WIP1* whose expression orchestrates male flower development, recruits the corepressor TOPLESS to the *CRC* promoter to suppress its expression through histone deacetylation. Impairing TOPLESS-WIP1 physical interaction leads to *CRC* expression, carpel determination, and consequently the expression of the stamina inhibitor, the aminocyclopropane-1-carboxylic acid synthase 7 (*CmACS7*), leading to female flower development. Our findings suggest that sex genes evolved to interfere with flower meristematic function, leading to unisexual flower development.

To increase genetic diversity and fitness of offspring, flowering plants have developed several systems to prevent self-fertilization. As a result of sex determination processes, unisexual male and female flowers may develop on the same plant (monoecy) or on separate individuals (dioecy). The evolutionary pathways from hermaphroditism to unisexuality have been associated with the emergence of sex determination genes (*1*, *2*).

[1]Université Paris-Saclay, CNRS, INRAE, Université Evry, Institute of Plant Sciences Paris-Saclay (IPS2); 91190 Gif sur Yvette, France. [2]INRAE, Génétique et Amélioration des Fruits et Légumes (GAFL), 84143 Montfavet, France.
***Corresponding author. Email: abdelhafid.bendahmane@inrae.fr**
†These authors contributed equally to this work.

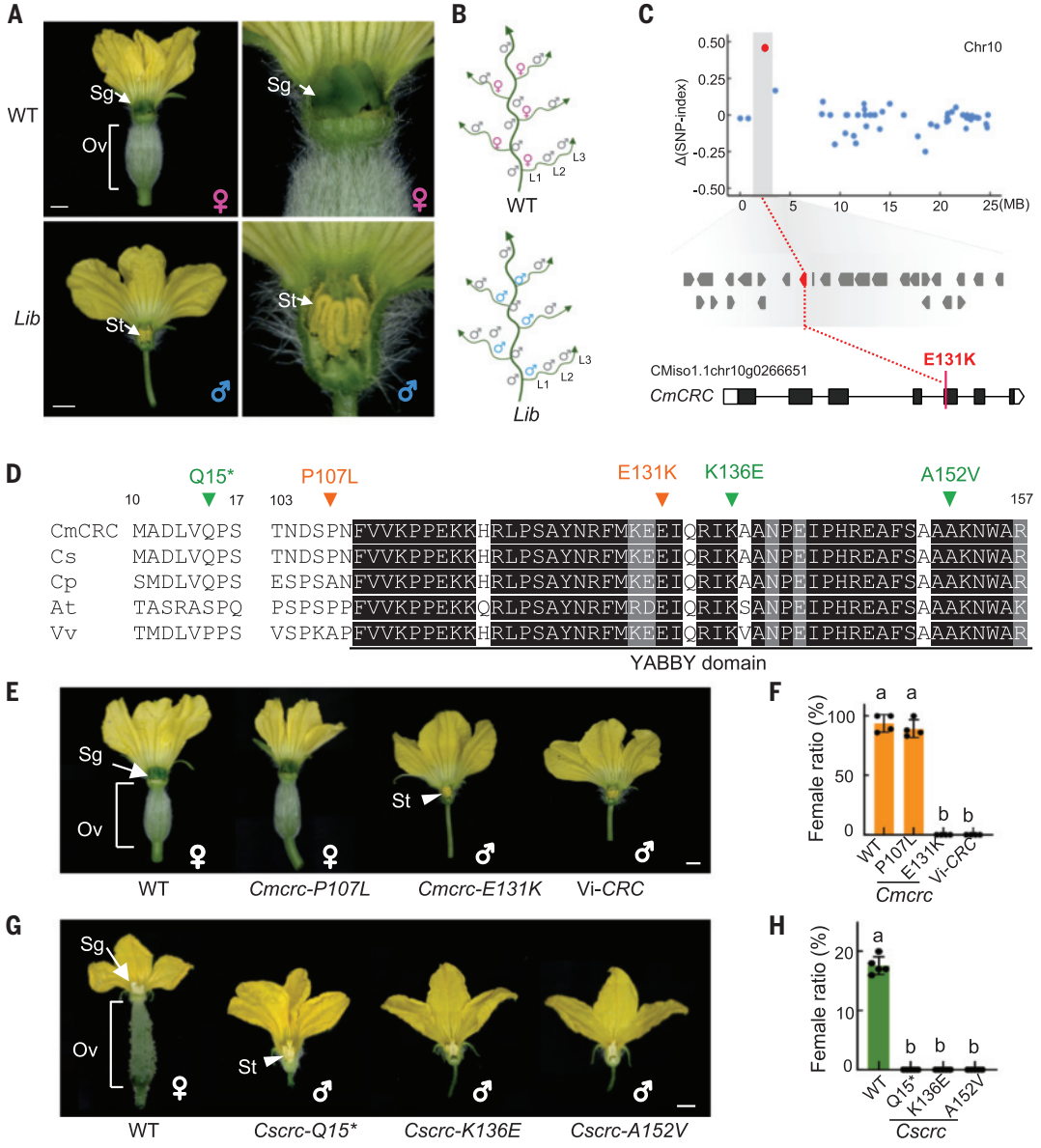


Fig. 1. Characterization of *Lib* mutants. (**A**) Sexual phenotype of monoecious melon (WT) and *Little Boy* (*Lib*) androecious mutant. Ov, ovary; Sg, stigma; St, stamen. (**B**) Schematic of sexual morphs. Female flowers on first nodes (L1) of lateral branches became male flowers in *Lib*. (**C**) Cloning of the *Lib* locus. ΔSNP index between monoecious and androecious bulks on chromosome 10. The highest ΔSNP index corresponds to an E-to-K missense mutation in the gene *CRC*. (**D**) Alignments of CmCRC with homologous proteins. Cs, *Cucumis sativus*; Cp, *Cucurbita pepo*; At, *Arabidopsis thaliana*; Vv, *Vitis vinifera*. Induced mutations in melon (orange) and cucumber (green) are shown. (**E** and **G**) Sexual phenotype of monoecious plant (WT), *crc* mutants and VIGS-*CmCRC* (Vi-*CRC*) in melon (E) and cucumber (G). (**F** and **H**) Statistical analysis of female flower ratio [females/(females + males)], in percent, of L1 nodes of lateral branches in melon (F) and nodes 1 to 20 on main stem in cucumber (H). Bars represent means ± SD (n = 4 to 5). Different letters indicate significant differences (P < 0.05, one-way ANOVA with Tukey's post hoc test). Scale bars, 5 mm in (A), (E), and (G).

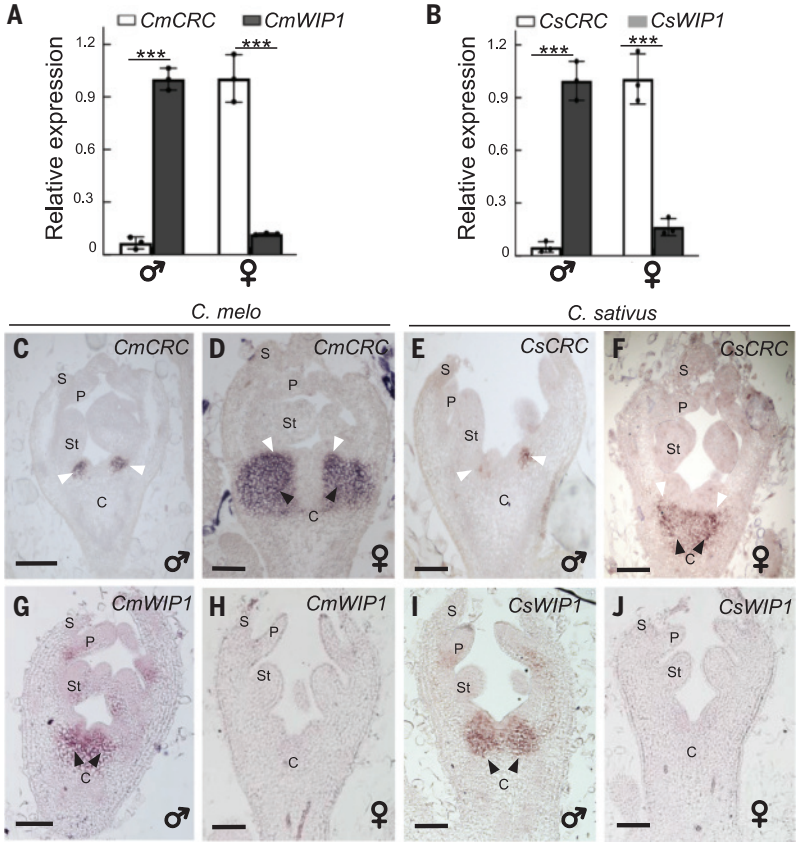
A typical hermaphroditic flower is built in four concentric whorls: the calyx, the corolla, the androecium, and the gynoecium. Following floral transition, these organs are produced from a pool of stem cells within the floral meristem. A signaling pathway involving the homeodomain protein WUSCHEL (WUS) manages the maintenance of stem cell activity in the floral meristem (*3*–*5*). Once floral organ primordia are formed, the homeotic gene *AGAMOUS* (*AG*) orchestrates *WUS* repression, leading to flower meristem termination (*6*). This process involves the expression of *KNUCKLES* and *CRABS CLAW* (*CRC*), downstream genes that act synergistically through parallel pathways to repress *WUS* expression (*7*, *8*). *CRC*-control of floral meristem termination involves the transcription of *YUCCA* auxin biosynthetic genes and transcriptional repression of *TORNADO2* (*TRN2*), a plasma membrane protein that modulates auxin homeostasis (*9*, *10*).

In this study, we investigated how sex determination genes lead to unisexual flower development in *Cucurbitaceae*, a large plant family containing species that display mostly unisexual flowers (*11*). In *Cucumis melo* (melon) most of the flowers are male, and female flowers develop only on the first nodes of branches. At early developmental stages, flowers are bisexual; sex determination then occurs through arrest of either the stamen or the carpel primordia, resulting in unisexual flowers. This sexual organ arrest is genetically determined by the interactions of the *andromonoecious* (*M*), *androecious* (*A*), and *gynoecious* (*G*) genes, which encode for *CmACS-7*, *CmACS11*, and *CmWIP1*, respectively (*12*–*14*). Interactions between the *M*, *A*, and *G* genes define the monoecy sex determination pathway in Cucurbits (*13*). We screened for sex transition mutants and analyzed the causative mutations in relation to the monoecy pathway in cucumber and melon.

Results

Little Boy sex transition mutant encodes for Crabs Claw

We conducted a forward genetic screen and uncovered a mutant for which female flowers develop into males (Fig. 1, A and B, and fig. S1). We named the gene *Little Boy* (*Lib*) and mapped the mutation to a single gene coding for a homolog of *CRC* (Fig. 1C and fig. S2), a transcription factor of the *YABBY* gene family controlling carpel and nectary development as well as flower meristem termination (*9*, *15*). We identified a nonsynonymous E131K mutation in the highly conserved YABBY domain (Fig. 1, C and D). Because there is no efficient



K

Genotype	Observed phenotype	Plant showing phenotype/ total	Flower sexuality
ACS11/WIP1/ACS7/CRC	monoecious	10/10	♀♂
acs11/WIP1/ACS7/CRC	androecious	10/10	♂
ACS11/wip1/ACS7/CRC	gynoecious	10/10	♀
ACS11/WIP1/acs7/CRC	andromonoecious	10/10	♂♀♂
ACS11/WIP1/ACS7/crc	androecious	10/10	♂
ACS11/wip1/acs7/CRC	hermaphrodite	5/5	♂♀
ACS11/wip1/ACS7/crc	androecious	5/5	♂

Fig. 2. *CRC* expression in unisexual flowers. (**A** and **B**) qRT-PCR analysis of *CRC* and *WIP1*. Bars represent means ± SD (n = 3). ***P < 0.001 (Student's t test). (**C** to **F**) *CRC in situ* expression. In male and female flowers, *CRC* transcripts are detected in cells between the stamen and carpel primordia where nectary primordia arise at stage 8 (white arrows). Black arrows denote *CRC* transcripts detected in carpel primordia of female flowers. (**G** to **J**) *WIP1* in situ expression. Black arrows denote *CmWIP1* and *CsWIP1* transcripts detected in carpel primordia of male flowers. No transcripts were detected in female flowers. C, carpel primordia; St, stamen primordia; P, petal; S, sepal. (**K**) Sexual morphs of melon plants across a combination of alleles at different sex loci. Flower buds at stage 6, from monoecious melon (Cm) and cucumber (Cs) were used in (A) and (B) as well as (C) to (J). Scale bars, 100 μm.

transformation protocol in cucurbits, we first used virus-induced gene silencing (VIGS) to knock down the accumulation of *Lib* transcript in monoecious plants and observed a complete female to male sexual transition in vines normally harboring female flowers (Fig. 1, E and F, and table S1). This sexual transition correlated with the silencing of the *Lib* transcript (fig. S3). To further validate the role of *Lib* in unisexual female flower development, we used TILLING (Targeting Induced Local Lesions IN Genomes) collections from monoecious melon and cucumber and screened for mutations in *Lib*. Of the induced mutations identified (35 in total), we observed one nonsense (Q15*) and three missense (E131K, K136E, and A152V) mutations altering highly conserved amino acid positions in the conserved YABBY domain (Fig. 1D and fig S4). We backcrossed the mutant lines harboring the missense and nonsense mutations to the wild type and followed the segregation of the mutations with the phenotypes. As predicted, plants homozygous for E131K, K136E, A152V, or Q15* mutations were androecious—female flowers transformed into male flowers (Fig. 1, E to H, and fig. S5). Consistent with this, silent conserved mutations had no effect on the sexual morph of the plant (fig. S4 and table S2). Based on the high-resolution genetic map, the VIGS study, and the TILLING mutants, we concluded that the *Lib* gene encodes for *CRC* in melon and cucumber.

WIP1 binds to the promoter of CRC to repress its expression

The gynoecy gene *WIP1* is a master regulator orchestrating sex determination in cucurbits. Expression of *WIP1* inhibits carpel primordia and leads to male flowers whereas its non-expression releases the carpel from this inhibition and leads to female flowers (*14*). In unisexual flowers of monoecious plants, the inappropriate sexual organs stop developing at stage 6, shortly after the elaboration of carpel and stamen primordia (fig. S6). Quantitative real-time PCR (qRT-PCR) analysis in monoecious melon and cucumber demonstrates that *CRC* is highly expressed in female flower buds at stage 6 and is weak in buds determined to develop into male flowers (Fig. 2, A and B). Hence, *WIP1* function is antagonistic to and may be the repressor of *CRC* function in male flowers. We examined the spatial expression patterns of *CRC* and *WIP1* using in situ hybridization. *WIP1* and *CRC* showed antagonistic expression patterns in carpel primordia (Fig. 2, C to J). *CRC* mRNA was detected only in carpel primordia of female flower buds at stage 6 and onward (Fig. 2, D and F). Independently from its carpel functions, CRC orchestrates nectary development between stamen and carpel primordia. Consistent with this, *CRC* expression was not altered in nectary precursor cells (Fig. 2, C to F, and fig. S7). To provide genetic support for the functional interaction between *CRC* and *WIP1*, we generated single and double mutants and analyzed the expression of the two genes. We found that *CRC* is expressed when WIP1 function is abolished and *Cmcrc/Cmwip1* double mutants are androecious (Fig. 2K and fig. S8). Further, in gynoecious plants VIGS suppression of *CRC* leads to male flower development (fig. S9 and table S1). Together these data indicate that *WIP1* acts upstream and is epistatic to *CRC* in the sex determination pathway.

To investigate whether WIP1 is a direct repressor of *CRC* expression, we mapped genome-wide WIP1 DNA binding using ampDAPseq (fig. S10). WIP1-binding sites were mostly identified in promoter and intergenic regions (data S1); a consensus motif (Fig. 3A) computed from these sequences corresponds to the binding site, as previously characterized by Chromatin Immunoprecipitation sequencing (ChIP-seq) and ampDAPseq for three *Arabidopsis* WIP proteins (*16*, *17*). In particular, we found that the

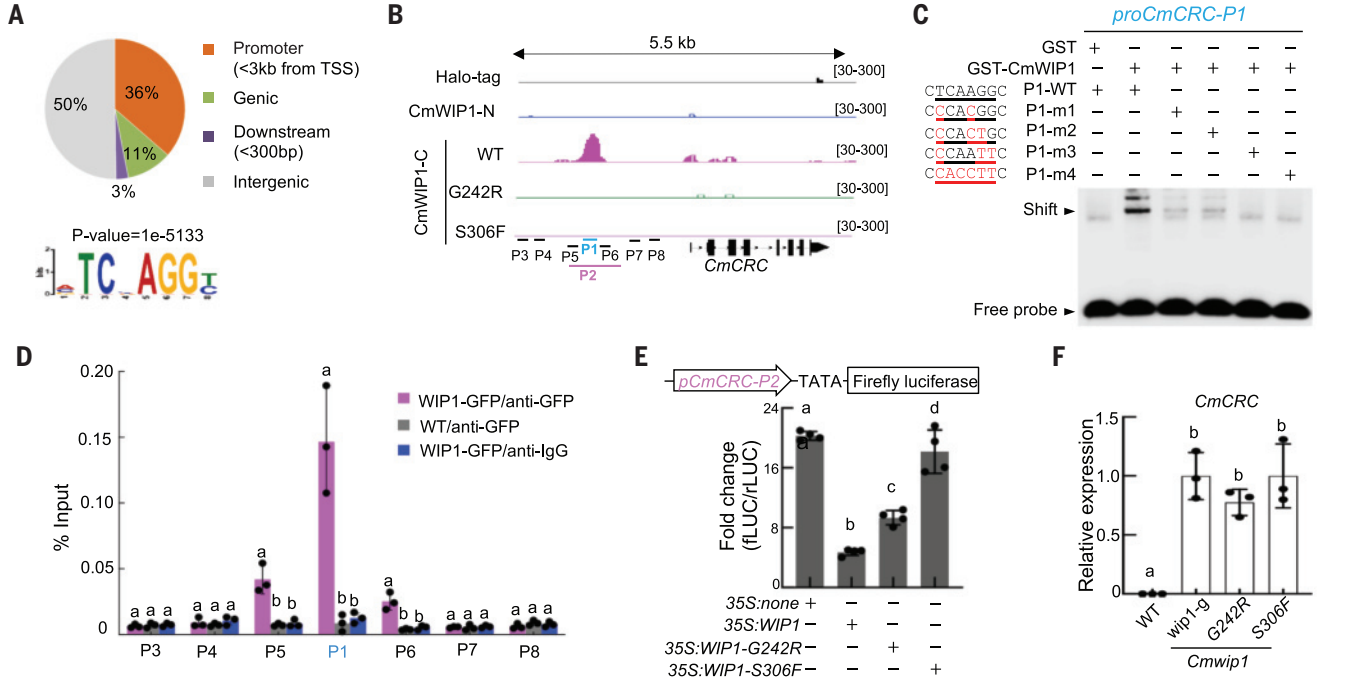


Fig. 3. CmWIP1 binds to the *CRC* promoter. (**A**) Distribution of CmWIP1 DAP-seq peaks and CmWIP1 binding motif. (**B**) CmWIP1 binding at the *CmCRC* locus. Halo-tag, negative control; -N, N terminus; -C, C terminus; P1 to P8, promoter sequences used in EMSA, ChIP, and promoter activity assays. G242R and S306F mutations in WIP1 DNA binding domain. (**C**) EMSA assay. A 5-μM GST or WIP1-GST protein and a 10-nM DNA probe were used. P1-m1 to P1-m4, mutant probes. GST, Glutathione S-transferase. (**D**) ChIP-qPCR assay in melon protoplast transformed with *35S:WIP1-GFP*. Results are expressed as a percentage of the INPUT fraction. Wild-type protoplasts and anti-IgG antibody were used as negative controls. (**E**) Promoter activity assays. Empty vector (*35S:none*), *35S:WIP1* or variants were cotransformed into melon protoplasts along with *pCmCRC-P2:fLUC*. Bars represent means ± SD (n = 4). (**F**) qRT-PCR analysis of *CmCRC*. Flower buds at stage 6 were used. *wip1-g*, a natural epigenetic mutant; G242R and S306F, TILLING mutants (*14*). In (D) to (F), bars represent mean ± SD (n = 3) and different letters denote significant differences (P < 0.05, one-way ANOVA with Tukey's post hoc test).

CmCRC promoter harbored the consensus CmWIP1 binding motif and was bound by CmWIP1 but not by its zinc-finger variants G242R and S306F (Fig. 3B). The identified motif was also conserved across monoecious *Cucurbitacea* species (fig. S11). To validate the binding of CmWIP1 to the *CmCRC* promoter, we used Electrophoretic Mobility Shift Assay (EMSA) and band shifts were obtained only when WT probes were incubated with the CmWIP1 protein (Fig. 3C and fig. S12). ChIP-qPCR analysis further validated the binding in vivo (Fig. 3D). We next tested the effect of the binding of CmWIP1 to the *CRC* promoter using a Luciferase reporter assay. We coexpressed *35S:WIP1* variants and *pCRC:LUC* reporter constructs in melon protoplasts. Expression of the reporter gene declined considerably in the samples cotransformed with *35S:WIP1* but less so in its variants harboring mutations within the DNA binding domain and in *pCRC:LUC* promoter mutant forms (Fig. 3E and fig. S12), suggesting that WIP1 indeed represses the transcription of *CRC* through binding to its promoter. Consistent with this, WIP1-mediated repression of *CRC* expression is released in gynoecious lines harboring CmWIP1-G242R or -S306F missense alleles (Fig. 3F), validating that WIP1 represses the transcription of *CRC* through direct binding to the *CRC* promoter.

WIP1 interacts with the corepressor TPL to repress CRC expression

To uncover the molecular mechanisms underlying WIP1-mediated transcriptional repression of *CRC*, we screened for WIP1 partners using the yeast two-hybrid system (Y2H). Sequencing and annotation of 125 positive clones revealed that 10 encode a melon protein with 97.8% amino acid identity to the *Arabidopsis* TPL protein, which we designated CmTPL (*18*). Less frequently, WIP1 also interacted with two other TPL-related proteins, TPR3 and TPR4 (fig. S13, A to D, and table S3). Consistent with this, we found *CmTPL* expressed five times more than *CmTPR3* and *CmTPR4* in both male and female flowers (fig. S13E). To further analyze the regions involved in the interaction, we tested constructs harboring different CmTPL and CmWIP1 domains. We found CmWIP1-TPL physical interactions involving the N-terminal domain of CmWIP1 and the LisH, CTLH, and CRA domains of TPL (fig. S13B). The *WIP* N-terminal domain harbors two conserved motifs, N1 and N2. N1 is a Leucine-rich motif and N2 fits with the canonical EAR motif (Fig. 4H). A model of the three-dimensional structure of WIP1 and TPL predicted that N1 and N2 motifs likely form a stem-loop structure recruited for the interaction with TPL (fig. S14). To test whether the predicted interaction involves N1 and/or N2 motifs we generated Alanine scanning mutants. We found that the single n1 and n2 mutant partially affected the interaction whereas the n1-n2 double mutant completely impaired the interaction (fig. S13C and table S4). This interaction was further verified by coimmunoprecipitation (Co-IP) assays using WIP-GFP and TPL-Flag constructs transiently expressed in melon protoplasts (Fig. 4, A and B). As in Y2H, the interactions were partial for the n1 and n2 mutants and completely absent in the n1 and -n2 double mutants. Next, we carried out a transient expression assay in melon protoplasts to examine the effect of WIP1-TPL interaction on *CRC* transcription. We found the p*CRC:LUC* reporter activity substantially recovered when melon protoplasts expressed n1 or n2 mutant forms of WIP1 (Fig. 4C), indicating that interference with WIP1-TPL interaction leads to *CRC* expression.

Mutations in WIP1-TPL interacting domains lead to expression of CRC and femaleness

To verify the biological relevance of WIP1-TPL interaction in *CRC* repression, we first silenced

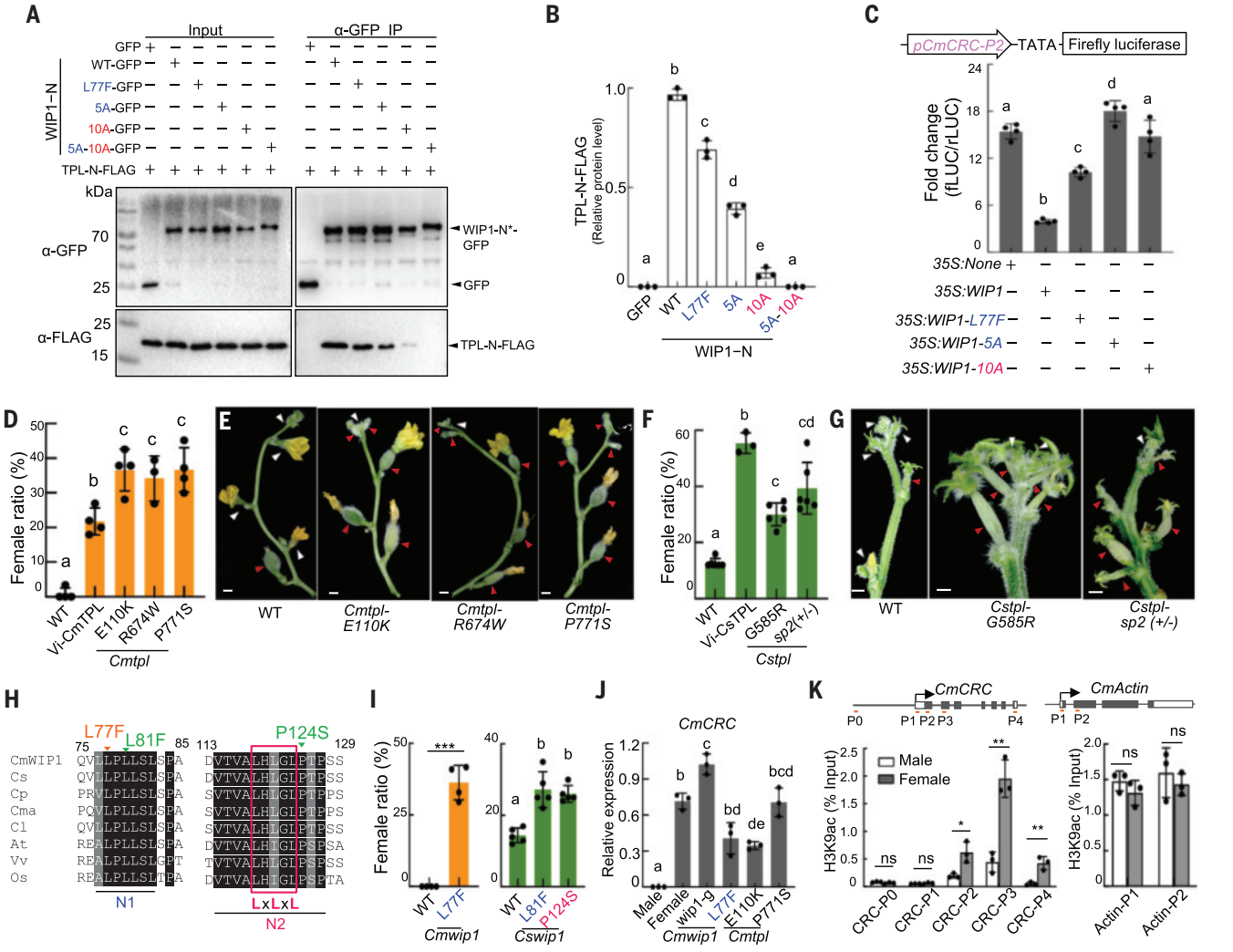


Fig. 4. WIP1 recruits Topless to repress *CRC*. (**A**) Co-IP assays. GFP-tagged WIP1–N or variants (asterisk) were cotransformed into melon protoplasts along with FLAG-tagged TPL-N. (**B**) Quantification of FLAG-tagged TPL-N from Co-IP assays in (A). (**C**) Promoter activity assay. Empty vector (*35S:none*), *35S:WIP1* or variants were cotransformed into melon protoplasts along with *pCmCRC-P2:fLUC*. Statistical analysis of female flower ratio in monoecious (WT), VIGS-*CmTPL* (Vi-*CmTPL*) and tpl mutants in melon (**D**) and cucumber (**F**). Flower phenotypes of tpl mutants in melon (**E**) and cucumber (**G**); white and red triangles denote male and female flowers, respectively; scale bars, 5 mm. (**H**) Sequence alignment of WIP1 and homologous proteins showing N1 and N2 motifs. Initials of species are indicated (fig. S4). LxLxL, EAR motif. Induced mutations in melon (orange) and cucumber (green) are shown. (**I**) The female ratio [females/(females + males)], in percent, of nodes 2 to 10 of lateral branches (melon) and nodes 1 to 20 of main stem (cucumber). qRT-PCR analysis of *CmCRC* (**J**) and ChIP-qPCR analysis of H3K9ac (**K**) at stage 6 flower buds. *CmACTIN1*, control. Bars represent means ± SD (n = 3 to 5); different letters denote significant differences ($P < 0.05$, one-way ANOVA with Tukey's post hoc test). *$P < 0.05$, **$P < 0.01$ (Student's t test).

the expression of TPL, TPR3, and TPR4. VIGS of TPR3 and TPR4 did not show any phenotype alteration (table S5). By contrast, TPL-silenced lines showed flowers ranging from partial feminization to complete male to female sex transition, both in melon and cucumber (Fig. 4, D and F, and fig. S15). This sexual transition was stronger in plants in which the VIGS vector targeted both *TPL* and *TPR3* (table S5). Consistent with the VIGS data, induced mutations in *TPR3* and *TPR4* did not show any alteration of either vegetative or flower development (table S6). By contrast, TPL loss-of-function mutants were unable to develop flowers (fig. S16). To circumvent the nonflowering phenotype, we phenotyped 10 missense mutants. We found the four mutations (E110K, G585R, R674W, and P771S)—all predicted to be deleterious—to lead to female flower development on vines determined to develop male flowers (Fig. 4, D to G). This sexual transition affected 30 to 40% of total male flowers, both in melon and cucumber. This sexual transition is likely caused by gene dosage as heterozygous *TPL* splicing mutants in cucumber showed enhanced femaleness (Fig. 4F).

The WIP1-TPL interaction implicates N1 and N2 motifs of WIP1 (fig. S13C and Fig. 4, A to C). To further characterize in planta their roles in sex determination, we screened for induced mutations in the two motifs. We identified three missense mutations—two in the N1 motif (L77F and L81F) and one in the N2 motif (P124S) (Fig. 4H). We observed for both n1 and n2 TILLING mutants the development of female features, such as an ovary with ovules, style, and stigma in flowers determined to be male (Fig. 4I and fig. S17). We next analyzed the expression of *CRC* in WIP1 n1 and n2 mutants. Consistent with the feminization of male flowers, *CRC* expression was derepressed (Fig. 4J). Because TPL recruits histone deacetylase to repress the expression of target genes, we analyzed the histone acetylation levels of *CRC* in male and female flowers. ChIP assays with anti-H3K9ac antibodies in both male and female flowers revealed a considerable decrease in H3K9ac in the core of the gene in male

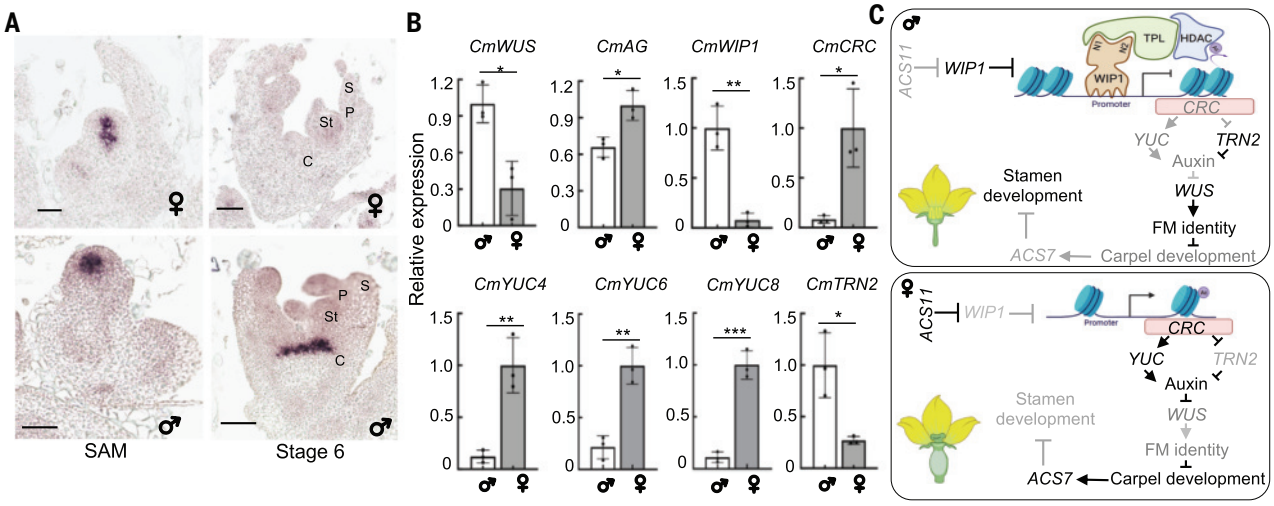


Fig. 5. *WIP1* delays floral stem cell termination. (**A**) *CmWUS* in situ expression in shoot apical meristem (SAM) and flower buds at stage 6 in melon. Stages 2, 4, and 7 are shown in fig. S18. Scale bars, 100 μm. *CmWUS* transcripts were detected in carpel primordia of male (but not female) flowers at stage 6. (**B**) qRT-PCR analysis of *CmWUS*, *CmAG*, *CmWIP1*, *CmCRC*, *CmYUC4*, *CmYUC6*, *CmYUC8*, and *CmTRN2* in laser microdissected carpel primordia from male or female flower buds at stage 6. Bars represent means ± SD (n = 3). *P < 0.05, **P < 0.01, ***P < 0.001 (Student's t test). (**C**) Model explaining how WIP1-TPL controls the expression of *CRC* to lead to male flower development.

flowers compared with female flowers (Fig. 4K). Collectively, these results support the statement that the WIP1-TPL complex binds to the promoter of *CRC* to inhibit its expression, thereby promoting the development of male flowers.

Repression of CRC by WIP1 delays floral stem cell termination in male flowers

Flower stem cell termination is a prerequisite for carpel development. We monitored the expression of *WUS* in male and female flowers during sex transition stages through in situ hybridization. Although no *WUS* mRNA was detected at stage 6 in female flowers, *WUS* mRNA levels were very high in carpel primordia of male flowers at the same stage (Fig. 5A and fig. S18). To quantify the differential expression, we laser microdissected carpel primordia of male and female flowers at stage 6 and analyzed the expression of *WUS* by qRT-PCR (fig. S19). Consistent with the results of the in situ hybridization, *WUS* was expressed three times more in that of male versus female carpel primordia (Fig. 5B). In *Arabidopsis*, CRC suppresses *WUS* expression through the up-regulation of *YUC4* and the down-regulation of *TRN2* (*9*, *10*). *YUC4* belongs to a multigene protein family that encodes flavin-containing monooxygenases that catalyze the rate-limiting step in auxin biosynthesis (*9*, *10*). As above, we analyzed the expression of *TRN2* and different *YUCCA* genes, expressed in melon flowers compared with leaf and root (fig. S20) in laser microdissected carpel primordia by qRT-PCR. We found three *YUC* genes up-regulated and *TRN2* down-regulated, in female versus male flowers, respectively (Fig. 5B). Taken together, these results suggest that *CmWIP1* promotes male flower development through interference with *CRC* function in floral meristem determinacy in the carpel primordia.

Discussion

During flower development, proliferation of stem cells is terminated in a timely manner to allow for carpel development. This process involves the expression of *CRC* in the carpel primordia, a mechanism conserved across angiosperms (*8*). In unisexual flowers, both the male- and female-promoting genes (*WIP1* and *ACS7*, respectively), are also expressed in the carpel primordia (*12*–*14*). The integration of *WIP1*, *ACS7*, and *CRC* into a genetic model of sex determination reveals a mechanism in which *WIP1* interferes with carpel determinacy to lead to male flower development whereas *ACS7* is expressed following carpel determinacy to lead to female flower development (Fig. 5C). WIP1-mediated transcription repression of *CRC* implicates the recruitment of TPL. However, how *ACS7* expression in the carpel is controlled is unclear. As in *Arabidopsis*, we found *CRC* expression leading to down regulation of *TRN2* and the up-regulation of at least 3 *YUC* genes (*9*, *10*). We suggest that the generated auxin maxima in the carpel primordia promote the expression of *ACS7*. Consistent with this, cucumber plants treated with auxins show enhanced femaleness through the ethylene pathway and this effect is blocked by ethylene inhibitors (*19*–*21*).

CRC is also required for nectary development (*15*), yet its expression is not affected in male flowers. We found *WIP1* and *CRC* expression patterns overlapping in the carpel primordia but not in the nectary, leading to normal development of the nectary in male flowers (fig. S21).

WIP proteins are limited to land plants and control key developmental functions. In Marchantia, *MpWIP* is necessary for air pore morphogenesis. In flowering plants, WIPs are implicated in transmitting tracts, primary root formation, and sex determination (*22*–*25*). Based on their sequence homology and complementation experiments, it has been suggested that *WIP* genes might show conserved functions across species (*16*). Our work reveals the mode of action of WIP proteins. The WIP zinc finger domain binds to a conserved cis-regulatory element (Fig. 3), and the N1 and N2 protein motifs cooperate to recruit the TPL family corepressors to repress gene transcription (Fig. 4). In conclusion, our findings reveal the molecular mechanisms driving the development of male and female unisexual flowers in cucurbits and help us to better understand how WIP proteins regulate growth and development in land plants.

REFERENCES AND NOTES

1. D. Charlesworth, *Annu. Rev. Plant Biol.* **67**, 397–420 (2016).
2. G. Feng *et al.*, *Curr. Opin. Plant Biol.* **54**, 61–68 (2020).
3. U. Brand, J. C. Fletcher, M. Hobe, E. M. Meyerowitz, R. Simon, *Science* **289**, 617–619 (2000).
4. H. Schoof *et al.*, *Cell* **100**, 635–644 (2000).
5. T. Laux, K. F. Mayer, J. Berger, G. Jürgens, *Development* **122**, 87–96 (1996).
6. X. Liu *et al.*, *Plant Cell* **23**, 3654–3670 (2011).
7. T. Payne, S. D. Johnson, A. M. Koltunow, *Development* **131**, 3737–3749 (2004).
8. B. Sun, Y. Xu, K.-H. Ng, T. Ito, *Genes Dev.* **23**, 1791–1804 (2009).
9. N. Yamaguchi, J. Huang, Y. Xu, K. Tanoi, T. Ito, *Nat. Commun.* **8**, 1125 (2017).
10. N. Yamaguchi *et al.*, *Nat. Commun.* **9**, 5290 (2018).
11. A. Kocyan, L.-B. Zhang, H. Schaefer, S. S. Renner, *Mol. Phylogenet. Evol.* **44**, 553–577 (2007).
12. A. Boualem *et al.*, *Science* **321**, 836–838 (2008).
13. A. Boualem *et al.*, *Science* **350**, 688–691 (2015).
14. A. Martin *et al.*, *Nature* **461**, 1135–1138 (2009).
15. J. L. Bowman, D. R. Smyth, *Development* **126**, 2387–2396 (1999).
16. M. V. G. Roldan *et al.*, *Commun. Biol.* **3**, 239 (2020).
17. R. C. O'Malley *et al.*, *Cell* **165**, 1280–1292 (2016).
18. H. Szemenyei, M. Hannon, J. A. Long, *Science* **319**, 1384–1386 (2008).

19. C. Shen, G. Li, L. Dreni, D. Zhang, *Front. Plant Sci.* **12**, 635500 (2021).
20. S. Shannon, M. D. de La Guardia, *Nature* **223**, 186 (1969).
21. T. Trebitsh, J. Rudich, J. Riov, *Plant Growth Regul.* **5**, 105–113 (1987).
22. B. C. Crawford *et al.*, *Science* **347**, 655–659 (2015).
23. V. A. Jones, L. Dolan, *Development* **144**, 1472–1476 (2017).
24. M. Sagasser, G.-H. Lu, K. Hahlbrock, B. Weisshaar, *Genes Dev.* **16**, 138–149 (2002).
25. B. C. Crawford, G. Ditta, M. F. Yanofsky, *Curr. Biol.* **17**, 1101–1108 (2007).

ACKNOWLEDGMENTS

The authors thank S. Grant, J. Szecsi, R. Sablowski, and O. Martin for critical reading of the manuscript. We thank V. Rittener for technical assistance and IPS2 glasshouse staff and the research facilities provided by GAFL, as well as the experimental unit for plant handling. **Funding:** This work was funded by the following: European Research Council, grant ERC-SEXYPARTH, 341076; Agence National de la Recherche, grant EPISEX, ANR-17-CE20-0019; Agence National de la Recherche, grant NECTAR, ANR-19-CE20-0023; Laboratoire d'Excellence Sciences des Plantes de Saclay, grant SPS, ANR-10-LABX-40-SPS; and the Initiative d'Excellence Paris-Saclay, grant Lidex-3P, ANR-11-IDEX-0003-02. **Author contributions:** Conceptualization: A.Be. and A.Bo. Methodology: S.Z., F.-Q.T., C.T., C.-H.C., F.S., H.M., and C.C. Investigation: A.Be., S.Z., F.-Q.T., A.Bo., and C.D. Visualization: S.Z. and F.-Q.T. Funding acquisition: A.Be. Project administration: A.Be. Supervision: A.Be., A.Bo., and C.D. Writing – original draft: A.Be., S.Z., and F.-Q.T. Writing – review and editing: A.Be., S.Z., F.-Q.T., A.Bo., and C.D. **Competing interests:** Authors declare that they have no competing interests. **Data and materials availability:** The raw NGS data used and generated in this study have been deposited in the SRA database under accession number PRJNA847166. All other data are available in the main text or supplementary materials. The described biological material can be obtained from A.Be. under a material transfer agreement with INRAE.
License information: Copyright © 2022 the authors, some rights reserved; exclusive licensee American Association for the Advancement of Science. No claim to original US government works. https://www.sciencemag.org/about/science-licenses-journal-article-reuse

SUPPLEMENTARY MATERIALS

science.org/doi/10.1126/science.add4250
Materials and Methods
Figs. S1 to S21
Tables S1 to S7
References (*26*–*50*)
MDAR Reproducibility Checklist
Data S1

Submitted 10 June 2022; accepted 5 October 2022
10.1126/science.add4250

REPORTS

STRUCTURAL BIOLOGY

Molecular glue CELMoD compounds are regulators of cereblon conformation

Edmond R. Watson[1], Scott Novick[2,3], Mary E. Matyskiela[4]†, Philip P. Chamberlain[4]†, Andres H. de la Peña[4]†, Jinyi Zhu[4], Eileen Tran[4], Patrick R. Griffin[2,3], Ingrid E. Wertz[4], Gabriel C. Lander[1]*

Cereblon (CRBN) is a ubiquitin ligase (E3) substrate receptor protein co-opted by CRBN E3 ligase modulatory drug (CELMoD) agents that target therapeutically relevant proteins for degradation. Prior crystallographic studies defined the drug-binding site within CRBN's thalidomide-binding domain (TBD), but the allostery of drug-induced neosubstrate binding remains unclear. We performed cryo–electron microscopy analyses of the DNA damage-binding protein 1 (DDB1)–CRBN apo complex and compared these structures with DDB1-CRBN in the presence of CELMoD compounds alone and complexed with neosubstrates. Association of CELMoD compounds to the TBD is necessary and sufficient for triggering CRBN allosteric rearrangement from an open conformation to the canonical closed conformation. The neosubstrate Ikaros only stably associates with the closed CRBN conformation, illustrating the importance of allostery for CELMoD compound efficacy and informing structure-guided design strategies to improve therapeutic efficacy.

Eukaryotic proteins are targeted for degradation through covalent attachment of ubiquitin moieties to specific residues, primarily lysine side chains (*1*). Ubiquitination is facilitated by ubiquitin ligases (E3s), which coordinate and position targeted substrates for ubiquitin ligation, often through adaptor proteins and interchangeable receptor modules. Substrate specificity of one such E3 complex, the Cullin-4 RING ligase (CRL4), is mediated by the cereblon (CRBN) substrate receptor. CRBN facilitates the transfer of ubiquitin to substrate proteins by reversibly interacting with the CRL4 core complex, which consists of the Cullin-4 scaffold, the DNA damage-binding protein 1 (DDB1) adaptor protein, and RING finger protein ROC1 (fig. S1A). CRBN is also the cellular receptor for a class of drugs known as CELMoD (CRBN E3 ligase modulatory drug) agents, which bind to a conserved hydrophobic pocket in CRBN to create a molecular surface capable of recruiting neosubstrates, that is, cellular proteins that are targeted only in response to drug. Such ligand-induced CRL4-CRBN recruitment facilitates neosubstrate ubiquitination and subsequent proteasomal degradation, thereby dictating therapeutic efficacy (*2*). The CELMoD agent lenalidomide (Revlimid) has been used as a first-line therapy for multiple myeloma and other hematological malignancies for more than a decade, and next-generation CELMoD compounds markedly improve patient outcomes in clinical trials (*3*). Although crystallographic structural snapshots of CRBN-DDB1 bound to a variety of drugs and neosubstrates have facilitated a molecular description of the stable quaternary complex, the allostery associated with substrate targeting remains unknown, and the structural features of the unliganded complex have yet to be described.

[1]Department of Integrative Structural and Computational Biology, Scripps Research, La Jolla, CA 92037, USA. [2]Department of Molecular Medicine, Scripps Research, Jupiter, FL 33458, USA. [3]UF Scripps Biomedical Research, University of Florida, Jupiter, FL 33458, USA. [4]Bristol-Myers Squibb, San Diego, CA 92121, USA.
†Present address: Neomorph, Inc., San Diego, CA 92121, USA.
***Corresponding author. Email: glander@scripps.edu**

CRBN is a 50-kDa protein containing three folded domains: an N-terminal Lon protease-like domain (hereafter, Lon domain), an intermedial helical bundle (HB), and a C-terminal thalidomide-binding domain (TBD) that harbors the drug-binding pocket. CRBN is recruited to the Cullin-4–ROC1 ligase module by the adaptor protein DDB1, which consists of three WD-40 beta propeller domains (BPA, BPB, and BPC). The HB of CRBN docks into a central hydrophobic cleft formed at the interface of BPA and BPC of DDB1, while the mobile BPB domain interacts with Cullin-4, positioning CRBN-bound substrates for ubiquitination. Over a dozen crystal structures of the CRBN-DDB1 complex show the Lon domain and TBD of CRBN tightly interacting with one another in what can be described as a closed conformation ($CRBN^{closed}$) (*2*, *4*–*10*). These structures of the closed conformer bound to small molecules have provided the basis for structure-guided drug design of next-generation CELMoD agents with enhanced neosubstrate specificity and potency, such as CC-92480 (mezigdomide). Although it is thought that association of the TBD and Lon domains is concomitant with drug and neosubstrate binding, this assumption is challenged by structures of the isolated TBD bound to ligands, demonstrating that the TBD is competent for drug binding in the absence of the Lon domain (*11*).

Two crystal structures have captured the Lon domain and TBD in an open conformation ($CRBN^{open}$) where the two domains are separated and positioned at a ~45° angle relative to one another. These reports raise questions about the assumed constraints associated with drug accessibility and binding, as well as the mechanisms by which ligands modify the surface chemistry of CRBN to enable neosubstrate recruitment and subsequent ubiquitination and degradation (*4*, *5*). If $CRBN^{open}$ represents a physiological conformer (i.e., not an artifact of crystallization), we must reconsider recruitment of drug and neosubstrates in the context of these two conformers. Additionally, the dynamics of interconversion between the open and closed conformers, the effect that

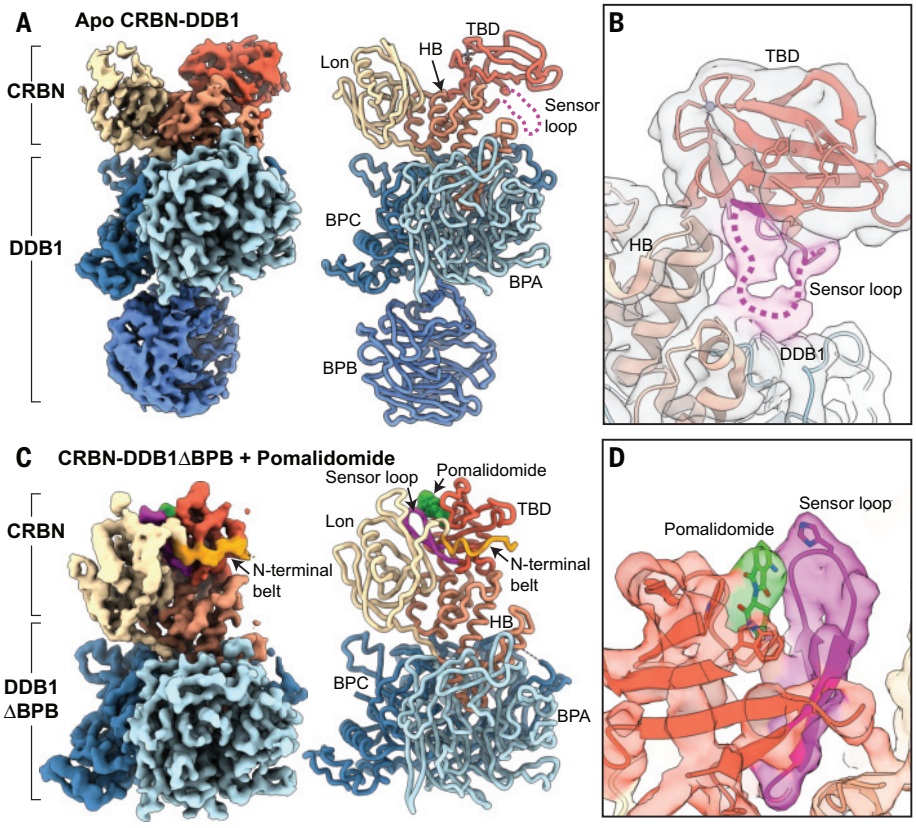


Fig. 1. CRBN^{open} is allosterically modulated to CRBN^{closed} by pomalidomide. (**A**) ~3.5-Å-resolution cryo-EM reconstruction of CRBN-DDB1 in the unliganded apo form. The Lon domain (tan) is separated from the TBD (red), while the helical bundle (HB, light red) mediates interaction with DDB1, composed of beta propeller A (BPA, light blue), beta propeller B (BPB, medium blue), and beta propeller C (BPC, steel blue). CRBN and DDB1 are thresholded independently to illustrate important features. To the right, a ribbon representation of the CRBN-DDB1 complex modeled from density is shown (same color scheme as on the left). The sensor loop is denoted as a dotted magenta line extending away from the TBD domain. (**B**) The unsharpened cryo-EM map shows the path of the sensor loop, which interacts with the HB and BPA of DDB1. (**C**) Surface representation of the ~3.9-Å-resolution cryo-EM reconstruction of CRBN-DDB1 in the closed form in complex with pomalidomide. The N-terminal belt (orange) wraps around the TBD domain. To the right, a ribbon representation of CRBN-DDB1$^{\Delta BPB}$ in complex with pomalidomide is shown, with the sensor loop (magenta) adopting a β-hairpin organization that is tightly packed between the TBD and Lon domains. (**D**) A detailed view of the density corresponding to pomalidomide (green) and the sensor loop (magenta) in CRBN^{closed}.

ligands and neosubstrates have on this process, and how these dynamics affect neosubstrate positioning and subsequent degradation may have profound effects on the design, and ultimately the therapeutic impact, of next-generation CELMoD compounds.

To better understand the spectrum of CRBN conformations, we used cryo–electron microscopy (cryo-EM) to examine the population ensemble of CRBN-DDB1 conformers present in solution under various conditions. To overcome preferred orientation and partial denaturation or dissociation of the complex during cryo-EM grid preparation, a combination of grid pretreatment with a CRBN-agnostic protein, incorporation of mild amphiphilic detergent, and sample dilution immediately before plunging improved particle homogeneity and distribution in ice (see methods in the supplementary materials). Unexpectedly, whether copurified with either full-length DDB1 or DDB1 lacking BPB (CRBN-DDB1$^{\Delta BPB}$, a construct commonly used for x-ray crystallography), apo-CRBN exclusively adopts an open conformation, with the TBD and Lon domains separated from one another (Fig. 1A and fig. S1B).

Our ~3.5-Å-resolution cryo-EM structure confirms the physiological existence of the open conformer and provides the first opportunity to examine this CRBN conformation in the absence of ligand or substrate. Notably, we do not observe density for the "sensor loop," a beta-insert hairpin within CRBN's TBD (residues ~341 to 361) that has been shown to directly bind immunomodulatory drugs and neosubstrates in prior structures (*2*, *12*), at its canonical position adjacent to the thalidomide-binding pocket. Instead, we observe strong, low-resolution density corresponding to the sensor loop engaged in previously unobserved interactions with a helix in CRBN's HB (residues ~210 to 220) and a loop of BPC in DDB1 (residues ~776 to 780) (Fig. 1B). These regions of the HB and DDB1 are usually disordered in crystal structures (*5*, *10*, *12*, *13*), consistent with the flexibility of this region observed in our cryo-EM density. However, the clearly observed association between the sensor loop and this HB-DDB1 interface in our cryo-EM structures suggests that interaction between these flexible loops plays a role in maintaining the TBD in the CRBN^{open} conformer.

To better understand how CELMoD agents interact with and influence this open CRBN conformation, we added saturating amounts of different compounds to CRBN-DDB1 for cryo-EM analyses. Addition of pomalidomide was sufficient to induce conformational rearrangement within CRBN for only ~20% of the particles. The ~3.9-Å-resolution structure of CRBN^{closed} arising from pomalidomide-bound particles shows the ~15-kDa TBD positioned adjacent to the Lon domain and unambiguous density within the ligand-binding pocket consistent with pomalidomide association (Fig. 1C). Necessarily, the sensor loop in CRBN^{closed} is observed in the canonical β-hairpin fold interfacing the TBD and Lon domain, and a portion of the CRBN N terminus (residues 48 to 63) that is disordered in the CRBN^{open} becomes ordered, extending from the Lon domain, trussing the TBD, and supporting the closed conformation (Fig. 1C). To better define the role of these N-terminal residues, hereafter referred to as the N-terminal belt, in CRBN closure, we truncated 63 residues from the CRBN N terminus (CRBN$^{\Delta NTD}$) and incubated the CRBN$^{\Delta NTD}$-DDB1 with saturating pomalidomide concentrations. Deletion of the N terminus all but abolishes CRBN closure, with less than ~2% of the complexes adopting a closed conformation with a poorly ordered sensor loop, underscoring the importance of the CRBN N-terminal belt in stabilizing the CRBN^{closed} conformer (fig. S2A).

We expected to observe the pomalidomide ligand in the binding pocket of only the CRBN^{closed} conformer, but we were surprised to find strong density corresponding to pomalidomide within the binding pocket of CRBN^{open} as well (fig. S3A). Even with the ligand bound—and in stark contrast to prior crystal structures of the CRBN^{open} conformer—the sensor loop of our cryo-EM CRBN^{open} conformer remains engaged in interactions with the CRBN HB and DDB1 as we observe in the apo-CRBN conformer (fig. S3B). These results indicate that limitations in neosubstrate recruitment, which directly translate to drug efficacy, may not solely correlate with CRBN-binding kinetics. Rather,

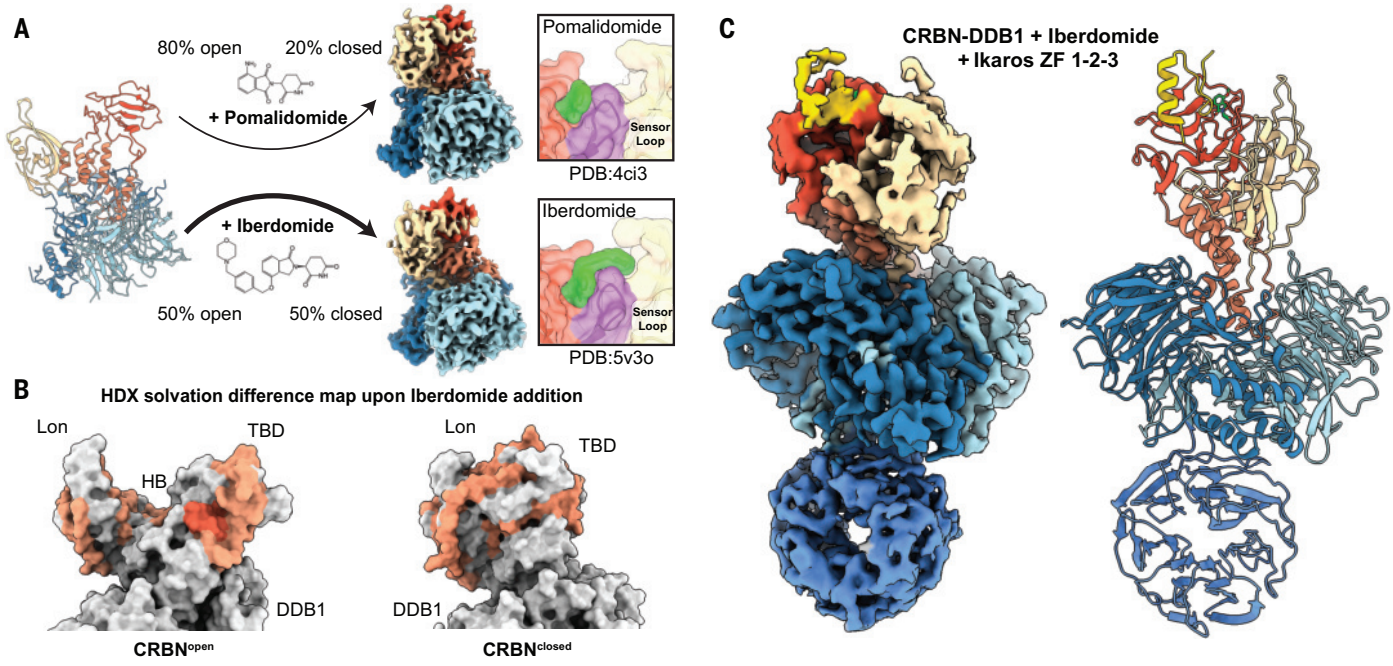


Fig. 2. Improved CELMoD compounds drive CRBN^{closed} and recruit Ikaros. (**A**) The CRBN^{open} transition to CRBN^{closed} is differentially regulated between pomalidomide (~20% of particles adopt CRBN^{closed}) and the CELMoD agent iberdomide (~50% of particles adopt CRBN^{closed}). (Top right) The ~3.9-Å-resolution cryo-EM structure of pomalidomide-induced CRBN^{closed}. (Bottom right) The ~3.7-Å-resolution reconstruction of iberdomide-induced CRBN^{closed}. The inset panels on the far right depict surface representations of published crystal structures illustrating the ligand (green) interactions with sensor loop (magenta). (**B**) Colored space-filling representation of CRBN models with residue-specific coloring according to changes in solvency upon addition of iberdomide as detected by HDX-MS. Orange residues correspond to peptides with mild HDX differential, and red residues correspond to peptides with large HDX differential. Mixed conformations are expected during the experiment, so CRBN^{open} and CRBN^{closed} are both shown. (**C**) The ~3.6-Å-resolution reconstruction of iberdomide-induced CRBN^{closed} in complex with Ikaros ZF1-ZF2-ZF3 (gold). DDB1 and CRBN are thresholded independently to illustrate important features.

conversion of the CRBN^{open} to the CRBN^{closed} conformation may be a key mechanistic bottleneck in the allosteric transformation of apo-CRBN to a neosubstrate-binding conformation after ligand association.

We were intrigued by the observation that saturating concentrations of pomalidomide did not induce widespread closure of the CRBN domains, despite high occupancy. We rationalized that next-generation CELMoD agents with improved binding affinity may also have a more pronounced allosteric effect through enhanced interactions with the sensor loop, contributing to adoption of the sensor loop to the CRBN^{closed}–competent β-hairpin conformation. Indeed, an analysis of CRBN-DDB1 in the presence of CC-220 (iberdomide), a molecule with ~20-fold improved affinity and ~24-fold enhanced Ikaros degradation (*13*), shows that nearly 50% of particles have shifted to the CRBN^{closed} conformer (Fig. 2A). As with pomalidomide, in the presence of excess ligand, we observe density consistent with iberdomide within the glutarimide-binding pocket of both the CRBN^{closed} and CRBN^{open} conformers, suggesting that drug occupancy within CRBN is not responsible for the increased allosteric transition. Two prior crystal structures of the iberdomide-bound CRBN show that the additional phenyl and morpholino moieties of the iberdomide molecule can arch over the top of the sensor loop β-hairpin (*13*, *14*), a conformation that may aid in the stabilization of this structural motif. These data support our proposed allosteric model whereby enhanced ligand interaction with the sensor loop stabilizes the β-hairpin conformation, which promotes the closure of the TBD and Lon domains and ultimately translates to improved neosubstrate ubiquitination and subsequent degradation efficacy. We note, however, that these extended moieties are limited in resolution in our cryo-EM structure (fig. S3C) and have high B-factors in published x-ray structures. This observation, coupled with recently described alternative positions of these extended ligand groups (*14*), suggests that iberdomide's interaction with the sensor loop may be dynamic. It is likely that a more stable interaction with the sensor loop could be attained with next-generation CELMoD agents.

To further investigate the allosteric influence of iberdomide on CRBN closure, we used hydrogen-deuterium exchange mass spectrometry (HDX-MS) to profile changes in solvent accessibility of CRBN-DDB1 peptides in the presence of iberdomide. Compared with unliganded CRBN-DDB1, addition of drug substantially reduced solvation for regions within the Lon, TBD, and HB domains found at the domain-domain interface of the closed conformation, consistent with transition from CRBN^{open} to CRBN^{closed} (Fig. 2B and fig. S4A), whereas the DDB1 surfaces were unchanged (fig. S4B). As expected, the most extreme change is observed for the sensor loop itself, consistent with formation of the buried hairpin we observe in CRBN^{closed} (Fig. 1C). These findings offer a potential new modality for drug development, wherein properties influencing not only binding kinetics for CRBN and neosubstrates (*15*) but also the capacity to stabilize the β-hairpin conformation of the sensor loop as a means of both initiating and maintaining the closed conformation should be considered. The CRBN^{closed} conformation may in turn be a prerequisite for substrate recruitment.

Indeed, the substantial population of ligand-bound CRBN^{open} conformers in our datasets indicates that ligand binding is not concurrent with adoption of the CRBN^{closed} conformation and that CRBN closure is dependent on subsequent allosteric triggers. We posit that ligand binding is involved in inducing the sensor loop's adoption of the β-hairpin arrangement, thereby untethering the TBD from the CRBN HB to enable the CRBN^{closed} conformation for substrate interaction. Despite extensive focused classification of the tether region, we were unable to identify a population of liganded CRBN^{open} conformers where the sensor loop is

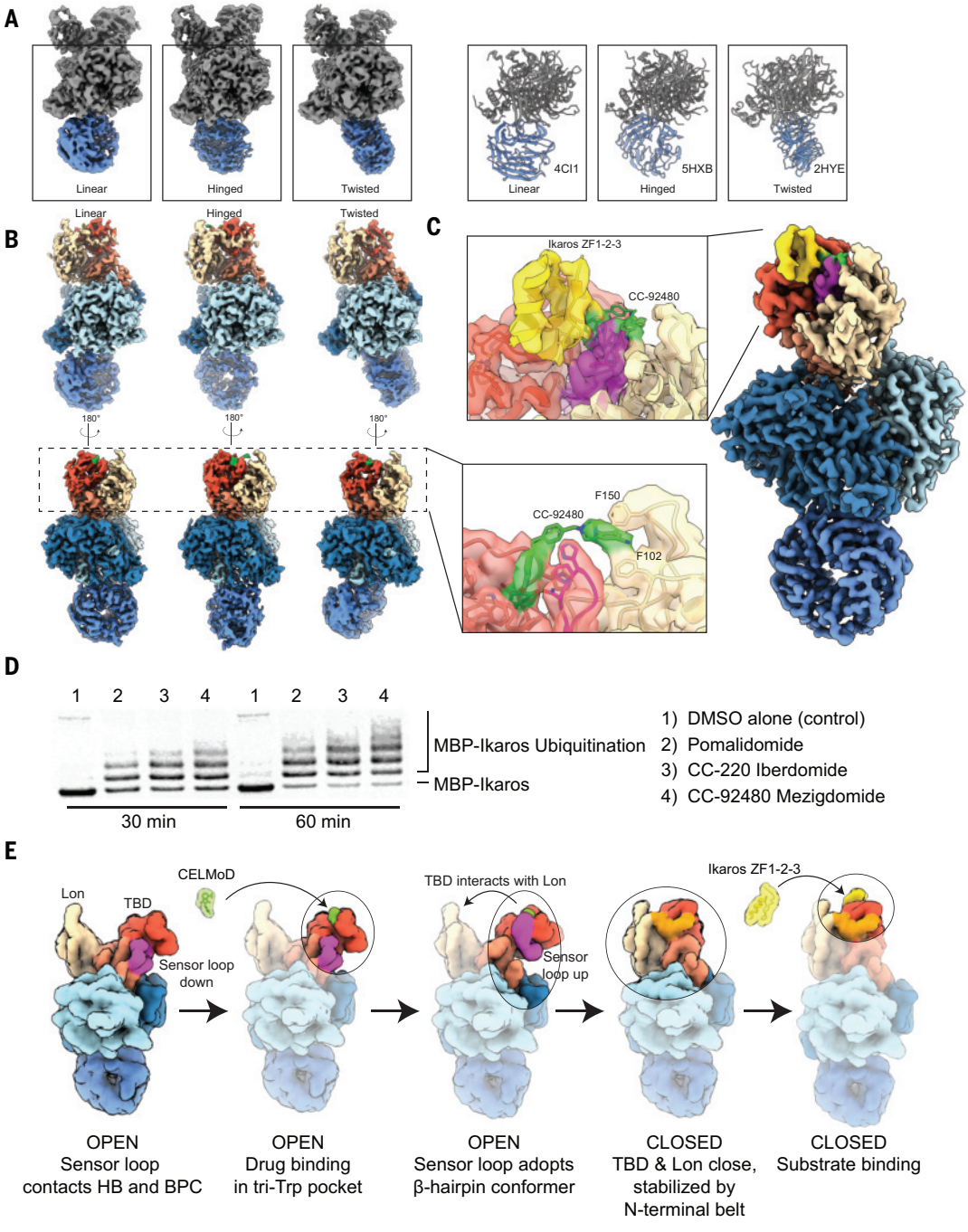


Fig. 3. DDB1 and next-generation CELMoD agents further poise CRBN substrates for ubiquitination in disease contexts. (**A**) Three-dimensional classification of unliganded CRBN-DDB1 yields three discrete positions of DDB1's mobile BPB propeller (colored blue). (Left) ~3.5-Å-resolution cryo-EM reconstructions of CRBN-DDB1 with BPB in a linear (left), hinged (middle), or twisted (right) position. (Right) Structural models in similar orientations for reference, adopting a linear (PDB ID 4CI1, left), hinged (PDB ID 5HXB, middle), or twisted (PDB ID 2HYE, right) position. (**B**) The ~3.2-Å-resolution cryo-EM reconstructions of CRBN-DDB1 complexed with mezigdomide with a linear (left), hinged (middle), or twisted (right) position of BPB. (Inset) ~3.1-Å-resolution focused refinement of particles from all three orientations reveal a connection between mezigdomide and the Lon domain, "stapling" the $CRBN^{closed}$ conformation. (**C**) The ~3.1-Å-resolution reconstruction of mezigdomide-induced $CRBN^{closed}$ bound to Ikaros ZF1-ZF2-ZF3. The inset shows a focused view of connection between mezigdomide and the Lon domain, stapling $CRBN^{closed}$ in the presence of Ikaros. (**D**) In vitro ubiquitination assay tracking MBP-Ikaros ubiquitination in the presence of different molecules used in this study (labeled on the right). (**E**) Mechanistic model illustrating pathway of assembly. First, unliganded CRBN is open with the sensor loop attached to HB. Second, ligand is added and associates with TBD in the hydrophobic pocket. Third, binding of ligand in the tri-Trp pocket stabilizes the sensor loop as a β-hairpin detached from the HB. Fourth, sensor loop refolding promotes transition of $CRBN^{open}$ to $CRBN^{closed}$ without an observed intermediate, and the N-terminal belt is seated (orange). Fifth, substrate is recruited to the $CRBN^{closed}$ conformation for subsequent ubiquitination by CRL4.

untethered from the HB in any of our datasets. This finding indicates that ligand-mediated detachment of the sensor loop from the HB is concomitant with adoption of the structured β-hairpin and triggers immediate closure of the CRBN TBD and Lon domains.

We next aimed to probe the role of drug binding in neosubstrate recruitment and positioning in the context of the $CRBN^{open}$ and $CRBN^{closed}$ conformers. Prior crystallographic studies yielded structures of $CRBN^{open}$ conformers bound to neosubstrates (*4*, *9*), although it was speculated that these conformations may have resulted from crystallization conditions and lattice contacts. To investigate drug-mediated CRBN-DDB1 recruitment of neosubstrates, we used the zinc finger (ZF) transcription factor Ikaros, a cellular target of pomalidomide and iberdomide. We generated different constructs containing tandem Ikaros ZF1, ZF2, and ZF3 domains (fig. S5A) for increased recruitment efficiency (*4*) and incubated each individually with CRBN-DDB1 in the presence of pomalidomide or iberdomide. Regardless of drug identity or Ikaros ZF construct design, our single-particle analyses reveal density consistent with the location and positioning of a single Ikaros ZF motif associated with the TBD domain of the $CRBN^{closed}$ conformer (Fig. 2C and fig. S5B), again confirmed in HDX-MS analyses showing even more pronounced changes for residues within the sensor loop that contact the known Ikaros recruitment motif (fig. S4, C and D). We

were unable to detect any Ikaros association with the $CRBN^{open}$ conformer, consistent with a mechanism whereby drug-induced CRBN closing occurs before substrate recruitment. This result further demonstrates the importance of an allosteric control mechanism, whereby drug-induced CRBN closing occurs prior to neosubstrate recruitment.

The Cullin-4–ROC1 ligase core recruits the DDB1-$CRBN^{closed}$-Ikaros complex by associating with the second beta propeller of DDB1 (called BPB), which is located distally to CRBN. BPB extends from the DDB1 core as a mobile element, and this flexibility has been implicated in the mechanism of DDB1 as a promiscuous adaptor that bridges Cullin-4 with structurally diverse substrate-binding modules. Correspondingly, BPB has been captured in a variety of conformations in several prior studies (*16*). We sought to describe the motion of BPB and its potential relevance to Ikaros positioning for ubiquitination in the context of the CRL4-CRBN complex assembly. Our image analyses of the BPB domain within our apo CRBN data reveal that, rather than demonstrating a full continuum of motion, the BPB position is limited to three metastable positions. Approximately 65% of the particles adopt a "linear" orientation, in which the broad face of BPB is in a similar orientation as BPC (Fig. 3A, left). A ~70° rotated "hinged" orientation, where the BPB face more closely matches BPA, is the second major class observed, with ~20 to 30% of particles (Fig. 3A, middle), and only a minor population contain BPB in the third, "twisted" orientation, rotated ~140° from the linear orientation (Fig. 3A, right). Further classification of particles contributing to each of these states reveals only minor positional variability for BPB, as has been previously described (*16*), centered around these discrete conformations.

These three principal orientations were observed in recent low-resolution cryo-EM structures of DDB1-DCAF1 (DDB1 and Cullin-4 associated factor 1) bound to Cullin-4 (*17*), and our structures demonstrate that the BPB likely switches between these three energetic minima irrespective of the substrate adaptor module or interaction with Cullin. Although we were unable to discern allosteric coordination upon ligand or Ikaros binding, the population distribution of the states varies greatly compared with those observed for the Cullin-bound DDB1 (*17*). Notably, the twisted orientation that we observe in <10% of our particles is the majority conformer when bound to Cullin (*17*), suggesting that association with Cullin may substantially modulate BPB positioning between these three states, thereby influencing proximity and positioning of neosubstrates for ubiquitination.

Given the potential clinical relevance of the observed CRBN allostery, we considered the mechanisms of action responsible for the improved efficacy of next-generation CELMoD molecules. Mezigdomide, for example, was recently shown to display efficient, rapid neosubstrate degradation kinetics and is considerably more efficacious in the treatment of relapse or refractory patients who no longer respond to primary treatment with lenalidomide and/or pomalidomide (*18*). To investigate the structural features responsible for the enhanced efficacy of this compound, we incubated mezigdomide with CRBN-DDB1 for cryo-EM analyses. One hundred percent of the complexes adopted the $CRBN^{closed}$ conformer. Density corresponding to mezigdomide is clearly observed in the canonical binding site in the ~3.2-Å-resolution structures of CRBN-DDB1 with BPB in the three discrete orientations (Fig. 3B). We also observe protruding drug density that extends to the distal Lon domain, a feature that had not been observed in the structures of any other liganded CRBN (Fig. 3B, right). We were able to unambiguously fit mezigdomide into the density to reveal that the benzonitrile moiety is likely stabilized by aromatic or cation-pi interactions with CRBN Phe^{102} and Phe^{150} of the Lon domain. Association of the glutarimide and the benzonitrile moieties to distinct domains within CRBN, that is, the TBD and Lon domains, respectively, both provides avidity for improved ligand affinity and serves to staple the domains together in the closed conformation, which is traditionally accomplished by the CRBN N-terminal belt (Fig. 1C). Ikaros is recruited to mezigdomide-bound CRBN-DDB1 (Fig. 3C), and its ubiquitination efficiency is enhanced in assays with Cullin-4–ROC1 (Fig. 3D). Within the mezigdomide-bound dataset, we observe a substantial population of $CRBN^{closed}$ particles that lack discernible density for the stabilizing N-terminal belt (fig. S2B). We thus propose that there is functional redundancy in securing the closed conformer and that mezigdomide further promotes neosubstrate recruitment and subsequent ubiquitination by prolonging the mechanistic cycle of closure, neosubstrate binding, N-terminal engagement, and stepwise reversal to the open conformation. These data elucidate a distinctive, previously unexplored compound design modality and describe the structural mechanism for enhanced therapeutic benefit of mezigdomide in patients unresponsive to pomalidomide, further illustrating the therapeutic value of allosteric control. Although not tested directly, we speculate that incorporation of these improved design elements to other molecular glues and heterobifunctional molecules would similarly improve their efficacy.

Our results provide mechanistic insights into the therapeutic efficacy of CELMoD compounds, a class of molecules that epitomize molecular glues and are central players in the field of targeted protein degradation. In so doing, we highlight previously unappreciated allosteric effects for consideration in the design of CRBN-directed molecular glue therapeutics (Fig. 3E). By characterizing the conformational rearrangements inherent to the CRBN-DDB1 system, and showing how three distinct degrader molecules affect allostery and neosubstrate-binding capacity, we reveal how conformational control of the mobile drug-binding TBD within CRBN has cryptically driven the therapeutic success of neosubstrate-targeting agents.

REFERENCES AND NOTES

1. K. N. Swatek, D. Komander, *Cell Res.* **26**, 399–422 (2016).
2. P. P. Chamberlain *et al.*, *Nat. Struct. Mol. Biol.* **21**, 803–809 (2014).
3. P. G. Richardson *et al.*, *Blood* **138** (suppl. 1), 2731 (2021).
4. Q. L. Sievers *et al.*, *Science* **362**, eaat0572 (2018).
5. G. Petzold, E. S. Fischer, N. H. Thomä, *Nature* **532**, 127–130 (2016).
6. M. E. Matyskiela *et al.*, *Nat. Struct. Mol. Biol.* **27**, 319–322 (2020).
7. C. Surka *et al.*, *Blood* **137**, 661–677 (2021).
8. E. S. Fischer *et al.*, *Nature* **512**, 49–53 (2014).
9. R. P. Nowak *et al.*, *Nat. Chem. Biol.* **14**, 706–714 (2018).
10. E. S. Wang *et al.*, *Nat. Chem. Biol.* **17**, 711–717 (2021).
11. M. D. Hartmann, I. Boichenko, M. Coles, A. N. Lupas, B. Hernandez Alvarez, *PLOS ONE* **10**, e0128342 (2015).
12. M. E. Matyskiela *et al.*, *Nature* **535**, 252–257 (2016).
13. M. E. Matyskiela *et al.*, *J. Med. Chem.* **61**, 535–542 (2018).
14. C. Heim, M. D. Hartmann, *Acta Crystallogr. D Struct. Biol.* **78**, 290–298 (2022).
15. N. R. Kong, H. Liu, J. Che, L. H. Jones, *ACS Med. Chem. Lett.* **12**, 1861–1865 (2021).
16. N. Bai *et al.*, *J. Biol. Chem.* **298**, 101653 (2022).
17. S. Banchenko *et al.*, *PLOS Pathog.* **17**, e1009775 (2021).
18. J. D. Hansen *et al.*, *J. Med. Chem.* **63**, 6648–6676 (2020).

ACKNOWLEDGMENTS

We thank J. C. Ducom at Scripps Research High Performance Computing and C. Bowman at Scripps Research for computational support, as well as B. Anderson at the Scripps Research Electron Microscopy Facility for microscopy support. Computational analyses of EM data were performed using shared instrumentation funded by NIH S10OD021634 to G.C.L. **Funding:** This work was supported by National Institutes of Health grant S10OD021634 (G.C.L.). **Author contributions:** Conceptualization: E.R.W., M.E.M., P.P.C., and G.C.L. Methodology: E.R.W., S.N., M.E.M., P.P.C., A.H.d.l.P., J.Z., E.T., P.R.G., I.E.W., and G.C.L. Investigation: E.R.W., J.Z., and G.C.L. Visualization: E.R.W., S.N., and J.Z. Project administration: P.P.C., I.E.W., and G.C.L. Supervision: P.P.C., I.E.W., and G.C.L. Writing – original draft: E.R.W. and G.C.L. Writing – review & editing: E.R.W., I.E.W., and G.C.L. **Competing interests:** M.E.M., P.P.C., A.H.d.l.P., J.Z., E.T., and I.E.W. are or were employees of Bristol-Myers Squibb and have received Bristol-Myers Squibb stock. G.C.L. has received research funding from Bristol-Myers Squibb. A provisional patent regarding aspects of this work has been filed under US Provisional Patent Application no. 63/293,402. E.R.W. has received consulting fees for service rendered in cryo-EM method applications. P.P.C. is a founder, employee, and equity holder of Neomorph Inc. M.E.M. and A.H.d.l.P. are employees and stockholders of Neomorph Inc. **Data and materials availability:** Atomic models have been deposited to the Protein Data Bank (PDB) under IDs 8CVP, 8D7U, 8D7V, 8D7W, 8D7X, 8D7Y, 8D7Z, 8D80, and 8D81, as described in table S2. Electron microscopy reconstructions have been deposited to the Electron Microscopy Databank (EMDB) under accession codes EMDB-27012, EMDB-27234, EMDB-27235, EMDB-27236, EMDB-27237, EMDB-27238, EMDB-27239, EMDB-27240, EMDB-27241, and EMDB-27242, as described in table S1.

License information: Copyright © 2022 the authors, some rights reserved; exclusive licensee American Association for the Advancement of Science. No claim to original US government works. https://www.science.org/about/science-licenses-journal-article-reuse

SUPPLEMENTARY MATERIALS

science.org/doi/10.1126/science.add7574
Materials and Methods
Figs. S1 to S9
Tables S1 to S3
References (*19*–*32*)
MDAR Reproducibility Checklist

Submitted 1 July 2022; accepted 5 October 2022
10.1126/science.add7574

VOLCANIC PLUMES

The January 2022 eruption of Hunga Tonga-Hunga Ha'apai volcano reached the mesosphere

Simon R. Proud[1,2]*, Andrew T. Prata[2], Simeon Schmauß[3]

Explosive volcanic eruptions can loft ash, gases, and water into the stratosphere, which affects both human activities and the climate. Using geostationary satellite images of the 15 January 2022 eruption of the Hunga Tonga-Hunga Ha'apai volcano, we find that the volcanic plume produced by this volcano reached an altitude of 57 kilometers at its highest extent. This places the plume in the lower mesosphere and provides observational evidence of a volcanic eruption injecting material through the stratosphere and directly into the mesosphere. We then discuss potential implications of this injection and suggest that the altitude reached by plumes from previous eruptions, such as the eruption of Mount Pinatubo in 1991, may have been underestimated because of a lack of observational data.

Large explosive volcanic eruptions are important because they can affect climate (*1*), disrupt aviation (*2*), and pose numerous hazards to communities living nearby (*3*, *4*). The degree to which explosive volcanic eruptions affect climate is largely dependent on the volcano's latitude, the plume height, and the amount of SO_2 gas that is released (*5*). When a substantial amount of SO_2 is released into the atmosphere, it is converted to sulfate aerosols that can, in the most extreme cases, persist for several years (*6*), and when injected at low latitudes, the aerosol disperses into both hemispheres (*1*, *7*). The persistent aerosol veil that is produced affects climate because of the reflection of incoming visible radiation and absorption of near-infrared radiation (*8*), which results in a cooling of the troposphere (*9*) and heating of the stratosphere (*10*). Within the satellite era, there are numerous examples of volcanic plumes reaching the upper troposphere–lower stratosphere (*11*); however, few have been observed to reach higher than 30 km and affect the climate (*12*). Notable examples that have been observed and quantified using satellite observations include the plumes of Mount Pinatubo (Philippines) in 1991, which injected ~20 Tg of SO_2 (*13*) and reached 40 km at its highest point (*14*), and El Chichón, which released ~7.5 Tg of SO_2 into the atmosphere (*15*) in 1982, reaching 31 km (*16*). Based on the satellite data record, in general, individual explosive volcanic eruptions are not expected to have a measurable climate impact unless >1 Tg SO_2 is released into the stratosphere (*12*).

The Hunga Tonga-Hunga Ha'apai (HTHH) volcano (20.536°S, 175.382°W) is an underwater caldera volcano located ~70 km north-northwest of Tonga's capital, Nukualofa. Recent Surtseyan-style eruptive activity was observed in 2009, from 2014 to 2015, and from 20 December 2021 to 15 January 2022 (*17*). In the lead-up to the 15 January 2022 eruption, described later in the text, a large phreatomagmatic eruption, similar to the December 2019 eruption of Anak Krakatau, Indonesia (*18*), was observed on 13 January in geostationary satellite data. The volcanological setting of HTHH is very different from those of the Mount Pinatubo and El Chichón volcanoes because of the abundance of seawater available for magma interaction. Initial estimates of the total mass of SO_2 released by the 15 January eruption from hyperspectral sounders and ultraviolet instruments were 0.2 to 0.4 Tg SO_2 (*19*, *20*). This amount of SO_2 is low and suggests that large amounts of SO_2 may have been scavenged through wet deposition (*18*, *21*).

On 15 January 2022, at about 04:06 UTC (17:06 local time), the HTHH volcano violently erupted, producing the large volcanic plume shown in Fig. 1. A second smaller eruption occurred at 08:00 UTC, with no further large eruptions occurring thereafter. This eruption was one of the most powerful in recent years, triggering a tsunami that was felt across the Pacific and atmospheric waves (*22*) that circled Earth multiple times, which were seen as fluctuations in global pressure sensor readings for several days. The volcano's location is well covered by satellite sensors, with three geostationary weather satellite platforms providing imagery of the area at visible and infrared

[1]National Centre for Earth Observation, RAL Space, STFC Rutherford Appleton Laboratory, Harwell OX11, UK. [2]Atmospheric, Oceanic and Planetary Physics, University of Oxford, Parks Road, Oxford OX1 3PU, UK. [3]Munich University of Applied Sciences, Lothstraße. 34, 80335 Munich, Germany.
*Corresponding author. Email: simon.proud@stfc.ac.uk

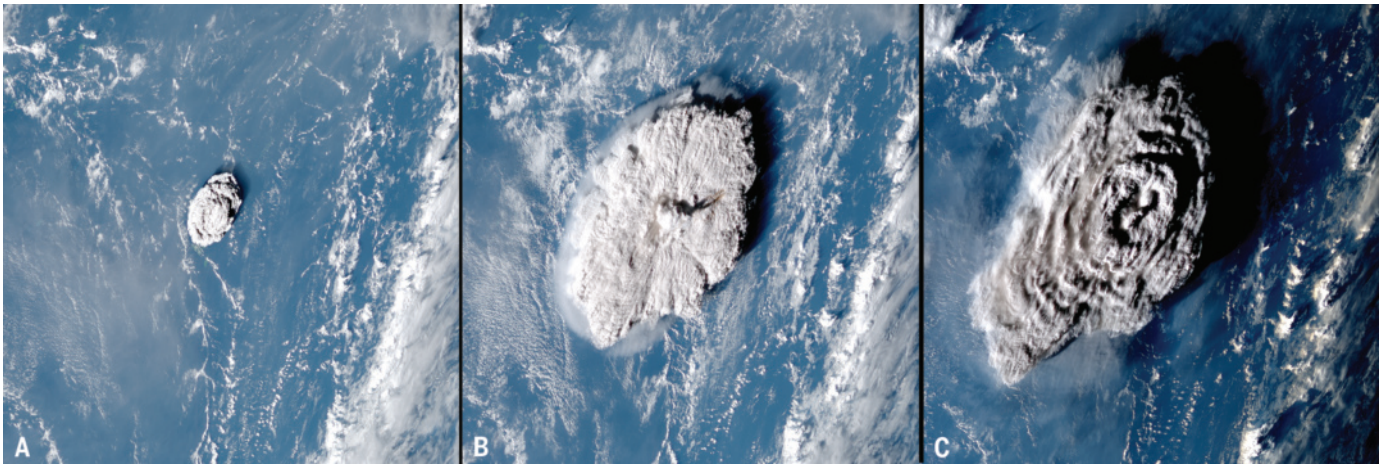


Fig. 1. The HTHH eruption as viewed from the Himawari-8 weather satellite. (**A**) At 04:10 UTC on 15 January 2022, ~10 min after the eruption began. (**B**) At 04:50 UTC, after the initial dome collapsed, leaving remnants at 55- to 58-km altitude that cast a shadow (to the right) onto the umbrella cloud at 34 km. (**C**) At 05:40 UTC, as the volcanic umbrella spreads south-westward and the Sun begins to set, emphasizing the shadows that we used to calculate plume altitude and highlighting wave structure in the umbrella top.

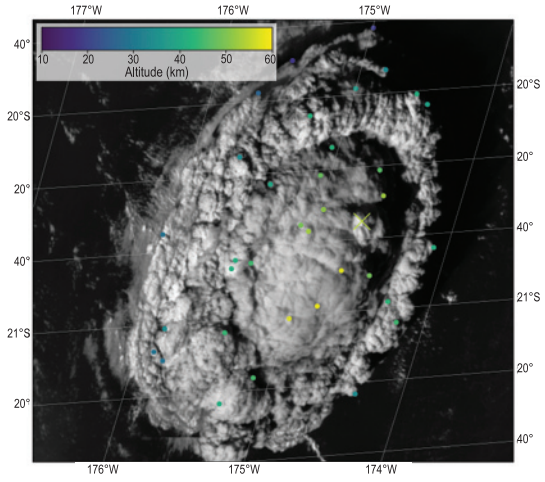


Fig. 2. Parallax-based retrievals of plume altitude at 04:30 UTC on 15 January 2022 overlaid on Himawari-8 high-resolution data for the same time frame. Colored circles represent Advanced Himawari Imager (AHI)–Advanced Meteorological Imager (AMI) retrievals, and the two crosses represent AHI-AMI–Advanced Baseline Imager (ABI) retrievals.

wavelengths every 10 min (summarized in table S1), and at about 07:05 UTC, the National Oceanic and Atmospheric Administration (NOAA) enabled a fast-scanning mesoscale sector over the volcano, producing imagery every minute.

Typically, the altitude of a volcanic plume is estimated from its top temperature measured by satellite and compared with a vertical profile of temperature from radiosonde measurements or weather model outputs such as those produced by the European Centre for Medium-Range Weather Forecasts (ECMWF) (*23*). This technique makes use of the relationship between decreasing atmospheric temperature—and hence cloud temperature for a cloud in thermodynamic equilibrium with its surroundings—and altitude in the troposphere (*24*). However, for large volcanic eruptions, the cloud penetrates the tropopause and enters the stratosphere, where temperature increases with altitude, thus rendering temperature-based techniques inaccurate: In such cases, the plume in the stratosphere will initially be cooler than the ambient air but will warm as the plume enters thermodynamic equilibrium with its surroundings, which presents several possible altitude solutions for a single cloud temperature. This is further complicated because the eruption itself is likely to affect local vertical temperature profiles. In this report, we make use of the multiple satellite sensors that viewed the eruption from very different viewing geometries to compute plume altitude based on the parallax effect, which does not suffer from the limitations described earlier in the text, and find that the HTHH eruption not only penetrated the stratosphere but also reached the lower mesosphere.

When a satellite views a high-altitude cloud, the cloud location within the satellite image will be incorrect because of a parallax shift, the magnitude of which depends on the viewing angle between satellite and cloud and upon the cloud altitude. If two or more satellites view a cloud from differing locations, then its actual position and altitude are found by iteratively adjusting estimated cloud altitude to minimize the difference in the parallax-corrected position between satellites (*25*). We have previously used this approach to successfully estimate the altitude and trajectory of the Chelyabinsk meteor (*26*), demonstrating that the technique is appropriate for high-altitude clouds. Here, we apply the approach to a series of manually selected cloud positions observed by Himawari-8 and GEO-KOMPSAT-2A (GK-2A) to the west of the eruption and the Geostationary Operational Environmental Satellite (GOES-17) to the east across images taken between 04:16 and 06:36 UTC, after which the Sun set. In addition, we perform a more detailed analysis of the 04:36 UTC imagery from Himawari-8 and GK-2A to map variations in altitude across the plume, which is shown in Fig. 2. Because these methods rely on manual point selection and analysis, they cannot map altitude across the whole plume. To gain a broad perspective of plume altitude, we therefore also applied a stereoscopic vision tool to estimate altitude, which is less accurate but can provide spatial information, and the standard temperature-based

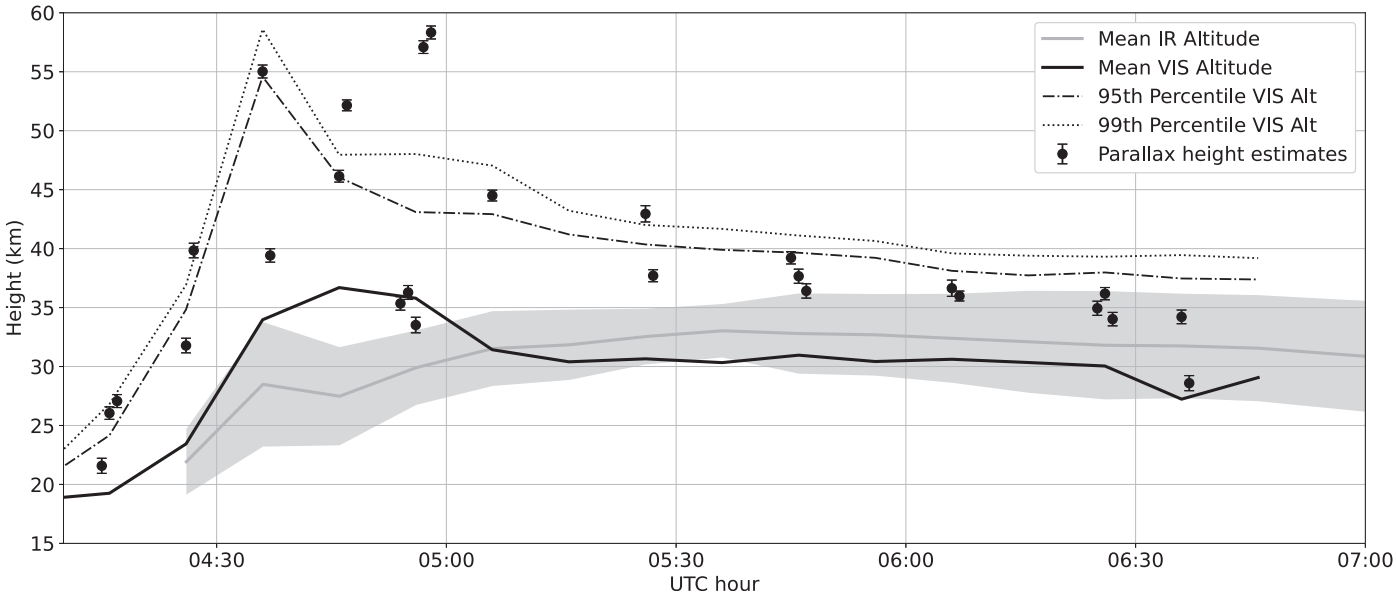


Fig. 3. Temporal evolution of volcanic plume altitude derived from visible and infrared data. Infrared (IR) heights are derived from Himawari-8 brightness temperature measurements and the ECMWF temperature profile. The gray-shaded area represents one standard deviation from the mean. The blue lines indicate altitudes estimated by the stereoscopic method applied to VIS (visible) data across the entire volcanic plume, and the green markers are parallax heights derived from a manual analysis of data from Himawari-8, GK-2A, and GOES-17. Error bars show the spread of estimated altitudes due to simulated geolocation uncertainty. Because of sunset, no visible altitudes are available after 06:46 UTC. All times given are for 15 January 2022.

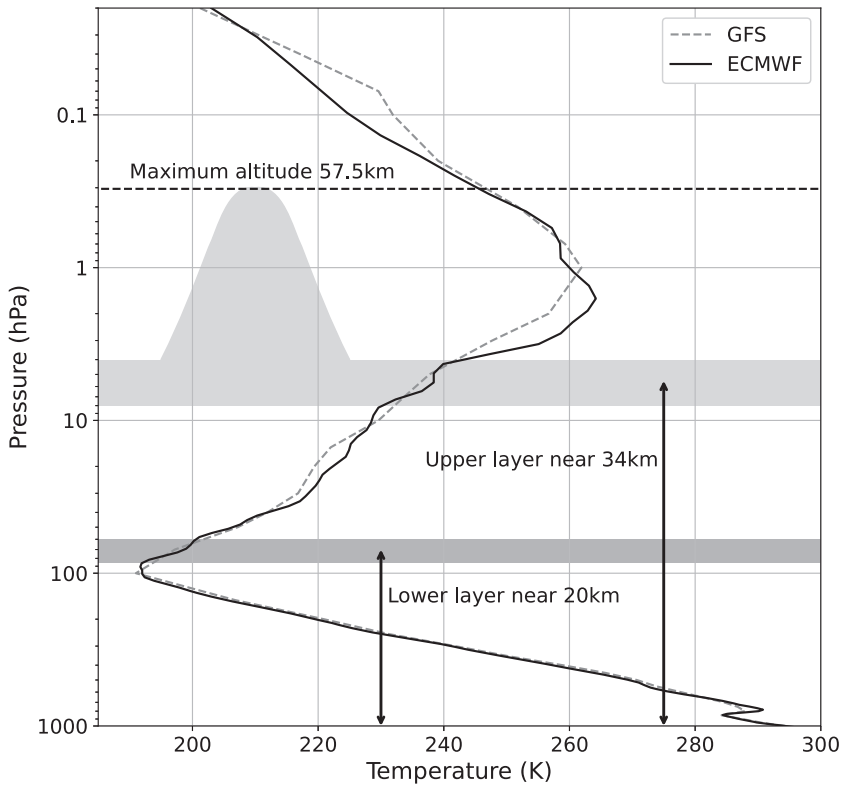


Fig. 4. Vertical structure of the volcanic plume. Represented are a lower near-tropopause layer, the altitude of which cannot be accurately determined; the main umbrella at higher altitude; and the dome-like protrusion seen in the 04:30 UTC satellite images from 15 January 2022. Layer thickness is computed from the spread of parallax-based altitude retrievals for each layer and, when optically thick, by using the infrared brightness temperature approach. Overlaid are the 00:00 UTC Global Forecast System (GFS) and ECMWF temperature profiles that show the tropopause near 100 hPa and the stratopause between 1 and 1.5 hPa.

retrieval described earlier in the text. The results of all three techniques are shown in Fig. 3. Further information on the methods used here, including tables of parallax-retrieved altitudes, is given in the supplementary materials.

Altitude retrievals from the early phase of the eruption show a rapidly ascending plume that reached 25 km about 15 min after the eruption began and 40 km, in the upper stratosphere, after 25 min. By 04:36 UTC, a half hour after the eruption began, a dome, ~90 km in diameter, was visible that extended from 34 km up to 57 km altitude (~0.3 hPa in the ECMWF analysis), which is 13 km above the local stratopause (1.5 hPa)—well within the mesosphere. We estimate the uncertainty on this altitude to be less than 1.5 km. Encircling this dome was a donut-shaped structure with altitudes peaking at 41 km (2.2 hPa) and a secondary layer just above the ECMWF tropopause at 17.5 km (91 hPa). A schematic of the eruption at this point is shown in Fig. 4. Ten minutes later, the dome collapsed to leave the expanding donut cloud, although the haziness visible in the central region above the volcano indicates that high-altitude aerosols such as sulfates or ash are likely to be present. This haze is too optically thin, though, to support altitude retrieval. By 04:56 UTC, the eruption had produced a vertical column stretching from the surface to the mesosphere, including two tendrils that reached 58 km (0.28 hPa). These tendrils cast a shadow onto the remaining volcanic cloud at 35-km altitude, and calculating tendril altitude from the shadow length gives an altitude of 57.5 km, which closely matches the parallax-derived altitude. Thereafter, as shown in Fig. 3, peak altitude decreased, and no further mesospheric intrusions were detected. Analysis of the infrared imagery shows two clouds over the next 12 hours: One moving south-west in the prevailing winds at 30 to 35 km altitude and one moving east at the tropopause.

The influence of volcanoes on the mesosphere is unclear. Previous eruptions into the stratosphere have indirectly affected the mesosphere through the upward-ascent transport of volcanic aerosols after an eruption (*27*), although the chemical processes acting on mesospheric volcanic aerosols are the subject of debate (*28*). Vertical propagation of gravity waves from volcanoes can affect the mesospheric temperature (*29*), whereas the aerosols and water vapor injected to high altitude by the 1883 Krakatoa eruption may have been responsible for subsequent apparent increases in mesospheric clouds. However, there is no agreement as to why some volcanic eruptions but not others are associated with mesospheric cloud increases (*30*). Our observations of the HTHH plume provide direct evidence that volcanic eruptions can inject material into the mesosphere and will enable a more detailed analysis of mesospheric chemistry and transport.

However, our work also raises questions: What mechanisms contributed to this eruption reaching such high altitude but with little SO_2 being observed? What is the composition of the hazy substance that is visible atop the highest portions of the plume, and how long will it persist in the mesosphere? In addition, we show that the mesospheric altitudes achieved by this plume were only visible in satellite images taken at two times (those starting at 04:30 and 04:50 UTC), highlighting the importance of frequent, every 10 min in this case, satellite observations. Previous eruptions were observed much less frequently by satellite, once every hour by only one satellite (GMS-4) in the case of Mount Pinatubo, meaning that the peak altitude reached by the volcanic plume is likely to have fallen between observations and that parallax-based height estimates were not possible. If the 2022 HTHH eruption had been observed by the same satellite as that in the case of Mount Pinatubo, the peak altitudes observed would have been substantially lower than those described here: 32 km per infrared data and 39 km using the shadow technique used for Mount Pinatubo (*14*).

REFERENCES AND NOTES

1. A. Robock, *Rev. Geophys.* **38**, 191–219 (2000).
2. T. J. Casadevall, Ed., "Volcanic ash and aviation safety: Proceedings of the first international symposium on volcanic ash and aviation safety" (US Geological Survey Bulletin 2047, US Government Printing Office, 1994).
3. S. C. Loughlin, S. Sparks, S. K. Brown, S. F. Jenkins, C. Vye-Brown, Eds., *Global Volcanic Hazards and Risk* (Cambridge Univ. Press, 2015).
4. T. M. Wilson, S. Jenkins, C. Stewart, in *Volcanic Hazards, Risks and Disasters*, J. F. Shroder, P. Papale, Eds. (Elsevier, 2015), pp. 47–86.
5. C. Schnetzler, G. Bluth, A. Krueger, L. Walter, *J. Geophys. Res.* **102**, 20087–20091 (1997).
6. S. Kremser *et al.*, *Rev. Geophys.* **54**, 278–335 (2016).
7. J. Hansen, A. Lacis, R. Ruedy, M. Sato, *Geophys. Res. Lett.* **19**, 215–218 (1992).
8. G. L. Stenchikov *et al.*, *J. Geophys. Res.* **103**, 13837–13857 (1998).
9. E. G. Dutton, J. R. Christy, *Geophys. Res. Lett.* **19**, 2313–2316 (1992).
10. K. Labitzke, M. P. McCormick, *Geophys. Res. Lett.* **19**, 207–210 (1992).
11. A. Bernard, W. I. Rose Jr., *Nat. Hazards* **3**, 59–67 (1990).
12. S. Carn, L. Clarisse, A. Prata, *J. Volcanol. Geotherm. Res.* **311**, 99–134 (2016).
13. S. Guo, G. J. Bluth, W. I. Rose, I. M. Watson, A. Prata, *Geochem. Geophys. Geosyst.* **5**, Q04001 (2004).
14. R. E. Holasek, S. Self, A. W. Woods, *J. Geophys. Res.* **101**, 27635–27655 (1996).
15. A. Krueger, N. Krotkov, S. Carn, *J. Volcanol. Geotherm. Res.* **175**, 408–414 (2008).
16. M. Matson, *J. Volcanol. Geotherm. Res.* **23**, 1–10 (1984).
17. M. Brenna *et al.*, *Lithos* **412-413**, 106614 (2022).
18. A. T. Prata *et al.*, *Sci. Rep.* **10**, 3584 (2020).
19. Global Volcanism Program, in vol. 47 of the *Bulletin of the Global Volcanism Network*, A. E. Crafford, E. Venzke, Eds. (Smithsonian Institution, 2022).

20. M. Zuo *et al.*, *Adv. Atmos. Sci.* 10.1007/s00376-022-2034-1 (2022).
21. W. I. Rose *et al.*, *Nature* **375**, 477–479 (1995).
22. D. A. Yuen *et al.*, *Earthquake Research Advances* **2**, 100134 (2022).
23. R. G. Owens, T. Hewson, "ECMWF forecast user guide" (European Centre for Medium-Range Weather Forecasts, 2018).
24. C. Oppenheimer, *Int. J. Remote Sens.* **19**, 2829–2864 (1998).
25. L. Merucci, K. Zakšek, E. Carboni, S. Corradini, *Remote Sens.* **8**, 206 (2016).
26. S. Proud, *Geophys. Res. Lett.* **40**, 3351–3355 (2013).
27. M. J. Mills, O. B. Toon, G. E. Thomas, *J. Geophys. Res. D Atmospheres* **110**, D24208 (2005).
28. C. George *et al.*, in *Atmospheric and Aerosol Chemistry*, V. McNeill, P. Ariya, Eds. (Topics in Current Chemistry 339, Springer, 2012), pp. 1–53.
29. C. von Savigny *et al.*, *Meteorol. Z.* **29**, 3–18 (2020).
30. C. Bertolin, F. Domínguez-Castro, *Holocene* **30**, 682–690 (2020).

ACKNOWLEDGMENTS

We thank J. Amos for the initial recognition that this eruption reached the mesosphere and acknowledge helpful discussions with E. Carboni and R. Grainger regarding the HTHH eruption and drafts of this paper. We also acknowledge the NOAA's Big Data Program for making GFS, GOES-17, and Himawari-8 data openly accessible; the Japan Meteorological Agency for its Himawari-8 data access; and the Korea Meteorological Administration (KMA) for making GEO-KOMPSAT-2A data available via its open application programming interface (API). We also thank the ECMWF for provision of the temperature vertical profile analysis used in this study. **Funding:** S.R.P.'s work on this study was funded as part of NERC's support of the National Centre for Earth Observation, award ref. NE/R016518/1; and by a NERC Innovation fellowship, award ref. NE/R013144/1. A.T.P. was funded by NERC's support of the Radar-supported Next-Generation Forecasting of Volcanic Ash Hazard project, award ref. NE/S003843/1. **Author contributions:** S.R.P. formulated the research, wrote the parallax and infrared retrieval code, and analyzed the results. A.T.P. also analyzed the results, and both S.R.P. and A.T.P. contributed to drafting the manuscript. S.S. devised and performed the stereoscopic height retrievals. **Competing interests:** The authors declare no competing interests. **Data and materials availability:** GOES-16 and Himawari-8 satellite data are available through NOAA's Big Data Program: https://www.noaa.gov/nodd/datasets. GK-2A data are available via KMA's open data API: https://datasvc.nmsc.kma.go.kr/. ECMWF and GFS profile data (filename TProfs.csv) and the Python code used to perform this analysis are available on GitHub: https://github.com/simonrp84/Tonga_Volcano_Code. The lists of points used for tri- and dual-satellite parallax calculations are also on the same GitHub page (filenames Points_Dual.csv and Points_Tri.csv). The infrared and stereoscopic retrieval outputs are in the Height_Out and Heightmap subdirectories, respectively. **License information:** Copyright © 2022 the authors, some rights reserved; exclusive licensee American Association for the Advancement of Science. No claim to original US government works. https://www.science.org/about/science-licenses-journal-article-reuse

SUPPLEMENTARY MATERIALS

science.org/doi/10.1126/science.abo4076
Materials and Methods
Table S1
References (*31*–*38*)

Submitted 1 February 2022; accepted 8 October 2022
10.1126/science.abo4076

QUANTUM TECHNOLOGY

Robust multi-qubit quantum network node with integrated error detection

P.-J. Stas[1]*, Y. Q. Huan[1]*, B. Machielse[1,2]*, E. N. Knall[3], A. Suleymanzade[1], B. Pingault[3,4,5], M. Sutula[1], S. W. Ding[3], C. M. Knaut[1], D. R. Assumpcao[3], Y.-C. Wei[1], M. K. Bhaskar[1,2], R. Riedinger[1,6,7], D. D. Sukachev[1,2], H. Park[1,8], M. Lončar[3], D. S. Levonian[1,2], M. D. Lukin[1]†

Long-distance quantum communication and networking require quantum memory nodes with efficient optical interfaces and long memory times. We report the realization of an integrated two-qubit network node based on silicon-vacancy centers (SiVs) in diamond nanophotonic cavities. Our qubit register consists of the SiV electron spin acting as a communication qubit and the strongly coupled silicon-29 nuclear spin acting as a memory qubit with a quantum memory time exceeding 2 seconds. By using a highly strained SiV, we realize electron-photon entangling gates at temperatures up to 1.5 kelvin and nucleus-photon entangling gates up to 4.3 kelvin. We also demonstrate efficient error detection in nuclear spin–photon gates by using the electron spin as a flag qubit, making this platform a promising candidate for scalable quantum repeaters.

The ability to distribute quantum information over extended distances (*1*, *2*) constitutes an important enabling technology in quantum information science, with applications in quantum key distribution (*3*, *4*), nonlocal sensing (*5*), and distributed quantum computation (*6*, *7*). A key requirement for the realization of such long-distance quantum networking involves the development of quantum repeaters (*8*) to mitigate photonic qubit loss during transmission over extended distances. These require network nodes containing multiple qubits that can collect, store, and process information communicated through photonic channels (*9*). Although theoretical proposals for all-photonic repeater schemes (*10*) potentially circumvent this requirement, they involve efficient sources of large-scale photonic states, which are very challenging to realize.

Color centers in diamond nanophotonic structures (*11*–*14*) have recently emerged as leading candidates for realizing such nodes owing to their long coherence times, high-fidelity single-qubit gates, efficient qubit-photon interfaces, and high experimental repetition rates. The integration of all these features into a single device has led to the demonstration of memory-enhanced quantum communication (*11*) with the silicon-vacancy (SiV) center. Important steps toward quantum networking have been taken by using multi-qubit registers based on nitrogen-vacancy (NV) centers and nearby nuclear spins (*15*), but the low coupling efficiency to photons makes scalability challenging. Although other promising platforms, such as trapped ions (*16*) and neutral atoms (*17*) in optical cavities, achieved efficient coupling to photons, scalable implementation of quantum repeaters requires access to auxiliary memory qubits to perform entanglement swapping, purification, and error detection (*8*, *9*), which thus far has been challenging to achieve in a single setting. For SiVs, the technical complexity associated with the need for operation at dilution refrigerator temperatures [required to avoid phonon-induced dephasing (*18*)] has thus far impeded the prospects for scalability. Here, we address this long-standing challenge by using a highly strained SiV (*18*, *19*) featuring the ^{29}Si isotope, with its nuclear spin (*20*) serving as a deterministic long-lived memory qubit. We demonstrate full control of this integrated two-qubit register at increased temperatures, including selective qubit readout via a phase-based readout method, enabling multiple electron state resets before deterioration of the nuclear spin memory.

The ^{29}SiV in an external magnetic field constitutes a two-qubit system of four spin states with nondegenerate transition frequencies (Fig. 1A). The electron and nuclear spin qubits are coherently controlled by using microwave (MW) and radiofrequency (RF) pulses, respectively, which are delivered through gold coplanar waveguides (Fig. 1B). The SiV is embedded in a nanophotonic cavity (Fig. 1C), which enhances optical transitions to the excited-state manifold at 737 nm (Fig. 1A, wavy arrows) that is used for state readout and spin-photon entanglement. The SiV-cavity system exhibits high-contrast spin-dependent reflection spectra (Fig. 1D) enabled by the strong cavity coupling [cooperativity $C = 1.6$ (*21*)].

High-fidelity resonant readout of the electron state is achieved by measuring the reflected intensity of a laser at the frequency of

[1]Department of Physics, Harvard University, Cambridge, MA 02138, USA. [2]AWS Center for Quantum Networking, Boston, MA 02210, USA. [3]John A. Paulson School of Engineering and Applied Sciences, Harvard University, Cambridge, MA 02138, USA. [4]QuTech, Delft University of Technology, 2600 GA Delft, Netherlands. [5]Kavli Institute of Nanoscience Delft, Delft University of Technology, 2600 GA Delft, Netherlands. [6]Institut für Laserphysik und Zentrum für Optische Quantentechnologien, Universität Hamburg, 22761 Hamburg, Germany. [7]The Hamburg Centre for Ultrafast Imaging, 22761 Hamburg, Germany. [8]Department of Chemistry and Chemical Biology, Harvard University, Cambridge, MA 02138, USA.
*These authors contributed equally to this work.
†Corresponding author. Email: lukin@physics.harvard.edu

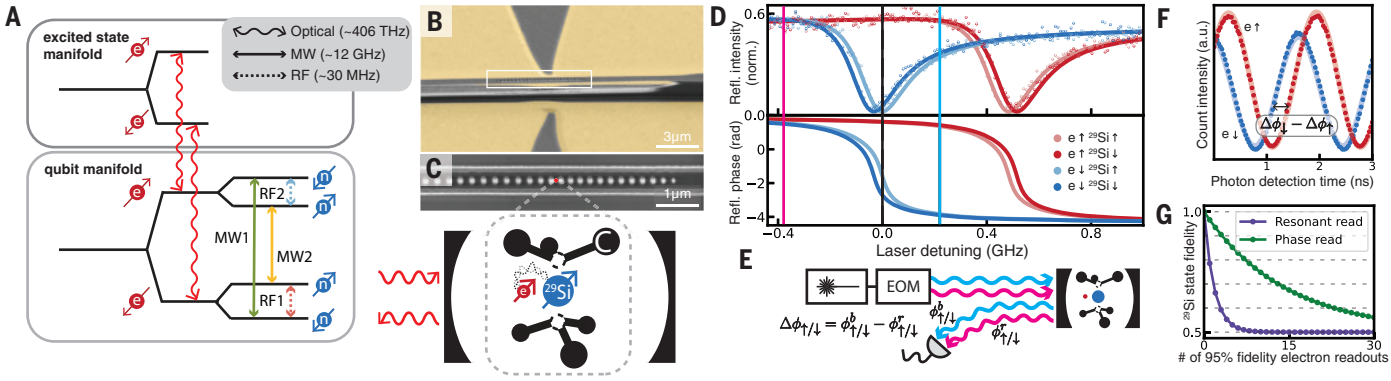


Fig. 1. Quantum network node based on ^{29}SiV. (**A**) Energy-level diagram of the ^{29}SiV. Allowed magnetic dipole transitions are shown by arrows in the qubit manifold for the case when the **B**-field is oriented along the symmetry axis. (**B**) False-color scanning electron microscope (SEM) image of the device, showing the gold coplanar waveguides in yellow. (**C**) Zoomed-in SEM image of the nanophotonic cavity in which the ^{29}SiV is located. (**D**) Spin-dependent reflection intensity (top) and phase (bottom) as a function of laser frequency with a cavity-SiV detuning of $\Delta = 69$ GHz chosen to maximize optical contrast. (**E**) Experimental setup for phase readout of the electron spin state. (**F**) Measured spin-dependent phase shift of the beating pattern between sidebands. (**G**) Coherence of a nuclear superposition state as a function of the number of electron readouts for resonant and phase readouts.

maximum reflection intensity contrast (Fig. 1D, black line) (*11*). However, the nuclear qubit experiences dephasing from the laser during readout, with the highest decoherence rate occurring when the laser is near the resonant readout frequency (*21*). To enable selective readout of the electronic spin qubit, we probe the system at laser frequencies at which minimal nuclear dephasing occurs and make use of the electron spin–dependent phase—instead of intensity—of reflected photons for readout. Using an electro-optic modulator (EOM) to generate sidebands (Fig. 1E), we send two tones (blue and magenta lines in Fig. 1D) along the same path and measure the spin-dependent reflected phase difference via the resulting beating pattern to determine the electron state (Fig. 1F) (*21*). With this phase-based readout, the electron can be read 14 times at 95% fidelity before causing a $1/e$ loss of nuclear coherence. This constitutes an eightfold improvement over the resonant readout method (Fig. 1G), with further improvements expected through cavity design and magnetic field optimization (*21*).

The two-qubit ^{29}SiV system is fully controlled by selectively driving the four single-spin–flipping transitions (Fig. 1A) to implement the four possible controlled-NOT (CNOT) gates: two electron-flipping gates C_nNOT_e (MW1) and $\overline{C_nNOT_e}$ (MW2), and two nucleus-flipping gates C_eNOT_n (RF1) and $\overline{C_eNOT_n}$ (RF2), where the absence (presence) of the overbar indicates conditioning on the control spin being in the down (up) state. We measure a fidelity of $99.9 \pm 0.1\%$ for the C_nNOT_e gate with a gate time of 30.0 ns. As the time to drive a nuclear π rotation (23 μs) is longer than the electron dephasing time $T^*_{2,e}$ (5 μs) (*21*), transfer of electron superposition states onto the nucleus is not possible with direct driving for the C_eNOT_n gate. To circumvent this problem, we increase the electron coherence time using a dynamical decoupling sequence and interleave it with stepwise nuclear rotations (*22*, *23*) to implement a decoupled C_eNOT_n (Fig. 2A). Specifically, we apply RF1 in the first window, and alternate it with applying RF2 after every subsequent unconditional electron π pulse to account for the flipping electron state while keeping the nuclear rotation conditional on the same initial electron state, achieving a gate fidelity of $93.7 \pm 0.7\%$ (*21*) within a gate time of 29.2 μs. With the decoupled C_eNOT_n, we can swap a superposition state from the electron onto the nuclear spin state (Fig. 2B), where it can be stored using an XY8 decoupling sequence. We find that the nuclear coherence time scales with n,

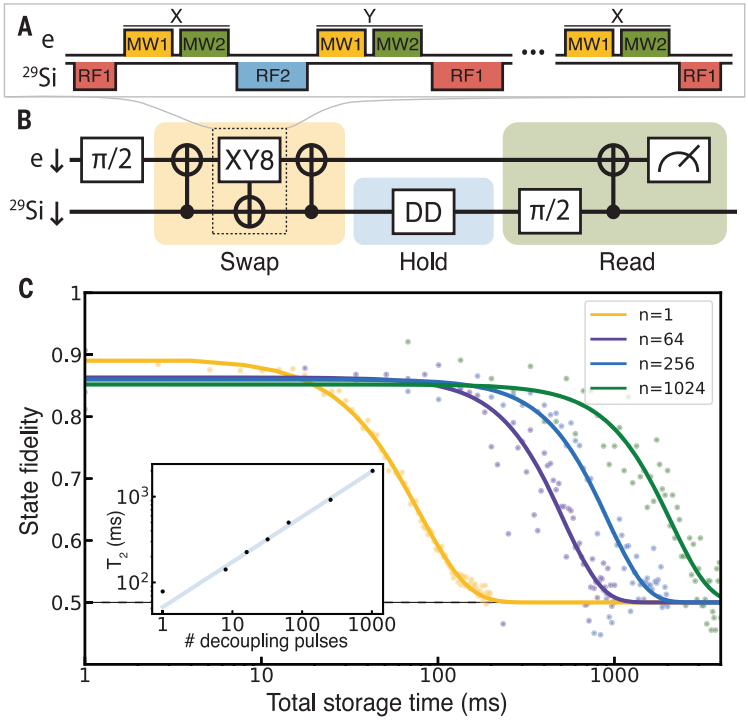


Fig. 2. Long-lived quantum memory based on ^{29}Si nuclear spin. (**A**) Pulse sequence for a decoupled C_eNOT_n gate. (**B**) Sequence for swapping the electron state onto the nucleus, after which a nuclear XY8 decoupling sequence with $n = 1, 64, 256, 1024$ pulses is applied and the nuclear state is measured through resonant readout of the electron. (**C**) Measured nuclear state fidelity after sequence (B). Inset: $T_{2,n}$ as a function of the number of decoupling pulses n fitted to $T_{2,n} \propto n^{\alpha}$ where $\alpha = 0.53$.

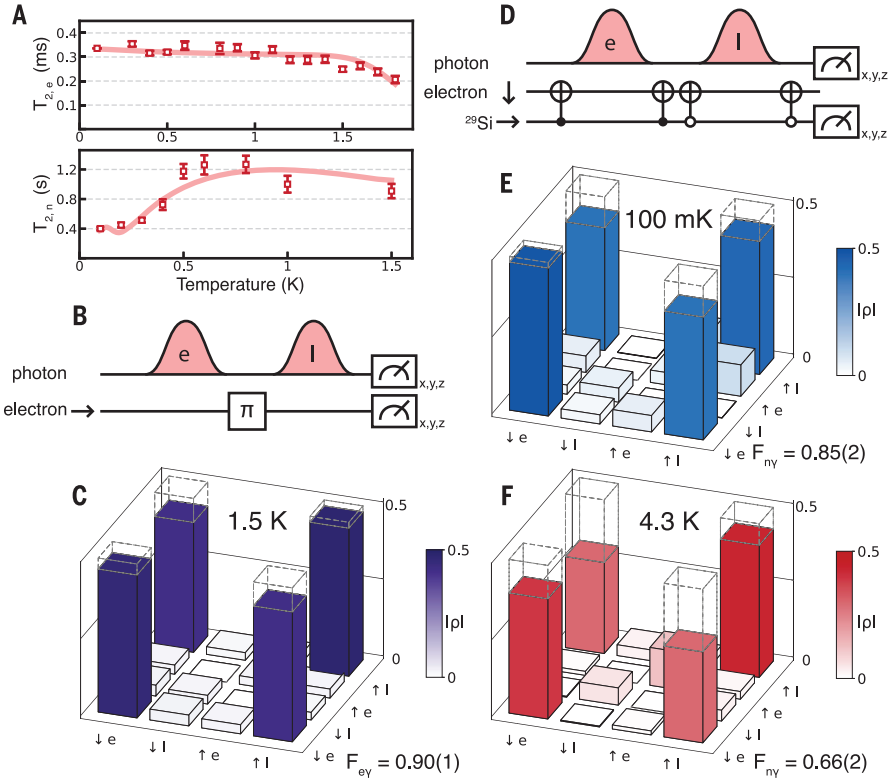


Fig. 3. Spin-photon entanglement at elevated temperatures. (**A**) Coherence time of the electron (top) and nucleus (bottom) obtained using 8-XY8 sequences as a function of temperature. Initial increase of the nuclear $T_{2,n}$ is due to motional averaging of the noise bath. Solid lines are fits to decoherence models of the spin environment described in (*21*). (**B**) Electron spin–photon gate implementation with (**C**) reconstructed density matrix at 1.5 K using resonant electron readout. (**D**) Circuit diagram for the photon-nucleus entangling (PHONE) gate. CNOT gates with black and white control dots refer to C_nNOT_e and $\overline{C_nNOT_e}$ gates, respectively. Reconstructed density matrices for photon-nuclear spin entanglement at (**E**) 100 mK and (**F**) 4.3 K.

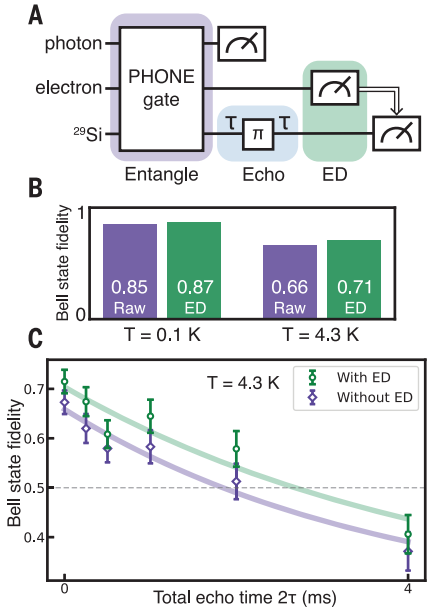


Fig. 4. Spin-photon entanglement with integrated error detection. (**A**) Gate sequence for entanglement between a photon and nucleus and subsequent state storage with error detection (ED) based on resonant readout of the electronic spin. (**B**) Bell state fidelity improvement with ED at 0.1 K and 4.3 K. (**C**) Bell state fidelity as a function of storage time for the sequence shown in (A) before and after error detection. Fits are exponential curves decaying to the maximally mixed-state fidelity $\Phi^+\rho_{mm}\Phi^+ = 0.25$ as the nuclear lifetime $T_{1,n}$ is comparable to the coherence time; fitted decay constants are 4.5 (3.8) ms with (without) ED.

the number of decoupling pulses applied, as $T_{2,n} \propto n^{0.53}$ with a maximum measured nuclear memory time of $T_{2,n} = 2.1 \pm 0.1$ s (Fig. 2C) when using a 128-XY8 sequence.

To enable robust spin-photon entanglement, we use a SiV with large residual strain [ground state splitting $\Delta_{GS} = 554$ GHz (*21*)], which greatly suppresses the rate of thermal decoherence processes (*19*), enabling operation at 1.5 K without an appreciable reduction in $T_{2,e}$ (Fig. 3A). We implement high-temperature spin-photon entangling gates between the electron spin and time-bin qubits in the $\{e, l\}$ basis, corresponding to the presence of a photon in either the early or late time bin. The entangling gate sequence (*11*) shown in Fig. 3B generates the entangled state $(e\downarrow_e + l\uparrow_e)/\sqrt{2}$ conditioned on the detection of a single reflected photon. We find a Bell state fidelity of $F_{e\gamma} = 0.91 \pm 0.02$ (0.90 ± 0.01) at 0.1 K (1.5 K) (Fig. 3C), which is primarily limited by residual reflections from the $\downarrow_e$ state and imperfect photonic state measurements.

To further extend the entanglement capabilities of our spin-photon interface, we introduce a photon-nucleus entangling (PHONE) gate that directly entangles the ^{29}Si nuclear spin with a photonic qubit using only fast MW gates and allows operating temperatures up to 4.3 K. In this scheme, the photon-nucleus-electron system is initialized in the $(e + l)(\uparrow_n + \downarrow_n)\downarrow_e/2$ state, and we apply a sequence of CNOTs as shown in Fig. 3D such that the electron state—and as a result, the SiV reflectivity—in each time bin is conditional on the nuclear state; the final entangled state is given by $(e\uparrow_n + l\downarrow_n)\downarrow_e/\sqrt{2}$. We measure the resulting Bell state fidelity to be $F_{n\gamma} = 0.85 \pm 0.02$ (0.66 ± 0.02) at 0.1 K (4.3 K) (Fig. 3, E and F), with dominant infidelities due to MW gate errors and the nuclear state dependence of the optical transition frequency, which prevents the photon frequency from being tuned to maximize contrast for both nuclear spin states simultaneously (Fig. 1D) (*21*).

A key feature of the PHONE gate is that the electron should always remain in the $\downarrow_e$ state after a successful gate application. Because the electron spin mediates the interface between the photon and the nucleus, electron spin flips can be used as an integrated error witness to detect gate errors. Similar to flag qubits in error correction protocols (*24*), PHONE gate errors can be reduced at the cost of some gate failure probability (*25*) by measuring the state of the electron spin qubit (Fig. 4A). Specifically, if the electron spin is measured to be in the $\uparrow_e$ state after a PHONE gate application, the prepared photon–nuclear spin entangled state is discarded. As shown in Fig. 4B, the use of the procedure results in a Bell state fidelity increase of 2% (7%) to $F_{n\gamma} = 0.87 \pm 0.02$ (0.71 ± 0.02) with an error detection rate of 8.4% (13.9%) at 0.1 K (4.3 K). In Fig. 4C, we combine all these components to implement a PHONE gate at 4.3 K with error detection and store the spin-photon entangled state in the nuclear spin memory using an echo sequence (Fig. 4A) for more than 2.5 ms above the threshold value of 50%, as compared to 1.5 ms without error detection. The error detection protocol detects MW gate errors and $T_{1,e}$- and $T_{2,e}$-limited depolarization and dephasing, and the large gain in fidelity at 4.3 K is due to the greater contribution of the detectable errors from short $T_{1,e}$ and $T_{2,e}$ times at this temperature (*21*). Conversely, the improvement from error detection at 0.1 K is limited as the

from photon state measurement and SiV optical contrast.

These observations open up several new avenues for realizing quantum networks and exploring their applications. The access to an additional memory qubit directly enables improved memory-enhanced quantum key distribution (*11*) by extending the time window for photons arriving from different communicating parties to the memory node for asynchronous Bell measurement, whereas the phase readout protocol facilitates electron resets between entanglement attempts while information is stored on the nucleus. A nuclear memory can additionally expand the capabilities of the SiV as a single photon source for the creation of photonic cluster states (*26*, *27*). The methods demonstrated here can also enable the deployment of scalable SiV-based quantum repeater networks. Based on a large-scale survey of a second chip fabricated using the current process (*21*), we find that more than 11% of all SiVs are sufficiently strained for operation at 1.5 K, indicating the possibility for a sizable number of highly strained devices in nanophotonic cavities that can operate at elevated temperatures. Moreover, recently demonstrated techniques for strain tuning of nanocavities (*28*) can enable fully deterministic access to high-strain operation. The fidelity gain from our error detection could be larger for more complex spin-photon entangling sequences, such as PHONE-type gates entangling successive photons with the nucleus or entangling a photon with multiple nuclei strongly coupled to the SiV. It also opens opportunities to operate more effectively in regimes where the SiV electron coherence properties deteriorate, including at higher temperatures as demonstrated here, and in a misaligned magnetic field as is required for acoustic spin control (*29*) and single-photon generation (*30*). The use of cavities with higher cooperativity as demonstrated previously (*11*) should allow for higher fidelity and efficiency of electron-spin photon and PHONE gates, as well as improved ^{29}Si state preservation during electron readout (*21*). Finally, nearby ^{13}C spins, such as one associated with the SiV used in this work (*21*), can be used as additional memory resources (*15*, *22*). Apart from realizing multi-node quantum network protocols (*8*, *9*), these systems can also allow for the generation of complex photonic tree cluster states that enable robust one-way long-distance quantum communication (*31*).

REFERENCES AND NOTES

1. H. J. Kimble, *Nature* **453**, 1023–1030 (2008).
2. S. Wehner, D. Elkouss, R. Hanson, *Science* **362**, eaam9288 (2018).
3. A. K. Ekert, *Phys. Rev. Lett.* **67**, 661–663 (1991).
4. H.-K. Lo, M. Curty, K. Tamaki, *Nat. Photonics* **8**, 595–604 (2014).
5. E. T. Khabiboulline, J. Borregaard, K. De Greve, M. D. Lukin, *Phys. Rev. Lett.* **123**, 070504 (2019).
6. H. Buhrman, H. Röhrig, *Mathematical Foundations of Computer Science 2003* (Springer Berlin Heidelberg, 2003), pp. 1–20.
7. D. Cuomo, M. Caleffi, A. S. Cacciapuoti, *IET Quantum Commun.* **1**, 3–8 (2020).
8. W. Dür, H.-J. Briegel, J. I. Cirac, P. Zoller, *Phys. Rev. A* **59**, 169–181 (1999).
9. L. Childress, J. M. Taylor, A. S. Sørensen, M. D. Lukin, *Phys. Rev. Lett.* **96**, 070504 (2006).
10. K. Azuma, K. Tamaki, H.-K. Lo, *Nat. Commun.* **6**, 6787 (2015).
11. M. K. Bhaskar *et al.*, *Nature* **580**, 60–64 (2020).
12. E. R. Schmidgall *et al.*, *Nano Lett.* **18**, 1175–1179 (2018).
13. A. E. Rugar *et al.*, *ACS Photonics* **7**, 2356–2361 (2020).
14. X. Guo *et al.*, *Nano Lett.* **21**, 10392–10399 (2021).
15. M. Pompili *et al.*, *Science* **372**, 259–264 (2021).
16. J. Schupp *et al.*, *PRX Quantum* **2**, 020331 (2021).
17. A. Reiserer, N. Kalb, G. Rempe, S. Ritter, *Nature* **508**, 237–240 (2014).
18. K. D. Jahnke *et al.*, *New J. Phys.* **17**, 043011 (2015).
19. S. Meesala *et al.*, *Phys. Rev. B* **97**, 205444 (2018).
20. B. Pingault *et al.*, *Nat. Commun.* **8**, 15579 (2017).
21. Further details on theoretical analysis and additional supporting experimental results are provided in the supplementary materials.
22. C. Bradley *et al.*, *Phys. Rev. X* **9**, 031045 (2019).
23. T. van der Sar *et al.*, *Nature* **484**, 82–86 (2012).
24. R. Chao, B. W. Reichardt, *Phys. Rev. Lett.* **121**, 050502 (2018).
25. J. Borregaard, P. Kómár, E. M. Kessler, A. S. Sørensen, M. D. Lukin, *Phys. Rev. Lett.* **114**, 110502 (2015).
26. A. Russo, E. Barnes, S. E. Economou, *Phys. Rev. B* **98**, 085303 (2018).
27. C. P. Michaels *et al.*, *Quantum* **5**, 565 (2021).
28. B. Machielse *et al.*, *Phys. Rev. X* **9**, 031022 (2019).
29. S. Maity *et al.*, *Phys. Rev. X* **12**, 011056 (2022).
30. E. N. Knall *et al.*, *Phys. Rev. Lett.* **129**, 053603 (2022).
31. J. Borregaard *et al.*, *Phys. Rev. X* **10**, 021071 (2020).
32. P.-J. Stas *et al.*, Zenodo (2022). https://doi.org/10.5281/zenodo.7101712.

ACKNOWLEDGMENTS

We thank J. Borregaard for discussions and J. MacArthur for assistance with electronics. **Funding:** This work was supported by the NSF, CUA, DoD/ARO DURIP, AFOSR MURI, and DOE (award no. DE-SC0020115). Devices were fabricated at Harvard CNS, NSF award no. 1541959. Y.Q.H. acknowledges support from the A*STAR National Science Scholarship. D.A., E.N.K., and B.M. acknowledge support from an NSF GRFP No. DGE1745303. B.P. acknowledges support through a Marie Skłodowska-Curie fellowship from the European Union's Horizon 2020 research and innovation programme under the Grant Agreement No. 840968 (COHESiV). M.S. acknowledges funding from the NASA Space Technology Graduate Research Fellowship Program. R.R. acknowledges support from the Alexander von Humboldt Foundation and the Cluster of Excellence 'Advanced Imaging of Matter' of the Deutsche Forschungsgemeinschaft (DFG) - EXC 2056 - project ID 390715994. **Author contributions:** P.-J.S., Y.Q.H., B.M., and D.S.L. performed the measurements and analyzed data. B.M. and E.N.K. fabricated the devices. A.S., B.P., M.S., S.D., C.M.K., D.R.A., Y.-C.W., M.B., R.R., and D.S. assisted with experiments. All work was supervised by H.P., M.L., and M.D.L. All authors discussed the results and contributed to the manuscript. **Competing interests:** The authors declare that there are no competing financial interests. **Data and materials availability:** Data and code can be found on Zenodo (*32*). **License information:** Copyright © 2022 the authors, some rights reserved; exclusive licensee American Association for the Advancement of Science. No claim to original US government works. https://www.science.org/about/science-licenses-journal-article-reuse

SUPPLEMENTARY MATERIALS

science.org/doi/10.1126/science.add9771
Supplementary Text
Figs. S1 to S15
Tables S1 to S6
References (*33*–*56*)

Submitted 17 July 2022; accepted 27 September 2022
10.1126/science.add9771

MONKEYPOX

Multiple lineages of monkeypox virus detected in the United States, 2021–2022

Crystal M. Gigante[1], Bette Korber[2], Matthew H. Seabolt[1,3], Kimberly Wilkins[1], Whitni Davidson[1], Agam K. Rao[1], Hui Zhao[1], Todd G. Smith[1], Christine M. Hughes[1], Faisal Minhaj[1], Michelle A. Waltenburg[1], James Theiler[4], Sandra Smole[5], Glen R. Gallagher[5], David Blythe[6], Robert Myers[6], Joann Schulte[7], Joey Stringer[7], Philip Lee[8], Rafael M. Mendoza[9], LaToya A. Griffin-Thomas[10], Jenny Crain[11], Jade Murray[12], Annette Atkinson[12], Anthony H. Gonzalez[13], June Nash[13], Dhwani Batra[1], Inger Damon[1], Jennifer McQuiston[1], Christina L. Hutson[1], Andrea M. McCollum[1], Yu Li[1]*

Monkeypox is a viral zoonotic disease endemic in Central and West Africa. In May 2022, dozens of non-endemic countries reported hundreds of monkeypox cases, most with no epidemiological link to Africa. We identified two lineages of monkeypox virus (MPXV) among two 2021 and seven 2022 US monkeypox cases: the major 2022 outbreak variant called B.1 and a minor contemporaneously sampled variant called A.2. Analyses of mutations among these two variants revealed an extreme preference for GA-to-AA mutations indicative of human APOBEC3 cytosine deaminase activity among Clade IIb MPXV (previously West African, Nigeria) sampled since 2017. Such mutations were not enriched within other MPXV clades. These findings suggest that APOBEC3 editing may be a recurrent and a dominant driver of MPXV evolution within the current outbreak.

Monkeypox is a viral zoonotic disease caused by monkeypox virus (MPXV) that is endemic in West and Central Africa. There have been several reported cases of travel-associated monkeypox in non-African countries in recent years. In 2003, an outbreak of monkeypox in the United States was linked to imported African small mammals (*1*). In 2017, the largest monkeypox outbreak in western Africa occurred in Nigeria after decades of no identified cases (*2*), and during 2018 to 2021, eight cases were exported from Nigeria to non-endemic countries (*2*–*5*). In 2021, there were two US monkeypox cases in travelers from Nigeria, one in Maryland and one in Texas (*4*, *5*). In May of 2022, this pattern of monkeypox cases in travelers from Nigeria shifted. As of 28 September 2022, 67,602 cases

of monkeypox were reported in 99 non-endemic countries, most with no epidemiological link to Africa (*6*), and 25,509 cases have been confirmed in the United States (*7*).

Comparison of MPXV sequences from nine US monkeypox cases from 2021 and 2022 (ON563414.3, ON674051, ON675438, ON676703, ON676704, ON676705, ON676706, ON676707, and ON676708) revealed two distinct lineages (Fig. 1) within MPXV Clade IIb (formerly named West African MPXV found east of the Dahomey Gap). Neutral nomenclature was chosen to reduce the stigmatization that can be associated with naming that is based on locations (*8*). We maintain the designation of two clades of MPXV, Clade I: formerly Congo Basin/Central African and Clade II: formerly West African, which are based on genetic distance and evidence-based clinical differences (*9*–*12*). Five of the seven May 2022 US sequences formed a monophyletic clade with 2022 MPXV sequences from Europe (Fig. 1), with most genomes within this clade containing zero to two nucleotide changes in nonrepeat regions (fig. S1 and table S1). This clade will be referred to as the current predominant 2022 MPXV outbreak variant, B.1 [which is based on proposed MPXV naming from Nextstrain (*13*)]. MPXV from a 2021 travel-associated case from Nigeria to Maryland (USA_2021_MD) displayed high similarity to variant B.1 sequences, with ~13 nucleotide differences (Fig. 1, fig. S1, and Table 1). The USA_2021_MD and 2022 outbreak sequences shared many mutations that separated them from MPXV sequences from Nigeria and travel-associated cases from 2017–2019 (table S2).

Two 2022 US MPXV sequences, USA_2022_FL001 and USA_2022_VA001, and one 2021 US sequence, USA_2021_TX, formed a monophyletic clade (variant A.2) that was polyphyletic to other 2022 MPXV sequences from the United States and Europe (Fig. 1). Each genome contained ~80 nucleotide changes relative to the variant B.1 MPXV sequences (fig. S1). The three variant A.2 genomes displayed ~30 unique nucleotide differences from each other (fig. S1 and table S3). Each case also reported travel to different countries in the Middle East and West Africa (table S4). This suggests that although the three MPXVs share a common ancestor, they likely represent separate introductions to the United States.

Real-time polymerase chain reaction (PCR) testing of USA_2021_MD and the five 2022 MPXV variant B.1 samples revealed a lower sensitivity (average Ct delay of 6.88, ranging from 5.3 to 8.3) in the *Orthopoxvirus* generic OPX3 real-time PCR assay (*14*) compared with the Monkeypox Clade II–specific real-time PCR assay (*15*) (table S5, when performed as described in Methods). By contrast, similar Ct values were observed for USA_2022_FL001, USA_2022_VA001, or USA_2021_TX samples (average difference of −0.78 Ct, ranging from −1.4 to 0.5). Careful comparison of Ct values between the two assays can, in theory, differentiate between cases belonging to variant B.1 and cases from other Clade IIb MPXV without sequencing. Sequence examination revealed a single nucleotide polymorphism (SNP) in the reverse primer-binding site for the OPX3 real-time PCR assay (DNA polymerase gene VACV-Cop E9L, C322T) in USA_2021_MD and variant B.1 sequences that was absent from other Clade IIb MPXV sequences. The decreased sensitivity in the OPX3 assay is unrelated to the US Food and Drug Administration–cleared VAC1 assay (*16*) used for MPXV screening. Use of different commercial reagents, run parameters, or PCR platforms may result in different results.

When we compared the 2022 outbreak MPXV sequences in Fig. 1 with other MPVX sequences in Lineage A, we noticed a marked preponderance of G-to-A mutations, specifically 5′ GA-to-AA or 5′ GG-to-AG, indicative of host Apolipoprotein B mRNA Editing Catalytic Polypeptide-like3 (APOBEC3) activity (*17*, *18*) (Fig. 2 and Table 2). Looking at this systematically, we found that a significant enrichment of APOBEC3 context G-to-A mutations was evident throughout Lineage A, among Clade IIb MPXV sequences sampled from 2017 to 2022 (Fig. 2 and Table 2). Overall, among unique mutations within Lineage A, 167 G-to-A mutations were in an APOBEC3 context, whereas nine G-to-A mutations were not in an APOBEC3 motif, and only 14 mutations were not G-to-A (Fig. 2 and Table 2). The vast majority of the APOBEC3 context G-to-A mutations were specifically GA-to-AA (156 of 167, or 95%; Fig. 2), indicating that if these mutations were generated by APOBEC3 editing, then APOBEC3G was not the major form because it produces GG-to-AG changes (*19*, *20*).

We explored the abundance of APOBEC3 motif G-to-A mutations along the evolutionary trajectory from the common ancestor of Lineage A to the variants A.2 and B.1 (Fig. 2 and fig. S2). The path from the estimated ancestor of Lineage A to the estimated ancestors of both variant B.1 and variant A.2, including each internal branch, revealed significantly increased APOBEC3 motif G-to-A changes, indicating that sequential acquisition of mutations in distinct individuals sampled historically since 2017 have contributed to the high proportions of GA-to-AA APOBEC3 (fig. S2 and table S6). Given the limited variation found in 2022 outbreak sequences in variant B.1, there were only a small number of SNPs relative to the ancestor for any one sequence. When considered together, however, all eight SNPs observed among the 12 variant B.1 genomes available in early May 2022 were GA-to-AA APOBEC3 context mutations (Fig. 2, fig. S2, and table S6). Outbreak-related sequence data have increased very rapidly, enabling the analysis of 397 outbreak genomes sampled between 1 May and 15 July 2022, available through the GISAID data sharing initiative (*21*). This greatly expanded dataset confirmed the pattern observed among the first 12 sequences: 275/308 (89%) of observed unique G-to-A mutations occurred in an APOBEC3 context, and 261/275 (95%) of these were specifically 5′ GA-to-AA (Fig. 2, fig. S3, and table S7). Beyond variant B.1, by partitioning Lineage A into sublineages (A.2, Nigeria 2017, and Nigeria 2017–2019; Fig. 2) we found that G-to-A mutations in variant A.2 were in an APOBEC3 context and were enriched throughout Lineage A (Fig. 2, fig. S2, and table S6). Four additional MPXV sequences belonging to variant A.2 have now been detected in India and Thailand (*22*); 45/47 (96%) G-to-A mutations were in an APOBEC3 context, and all 45 of these were specifically 5′ GA-to-AA (table S7).

By contrast, APOBEC3 context G-to-A changes were lower than would be expected by chance relative to other G-to-A changes across Clade I and Clade IIa MPXV (Fig. 2, fig. S2, and table S8). To better resolve where within the phylogeny the switch in mutational patterns arose, we evaluated the mutational frequencies along the internal branches in Clade IIb leading into Lineage A (Fig. 2, fig. S2, and table S8), and these were not found to be statistically enriched for APOBEC3 context G-to-A changes.

In the 15 July 2022 GISAID sample, there were three highly related sequences, one each from Italy, Spain, and France. These were chimeric in that most of the genome was typical of variant B.1, but each inverted terminal repeat region carried five consecutive bases that were typically found among other Lineage A and Clade IIb MPXV, but not among B.1 sequences. A detailed analysis of these sequences is provided in fig. S4, and they were excluded from the analysis shown in fig. S3. This pattern is potentially indicative of recombination, an important aspect of poxvirus evolution (*23*); however, assembly errors caused by reference calling in low coverage

[1]National Center for Emerging and Zoonotic Infectious Diseases, Centers for Disease Control and Prevention, Atlanta, GA, USA. [2]T-6: Theoretical Biology and Biophysics, Los Alamos National Laboratory, Los Alamos, New Mexico, USA; New Mexico Consortium, Los Alamos, NM, USA. [3]Leidos Inc., Reston, VA 20190, USA. [4]ISR-3: Space Data Science and Systems, Los Alamos National Laboratory, Los Alamos, NM, USA. [5]Massachusetts Department of Public Health, Jamaica Plain, MA, USA. [6]Infectious Disease Epidemiology and Outbreak Response Bureau, Maryland Department of Health, Baltimore, MD, USA. [7]Dallas County Health and Human Services Public Health Laboratory, Dallas, Texas, USA. [8]Florida Department of Health Bureau of Public Health Laboratories-Jacksonville, Jacksonville, FL, USA. [9]Florida Department of Health in Broward County, Hollywood, FL, USA. [10]Virginia Department of General Services, Division of Consolidated Laboratory Services, Richmond, VA, USA. [11]Virginia Department of Health, Richmond, VA, USA. [12]Utah Department of Health and Human Services, Salt Lake City, UT, USA. [13]Sacramento County Public Health, Sacramento, CA, USA.
***Corresponding author. Email: yuli@cdc.gov**

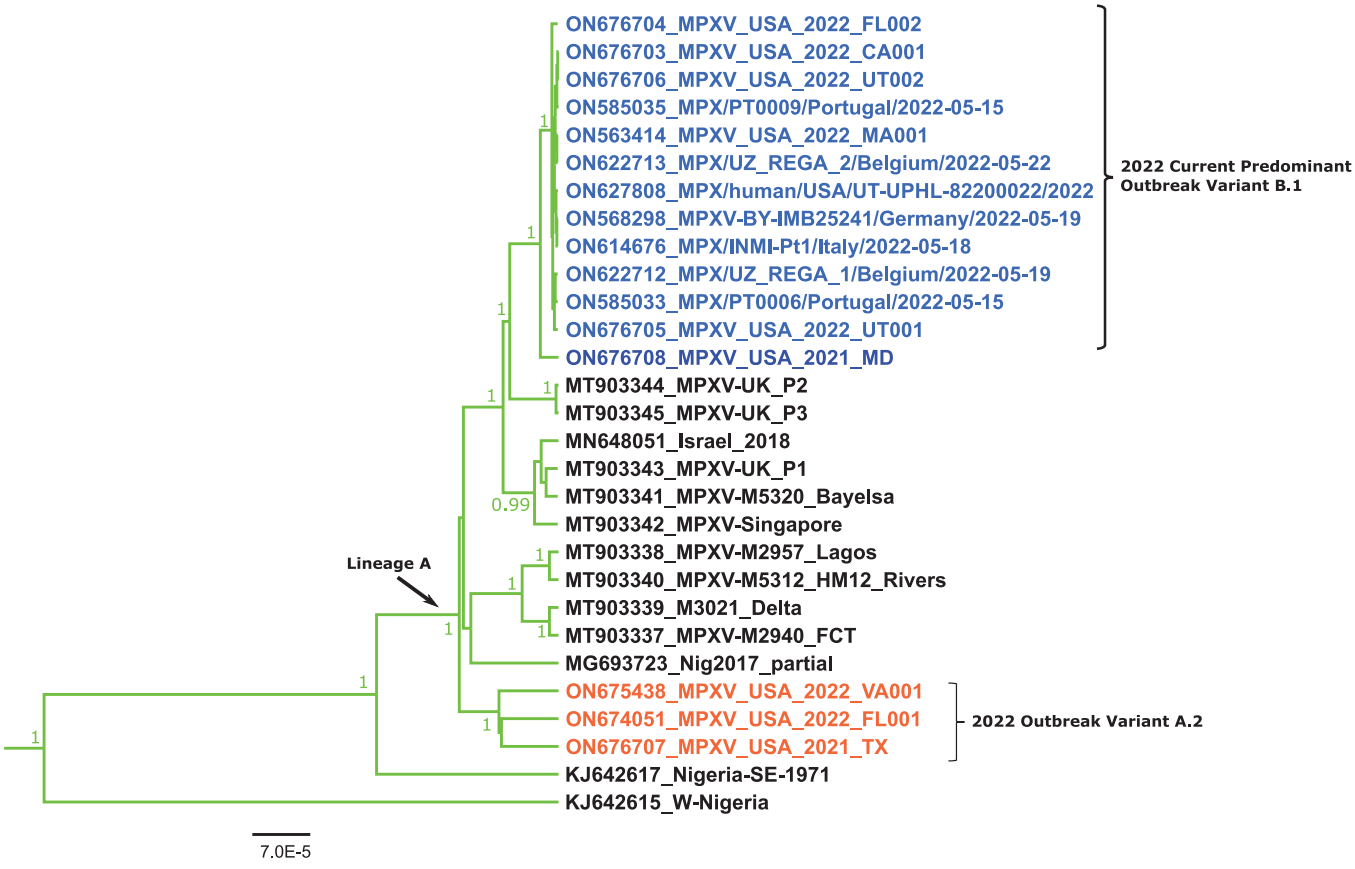


Fig. 1. Phylogenetic analysis of Clade IIb MPXV genome sequences. Variant B.1 sequences are shown in blue text, variant A.2 sequences in orange text, and green branches indicate Clade IIb. Phylogenetic analysis was performed in BEAST v1.8.3 using the HKY+G model and constant coalescent prior on complete genome alignments after removing all sites containing gaps. Scale bar is in substitutions per site; posterior support values are shown at branch points.

regions could not be ruled out as a possible explanation.

Given the clear transition in the mutational pattern in Lineage A relative to Clades I and IIa (Fig. 2), we explored the hypothesis that there was a concomitant change in the evolutionary rate in Lineage A. First, we used the fixed local clock model as implemented in BEAST to compare the estimated mean evolutionary rate of Lineage A ($7.2 \times 10^{-6} \pm 8.9 \times 10^{-7}$ SD) with those of Clade I ($1.9 \times 10^{-6} \pm 3.1 \times 10^{-7}$ SD) and Clade IIa ($3.9 \times 10^{-6} \pm 8.9 \times 10^{-7}$ SD) (table S9). We also separated Lineage A, retaining Nigerian-SE-1971 as an outgroup, from Clade I and IIa and repeated the analysis using two trees. We felt this to be the more appropriate alternative given the transition in the underlying evolutionary model. In this analysis, we found that Lineage A had an even higher evolutionary rate estimate of $2.8 \times 10^{-5} \pm 8.8 \times 10^{-6}$ SD, whereas estimates for Clades I and IIa were essentially unchanged (table S9). Thus, using either approach, we observed higher evolutionary rates within Lineage A, consistent with mutations being driven by host editing mediated through APOBEC3 over what is expected by errors in the viral polymerase.

Table 1. Unique coding nucleotide changes in 2022 predominant MPXV outbreak variant B.1. Mutations listed (all SNPs) were shared among all MPXV Clade IIb variant B.1 sequences examined in Fig. 1 and were not present in USA_2021_MD or UK-P2 (MT903344.1). Gene homologs in vaccinia virus Copenhagen (VACV-Cop) are given for each gene. Additional information can be found in table S2.

Position*	MD 2021	2022 Outbreak	Effect	Amino acid change	Note
3120, 194114	G	A	Synonymous		VACV-Cop C19L ankyrin-like
39148	C	T	Missense	Glu353Lys	VACV-Cop F13L major envelope antigen of EEV
73248	G	A	Missense	Asp88Asn	VACV-Cop G8R VLTF-1 (late transcription factor 1)
74214	G	A	Missense	Met142Ile	VACV-Cop G9R entry/fusion complex component
77392	G	A	Missense	Glu162Lys	VACV-Cop L4R ss/dsDNA binding protein
84596	C	T	Synonymous		VACV-Cop J6R RNA polymerase subunit (RPO147)
150480	C	T	Missense	His221Tyr	VACV-Cop A46R IL-1/TLR signaling inhibitor
170273	G	A	Synonymous		VACV-Cop B12R Ser/Thr kinase
183534	C	T	Missense	Pro722Ser	VACV-Cop B21R membrane-associated glycoprotein

*Position in MT903344.1.

An enriched evolutionary rate for Clade B.1 outbreak viruses has been similarly reported by others (*18*, *22*). A cautionary note regarding the robustness of estimates of rates of evolutionary change is that molecular clock assumptions may be violated in a scenario where mutations are dominated by host-mediated APOBEC3 deaminase activity, as different people may have different levels of APOBEC3 activity, and this may vary during the course of an infection. For example, transient increases in G-to-A ABOBEC3 motif–enriched mutations in HIV genomes in single infected hosts have been observed both in HIV-1 infection in humans and simian-HIV (SHIV) infections in monkeys (*24*, *25*)

All publicly available MPXV genomes from the 2022 monkeypox outbreak to date belong to Clade II, which may cause less severe disease and have a lower case fatality rate than Clade I MPXV (*10*–*13*). Genomes published during the 2022 outbreak share a common ancestor with MPXV sequences from Nigeria (Clade IIb); however, sequences from surrounding countries are limited, and most of our understanding of these relationships comes from viruses linked to or identified in Nigeria. The high similarity among the current predominant 2022 MPXV outbreak variant B.1 sequences analyzed here is similar to the 0.4 to 1.5 SNPs reported between genomes from epidemiologically linked samples from the same transmission chain (*3*). Among Clade IIb sequences, many unique mutations were shared between USA_2021_MD and variant B.1 genomes, further indicating that any evolutionary force leading to these changes most likely preceded the 2022 outbreak and were found in a common ancestor shared between the variant B.1 and USA_2021_MD. By contrast, there were sufficient differences (>30 SNPs) among the three variant A.2 sequences to suggest that they likely represent separate introductions into the United States.

After the reemergence of MPXV in Nigeria in 2017 and before 2022, there had only been two reported events of person-to-person transmission of MPXV outside of Africa (*3*, *26*). Several factors may be contributing to this recent increased spread between humans, including behaviors involving close contact and failure to recognize or diagnose monkeypox to prevent spread. It is currently unclear whether the APOBEC3 motif or other mutations observed in the 2022 outbreak MPXV variants have affected or will affect viral transmissibility or pathogenicity. An E353K mutation in F13L (which codes for the target of tecovirimat, an antiviral agent indicated for the treatment of smallpox) was shared by all sequences in the predominant 2022 outbreak cluster; functional studies revealed no effect on the efficacy of tecovirimat (the median effective concentration was 0.007731 ± 0.002 μM for 353E and 0.002860 ± 0.001 μM for 353K) (fig. S5).

APOBEC3 proteins are an important component of the vertebrate innate immune system and restrict the replication of exogenous viruses through cytosine-to-uracil deaminase activity (*19*, *27*). APOBEC3 proteins act mainly on single-stranded DNA and have been extensively studied in RNA viruses, including HIV (*20*), but can also act on DNA viruses (*28*, *29*). It is unlikely that the GA-to-AA substitutions we report here were caused by sequencing error because the sequences used in the analyses were produced across many different laboratories

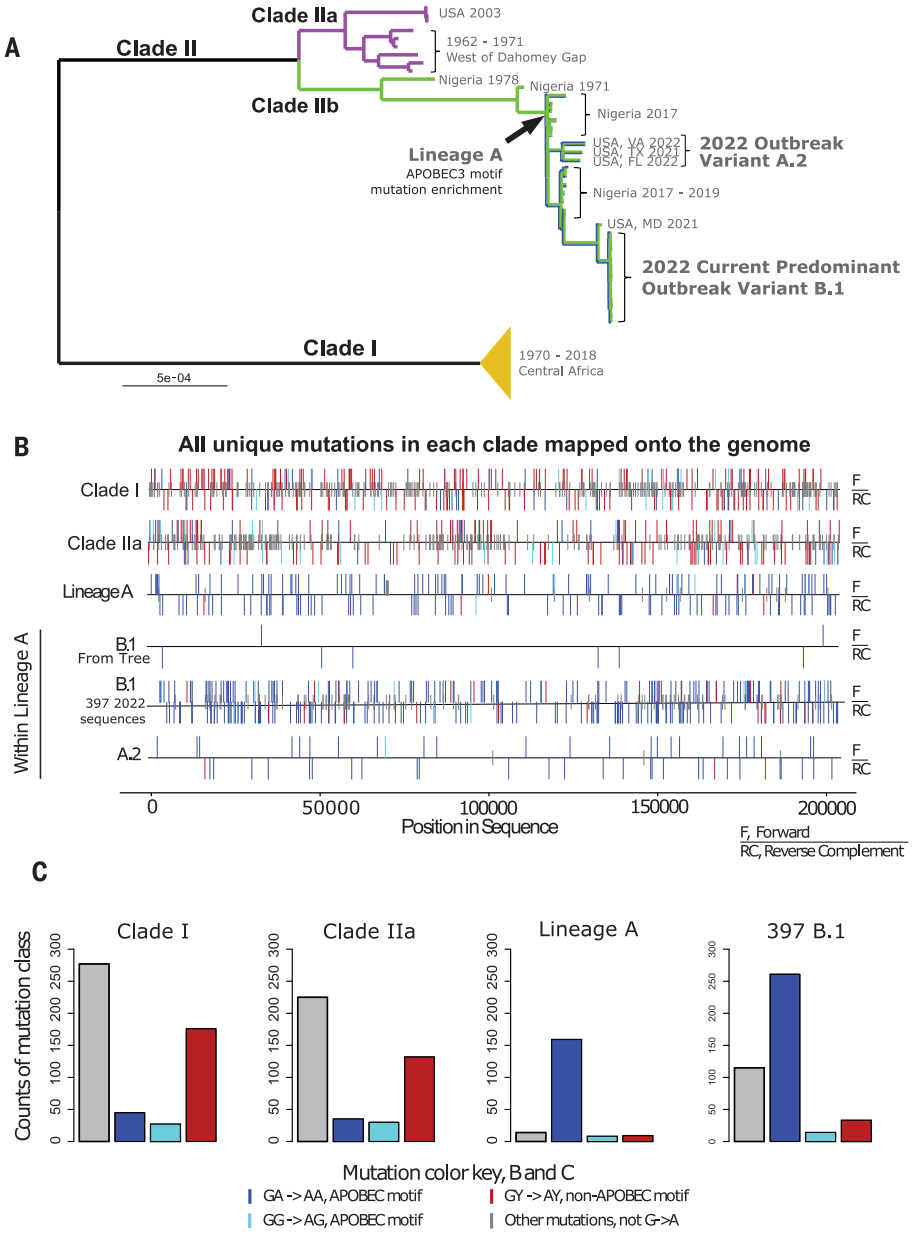


Fig. 2. Analysis of APOBEC3 motif mutations in MPXV. (**A**) Maximum likelihood phylogenetic tree using IQ-TREE. Enrichment for G-to-A APOBEC context mutations (blue line) was found in Lineage A, within Clade IIb (green branches). A detailed version of this tree with taxa names is included in fig. S2. The scale bar indicates the number of substitutions per sequence site. (**B**) Mutational patterns found among Clade I, Clade IIa, and Lineage A in the phylogeny above. All unique mutations in a clade relative to the most recent common ancestor of that clade are shown in a single panel, and the class of each mutation is shown on either the forward or reverse complement strand. The increased number of APOBEC3 context mutations, indicated by blue ticks, in Lineage A, versus red and gray captures the dominance of GA-to-AA APOBEC3 context mutations in this lineage and contrasts with Clades I and IIa. The exact numbers and statistics are provided in Table 2. The A.2 and B.1 variants within Lineage A in the tree and an updated analysis of 397 variant B.1 sequences from GISAID demonstrate the continuing dominance of GA-to-AA APOBEC3 context mutations among currently sampled outbreak sequences. (**C**) Bar charts showing the total number of each class of unique mutations within each clade shown in (B) for Clade I, Clade IIa, and lineage A, as well as for 397 sequences from lineage B.1 from fig. S3A.

Table 2. Summary of the counts of different classes of all unique mutations observed in the different clades shown in Fig. 2. C-to-T mutations in the forward strand are included as G-to-A in the reverse complement as a simplified way of tallying all mutations that occurred in the context of an APOBEC3 motif in the viral genome relative to those that did not. *P* values are derived from a Fisher's exact test of a contingency table based on columns 4 to 7. First, we identified all G's either in an APOBEC context (GA or GG) or not in an APOBEC context (GC or GT), and then we determined the number that had undergone G-to-A substitutions and the number where the G was unchanged within each of the two contexts. An ABOBEC motif odds ratio >1 indicates APOBEC context enrichment. The final column shows the number of GA-to-AA and GG-to-AG mutations that constitute the total G-to-A APOBEC context mutations in column 4.

	Clade	All other mutations	G-to-A APOBEC context	G in APOBEC context, no change	G-to-A non APOBEC context	G not in APOBEC context, no change	*P* value (two-sided)	*q* value	Odds ratio	GA-to-AA + GG-to-AG
Non-APOBEC context	I	277	72	36552	176	30580	<0.000001	0.000006	0.3423	45 + 27
	IIa	225	65	36548	132	30578	<0.000001	0.000006	0.412	35 + 30
APOBEC context enriched	Lineage A	14	167	36415	9	30669	<0.000001	0.000006	15.63	159 + 8
	B.1 (*n* = 12)	0	8	36517	0	30675	0.0095	0.022	Infinity	8 + 0
	B.1 (*n* = 397)	115	275	35064	33	29705	<0.000001	0.000006	7.06	261 + 14

using multiple methods, including both short- and long-read approaches and with and without PCR. The presence of mutations consistent with APOBEC3 editing in several branches of the Clade IIb MPXV will cause discordance in estimates of evolutionary rate and divergence time using many standard methods.

Specific enrichment of the APOBEC3 motif mutations in Clade IIb MPXV since 2017 may suggest something different in virus-host interactions, facilitating this mutational pattern. Such a pattern might be caused by sustained transmission in a new host or a new route of infection. The APOBEC3 (A-to-G) locus carries seven genes or pseudogenes and is a primate-specific expansion of the APOBEC family of genes; APOBEC3 is not found in rodents (*30*), which are thought to be the primary reservoir of monkeypox virus in Africa. Additionally, APOBEC3 has been found at higher levels in mucosal tissues than in skin in humans (*31*), so permucosal transmission may provide increased opportunity for APOBEC3 editing of MPXV. Before this outbreak, APOBEC3 editing was not recognized or appreciated as a mechanism of poxvirus mutation. Two studies in vaccinia virus found that the overexpression of APOBEC3 had no effect on viral replication and that endogenous or overexpressed APOBEC3 was not degraded by vaccinia virus, as it is by other viruses (*32*, *33*). However, neither of these studies performed sequencing. The fact that the enrichment can be observed at essentially all levels within Clade IIb MPXV since 2017 suggests that it is a recurrent and dominant mutational effect in recent MPXV evolution. Furthermore, the majority of the mutations detected among expanding outbreak samples were 5′ GA-to-AA (Fig. 2 and table S7), indicating that this mutational bias is continuing.

REFERENCES AND NOTES

1. Centers for Disease Control and Prevention (CDC), *MMWR Morb. Mortal. Wkly. Rep.* **52**, 561–564 (2003).
2. A. Yinka-Ogunleye *et al*., *Lancet Infect. Dis.* **19**, 872–879 (2019).
3. M. R. Mauldin *et al*., *J. Infect. Dis.* **225**, 1367–1376 (2022).
4. V. Costello *et al*., *Emerg. Infect. Dis.* **28**, 1002–1005 (2022).
5. A. K. Rao *et al*., *MMWR Morb. Mortal. Wkly. Rep.* **71**, 509–516 (2022).
6. Centers for Disease Control and Prevention, "2022 global map & case count" (CDC, 2022); https://www.cdc.gov/poxvirus/monkeypox/response/2022/world-map.html.
7. Centers for Disease Control and Prevention, "2022 U.S. map & case count" (CDC, (2022); https://www.cdc.gov/poxvirus/monkeypox/response/2022/us-map.html.
8. C. Happi *et al*., *PLOS Biol.* **20**, e3001769 (2022).
9. A. M. Likos *et al*., *J. Gen. Virol.* **86**, 2661–2672 (2005).
10. K. Brown, P. A. Leggat, *Trop. Med. Infect. Dis.* **1**, 8 (2016).
11. M. G. Reynolds *et al*., *Emerg. Infect. Dis.* **13**, 1332–1339 (2007).
12. C. L. Hutson *et al*., *BioMed Res. Int.* **2015**, 965710 (2015).
13. J. Hadfield *et al*., *Bioinformatics* **34**, 4121–4123 (2018).
14. M. G. Reynolds *et al*., *Am. J. Trop. Med. Hyg.* **82**, 746–754 (2010).
15. Y. Li, H. Zhao, K. Wilkins, C. Hughes, I. K. Damon,*J. Virol. Methods* **169**, 223–227 (2010).
16. Y. Li, V. A. Olson, T. Laue, M. T. Laker, I. K. Damon, *J. Clin. Virol.* **36**, 194–203 (2006).
17. A. R. O'Toole, A. Rambaut, "Initial observations about putative APOBEC3 deaminase editing driving short-term evolution of MPXV since 2017" (Virological.org, 2022); https://virological.org/t/initial-observations-about-putative-apobec3-deaminase-editing-driving-short-term-evolution-of-mpxv-since-2017/830.
18. J. Isidro *et al*., *Nat. Med.* **28**, 1569–1572 (2022).
19. R. S. Harris, J. P. Dudley, *Virology* **479-480**, 131–145 (2015).
20. M. T. Liddament, W. L. Brown, A. J. Schumacher, R. S. Harris, *Curr. Biol.* **14**, 1385–1391 (2004).
21. GISAID, www.gisaid.org
22. B. Jolly, V. Scaria, *J. Infect.* **22**, 0.1016/j.jinf.2022.08.013 (2022).
23. J. J. Esposito *et al*., *Science* **313**, 807–812 (2006).
24. E. E. Giorgi, H. Li, T. Bhattacharya, G. M. Shaw, B. Korber, *mBio* **11**, e00324-e20 (2020).
25. B. F. Keele *et al*., *Proc. Natl. Acad. Sci. U.S.A.* **105**, 7552–7557 (2008).
26. G. Hobson *et al*., *Euro Surveill.* **26**, 2100745 (2021).
27. J. D. Salter, R. P. Bennett, H. C. Smith, *Trends Biochem. Sci.* **41**, 578–594 (2016).
28. J. P. Vartanian, D. Guétard, M. Henry, S. Wain-Hobson, *Science* **320**, 230–233 (2008).
29. J. P. Vartanian *et al*., *PLOS Pathog.* **6**, e1000928 (2010).
30. A. Jarmuz *et al*., *Genomics* **79**, 285–296 (2002).
31. C. J. Warren, K. Van Doorslaer, A. Pandey, J. M. Espinosa, D. Pyeon, *Virus Evol.* **1**, vev015 (2015).
32. M. Kremer *et al*., *Virol. J.* **3**, 86 (2006).
33. L. Soday *et al*., *Cell Rep.* **27**, 1920–1933.e7 (2019).
34. Sequence alignments for: C. M. Gigante, B. Korber, M. H. Seabolt, K. Wilkins, W. Davidson, A. K. Rao, H. Zhao, T. G. Smith, C. M. Hughes, F. Minhaj, M. A. Waltenburg, J. Theiler, S. Smole, G. R. Gallagher, D. Blythe, R. Myers, J. Schulte, J. Stringer, P. Lee, R. M. Mendoza, L. A. Griffin-Thomas, J. Crain, J. Murray, A. Atkinson, A. H. Gonzalez, J. Nash, D. Batra, I. Damon, J. McQuiston, C. L. Hutson, A. M. McCollum, Y. Li, Multiple lineages of monkeypox virus detected in the United States, 2021- 2022, Dryad (2022); https://doi.org/10.5061/dryad.jq2bvq8cd.
35. GISAID sequence alignment for: C. M. Gigante, B. Korber, M. H. Seabolt, K. Wilkins, W. Davidson, A. K. Rao, H. Zhao, T. G. Smith, C. M. Hughes, F. Minhaj, M. A. Waltenburg, J. Theiler, S. Smole, G. R. Gallagher, D. Blythe, R. Myers, J. Schulte, J. Stringer, P. Lee, R. M. Mendoza, L. A. Griffin-Thomas, J. Crain, J. Murray, A. Atkinson, A. H. Gonzalez, J. Nash, D. Batra, I. Damon, J. McQuiston, C. L. Hutson, A. M. McCollum, Y. Li, Multiple lineages of monkeypox virus detected in the United States, 2021- 2022, GISAID EpiPox Downloads (2022); https://doi.org/10.55876/gis8.220715bk.
36. Code used for APOBEC3 analysis for: C. M. Gigante, B. Korber, M. H. Seabolt, K. Wilkins, W. Davidson, A. K. Rao, H. Zhao, T. G. Smith, C. M. Hughes, F. Minhaj, M. A. Waltenburg, J. Theiler, S. Smole, G. R. Gallagher, D. Blythe, R. Myers, J. Schulte, J. Stringer, P. Lee, R. M. Mendoza, L. A. Griffin-Thomas, J. Crain, J. Murray, A. Atkinson, A. H. Gonzalez, J. Nash, D. Batra, I. Damon, J. McQuiston, C. L. Hutson, A. M. McCollum, Y. Li, Multiple lineages of monkeypox virus detected in the United States, 2021- 2022, Zenodo (2022); https://doi.org/10.5281/zenodo.6970457.

ACKNOWLEDGMENTS

We thank B. Foley for providing a draft alignment of MPXV; D. MacCannell, K. Patel, Y. Tao, S. Tong, B. Cherney, and J. Barnes from the US Centers for Disease Control and Prevention; A. Kim and S. Lukula from the Maryland Department of Health Laboratory; B. Downes from Fairfax County, Virginia Department of Health; C. Brown, L. Madoff, M. DeMartino, E. Buzby, S. Ash, and J. Hall from the Massachusetts Department of Health; J. Jaramillo from Dallas County LRN; D. Hairfield and K. Stratton from the Virginia Department of General Services, Division of Consolidated Laboratory Services; and the authors from the originating laboratories and the submitting laboratories who generated and shared the GISAID genetic sequence data on which this research is based (GISAID acknowledgments tables S10 and S11 are provided in the supplementary materials). **Funding:** No external funding was used for the Centers for Disease Control and Prevention (CDC) effort in this investigation. B.K. was supported by the Laboratory Directed Research and Development program of Los Alamos National Laboratory under project number 20220660ER. **Author contributions:** Conceptualization: Y.L., C.M.G., B.K., J.M., I.D.; Funding acquisition: Y.L., C.M.G., B.K.; Investigation: M.H.S., K.W., W.D., A.K.R., H.Z., C.M.H., F.M., M.A.W., J.T., S.S., G.R.G., D.B., R.M., J.S., P.L., R.M.M., L.A.G., J.C., J.M., A.A., A.H.G., J.N., D.B., A.M.M., T.G.S.; Methodology: Y.L., B.K., J.T., C.M.G., M.H.S.; Visualization: C.M.G., B.K., J.T., Y.L.; Writing – original draft: C.M.G., B.K.; Writing – review and editing: C.M.G., B.K., Y.L., I.D., A.M.M.,

C.L.H., J.M. **Competing interests:** The authors declare no competing interests. **Data and materials availability:** All data are available in the main text or public databases and GISAID. MPXV genomes were deposited to GenBank under accession numbers ON563414.3, ON674051, ON675438, ON676703, ON676704, ON676705, ON676706, ON676707, and ON676708. Alignments and code have been made available online (*34*–*36*). **License information:** Copyright © 2022 the authors, some rights reserved; exclusive licensee American Association for the Advancement of Science. No claim to original US government works. https://www.science.org/about/science-licenses-journal-article-reuse. In the interest of rapid dissemination of results with immediate public health relevance, the author will make the Author Accepted Manuscript (AAM) version available under a CC BY public copyright license.

SUPPLEMENTARY MATERIALS

science.org/doi/10.1126/science.add4153
Materials and Methods
Figs. S1 to S5
Tables S1 to S9
References (*37*–*43*)
MDAR Reproducibility Checklist
GISAID Acknowledgment Tables S10 and S11

Submitted 12 June 2022; accepted 10 October 2022
Published online 20 October 2022
10.1126/science.add4153

INDIANA UNIVERSITY
SCHOOL OF PUBLIC HEALTH
Bloomington

THE TIME IS *NOW*

We strive for excellence in research, teaching, and service, while fostering a robust exchange of ideas on local and global health–related issues.

The **Indiana University School of Public Health – Bloomington** invites applications for multiple openings in administrative faculty, tenured/tenure-track faculty, and post-doctoral fellows in all departments. SPH-B seeks individuals passionate about our mission to promote health for all members of society through rigorous and impactful research, excellence in teaching and mentoring, and service to the university, profession, and the community.

SPH-B is committed to growing and sustaining a multi-culturally diverse, equitable, and inclusive living, learning, and working environment. Of the current 100 T/TT faculty, 35% are from underrepresented racial and ethnic groups as defined by the National Science Foundation (NSF).

We are currently accepting applications for the following administrative faculty positions:

- Chairperson of the Department of Environmental and Occupational Health
- Associate Dean for Faculty Affairs
- Associate or Executive Assistant Dean for Academic Affairs and Enrollment

We are currently accepting applications for multiple tenured/tenure-track positions in the departments of:

- Applied Health Science
- Environmental and Occupational Health
- Epidemiology and Biostatistics
- Kinesiology
- Health & Wellness Design

Learn more about these and other openings at **go.iu.edu/4BrJ**



#YearOfLeverage

The UNIVERSITY of OKLAHOMA

EXECUTIVE DIRECTOR,
INTEGRATIVE LIFE SCIENCES INSTITUTE (ILSI)
UNIVERSITY OF OKLAHOMA (NORMAN, OK)

TO APPLY: APPLY.INTERFOLIO.COM/113559

The University of Oklahoma is seeking nominations and applications for the position of inaugural **Executive Director of the ILSI** and at the rank of **Full Professor**. The academic home department will be aligned with the successful candidate's disciplinary interests.

The Executive Director, who will report directly to OU's Vice President for Research and Partnerships, will provide strong leadership in guiding the mission of ILSI, which is to advance positive health outcomes through convergence research to create new diagnostics, therapies, policies, and practices that will enable recognition of and response to continuing and emerging disease threats and address social and environmental risk factors impacting health equity.

The successful candidate will be an experienced and dynamic leader with exceptional scholarly credentials in life sciences research. The candidate will promote and strengthen collaborative efforts between the faculty, students, and staff across our three campuses, to incentivize and develop transdisciplinary teams in areas of strategic importance to the ILSI. Establishing strong partnerships with OU Health Sciences Center and the Oklahoma Medical Research Foundation is an important objective for ILSI. In addition, the successful candidate will build a robust and sustainable financial portfolio of dedicated internal and extramural funding for the operational costs of the institute and in support of its convergence research mission. Applicants must hold a Ph.D. and/or M.D. in life sciences research or related area, have at least two years of relevant academic or corporate leadership experience, and show evidence of a nationally recognized and well-funded research program.

For more information contact: Ann West (**awest@ou.edu**)
The University of Oklahoma is an equal opportunity institution.
For more information, please visit **http://www.ou.edu/eoo/**

UCLA College | Life Sciences Ecology & Evolutionary Biology

TENURE TRACK ASSISTANT PROFESSOR POSITION IN POPULATION BIOLOGY

The Department of Ecology and Evolutionary Biology (EEB) at UCLA is searching for a tenure track **Assistant Professor** in population biology. We seek candidates who apply quantitative approaches to test theory-driven questions on the ecology or evolution of populations. The successful candidate will be expected to develop a rigorous, externally funded research program and teach at both the undergraduate and graduate levels with innovative pedagogical approaches. We are especially interested in candidates who can develop courses that satisfy the UCLA diversity requirement or include topics of diversity, equity and inclusion and how they relate to our field. We welcome candidates who demonstrate a commitment to equity and inclusion through research, teaching, mentoring, community engagement and/or service and who apply inclusive mentoring practices. Necessary qualifications include a PhD degree in a relevant discipline and a strong background in quantitative methods. Evidence of sustained research productivity through journal publications is required.

Submit application packages online through **https://recruit.apo.ucla.edu/JPF07931** and include the following: **1)** cover letter; **2)** curriculum vita; **3)** statement of research interests; **4)** statement of teaching expertise; **5)** statement of formal and informal activities to promote equity, diversity and inclusion; **6)** names and contact info of three referees (reference letters will only be requested of select candidates), and **7)** reference check authorization release form. The University of California seeks to recruit and retain a diverse workforce as a reflection of our commitment to serve the people of California, to maintain the excellence of the University, and to offer our students richly varied disciplines, perspectives, and ways of knowing and learning. Complete applications must be submitted by **November 16, 2022**. For full information about this position, please visit: **https://recruit.apo.ucla.edu/JPF07931**.

The University of California is an Equal Opportunity/Affirmative Action Employer. All qualified applicants will receive consideration for employment without regard to race, color, religion, sex, sexual orientation, gender identity, national origin, disability, age or protected veteran status. For the complete University of California nondiscrimination and affirmative action policy, see: UC Nondiscrimination & Affirmative Action Policy. (http://policy.ucop.edu/doc/4000376/NondiscrimAffirmAct)

COLUMBIA | VAGELOS COLLEGE OF PHYSICIANS AND SURGEONS

2023 Schaefer Research Scholars Program Awards

The Vagelos College of Physicians and Surgeons (VP&S) is pleased to announce the *2023 Schaefer Research Scholars Program Awards.* The *Awards,* made possible through a bequest from Dr. Ludwig Schaefer, are made annually to four research scientists who have distinguished themselves in human physiology, as broadly defined, and whose current work is of outstanding merit. The proposed research must have the potential to illuminate the field. Two awards are made to research scientists residing or working in North or South America, and two awards are made to research scientists residing or working outside North or South America. Each award consists of a $50,000 cash prize and up to $200,000 in direct research support.

Applications must include a cover sheet; a research proposal (one page); a research budget (not to exceed $200,000 in total direct costs) delineated by cost category (salary, fringe, supplies, etc.) for one year (7/1/2023–6/30/2024); a curriculum vitae (not to exceed 10 pages); and a page summarizing applicant's research support. Internal candidates must obtain a nomination letter from their Department Chair. External candidates must present letters from the Dean or equivalent in their home institution as well as from the Columbia University Irving Medical Center collaborator, if applicable.

Nomination deadline: December 12, 2022, at 5:00 p.m. (EST)
To apply visit https://www.ps.columbia.edu/schaefer
and submit all required materials.
Awardees will be notified in February 2023.



Vice Chair & Director of the Radiation and Molecular Oncology Section

The Department of Radiation Oncology at the University of Texas Southwestern Medical Center is recruiting a **senior biology faculty member and/or physician-scientist in biology** to join, build, and lead the department's Radiation and Molecular Oncology section. The section has existing strengths within mechanistic studies of DNA damage/repair and radiotherapy translation in combination with novel systemic therapies, and there is a strong desire to expand/enhance research into realms of immune and metabolic modulation of cancer behavior and therapy responsiveness.

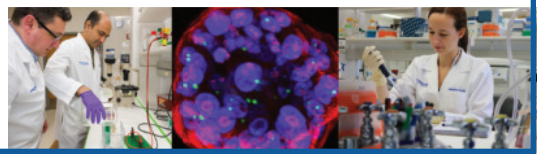
The director will provide section leadership and oversee research investigators and day-to-day operations of a large research infrastructure, including existing core facilities and 25,000 sq. ft. of laboratory space assigned to multiple researchers in the department. Candidate will report directly to the department Chair. The section currently has 18 faculty, including 10 principal investigators. Successful candidate will be provided resources to develop integrated programs with both the Clinical and Medical Physics and Engineering divisions of the department as well as the ability to pursue novel investigations and treatments. Candidates should have an interest in initiating new translational projects and collaborative research both within and outside the department, as well as those associated with the Harold C. Simmons Comprehensive Cancer Center. If close to promotion timeline, associate professor candidates may be taken.

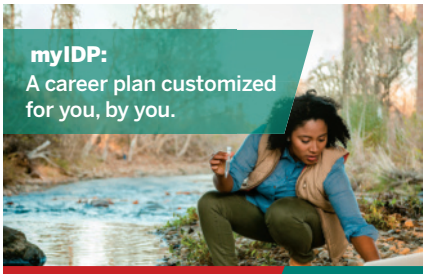
Skills & Qualifications:

- Required record of excellence in research accompanied by a strong publication and funding history.
- Interest in some of the following topics that include but are not limited to radiation biology/oncology, cancer biology, immunology, metabolic study, DNA repair, combination therapies, and the development of biomarkers.
- Open to initiating translational projects and collaborative research with clinicians and scientists across disciplines.
- Strong interpersonal skills and motivation for program building, as well as interests in basic and translational science training.
- Must have a Ph.D., M.D., or M.D./Ph.D. degree or equivalent. Candidates who intend to maintain a clinical practice must have a medical degree from an ACGME-approved medical school or equivalent and have completed a radiation oncology residency program from an approved institution.

To learn more about this position or to apply:

UT Southwestern
Harold C. Simmons Comprehensive Cancer Center
NCI Designated Comprehensive Cancer Center
Department of Radiation Oncology





Features in myIDP include:

- Exercises to help you examine your skills, interests, and values.
- A list of 20 scientific career paths with a prediction of which ones best fit your skills and interests.

myIDP
Visit the website and start planning today!
myIDP.sciencecareers.org

Science Careers
In partnership with:

UCSF University of California San Francisco
UIC
BURROUGHS WELLCOME FUND
University of Massachusetts Medical School
FASEB Federation of American Societies for Experimental Biology

McGOVERN INSTITUTE

CALL FOR NOMINATIONS: SCOLNICK PRIZE IN NEUROSCIENCE

The McGovern Institute for Brain Research is accepting nominations for the **19th annual Edward M. Scolnick Prize in Neuroscience**. The Prize recognizes an outstanding discovery or significant advance in the field of neuroscience. The prize is $200,000. The recipient presents a public lecture at MIT, hosted by the McGovern Institute and followed by a dinner in Spring 2023.

Nomination Deadline: December 15, 2022

Nomination procedures:
Candidates for the award must be nominated by individuals affiliated with universities, hospitals, medicals schools, or research institutes, with a background in neuroscience. Self-nomination is not permitted. Each nomination should include:

- A biosketch or CV of the nominee;
- A letter of nomination with a summary and analysis of the major contributions of the nominee to the field of neuroscience.
- Up to two representative reprints will be accepted.

Selection Procedure:

- Members of the selection committee and faculty affiliated with MIT are not eligible.
- Announcement of the award recipient will be made in January 2023.
- Recipient must attend all events to be awarded the prize.

Past Scolnick Prize Recipients:
2022: David Ginty, Harvard University; 2020: Joshua Sanes, Harvard University; 2019: Richard Huganir, Johns Hopkins University; 2018: David J. Anderson, HHMI, Caltech; 2017: Catherine Dulac, HHMI, Harvard University; 2016: Cornelia Bargmann, HHMI, The Rockefeller University; 2015: Charles Gilbert, The Rockefeller University; 2014: Huda Zoghbi, HHMI, Baylor University; 2013: Thomas Jessell, HHMI, Columbia University; 2012: Roger Nicoll, UCSF; 2011: Bruce McEwen, The Rockefeller University; 2010: Lily and Yuh-Nung Jan, UCSF; 2009: Jeremy Nathans, Johns Hopkins University; 2008: Michael Davis, Emory University; 2007: David Julius, UCSF; 2006: Michael Greenberg, Children's Hospital/HMS; 2005: Judith Rapoport, NIH; 2004: Masakazu Konishi, CalTech

Send nomination packet to: **gwolf@mit.edu**

JOB FOCUS: DIVERSITY

COLLEGE OF MEDICINE TUCSON
Immunobiology

ASSISTANT PROFESSOR - BACTERIOLOGIST
Department of Immunobiology
College of Medicine, University of Arizona Health Sciences

The Department of Immunobiology at the University of Arizona (UA) College of Medicine-Tucson (COM-T) is seeking applicants for a tenure-track **Assistant Professor** position in bacteriology. We recognize the power of a diverse community and strongly encourage qualified individuals with varied experiences, perspectives, and backgrounds to apply.

Applicants must have demonstrated the ability to establish an independent research program and obtain extramural funding. Individuals whose research advances the understanding of host-microbe interactions, including but not limited to respiratory diseases with a bacterial etiology, bacterial metabolism, regulation of host responses, microbiomes and/or mucosal immunology during dysbiosis and/or pathogenesis are strongly encouraged to apply. Applicants must have postdoctoral experience and a PhD, MD, or equivalent degree in their field of study. The successful applicant is expected to obtain extramural funding for their research program and participate in graduate student mentoring and graduate and medical student teaching. They are also expected to interact with other faculty on larger collaborative scientific projects. Along with submitting your CV and Cover Letter, the applicant should arrange for 3 letters of recommendation to be sent separately by senior faculty with extensive knowledge of the candidate. These letters should be sent to Tonya Fotheringham (**tonyah@arizona.edu**). Salary and start-up funds will be commensurate with the applicant's qualifications and the nature of the applicant's project.

Information on the highly collaborative nature of the Department of Immunobiology and the interdepartmental/interdisciplinary ABBS graduate (PhD) program to which it belongs can be obtained through the links on the department website (**immunobiology.arizona.edu**). Additional information on UA Centers, Institutes, and core facilities can be found at the UA COM-T website (**medicine.arizona.edu/about-college/centers**). UA is in the midst of the 4th Industrial Revolution strategic plan designed to significantly increase its research capacity over the next 10 years.

The University of Arizona has been recognized on Forbes list of America's Best Employers in the United States and has been awarded the Work-Life Seal of Distinction by World@Work! For more information about working at the University of Arizona and relocations services, please go to **talent.arizona.edu**.

For full details and qualifications, and to complete an on-line application, see **req12237** at **talent.arizona.edu**.

Outstanding UA Benefits! The University of Arizona is an Equal Opportunity Employer Minorities/Women/Vets/Disabled.



What's Your Next Career Move?

From networking to mentoring to evaluating your skills, find answers to your career questions on *Science* Careers

To view the complete collection, visit **ScienceCareers.org/booklets**



Science Careers
AAAS

Shenzhen Institute of Advanced Technology
Chinese Academy of Sciences



Established in partnership between the Chinese Academy of Sciences and the Shenzhen Municipal Government, the Shenzhen Institute of Advanced Technology (SIAT) is a newly-created university with an objective to become the world's preeminent institute for emerging science and engineering programs. SIAT is equipped with state-of-art teaching and research facilities and is dedicated to cultivating international, visionary, and interdisciplinary talents while delivering research support to pursue innovation-driven development.

SIAT is located in Shenzhen, also known as the "Silicon Valley of China," a modern, clean, and green city, well-known for its stunning architecture, vibrant economy, and its status as a leading global technology hub. SIAT is seeking applications for faculty positions of all ranks in the following academic programs: Computer Science and Engineering, Bioinformatics, Robotics, Life Sciences, Material Science and Engineering, Biomedical Engineering, Pharmaceutical Sciences, Synthetic Biology, Neurosciences, etc. SIAT seeks individuals with a strong record of scholarship who possess the ability to develop and lead high-quality teaching and research programs. SIAT offers a comprehensive benefits package and is committed to faculty success throughout the academic career trajectory, providing support for ambitious and world-class research projects and innovative, interactive teaching methods.

Further information:
https://www.siat-sz.edu.cn/

LINKÖPING UNIVERSITY

EUROSCIENCE POSTDOCTORAL PROGRAMME

Linköping University is one of Sweden's six large universities, currently enrolling 35 900 students. The Centre for Systems Neurobiology involves some 50 independent research groups, from the Faculty of Medicine and the Faculty of Science and Engineering, as well as the University Hospital.

The Centre for Systems Neurobiology is now seeking **Postdoctoral Fellows** within several neuroscience research areas: Animal behavior/Behavioral genetics/ Evolution (Urban Friberg, Per Jensen), Clinical neurophysiology and neuromodulation (Magnus Thordstein), Ion channels (Antonios Pantazis), Neurodegenerative disease (Peter Nilsson), Neuroendocrinology/neuroimmunology (Anders Blomqvist, David Engblom), Psychiatric neuroscience and addiction (Eric Augier), and Sensory and cognitive systems and pain (Sarah McIntyre, Saad Nagi, Håkan Olausson, Marcin Szczot).

For full consideration please apply as soon as possible, and no later than **November 30th**.

For more details regarding the Centre, the different research labs involved in the programme, and to submit a letter-of-intent please go to: **https://liu.se/en/research/center-for-systems-neurobiology**.

For information regarding the university and the region, please go to: **liu.se, eastsweden.com**.

EPFL

Faculty position in Hydraulic Engineering & Fluid-Structure Interactions

at the Ecole polytechnique fédérale de Lausanne (EPFL)

The EPFL School of Architecture, Civil and Environmental Engineering (ENAC) invites applications for an Assistant (tenure-track) or Associate (tenured) Professor of **Hydraulic Engineering & Fluid-Structure Interactions** in the Institute of Civil Engineering.

The Institute of Civil Engineering in ENAC carries out basic and translational research spanning fundamental understanding of Hydraulic Engineering, Structures and Materials, Transportation and Networks, and Geosystems and Geomechanics. It covers a diverse portfolio in research, teaching and innovative technology development across transversal themes: understanding and adapting to climate change, natural hazards, infrastructure resilience and sustainability, design for re-use, geo-energy and geosystems.

Areas of interest include but are not limited to: fundamental research in the development of renewable energy systems such as dams and hydropower systems, advanced modelling of hydraulic infrastructure, fluid-structure interactions, resource conservation, and risk analysis for extremes. Additional areas include experimental methods as well as sensing data for the development of techniques that leverage digital twins for reliable maintenance and safety assessment of hydraulic infrastructure, as well as analysis of extreme natural hazards and adaptation to climate change.

The successful candidate will have a strong research background in Hydraulic Engineering and Fluid-Structure Interactions as well as the potential to develop an innovative and internationally recognized research program.

As a faculty member in the Civil Engineering Section, the appointee will excel in undergraduate and graduate teaching and in guiding research students.

EPFL, with its main campus located in Lausanne on the shores of Lake Geneva, is a dynamically growing and well-funded institution fostering excellence and diversity. It is well equipped with experimental and computational infrastructure and offers a fertile environment for research collaboration between various disciplines. The EPFL environment is multilingual and multicultural, with English serving as a common interface. EPFL offers significant start-up resources and internationally competitive salaries and benefits as well as excellent experimental and computational facilities.

The following documents are requested in PDF format: cover letter including a statement of motivation, curriculum vitae, publication list, concise statements of research vision and teaching interests (up to five pages for each), and the names and addresses (including e-mail) of at least three (for the rank of Assistant Professor) or five (for the rank of Associate Professor) references who have already agreed to supply a letter upon request. Applications should be uploaded to the EPFL recruitment web site:

https://facultyrecruiting.epfl.ch/position/40599565

Formal evaluation of the applications will begin on **December 1st, 2022**.

Further enquiries should be made to:
Prof. Dimitrios Lignos
Chair of the Search Committee
e-mail: SearchHydraulics@epfl.ch

For additional information on EPFL, please consult the websites: www.epfl.ch, enac.epfl.ch, iic.epfl.ch, sgc.epfl.ch.

EPFL is an equal opportunity employer and a family-friendly university that is committed to increasing the diversity of its faculty. It strongly encourages women to apply.

Science Careers online @sciencecareers.org

By **Isabella Bennett**

Our labor isn't free

I saw the bright yellow envelope tucked beneath my windshield wiper and my heart sank. Another parking ticket. Without looking at the amount, I slid the ticket into my glovebox next to its twin, opened the trunk, and handed the faculty candidate beside me the suitcase I had stored for them. I was in the second year of my Ph.D. and the fifth month of serving on a faculty search committee. When I was invited to join the committee, the faculty members in charge told me it would be "a lot of reading but a good experience and some fancy dinners." I felt honored to be included. Little did I know the costs my volunteer commitment would entail.

It started off great. I read about 40 applications and the associated novella-length CVs, evaluating each using an extensive rubric. But my stress level rose when two grants I'd submitted—the first I'd ever written, with little expectation of success—were funded. I worried the faculty search would mean I couldn't give my newly funded project the time and energy it deserved, but I felt I owed it to the candidates and my mentors on the committee to continue. So, I stretched myself to the limit. I told my partner not to expect to see much of me, much less have any help around the house. I stopped responding to calls from friends and family.

After several weeks, my stress started to manifest physically. An old back injury flared up and I found myself lying on the floor, unable to walk. With the help of muscle relaxers and treatment, I managed to attend the virtual candidate interviews from my couch, and eventually got back on my feet. But there was no question I had too many responsibilities, too little time, and now a handful of hospital bills to top it off. Still, I'd come this far, and I was committed to seeing the search through.

Months later, when we brought the top candidates to campus for in-person interviews, I shared meals with them, introduced them before their lectures, and drove them around the campus, accumulating those yellow university parking tickets. I didn't have the time or energy to dispute them. I was behind on my research, drained, and socially starved.

After the last interview, the department sent an email thanking me for my work with a $25 gift card to the university coffee shop. I appreciated the recognition and figured the caffeine would help as I tried to catch up on my research. I thought that was that.



"The expectation should never be that experience and a line on your resume ... are fair compensation."

A couple weeks after the search concluded, however, I reconnected with a mentor at another institution. As we caught up, she asked how the university had compensated me for such a significant commitment. When I said something about food and experience, she told me how she arranges for students in her department to be paid for any service work, at well above minimum wage. The thought had never occurred to me.

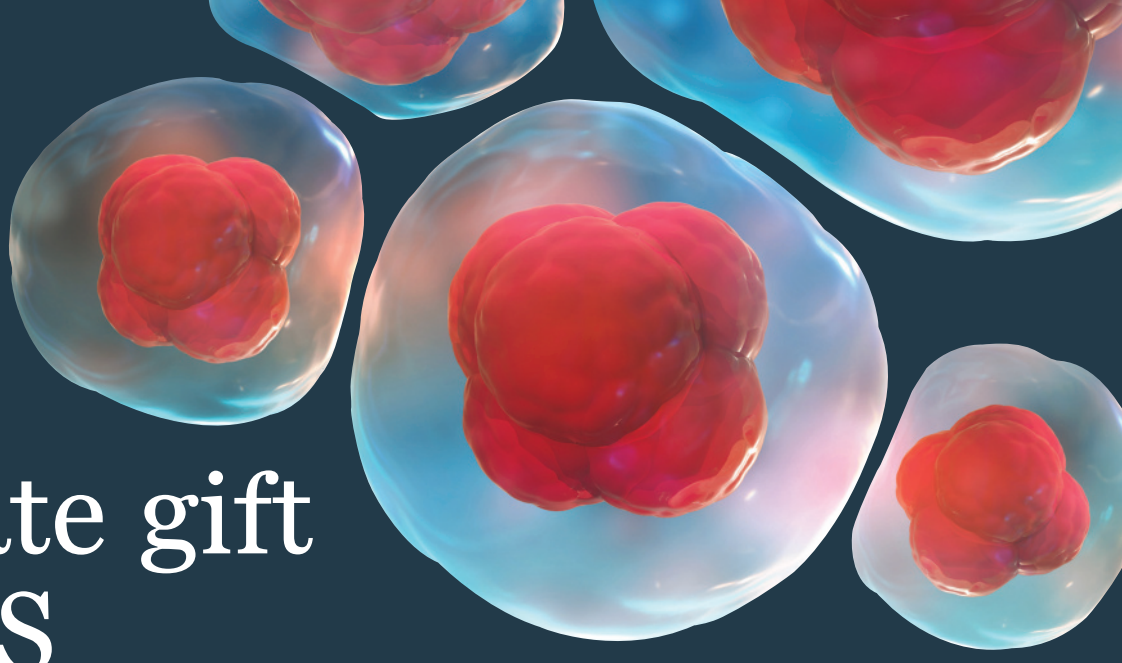
After that call, I couldn't stop thinking about why I wasn't paid for those 5 months of work. A parking pass and gas reimbursement would have been helpful, at least. But as an early-career grad student still finding my footing, it didn't occur to me to advocate for myself. I don't think anyone was maliciously trying to take advantage of me; it's just so ingrained in academic culture that graduate students will perform uncompensated labor that no one—including me—gave it a second thought.

Countless other students have served their universities essentially for free, too. This needs to change. I spent more than 200 hours on this search, and although it was a good learning experience, it cost me a lot more than a pair of $25 parking tickets. My research, health, and personal life suffered. The expectation should never be that experience and a line on your resume—and perhaps a gift card—are fair compensation. ■

Isabella Bennett is a graduate student at the University of Vermont. Send your career story to SciCareerEditor@aaas.org.

ILLUSTRATION: ROBERT NEUBECKER

1848 SOCIETY
AAAS



An estate gift to AAAS

Going all the way back to 1848, our founding year, the American Association for the Advancement of Science (AAAS) has been deeply committed to advancing science, engineering and innovation around the world for the benefit of all people.

Today, we are dedicated to advocating for science and scientific evidence to be fully and positively integrated into public policy and for the community to speak with one voice to advance science and engineering in the United States and around the world.

By making AAAS a beneficiary of your will, trust, retirement plan or life insurance policy, you will become a member of our 1848 Society and will help fuel our work on behalf of science and society – including publishing the world's most promising, innovative research in the *Science* family of journals and engaging in the issues that matter locally, nationally and around the world.

"As a teacher and instructor, I bear responsibility for the younger generations. If you have extra resources, concentrate them on organizations, like AAAS, that are doing work for all."

—Prof. Elisabeth Ervin-Blankenheim, 1848 Society member

If you intend to include AAAS in your estate plans, provide this information to your lawyer or financial adviser:

Legal Name: American Association for the Advancement of Science
Federal Tax ID Number: 53-0196568
Address: 1200 New York Avenue, NW, Washington, DC 20005

If you would like more information on making an estate gift to AAAS, cut out and return the form below or send an email to philanthropy@aaas.org. Additional details are also available online at **www.aaas.org/1848Society**.

AMERICAN ASSOCIATION FOR THE ADVANCEMENT OF SCIENCE

cut here

Yes, I would like more information about joining the AAAS 1848 Society.

1848 SOCIETY
AAAS

PLEASE CONTACT ME AT:

Name: _____

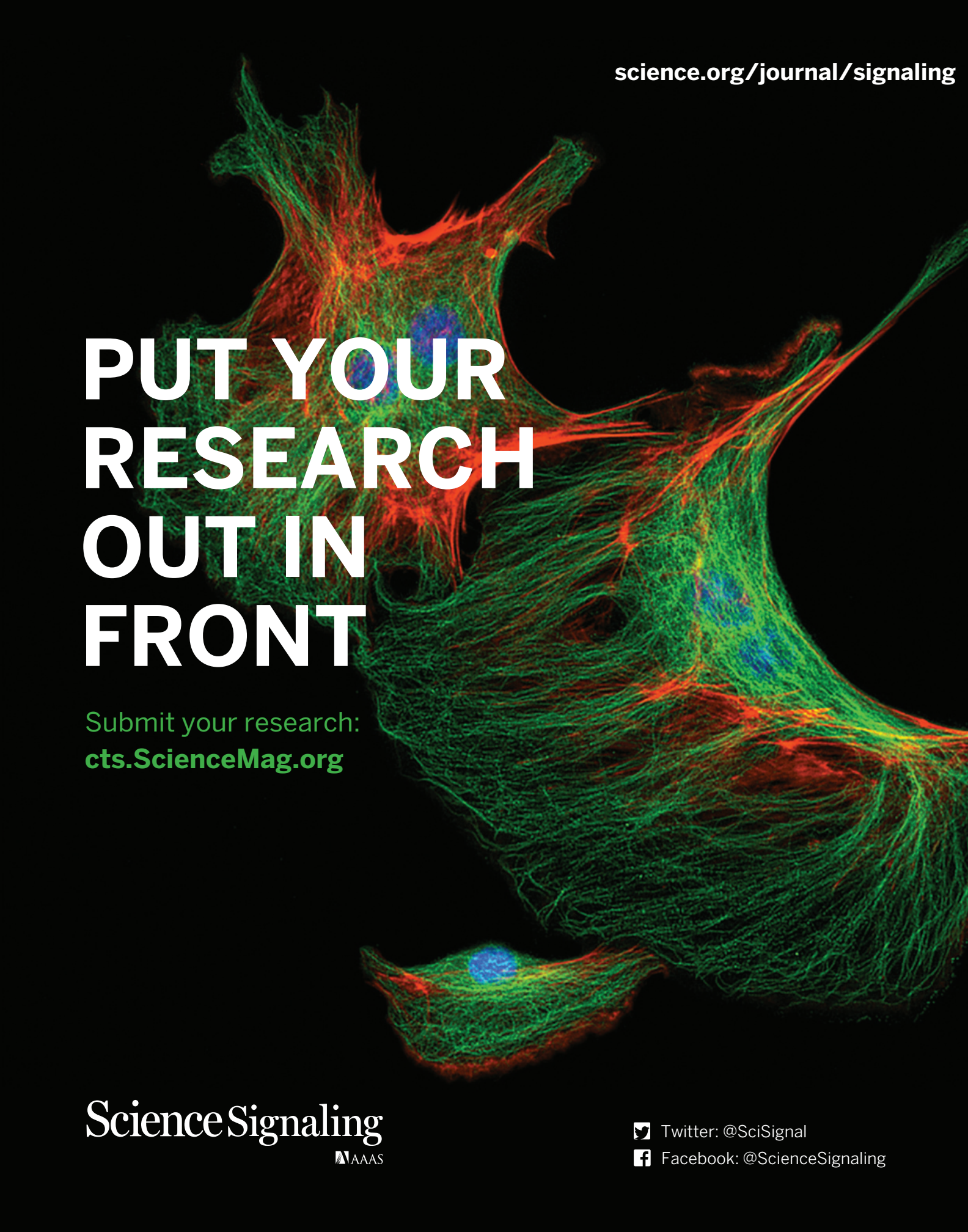
Address: _____

City: _____ State: _____ Zip code: _____ Country: _____

Email: _____ Phone: _____

RETURN THIS FORM TO:
AAAS Office of Philanthropy and Strategic Partnerships • 1200 New York Avenue, NW • Washington, DC 20005 USA

science.org/journal/signaling



PUT YOUR RESEARCH OUT IN FRONT

Submit your research:
cts.ScienceMag.org

Science Signaling
AAAS

Twitter: @SciSignal
Facebook: @ScienceSignaling